

AD-A241 311



OCT 02 1991



Proceedings of Damping '91

**13-15 February 1991
San Diego, California**

(Pages AAC-1 through DCC-19)

August 1991

Final Report for Period February 1989 to February 1991

Approved for public release; distribution is unlimited

Sponsored by:

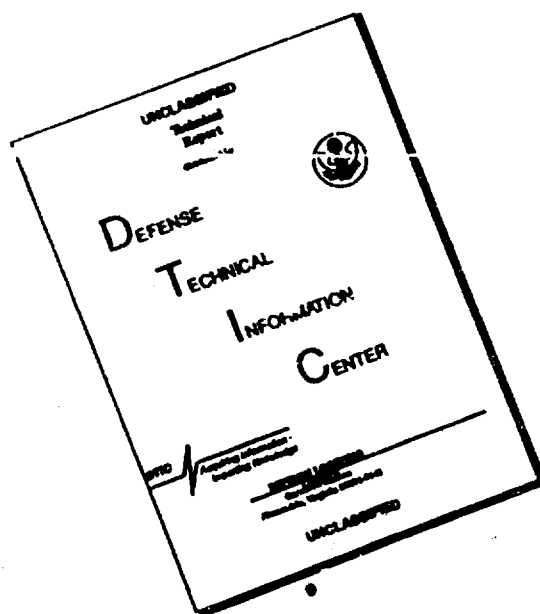
Wright Laboratory

Flight Dynamics Directorate

91-12019



DISCLAIMER NOTICE



THIS DOCUMENT IS BEST
QUALITY AVAILABLE. THE COPY
FURNISHED TO DTIC CONTAINED
A SIGNIFICANT NUMBER OF
PAGES WHICH DO NOT
REPRODUCE LEGIBLY.


NOTICE

When Government drawings, specifications, or other data are used for any purpose other than in connection with a definitely Government-related procurement, the United States Government incurs no responsibility or any obligation whatsoever. The fact that the government may have formulated or in any way supplied the said drawings, specifications, or other data, is not to be regarded by implication, or otherwise in any manner construed, as licensing the holder, or any other person or corporation; or as conveying any rights or permission to manufacture, use, or sell any patented invention that may in any way be related thereto.

This report is releasable to the National Technical Information Service (NTIS). At NTIS, it will be available to the general public, including foreign nations.

This technical report has been reviewed and is approved for publication.


JEROME PEARSON, Chief
Structural Dynamics Branch


LYNN ROGERS, PhD
Principal Engineer
Structural Dynamics Branch

If your address has changed, if you wish to be removed from our mailing list, or if the addressee is no longer employed by your organization please notify WL/ENIG, WPAFB, OH 45433-6883 to help us maintain a current mailing list.

Copies of this report should not be returned unless return is required by security considerations, contractual obligations, or notice on a specific document.

REPORT DOCUMENTATION PAGE				Form Approved OMB No. 0704-0188	
1a. REPORT SECURITY CLASSIFICATION Unclassified			1b. RESTRICTIVE MARKINGS		
2a. SECURITY CLASSIFICATION AUTHORITY			3. DISTRIBUTION / AVAILABILITY OF REPORT		
2b. DECLASSIFICATION / DOWNGRADING SCHEDULE			Approved for public release; distribution unlimited		
4. PERFORMING ORGANIZATION REPORT NUMBER(S) WL-TR-91-3078 Volume I			5. MONITORING ORGANIZATION REPORT NUMBER(S)		
6a. NAME OF PERFORMING ORGANIZATION Flight Dynamics Directorate Wright Laboratory		6b. OFFICE SYMBOL (If applicable) WL/FIBG	7a. NAME OF MONITORING ORGANIZATION		
6c. ADDRESS (City, State, and ZIP Code) Wright-Patterson AFB, OH 45433-6553			7b. ADDRESS (City, State, and ZIP Code)		
8a. NAME OF FUNDING / SPONSORING ORGANIZATION		8b. OFFICE SYMBOL (If applicable)	9. PROCUREMENT INSTRUMENT IDENTIFICATION NUMBER		
8c. ADDRESS (City, State, and ZIP Code)			10. SOURCE OF FUNDING NUMBERS		
			PROGRAM ELEMENT NO. 62201F	PROJECT NO. 2401	TASK NO. 04
				WORK UNIT ACCESSION NO. 23	
11. TITLE (Include Security Classification) Proceedings of Damping '91					
12. PERSONAL AUTHOR(S)					
13a. TYPE OF REPORT Final		13b. TIME COVERED FROM FEB 89 TO FEB 91		14. DATE OF REPORT (Year, Month, Day) August 1991	
15. PAGE COUNT 514					
16. SUPPLEMENTARY NOTATION Pages AAC-1 through DCC-19					
17. COSATI CODES			18. SUBJECT TERMS (Continue on reverse if necessary and identify by block number)		
FIELD	GROUP	SUB-GROUP			
			Vibration Damping, controls/structure interaction.		
19. ABSTRACT (Continue on reverse if necessary and identify by block number)					
Individual papers of Damping '91 held 13-15 February 1991 in San Diego CA are presented. The subjects included: Viscoelastic Material Testing and Characterization, Passive Damping Concepts, Passive Damping Analysis and Design Techniques, Optimization, Damped Control/Structure Interaction, Viscous Dampers, Friction Damping, Other Vibration Suppression Techniques, Damping Identification and Dynamic Testing, Applications to Aircraft, Space Structures, Marine Structures, Commercial Products, Defense Applications, and Payoffs of Vibration Suppression.					
20. DISTRIBUTION / AVAILABILITY OF ABSTRACT <input checked="" type="checkbox"/> UNCLASSIFIED/UNLIMITED <input type="checkbox"/> SAME AS RPT <input type="checkbox"/> DTIC USERS			21. ABSTRACT SECURITY CLASSIFICATION Unclassified		
22a. NAME OF RESPONSIBLE INDIVIDUAL Dr. Lynn Rogers			22b. TELEPHONE (Include Area Code) (513) 255-6622		22c. OFFICE SYMBOL WL/FIBG

Workshop Administration

Director

Dr. Lynn C. Rogers
Wright Laboratory
Flight Dynamics Directorate

Technical Chairman

Dr. Conor D. Johnson
CSA Engineering, Inc.

Administrative Chairman

Mrs. Beryl D. Deremigio
CSA Engineering, Inc.

Assistant Administrative Chairman

Ms. Bonnie L. Portis
CSA Engineering, Inc.

Session Chairmen

Mr. Bradley Allen, *CSA Engineering, Inc.*
Capt. Walter Address, *Space Systems Division*
Dr. Mohan Aswani, *Aerospace Corporation*
Capt. Mark Arnold, *Wright Laboratory, Flight Dynamics Directorate*
Mr. Eric Austin, *CSA Engineering, Inc.*
Lt. Col. Ronald L. Bagley, *Air Force Institute of Technology*
Dr. Andrew S. Bicos, *McDonnell Douglas Space Systems Company*
Mr. Daniel Cyphers, *W. J. Schafer Associates, Inc.*
Mr. Eric Dalton, *Teledyne Brown*
Mr. Ralph Dornsife, *US Army / CERL*
Mr. William Driscoll, *3M / Industrial Specialties Division*
Mr. Robert Dunning, *TRW*
Mr. Rod Eddleman, *US Army Strategic Defense*
Mr. Richard Ely, *LTV Aircraft Group*
Dr. James Fanson, *Jet Propulsion Laboratory*
Mr. Bryce Fowler, *CSA Engineering, Inc.*
Dr. Joseph Garibotti, *Ketema, Inc.*
Mr. Russell Gehling, *Martin Marietta Astronautics Group*
Dr. Steven Ginter, *Honeywell Satellite Systems*
Dr. John Gubser, *McDonnell Douglas Missile System Company*
Dr. John Henderson, *Consultant*
Mr. Dennis Hill, *GE Astro Space Division*

Dr. Philip Hipol, *The Aerospace Corporation*
 Dr. Robert Holman, *Hughes Aircraft Company*
 Mr. J. Warren Hoskins, *Lockheed Missiles and Space Company*
 Dr. Roy Ikegami, *Boeing Aerospace*
 Dr. Conor Johnson, *CSA Engineering, Inc.*
 Mr. Derrick Johnson, *Boeing Aerospace*
 Dr. David I. G. Jones, *Wright Laboratory, Flight Dynamics Directorate*
 Dr. Edward Kerwin, *Bolt, Beranek and Newman, Inc.*
 Mr. John Lassiter, *Warner - Robins ALC*
 Mr. Paul Lindquist, *Wright Laboratory, Flight Dynamics Directorate*
 Lt. John Mackaman, *Wright Laboratory, Flight Dynamics Directorate*
 Dr. Ray Manning, *TRW, Space and Technology Group*
 Mr. Daniel Morgenthaier, *Martin Marietta Space Systems*
 Mr. Ahid Nashif, *Anatrol Corporation*
 Mr. Rory Ninneman, *Phillips Laboratory*
 Mr. Earl Pinson, *Lockheed Missiles and Space Company*
 Mr. Ken Qassim, *Phillips Laboratory*
 Mr. Keith Quinn, *Nichols Research Corporation*
 Dr. Dantam Rao, *Mechanical Technology, Inc.*
 Dr. Wayne Reader, *Vector Research Company, Inc.*
 Dr. Kenneth Richards, *Martin Marietta*
 Mr. Stanley Sattinger, *Westinghouse Science and Technology Center*
 Dr. Daniel Segalman, *Sandia National Laboratories*
 Mr. Leonard Shaw, *Wright Laboratory, Flight Dynamics Directorate*
 Professor Young Shin, *Naval Postgraduate School*
 Dr. Stepan Simonian, *TRW, Space and Technology Group*
 Mr. Kevin Slimak, *Phillips Laboratory, Astronautics Directorate*
 Dr. Jaak Soovere, *Lockheed Missiles and Space Company*
 Mr. Clyde Stahle, *GE Astro Space*
 Mr. Ralph Tate, *LTV Aircraft Products Group*
 Mr. Roger Thaller, *Aeronautical Systems Division*
 Capt. Steven G. Webb, *US Air Force Academy*
 Mr. Kenneth R. Wentz, *Wright Laboratory, Flight Dynamics Directorate*
 Maj. Stephen Whitehouse, *Wright Laboratory, Flight Dynamics Directorate*
 Dr. William Witt, *The CORE Group*
 Dr. Y. C. Yiu, *Lockheed Missiles and Space Company*
 Mr. Wayne Yuen, *Wright Laboratory, Flight Dynamics Directorate*
 Mr. Michael L. Zeigler, *Wright Laboratory, Flight Dynamics Directorate*

FOREWORD

This publication includes individual papers of **Damping '91** held February 13-15, 1991, San Diego, California. The Conference was sponsored by the Wright Laboratory, Flight Dynamics Directorate, Wright-Patterson Air Force Base, Ohio.

It is desired to transfer vibration damping technology in a timely manner within the aerospace community, thereby, stimulating research, development and applications.

Accession For	
NTIS - CR&I DHEC 148 In Compliance with 49 CFR 171.101	
by	
District of	
Availability Codes	
Date	
A-1	



TABLE OF CONTENTS

	<u>Paper No.</u>
The F-117 Stealth Aircraft (Keynote Address) Mr. Paul Martin	AAA*
Use of Passive Damping for Aircraft Cabin Noise Control (Invited Speaker) Dr. Leo Butzel	AAB*
The Society of Damping Technology in Japan and its Activities (Invited Speaker) Dr. Yasuo Tokita and Hiroshi Okamura	AAC
<hr/> SESSION BA - Aircraft Applications <hr/>	
Integral Damping Treatment for Primary Aircraft Structures Sal Liguore, Marty Ferman, and Rudy Yurkovich	BAA
An Investigation of Add-on Damping Treatment for Life Extension of the F-15 Upper Outer Wing Skin Michael Parin, V. Levraea, Jr., Dr. Lynn Rogers, and A. Pacia	BAB
Damping Treatments for Aircraft Hardmounted Antennae Ralph E. Tate and Carl L. Rupert	BAC*
<hr/> SESSION BB - Plates and Beams <hr/>	
Examination of Boundary Conditions for Sixth-Order Damped Beam Theory Ralph E. Tate	BBA
The Effect of Compliant Layering on Damped Beams David John Barrett	BBB
The Damping Property of Laminated Steel Sheet after Deep Drawing Hiroshi Okamura	BBC

TABLE OF CONTENTS (continued)

	<u>Paper No.</u>
<hr/> SESSION BC - Analysis and Design 1 <hr/>	
Practical Design and Analysis of Systems with Fractional Derivative Materials and Active Controls Daniel R. Morgenthaler	BCA
An Implicit Fourier Transform Method for Nonlinear Dynamic Analysis with Frequency Dependent Damping Prof. F. Venancio-Filho and A. M. Claret	BCB
On a Linear Property of Lightly Damped Systems Z. Liang, M. Tong, and G. C. Lee	BCC
<hr/> SESSION CA - Control Structure <hr/>	
Active Vibration Suppression via LQG/LTR: Analytic and Experimental Results for the PACOSS Dynamic Test Article Russell N. Gehling	CAA
H∞ Control for the PACOSS DTA Christopher T. Voth and R. Michael Stoughton	CAB
Active Damping of a Cantilever Beam Dr. Hung V. Vu, Stein Husher, and D. E. Zimmerman	CAC
The Investigation of Large Space Structure Passive Electrodynamic Dampers Dr. Roger Stettner and Dr. Paul Mlakar	CAD
<hr/> SESSION CB - Damping Material and Measurements <hr/>	
A Method for the Measurement of the Complex Compressional Modulus of Thin Layers Dr. Jonathan D. Rogers and Dr. Daniel J. Segalman	CBA*

TABLE OF CONTENTS (continued)

	<u>Paper No.</u>
The Evaluation of Young's Complex Modulus of Viscoelastic Materials Marc Tardif and Prof. Germain Ostiguy	CBB
Role of Morphology in Damping Efficiency Dr. L. H. Sperling, J. J. Fay, and Dr. D. A. Thomas	CBC*
The Thermorheologically Complex Material Lt. Col. Ronald L. Bagley	CBD*
<hr/>	
SESSION CC - Analysis and Design 2	
<hr/>	
Methods of Reduction of Wind Induced Dynamic Response in Solar Concentrators and Other Small Lightweight Structures Monte A. McGlaun	CCA
Analysis of a Five-Layer, Viscoelastic, Constrained-Layer Beam Michael A. Falugi	CCB
Dynamics of a Class of Viscously Damped Struts Dr. Y. C. Yiu and Dr. Steven Ginter	CCC
A Study of a Vibration Absorber to Control the Vibration of a Rectangular Plate Akio Sugimoto, Hideo Utsuno, and Toshimitsu Tanaka	CCD
<hr/>	
SESSION DA - Analysis and Testing	
<hr/>	
Impedance Matched Mass-Dampers: A New Approach for Improving Structural Damping Craig Gardner and Prof. Richard H. Lyon	DAA
Analytical and Experimental Modal Analysis of a Two-Tiered Structure Dr. Hung V. Vu, William C. Flynn, and T. K. Vuong	DAB

TABLE OF CONTENTS (continued)

	<u>Paper No.</u>
Development of a Magnetic Suspension System for Reliable Vibration Damping Measurement Dr. Dantam K. Rao	DAC*
<hr/> SESSION DB - Viscoelastic Material <hr/>	
VEM Characterization Program Bryce L. Fowler	DBA
Data Base of the Dynamic Properties of Materials Ahid D. Nashif and Thomas M. Lewis	DBB
Establishing the Validity of the Master Curve Technique for Complex Modulus Data Reduction Dr. S. O. Oyadiji and Prof. G. R. Tomlinson	DBC
<hr/> SESSION DC - Optimization <hr/>	
Integrated Optimization of Composite Structures for Advanced Damped Dynamic Characteristics Dr. Dimitris A. Saravanos and Christos C. Chamis	DCA
An Optimum Design Methodology for Passively Damped Truss Structures Dr. Ray Manning	DCB
On An Application of Complex Damping Coefficients Z. Liang, M. Tong and G. C. Lee	DCC
<hr/> SESSION EA - DAMMPS I <hr/>	
Statistical and Worst Case Evaluation of Orbital Jitter Reduction Using Passive Damping J. Molnar, Dennis Hill, and Clyde Stahle	EAA

TABLE OF CONTENTS (continued)

	<u>Paper No.</u>
LMSC DAMMPS Program Status J. Warren Hoskins and Dr. Y. C. Yiu	FAB
Damping of Precision Metal Matrix Trusses Dr. Stepan S. Simonian	EAC
Development of Low Modulus Damping Material for Precision Mounting Platforms Steven Kirshenbaum, Dennis Hill, and Clyde Stahle	EAD
Complex Stiffness Test Data for Three Viscoelastic Materials by the Direct Complex Stiffness Method Bradley R. Allen and Earl Pinson	EAE
<hr/> SESSION EB - Viscoelastic Material Measurements <hr/>	
Direct Measurement of the Dynamic Material Properties of Polymers for Low Frequencies Ahid D. Nashif, Thomas M. Lewis, and Paul J. Macioce	EBA
Correlation of Complex Modulus Data by Direct Stiffness and Indirect Resonant Beam Test Techniques T. Lewis, Mona P. Khoury, and Dr. David I. G. Jones	EBB
Constitutive Modeling of Nonlinear Damping Materials Dr. Jerome Sackman, Prof. J. M. Kelly, and A. E. Javid	EBC
Results of a Round Robin Test Series to Evaluate Complex Moduli of a Selected Damping Material Dr. David I. G. Jones	EBD
<hr/> SESSION EC- Analysis and Design 3 <hr/>	
A Mathematical Framework for the Study of Indirect Damping Mechanisms David L. Russell	ECA*

TABLE OF CONTENTS (continued)

	<u>Paper No.</u>
Techniques of Design and Using Viscoelastic Dampers Z. Liang, M. Tong, and G. C. Lee	ECB
Modeling of Constrained Layer Damping in Trusses Dr. Daniel J. Inman, Joseph C. Slater, and W. Keith Belvin	ECC
A Strong Criterion for Testing Proportionally Damped Systems Z. Liang, M. Tong, and G. C. Lee	ECD
<hr/>	
SESSION ED - Applications	
Abbreviated Papers	
<hr/>	
The PACOSS Dynamic Test Article Russell N. Gehling	EDA
Retrofitted Damping Treatment for a Three Stage Booster System Dr. Daniel J. Segalman and E. L. Marek	EDB*
Damping Design for a Disk Drive Head Flexure Eric M. Austin, James C. Goodding, and William A. Driscoll	EDC
Damping Jet Engine Front Frame Struts Capt. Vance Johnson, Kurt Nichol, and Dennis Murphy	EDD*
Isolation Joint for Flexural and Compressional Isolation Al Wignall and J. Aron	EDE
Characterization of Viscoelastic Damping in an Antenna Structure Dr. Ephraim Garcia, James M. Argento, and Robert Alan Carlin	EDF
Laminar Blade Damper Michael Kolela	EDG
Experimental Study on Noise Reduction due to Damping Treatments Ken Okada and Junichi Kanazawa	EDH*

TABLE OF CONTENTS (continued)

	Paper No.
<hr/> SESSION FA - DAMMPS 2 <hr/>	
Evaluation of Damping Concepts for Precision Mounting Platforms Dennis Hill, Clyde Stahie, and James Staley	FAA
Synergistic Design of Passive Damping and Metal Matrix Composites Earl D. Pinson, Eric M. Austin, and Michael L. Zeigler	FAB
A Three Element Viscoelastic Isolator Dr. Stepan S. Simonian	FAC
<hr/> SESSION FB - Noise and Acoustics <hr/>	
Integrally Damped Honeycomb Structural Concepts to Increase Noise Transmission Loss Jefferson F. Newton, Dr. Roy Ikegami, and D. J. Carbery	FBA
Reduction of Acoustic Responses Using Viscoelastic Damping Materials Dr. David Chu, C. Stahle, J. Staley, J. Peir, and M. McMeekin	FBB
Design Method of Damping Treatment for Structure-Borne Noise Reduction Iwao Honda, Tadao Nakamura, Yoshihiko Irie, and Kazuo Yamamoto	FBC*
<hr/> SESSION FC - Civil Structures <hr/>	
Earthquake Simulator Testing of Two Damping Systems for Multistory Structures Ian D. Aiken and James M. Kelly	FCA
Correlation of Experimental Results with Predictions of Viscoelastic Damping for a Model Structure T. T. Soong and Dr. Ming Lai	FCB

TABLE OF CONTENTS (continued)

	<u>Paper No.</u>
Damping Capacity of Reinforced Concrete External Beam Column Connections Dr. Alexander G. Tsonos, Ioannis A. Tegos, and Prof. Georgios G. Penelis	FCC*
<hr/>	
SESSION FD - Analysis and Damping Mechanisms	
Abbreviated Papers	
<hr/>	
Eddy Current-based Vibration Damping for Aerospace Structures James Goldie	FDA
The Absolute Value Modal Strain Energy Method Daniel R. Morgenthaler	FDB
An Analytical Model for the Vibration of Viscoelastically Damped Curved Sandwich Beams Dr. Mohan D. Rao and Shulin He	FDC
Bibliography of Environmental Data Measured In-Flight Lt. Col. Raymond F. Hain, III	FDD
General Motion of an Inclined Impact Damper with Friction C. N. Bapat	FDE
The Shock and Vibration Information Analysis Center (SAVIAC) Harold D. Kohn	FDF
<hr/>	
SESSION GA - Electro-Rheological Fluids and Fluids	
<hr/>	
The Vibration Damping Effect of an Electrorheological Fluid Stephen A. Austin	GAB
Modelling of Nonlinear Dilatation Response of Fluids Containing Columns Plastic and Shear Relaxation Considered Dr. Bernd Wendlandt	GAC

TABLE OF CONTENTS (continued)

	<u>Paper No.</u>
Electro-Rheological Fluids Characterization by Dynamic Mechanical Thermal Analysis under Applied Fields Dr. R. E. Wetton and Dr. J. C. Duncan	GAD*
<hr/>	
SESSION GB - Control Structure Interaction 2	
<hr/>	
On Piezoelectric Energy Conversion for Electronic Passive Damping Enhancement Dr. Donald L. Edberg, Dr. Andrew S. Bicos, and J. S. Fechter	GBA
The Need for Passive Damping in Feedback Controlled Flexible Structures Dr. Andreas von Flotow and D. W. Vos	GBB
Passive Control of a Flexible Planar Truss Using A Reaction Mass Actuator Capt. Steven G. Webb and Lt. David R. Lee	GBC
<hr/>	
SESSION GC - Damping Identification	
<hr/>	
A Identification Technique for Damped Distributed Structural Systems Using the Method of Collocation R. Chander, M. Meyyappa, and S. V. Hanagud	GCA
Correlation Techniques to Determine Model Form in Robust Nonlinear System Realization/Identification Greselda Stry and D. Joseph Mook	GCB
System Level Design and Analysis of Truss Structures Damped by Viscous Struts Dr. Y. C. Yiu	GCC
Damping Ratio Estimates from Autocorrelation Functions Prof. Luigi Balis-Crema and Prof. A. Agneni	GCD

TABLE OF CONTENTS (continued)

	<u>Paper No.</u>
<hr/>	
SESSION GD - Damping Materials	
<hr/>	
Dynamic Moduli of Fluorocarbon Compounds Dr. Wayne T. Reader and Robert W. Megill	GDA*
Passive Vibration Damping with Noncohesive Granular Materials Dr. Monen Abdel-Gawad	GDB
VEM Database Program Bryce L. Fowler	GDC
Measurement of the Mechanical Properties of Viscoelastics by the Direct Complex Stiffness Method Bradley R. Allen and Dr. David A. Kienholz	GDD
The Effect of Porosity on the Microstructural Damping Response of a 6061 Aluminum Alloy Jinmin Zhang, M. N. Gungor, and E. J. Lavernia	GDE
Damping Properties of Aliphatic Polyurethanes from 4, 4' - Dicyclohexylmethane Diisocyanate John D. Lee, Gilbert F. Lee, and Bruce Hartmann	GDF
An Apparatus for Measuring the Low Frequency Dynamic Characteristics of Materials Mona P. Khoury and Francis Olivier	GDG
<hr/>	
SESSION HA - Composite and Metal Matrix	
<hr/>	
Controlling the Damping Behavior of Pitch-based Carbon Fibers Andrew J. Eckel and Steven P. Jones	HAA
Internal Damping of Metal Matrix Composites: A Technical Assessment Jacques E. Schoutens	HAB
Vibration Suppression of Thin-Walled Composite Tubes Using Embedded Viscoelastic Layers F. M. Belknap and Professor J. B. Kosmatka	HAC
<hr/>	

*Not available for publication

TABLE OF CONTENTS (continued)

	Paper No.
<hr/> SESSION HB - Tubes and Shells <hr/>	
Directional Damping of the Global Vibration Modes of Tubular Structures by Constrained-Layer Treatments Stanley S. Sattinger	HBA
Damped Response of Viscoelastic Thick Cylinders of Infinite Extent Dr. Hamid Hamidzadeh, D. J. Nunez, and D. E. Chandler	HBB
<hr/> SESSION HC - Circular Plates <hr/>	
Dynamic Analysis of Finite, Three Dimensional, Linear, Elastic Solids with Kelvin Viscoelastic Inclusions: Theory with Applications to Asymmetrically Damped Circular Plates Prof. C. D. Mote, Jr. and I. Y. Shen	HCA
Modal Analysis of Kelvin Viscoelastic Solids Under Arbitrary Excitation: Circular Plates Under Moving Loads I. Y. Shen and Prof. C. D. Mote, Jr.	HCB
Response of a Circular Plate with Patch Damping Prof. Douglas Muster, Mahmoud Mezache, and G. H. Koopmann	HCC
<hr/> SESSION IA - Viscous <hr/>	
Development of the PACOSS D-Strut David Cunningham	IAA
Design, Analysis, and Testing of the PACOSS D-Strut Truss Daniel R. Morgenthaler	IAB
An Advanced D-Strut L. Porter Davis and Dr. Steve Ginter	IAC

TABLE OF CONTENTS (continued)

	<u>Paper No.</u>
Testing of a Viscous Damped Isolator Bradley R. Allen and David Cunningham	IAD
<hr/> SESSION IB - Experimental Measurements <hr/>	
The Effect of Source Impedance on Damping Measurements Using Resonance Dwell Testing Ralph E. Tate	IBA
The Dependency of Vibration Energy Dissipation on the Amplitude of Structural Motion Dale L. Jensen	IBB*
Low-deflection Loss and Hysteresis Measurements on a Spacecraft Test Joint Eric M. Austin, James C. Goodding, and Timothy L. Flora	IBC
Damping Ratio Measurements in Kevlar Sandwich Samples Prof. Luigi Balis-Crema, Prof. A. Castellani, and Prof. A. Agneni	IBD
<hr/> SESSION IC - Metals <hr/>	
Characterization of the Damping Properties of High Damping Alloys Dr. Iain G. Ritchie and Z-L. Pan	ICA
Viscoelastic and Structural Damping Analysis Prof. Harry H. Hilton	ICB
Analysis of Strain Dependent Damping in Metals via Modeling of Material Point Hysteresis Dr. E. J. Graesser and C. R. Wong	ICC
Non-Obstructive Particle Damping Tests on Aluminum Beams Dr. Hagop V. Panossian	ICD

TABLE OF CONTENTS (continued)

	<u>Paper No.</u>
<hr/> SESSION JA - Experimental Measurements of Damping <hr/>	
Complex Dynamic Modulus of Nitinal-reinforced Composites Dr. Amr M. Baz, R. Deigan, and Dr. J. Gilheany	JAA*
Estimation of Nonproportional Damping from Experimental Measurements Dr. T. K. Hasselman and Jon D. Chrostowski	JAB*
Load Unit Deflection Correction for Forced Vibration Test System Kirk R. Biegler	JAC
<hr/> SESSION JB - Friction <hr/>	
An Analytical Approach to Designing Friction Dampers in Turbomachinery Blading Joe Panovsky, D. Hendley, and R. MacKay	JBA
Micro Slip Damping Mechanism in Bolted Joints Prof. M. Groper	JBB*
<hr/> SESSION JC - Analysis and Design 4 <hr/>	
On a Theory of Complex Damping Z. Liang, M. Tong, and G. C. Lee	JCA
An Iterative Method in Dynamic Structural Analyses with Nonproportional Damping Dr. Wan T. Tsai and J.T. Leang	JCB

✻

<Damping '91 Conference> in San Diego

The 'Society of Damping Technology' in Japan and Activities

with the trends of the damping materials & technology in Japan

1991. 2. 13~15.

Yasuo Tokita *¹
Hiroshi Okamura *²

Society of Damping Technology, in Japan

*1) President, SDT in Japan ; Derector, Aircraft Nuisance Prevention Association
Reseach Center.

*2) Memeber, SDT in Japan ; Manager, Component Eng. Dept. Truck & Bus Eng. Center,
Mitsubishi Motors Corporation.

The 'Society of Damping Technology' in Japan and the Activities
with the trends of the damping materials & technology in Japan

Abstract

The development activities of damping materials and their technologies in Japan have been given an active life speedily in the past several years. As the examples, the application of damping materials to the floor panel of motor vehicle body and the utilization of laminated damping steel sheets by various industries in Japan will be reviewed in this report.

Then, a report will be made on the activities of Society of Damping Technology in Japan, a society which was inaugurated with the background situation as indicated in the above. Among various activities performed by the society, a report will be made particularly on the outline of round robin test which was conducted by the society. The report will be concluded by a summary of the future trends to be realized in Japan and the role of the society to be played in the accomplishment of such targets.

1 Background

1.1. The Trends of Damping Materials in Japan

Stimulated by the enforcement of the regulations for the prevention of environmental pollution by the Japanese Government, particularly of the noise control regulations on motor vehicles, the application of damping materials has been rapidly and widely spread among various industries in Japan. This trend has been further enhanced by the fact that the industries become aware that the reduction of vibration and noise in products will heighten the value of their products in the market.

It has been realized that an appropriate damping effect can be achieved by an addition of damping material (such as free layer bonding type) or by replacement (such as laminated damping steel sheet) without altering a structure of product to a large extent.

Damping mechanism and material characteristics, however, are not known well by the people in Japan except for a certain number of technical experts and researchers. When an application of damping material is not made appropriately, the damping effect could be reduced drastically or sometimes may bring an

advers effect- and ends up with a wrong appraisal being cast upon it. Having such a situation in the background, interests in damping materials among the industries in Japan had been increased to an extent that Society of Damping Technology in Japan was inaugurated.

In the following, an application of damping material to the floor panel of motor vehicle body and a utilization of laminated damping steel sheet by various industries in Japan will be discussed.

1.2. Application of Damping Material to Floor Panel of Motor Vehicle Body

The historical trend of patent application in Japan for the damping materials for a use of damping floor panels of motor vehicle body is shown in Fig.1. ⁽¹⁾ Applications for materials used for sound absorption, sound insulation and damping are included in this figure and the hatched portion in it corresponds to the number of patent application for the damping materials. It is obvious that the number of patent application increased quite remarkably with the advent of 1980. As stated in the above, the trend clearly shows the heightening of technical interests in noise reduction obviously as the result of the stimulation given by the enforcement of noise control regulation.

Fig. 2 shows the historical trend of noise level prevailing in the interior of passenger cars produced and marketed in Japan. ⁽²⁾ The chart shows that noise reduction of some 8 dB(A) was realized in the past 10 years. This is obviously the result of the application of noise reduction methods stated in the above.

Fig. 3 shows the proportions by weight of noise control materials used in passenger cars. ⁽²⁾ Approximately half of the weight is taken by the damping materials. Majority of the damping materials indicated in this diagram are of asphalt materials and will be bonded as free layers type.

While damping materials are used widely as the principal means for noise control, materials having much better damping capabilities and lighter weight are being sought after earnestly with an aim of further reduction of noise level as well as vehicle weight. In order to achieve such purposes, adoption of composite materials and constrained layer damping system, foaming of damping layer, etc. have already been tried.

1.3. Laminated Damping Steel Sheet

Fig. 4 shows the transition of production volume of laminated damping sheet in Japan. ⁽²⁾ A sudden increase in production is seen in the latter half of 80s. After the enforcement of Phase II of the noise control regulation in '83, the

use of laminated damping steel sheet for the stamp formed engine oil pan was commenced. The consumption of the material by the electric home appliance industry was increased much after they adopted it for foaming the outer panel of home washing machine.

Fig. 5 shows the breakdown by weight of the application of this material for various industries in Japan.⁽³⁾ The consumption by the motor and electric appliance industries are by far the largest, however, the applications for building materials and general machineries are being increase gradually. Table 1 shows examples of laminated damping steel sheet application by various industries. Obviously the materials are used for noise reduction of various products.

2 Society of Damping Technology in Japan

2.1. Inauguration of Society

As elaborated in the above, the application of damping materials for the purpose of vibration and noise reduction has become very popular in Japan and the market segments of products where the super great quality is given by damping materials have been expanded. But there are many subjects left unsolved in the technical aspects of damping materials. Mutual recognition of such problems, efforts in exploring their solutions and deepening people's understanding in damping materials are essential for their popularization and growth. Society of Damping Technology in Japan was inaugurated for the achievement of those objectives.

2.2. General Policies of Society's Activities

The general policies of this society's activities shall be;

- Activities will be centered in the industries, that is, the various seeds and needs for damping materials and technologies present in the industries would be picked up widely and discussed in various aspects.
- Public relations activities to be made by each member company in auxiliary to the above activities will be permitted.
- Exchange of informations and conversations between and among makers, users and neutral organizations (such as research institutions, universities, instrument manufacturers, etc.) on the subject of damping materials will be promoted.
- Research and study will be made jointly on the subjects relative to the damping. These studies will be made principally by the study and technical committees and working groups subordinate to those committees.

- Publicity-activities on damping materials and technologies in such forms as lecture class, issuing manuals on measuring methods and utilization technologies.

2.3. Organization of Society

The society was inaugurated in July 1988 with the assistance of Tokyo Metropolitan Industrial Technology Center. The society's secretariat is located in that center. When the first general assembly of the society was held at the time of inauguration, there were 39 corporate members, 6 private members and 3 special members making the total of 48 members. The society now has the total of 145 members which consist of 120 corporate, 22 private and 3 special members. The number is still being increased by the enrollment of several new members in every month.

Fig. 6 shows the main business activities and involvement in damping materials by the society members.⁽⁴⁾ About a half of the members are in nonmetallic industries (many are in polymer industries) and belong to the maker's side of damping materials. About 35 % are on the user's side coming from fairly wide range of industries. The rest are from the neutral institutions and industries. In an aspect of involvement in damping materials, it is recognized that members representing many sections are in a good harmonious balance.

Fig. 7 shows the organization structure and activities of the society. Under the executive committee formed by President, Vice President and chairman of each committee, there are a secretariat and 5 committees (2 in business handling and 3 in research and study). There are number of working group under the supervision of each research and study committee and the main activities of the society are pursued by those people.

2.4. Activities of Research and Study Committees

Researches and studies in various subjects related to the damping materials and technologies are actually carried out by 3 research and study committees together with working groups (W/G) placed under them as shown in Fig. 7.

Domestic and international literature study W/G collects the literatures and papers on the damping materials and technologies issued widely in Japan and overseas countries mostly supplied by the members and put them in a data base. Damping '89 W/G was formed for the study of technical reports in Proceedings of Damping '89 Conference.

Round robin test W/G performed in the last year a round robin test on a free layer damping material bonded to steel beam test piece. 25 members joined in this test. The details of the test result will be discussed later in this report. Similar test is being performed on laminated damping steel sheets, now.

Standard study W/G collects and studies the standards issued for the administration of damping characteristic measurement methods in many countries. It will also be issuing a measurement manual for the members by compiling the results of their study, the results of round robin tests performed in supplement. These results will also be studies for reflecting them into the official standardization of damping characteristic measurements in Japan.

Examples of damping material application have been announced to and discussed by the members. Problems in the utilization technology unique to each individual section will be studied and solved by such method as organizing new W/Gs for motor vehicles and building materials.

3. Round Robin Test

3.1. Objective and Principal Test Conditions

The objective of this test is to have each member get mutually acquainted with other member's technical levels in the measurement method and to make clear the subjects and problems on the measurement which have been carried by each individual member. The test results will be further utilized in the compilation of manual on the measurement guideline to be issued for the distribution to all members. They will also be used in the society's cooperation to the official standardization of damping characteristic measurement.

1. Test specimen and test method

1-1. Type of test piece: test piece bonded with free layer damping materials.

1-2. Damping material: type of EVA (elastic)

1-3. Adhesive: type of SBR (styrene butadiene rubber)

1-4. Test method: constant strain method

Measurement method and test piece method can be determined at an option by the members. Details will be referred to the details.

2. Test conditions: test piece will be tested under free and fixed with center support and center support. When the attached test piece parts, will be tested under the same conditions.

3. Test results

Fig. 8 shows all measurement data obtained by the cantilever method. As the end clamping was not rigid enough, dispersal of damping characteristic in bending mode of first order, where the influence of boundary condition is largest, is noted. It was also revealed that several test data contained problems due to data analysis by FFT (Fast Fourier Transform).

Fig. 9 shows a graph in which data with the above problems are all omitted. The dispersal of damping characteristic measurement data is also made smaller. The results of measurement by the members, except for data B of an original steel beam having a small loss factor η -value, are fundamentally consistent even though somewhat smaller data dispersal is still evident. Further study to explore the cause of such dispersal is required.

3.3. Both End Free with Center Excitation Method

All measurement data obtained by both end free with center excitation method are shown in Fig.10. An impedance head is installed in this method on the center portion where an excitation is applied. The exciting input and the vibration response are measured by it. Data with fairly large dispersal are included in this case, too.

Fig. 11 shows the excitation structure applied in the test. The method in which a nut is used for clamping as shown in the figure will present a problem in processing the damping layer at the portion where it is tightened by the nut, for example, damping layer is cut or tightened together with steel sheet. In a method where an extension rod is used, it is noted that the bending mode of steel beam, the main target of measurement, tends to be mixed with unnecessary mode because the excitation structure is not installed accurately on the center of a test piece.

Fig.12 shows the graph where the data containing problems are all omitted. As in the cantilever method, all the measurements are consistent except for data B. Further exploration is also necessary to the cause of data dispersal still left on this graph.

3.4. Summary

All the results obtained from the round robin test performed by the society, this time, except for the data of steel beam having smaller η -value (smaller than 0.01) and for the measurement data in which the cause of large dispersal is clarified, are found to be fundamentally consistent with each other. It means that as long as the basic rules for the measurement are carefully

observed, a dispersal of measurement can be minimized.

The values shown in Fig. 9 to 12 are consistent with each other and the fact suggests that the variation due to different methods of measurement can also be minimized.

However, some significant dispersal of data is still present even after those data are screened and, therefore, further exploration is still required. It is intended that supplementary tests on the dispersal of data on steel beam bonded with free layer damping material and round robin on laminated damping steel sheet will be carried out in this year for the clarification of the subjects and problems associated with the measurement methods.

4 Conclusion

4.1. Damping Materials and Technologies in Japan

(1) The product value of damping material has been recognized by the people quite recently.

- ① They are very effective means for the reduction of noise and vibration.
- ② The spreading of use has been expedited by turning them into massproduction.

(2) New problems have appeared, on the contrary.

- ① The damping method alone can not, in many cases, insure a satisfactory results.
- ② Improvements in the ratio of cost and weight vs η -value and in the total performance of the materials are required.

(3) Under the circumstances, the future course shall be;

① High performance

- High η -value (loss factor)
 - Free layer damping type \rightarrow Constrained layer damping type,
 - Material improvements, etc.
- Multiple functions (multilayers, composition)

② Heightened level of employment technology

- Establishment of predicting technique
- Optimum design (ratio of cost and weight vs η -value)
- Build up of data base

4.2. Society's Future Role

- (1) Contribution to new developments in the damping by the study and research works to be made on this subject.
- (2) Engaging in the publicity activities of the damping materials and technologies to expand the bottom layer of the needs.
- (3) Grasping the needs and seeds through the exchanges of information and conversations among and between the makers and users of damping materials and neutral institutions and industries, and feeding them back to all members.

4.3. Final Conclusion

It is my great honor and pleasure to have been given an opportunity of making a presentation on the trend of the study in damping and the activities of Society of Damping Technology in Japan to this conference in the presence of the most prominent people of the damping technologies in the world.

It is my strong personal belief that the society in Japan should also try to enhance their international activities from now on. I believe the cooperation of all the members present here will be honored and appreciated by all the members of the society in Japan. Thank you very much.

Reference

- (1) J.Satoh; Technical trends of damping, sound absorption and sound insulation materials used in passenger car, Toyota Gosei Technical Review, Vol.28 No.3, (1986), p121-127. (in Japanese)
- (2) T.Nitta, M.Momozawa; On vibration damping by mean of visco-elastic materials, The Journal of INCE of Japan, Vol.15 No.1 (1991) (in Japanese)
- (3) Based on the investigation of statistics reported in newspapers, journals, etc.
- (4) According to the questionnaire for the members of SDT in Japan.
- (5) S.Takada, K.Okada, S.Daimon and M.Yamaguchi; Results of the round robin tests on 2-layer type damping beam", Proceedings of the 1990 Meeting, Acoustics Society Japan (1990), p579-580. (in Japanese)
- (6) M. Yamaguchi, S. Takada, T. Aoki, K. Okada and S. Daimon; Results of the round robin tests on 2-layer type damping beams, proceedings of the 1990 Meeting, INCE / Japan (1990), p309-312 (in Japanese) □

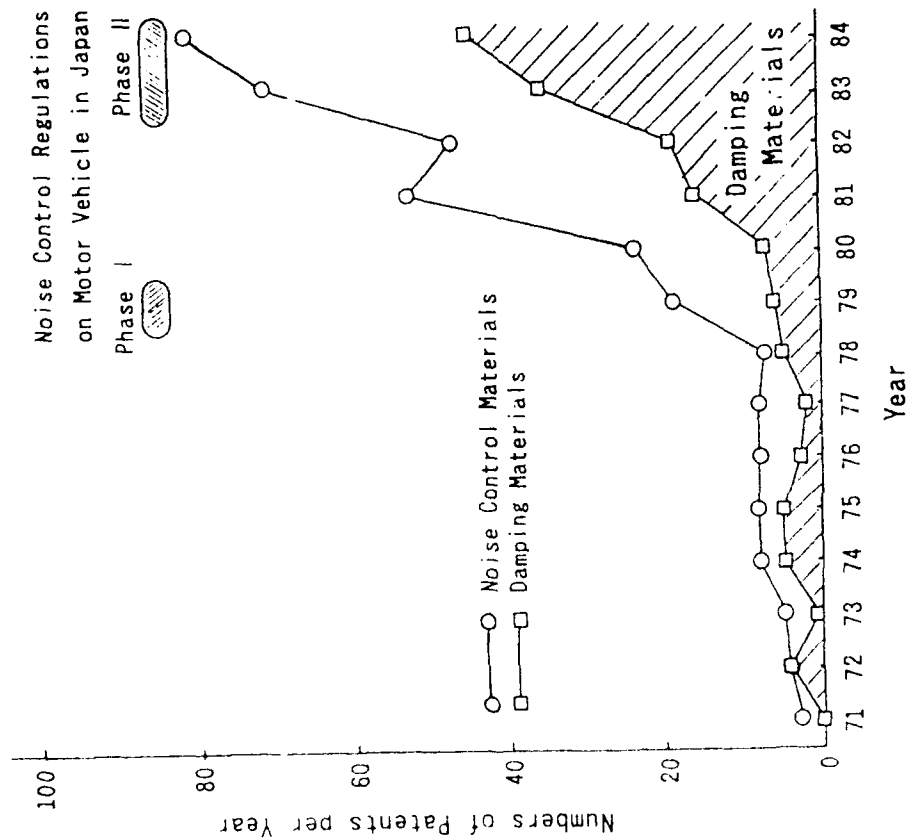


Fig. 1 Trends in Patents about Noise Control Materials for the Floor Panels of Vehicle Body

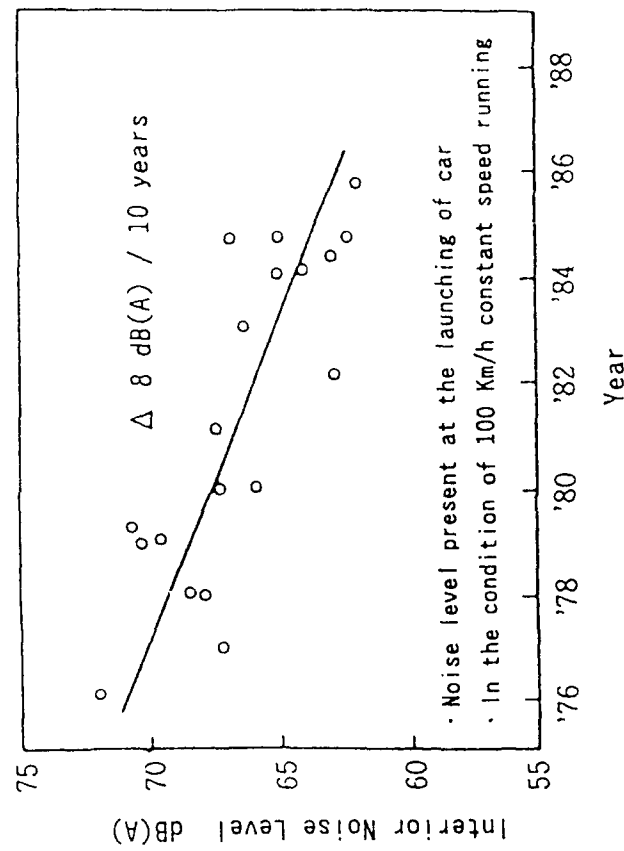


Fig. 2 The Historical Trend of Noise Level in Interior of Passenger Cars with 2000 cc Class Engine

Noise Control Materials

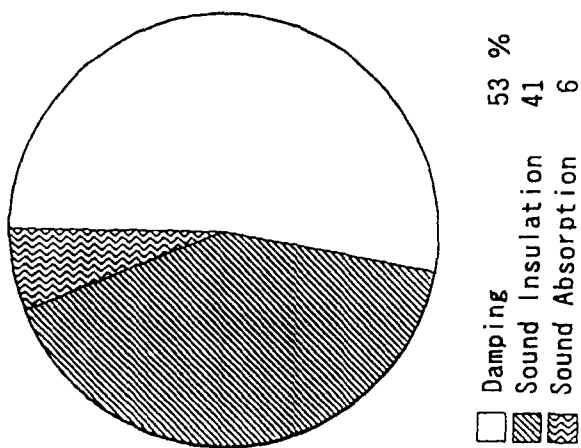


Fig. 3 Breakdown by Weight for the Purposes of Noise Control Materials used in Passenger Car (with 0.65~4.0 liter class engine)

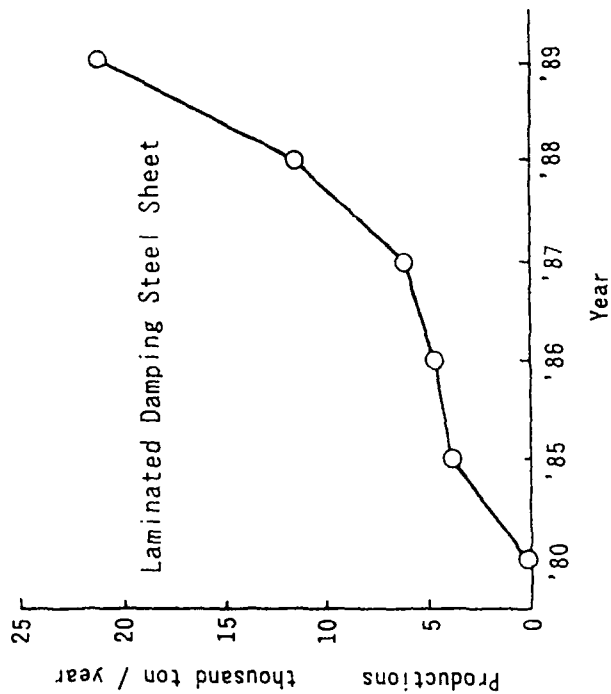


Fig. 4 The Productions of Laminated Damping Steel Sheet in Japan

Laminated Damping Steel Sheets

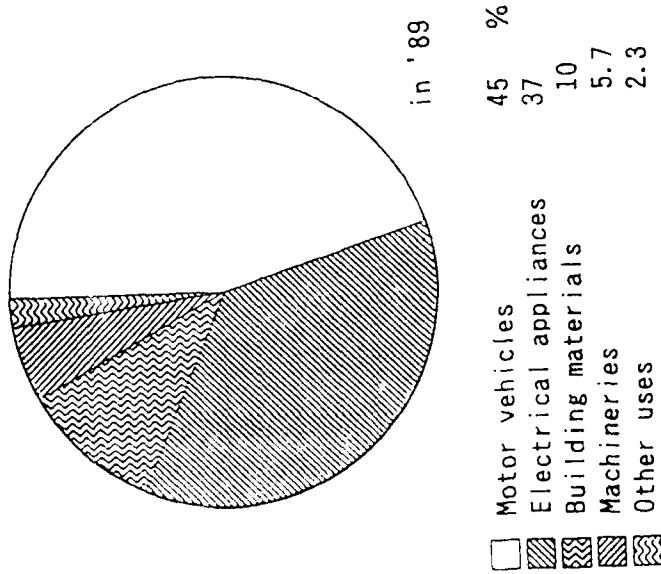
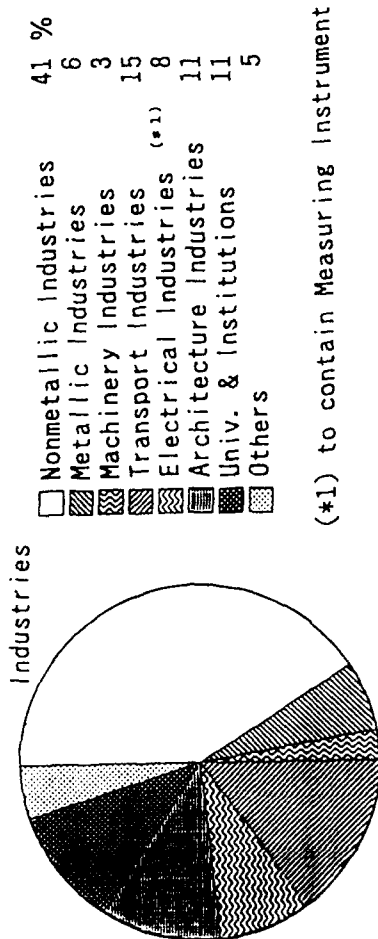


Fig. 5 Breakdown by Weight for the Use of Laminated Damping Steel Sheets

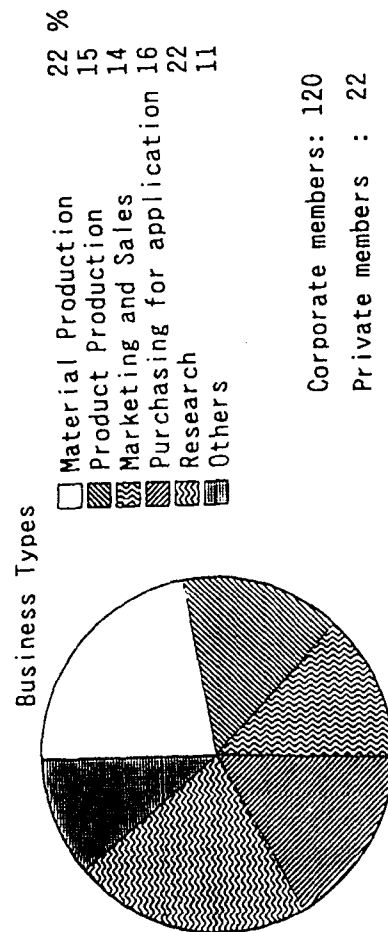
Table 1 Application Example of Laminated Damping Steel Sheet

Industry	Application Example
Motor Vehicle	Engine (oil Pan, front cover, rocker cover), Vehicle Body (floor, door, tire house, dash panel) Transmission cover, Parking brake cover
Electrical Home Appliance	Outer panel of washing machine, OA equipment cover(printer,etc.), Audio Equipment Components, Electric Generator
Building	Roof, Floor, Stairway, Shutter, Railway bridge (steel)
Machineries	Hoppers, Ducts, Partially enclosed cover

(A) Type of Member's Industries



(B) Member's Business Relations with Damping Materials



Corporate members: 120
Private members : 22
Special members : 3
Total members : 145

Fig. 6 Membership Structure

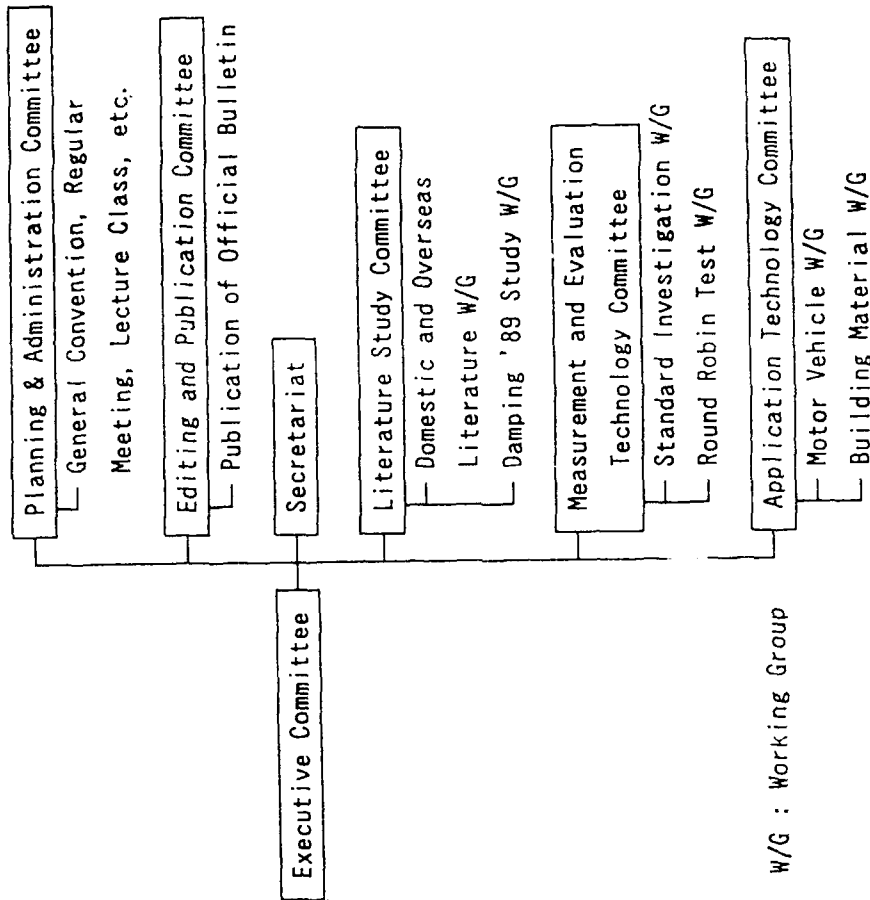


Fig. 7 Society's Organization and Activities

Table 2 Condition for Round Robin Test

Measurement Method	Strain & Stress Method	Cantilever Beam	Both Ends Clamping Beam	Both Ends Free Beam (1)	Both Ends Free Beam (2)
Damping Base (H+B)	0.5~2.5	2.5/ 1.0	2.5/ 1.0	2.5/ 1.0	15 / 9
Layer Plate (M+B)	"	1.5/ 1.0	1.5/ 1.0	1.5/ 1.0	"
t_0 mm / t_p mm (L+B)	"	"	"	"	"
Effective Length mm	20 ~ 50	220	300	280	500
Width mm	2.4 ~ 5	10	10	25	50
No. of Participants	3	13	2	9	3
Measurement Order	parallel	round robin test			

(Note) ① H,M :PVC damping materials, L :SBR rubber,

B :Base Plate of Steel Sheet

② Temperature for measurement... 25 ° C

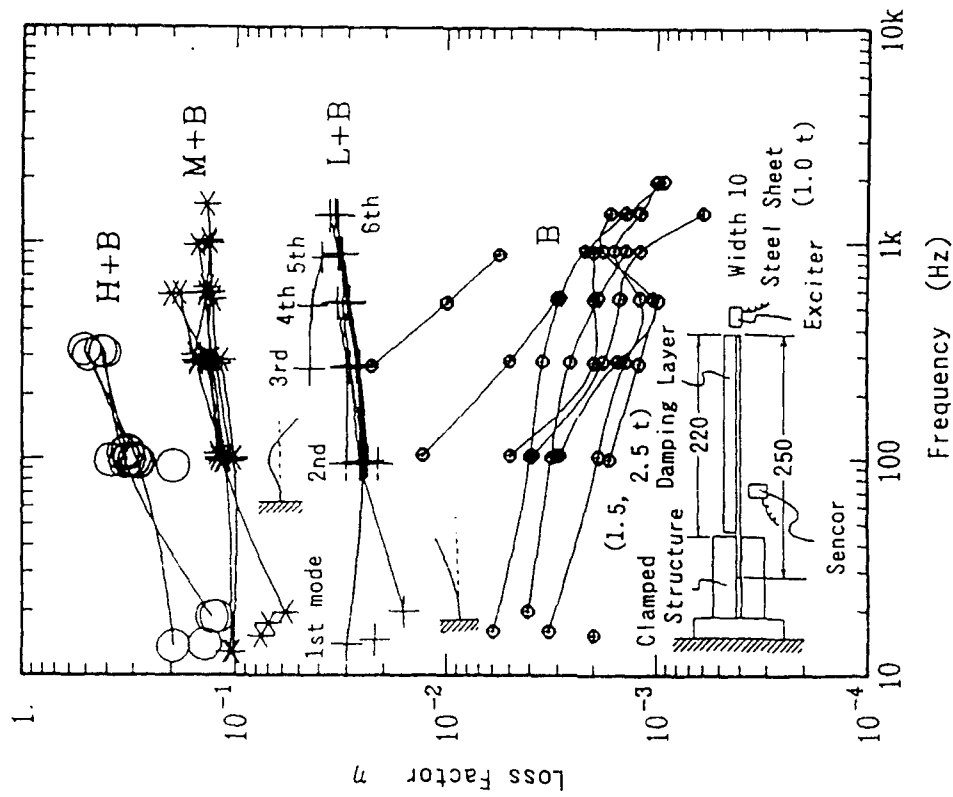


Fig. 8 Round Robin Test Measurements (all data)
by Cantilever Beam Method

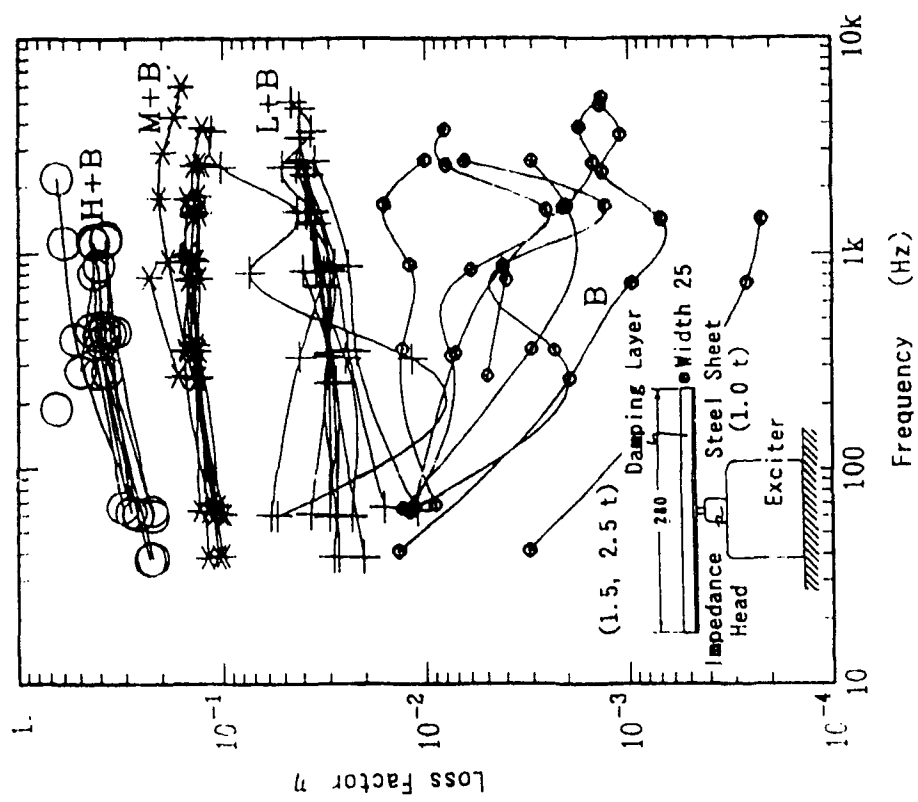


Fig. 9 Round Robin Test Measurements by Cantilever Beam Method (Data partially omitted)

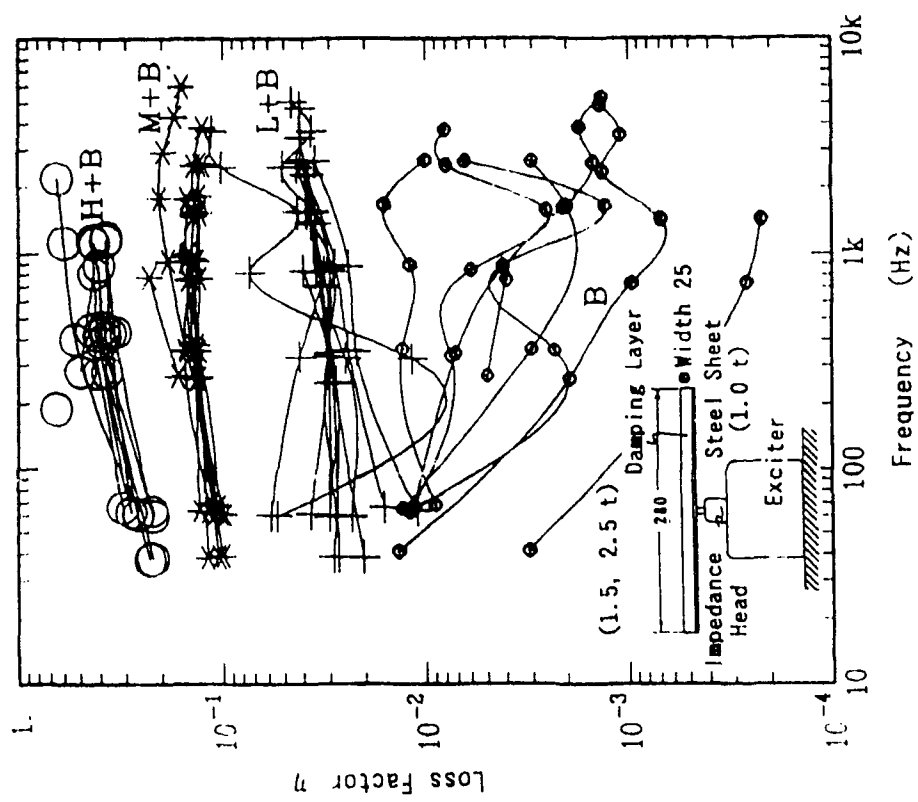


Fig. 10 Round Robin Test Measurements by Both Ends Free Beam with Center Excitation Method (all data)

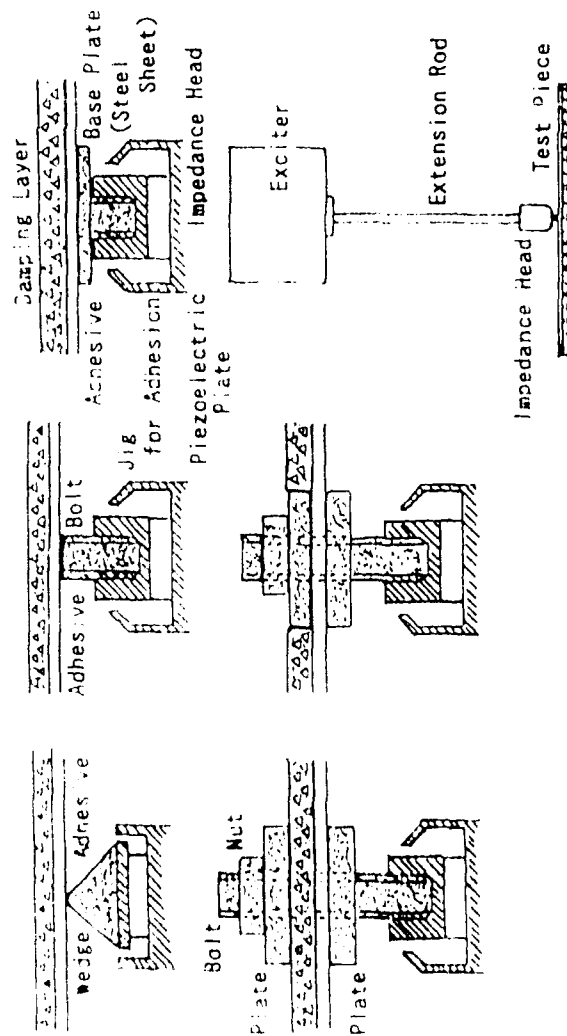


Fig. 11 Installation of Test Piece in Both Ends Free Beam with Center Excitation Method

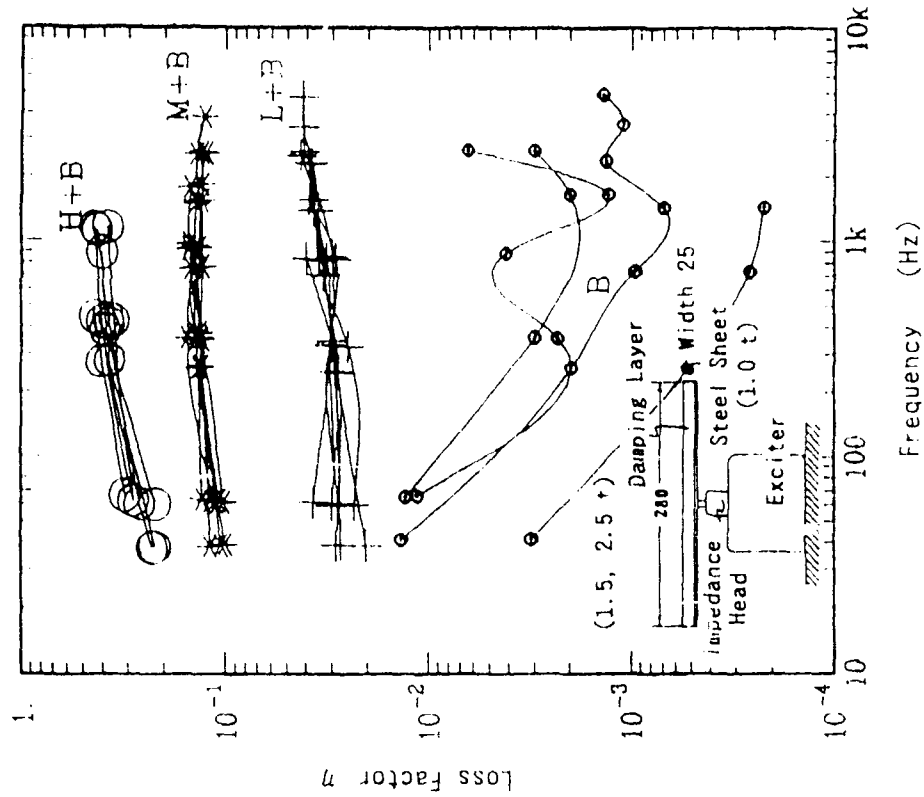


Fig. 12 Round Robin Test Measurements by Both Ends Free Beam with Center Excitation Method (Data partially omitted)

Integral Damping Treatment for Primary Aircraft Structures

by

Sal Liguore¹, Marty Ferman², Rudy Yurkovich³

McDonnell Aircraft Company
McDonnell Douglas Corporation
St. Louis, Missouri

ABSTRACT

The dynamic response of primary aircraft structure to buffeting flows, high acoustic levels, and shock boundary layer interaction has led to premature structural fatigue failures on current aircraft and is anticipated to be a continuing problem in the future. Increasing structural strength/stiffness can be a solution but this approach adds weight to the aircraft. Since the problem is dynamic response, increasing the amount of damping in the structure can also be a solution. If integral damping is considered as a part of the original design, a lighter weight design can result. The application of integral damping to primary aircraft structure was investigated and its effectiveness in controlling the primary structural modes was assessed. The findings show the approach is feasible. A simulated aircraft structure was tested with damping treatments applied. The most promising damping concepts were then analytically evaluated on the F/A-18 vertical tail.

-
1. Engineer, Structural Dynamics and Loads
P.O. Box 516, Saint Louis, Missouri 63166-0516
Mail Code 0341180, (314) 232-3109
 2. Pr. Tech. Specialist, Structural Dynamics and Loads
 3. Sr. Pr. Tech. Specialist, Structural Dynamics and Loads

BACKGROUND

Adding significant damping to reduce the primary structural mode response of lifting surfaces on aircraft can be challenging. The damping in these modes during flight can be high due to the aerodynamics present. For example, a 10 percent structural damping coefficient in the wing first bending mode is typical. Thus, in order to reduce the response by half, this aerodynamic damping level must be exceeded if the damping treatment is to be effective.

In 1987 as part of McDonnell Aircraft Company's Internal Research and Development (IRAD) program, a combined analytical and experimental program to explore the usage of viscoelastic damping in primary aircraft structure was initiated. As part of this study, the F/A-18 horizontal tail was selected for a primary structure damping treatment, Reference 1. The goal was to cut the stabilator response in half. The damping treatment consisted of a stiff graphite epoxy constraining layer adhesively bonded to the stabilator by 3M ISD-113 viscoelastic material. Modal loss factors as a function of temperature, as predicted by analysis and as measured by the experiment, are shown in Figure 1. As can be seen from the figure, the measured damping is considerably less than predicted from the analysis. The discrepancy between measured and predicted values was attributed to only having a 60 percent bond between the stabilator and patch. The difficulties of applying a stiff sheet to a sculpted surface produced poor bonding, thus limiting the effectiveness of the treatment.

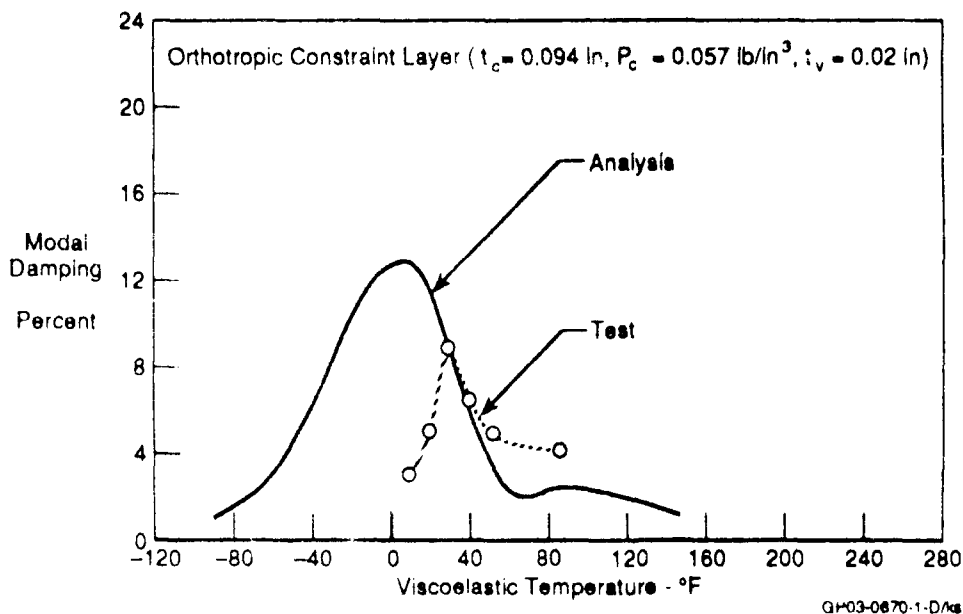


Figure 1. F/A-18 Horizontal Tail Constrained Layer Damping Treatment
Second Bending Mode

During 1988, as part of the above research program, several integral damping treatment concepts for the F/A-18 vertical tail were analyzed, Reference 2. The scope of the study was expanded to include not only the constrained-layer damping but also damped-link and tuned-mass damper concepts. In general, the modal strain energy (MSE), other than that concentrated at the root support was evenly distributed throughout the skin

structure. This type of MSE distribution is inhibitive to layered damping treatments. The reason is that a constraining layer thickness that effectively extracts MSE from the first bending mode is unlikely to be successful on the first torsion mode. Also, the F/A-18's tail surface is not conducive to a constrained-layer damping treatment due to the unevenness of the composite skin. The conclusion from this study was that none of the constrained-layer damping treatments produce the desired levels of structural damping. The main reason cited was that global modes require a global treatment unless concentrations of MSE can be identified. The damped-link failed to produce the required levels of damping because there was not enough relative motion to add any significant damping. Damped-links are analogous to a shock-absorber and require that their end-points have large relative displacements. The tuned-mass-dampers (TMD) did offer some promise; however, the difficulty in practically applying this technology makes it the least favorable alternative. Some of the inherent problems in the construction of the TMD are creep and displacement control. For the F/A-18 vertical tail application, the most critical parameters are the control of modes over a wide frequency and temperature range. TMD designs are limited to one condition or one modal effect.

In a parallel effort to design a damping treatment for the F/A-18 vertical tail, Reference 3, a scaled test article was developed to quickly and economically demonstrate the viability of an add-on damping treatment concept. Using this test article, viscoelastic tuned beam damper concepts were demonstrated in controlling the primary modes. A response plot with and without the viscoelastic tuned beam damper is shown in Figure 2. There is a significant reduction in the response of the second mode with the damper installed. The tuned beam damper was found to be effective in controlling the important modes of the beam structure within the weight limitations.

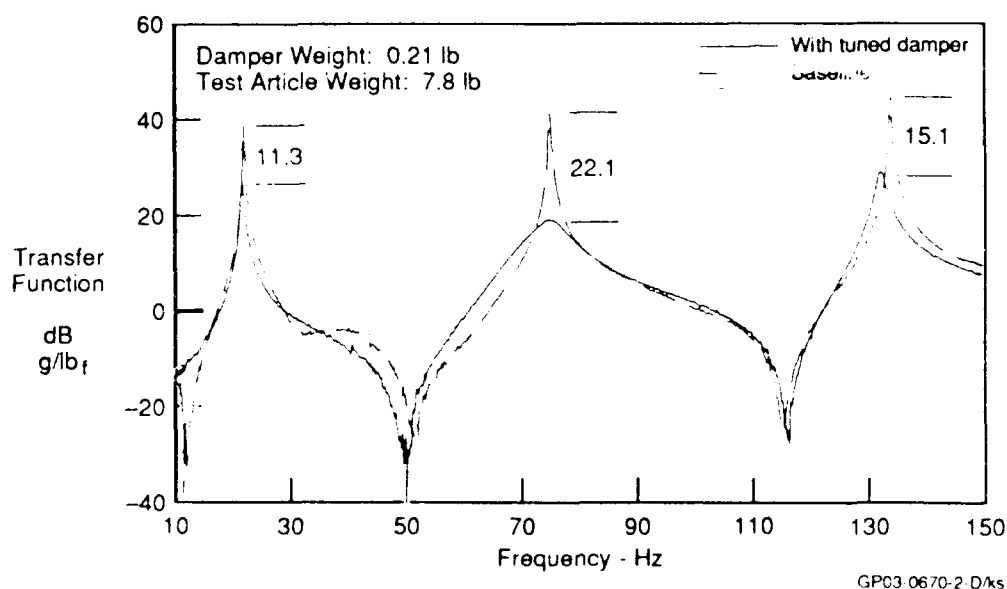
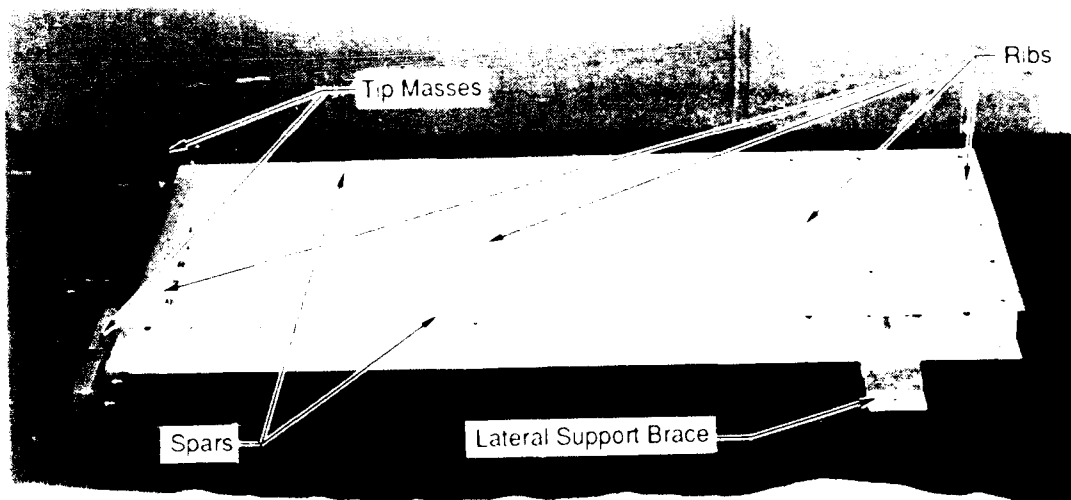


Figure 2. Response Data for Cantilever Beam With and Without TMD

SUBSCALE STRUCTURE STUDY

The previous studies had identified many damping concepts and provided data on the damping of empennage structural response. In continuing this research, our thrust was to investigate, in a more controlled manner, the previously identified damping concepts. We used a subscale structure that simulated the vibrational characteristics of the F/A-18 vertical tail. Two damping treatments were tested using this subscale structure which is a simple box beam shown in Figure 3. The box beam was of a single cell construction with all aluminum structure. The box beam is 48 inches long (of which 12 inches is a support root) by 18 inches wide and 3 inches deep. A tip mass was added to simulate the lowest frequencies of the F/A-18 vertical tail.

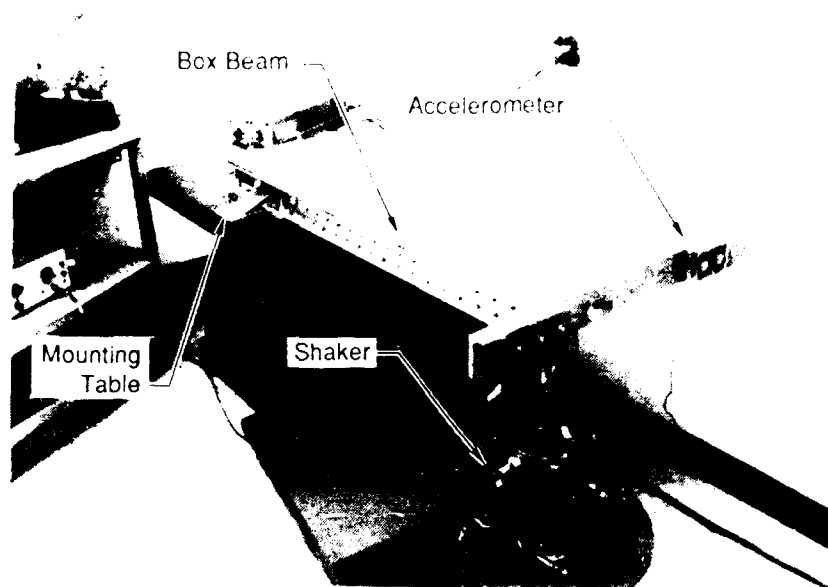


GP03-06-10-3-KWS

Figure 3. Single Cell Box Beam Structural Configuration

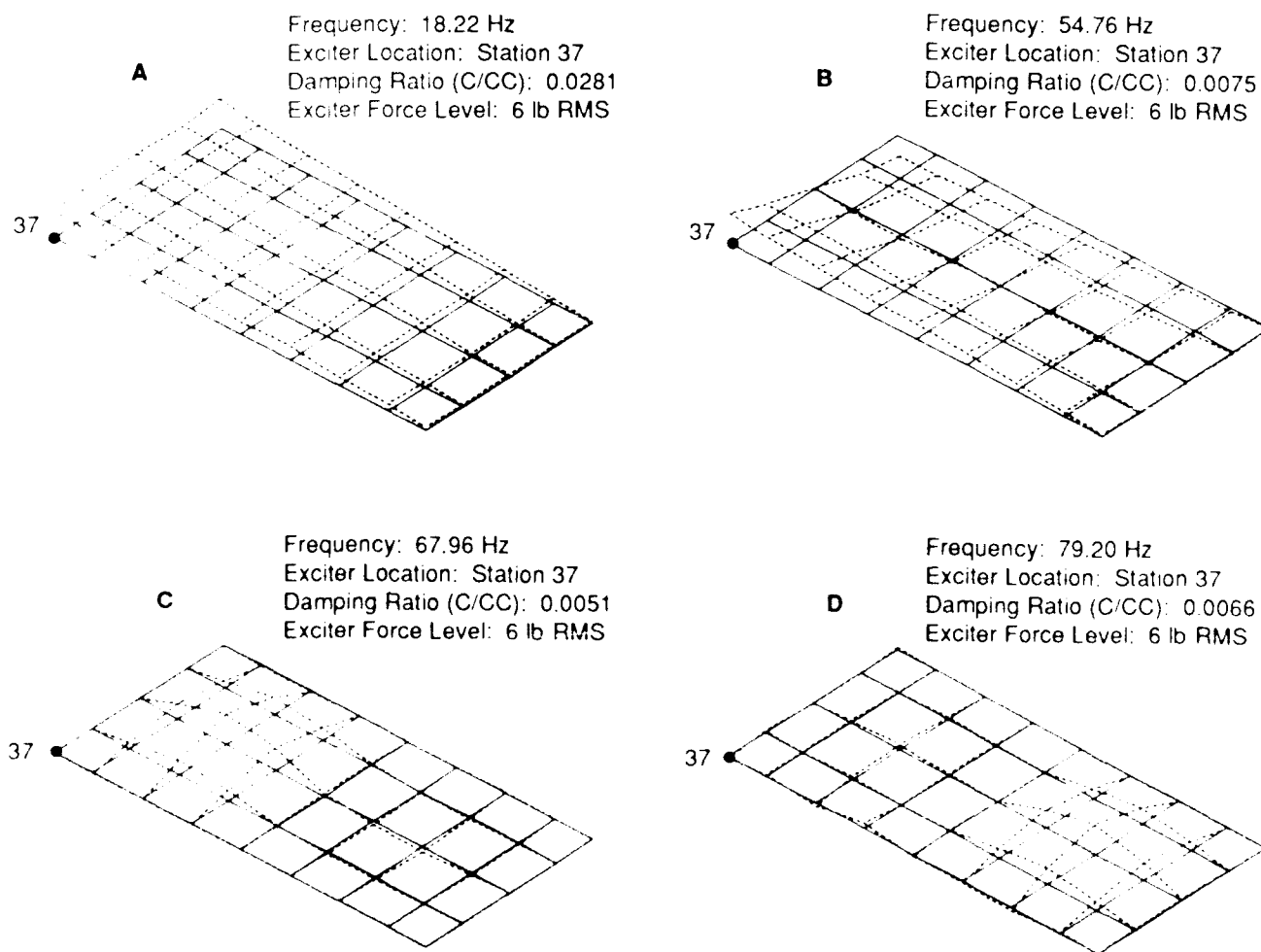
Using the single cell box beam test article, two damping concepts were evaluated: a partial exterior add-on treatment and an integrally damped interior treatment. Modal and dynamic response tests were performed to verify increased levels of damping in the primary (first bending and first torsion) and secondary (panel) modes of the box beam.

The box was tested in a cantilevered configuration, Figure 4. A complete baseline modal survey was conducted to establish frequencies, mode shapes, and damping values for the first bending and torsion modes and the first panel modes of the skins. The mode shapes, frequencies, and damping are shown in Figure 5. Forced vibration tests using random and sine excitation were conducted. During these tests transfer functions were measured at various locations on the untreated structure to provide a baseline from which the response of the damped structure could be compared.



GPC3-0670-4-KAS

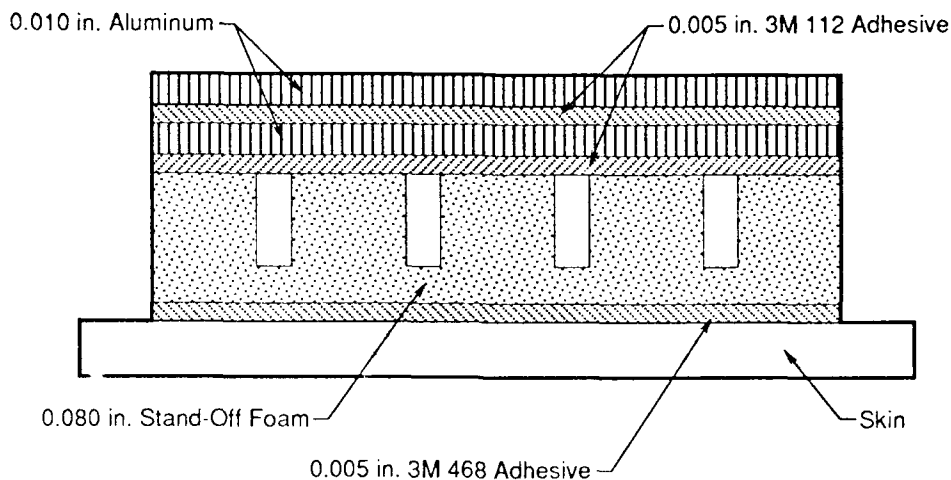
Figure 4. Box Beam Vibration Test Setup



GPC3-0670-4-KAS

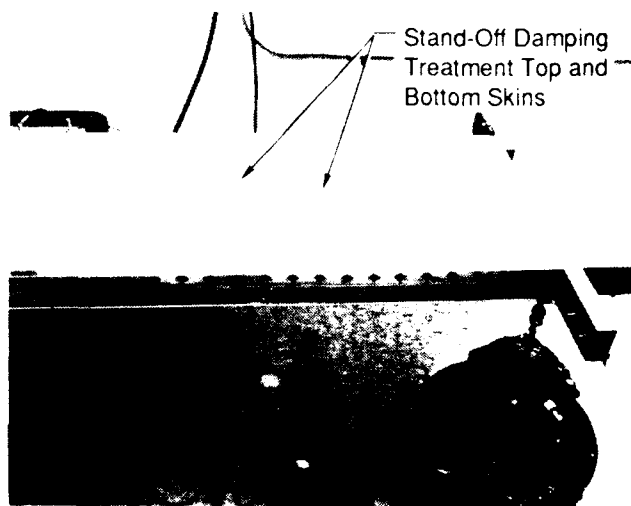
Figure 5. Mode Shape Plots of the Primary Modes of the Baseline Box Beam

The damping treatments tested consisted of: a stand-off damping treatment applied to the outer skin, and an adhesive or "interface" damping layer applied between the skin and spar-caps. The stand-off treatment consisted of an 0.080 inch thick syntactic foam layer adhesively applied to the skin with a 0.005 inch thick layer of 3M 468 and a double application of 0.005 inch thick 3M ISD-112 and 0.010 inch thick soft aluminum constraining layer, Figure 6. The treatment was applied in 12 by 15 inch sized patches to all four exposed panel areas (top and bottom) on the box beam, Figure 7.



GP03-0670-6-D/dpt

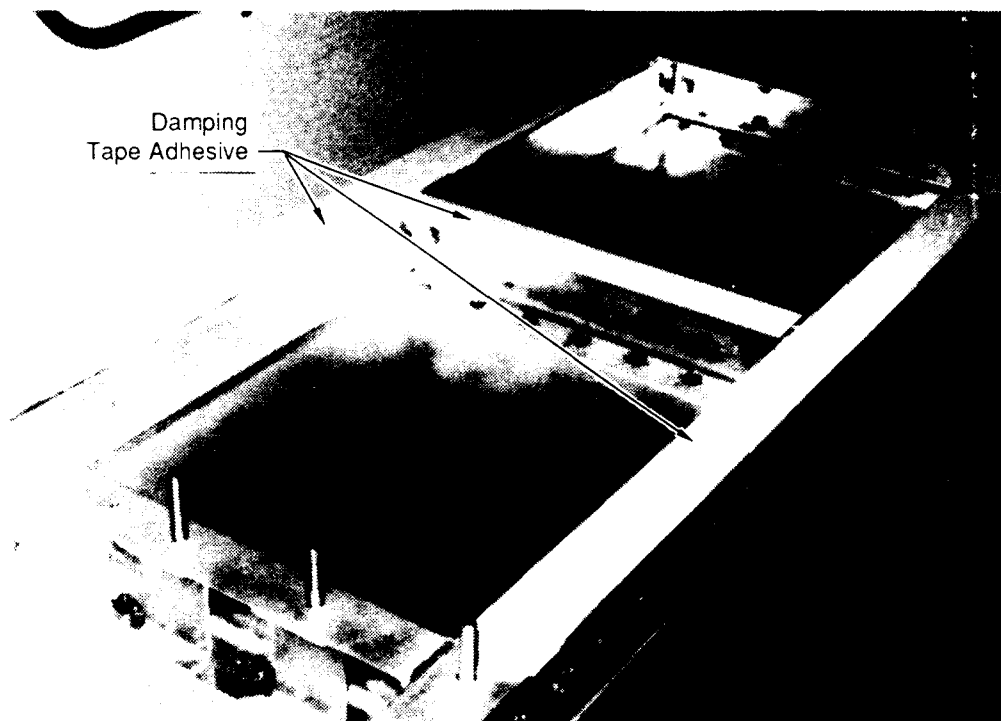
Figure 6. Stand-Off Damping Treatment Design Configuration



GP03-0670 7 kas

Figure 7. Stand-Off Damping Treatment on the Box Beam

For the "interface" damping treatment, a 0.02 inch thick damping layer of 3M ISD-113 was bonded to the spar caps and then the skins were fastened in place with adhesive, Figure 8. The previous damping treatment of the stand-off material was not removed (the effect on the primary mode response was minimal and the accelerance frequency response functions were less noisy.) The effects of the two treatments were assumed to be additive, with the initial effect known.



Box Beam With Top Skin Removed to Show Adhesive

GP03-0670-8'kas

Figure 8. Spar/Skin Joint Damping Treatment on the Box Beam

The vibration test results are summarized in Figure 9. These results indicate that the exterior damping treatment is effective in reducing the response of the primary structure, but it is even more effective in reducing response in the local panel modes of vibration, Figure 10. An increase in damping of 29 percent in the first bending mode was observed. This is a significant increase in damping, considering that the baseline first bending modal loss factor was 0.064. A 94 percent reduction and a 77 percent reduction from baseline response in the first and second panel modes was measured.

Mode Shape	Baseline		Stand-Off		Interface	
	Freq (Hz)	Modal Loss Factor	Freq (Hz)	Modal Loss Factor	Freq (Hz)	Modal Loss Factor
First Bending Primary	18.22	0.056	17.87	0.092	19.30	0.103
First Torsion Primary	54.76	0.015	54.77	0.026	44.09	0.082
First Panel (Front Panel)	67.69	0.010	78.89	0.163	Not Determined	
Second Panel (Back Panel)	79.20	0.013	89.03	0.052	Not Determined	

GP03-0670-9 D:dpt

Figure 9. Box Beam Damping Test Results Summary

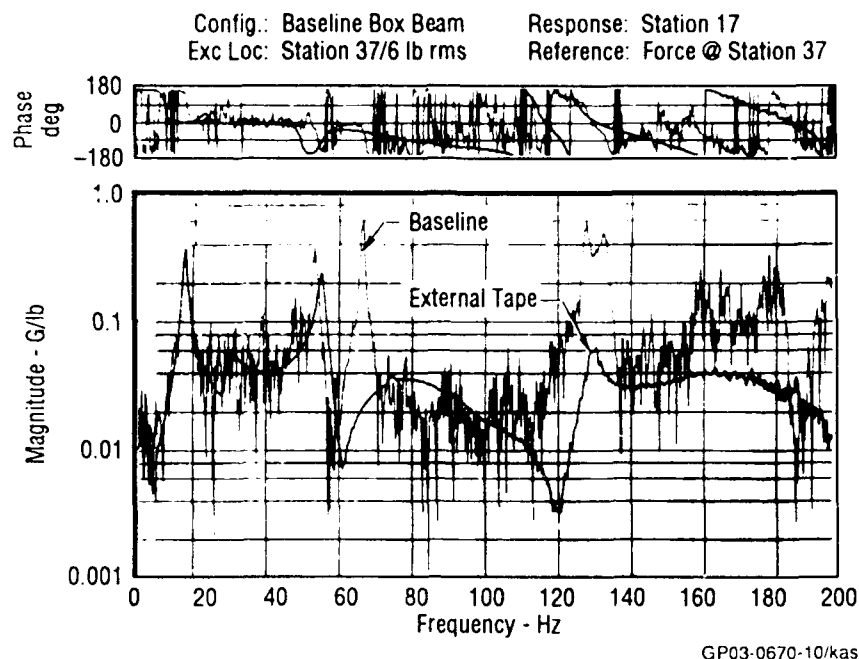


Figure 10. Overlay of the Box Beam Baseline and External Tape Random Response Transfer Function

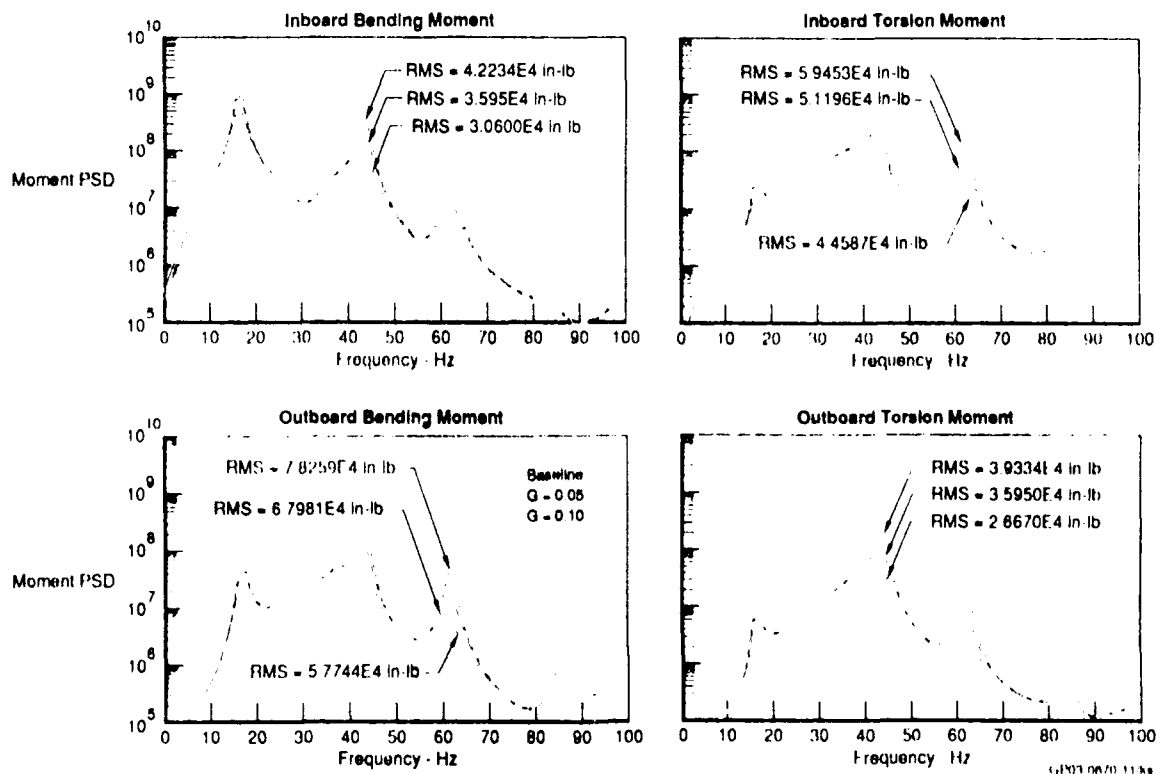
The interface damping concept increased the damping in the first bending mode and caused an additional 13 percent reduction in response or a 39 percent reduction overall from the baseline response. The damping treatment was more effective in damping the first torsion mode. The combined effects of the standoff and the interface damping treatments caused an 82 percent reduction from the baseline torsion mode response. A decrease in stiffness of 19.5 percent from the baseline torsion mode frequency was observed which was observed by the decrease in the modal frequency from 54.77 Hz to 44.09 Hz.

F/A-18 VERTICAL TAIL APPLICATION

For the major case of interest here, the F/A-18 vertical tail is subjected to severe buffeting forces at angles of attack above 20 degrees. These buffeting forces cause very high dynamic response in the primary modes of the tail; i.e., zero to peak amplitudes in excess of 500g have been observed in flight. If the objective is to cut the buffet response in half, then the level of structural damping in the vertical tail needs to be significantly increased.

In order to investigate the effectiveness of damping to control the vertical tail response during buffeting flow conditions, buffet response calculations were made using simulated levels of structural damping. The simulated damping levels are assumed to come from the inclusion of the damping treatment to the structure. Unsteady pressures during buffet were measured during the wind tunnel program described in Reference 4. These pressures were scaled to aircraft size and were used as the forcing function in the response calculation. The scaling method and calculation approach are also described in Reference 4. The results of the calculations are shown in Figure 11. The

F/A-18 Vertical Tail Buffet Response Predictions With/Without Damping



data are presented in the form of bending and torsion moment PSD's for a 14 percent and 66 percent span station. For the condition of Angle of Attack of 32 degrees, Dynamic Pressure of 347 psf and Mach Number of 0.6, the first bending mode dominates inboard bending moment responses, and the second bending mode dominates the outboard bending moment responses. The overall RMS response reductions, (Figure 12), suggest that 50 percent is the maximum that can be obtained from a damping increase alone.

As previously mentioned, analytical studies for primary structure damping treatments for the F/A-18 vertical tail, Reference 2, had concluded that constrained-layer damping could not be effectively included because the structure itself was well designed with no areas of major strain energy concentrations. For the F/A-18 vertical tail application two treatments were analyzed. These consisted of a "hybrid" design of the solid spacer treatments identified in Reference 2 and the interface concept which was tested using the subscale structure. Analyses of these two treatments required extensive modification of the existing F/A-18 dynamic finite element model, shown in Figure 13, in order to examine the damping treatments. The damping concepts were each individually modeled and extensively analyzed using the MSE Method, Reference 5, for various damping configurations.

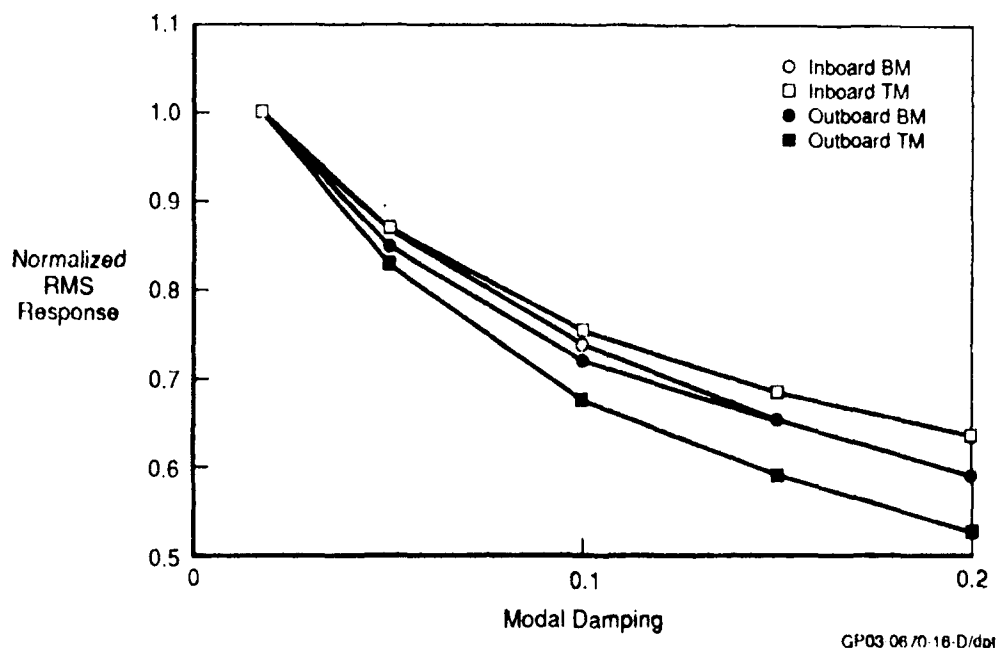


Figure 12. RMS Damping Response Normalized to the Baseline RMS Response

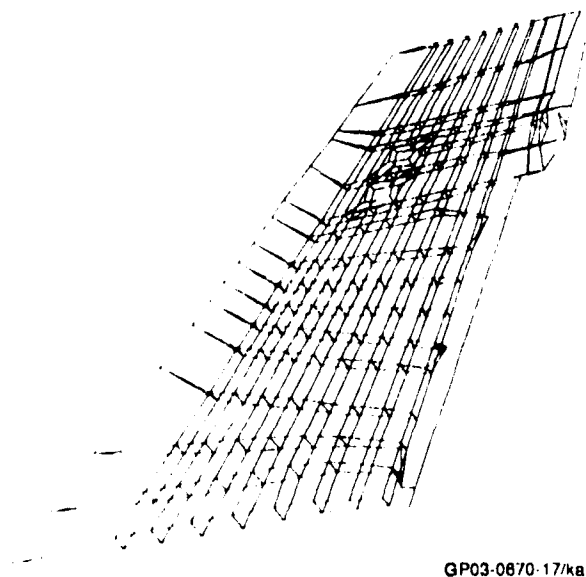
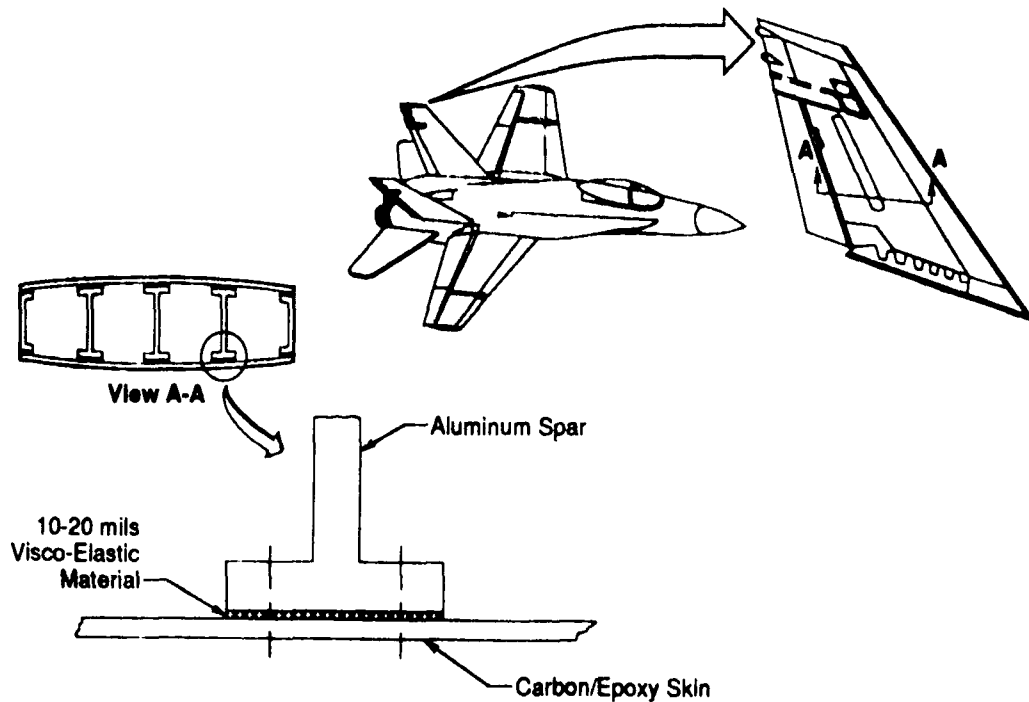


Figure 13. MSC/NASTRAN Dynamics Model of the F/A-18 Vertical Tail

INTERFACE DAMPING CONCEPT

The interface damping treatment required that a layer of shear deformable elements be included between the spar cap and skin. Hence, an extra set of nodes was placed underneath the existing spar cap nodes. This model reflects the detail in the primary load path (skin through fastener to spar) needed to analyze the problem sufficiently. In this concept, Figure 14, a portion of the beam shear load is transferred through the VEM located between the moldline skin and substructure. The remaining load is carried through by the fasteners. In the study, fasteners were assumed to be either widely spaced or were excluded from the model. Both variations of the interface concept will be discussed.



GP03 0870-18 D/Aa

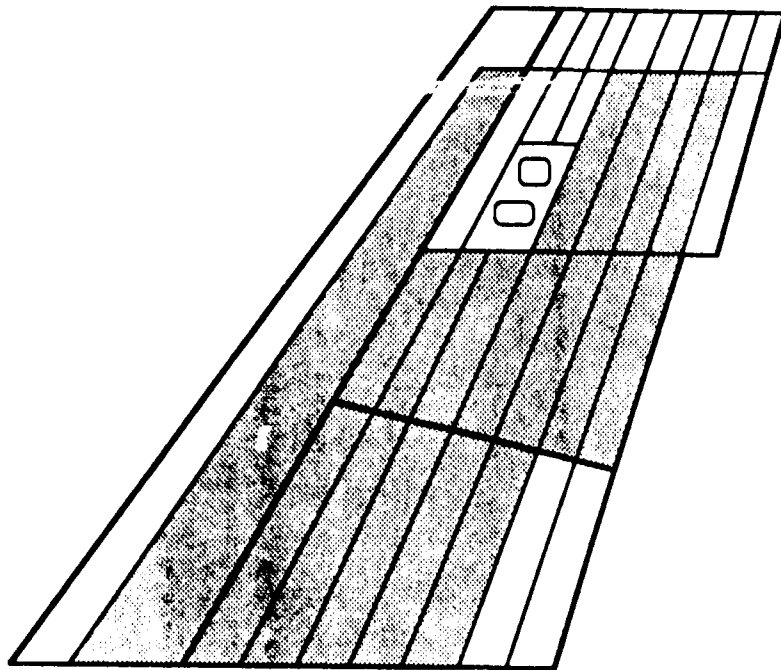
Figure 14. A Structurally Integrated Passive Damping Concept

The interface layer was included into the detailed F/A-18 vertical tail as a shear panel with the transverse degree-of-freedom (DOF) rigidly constrained between the spar cap and skin element DOF. When the fastener effects were included, they were modeled with rigid bar-type elements in all DOF. The treated areas of the structure are shown in Figure 15. With fasteners, this treatment only produced 1.5 percent and 2.0 percent MSE in the first and second bending modes and nearly 8 percent MSE in the first torsion mode of the vertical tail. Without the fasteners, 3 percent and 4 percent MSE were produced from the first bending and second bending modes, respectively. When no fasteners were assumed to be in place, the modal strain energy produced in the first torsion mode increased to a peak MSE of 12 percent (Figure 16), but at a subsequent loss in stiffness of the structure noticed as a decrease in frequency, Figure 17.

SOLID SPACER DAMPING CONCEPT

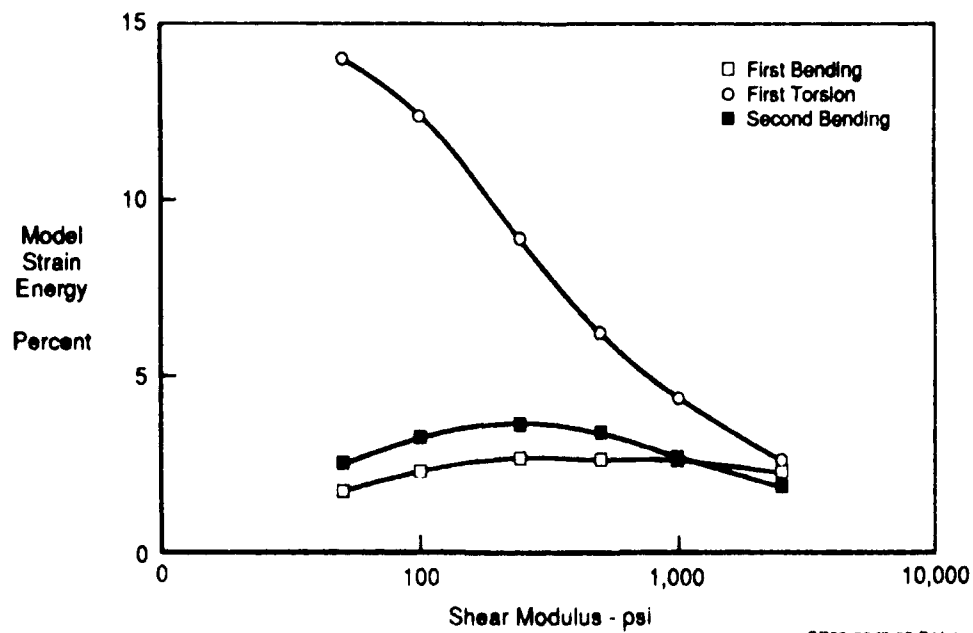
Previously, this concept had been analyzed in two solid spacer arrangements, Figure 18, and neither concept showed any significant benefit for further evaluation. However, it was thought that a combination of the two concepts, Figure 19, would show the necessary levels in damping that would make this concept a candidate for future design application. Thus, the damping treatment was evaluated.

The combination of the three damping layers allows for shear deformation to take place in all three layers. If only the center-plane layer existed with the two rigid spacers rigidly attached to the skins, then no relative shearing could take place in that layer. This is because the vertical tail is



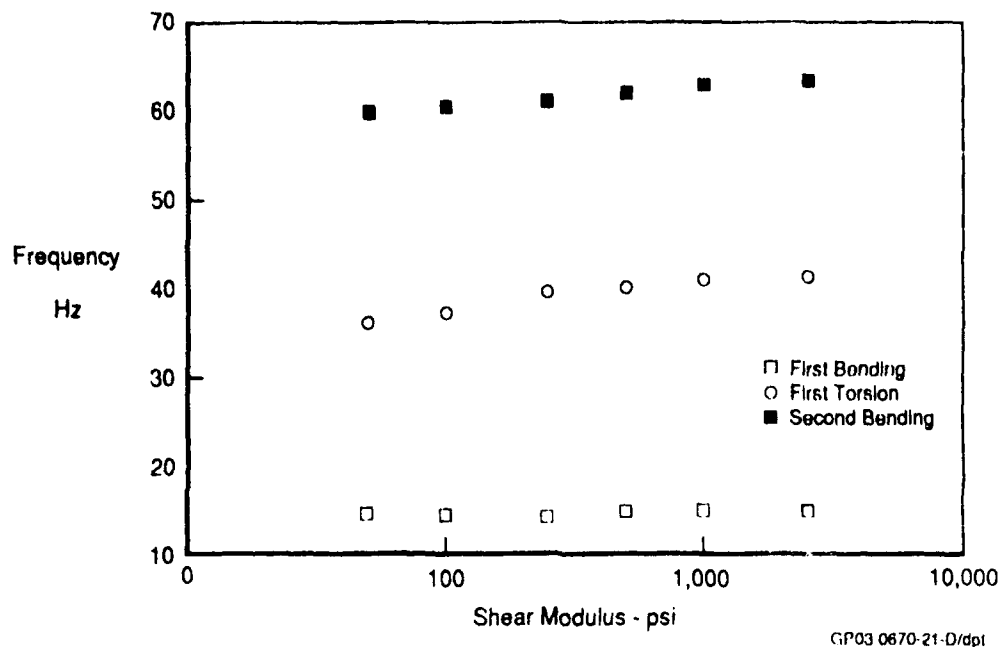
GP03-0670-19 D/dpt

Figure 15. Solid Spacer Damping Treatment Coverage on the Vertical Tail



GP03 06/0 20 D/dpt

Figure 16. Interface Damping Treatment With No Fasteners



**Figure 17. Interface Damping Treatment With No Fasteners
Modal Frequency Dependence on Shear Modulus**

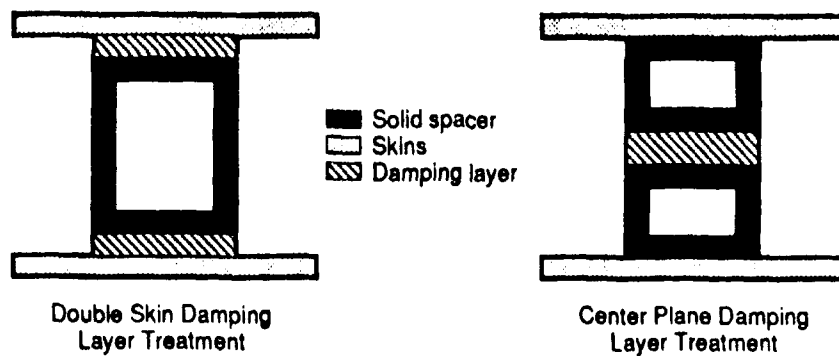


**Figure 18. Solid Spacer Damping Treatment Concepts
Reference 2**



Figure 19. Hybrid Solid Spacer Damping Concepts

constructed of skin and multiple spar which is thus quite rigid in shear with no relative shearing motion between the skins of the tail. When two skin damping layers are held by one solid spacer, only a minimal amount of damping can be produced from these layers. This is similar to trying to damp a very thick beam with two very thin constrained-layer damping treatments applied to either side. But, when the solid spacers are decoupled from both skins and at their center plane by a soft viscoelastic layer, dramatic shear relief is exhibited in all of the layers. In fact, as the center layer becomes weaker and thicker, the damping in the skin layers will begin to maximize shear effects by increasing the amount of relative displacement between the skin and solid spacer.

This treatment was applied continuously between the spars over the shaded portions of Figure 15. It includes an integral damping treatment for the leading edge as well as the main torque box. Sensitivity studies were performed on the effect of the shear moduli in the different layers including the shear stiffness of the solid spacers. The first bending mode has very little dependence on any of the parameters considered. Damping of this mode is heavily dependent on the stiffness at the root of the tail. For the first torsion and second bending modes, the parameters that optimize the strain energy in these modes is opposing. For instance, the torsion mode yields 9.2 percent modal strain energy at a $G_{\text{skin}}/G_{\text{core}} = 500 \text{ psi}/1000 \text{ psi}$, where G_{skin} is the shear modulus of the skin side damping layer and G_{core} is the shear modulus for the damping layer at the center plane, and the second bending mode maximizes at 7.7 percent at $G_{\text{skin}}/G_{\text{core}} = 20 \text{ psi}/100 \text{ psi}$. Finally, more strain energy can be produced in the bending modes when the solid spacer is assumed to be very rigid. The above studies assumed the shear modulus of the solid spacer to be $G_{\text{spacer}} = 500,000 \text{ psi}$. As an upper limit, 22.0 percent MSE was produced in the VEM for the second bending mode, 4.7 percent MSE for the first bending mode and 6.0 percent MSE for the torsion mode when $G_{\text{skin}}/G_{\text{core}} = 20 \text{ psi}/100 \text{ psi}$ with a rigid spacer, $G_{\text{spacer}} = 50 \times 10^6 \text{ psi}$.

The negative aspect of this treatment is that it adds nearly 40 pounds per tail. This does not reflect any optimization by placement or geometry to reduce the weight penalty. The weight penalty was imposed by the use of the spacers which accounted for 85 percent of the weight increase. These spacers were modeled with solid finite elements which were assumed to represent hollow tubes made of composite materials and very stiff in shear. The overall weight of the damping treatment could be reduced by removing the treatment from certain areas of the structure that had little effect on the modes of interest. For instance in the first bending mode, the leading edge and lower to mid tail regions contribute the most to the damping increase. In the second bending mode, the mid region contributes the most to the damping increase. In the present vertical tail structural arrangement, it would not be practical to try to use this treatment in areas obstructed by wire bundles, hydraulics, and fuel lines.

CONCLUSIONS

Viable integral damping concept have been shown to merit further full scale evaluation. The analysis of the interface damping concept shows that it can be tailored for specific damping, strength and stiffness requirements by altering the structure fastener spacing. Evidence from the study shows that a reduced number of fasteners is required for the interface concept because

aircraft standards for fastener spacing along a spar results in an overly rigid structure which inhibits any shear relief through the VEM. The analysis of the solid spacer concept proved the proof-of-concept and showed that it would be a candidate for future aircraft. However, a damping concept of this sort will need to be considered in the initial design phase in order to make the concept more weight efficient.

ACKNOWLEDGMENTS

The research studies reported in this paper were conducted under the McDonnell Aircraft Company's Independent Research and Development Program. Special assistance from the McDonnell Aircraft Structural Dynamics Lab Group was given in the set-up and conduct of lab tests. Also, the damping materials were graciously supplied by the 3M Company Industrial Specialities Division and Wright Laboratory "Damping Clearing Center."

REFERENCES

- [1] Yurkovich R.N., "Application of Constrained Layer Damping to the F/A-18 Horizontal Tail," Damping 89, West Palm Beach, FL., February 1989.
- [2] Gibson, W.C., Maly J.R., and Austin E.M., "Conceptual Design of the Damping Treatments for the F/A-18 Vertical Tail," CSA Report No. 88-11-02, November 1988.
- [3] Parin, M. and Nashif, A.D., "Development of Vibration Control Measures for the F/A-18 Vertical Tail," Anatrol Report No. 88024, February 15, 1989.
- [4] Ferman, M.A., and Zimmerman, N.H., "Prediction of Tail Buffet Loads for Design Application," NADC-880434-60, July 1987.
- [5] Johnson, C.D., Keinholz D.A., and Rogers, L.C., "The Modal Strain Energy Finite Element Analysis Method and its Application to Damped Laminated Beams," 51st Shock and Vibration Symposium, San Diego, CA, October 21-23, 1980.

AN INVESTIGATION OF ADD-ON DAMPING TREATMENT FOR LIFE EXTENSION OF THE F-15 UPPER OUTER WING SKIN

M. Parin, V. Levraca, A. Pacia, and L. Rogers

Flight Dynamics Directorate
Wright Laboratory
Wright-Patterson AFB, OH

ABSTRACT

The purpose of this investigation was to design, fabricate, and verify candidate add-on damping treatments for the F-15 upper-outer wing skin. The F-15 upper-outer wing skin has experienced high cycle fatigue cracks caused by separated flow on the upper wing surface. The separated flow results during high load factor maneuvers and in turn induces large vibratory loads on the upper wing skin and associated substructure. The capability of the F-15 to sustain these maneuvers allows the excitation to occur for sufficiently long periods of time to result in damage. Damage accumulates due to the resonant vibration of local skin/stiffener modes. The cracks initiate at the fastener holes adjacent to the integrally machined "T" stiffeners and tend to propagate parallel to the stiffeners. Two damping treatments resulted from the investigation and are recommended for F-15 fleet retrofit. One was an external constrained-layer treatment and the other was an internal "stand-off" treatment. Laboratory vibration, corrosion, and thermal aging tests were conducted as part of the development of the add-on damping treatments. Life extension factors were estimated for both damping treatments.

INTRODUCTION

The requirement for high performance fighter aircraft places tremendous demands on the components and materials from which these aircraft are constructed. Inherent with high performance are high vibration levels. One possible cause of large vibratory loads is separated flow. Separated flow presents an unpredictable and complex environment. Within this environment it is often impossible to estimate the precise dynamic flow characteristics or loading conditions aircraft components may experience during flight. If not properly accounted for in the design phase, large vibratory loads can result in high cycle fatigue and a substantial reduction of the useful service life of the component. Skin type components, in particular outboard wing

skins, are relatively light weight structures which are extremely susceptible to vibration response induced by separated flow.

The F-15 upper-outer wing skin (UOWS) panel has experienced cracks resulting from high cycle fatigue. The F-15 aircraft, shown in Figure 1, has sufficient thrust to perform sustained, high load factor maneuvers. Consequent separated flow over the wing panel contains high-level broad band random pressure fluctuations and induces large vibratory response in the UOWS panel and associated wing substructure. The resulting elevated stresses over time cause high cycle fatigue cracks to form in the wing skin. Historically, UOWS cracking dates to the late 1970's and early 1980's. At that time, the cracks were considered to occur only over a small portion of the skin closest to the wing tip. Subsequent finding show that the entire UOWS is prone to cracking.

The UOWS was originally designed for a service life of 8000 hours. Unfortunately the initial service life realized was only 250 hours. Several modifications were incorporated to improve the fatigue life of the skin, including fortifying critical locations on the wing skin. The modifications were initially thought to have resolved the fatigue cracking problem. In reality these changes only increased the life of the skin to approximately 1250 hours. The need still remained to increase the service life to the original design value of 8000 hours.

The purpose of this investigation was to design, fabricate, and verify candidate add-on damping treatments for the F-15 UOWS which would alleviate the occurrence of fatigue cracks caused by separated flow on the upper wing surface and increase the UOWS service life to the desired 8000 hours. Two candidate damping treatments resulted from the investigation and were recommended for F-15 fleet retrofit. One treatment was a field installable external system and the other an internal depot installable system. Neither system required modifications to the existing wing structure.

BACKGROUND

The F-15 UOWS is machined from a single block of 2024 Aluminum (Al) and consist of the skin, integrally machined "T" stiffeners, and chemically milled pockets between the stiffeners. The thickness varies from location to location on the panel, however assuming a constant thickness of 0.080" is sufficient for understanding the problem. Figure 2 shows the major substructure for the left wing. The UOWS extends from rib 153 to rib 224, and from the front spar to the rear spar. There are intermediate ribs at locations 172, 188, and 206. At rib 188, the front, main, and rear spars are at 10%, 45%, and 65% chord,

respectively. Collectively, the above mentioned members constitute the outer wing torque box. The wing skin measures approximately 5 feet wide by 7 feet long measuring along rib 188 and the main spar, respectively. Inboard of rib 155 the wing is "wet", that is, the volume is used for fuel storage. The outer torque box is "dry". Blind threaded, flush fasteners are used to attach the skin to the rib and spar substructure. A scrapped right hand UOWS is shown in Figure 3. Visible in Figure 3 are the integral stiffeners, their runouts, spar and rib fastener holes, and various panel access holes. Stiffeners are numbered consecutively starting at the UOWS leading edge. The stiffeners are not clipped to the ribs but are allowed to move freely within the rib notch. The cracks develop in the rib fastener holes adjacent to the stiffeners. Predominately, the cracks initiate either perpendicular to the ribs or parallel to the stiffeners. A damaged UOWS, showing the crack pattern, is presented in Figure 4. Figure 5 shows close-ups of the cracks. Based on the crack patterns and the unclipped stiffener design, it was concluded that the UOWS cracks were most likely induced by stiffener rotation. Figure 6 gives a convenient shorthand designation for the spar-rib bays which will be used throughout the remainder of this paper to aid the reader in locating specific portions of the UOWS.

The UOWS cracks are caused by high cycle fatigue. Damage accumulates due to resonant vibration of local skin/stiffener modes, excited by external oscillatory pressure resulting from separated flow. The excitation occurs during high load factor maneuvers. The capability of the F-15 to sustain these maneuvers causes the excitation to occur for sufficiently long periods of time to result in damage. Other investigations concerning the aerodynamic characteristics of the F-15 suggest that 12° angle-of-attack provides the most severe disturbances and consequently the most damage.

The location of UOWS fatigue cracks evolved during the course of this investigation. Initially, the concern was for the web of stiffener 4 in bay L1 (see Figure 6) and over rib 206 between bays L1 and L2. Next, it was observed that cracks also occurred over rib 188 between bays L2 and L3. Finally, it was learned that cracks occur over ribs 188 and 206 between the main and rear spars. Ribs 188 and 206 themselves crack, but were not specifically addressed in this study. The numerous access holes in bays L4 and R4 result in a significantly heavier structure and made this area less susceptible to fatigue cracking. Thus, with the exception of bays L4 and R4, high cycle fatigue cracks were observed over the entire UOWS panel.

FLIGHT DATA

Flight data were gathered to obtain UOWS response information during high load factor maneuvers and to assess the effectiveness of the damping system. These tests were conducted by McDonnell Aircraft Corporation, St. Louis MO (MCAIR), at the request and sponsorship of Warner-Robins Air Logistics Center. Numerous other investigations have provided some flight data along with data reduction and analysis. These investigations showed that obtaining accurate UOWS panel response data was highly dependent on whether the panel had been installed properly and the instrumentation used effectively. Inconsistencies in these two areas, among others, can easily lead the investigator to erroneous results. The flight test data collected for this investigation included the baseline response of the F-15 UOWS as well as the UOWS response with various candidate damping treatment configurations. Strain gages placed on internal and external surfaces of the panel were used to record the bulk of the response data. In some cases internal accelerometers were also used. Figure 7 shows the location of some of the strain gages used to obtain flight data. The strain gages were mounted adjacent to stiffener #4 at rib 188. One was positioned between the two rows of rib 188 fastener holes and the other was located just inboard of the fastener holes. The location and orientation of these strain gages were such that the strains inducing the fatigue cracks should be measured. Historically, many cracks have been discovered along stringer #4. Based on past analyses, it was observed that the response data obtained at the intersection of stiffener #4 and rib 188 could be used to represent the response over the remaining panel. Thus, the analyses performed centered on the UOWS response measurements taken at this location.

A plot of angle-of-attack (AOA) versus dynamic pressure (q) is given in Figure 8 for typical flight conditions for which high load factor maneuver data was gathered. The range of dynamic pressure, 350 psf to 500 psf, for the 12° AOA shown in this plot illustrates the difficulty, if not impossibility, of duplicating the service conditions for which damage is induced. The power spectral density (PSD), shown in Figure 9, is typical of the UOWS response at the strain gage locations shown in Figure 7 for an undamped panel. The flight conditions for this PSD were: 11° AOA, 5.9g load factor, 0.80 Mach, 20,000 feet altitude, and 424 psf dynamic pressure. Figure 9 shows high strain levels occur in the 300 to 400 Hertz (Hz) band. It is obvious that this peak makes the most significant contribution to cumulative high cycle fatigue crack damage.

Several damping treatment configurations were flight tested. The external and internal treatments which were recommended for F-15 retrofit were included in the flight tested damping treatments. Unfortunately detailed data is not yet available and will not be available before printing of this report; thus no

specific flight test results can be presented. The preliminary flight test results received from MCAIR are very promising and appear to significantly improve the UOWS fatigue life. MCAIR will release the final report near the end of calendar year 1991. The above mentioned damping treatments will be discussed in detail in the next section.

DAMPING TREATMENTS

This study investigated the performance of 13 different candidate add-on damping treatment configurations under laboratory conditions. For brevity only the "1980 Damping Treatment" and the two new damping treatments which were recommended to Warner-Robins Air Logistics Center are discussed in this section. Past damping experience suggested that a constrained-layer type damping treatment would offer the most viable, cost effective solution. A constrained-layer damping system consists of a layer of viscoelastic material (VEM) which is constrained by a metal layer. The layers of viscoelastic material and metal taken together are called a constrained-layer. Often these types of damping system will be constructed of multiple constrained-layers to achieve the desired level of damping. Whenever the structure undergoes bending, the metal layer will constrain the viscoelastic material, resulting in shear deformation of the VEM. Energy is dissipated due to this shear deformation.

An important part of designing a damping treatment is determining the environmental condition to which the treatment will be exposed and insuring the selected treatment will withstand and perform properly under these conditions. Critical environmental considerations include the operational temperature range for which damping is desired, the effects of the damping treatment on corrosion of the structure, and the effects of thermal aging on the performance of the damping treatment. Recent laboratory corrosion testing shows no degradation in corrosion resistance caused by the application of the recommended damping treatments. The corrosion test panels were exposed to a standard 30 day humidity corrosion environment in the laboratory consisting of 120° F, 98% relative humidity (RH), and salt spray. The addition of the damping treatments had no affect on corrosion, primarily because the paint was not disturbed during installation. Extensive service experience with similar damping treatments has not revealed any corrosion problems. For example, the "1980 Damping Treatment" has flown externally on approximately 300 aircraft for 10 years with no adverse affects on corrosion. Although the requirements used to develop the thermal aging tests were judged to be excessive, satisfactory thermal aging characteristics have been demonstrated in the laboratory for all materials used in the new damping treatments.

The temperature exposure of 8 hours at 340° F plus 48 hours at 270° F was intended to be a conservative design condition for the 8000 hour life; however, these exposure levels are believed to be more severe than necessary. Thousands of hours of F-111 service data establish that total outside air temperature (TOAT) exceeds 125° F less than 1% of the time. Laboratory tests confirmed that thermal aging caused the damping material to slightly stiffen which tended to increase damping treatment effectiveness. An additional issue of practicality includes being able to inspect the UOWS for structural integrity while the damping treatment is installed. The damping treatment configurations used in no instance covered up fasteners or locations where the cracks initiate. Therefore, the damping treatments will not hinder inspection of the UOWS either visually or radiographically and the treatments also will not impact removal or installation of the UOWS or other maintenance functions. A discussion on the selection of the damping treatment design temperature follows.

A plot of Mach number versus altitude is presented in Figure 10 for the F-15 aircraft. Included on the plot are standard day constant value curves for the following parameters: dynamic pressure (q), total outside air temperature (TOAT), and maneuver load factor. The load factor is for an F-15 with a gross weight of 42,000 pounds flying at a 12° AOA. The equilibrium temperature for the wing skin and the installed damping treatment will fall between the TOAT and the ambient temperature. The large dash marks in Figure 10 indicate planned data gathering flight conditions. Because the ratio of oscillatory pressure to dynamic pressure tends to be a constant in the subsonic flight regime, the oscillatory pressure (thus the cumulative damage) increases as Mach 1.0 at sea level is approached from the upper left on the graph. The structural limit of the F-15 is 8g's. Based on this, a temperature range from 50° F to 75° F was selected for the damping design. No cumulative damage was expected below 0° F or above 125° F.

A previous attempt by MCAIR to correct the UOWS fatigue cracking included the application of a multiple constrained-layer damping treatment referred to as the "1980 Damping Treatment". The treatment was applied externally over bay 11 of the skin (see Figure 6) because at the time, the fatigue cracks were considered to occur only in this outer spar-rib bay. It consisted of 3 constrained-layers each of which contained a 0.002" layer of ISD-112 VEM and a 0.005" layer of aluminum. Figure 11 illustrates the "1980 Damping Treatment". The "1980 Damping Treatment" was installed and flown on numerous operational F-15 aircraft but it proved to be unsuccessful in eliminating the UOWS fatigue cracks.

As previously mentioned, the Flight Dynamics Directorate developed two new damping treatments which were recommended to W-R ALC for F-15 fleet retrofit. The treatments consisted of an externally applied, field installable system and an internally applied, depot installable system. Figure 12 shows the recommended external treatment's multiple (4) constrained-layer

configuration. Two different constrained-layers were used in the design. One consisted of a 0.002" layer of ISD-112 VEM which was constrained by 0.005" of aluminum and the other was made of a 0.002" layer of ISD-113 VEM also constrained by 0.005" of aluminum. Two each of these different constrained-layers were used to build-up the total of four constrained-layers in the external treatment design. The use of two VEMs broadened the effective temperature range relative to the "1980 Damping Treatment". The six outer most spar-rib bays were covered (R1, R2, R3, L1, L2, and L3) by the external treatment. Figure 13 is a photo of the external treatment installed on an F-15 wing.

The recommended internal treatment is summarized in Figure 14. Starting at the wing skin, there was a 0.004" layer of pressure sensitive adhesive (VEM). Next there was an 0.080" stand-off layer of syntactic foam configured to maintain high shear stiffness and low flexural stiffness. This was achieved by cutting a checker board pattern into the syntactic foam. Finally, three constrained-layers of damping material were placed on top of the stand-off layer. The first constrained-layer (from the bottom) consisted of 0.004" of VEM and 0.005" of aluminum. The other 2 constrained-layer each consisted of 0.002" of VEM and 0.005" of aluminum. For all layers the Hueston Industries F-440 VEM was used. The internal damping treatment was applied in the chemically milled pockets between the integral stiffeners for all 8 spar-rib bays shown in Figure 6. Additionally, there were viscoelastic links (VELs) placed between the caps of the integral stiffeners and the notches in the rib. The VELs were located in all rib notch locations. The VEL material was slightly tacky at room temperature. A VEL thickness of 0.50" was used to provide an interference fit. The purpose of the VEL was to provide a link (having both stiffness and damping) from the stiffener cap to ground (rib notch) thereby reducing stiffener rotation. Figure 15 shows the stand-off damping treatment applied to the internal surface of the wing skin. Figure 16 shows the VELs located in the rib notches.

The installation of the damping treatments was simple and straight forward. First the UOWS was cleaned to remove all oil and dirt. Next, the external damping treatment was pre-cut to fit between the fastener rows for each spar-rib bay. The treatment was cut to insure that access to the fasteners was not impaired. A small amount of split peel ply or release paper was removed from the bottom of the damping treatment, exposing the first layer of VEM. The damping treatment was then carefully centered onto the appropriate spar-rib bay. Finally, the procedure was to gradually remove the release paper from under the damping treatment while simultaneously adhering the treatment. Special care was necessary to minimize entrapped air bubbles. A small, flat plastic scraper was rubbed over the surface of the external treatment as it was applied to squeegee out as much air as possible. This step is illustrated in Figure 17. A nice feature of the external damping treatment was that small amounts of compound curvature could be accommodated without

adversely affecting the quality of the application.

The internal stand-off treatment was applied in a similar manner except additional effort was required to avoid damaging the brittle stand-off layer. The pieces of internal damping treatment were much smaller than the external damping pieces and therefore air entrapment was not a problem. Hand pressure was sufficient to apply the internal treatment so the plastic scraper was not used. The VELs were provided with release paper on the surfaces which were to adhere to the skin stiffener and the rib notch. During installation, the release paper on the rib notch side is removed and the VEL is positioned in the rib notch. Just before installing the skin, the second release paper is removed. The thickness of the VEL was such that an interference fit resulted; however, the force required to install the UOWS tightly to the substructure was nominal and easily provided by advancing the fasteners.

Life Extension

A comparison between the response of the baseline UOWS and the UOWS with the external damping treatment installed is presented in Figure 18. The frequency response functions (FRFs) are the acceleration FRFs which were integrated twice to obtain the compliance (displacement) FRFs; the compliance FRFs were assumed to be proportional to strain. Figure 19 makes a similar comparison for the internal damping configuration. Notice the dramatic, beneficial reduction in response. The comparisons in this report were made on the basis of RMS stress rather than comparing peaks. Figure 20 presents the equation used to calculate a life extension factor. The ratio of the damped to the baseline response is raised to the proper exponential to give the life extension (ie, ratio of life). The RMS of the compliance FRF between 300 and 400 Hz was the basis of the calculation. Calculations made in this manner revealed that the UOWS with the "1980 Damping Treatment" would last 4 times as long as the baseline UOWS (bare UOWS), thus the life extension was a factor of 4. The life of the baseline UOWS is approximately 1250 hours, therefore the projected life with the 1980 Damping Treatment is 5000 hours. Obviously, this is an estimate; however, it does provide a measure of the damping treatment's performance. Similar estimates gave life extension factors for the new recommended external and internal treatments of 5 and 34, respectively. The internal treatment is considered the primary solution to resolve the UOWS high cycle fatigue cracking. This is because of the dramatic reduction in response achieved when it was installed. Its large life extension factor should offset a variety of uncertainties not accounted for by this investigation, such as precise temperature at which damage accumulates, the fact that RMS stresses were used instead of peak stresses, and

potential changes in future operational usage.

CONCLUSIONS

The Flight Dynamics Directorate, at the request and sponsorship of Warner-Robins Air Logistic Center tested 13 candidate add-on damping treatments for the F-15 UOWS. Of those tested, two damping treatments were recommended for F-15 fleet retrofit. One treatment was an externally applied constrained-layer treatment and the other was an internally applied stand-off treatment with viscoelastic links in the rib notches. The external and internal treatments resulted in life extension factors of 5 and 34, respectively. Thermal aging and corrosion tests were performed on the damping treatments with no adverse effects noted. At this time, there is no evidence to indicate that the recommended damping treatments should not be used to alleviate the UOWS fatigue cracking. Three hundred F-15 aircraft have accumulated ten years of service experience with the "1980 Damping Treatment" and to the authors knowledge there have been no reports of concerns or adverse effects associated with add-on damping treatments. It is projected that retrofit of the F-15 fleet with UOWS containing the internal treatment will result in a net savings of \$100M in maintenance and repair costs over the next 25 years. The recommended damping treatments are fully qualified for F-15 fleet retrofit and represent a viable, cost effective solution which will substantially improve the F-15 UOWS service life.

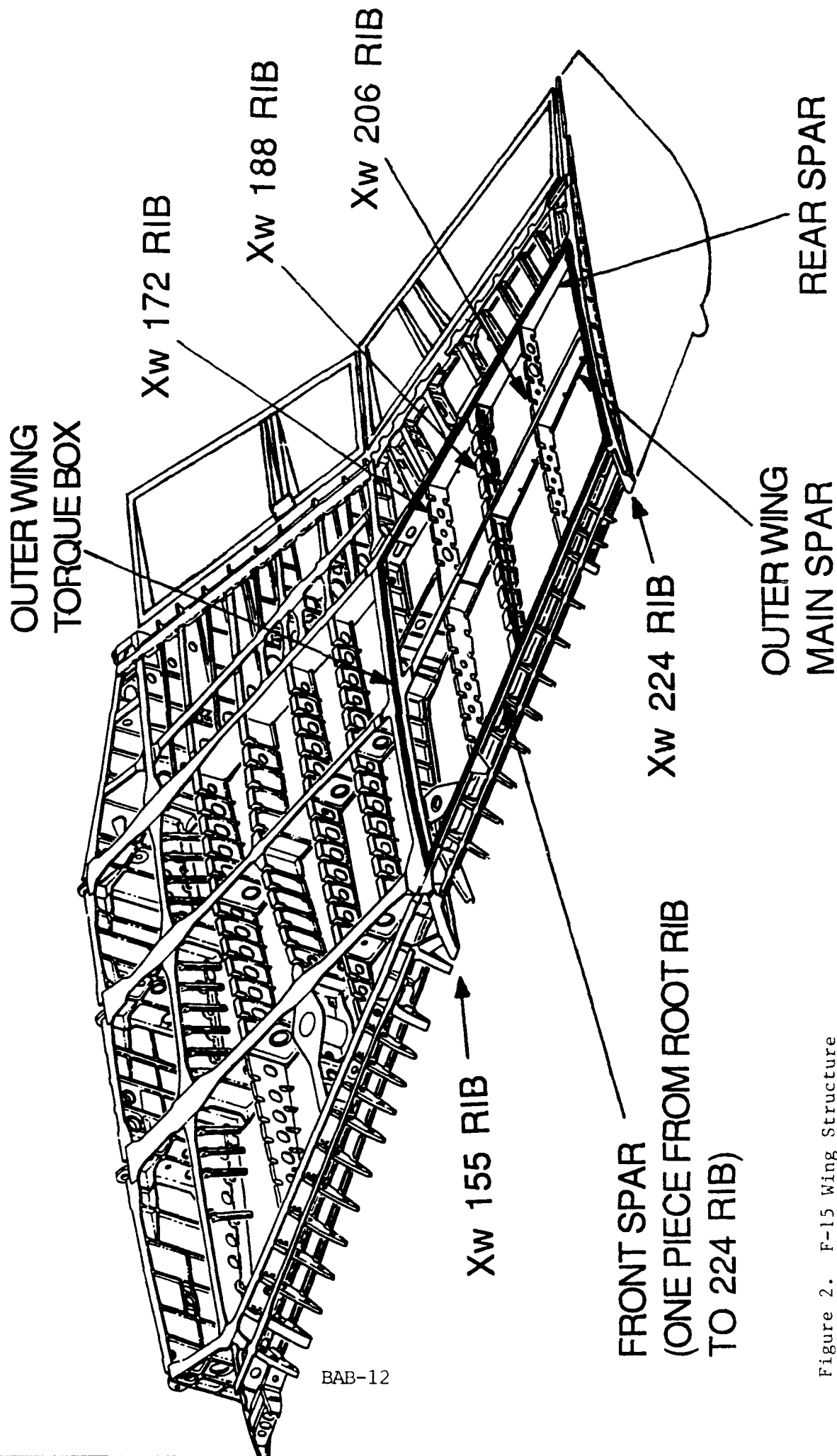
REFERENCES

1. Levraea, V., Parin, M., Pacia, A., and Rogers, L., "Add-on Damping Treatment for Life Extension of the F-15 Upper-Outer Wing Skin", WL-TM-91-307, WPAFB, OH, 1991.
2. Parin, M., Rogers L., Moon Y., and Falugi M. "Practical Stand Off Damping Treatment for Sheet Metal," Proceedings of Damping '89, Volume II, Paper No. IBA, February 1989.
3. Ferman, M., Patel, S., Zimmerman, N., and Gerstenkorn, G. "A Unified Approach to Buffet Response of Fighter Aircraft Empennage," Proceedings of the AGARD Specialists' Meeting on Aircraft Dynamic Loads Due to Flow Separation, Sorrento, Italy. AGARD-CP-483, April 1990.

4. Nashif, A., Jones, D., and Henderson, J., Vibration Damping, John Wiley & Sons, 1985.
5. Miles, R. "The Prediction of the Damping Effectiveness of Multiple Constrained Layer Damping Treatments" Presented at Acoustical Society of America, Massachusetts Institute of Technology, June 11-15, 1979.
6. Ross, D., Ungar, E., and Kerwin E. "Structural Damping" J. Ruzicka Ed., American Society of Mechanical Engineers, 1959.



F-15 WING STRUCTURE

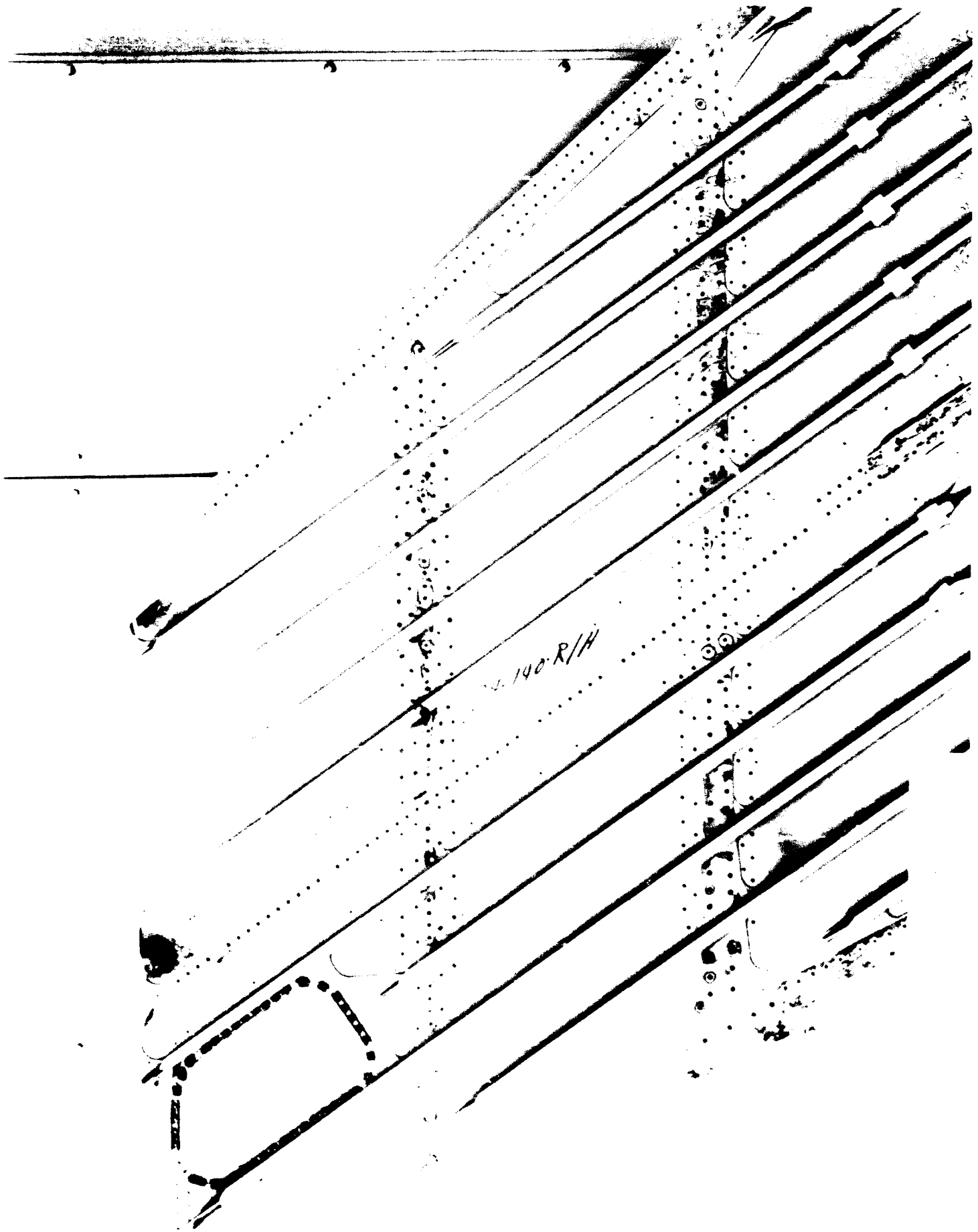


BAB-12

Figure 2. F-15 Wing Structure



Figure 3. E-15 Upper-Outboard Wing Skin Panel



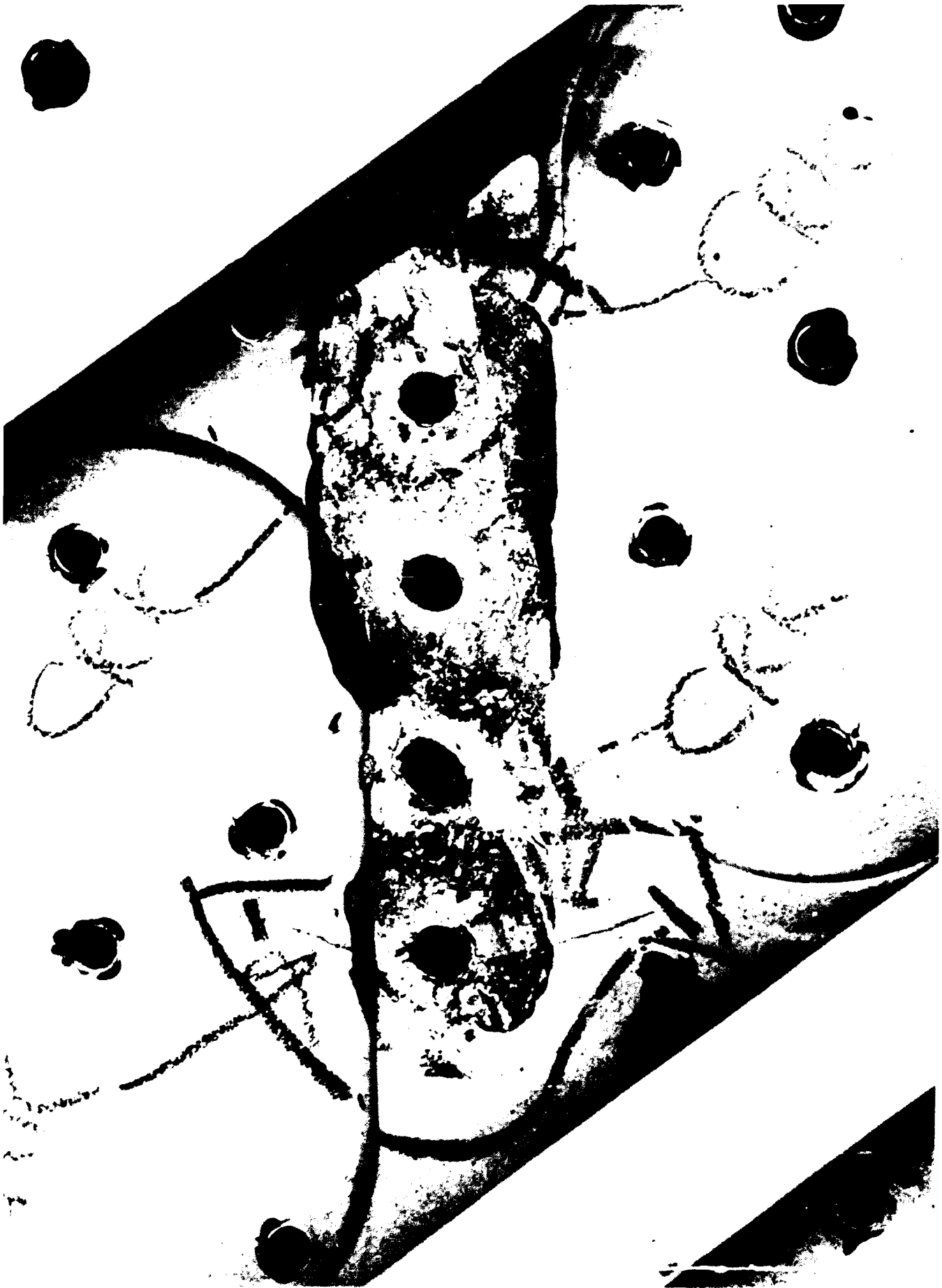
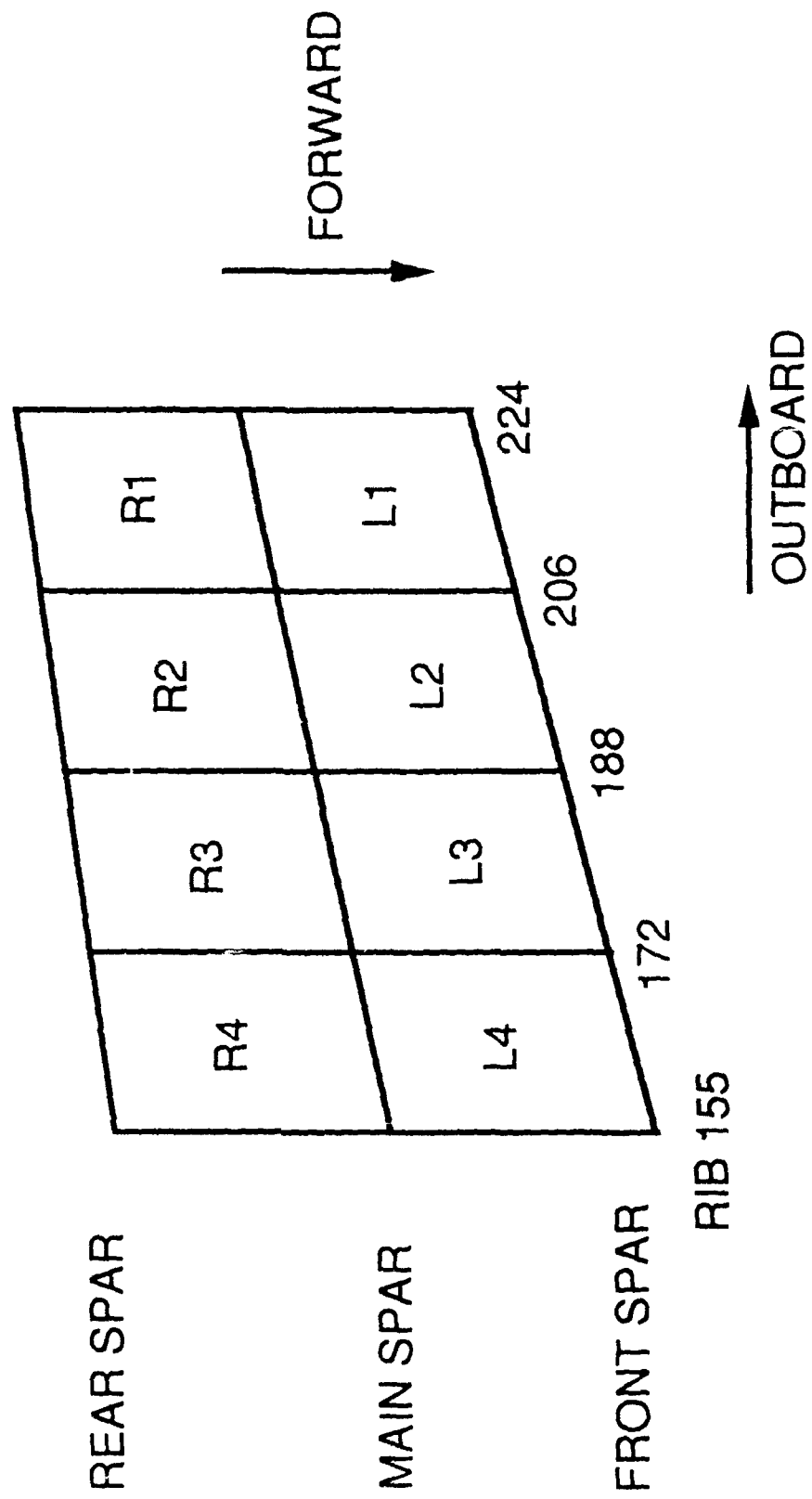


Figure 5. Close-up of UOWS Fatigue Cracks

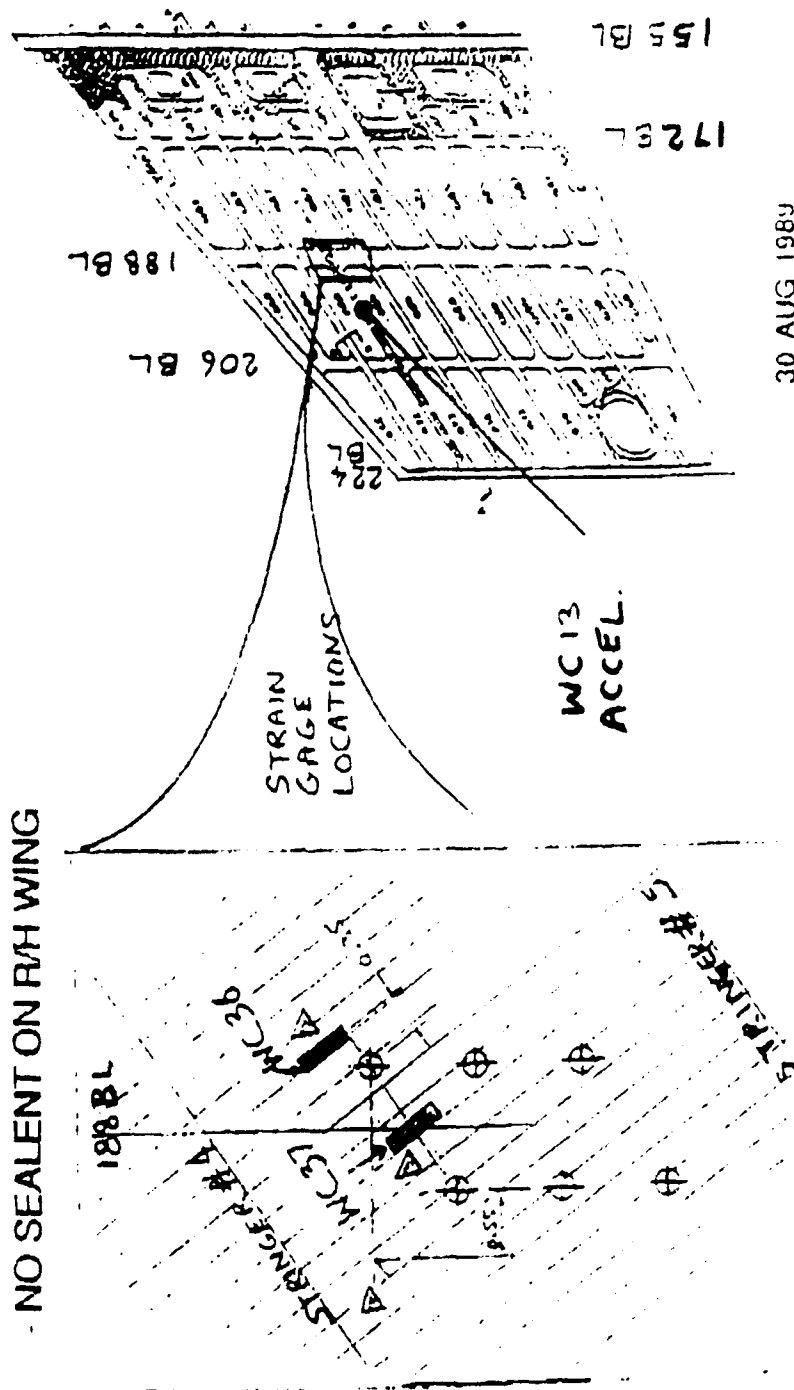
SPAR-RIB BAY DESIGNATION

TOP VIEW OF LEFT WING



FLIGHT TEST INSTRUMENTATION FOR SEALENT EVALUATION

- L/H AND R/H WINGS INSTRUMENTED
- SEALENT BETWEEN SKIN AND RIBS & SPARS ON L/H OUTER WING
- NO SEALENT ON R/H WING



30 AUG 1989
MCDONNELL AIRCRAFT

Figure 1. Flight Test Instrumentation

FLIGHT 994 WB21 AOA VS Q

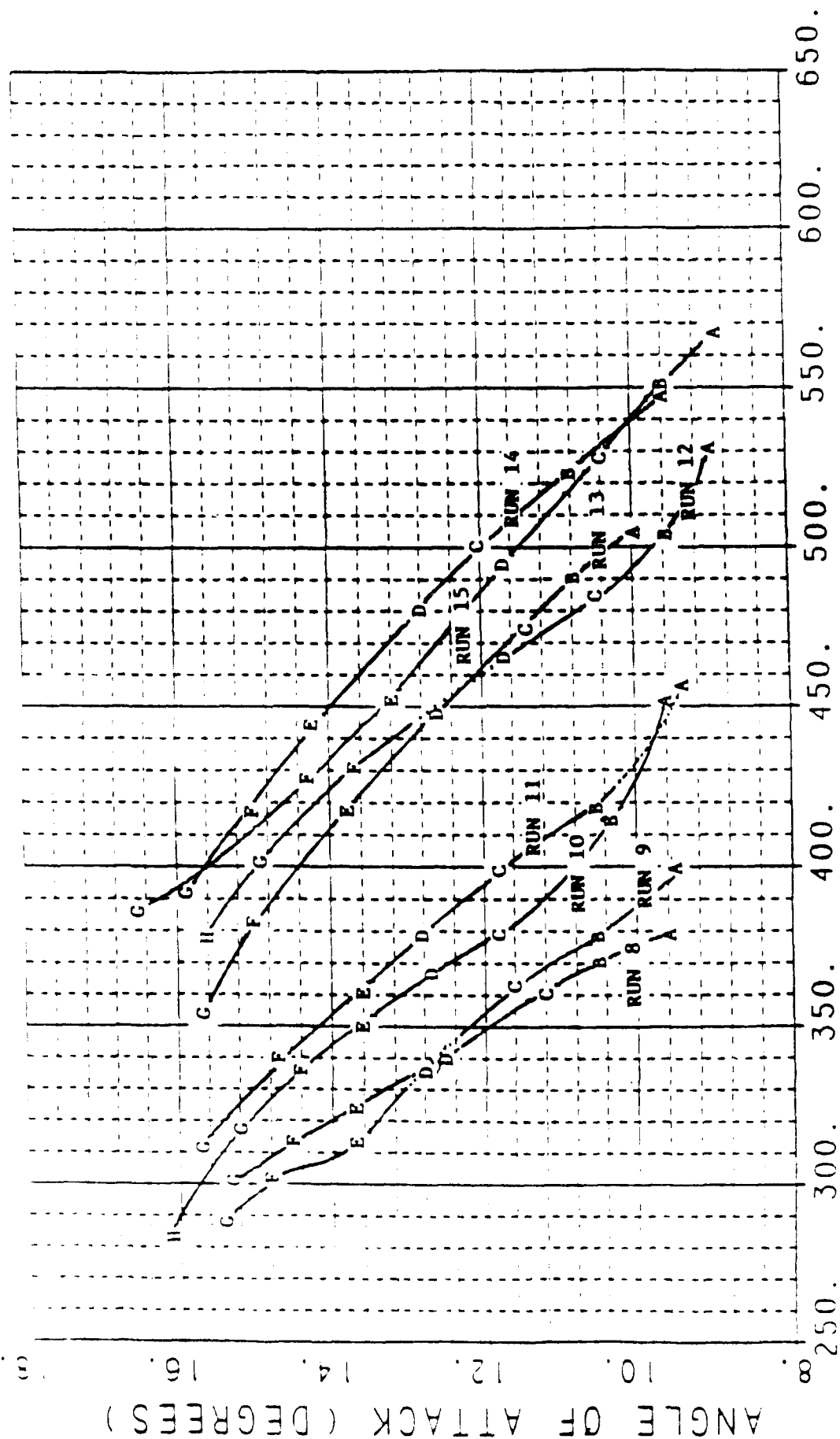


Figure 8. AOA vs Dynamic Pressure for F-15 Flight Conditions

F-15 UPPER OUTER WING SKIN LIFE EXTENSION

FLIGHT DATA PSD OF STRAIN GAGE

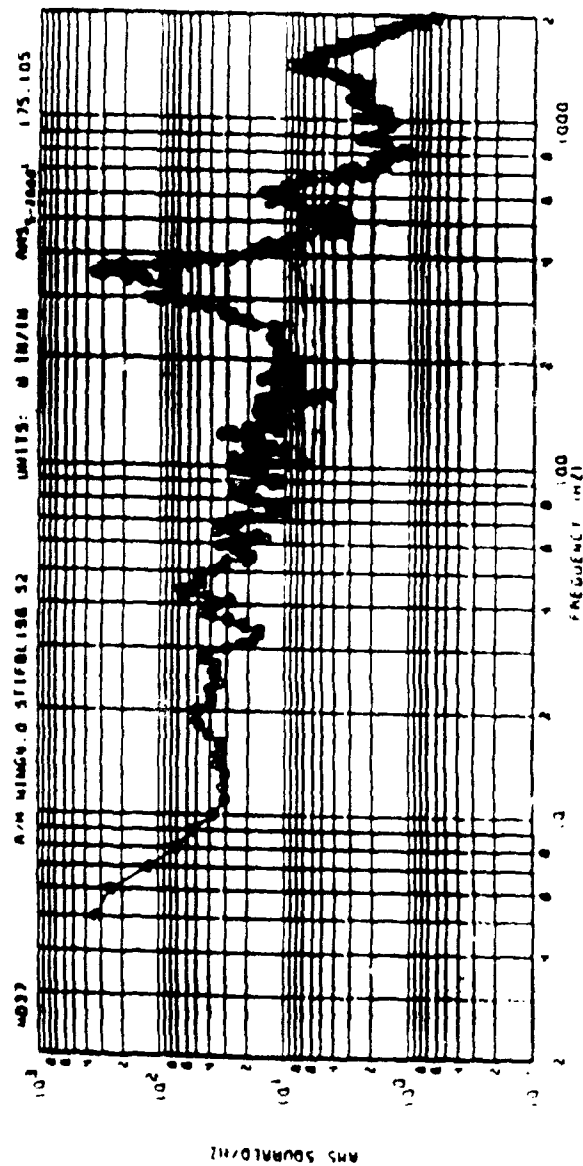


Figure 1. PSD of Strain Gage Flight Data

F-15 AIRCRAFT

GROSS WEIGHT = 42000 lbs

AOA = 12°

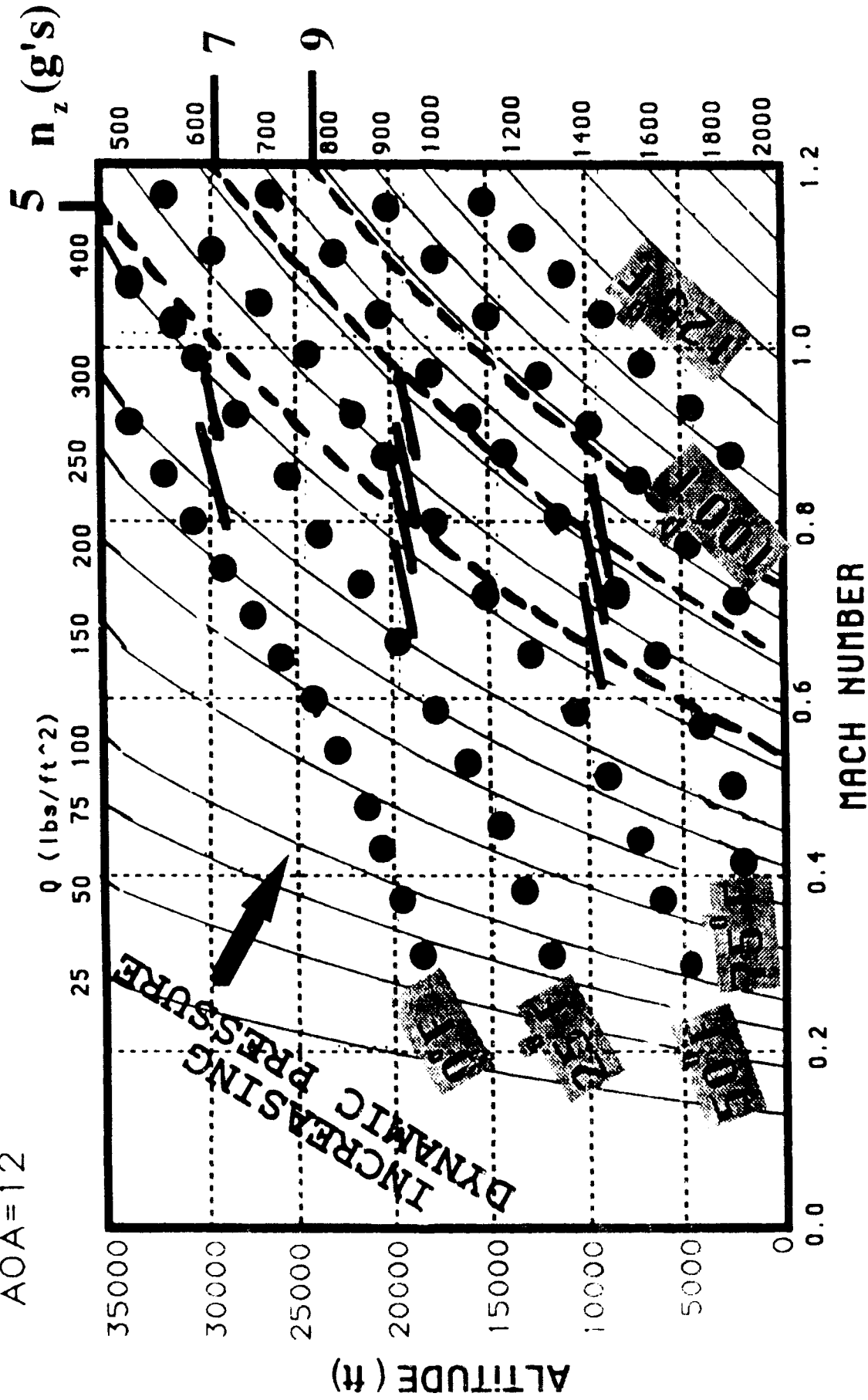


Figure 10. F-15 Flight Characteristics

F-15 UPPER OUTER WING SKIN

TEST CONFIGURATION 1

1980 DAMPING TREATMENT

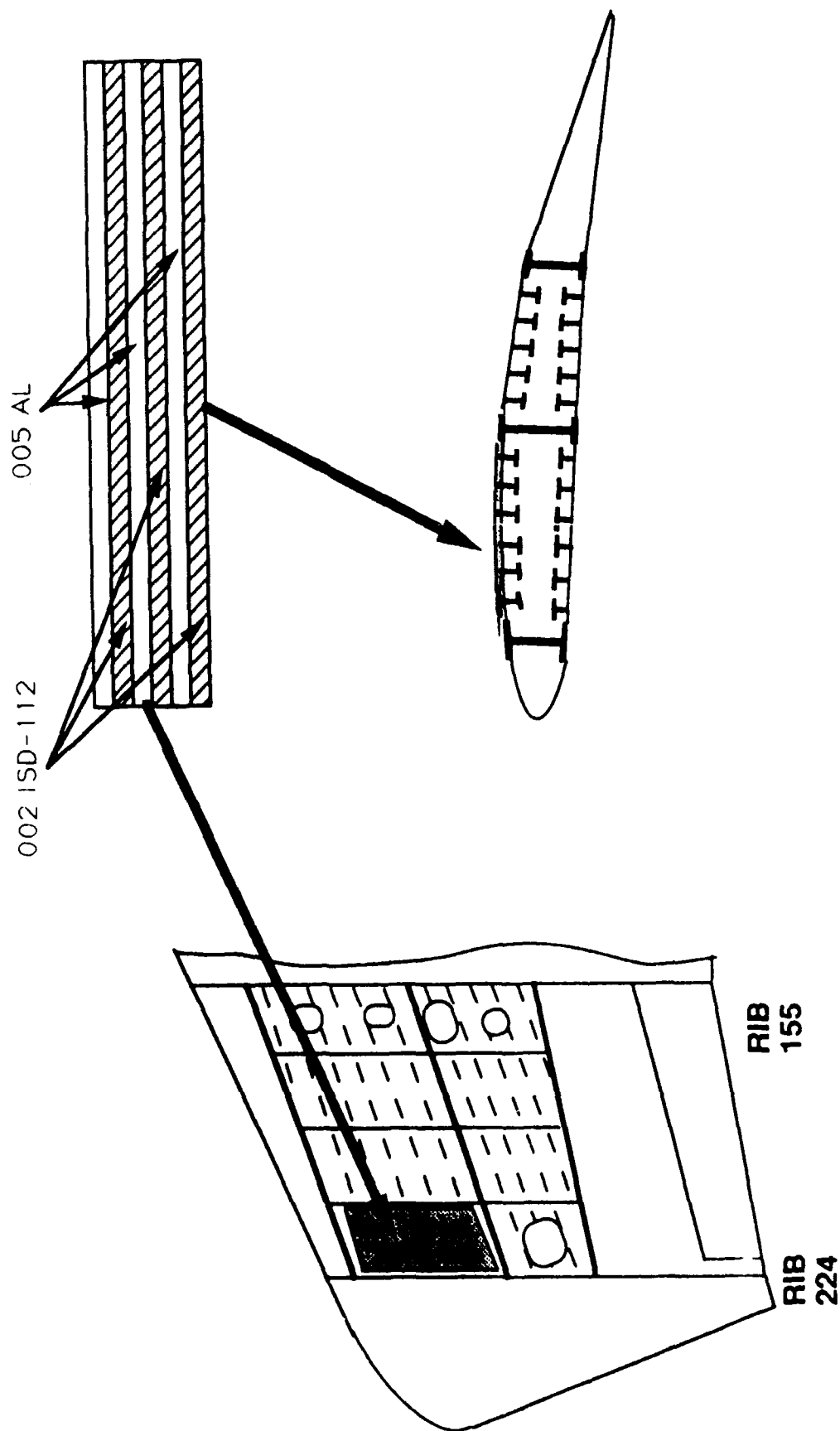


Figure 11. 1980 Damping Treatment

F-15 UPPER OUTER WING SKIN

RECOMMENDED EXTERNAL DAMPING TREATMENT

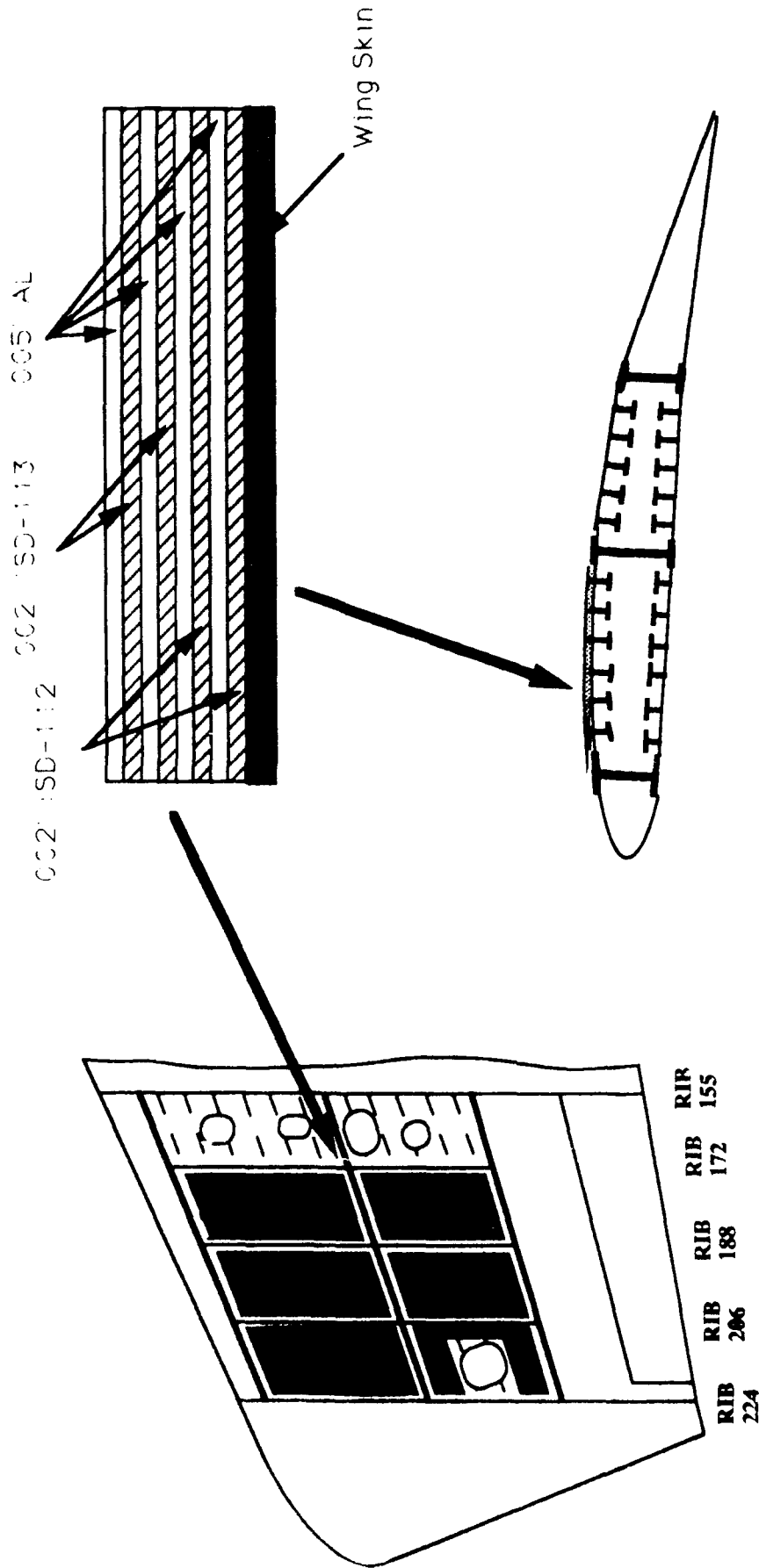


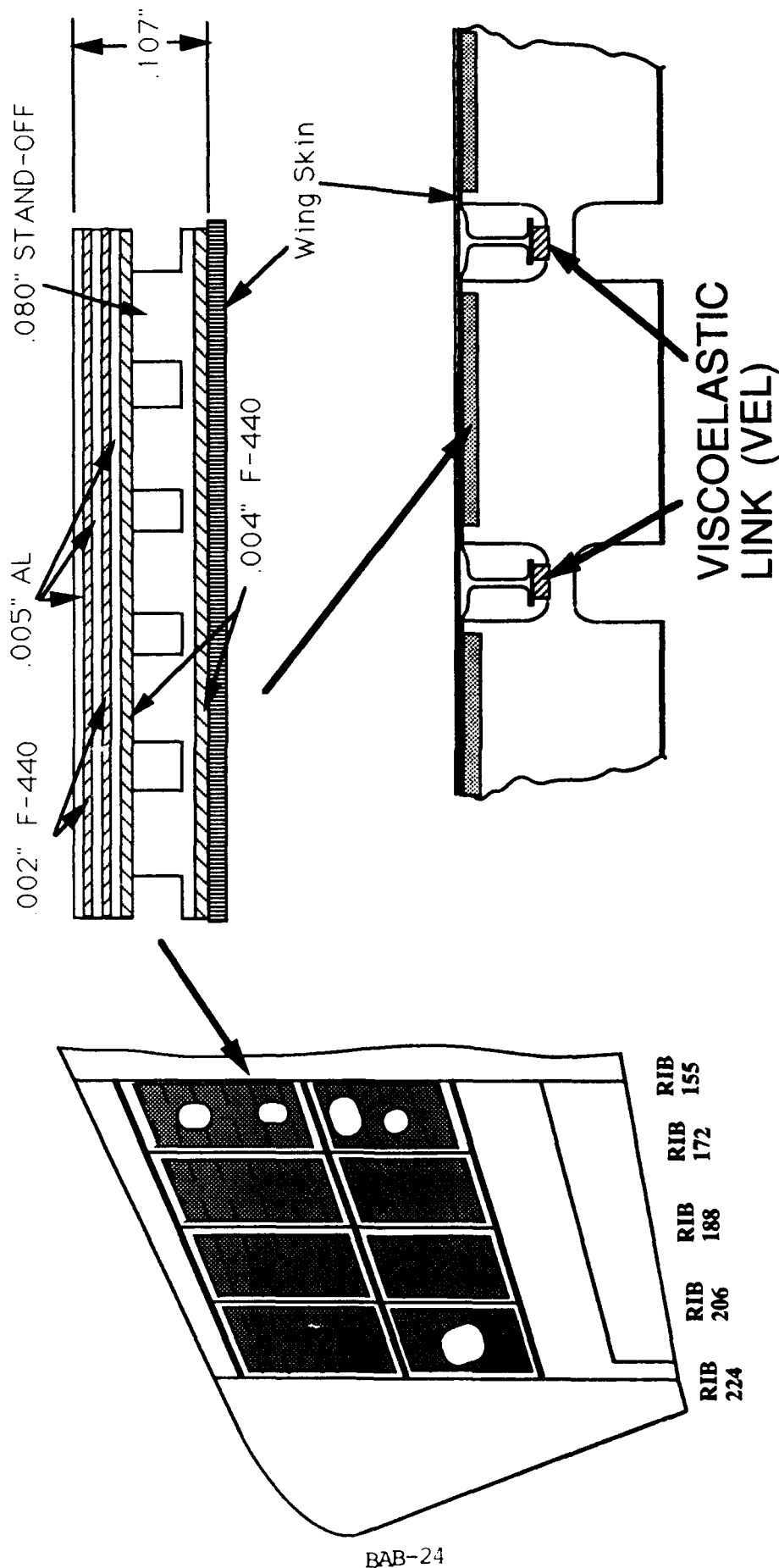
Figure 12. New External Damping Treatment



Ship's hull and rigging, 1940

F-15 UPPER OUTER WING SKIN

RECOMMENDED INTERNAL DAMPING TREATMENT

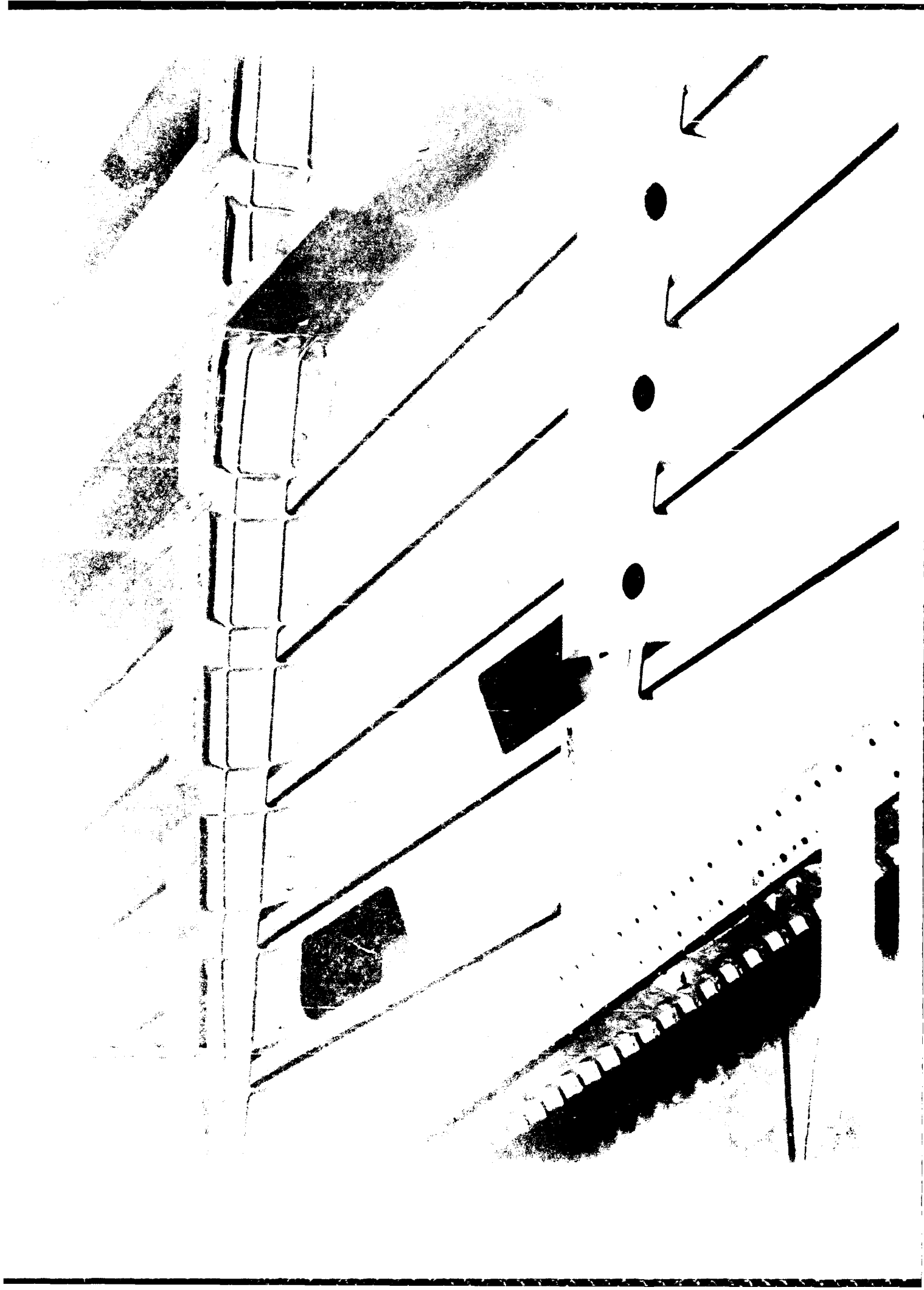


NOTE: DAMPING TREATMENT APPLIED TO INTERIOR SURFACE OF WING SKIN BETWEEN STIFFENERS.

NOTE: VEL APPLIED IN RIB NOTCH

Figure 14. New Internal Damping Treatment







F-15 WING DAMPING TREATMENT TEST

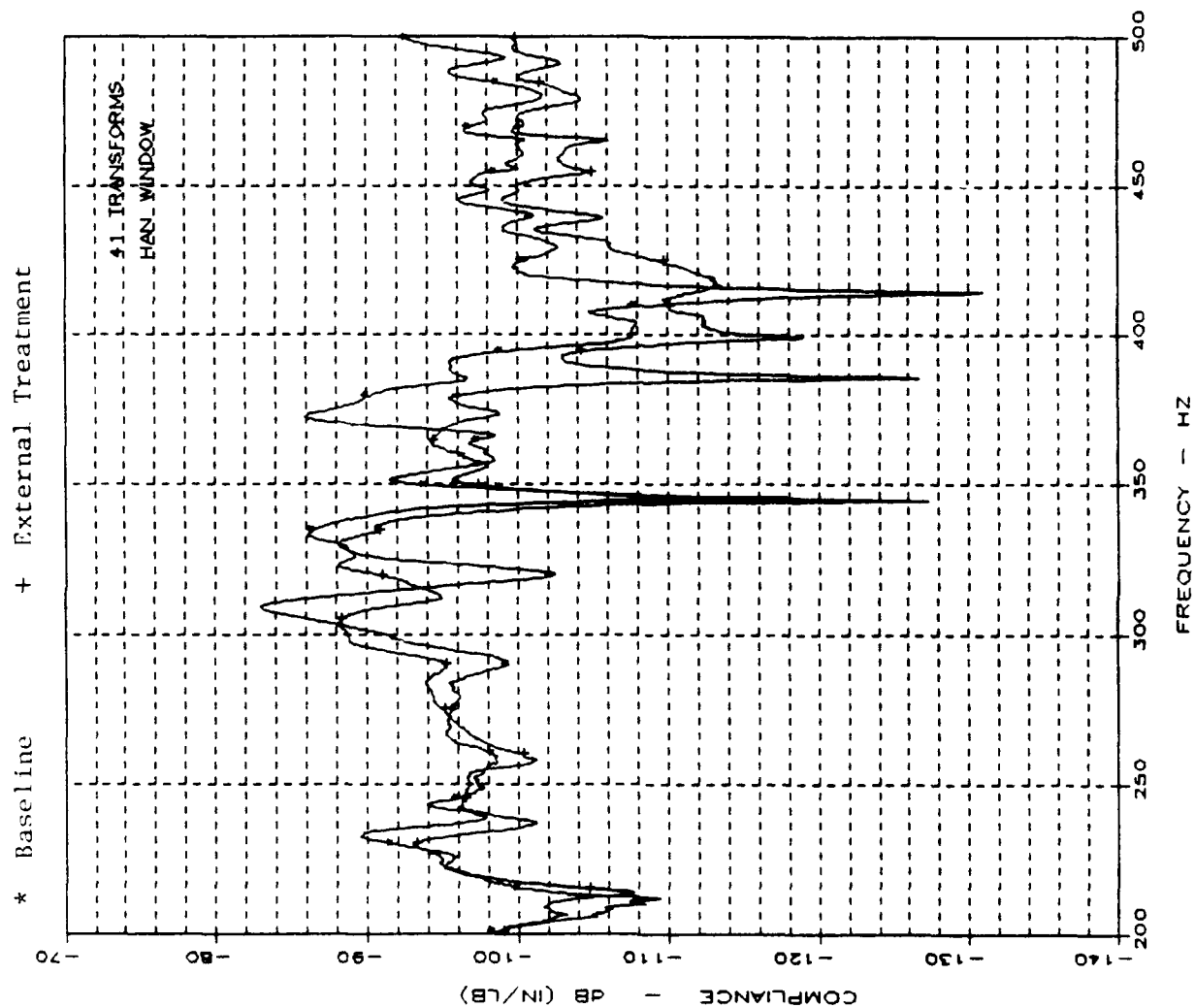


Figure 18. Comparison of Baseline UOWS and Externally Damped UOWS

F-15 WING DAMPING TREATMENT TEST

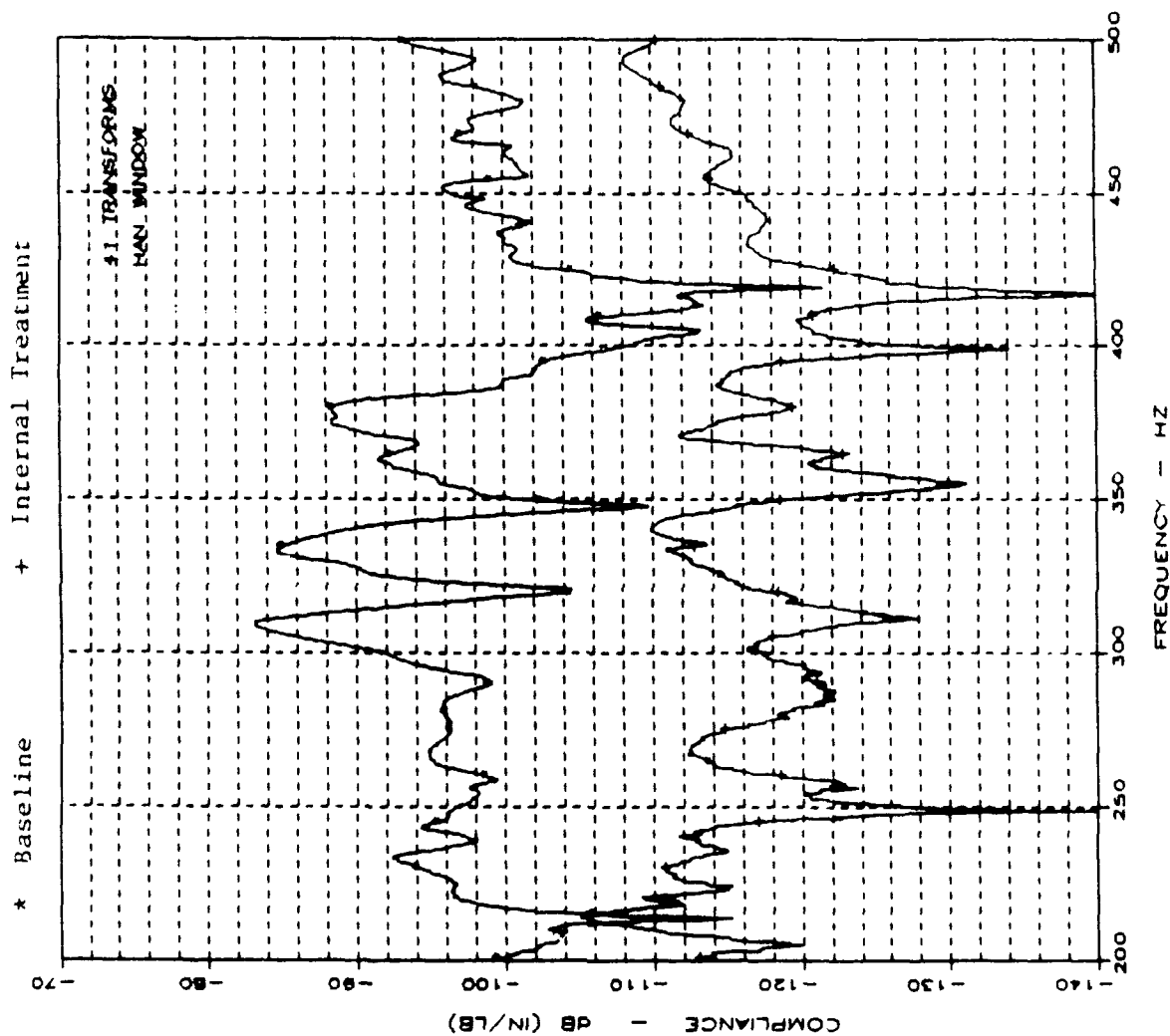


Figure 19. Comparison of Baseline UOWS and Internally Damped UOWS

F-15 UPPER OUTER WING SKIN LIFE EXTENSION

LIFE EXTENSION FACTOR CALCULATION

$$\text{Nd/Nu} = (\text{Sd/Su})^{-3.323}$$

WHERE

Nd = DAMPED LIFE

Nu = UNDAMPED LIFE

Sd = DAMPED STRESS

Su = UNDAMPED STRESS

Figure 20. Equation for Life Extension Calculation

DAMPING TREATMENTS FOR AIRCRAFT HARDMOUNTED ANTENNAE

Ralph E. Tate, Sr.¹
LTV Aircraft Products Group
Dallas, TX

Carl L. Rupert
LTV Aircraft Products Group (Ret.)
Dallas, TX

ABSTRACT

The Air Force Wright Research and Development Center's Aircraft Integral Damping Demonstration Program is being conducted by LTV to illustrate the advantages of incorporating damping into aircraft structure during the design phase of development. The present study deals with the important Band 6, 7, 8 antennae packages on the B-1B Aft Equipment Bay, where equipment failures are routinely occurring during take-off maneuvers at maximum afterburner throttle settings. That damage results from the intense vibroacoustical environment generated by the four three-stage afterburning engines. Failure rates have been sufficiently high to warrant a departure from the basic study to develop a "quick fix" solution involving add-on damping treatments, that can be installed in a short time with minimal modification to the existing structure.

The approach used in this program was to analyze operating ground test data that were generated on the antennae components, in conjunction with analytical models. Modal testing identified areas where damping treatments could be applied to reduce the resonant effects of the local system. Various treatments were developed, analyzed, and tested in situ on the aircraft. Thus, a cost effective and technically viable solution to acoustically induced failures was achieved.

FULL PAPER NOT AVAILABLE FOR PUBLICATION

¹Sr. Engineering Specialist, LTV Aircraft Products Group, P.O. Box 655907, M/S-194/26, Dallas, TX 75265-5907, (214) 266-8126

**EXAMINATION OF BOUNDARY CONDITIONS
FOR
SIXTH-ORDER DAMPED BEAM THEORY**

by
Ralph E. Tate
LTV Aircraft Products Group
Dallas, TX

ABSTRACT

The purpose of sixth-order beam theory is to include the effects of core shearing due to extentional deformation in terms of the transverse displacements. The constraint to eliminate the extentional motion reduces a twelfth-order system of equations into a single sixth-order equation.

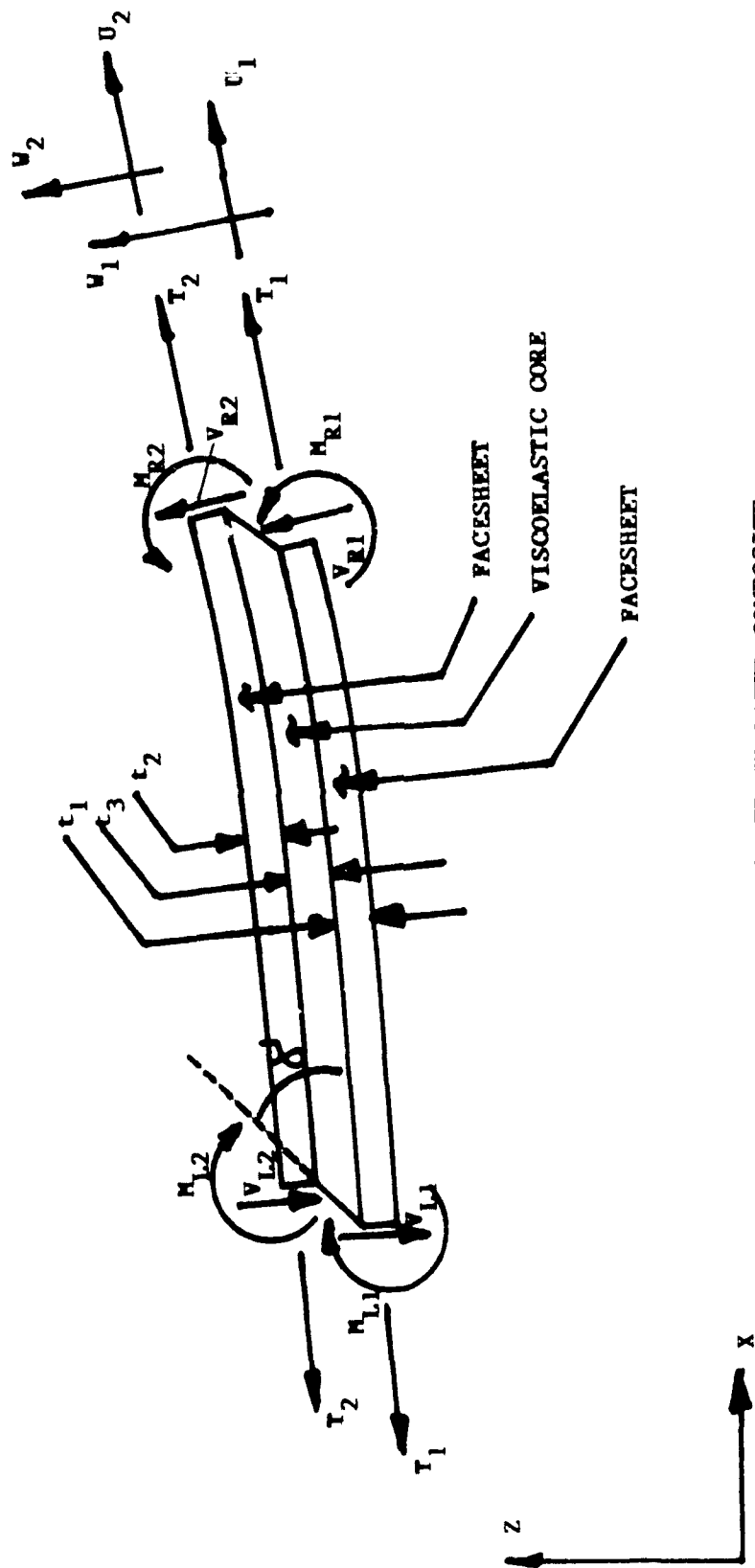
Since boundary conditions are necessary to completely specify the solution of partial differential equations, the author purposes to use this forum to present a detailed derivation of the sixth-order equation of motion using energy method techniques. The boundary conditions follow naturally as a consequence of the energy method formulation. The author show how two "natural" boundary conditions are lost, and must be replaced by two "kinematic" boundary conditions. The author interprets the boundary conditions and their consequences in the analysis of damped beams.

1.0 INTRODUCTION

Usage of constrained-layer damping composites for sound and vibration suppression originated in the 1950's, perhaps earlier[k]; however, the underlying theory was based on 4th-order beam theory and presumed no extensional deformation of the laminate. In order to include the extensional flexibility, several authors developed 6th-order beam and plate theories to describe the dynamic behavior of damped composite laminates [a,b,c,g,h,i]. The purpose of the 6th-order theories is to include the effects of core shearing due to the extension of the face sheets, in terms of the transverse bending displacements. The constraint to eliminate the extensional motion causes the equations of motion to be of 6th-order.

Dowell[h] and Miles[c] derive the laminate equations using an energy method approach to obtain the equations of motion. Dowell then retains terms only to 4th-order, since the adhesive shear layer is assumed stiff. The resulting boundary conditions are those found for 4th-order beam and plate theory. Dowell's formulation is useful in evaluating the interlaminar shear in fiber composites. Miles' obtains the 6th-order equations as a side discussion to validate his model; he does not elaborate on the boundary conditions required for solution for the 6th-order system. Miles study proceeds to thickness effects on damping.

Mead[a,b] and Abdulhadi[g] derive the equations of motion from a standard strength of materials perspective. This approach does not directly yield the boundary conditions as part of the formulation. Abdulhadi also does not articulate the boundary conditions necessary for solution: simply supported boundary conditions are presumed. Mead develops the boundary conditions and discusses the solutions for various boundary conditions. Maynor [j] numerically evaluated the effect of Mead's boundary conditions on loss factor estimates. He also observed that Abdulhadi deleted two boundary conditions in obtaining his solution. Essentially, Abdulhadi's equations of motion are equivalent to the 4th-order PKU equations [k]. Maynor delineated the difficulties and limitations in using the 6th-order equations.



FREE-BODY DIAGRAM FOR THREE-LAYER COMPOSITE

In the attached paragraphs, the 6th-order partial differential equation is obtained using energy methods. Subsequently, the boundary conditions are obtained. The limiting procedure shows how two "natural" boundary conditions are lost. Thus, two "kinematic" boundary conditions must be specified, that further reduce the generality of the 6th-order equation. The basic outline of the paper begins with the derivation of the equations of motions following Miles' assumptions, then validating the required boundary conditions used by Mead. The ramifications of those boundary conditions are discussed.

2.0 VARIATIONAL FORMULATION OF THE SIXTH-ORDER BEAM EQUATIONS

The sixth-order differential equation governing the vibration of a three layer sandwich beam will be derived using a variational approach. The beam geometry is depicted in the preceeding Figure.

The kinetic energy of a the vibrating beam is given by:

$$T = 1/2 \int_0^L \left[m_1 [(\dot{w}_1)^2 + (\dot{u}_1)^2] + m_2 [(\dot{w}_2)^2 + (\dot{u}_2)^2] \right] dx. \quad (2-1)$$

Similarly the elastic energy due to deflection of the constraining skin materials is given by:

$$V_s = 1/2 \int_0^L \left[(EI)_1 (w_1'')^2 + (EI)_2 (w_2'')^2 + (EA)_1 (u_1')^2 + (EA)_2 (u_2')^2 \right] dx. \quad (2-2)$$

The strain energy due to shearing of the adhesive core material is[d]:

$$V_a = 1/2 \int_0^L Gb \int_0^{t_3} \gamma^2 dz dx, \text{ where } \gamma = \frac{\partial w}{\partial x} + \frac{\partial u}{\partial z}. \quad (2-3)$$

The shear traction at the upper and lower surfaces of the adhesive is found to be:

$$\gamma_1 = w_1' + \left(\frac{t_1}{2t_3} \right) w_1' + \left(\frac{t_2}{2t_3} \right) w_2' + \left(\frac{u_1 - u_2}{t_3} \right). \quad (2-4a)$$

$$\gamma_2 = w_2' + \left(\frac{t_2}{2t_3} \right) w_2' + \left(\frac{t_1}{2t_3} \right) w_1' + \left(\frac{u_1 - u_2}{t_3} \right). \quad (2-4b)$$

The distributed shear strain throughout the adhesive thickness is:

$$\gamma = \gamma_1 + \tau \left(\frac{(\gamma_1 - \gamma_2)}{t_3} \right) \quad (2-5)$$

After substitution and integration over the thickness, the strain energy due to shearing of the adhesive is found to be:

$$V_s = 1/2 \int_0^L Gbt_3 \left\{ \gamma_1 \gamma_2 + \frac{(\gamma_2 - \gamma_1)^2}{3} \right\} dx \quad (2-6)$$

In order to apply Hamilton's Principle, the total energy in the vibrating beam is given as $Q = T - V_s - V_b + W_{nc}$, where

$$Q = \int_0^L F(\dot{u}_1, \dot{u}_2, \dot{w}_1, \dot{w}_2, u_1, u_2, w_1, w_2, u_1', u_2', w_1', w_2', w_1'', w_2''; x, t) dx. \quad (2-7)$$

Applying Hamilton's Principle, the variational of the energy is minimized, that is:

$$\delta J = \delta \int_1^2 Q(.) dt = 0.$$

Hence, the differential of $J(.)$ is:

$$\begin{aligned} \delta J = & \int_1^2 \left\{ \int_0^L \left[\left(\frac{\partial F}{\partial \dot{u}_1} \delta \dot{u}_1 + \frac{\partial F}{\partial u_1} \delta u_1 + \frac{\partial F}{\partial u_1'} \delta u_1' \right) \right. \right. \\ & + \left[\frac{\partial F}{\partial \dot{u}_2} \delta \dot{u}_2 + \frac{\partial F}{\partial u_2} \delta u_2 + \frac{\partial F}{\partial u_2'} \delta u_2' \right] + \left[\frac{\partial F}{\partial \dot{w}_1} \delta \dot{w}_1 + \frac{\partial F}{\partial w_1} \delta w_1 + \frac{\partial F}{\partial w_1'} \delta w_1' + \frac{\partial F}{\partial w_1''} \delta w_1'' \right] \\ & \left. \left. + \left[\frac{\partial F}{\partial \dot{w}_2} \delta \dot{w}_2 + \frac{\partial F}{\partial w_2} \delta w_2 + \frac{\partial F}{\partial w_2'} \delta w_2' + \frac{\partial F}{\partial w_2''} \delta w_2'' \right] \right] dx \right\} dt. \quad (2-8) \end{aligned}$$

After integration by parts, the integral appears as:

$$\begin{aligned} \delta J = & \int_1^2 \left(\int_0^L \left[\left(\frac{\partial F}{\partial u_1} - \frac{d}{dt} \left(\frac{\partial F}{\partial \dot{u}_1} \right) - \frac{d}{dx} \left(\frac{\partial F}{\partial u_1'} \right) \right) \delta u_1 + \left(\frac{\partial F}{\partial u_2} - \frac{d}{dt} \left(\frac{\partial F}{\partial \dot{u}_2} \right) - \frac{d}{dx} \left(\frac{\partial F}{\partial u_2'} \right) \right) \delta u_2 \right. \right. \\ & + \left[\frac{\partial F}{\partial w_1} - \frac{d}{dt} \left(\frac{\partial F}{\partial \dot{w}_1} \right) - \frac{d}{dx} \left(\frac{\partial F}{\partial w_1'} \right) + \frac{d^2}{dx^2} \left(\frac{\partial F}{\partial w_1''} \right) - P_1(x, t) \right] \delta w_1 \\ & \left. + \left[\frac{\partial F}{\partial w_2} - \frac{d}{dt} \left(\frac{\partial F}{\partial \dot{w}_2} \right) - \frac{d}{dx} \left(\frac{\partial F}{\partial w_2'} \right) + \frac{d^2}{dx^2} \left(\frac{\partial F}{\partial w_2''} \right) - P_2(x, t) \right] \delta w_2 \right] dx \\ & + \left[\frac{\partial F}{\partial u_1'} - T_1 \right]_{x=L} \delta u_1 + \left[\frac{\partial F}{\partial u_2'} - T_2 \right]_{x=L} \delta u_2 + \left[\frac{\partial F}{\partial w_1'} - \frac{d}{dx} \left(\frac{\partial F}{\partial w_1''} \right) - V_{R1} \right]_{x=L} \delta w_1 \\ & - \left[\frac{\partial F}{\partial w_1'} - \frac{d}{dx} \left(\frac{\partial F}{\partial w_1''} \right) + V_{L1} \right]_{x=0} \delta w_1 + \left[\frac{\partial F}{\partial w_2'} - \frac{d}{dx} \left(\frac{\partial F}{\partial w_2''} \right) - V_{R2} \right]_{x=L} \delta w_2 \quad (2-9) \end{aligned}$$

$$\begin{aligned}
& - \left[\frac{\partial F}{\partial w_2'} - \frac{d}{dx} \left(\frac{\partial F}{\partial w_2''} \right) + V_{L2} \right] \delta w_2 \Big|_{x=0} + \left[\frac{\partial F}{\partial w_1''} - M_{R1}' \right] \delta w_1' \Big|_{x=L} - \left[\frac{\partial F}{\partial w_1''} + M_{L1}' \right] \delta w_1' \Big|_{x=0} \\
& + \left[\frac{\partial F}{\partial w_2''} - M_{R2}' \right] \delta w_2' \Big|_{x=L} - \left[\frac{\partial F}{\partial w_2''} + M_{L2}' \right] \delta w_2' \Big|_{x=0} - \left[\frac{\partial F}{\partial u_1'} + T_1 \right] \delta u_1 \Big|_{x=0} - \left[\frac{\partial F}{\partial u_2'} + T_2 \right] \delta u_2 \Big|_{x=0} \Big| dt.
\end{aligned}$$

Equating each variational term to zero then yields the equations of motion and the required "natural" (or force-type) boundary conditions. Thus, the complete system of equations is found to be:

$$\begin{aligned}
\frac{\partial F}{\partial u_1} - \frac{d}{dt} \left(\frac{\partial F}{\partial \dot{u}_1} \right) - \frac{d}{dx} \left(\frac{\partial F}{\partial u_1'} \right) &= 0, \quad \frac{\partial F}{\partial u_2} - \frac{d}{dt} \left(\frac{\partial F}{\partial \dot{u}_2} \right) - \frac{d}{dx} \left(\frac{\partial F}{\partial u_2'} \right) = 0, \\
\frac{\partial F}{\partial w_1} - \frac{d}{dt} \left(\frac{\partial F}{\partial \dot{w}_1} \right) - \frac{d}{dx} \left(\frac{\partial F}{\partial w_1'} \right) + \frac{d^2}{dx^2} \left(\frac{\partial F}{\partial w_1''} \right) &= P_1(x, t), \\
\text{and } \frac{\partial F}{\partial w_2} - \frac{d}{dt} \left(\frac{\partial F}{\partial \dot{w}_2} \right) - \frac{d}{dx} \left(\frac{\partial F}{\partial w_2'} \right) + \frac{d^2}{dx^2} \left(\frac{\partial F}{\partial w_2''} \right) &= P_2(x, t)
\end{aligned} \tag{Eqns. 2-10}$$

The system is subject to the following boundary conditions:

$$\begin{aligned}
\frac{\partial F}{\partial u_1'} - T_1 \Big|_{x=L} &= 0, \quad \frac{\partial F}{\partial u_2'} - T_2 \Big|_{x=L} = 0, \quad \frac{\partial F}{\partial w_1'} - \frac{d}{dx} \left(\frac{\partial F}{\partial w_1''} \right) - V_{R1} \Big|_{x=L} = 0, \\
\frac{\partial F}{\partial w_1'} - \frac{d}{dx} \left(\frac{\partial F}{\partial w_1''} \right) + V_{L1} \Big|_{x=0} &= 0, \quad \frac{\partial F}{\partial w_2'} - \frac{d}{dx} \left(\frac{\partial F}{\partial w_2''} \right) - V_{R2} \Big|_{x=L} = 0, \\
\frac{\partial F}{\partial w_2'} - \frac{d}{dx} \left(\frac{\partial F}{\partial w_2''} \right) + V_{L2} \Big|_{x=0} &= 0, \quad \frac{\partial F}{\partial w_1''} - M_{R1}' \Big|_{x=L} = 0, \quad \frac{\partial F}{\partial w_1''} + M_{L1}' \Big|_{x=0} = 0, \\
\frac{\partial F}{\partial w_2''} - M_{R2}' \Big|_{x=L} &= 0, \quad \frac{\partial F}{\partial w_2''} + M_{L2}' \Big|_{x=0} = 0, \quad \frac{\partial F}{\partial u_1} + T_1 \Big|_{x=0} = 0, \quad \text{and } \frac{\partial F}{\partial u_2} + T_2 \Big|_{x=0} = 0.
\end{aligned} \tag{Eqns. 2-11}$$

The system is comprised of two fourth-order equations and two second-order equations. The twelve "natural" boundary conditions completely specify the solution. Hence, this set of differential equations is well-posed, as should be expected.

Next, the various partial derivatives of $F(\cdot)$ are derived:

$$\begin{aligned}
\frac{\partial F}{\partial \dot{u}_1} &= m_1 \dot{u}_1, \quad \frac{\partial F}{\partial \dot{u}_2} = m_2 \dot{u}_2, \quad \frac{\partial F}{\partial \dot{w}_1} = m_1 \dot{w}_1, \quad \frac{\partial F}{\partial \dot{w}_2} = m_2 \dot{w}_2, \quad \frac{\partial F}{\partial w_1''} = -(EI)_1 w_1'', \quad \frac{\partial F}{\partial w_2''} = -(EI)_2 w_2'', \\
\frac{\partial F}{\partial u_1'} &= -(EA)_1 u_1', \quad \frac{\partial F}{\partial u_2'} = -(EA)_2 u_2', \\
\frac{\partial F}{\partial u_1} &= -(1/2) Gb \left\{ (1+2\alpha_1) w_1' + (1+2\alpha_2) w_2' + 2 \left(\frac{u_1 - u_2}{t_3} \right) \right\}, \\
\frac{\partial F}{\partial u_2} &= (1/2) Gb \left\{ (1+2\alpha_1) w_1' + (1+2\alpha_2) w_2' + 2 \left(\frac{u_1 - u_2}{t_3} \right) \right\},
\end{aligned}$$

$$\frac{\partial F}{\partial w_1} = -(1/2) Gbt_3 \left\{ [2/3 + 2\alpha_1(1+\alpha_1)] w_1' + [-2/3 + (1+\alpha_1)(1+\alpha_2) + \alpha_1\alpha_2] w_2' + (1+2\alpha_1) \left(\frac{u_1 - u_2}{t_3} \right) \right\}, \text{ and}$$

$$\frac{\partial F}{\partial w_2} = -(1/2) Gbt_3 \left\{ [-2/3 + (1+\alpha_1)(1+\alpha_2) + \alpha_1\alpha_2] w_1' + [2/3 + 2\alpha_2(1+\alpha_2)] w_2' + (1+2\alpha_2) \left(\frac{u_1 - u_2}{t_3} \right) \right\}.$$

After substitution into the (2-10) and (2-11), the equations of motion for the system are obtained:

$$m_1 \ddot{w}_1 + (EI)_1 w_1^{(4)} - (1/2) Gbt_3 \left\{ [2/3 + 2\alpha_1(1+\alpha_1)] w_1'' + [-2/3 + (1+\alpha_1)(1+\alpha_2) + \alpha_1\alpha_2] w_2'' + (1+2\alpha_1) \left(\frac{u_1' - u_2'}{t_3} \right) \right\} = P_1(x, t), \quad (2-12a)$$

$$m_2 \ddot{w}_2 + (EI)_2 w_2^{(4)} - (1/2) Gbt_3 \left\{ [-2/3 + (1+\alpha_1)(1+\alpha_2) + \alpha_1\alpha_2] w_1'' + [2/3 + 2\alpha_2(1+\alpha_2)] w_2'' + (1+2\alpha_2) \left(\frac{u_1' - u_2'}{t_3} \right) \right\} = P_2(x, t), \quad (2-12b)$$

$$m_1 \ddot{u}_1 - (EA)_1 u_1'' - (1/2) Gb \left\{ (1+2\alpha_1) w_1' + (1+2\alpha_2) w_2' + 2 \left(\frac{u_1 - u_2}{t_3} \right) \right\} = 0, \quad (2-12c)$$

$$m_2 \ddot{u}_2 - (EA)_2 u_2'' + (1/2) Gb \left\{ (1+2\alpha_1) w_1' + (1+2\alpha_2) w_2' + 2 \left(\frac{u_1 - u_2}{t_3} \right) \right\} = 0. \quad (2-12d)$$

Correspondingly, the boundary conditions become:

$$(EI)_1 w_1^{(3)} - (1/2) Gbt_3 \left\{ [2/3 + 2\alpha_1(1+\alpha_1)] w_1' + [-2/3 + (1+\alpha_1)(1+\alpha_2) + \alpha_1\alpha_2] w_2' + (1+2\alpha_1) \left(\frac{u_1 - u_2}{t_3} \right) \right\} \Big|_{x=L} = V_{R1} \quad (2-13a)$$

$$(EI)_1 w_1^{(3)} - (1/2) Gbt_3 \left\{ [2/3 + 2\alpha_1(1+\alpha_1)] w_1' + [-2/3 + (1+\alpha_1)(1+\alpha_2) + \alpha_1\alpha_2] w_2' + (1+2\alpha_1) \left(\frac{u_1 - u_2}{t_3} \right) \right\} \Big|_{x=0} = -V_{L1} \quad (2-13b)$$

$$(EI)_2 w_2^{(3)} - (1/2) Gbt_3 \left\{ [-2/3 + (1+\alpha_1)(1+\alpha_2) + \alpha_1\alpha_2] w_1' + [2/3 + 2\alpha_2(1+\alpha_2)] w_2' + (1+2\alpha_2) \left(\frac{u_1 - u_2}{t_3} \right) \right\} \Big|_{x=L} = V_{R2} \quad (2-13c)$$

$$(EI)_2 w_2^{(3)} - (1/2) Gbt_3 \left\{ [-2/3 + (1+\alpha_1)(1+\alpha_2) + \alpha_1\alpha_2] w_1' + [2/3 + 2\alpha_2(1+\alpha_2)] w_2' + (1+2\alpha_2) \left(\frac{u_1 - u_2}{t_3} \right) \right\} \Big|_{x=0} = -V_{L2} \quad (2-13d)$$

$$\begin{aligned}
(EI)_1 w_1'' - M_{L1} \Big|_{x=L} &= 0 \quad (2-13e), & (EI)_2 w_2'' - M_{L2} \Big|_{x=L} &= 0 \quad (2-13f), \\
(EI)_1 w_1'' + M_{L1} \Big|_{x=0} &= 0 \quad (2-13g), & (EI)_2 w_2'' + M_{L2} \Big|_{x=0} &= 0 \quad (2-13h), \\
(EA)_1 u_1' - T_1 \Big|_{x=L} &= 0 \quad (2-13i), & (EA)_2 u_2' - T_2 \Big|_{x=L} &= 0 \quad (2-13j), \\
(EA)_1 u_1' + T_1 \Big|_{x=0} &= 0 \quad (2-13k), \text{ and } & (EA)_2 u_2' + T_2 \Big|_{x=0} &= 0 \quad (2-13l).
\end{aligned}$$

The procedure of Miles and Reinhall[c] will be followed to reduce the system of equations to sixth-order. First, the two bending equations are added, then the two longitudinal equations are subtracted, respectively:

$$\begin{aligned}
m_1 \ddot{w}_1 + m_2 \ddot{w}_2 + (EI)_1 w_1^{(4)} + (EI)_2 w_2^{(4)} \\
- (1/2) G b t_3 \left\{ [2/3 + 2\alpha_1(1+\alpha_1)] w_1'' + [-2/3 + (1+\alpha_1)(1+\alpha_2) + \alpha_1\alpha_2] w_2'' \right. \\
\left. + (1+2\alpha_1) \left(\frac{u_1' - u_2'}{t_3} \right) \right\} \\
- (1/2) G b t_3 \left\{ [-2/3 + (1+\alpha_1)(1+\alpha_2) + \alpha_1\alpha_2] w_1'' + [2/3 + 2\alpha_2(1+\alpha_2)] w_2'' \right. \\
\left. + (1+2\alpha_2) \left(\frac{u_1' - u_2'}{t_3} \right) \right\} \\
= P_1(x, t) + P_2(x, t) = P(x), \text{ and} \\
m_1 \ddot{u}_1 - m_2 \ddot{u}_2 - (EA)_1 u_1'' + (EA)_2 u_2'' \\
- (1/2) G b \left\{ (1+2\alpha_1) w_1' + (1+2\alpha_2) w_2' + 2 \left(\frac{u_1 - u_2}{t_3} \right) \right\} \\
- (1/2) G b \left\{ (1+2\alpha_1) w_1' + (1+2\alpha_2) w_2' + 2 \left(\frac{u_1 - u_2}{t_3} \right) \right\} = 0.
\end{aligned}$$

Now allowing $w_1 = w_2$, the equations reduce to:

$$D_t w^{(4)} - G b t_3 (1+\alpha_1+\alpha_2)^2 w^{(2)} - G b (1+\alpha_1+\alpha_2) (u_1' - u_2') = P'(x), \text{ and } (2-14a)$$

$$\left(\frac{u_1 - u_2}{t_3} \right) = -(1+\alpha_1+\alpha_2) w' + \left(\frac{(EA)_1 u_1'' - (EA)_2 u_2''}{2Gb} \right). \quad (2-14b)$$

$P'(x) = P(x) - (m_1 + m_2) \ddot{w}$. The effect of longitudinal inertia is also neglected. Since the each cross-section must remain balanced in tension, $(EA)_1 u_1' = -(EA)_2 u_2'$. Using this relation and after substituting (2-14b) into (2-14a)

the former, the following equations are obtained:

$$D_t w^{(4)} - Gbt_3(1+\alpha_1+\alpha_2)^2 w^{(2)} - Gb(1+\alpha_1+\alpha_2) \left(\frac{1}{(EA)_1} + \frac{1}{(EA)_2} \right) (EA)_1 u_1' = P'(x), \quad (2-15a)$$

and

$$D_t w^{(4)} - t_3 (EA)_1 (1+\alpha_1+\alpha_2) u_1^{(3)} = P'(x). \quad (2-15b)$$

The equations can be greatly simplified using two scale factors [D, C]:

$$G' = \frac{Gb}{t_3} \left(\frac{1}{(EA)_1} + \frac{1}{(EA)_2} \right), \text{ and } Y = \frac{t_3^2}{D_t} \left(\frac{(EA)_1 (EA)_2}{(EA)_1 + (EA)_2} \right); \text{ thus, } (2-16)$$

$$w^{(4)} - G' Y w^{(2)} - (G' t_3 / D_t) (1+\alpha_1+\alpha_2) u_1' = P'(x) / D_t, \text{ and } (2-17a)$$

$$w^{(4)} - [t_3 (EA)_1 / D_t] (1+\alpha_1+\alpha_2) u_1^{(3)} = P'(x) / D_t. \quad (2-17b)$$

The final step is to eliminate u_1 from the equations. This is accomplished by taking the second partial with respect to "x" of the first equation and multiplying the second equation by G' , then subtracting:

$$w^{(6)} - (1+Y)G' w^{(4)} = \frac{1}{D_t} \left(\frac{\partial^2 P'}{\partial x^2} - G' P' \right), \text{ or}$$

$$w^{(6)} - (1+Y)G' w^{(4)} + \frac{(m_1+m_2)}{D_t} \left(\frac{\partial^2 \ddot{w}}{\partial x^2} - G' \ddot{w} \right) = \frac{1}{D_t} \left(\frac{\partial^2 P}{\partial x^2} - G' P \right) \quad (2-18) //.$$

The corresponding reduction in the boundary conditions follows in the following section.

3.0 BOUNDARY CONDITIONS FOR THE SIXTH-ORDER BEAM EQUATIONS

The procedure for reducing combining the boundary conditions follows the same prescription as above. After adding the shear terms together, the boundary equations become ($w_1 = w_2$):

$$D_t w^{(3)} - Gbt_3(1+\alpha_1+\alpha_2)^2 w' - Gb(1+\alpha_1+\alpha_2)(u_1 - u_2) \Big|_{x=L} = V_R = V_{R1} + V_{R2}, \text{ and } (3-1)$$

$$D_t w^{(3)} - Gbt_3(1+\alpha_1+\alpha_2)^2 w' - Gb(1+\alpha_1+\alpha_2)(u_1 - u_2) \Big|_{x=0} = -V_L = -V_{L1} - V_{L2}. (3-2)$$

The following equation is valid throughout the beam and can be shown to be equivalent to the extentional boundary conditions (after a lot of work):

$$\left(\frac{u_1 - u_2}{t_3} \right) \Big|_0^L = -(1+\alpha_1+\alpha_2)w' + \left(\frac{(EA)_1 u_1'' - (EA)_2 u_2''}{2Gb} \right) \Big|_0^L. (3-3)$$

Since the procedure is identical for both equations, the derivation will proceed using only the first equation. After direct substitution of the extentional terms, the boundary condition becomes:

$$w^{(3)} - [t_3(1+\alpha_1+\alpha_2)/D_t](EA)_1 u_1'' \Big|_{x=L} = V_R/D_t. (3-4)$$

Taking the second derivative of (3-1) yields:

$$w^{(5)} - G'Yw^{(3)} - [G't_3(1+\alpha_1+\alpha_2)/D_t](EA)_1 u_1'' \Big|_{x=L} = 0. (3-5)$$

Eliminating the u_1 from the preceeding equation:

$$-w^{(5)} + (1+Y)G' w^{(3)} \Big|_{x=L} = (G'/D_t) V_R. (3-6)$$

Thus, the set "natural" boundary conditions become[a,b]:

$$-w^{(5)} + (1+Y)G' w^{(3)} \Big|_{x=L} = (G'/D_t) V_R. (3-7a)$$

$$-w^{(5)} + (1+Y)G' w^{(3)} \Big|_{x=0} = - (G'/D_t) V_L, (3-7b)$$

$$D_t w'' - M_R' \Big|_{x=L} = 0 \text{ (3-7c), and } D_t w'' + M_L' \Big|_{x=0} = 0 \text{ (3-7d).}$$

Analogously, the moment boundaries are evaluated. Again, right hand boundary alone will be evaluated, since the process for the left hand is identical. Thus, the moment equation becomes:

$$D_t w'' - (M_{R1} + M_{R2}) - \frac{(T_1 - T_2) t_3 (1 + \alpha_1 + \alpha_2)}{2} \Big|_{x=L} = 0. \quad (3-10)$$

After substituting for T_1 and T_2 , the resulting equation is:

$$D_t w'' - M_R - \frac{[(EA)_1 u_1' - (EA)_2 u_2'] t_3 (1 + \alpha_1 + \alpha_2)}{2} \Big|_{x=L} = 0, \text{ or } (3-11a)$$

since $(EA)_1 u_1' = -(EA)_2 u_2'$ throughout the beam, the equation reduces to,

$$D_t w'' - M_R - (EA)_1 u_1' [t_3 (1 + \alpha_1 + \alpha_2)] \Big|_{x=L} = 0. \quad (3-11b)$$

Taking the second partial derivative with respect to "x" of (3-11a) yields:

$$D_t w^{(4)} - M_R - \frac{[(EA)_1 u_1^{(3)} - (EA)_2 u_2^{(3)}] t_3 (1 + \alpha_1 + \alpha_2)}{2} \Big|_{x=L} = 0. \quad (3-12)$$

Substituting (3-3), this equation becomes:

$$D_t w^{(4)} - Gbt_3 (1 + \alpha_1 + \alpha_2)^2 w'' - Gb(1 + \alpha_1 + \alpha_2) (u_1' - u_2') \Big|_{x=L} = 0. \quad (3-13)$$

This can be re-written as:

$$D_t w^{(4)} - Gbt_3 (1 + \alpha_1 + \alpha_2)^2 w'' - Gb(1 + \alpha_1 + \alpha_2) \left(\frac{1}{(EA)_1} + \frac{1}{(EA)_2} \right) (EA)_1 u_1' \Big|_{x=L} = 0. \quad (3-14)$$

After applying the scale factors,

$$D_t w^{(4)} - G'Y w^{(2)} - [G't_3 (1 + \alpha_1 + \alpha_2)/D_t] (EA)_1 u_1' = 0. \quad (3-15)$$

Eliminating u_1 using (3-11b), the moment boundary condition reduces to:

$$M_R = \frac{D_t}{G'} \left(-w^{(4)} + (1 + G') w^{(2)} \right) \Big|_{x=L}. \quad (3-16)$$

Thus, the set of "natural" boundary conditions become:

$$-w^{(5)} + (1+Y)G' w^{(3)} \Big|_{x=L} = (G'/D_t) V_R, \quad (3-17a)$$

$$-w^{(5)} + (1+Y)G' w^{(3)} \Big|_{x=0} = -(G'/D_t) V_L, \quad (3-17b)$$

$$M_R = \frac{D_t}{G'} \left(-w^{(4)} + (1+G') w^{(2)} \right) \Big|_{x=L}, \text{ and} \quad (3-17c)$$

$$M_L = - \frac{D_t}{G'} \left(-w^{(4)} + (1+G') w^{(2)} \right) \Big|_{x=0}. \quad (3-17d)$$

These force-type boundary conditions agree with those obtained by Mead and Markus [a,b]. Only four "natural" boundary conditions now remain to specify the sixth-order equation. Thus, it is necessary to specify two addition "kinematic" constraints; otherwise, the problem is not well-posed. Representative "kinematic" constraints are:

clamped-free-

$$w_R = w_R' = 0 \text{ or } w_L = w_L' = 0, \quad (3-18a)$$

simply supported-

$$w_R = w_L = 0, \quad (3-18b)$$

simple-roller-

$$w_R = w_L' = 0 \text{ or } w_R' = w_L = 0, \text{ and} \quad (3-18c)$$

no rotation-

$$w_R' = w_L' = 0. \quad (3-18d)$$

Mead [a] discusses other exotic boundary conditions that are permutations of the above "natural" and "kinematic" end conditions through relaxing the various boundary tractions.

4.0 DISCUSSION/OBSERVATION

The equations of motion and associated boundary conditions for a three-layer composite laminate were derived in Section 2.0 (Eqns. 2-12a thru 2-13l). The "natural" or force type boundary conditions are a consequence of the energy method formulation [e,1]. That system of equations is of twelfth-

order and the solution is completely specified by the "natural" boundary conditions; thus, the equations of motion are well-posed. Consequently, since the system solution is completely specified by its "natural" boundary conditions, the formulation can be employed in the analysis of built-up structures (eg. a finite element analysis), albeit cumbersome. The existence of all "natural" boundary conditions permits the universal satisfaction of internal compatibility conditions required in a finite element type solution. Miles and Reinhall [c] proceed to perform an assumed modes solution to examine the thickness deformations in a three-layer composite. Their studies showed that thickness deformation is an important damping mechanism, especially in higher order modes.

The twelfth-order system was reduced to a single sixth-order partial differential equation (2-18), as shown in Section 2.0. By a similar process, the "natural" boundary conditions are reduced to four in number (3-17a thru 3-17d). Both the boundary conditions and the sixth-order equations agree with those derived by Mead [a,b].

The point to be observed here is that only four "natural" boundary conditions remain to specify the solution of a sixth-order differential equations; that is, a deficit of two differential equations. By constraining the extensional degrees of freedom (3-3), two boundary conditions are lost. Thus, two geometric or "kinematic" boundary conditions must be specified for the solution to be well-posed. Several possible "kinematic" boundary conditions are provided in Section 3.0 (3-18a thru 3-18d) to augment the "natural" boundary conditions. Mead discusses other admissible boundary conditions [a, b].

Since the sixth-order partial differential equation cannot be completely specified by the "natural" boundary conditions, a complex built-up structure cannot be modelled. Only simple structures (eg. single span beams and plates) can be evaluated. For example, element compatibility conditions in a finite element formulation cannot be universally satisfied without the imposition of a "kinematic" constraint; thus, the type of structure evaluated is limited, that is a general sixth-order beam or plate finite element cannot be

formulated.

Further, Mead demonstrated that all solutions to the sixth-order equation are complex-valued functions, with the sole exception of the case with simply supported boundaries. (The solution to the simply supported case is a real-valued function. This case can be further reduced to the standard RKU equations [c, k].) Thus, computationally, the sixth-order equation is effectively a twelfth-order system. No gain in computational efficiency is obtained.

The principal benefit derived from the sixth-order equation is when the relative extensional motion of the face sheets becomes significant, that is when one or both of the face sheets possess a low stiffness relative to the core shear stiffness. In this case, Maynor [j] has shown that numerical solution is neither particularly easy nor necessarily guaranteed. For the majority of engineering applications, a fourth-order (RKU) formulation is adequate to describe the dynamic behavior of damped laminate beams and plates [j].

5.0 SUMMARY

The author has presented a detailed derivation of the sixth-order beam equation and attendant boundary conditions. The author has shown how these boundary conditions naturally arise as a consequence of the variational energy method approach. The author shows how the boundary conditions vanish as a result of constraining the extensional motion of the face sheets, thereby requiring the imposition of "kinematic" constraints for a well-posed solution. These additional restraints restrict the types of structures which can be evaluated using the sixth-order equation. A useful modification to these boundary conditions is the inclusion of damping into the boundary conditions [m]. Inman has observed that such terms in the boundary conditions are important in the mechanics of line-of-sight/slewing or pointing/control applications of articulating structures.

REFERENCES

- a) DJ Mead and S Markus, "The Forced Vibration of a Three-Layer Damped Sandwich Beam with Arbitrary Boundary Conditions", J. Sound and Vibration, (1969) 10 (2), pp 163-175.
- b) DJ Mead and S Markus, "Loss Factors and Resonant Frequencies of Encastre' Damped Sandwich Beams", J. Sound and Vibration, (1970) 12 (1), pp 99-112.
- c) RN Miles and PG Reinhall, "An Analytical Model for the Vibration of Laminated Beams Including the Effects of Both Shear and Thickness Deformation in the Adhesive Layer", J. of Vibration, Acoustics, Stress and Reliability in Design, ASME, Vol. 108, January 1986.
- d) SP Timoshenko and JM Goodier, Mechanics of Materials, M^cGraw-Hill, NY(1972).
- e) HL Langhaar, Energy Methods in Applied Mechanics, John Wiley, NY(1962).
- f) IM Gel'fand, SV Fomin and RA Silverman (tr.), Calculus of Variations, Prentice-Hall, Englewood Cliffs, NJ(1963).
- g) F Abdulhadi, "Transverse Vibrations of Laminated Plates with Viscoelastic Layer Damping", Shock and Vibration Bulletin, 40(5), December 1969.
- h) EH Dowell and M-J Yan, "Governing Equations for Vibrating Constrained-Layer Damping Sandwich Plates and Beams", J. of Applied Mechanics, ASME, Vol. 94, December 1972.
- i) RA DiTaranto, "Theory of the Vibratory Bending for Elastic and Viscoelastic Finite Length Beams", J. of Applied Mechanics, ASME, Vol. 32, 1965.
- j) JW Maynor, "INTERIM PROGRESS REPORT - The Effect of End Fixity on Loss Factors Obtained Using Abdulhadi's Equation", LTV 9-51240/7AVO-054, Dtd. 31 July 1987.

JW Maynor, "FINAL REPORT - The Effect of End Fixity on Loss Factors Obtained Using Abdulhadi's Equations", LTV 9-51240/7AVO-111, Dtd. 18 December 1987.
- k) L Cremer, M Heckl, and EE Ungar(tr.), Structure-Borne Sound, 2nd Ed., Springer-Verlag, Berlin(1988).
- l) RR Craig, Structural Dynamics: An Introduction to Computer Methods, Wiley, New York(1981).
- m) DJ Inman, Vibration with Control, Measurement, and Stability, Prentice Hall, Englewood Cliffs, NJ (1989).

The Effect of Compliant Layering on Damped Beams

David John Barrett

Advanced Structures Technology Branch (Code 6043)
Naval Air Development Center
Warminster, Pa. 18974-5000
(215) 441-3770

ABSTRACT

This paper reports the results of an analytical investigation into the effects of compliant layering on damped beams. The beams consist of laminated face sheets sandwiching a single damping layer. Compliant layering is introduced into this construction by making the extensional modulus of the inner layers of the face sheets substantially less than that of the outer layers. The analytical model, that is used to determine the mechanical response of this type of structure, is based upon a generalization of constrained layer theory. The analysis predicts that compliant layering can be used to reduce the forced response and improve the modal damping.

March 12, 1991

1.0 INTRODUCTION

Damping treatments for bending components typically consist of adjacent layers of stiffness and damping materials. In these components the damping layers are sandwiched by the stiffness layers so that, when the stiffness layers deform under transverse loads, their bending will shear the damping layers. Because of their viscosity, the damping layers convert part of the strain energy of shearing into heat and thereby provide a means for dissipating the energies of shock and vibration [1, 2].

Any design approach that increases the rate or amount of shearing in the damping layers has the potential of improving the structural damping. Compliant layering, which in a layered design is the direct substitution of compliant material for stiffness material, offers such a possibility. The stiffness layers of conventional damping treatments consist of either monolithic isotropic, laminated quasi-isotropic or laminated unidirectional materials. This design practice results in in-plane moduli that are essentially constant over the depth of the stiffness layer. In these designs compliant layering would replace that part of the stiffness material that is adjacent to the damping layer with a material of lesser modulus. The in-plane modulus would no longer be constant over the stiffness layer and the in-plane extensional stiffness would be reduced. The hypothesis to be examined in this paper is that, under cyclic vibration, the use of compliant layers to reduce the in-plane extensional stiffness of damped treatments allows the stiffness layers on either side of the damping layer to undergo greater in-plane translations. This increases the rate of core shearing and thereby leads to higher levels of energy dissipation.

In a previous work [3, 4] a lamination theory was formulated that is applicable to a general class of damped bending structures, including structures with compliant layering. The lamination theory was used to examine the effects of stress coupling, lamination and compliant layering on damped plates. Here the original analytical theory is reduced for application to damped beams. Relevant parts of the previous analytical results are repeated and expanded here for the study of compliant layering in damped beams.

2.0 OUTLINE OF THE FORMULATION

The analytical model is a damped beam consisting of top and bottom face sheets sandwiching a single damping layer (see Figure 1). The face sheets are layered with a total of N^T layers in the top face sheet and N^B layers in the bottom face sheet. The thicknesses of the individual layers are designated by t_n^T for the top layers, t_n^B for the bottom layers and t^D for the damping layer. (Here the subscript n identifies individual stiffness layers while the superscripts T (top), D (damping), and B (bottom) refer to specific parts of the structure). The global coordinate system shown in Figure 1 and used in the development consists of the axial coordinate x_1 which is located in the mid surface of the damping layer (the reference surface), and the transverse coordinate x_2 .

To analytically model this structure the following assumptions are made:

1. The in-plane deformations of the face sheets vary linearly through the face sheet thickness;
2. The in-plane deformations of the damping layer vary linearly through it's thickness;
3. The in-plane displacement fields are continuous across the interfaces (perfect bonding);
4. The transverse displacement is the same for all parts of the cross section.
5. The moduli of all of the materials of construction can be treated by the Complex Modulus model;
6. The material model for the stiffness layers is transversely isotropic but neglects the thickness normal stresses. The axis of isotropy is parallel to the mid-surface;
7. The material model for the damping layer is isotropic but neglects all of the normal stresses.

Using assumptions 1 through 4, the motion of the structure can be expressed in terms of five displacement degrees of freedom (see Figure 2). These degrees of freedom are the reference surface displacements (u_1^0 and u_3^0), the rotation of the damping layer about the reference surface (α_1^D), and the rotations of the top and bottom face sheets (α_1^T and α_1^B). The degrees of freedom of this structural model are therefore a generalization of those found in constrained layer theory in that the top and bottom face sheets are allowed to rotate independently.

The displacements in terms of the degrees of freedom are

Top Face Sheet

$$u_1 = u_1^0(x_1, \tau) + \frac{1}{2}t^D \alpha_1^D(x_1, \tau) + (x_3 - \frac{1}{2}t^D) \alpha_1^T(x_1, \tau) \quad (1)$$

Damping Layer

$$u_1 = u_1^0(x_1, \tau) + x_3 \alpha_1^D(x_1, \tau) \quad (2)$$

Bottom Face Sheet

$$u_1 = u_1^0(x_1, \tau) - \frac{1}{2}t^D \alpha_1^D(x_1, \tau) + (x_3 + \frac{1}{2}t^D) \alpha_1^B(x_1, \tau) \quad (3)$$

Complete Construction

$$u_3 = u_3^0(x_1, x_2, \tau) \quad (4)$$

where the symbol τ is used to refer to the time variable. From these assumed displacements, the strain fields are computed using the strain-displacement equations. The stress fields are then found by applying the constitutive laws.

The equations of motion for the damped beam structure are derived using Hamilton's Principle in conjunction with Reissner's Variational Theorem. Since Hamilton's Principle is only applicable to conservative systems, the material properties

are initially treated as being purely elastic without any damping. The energy integrals, the integrands of which are formed from the field variables, are then minimized for this provisional, fully elastic system. The stress resultants are included by performing the thickness integration of these integrals. Taking the variation of the integrals with respect to the generalized displacements and forces and setting the coefficients of like variations to zero yields the governing system of differential equations. These equations include the force-displacement relations, the boundary conditions and the following equations of motion

$$-F_{11,1}^I - F_{11,1}^B - P_1 + M\ddot{u}_1^0 + I_1^D \ddot{\alpha}_1^D + I_1^I \ddot{\alpha}_1^I + I_1^B \ddot{\alpha}_1^B = 0 \quad (5)$$

$$-F_{13,1}^I - F_{13,1}^B - F_{13,1}^D - P_3 + M\ddot{u}_3^0 = 0 \quad (6)$$

$$\frac{1}{2} I^D (-F_{11,1}^I + F_{11,1}^B) + F_{13}^D + I_1^D \ddot{u}_1^0 + I_2^D \ddot{\alpha}_1^D + I_2^I \ddot{\alpha}_1^I + I_2^B \ddot{\alpha}_1^B = 0 \quad (7)$$

$$\frac{1}{2} I^D (-F_{11,1}^I + F_{11,1}^B) - M_{11,1}^I + I_1^I \ddot{u}_1^0 + I_2^I \ddot{\alpha}_1^D + I_3^I \ddot{\alpha}_1^I = 0 \quad (8)$$

$$-\frac{1}{2} I^D (-F_{11,1}^I + F_{11,1}^B) - M_{11,1}^B + I_1^B \ddot{u}_1^0 + I_2^B \ddot{\alpha}_1^D + I_3^B \ddot{\alpha}_1^B = 0 \quad (9)$$

in which the F_{ij}^I , F_{ij}^D , F_{ij}^B , M_{11}^I , M_{11}^D and M_{11}^B are the face sheet and damping layer force and moment stress resultants, the P_i are the applied tractions and the M , I_1^D , etc., are inertial constants.

At this point the force-displacement relations are substituted into the equations of motion. This yields a set of five displacement-equilibrium equations the unknowns of which are the five functional displacement degrees of freedom. Solutions to specific problems are found by applying the appropriate set of boundary conditions and solving these equations. In matrix notation these equations take the form

$$[M][\ddot{u}] + [D][u] = [P] \quad (10)$$

where $[M]$ is the mass matrix, $[D]$ is a differential operator matrix, $[u]$ is a vector of unknown displacement functions and $[P]$ is a load vector.

Once an elastic solution is obtained, damping can be introduced by invoking the Correspondence Principle in which the elastic moduli are replaced by the complex viscoelastic moduli of the Complex Modulus model. Application of the damped beam model is therefore limited to steady state harmonic vibrations.

3.0 SOLUTION FOR SIMPLY SUPPORTED BEAMS

Consider a beam of length a in the x_1 direction. On the $x_1 = 0$ and $x_1 = a$ edges the beam is simply supported. For these boundary conditions the Fourier series method can be applied to solve equation (10) using the following series expansions for the displacement degrees of freedom

$$u_1^0 = \sum_{m=1}^{\infty} U_1^{(0)}(x_1) \cos \frac{m\pi x_1}{a} e^{i\Omega t} \quad (11)$$

$$u_3^0 = \sum_{m=1}^{\infty} U_3^{(0)}(x_1) \cos \frac{m\pi x_1}{a} e^{i\Omega t} \quad (12)$$

$$\alpha_1^D = \sum_{m=1}^{\infty} A_1^{mD} \cos\left(\frac{m\pi x_1}{a}\right) e^{i\Omega\tau} \quad (13)$$

$$\alpha_1^T = \sum_{m=1}^{\infty} A_1^{mT} \cos\left(\frac{m\pi x_1}{a}\right) e^{i\Omega\tau} \quad (14)$$

$$\alpha_1^B = \sum_{m=1}^{\infty} A_1^{mB} \cos\left(\frac{m\pi x_1}{a}\right) e^{i\Omega\tau} \quad (15)$$

In these equations the superscripted constants are Fourier coefficients and Ω is the frequency of the steady state excitation.

The harmonically varying excitations (with respect to time) are also expressed in terms of Fourier series expansions

$$P_1(x_1, \tau) = \sum_{m=1}^{\infty} P_1^m \cos\left(\frac{m\pi x_1}{a}\right) e^{i\Omega\tau} \quad (16)$$

$$P_3(x_1, \tau) = \sum_{m=1}^{\infty} P_3^m \sin\left(\frac{m\pi x_1}{a}\right) e^{i\Omega\tau} \quad (17)$$

where the P_i^m are the Fourier coefficients determined from the Fourier formulae.

Substituting the above expansions into equation (10) results in an infinite number of uncoupled equations that can be grouped into sets by common indicial values. Thus a set of five equations and five unknowns is obtained for each indicial value where the unknowns of these equations are the Fourier coefficients of the displacement series. Expressing these equations in matrix form leads to the following general expression for each indicial value

$$-\Omega^2[M][U^m] + [B_m][U^m] = [P^m] \quad (18)$$

where $[U^m]$ is a vector of Fourier displacement coefficients, $[B_m]$ is a modal stiffness matrix whose elements are determined by the material and geometric properties of the structure, and $[P^m]$ is a vector of the Fourier loading coefficients.

The analysis can be completed in several ways depending upon the type of information desired. For instance, the dynamic response of a damped beam to a specific excitation can be found through the direct solution of equation (18). If however, the modal loss factors are to be determined then the Forced Mode Method [5] is applied.

4.0 APPLICATIONS

4.1 STRUCTURAL DESCRIPTION

The beam examined in this analytical study has a length of 25.4 cm. The top and bottom face sheets of the beam consist of 6 stiffness layers with each layer having a thickness of 0.1725 mm. The damping layer has a thickness of .0965 mm. The stiffness layers consist of IM6/3501-6 carbon-epoxy with a fiber volume fraction of 60%. The properties of this material are shown in Table 1 where the disparity in the axial and transverse extensional moduli should be noted. The damping layer consists

of ISD 112 Scotchdamp SJ2015x. The frequency dependence of the storage and loss moduli of this material are accounted for in the analysis. The mass density of the damping material is .98 gm/cc.

To study the effects of compliant layering on structural damping, the fiber reinforced layers adjacent to the damping layer are given a 90 degree off-axis orientation with respect to the x_1 coordinate direction. The off-axis orientation of the inner layers makes these layers compliant with respect to the x_1 coordinate direction. Therefore this particular type of lamination serves as a compliant layer design.

The notation used to specify the structural arrangement of the damped beams is identical to that used for laminations of advanced composites except for the addition of the symbol d which will indicate the presence of a damping layer. For instance, the baseline structure for this study, so called because it does not include compliant layering effects, is designated $0_6/d/0_6$.

4.2 NUMERICAL RESULTS

Figure 3 shows the loss factors of four different damped beams for the first five bending modes of vibration (Figures 3 to 6 repeat results that can be found in References 3 and 4). Here it is seen that there is little or no gain in damping for the fundamental mode but that in the higher modes the compliant layered laminates have significantly greater loss factors. (The matching of natural frequencies of the beams indicates that the gain in damping is not due to changing material properties.)

The goal of a damping design is to reduce resonant stresses and displacements. This is achieved by increasing the structural loss factor which in a compliant layer design is accomplished by sacrificing static stiffness (i.e. through the use of 90 degree layer orientations). It is necessary then to verify that the structural response actually decreases in the highly damped but more flexible compliant layer designs. To analytically test the response, the structures are subjected to forcing functions that approximately excite the resonant response (the approximation is introduced by not accounting for the negligible moment and in-plane components of the load vector that are required by the Forced Mode method for a strict proportionality to the inertia loading). Figure 4 shows the result of this computation where the amplitude of the transverse displacements have been normalized with respect to the modal response of the baseline beam. Except for the fundamental mode where virtually no improvement is achieved, the analysis predicts reduced resonant responses. (The failure of complaint layering to aid in controlling the response of the fundamental mode is attributed to the dimensions of the particular configuration being examined.)

The controlling parameter in increasing the damping in the compliant layered designs is the extensional modulus of the compliant layers. This is seen in Figure 5 where the modulus of the inner layers is varied parametrically as a percentage of the modulus of the outer layers. The loss factor directly increases with decreasing modulus. This modulus also controls the phase lag between the damping layer rotation (α^P) and the other displacement degrees of freedom (which respond approximately in phase). Figure 6 shows that this phase lag increases with decreasing modulus.

To test the hypothesis that compliant layering leads to higher energy dissipation through greater in-plane translations of the face sheets, the following ratios are formed

$$R_i^D = \frac{|\alpha_i^D|}{|U_3^0|_i} \quad (19)$$

$$R_i = \frac{|U_3^0|_i}{|U_3^0|_{Baseline}} \quad (20)$$

in which the subscript i is used to refer to a particular design and the vertical bars indicate the amplitude of the listed degree of freedom. The ratio R_i^D is a measure of the amount of core rotation (shearing) that occurs per transverse displacement. The ratio R_i is a relative measure of the resonant response. For the first four modes of response Table 2 shows these ratios and the corresponding loss factors for the baseline beam and three compliant layer designs. In each mode it is seen that the design that leads to the highest R_i^D also has the lowest resonant response and the highest loss factor. This indicates that compliant layering affects the response by increasing the rate of core shearing.

It can be argued that the relationship between the material properties, the structural configuration and the dynamic response is very complex and that the benefits in mechanical behavior obtained in the compliant layer design can be attributed to reaching an optimum balance of conventional design parameters rather than to the compliant layering. Since in the previous analysis the thicknesses of the stiffness and damping layers were restricted to commercially available sizes this may very well be the case. To examine this issue an additional analytical test is performed. For an excitation that excites specific modes of response, fix the thicknesses of the face sheets and vary the thickness of the damping layer until the response is minimized. The result is an optimized damping design for that specific excitation using conventional design practice. At this point compliant layering is introduced to see if a further reduction in response can be achieved. Table 3 shows the results of such an analysis for each of the first four modes of response. In each mode the compliant layering design yields an improvement over the optimized conventional design. Figures 7 and 8, which show this information plotted against the resonant frequency, indicate that the improvements are not due to changes in the amplitude of the forcing function or to changes in the frequency dependent material properties.

5.0 CONCLUSIONS

In order to examine the use of compliant layering in damped structures a structural theory was developed and applied to a simple but representative structural system. The analytical study revealed that compliant layering can increase the efficiency of damping designs by increasing the modal damping and reducing the forced response. The work presented here supports the following conclusions that were previously reported in References 3 and 4.

Compliant layering, which is the replacement of face sheet material with a less stiff material at the interface of the face sheets and the damping layer, affects the

dynamic response of the beam through the alteration of in-plane extensional stiffness properties. This creates a mechanism for increasing the rate of shearing in the damping material by increasing the relative in-plane displacements of the face sheets. The rate of shearing and the associated energy dissipation were found to increase as the modulus of the compliant layer was reduced. However, there is a limitation to this process since the moduli of the compliant layer must be high enough to confine the shear deformation to the damping layer.

Compliant layering can also be used to reduce the weight of damped structures since compliant materials are generally less massive than stiff materials. For instance, metallic face sheets that incorporate a glass-epoxy compliant layer can have improved dynamic resistance at a reduction in weight. This same effect can be achieved by merely removing some of the material on the inner side of the face sheets through grooving, waffling or scoring this surface.

Compliant layering introduces challenges to the fabrication process since it involves either the mating of dissimilar materials [6] or the unbalancing of quasi-isotropic laminates. Also, there will be additional steps in the laminate fabrication which will add to the cost of building these components. Nevertheless, depending upon the total cost of construction, compliant layering offers an important design option in the use of damped bending structures.

REFERENCES

1. Soovere, J. and Drake, M. L., "Aerospace Structures Technology Damping Design Guide," AFWAL-TR-84-3089, 1985.
2. Nashif, A. D., Jones, D. I. G., and Henderson, J. P., "Vibration Damping," New York: John Wiley and Sons, 1985.
3. Barrett, D. J., "An Anisotropic Laminated Damped Plate Theory," NADC-9006660, 1990.
4. Barrett, D. J., "An Anisotropic Laminated Damped Plate Theory," Accepted for publication in the Journal of Sound and Vibration.
5. Mead, D. J. and Markus, S., "The Forced Vibration of a Three Layer Damped Sandwich Beam with Arbitrary Boundary Conditions," Journal of Sound and Vibration 10(2), 163-175, 1969.
6. Rotz, C. A. and Barrett, D. J., "Cocured Damped Layers in Composite Structures," To be submitted for publication in the SAMPE Quarterly.

Axial Extensional Modulus	148. GPa
Transverse Extensional Modulus	8.96 GPa
Axial Poisson's Ratio	.35
Axial Shear Modulus	4.48 GPa
Transverse Shear Modulus	2.07 GPa
Axial Loss Factor	.00128
Transverse Loss Factor	.0110
Shear Loss Factor	.0110
Mass Density	1.52 gm/cc

Table 1 Material Properties of IM6/3501-6 Carbon-Epoxy

Beam Structure		Mode 1			Mode 2		
Design i	Lay-Up Specifications	R_i^D / R_1^D	R_i	η_S	R_i^D / R_1^D	R_i	η_S
1	$0_6/d/0_6$ (Baseline)	1.00	1.00	.26	1.00	1.00	.33
2	$0_5/90/d/90/0_5$	1.04	0.94	.28	1.08	0.88	.39
3	$0_4/90_2/d/90_2/0_4$	1.02	0.98	.26	1.10	0.85	.40
4	$0_3/90_3/d/90_3/0_3$	0.92	1.18	.23	1.06	0.92	.37

Beam Structure		Mode 3			Mode 4		
Design i	Lay-Up Specifications	R_i^D / R_1^D	R_i	η_S	R_i^D / R_1^D	R_i	η_S
1	$0_6/d/0_6$ (Baseline)	1.00	1.00	.34	1.00	1.00	.30
2	$0_5/90/d/90/0_5$	1.11	0.85	.43	1.12	0.83	.42
3	$0_4/90_2/d/90_2/0_4$	1.17	0.78	.48	1.21	0.73	.50
4	$0_3/90_3/d/90_3/0_3$	1.16	0.79	.46	1.24	0.70	.52

Measure of the Rate of Core Rotation $R_i^D = \frac{|\alpha_1^D|_i}{|U_3^0|_i}$

Measure of the Relative Resonant Response $R_i = \frac{|U_3^0|_i}{|U_3^0|_{Baseline}}$

The Modal Structural Loss Factor η_S

Table 2 Core Rotation per Transverse Deflection for Four Damping Designs

Mode	Design (1)	t^1 mm	t^2 mm	t^d mm	η_L	Displacement (2)
1	B	.000	1.035	.185	.36	1.00
	C	.310	.725	.185	.42	.86
2	B	.000	1.035	.085	.32	1.00
	C	.290	.745	.085	.37	.87
3	B	.000	1.035	.050	.29	1.00
	C	.270	.765	.050	.34	.88
4	B	.000	1.035	.035	.28	1.00
	C	.290	.745	.035	.33	.87

Notation:

t^1 The total thickness of the layers with a 90 degree orientation (Compliant Layer).

t^2 The total thickness of the layers with a 0 degree orientation.

t^d The thickness of the viscoelastic layer.

(1) Structural design.

B = Optimized design using conventional design practice.

C = Optimized design using compliant layering.

(2) The amplitude of the transverse displacement is normalized with respect to the response found for the conventional design.

Table 3 Optimized Designs

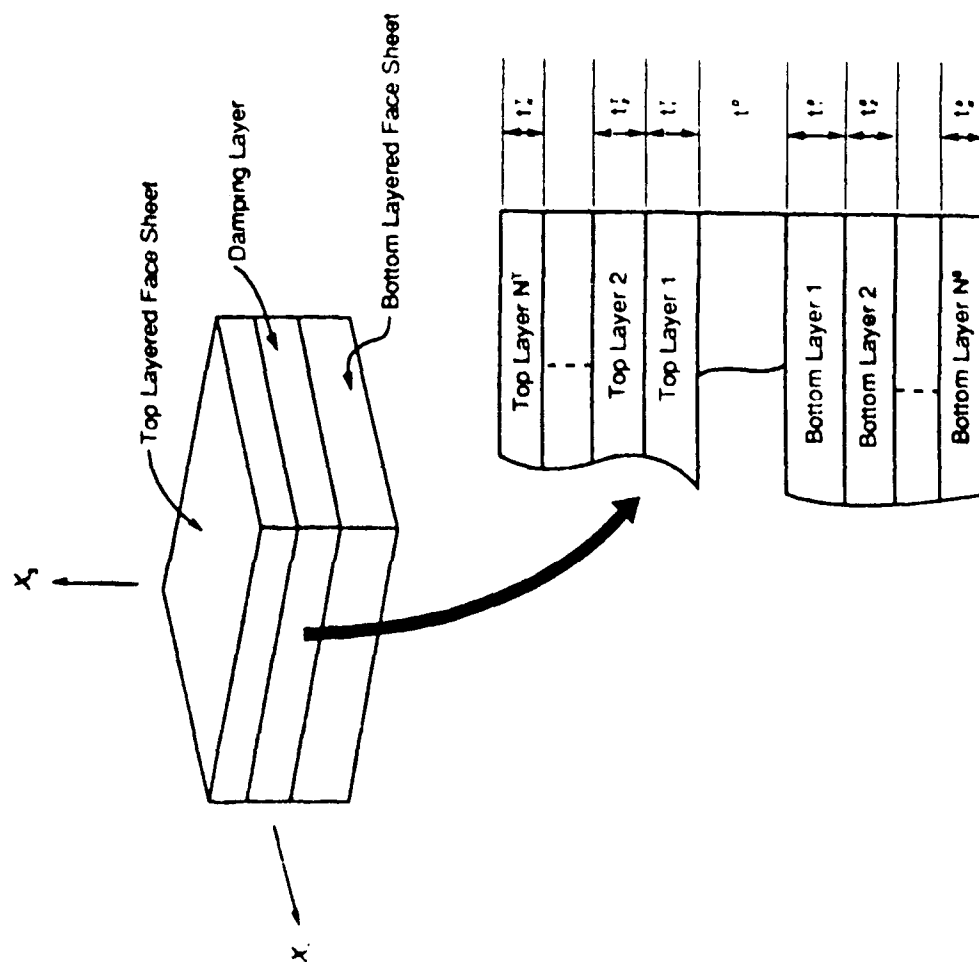


Figure 1 Damped Sandwich Beam

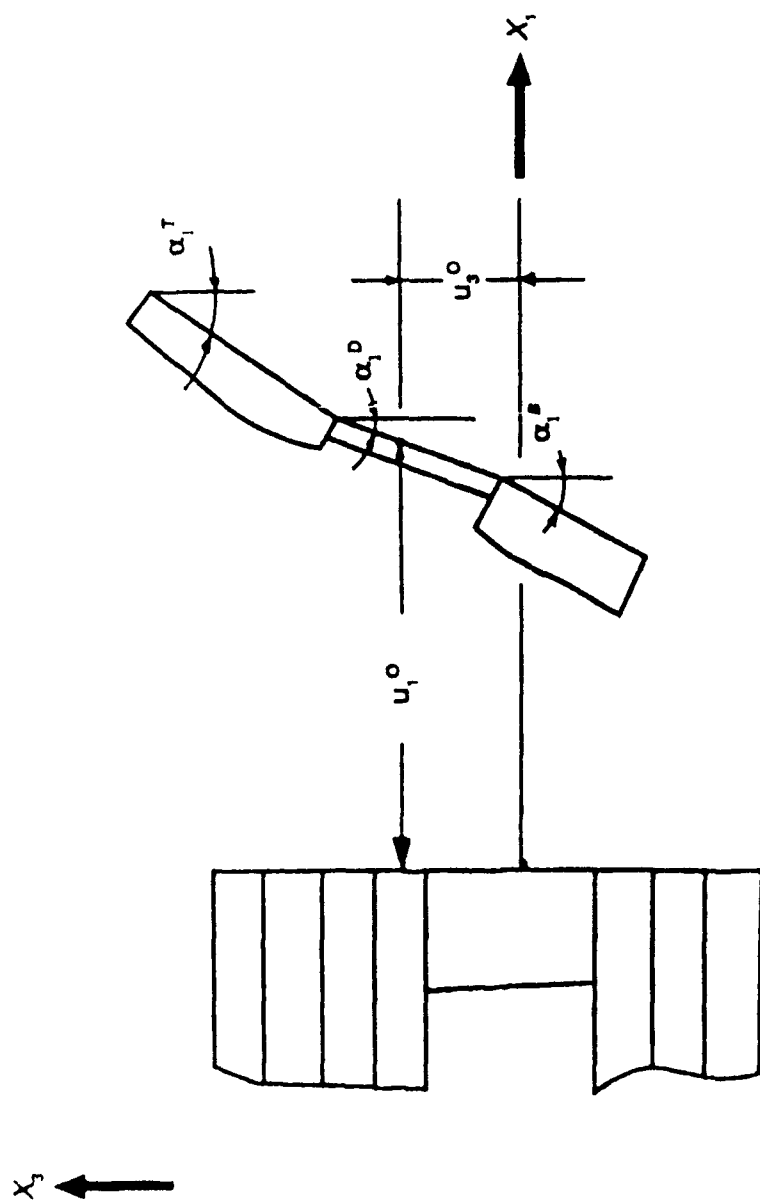


Figure 2 The Displacement Degrees of Freedom

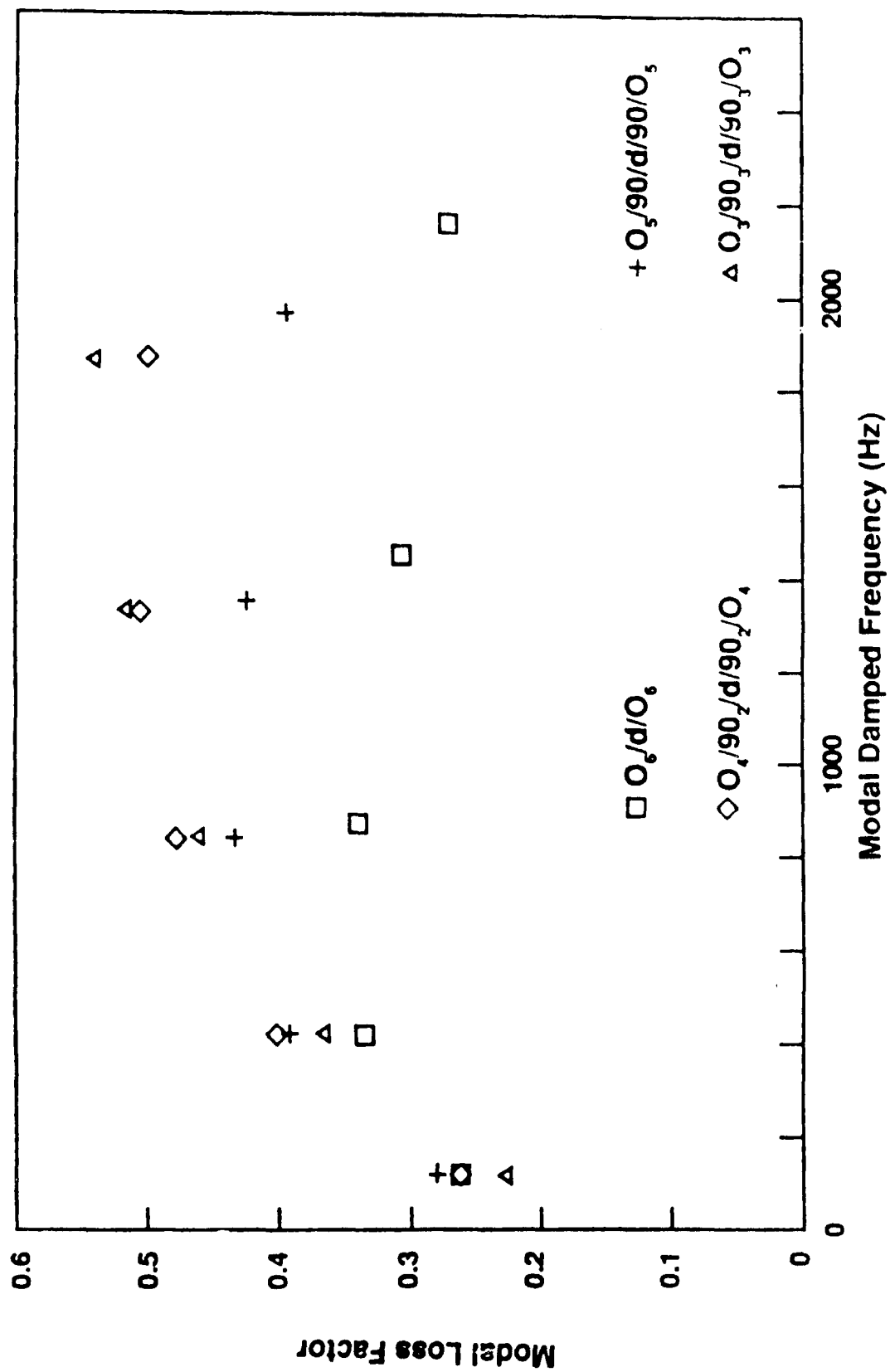


Figure 3 Modal Damping for Bending Modes 1 to 5

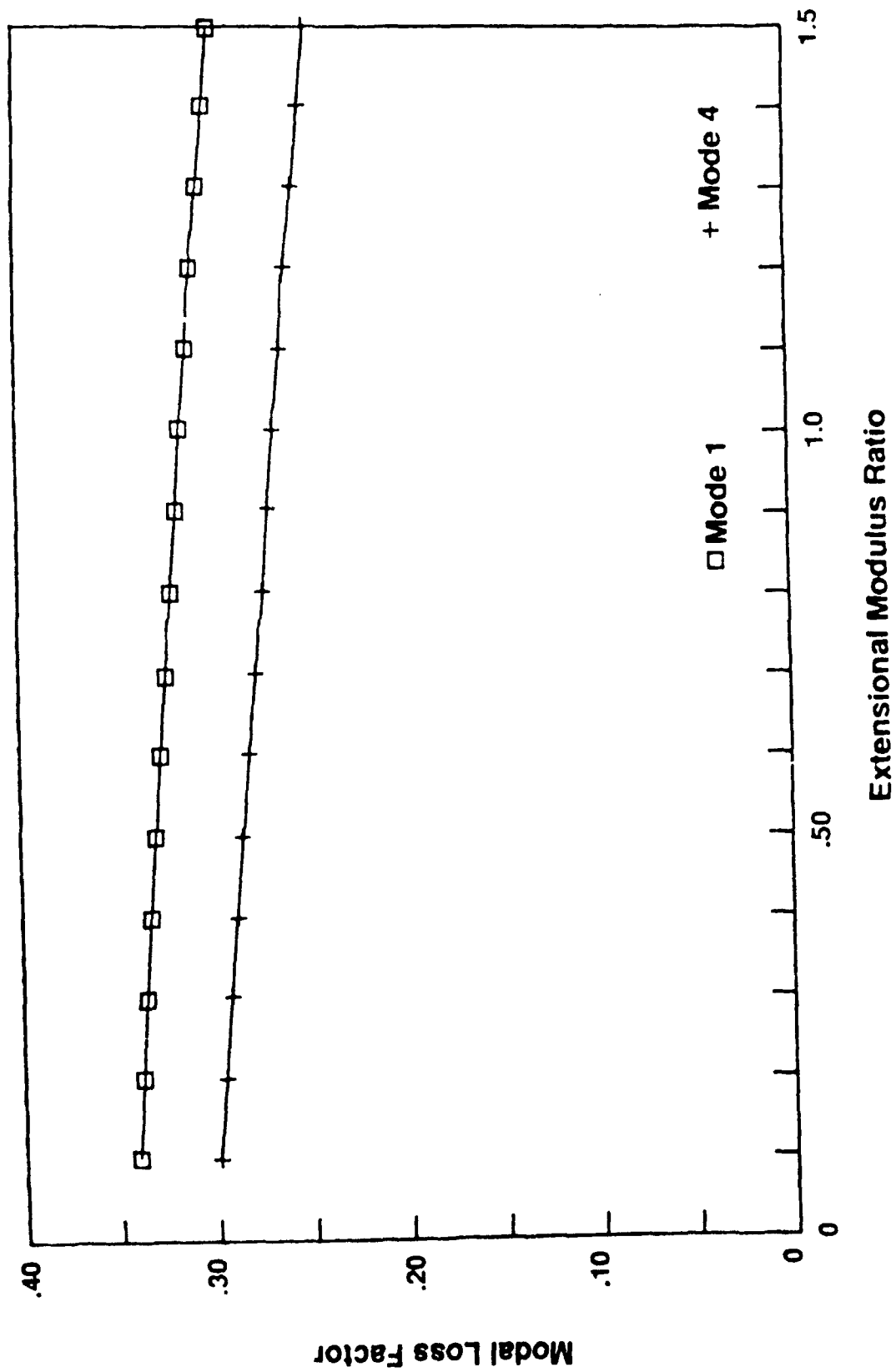


Figure 5 Modal Damping vs the Modulus of the Compliant Layer

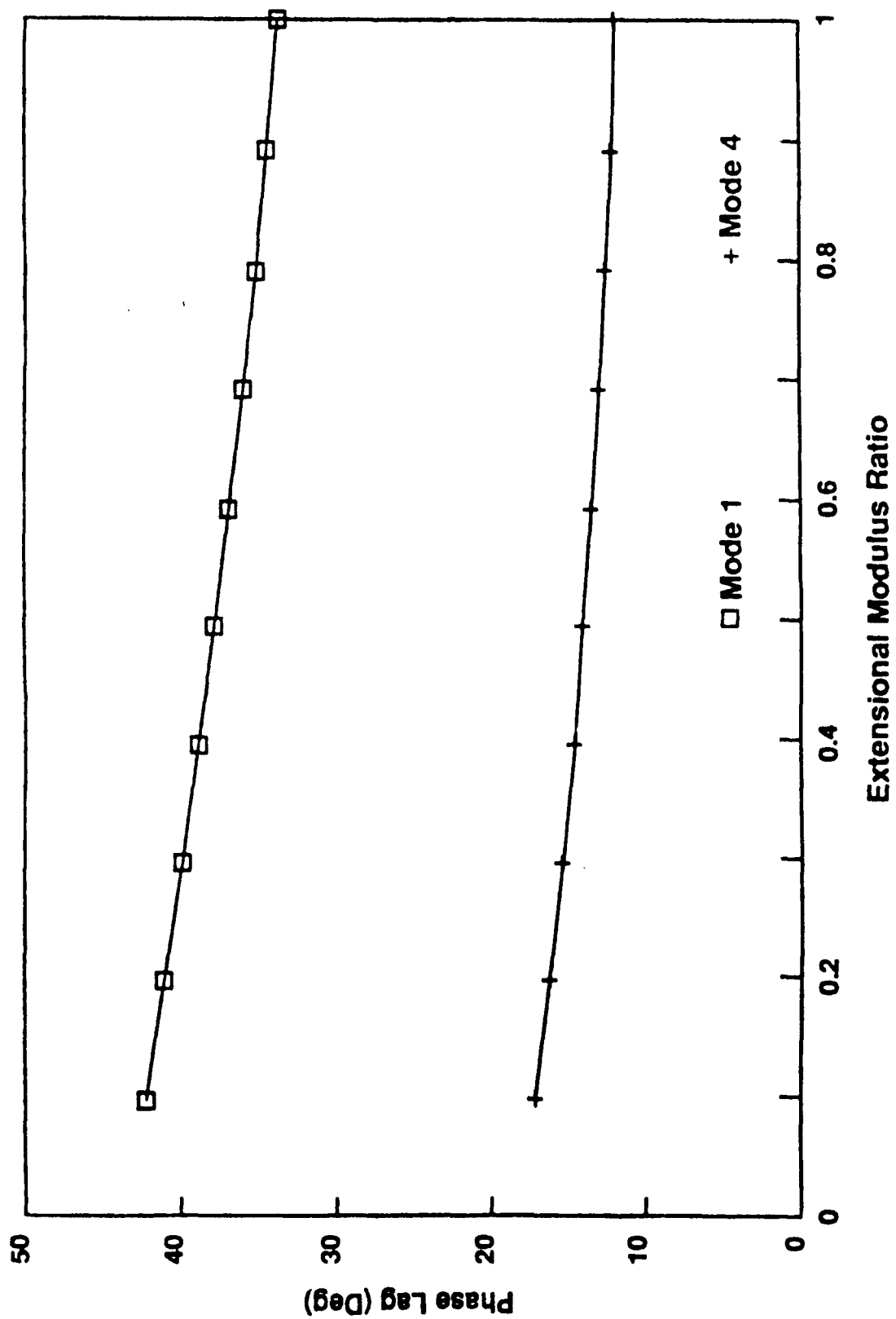


Figure 6 The Phase Lag of the Core Rotation vs the Modulus of the Compliant Layer

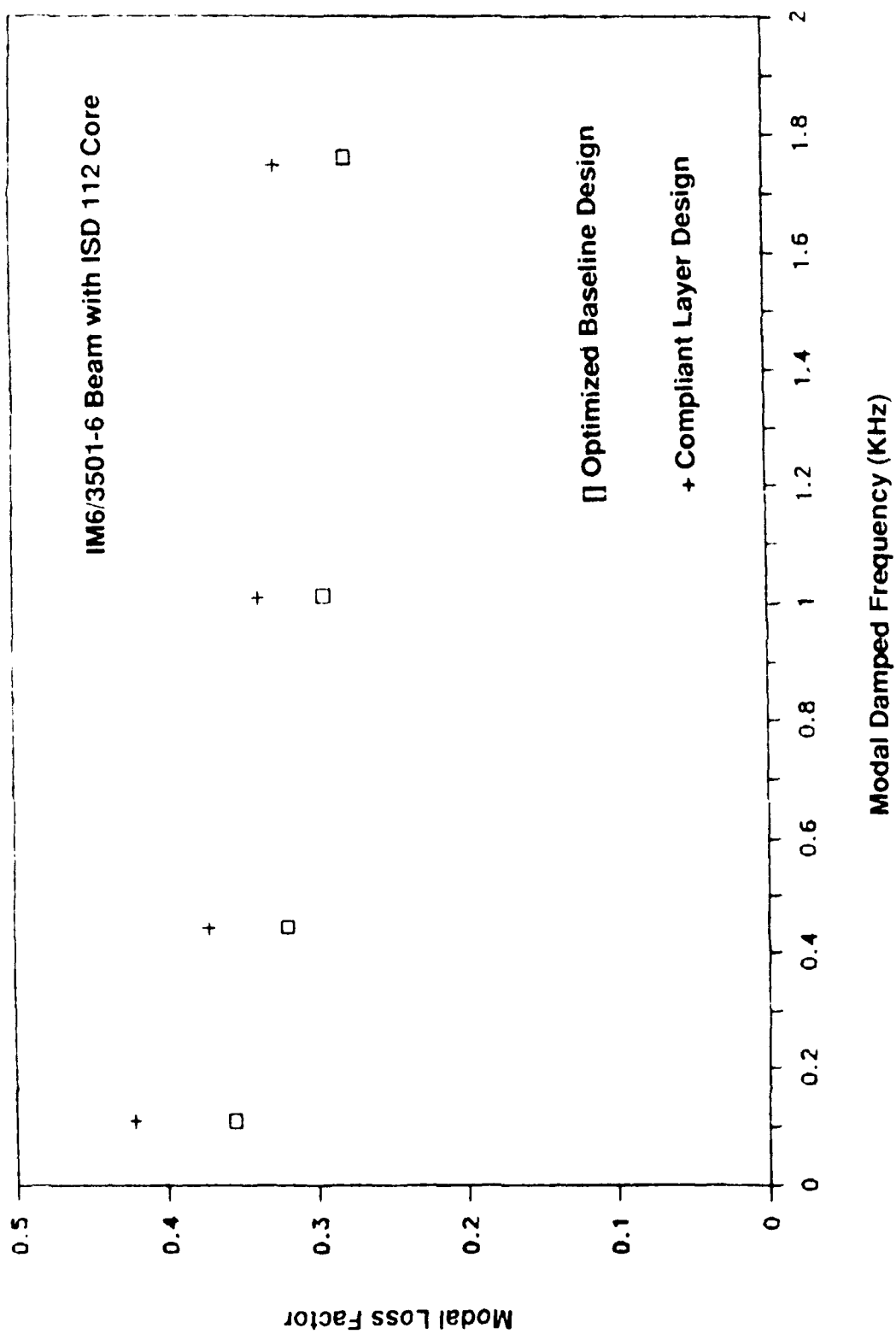


Figure 7 Modal Damping for Optimized Designs

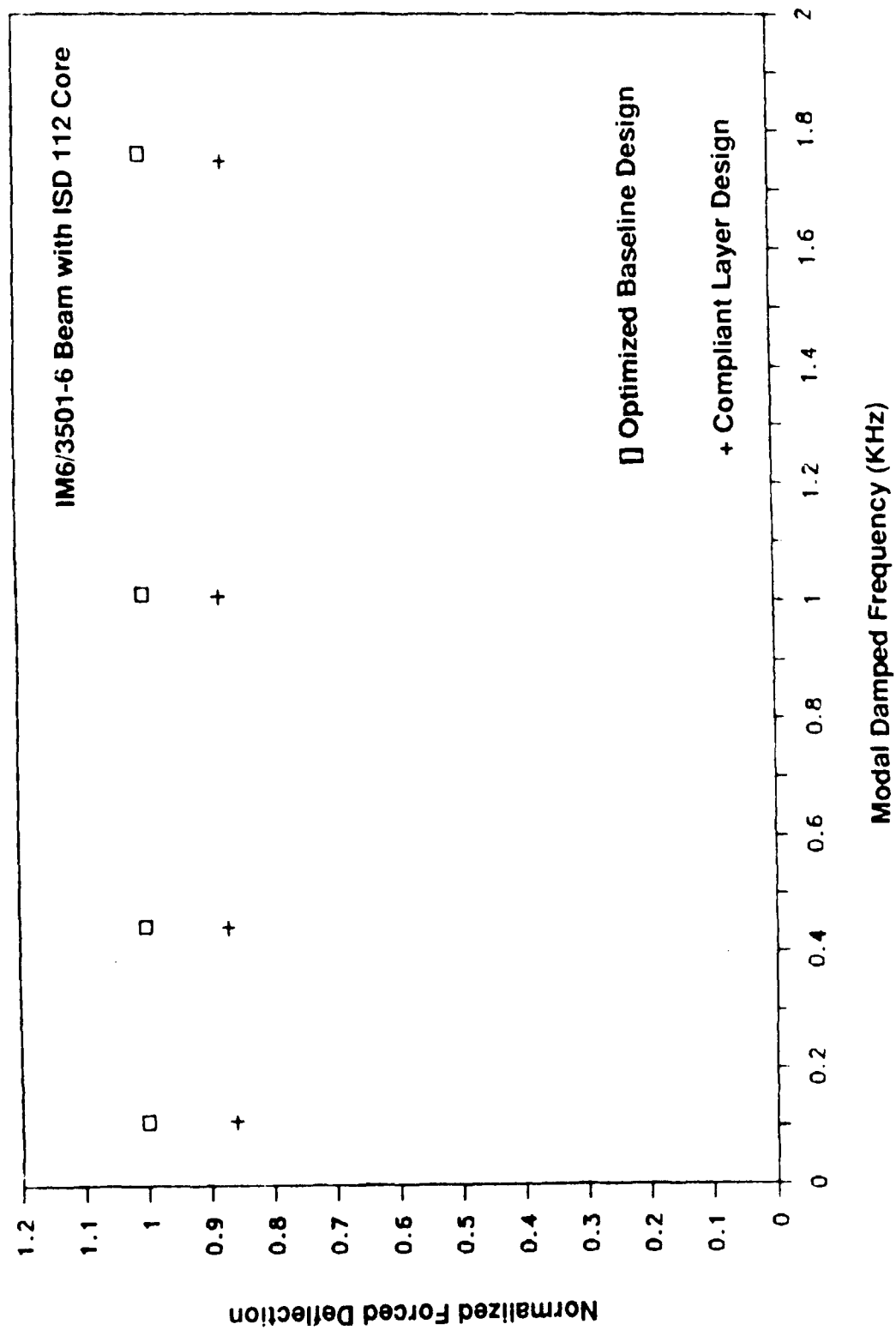


Figure 8 Normalized Forced Deflection for Optimized Designs

<Damping '91 Conference> in San Diego

The Damping Property of Laminated

Damping Steel Sheet after Deep Drawing

1991.2.13~15.

Hiroshi Okamura *

*1) Manager, Component Eng. Dept., Truck & Bus Eng. Center, Mitsubishi Motors Co.

Abstract

The damping property of laminated damping steel sheet is affected by shear deformation of viscoelastic layer, a constraint produced by the mutual slip between two steel sheets under a bending vibration mode. So, the bonding of the viscoelastic layer to steel sheets is critical to the damping property.

Sometimes, laminated damping steel sheet becomes unbonded locally from the viscoelastic layer because of an excessive relative slip between two steel sheets caused by a deep drawing.

It was found that by using the transmittance of ultrasonic wave, the unbonded area of laminated damping steel sheet can be detected without cutting it off. The validity of this method was confirmed by the T-Peel test which was conducted after the sheet was cut off.

The damping property measured at the wall of a deep drawn oil pan, was compared with a one for a laminated damping steel sheet not drawn yet.

It was found that the damping property and the noise reduction effect of a sheet after deep drawing were reduced in reverse proportion to the widening unbonded area.

1 Introduction

Steel sheet panels used for main components of a structure induce, in many cases, vibrations of bending modes and become a source of big noises.

The laminated damping steel sheet is incorporated not only with a normal function of steel sheet but also with a damping characteristic and, therefore, a substantial degree of reduction in vibration and noise can be achieved when it replaces an original steel sheet. This is an attractive feature from the design point of view since a basic structure of design can be retained as it is without making any modifications or alterations. The range of application for the material of this type has been expanded remarkably after an application to a deep drawn component part was made feasible by great improvements achieved in the sheet formability.

There are many covers attached to the exterior of reciprocating engines used

in the motor vehicles. They are the major sources of noises and, in particular, an oil pan has been known as being one of the big noise sources.

An example of noise contribution ratio of various engine components is shown in Fig. 1. A press formed steel sheet oil pans are generally used by the Japanese motor industries. Since a press die used for forming an oil pan of original steel sheet can be used without supplementing a major modification and also assisted by improvements achieved in the formability as mentioned above, the use of laminated damping steel sheet for the oil pan production was spread quite rapidly.

Stimulated by such application in massproduction system of the motor industries, applications by other industries were commenced and grew in a short period of time. The consumption of such materials, therefore, has grown in an amazing speed in Japan for the last few years.

The laminated damping steel sheet, however, has problems still to be solved. They are weldability, formability, bolt loosening, loss of bending stiffness, etc. Those problems can be solved not only by the improvement in steel sheets and damping films but also by the special design considerations given to a portion of structure where such a material is used. In order to acquire satisfactory solutions to such problems, it is essential to get a full knowledge of the nature of problem.

In this paper, a consideration will be given to the effect of deep drawing to the damping characteristic of the sheet. This is a critical problem as it is closely associated with a loss of fundamental mechanism of the damping effect. An oil pan is typically a deep drawn component part and can be a good example representing an involvement with this problem. It was quite incidental that the first full scale use of this material in Japan was directly involved with one of the most difficult problems.

2 Shear Deformation of Damping Layer

When a bending deformation is brought to a laminated damping steel sheet in a press operation, the deformations as shown in Fig. 2 takes place in the damping layer due to the tensile or compression deformation similar to the ones given to two steel sheet and the shear deformation caused by the mutual slip appeared between those two sheets.

The damping layer is a film of high polymer resin and, therefore, is able to withstand substantially layer deformation than steel sheets. The tensile and compression deformations on high polymer resin are in the same magnitude as those on surrounding steel sheets and will not create any problems by

themselves, however, since the shear deformation of damping layer is formed by a force generated by the mutual slip two of steel sheets and the magnitude is considerably larger, it is sometimes brought into a zone where some problems may start to appear.

As obvious in Fig. 3, damping layer's shear curve has a linear elasticity zone and a plastic deformation zone even though they are not defined as distinctively as a metal. The curve goes through the maximum shear stress point and is terminated by a rupture of layer, that is, a separation.⁽¹⁾ Maximum slip δ_{max} , prevailing in such an instance will be in a magnitude inherent to the material and proportional to the thickness of damping layer.

Fig. 4 shows the distribution of mutual slip appeared between two steel sheets of laminated damping steel sheet when it was bent to most fundamental V form by a press. Slits were provided on the side of rectangular piece of laminated damping steel sheet and the rate of slippage between two steel sheets was measured after the piece was bent by a press. Obviously in the figure, the slip becomes largest in the border zone between circular arc and flat flange areas.

Fig. 5 shows the distribution of mutual slip between two steel sheets when a test strip piece is drawn into a channel form.⁽³⁾ The cross section of the piece is resembled to that of an oil pan. Since the flange zone C~D was held firmly to prevent wrinkling during the formation and the bottom line A~B has a symmetry against the center line which passes through point A, the mutual slips between two steel sheets in those two zones are virtually nil. A large mutual slip appear on the side portion B~C, a portion located between the said two portions, simply because of the right angle bendings provided at both ends of this portion. The magnitude of mutual slip movement varies extensively and complexly while the piece is formed in a press. Details of mechanism, therefore, have not been clarified yet.

When a laminated damping steel sheet is used for an oil pan having a cross section in a form as shown in Fig.5, therefore, the damping layer in the side wall will be subjected to a large shear deformation. Fig. 5 (b) shows that as a die corner radius is increased, the maximum mutual slip becomes smaller. This shows that a shear deformation of damping layer can be reduced by a modification of pressing die. However it results in restricting die radius R_d necessary for securing the width of flat range portion.

As shown in fig. 6, the damping effect demonstrated by the laminated damping steel sheet in bending vibration mode is brought forth by the shear deformation of high polymer resin layer sandwiched between two steel sheets. Under such circumstance, therefore, if an excessive shear deformation is loaded on a

damping layer by a press operation and the layer is separated from the steel sheet, the basic function of the damping layer is lost.

3 Ultrasonic Transmittance Measurement of Adhesion of Damping layer

The measurement of adhesion of damping layer by an ultrasonic transmittance method is shown in Fig. 7. Since the condition of adhesion can be checked by this method without destroying a product, it becomes much easier to check for a damage of damping layer caused by a press operation as shown in the above the method can also be applied to an evaluation of laminated damping steel sheet in the development stage as well as to an conditioning made in a production line.

The gain of ultrasonic transmittance indication should be adjusted to a full scale '10' on a sheet having a good adhesion before it is formed by a press machine. The evaluation criteria for a good adhesion should be scale 8 or above, no good adhesion scale 2 or below and uncertain and unreliable adhesion scale between 2 to 8.

Those criteria are compared with T-Peel strength in Fig. 8 (2). Though they do not match perfectly, the correlation between two systems verifies the sufficient practicability of such evaluation.

Fig. 9 shows the result of ultrasonic transmittance test performed by the method shown in Fig. 7 on the adhesion of damping layer of an engine oil pan as an example of laminated damping steel sheet with a major press formation. It indicates that separations of damping layer took place locally. The evaluation was verified by a T-Peel strength test which was performed later on the same specimen. The result, meanwhile, indicates that an application in a deep drawn oil pan gives a laminated damping steel sheet a very harsh processing.

Shear deformation caused on the damping layer is large on the side wall as shown in Fig. 5 and, therefore, this area is more susceptible to an incomplete adhesion which means separation. The possibility of separation is reduced on the right wall because of a local protrusion provided on it. Some separation is noted on the bottom surface due to nonsymmetry of the left and the right as well as the front and the rear walls. It is a very complicated phenomenon.

Fig. 10 shows the result of vibration test performed on pieces of laminated damping steel sheet derived from the side and the bottom walls of oil pan as shown in Fig. 9. It is indicated that the piece retain good damping property from the bottom wall and no good one from the side wall. The evaluation, meanwhile, obtained by the ultrasonic transmittance test was found no good on the side wall and good for the bottom. So, reduction of damping characteristic due to partial separations of damping layer can be seen in the graph.

4 Structure Damping in Complex Structure and η Value

Required for Damping Treatment

Fig.11 shows an example of structure damping measured on a reciprocating engine. The basic structure of an engine is constituted by cast iron cylinder block, cylinder head, etc. and η value of those component materials is approximately 0.001. According to Fig.11, η value for engine structure is between 0.01 and 0.04, about 10 times as large as η of materials.

This is due to the structure damping, a combination of friction damping produced by each bolt joint face, etc. and oil damping produced by an oil film formed on the bearings of various rotating shafts. Larger η values, shown there while the engine is in a running condition, are realized by the damping effect of oil films formed on the bearings by the rotation of shafts.

For the purpose of an accomplishment of damping treatment for the reduction of vibration and noise on a very complicated structure as engine, a target η to be set is recommended to be larger than 0.1 by the past experiences because the effect of original structure damping is quite large.

5 η Value of Pressed Laminated Damping Steel Sheet Component and its Effect

Fig.12 shows the cantilever beam measurement method of loss factor η for a laminated damping steel sheet. A steel spacer is inserted between two steel sheets in lieu of a damping resin layer in the portion where the beam is fixed to the clamping block to accommodate an adaptability to boundary condition.

η of laminated damping steel sheet measured by the method shown in Fig.12 before it is formed by a press is shown in Fig.13. Nomogram and shift factor calculated by the data in Fig.13 are shown in Fig.14. Fig.15 shows the temperature and frequency characteristic of viscoelastic material itself.

In consideration of the structure damping in a bolted condition, the method of η measurement, on an oil pan made of laminated damping steel sheet and installed on an engine, is shown in Fig.16. The temperature of oil in the oil pan is constantly regulated to a certain level because the damping characteristic of laminated damping steel sheet is greatly influenced by the temperature. Fig.17 shows the result of test in Fig.16.

The solid line in Fig.17 is the damping characteristic derived from the calculation of viscoelastic data shown in Fig.15. The line indicates η which is the same as the one for the laminated damping steel sheet not processed by a press, obviously clear of mutual slip of steel sheets, and subjected to the same vibration mode. This sheet is a high temperature type which delivers the

maximum η value at around 70 °C, a temperature at which an oil pan is usually kept while an engine is in operation. It has η value exceeding 0.1 in a wider range.

In comparison to this solid line, there is a substantial reduction of η value on a laminated damping steel sheet after it is formed into an oil pan. As shown in Fig.9, separation of damping layer takes place more often on the left side wall of oil pan. For this reason, the reduction of η on the left side wall becomes larger to an extent that it goes under 0.1, the value which is put up as the target for η by the past experiences. ⁽⁴⁾

Fig.18 shows the effect of laminated damping steel sheet realized on sound power level at various points on an outer surface of oil pan while an engine is in operation. It is noted that a close correlation exists between this effect and the adhesion of damping layer shown in Fig.9 as well as η value shown in Fig.17.

Fig.19 shows sound pressure measured on the left side wall and the bottom of oil pan. The plots show that a noise reduction ranging from 1 to 2 dB(A) was accomplished on the left side wall and 2 to 3 dB(A) on the bottom. Both indicate that substantial damping was accomplished. Even though an accurate comparison was not made in this case, 60 % to 80 % sound power of the oil pan is normally supplied by the resonant peak of an outer panel which yields to a damping effectively. And, therefore, if a large η value is made available, much larger noise reduction will become feasible. ⁽⁵⁾

6 Summary

From the above, it can be said that a laminated damping steel sheet before it undergoes a press forming operation will have a substantially large η value than those of general structured components but if a separation of damping layer from steel sheets are caused by the bending operation of press, there could be a large reduction of η value to an extent that sometimes it goes under the expected value though all the damping effect is not necessarily lost. For the compensation of such reduction, an increase of maximum permissible mutual slip, δ_{max} , of damping layer by material improvement, review of press operation conditions, increase of layer thickness, etc. are being studied, however, a modification in pressed form where the mutual slip can further be restrained should be explored, too. Increasing the thickness of damping layer is relatively simple method but it may create new problems in bolt loosening or press formability of steel sheet and, therefore, its application is rather limited. ^{(6) (7)}

Under the circumstances, diversified studies in applied engineerings in the fields of materials, production engineering, designs, etc. as mentioned above should be carried out for an accomplishment of noise reduction in a deep drawn product such as an engine oil pan as it was discussed in this paper.

Reference

- (1) A.Nishimoto, M.Yoshida; Press Formability and Shearing Properties of Steel-Plastics-Steel laminated Sheets, Nkk Technical Report, No.127 (1989), p14~19 (in Japanese)
- (2) H.Okamura et al.; Application of Damping Steel Sheet to Oil Pan, Journal of SAE of Japan, Vol.41 No.7 (1987), p729~737. (in Japanese)
- (3) M.Yoshida; Press Formability of Vibration-Damping Sheets, Proceedings of the 37th Japanese Joint Conference for the Technology of Plasticity, No.37 (1986-11), p7~12 (in Japanese)
- (4) H.Okamura et al.; Study of Noise Reduction of Engine Parts by Application of Plastic Materials, JSAE Review, Vol.9 No.2 (1988), p34~42
- (5) S.Wada, H.Okamura et al.; Transient Response of Engine Structures by Impulse Excitation, Mitsubishi Heavy Industry Technical Review, Vol.20 No.5 (1983)
- (6) Y.Watanabe et al.; Development of Vibration-Damping Sheets, SAE Paper, No. No.850325 (1985)
- (7) M.Yoshida; Press Formability of Vibration-Damping Sheets, Journal of the JSTP, Vol.26 No.291(1985-4), p394~399 (in Japanese) □

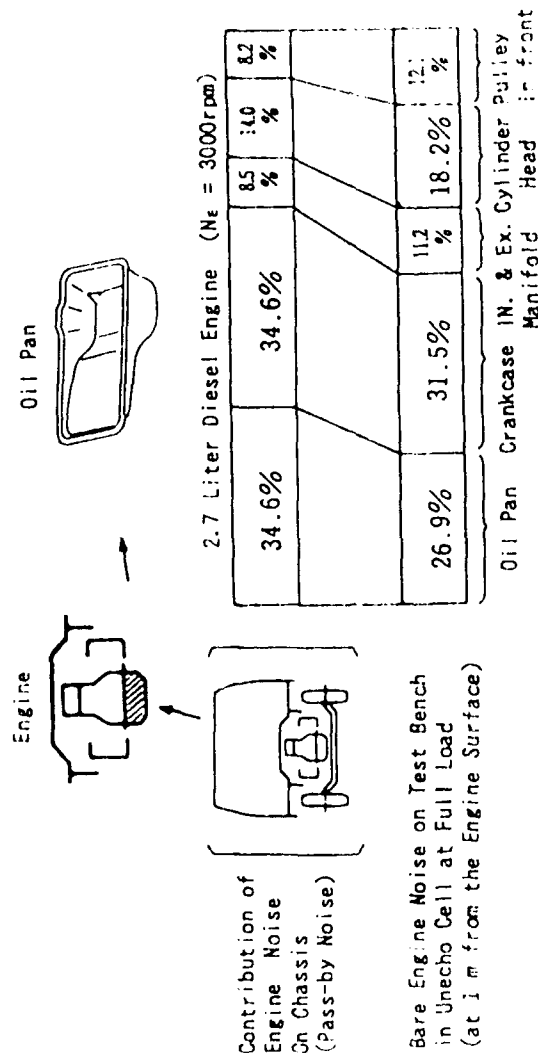


Fig. 1 Noise Contribution Ratio of Various Engine Components

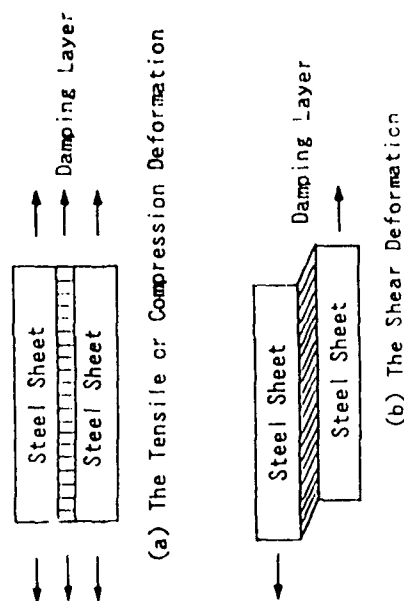


Fig. 2 Deformations of Damping Layer in a Press Operation

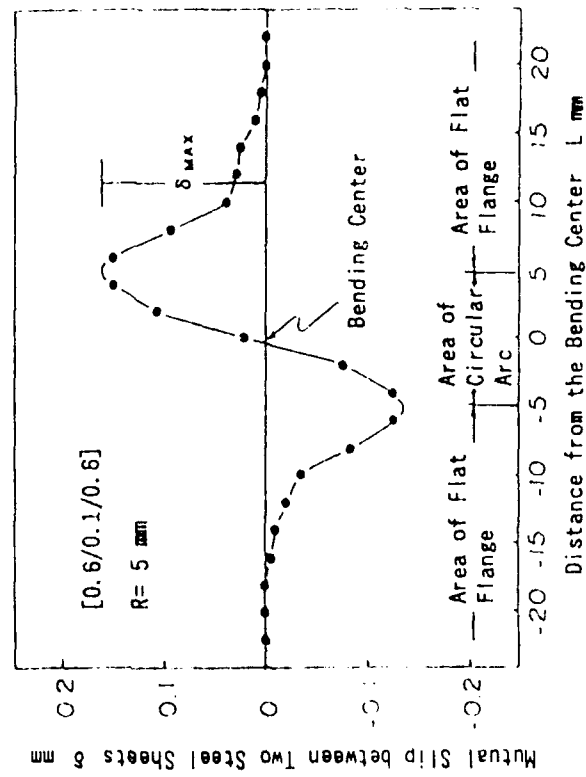
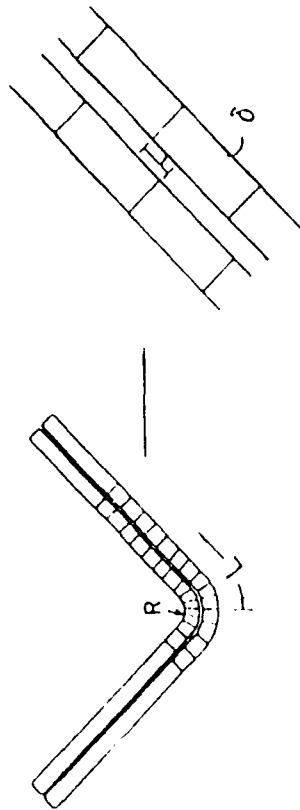


Fig. 4 Mutual Slip between Two Steel Sheets of Laminated Damping Steel Sheet after V-Press Bending

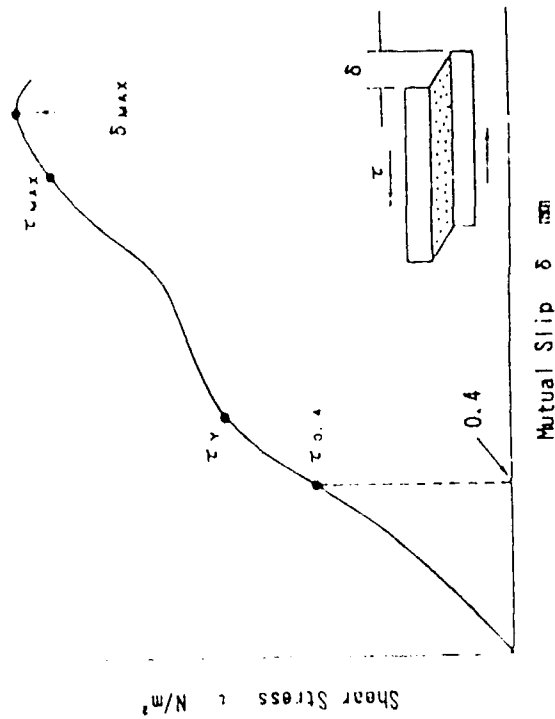
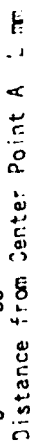


Fig. 3 Schematic Curve of Shear Stress vs Mutual Slip



(a) Distribution of Mutual Slip

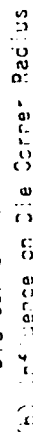
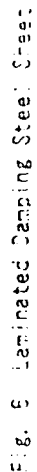


Fig. 5
Vertical Spacing between Two Steel Sheets of Laminated
Channeling Steel Sheets after Channel Type Drawing



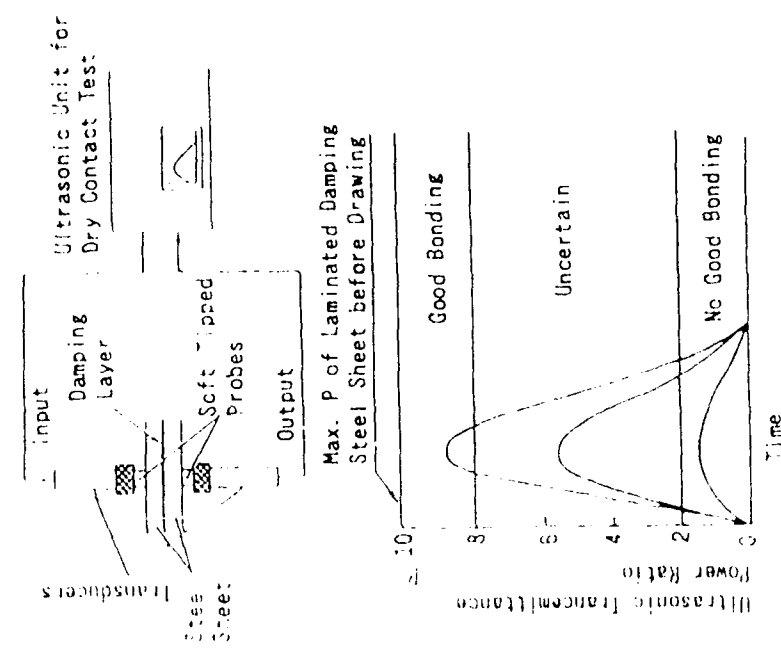


Fig. 7 Measurement of Adhesion of Damping Layer by an Ultrasonic Transmittance Method

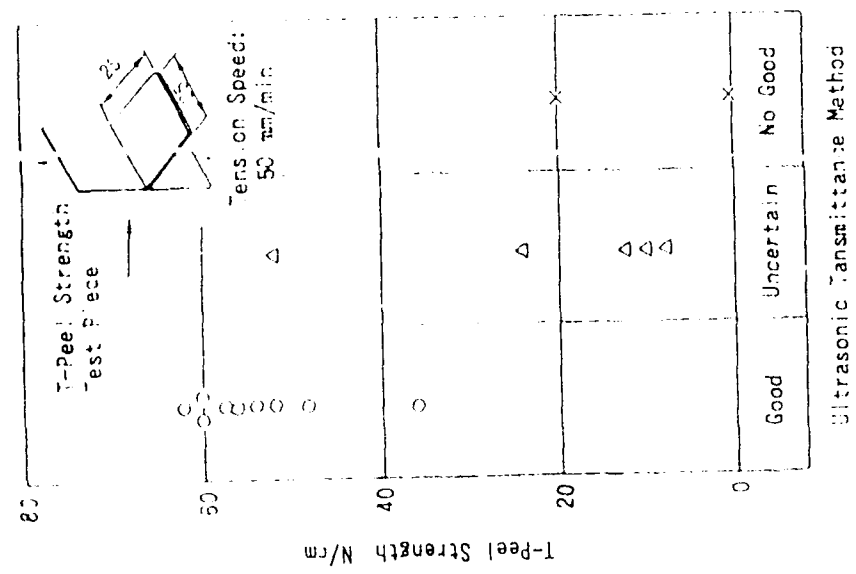


Fig. 8 Correlation between Ultrasonic Transmittance Method and T-Peel Strength Test Method about the Adhesion of Damping Layer

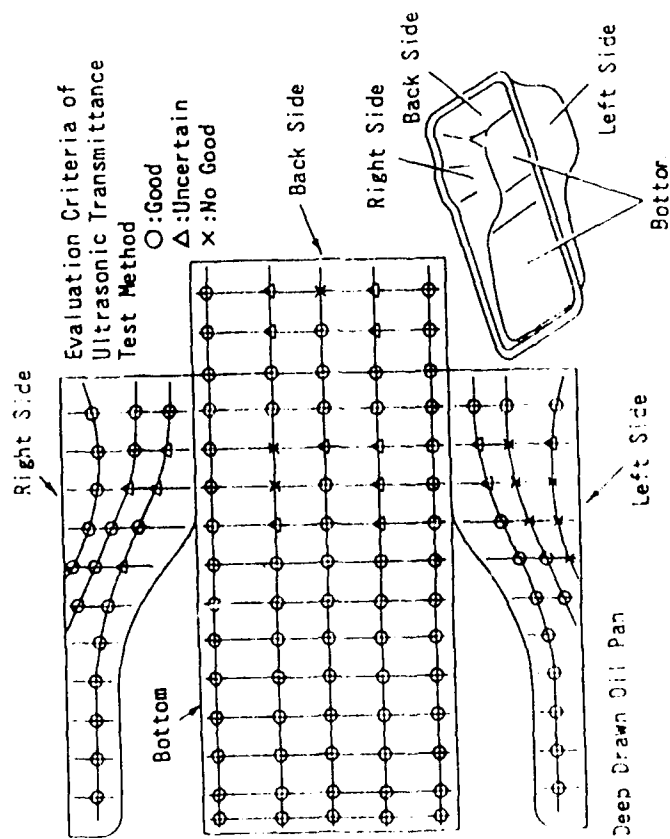


Fig. 9 The Result of Ultrasonic Transmittance Test on the Adhesion of Damping Layer of an Engine Oil Pan

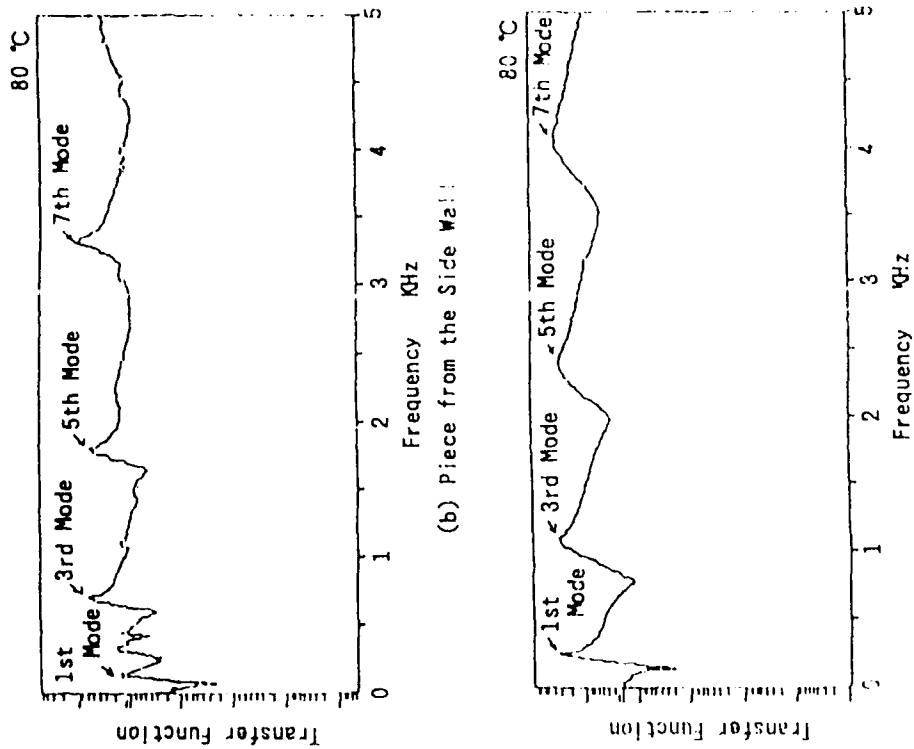


Fig. 10 Loss Factor of Laminated Damping Steel Sheet Test Piece Derived from the Wall of Oil Pan

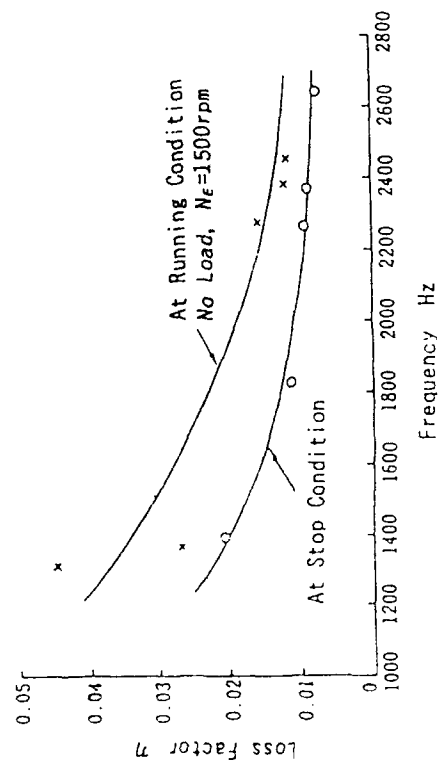


Fig. 11 Structure Damping of Reciprocating Engine

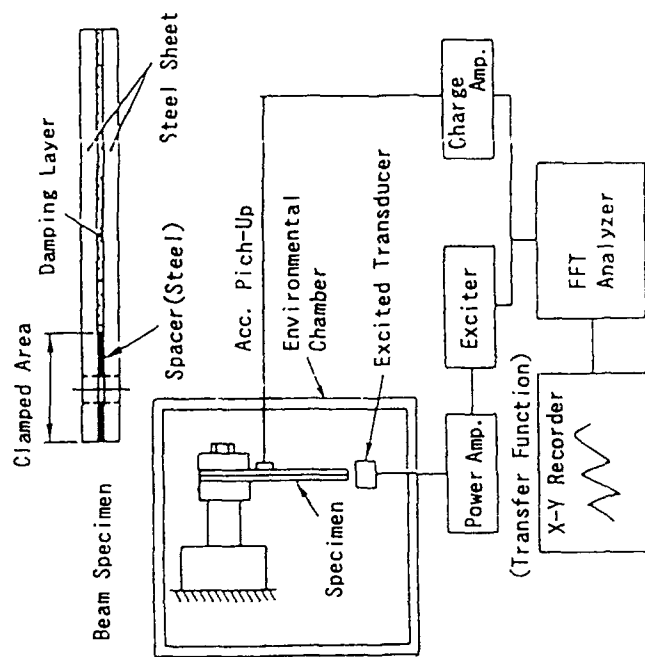


Fig. 12 Measurement Method of η Value for Cantilever Test Beam Piece

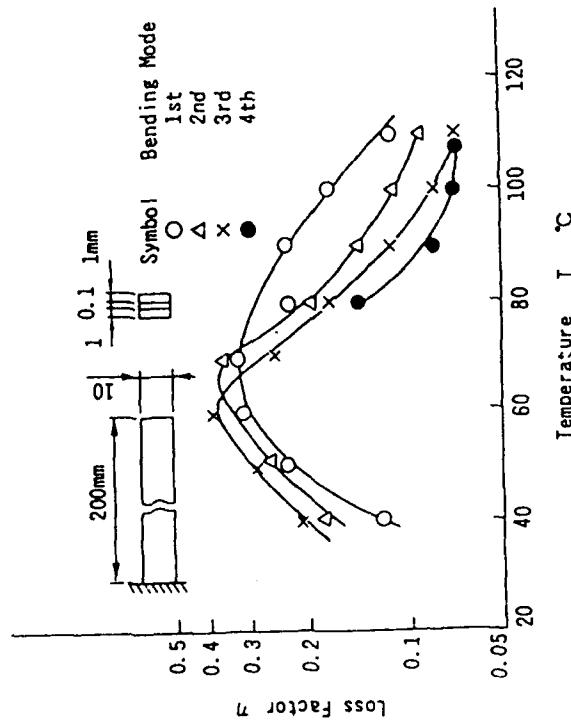


Fig. 13 Damping Property of Laminated Damping Steel Sheet Cantilever Test Beam Piece

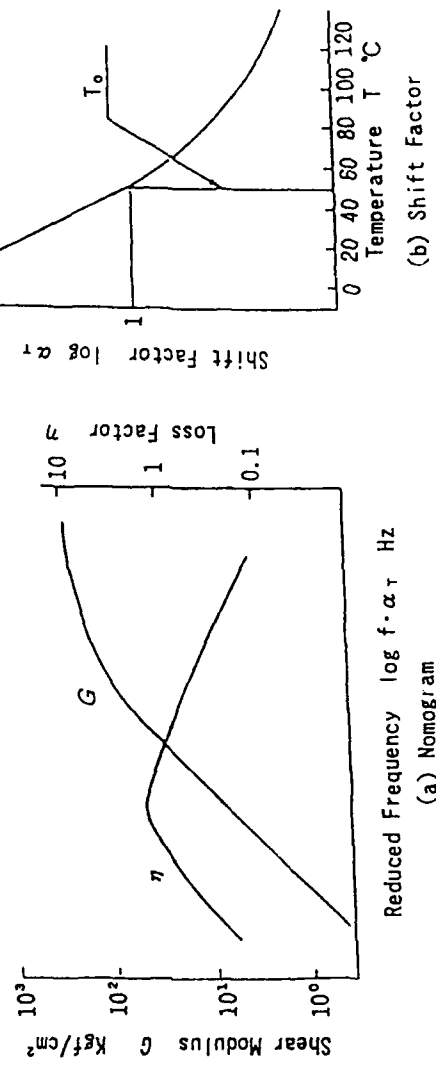


Fig. 14 Damping Characteristic of Viscoelastic Material (Damping Layer of Laminated Sheet)

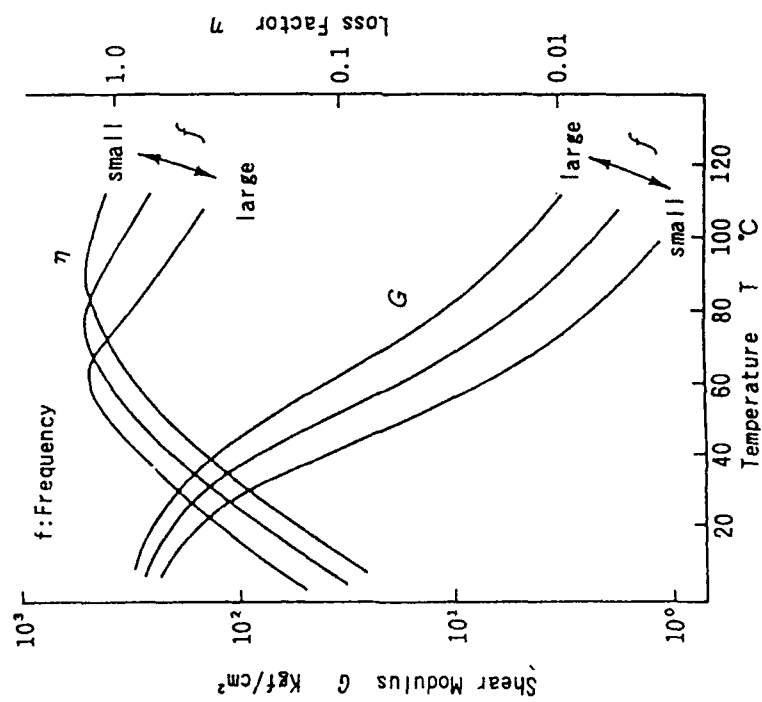


Fig. 15 Temperature and Frequency Characteristic of Viscoelastic Material (Damping Layer of Laminated Sheet)

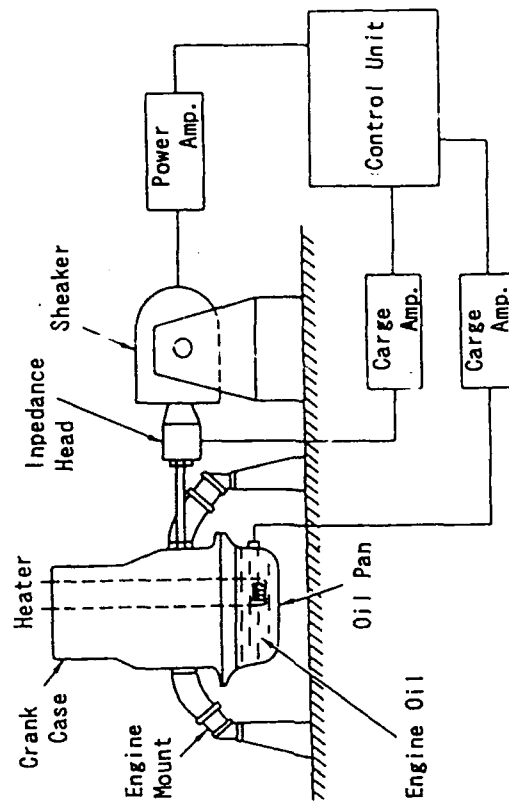


Fig. 16 Measurement Method of η Value for Oil Pan

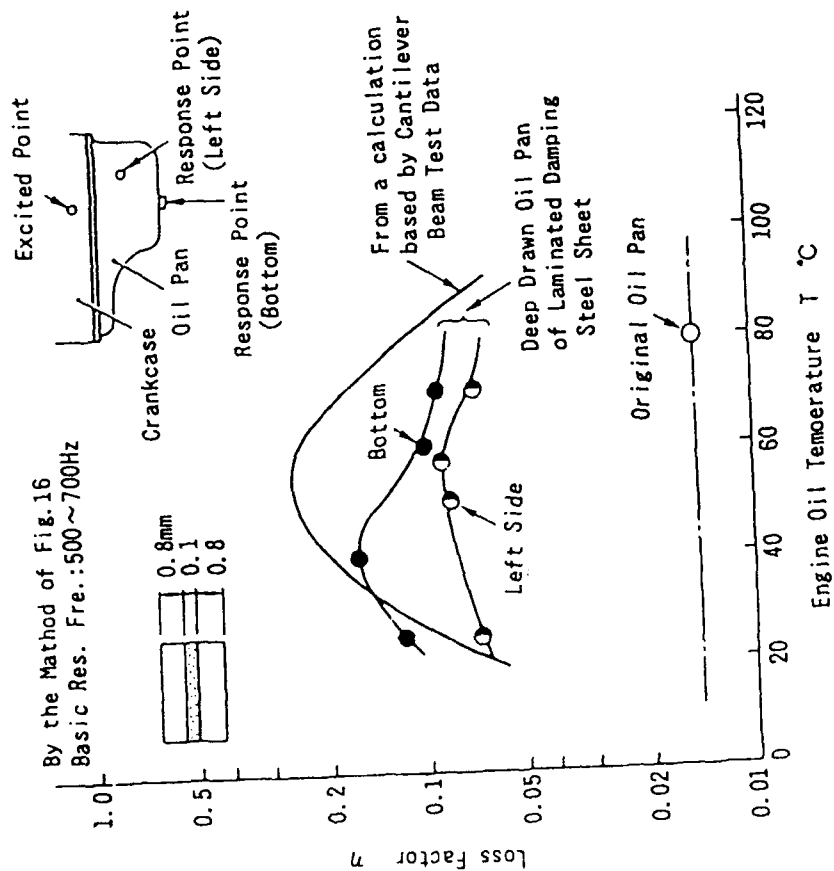


Fig. 17 η Value of Laminated Damping Steel Sheet Oil Pan

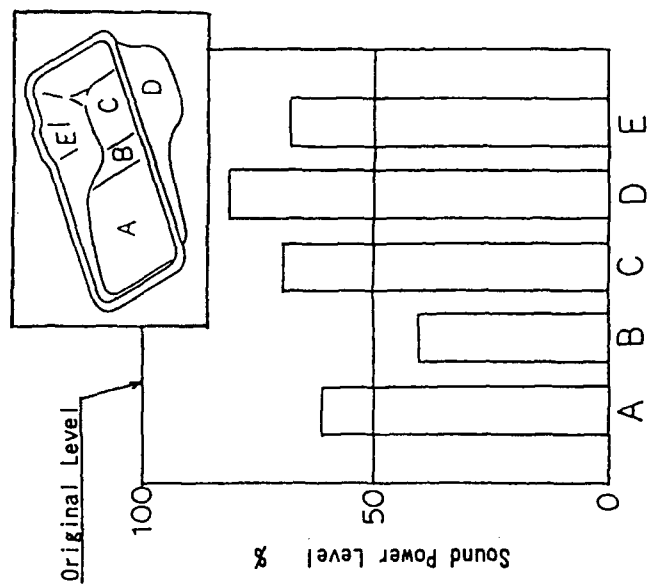


Fig. 18 Noise Reduction Effect on Sound Power Level of the Outer Surfaces of Laminated Damping Steel Sheet Oil Pan

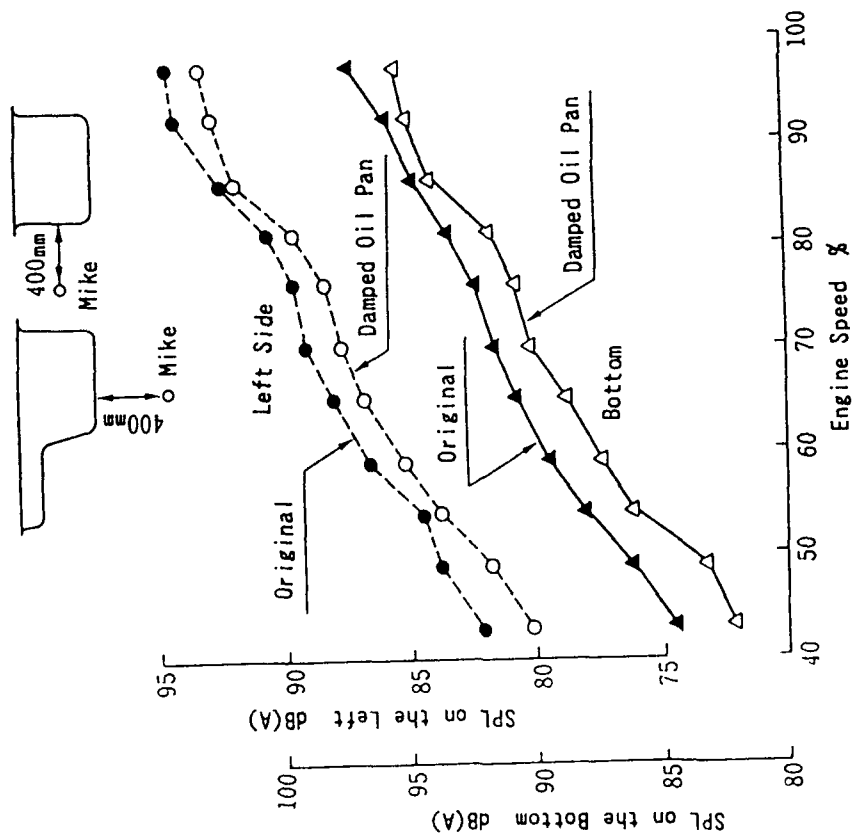


Fig. 19 Scund Pressure Level of Oil Pan

PRACTICAL DESIGN AND ANALYSIS OF SYSTEMS WITH FRACTIONAL DERIVATIVE MATERIALS AND ACTIVE CONTROLS

Daniel R. Morgenthaler *
Martin Marietta Astronautics Group
Denver, CO

ABSTRACT

The fractional derivative model of viscoelasticity is considered to be the most exact representation of viscoelastic material behavior, as it is based on the molecular theory of polymers. The classical fractional derivative expanded equations of motion, however, result in extremely large eigenproblems which are intractable for typical damped structural systems.

This paper discusses a procedure and numerical algorithms which can be used in the design and analysis of structures incorporating viscoelastic materials. Modal strain energy methods are used during the preliminary design phases, permitting inexpensive design iterations and structural modifications. After a satisfactory design is achieved, the solution to the problem is then generated using the frequency-dependent complex impedance matrix implied by the fractional derivative model. The eigensolution is generated using an accelerated complex subspace iteration procedure with spectral shifting. This technique provides the accurate solution to the fractional derivative eigenproblem with minimal computational requirements. When the complex open-loop modes are placed in an appropriate state-space form, active controls can then be directly applied to the reduced-order model.

The application of the method to an example problem with many degrees of freedom demonstrates that the method provides accurate closed-loop results, and can be implemented inexpensively on large-scale structural systems. Most importantly, the results show that the technique will be required for the application of sophisticated modern control algorithms to damped systems, and that the use of the modal strain energy technique to generate the open-loop system model for use in closed-loop analyses can provide results which are significantly in error.

* Mail Stop H4330
P. O. Box 179
Denver, CO 80201
(303)-971-9387

1.0 Introduction

Vibration control through the combined use of passive and active means has become an accepted method of performance enhancement for space systems with requirements for dimensional precision and stability. The Passive and Active Control of Space Structures (PACOSS) Program has shown that very accurate models of damped or undamped structures are required for successful implementation of modern control strategies. The Modal Strain Energy (MSE) method is a well known analytic method of approximating the behavior of damped systems with viscoelastic damping treatments, and this method serves as an outstanding tool for the design of complex structural systems with damping. As the MSE method is an approximation of the behavior of the damped system, the results of analyses using the MSE solution must be used cautiously.

The representation of the behavior of viscoelastic materials is most accurately described using fractional derivative models [1-5]. These models have their origin in the molecular behavior of polymers, and have been shown to accurately describe the behavior of many materials which lose energy in cyclic vibration. However, the fractional derivative representation of material behavior in the modeling of large-scale structural systems has generally been disregarded, due to the absence of numerical procedures which solve the equations of motion in an efficient manner.

This paper discusses a procedure which has been developed to efficiently design and analyze structural systems with materials which can be described by fractional derivative models, and provides an accurate reduced-order state-space form which can be used to design high-authority modern control systems and predict system performance. This method relies on an iterative solution of the differential equations of motion in the Laplace domain, which is termed spectral iteration. This method is used in conjunction with the subspace iteration eigensolution procedure to develop an efficient numerical algorithm for the solution of large fractional derivative eigenproblems typical of those which may be encountered in realistic structural applications.

The MSE method is the first step in this iterative process. Therefore, the new technique can be incorporated into an efficient design and analysis methodology which uses the MSE approximation during preliminary design stages, and improves the accuracy of the analysis as the design matures.

Through a sufficiently complex example problem, the new technique is shown to provide a system representation which may be used in the design of high-authority control systems, and to predict the closed-loop performance of passive/active systems. The number of the degrees of freedom of the example problem is large enough to demonstrate that the procedure can be used for the solution of realistic problems with viscoelastic damping treatments. It is also shown, however, that control designs which are generated based on a MSE plant model and exercised on the fractional derivative plant may have performance which is seriously degraded when compared with analytic predictions, and may even be unstable.

The new technique can be successfully used for materials represented using any order fractional derivative constitutive model, and indeed for any representation of the material behavior in the Laplace domain. The procedure may even prove to be more efficient in the eigensolution of large-scale problems which incorporate classical viscous damping than those which are presently available in many finite element codes. Further development of this and similar methods should result in techniques which can be effectively used on large-scale systems of the future with vibration control requirements.

2.0 The Fractional Derivative Representation of Material Behavior

The fractional derivative model of viscoelasticity is developed, based on a fractional derivative representation of the relationship between stress and strain within a viscoelastic material [1,2].

$$\sum_{m=1}^M b_m D^{\beta_m} \{ \tau(t) \} + \tau(t) = G_0 \gamma(t) + \sum_{n=1}^N G_n D^{\alpha_n} \{ \gamma(t) \} \quad (1)$$

where $\tau(t)$ is the material stress, $\gamma(t)$ is the material strain, the b_m and G_n are real constants, and D^k is the fractional derivative operator of order k .

A 5-parameter model can be developed which includes a single fractional derivative of both stress and strain. In the Laplace domain, this provides a Young's modulus and shear modulus which are the ratios of the Laplace transforms of stress and strain, and depend on the Laplace variable (frequency). Using the 5-parameter model, the shear modulus can be expressed:

$$G(s) = \frac{\tau(\omega)}{\gamma(\omega)} = \frac{G_0 + G_1 s^\alpha}{1 + b s^\beta} \quad (2)$$

An additional constraint on the representation in equation (2) is that the values of the powers α and β must be equal to be consistent with thermodynamic considerations [3]. This representation of material behavior is consistent with the macroscopic behavior of many rubbery and glassy materials, and is based on the molecular theory of polymers. Experimental data of the frequency-dependent behavior of a material can be fit using the fractional derivative model to allow the description of the material behavior in the frequency domain.

As an example, consider the viscoelastic material DYAD-606 from Soundcoat. Experimental data previously gathered for use on the PACOSS program was available for this material at 68°F in the frequency range from 1 to 46 Hz. This raw experimental data was fit using the 5-parameter model and a nonlinear error-norm minimization process. Using this technique, the five parameters of the model which best fit the data were:

$$G_0 = 246.45 \text{ psi}, G_1 = 534.22 \text{ psi}, b = 0.1043 (\text{sec})^{0.7049}, \alpha = 0.7049, \beta = 0.4885$$

Graphs of the experimental data and the resulting fractional derivative representation of the frequency-dependent shear modulus and material loss factor are given in Figures 1 and 2. Notice that the agreement between the experimental data and the fractional derivative model are exceptional for this material. However, the two fractional powers (α and β) differ for this fit of the material properties. The cause of this anomaly is unknown, and a higher-order fractional derivative model may be required. The above parameters were used in the subsequent example problem which included this viscoelastic.

A similar fit was performed for the viscoelastic material 3M-966, and 68°F experimental data was also available for this material from previous PACOSS work. The optimum model parameters for this material were:

$$G_0 = 7.9856 \text{ psi}, G_1 = 7.6992 \text{ psi}, b = 5.29 \times 10^{-4} (\text{sec})^{0.6053}, \alpha = 0.6053, \beta = 0.6053$$

The agreement between the experimental data and the fractional derivative model were equivalent to those found for DYAD-606. In this case, however, even though no constraints were imposed on the model parameters, the optimum values of the fractional derivative orders were the same. This is consistent with the thermodynamic requirements of the 5-parameter model. For both of these materials, an outstanding representation of the frequency-dependent material properties was achieved using the 5-parameter model. This agreement demonstrates the applicability of the fractional derivative model to many viscoelastic materials.

3.0 The Modal Strain Energy Method In the Approximate Solution of the Open-Loop System

The MSE method is a well known method of approximating the eigenvalues and eigenvectors of a dynamic system which includes viscoelastic material damping treatments. This method assumes that the real modes associated with the real part of the system stiffness matrix evaluated in the neighborhood of the eigenvalue are a sufficiently accurate approximation to the complex system eigenvectors. The importance of the MSE method as a design tool cannot be overemphasized, and the method allows the economical design of damping treatments for complex structures. This method approximates the solution to the frequency-dependent complex eigenvalue problem, and provides insight to facilitate effective structural modifications.

In general, the frequency-dependent complex stiffness matrix (complex impedance matrix) of a system which includes fractional derivative materials can be written as a sum of contributions from elastic elements and from each type of viscoelastic material. If the Poisson's ratio of the material is frequency independent, the total stiffness matrix can be written:

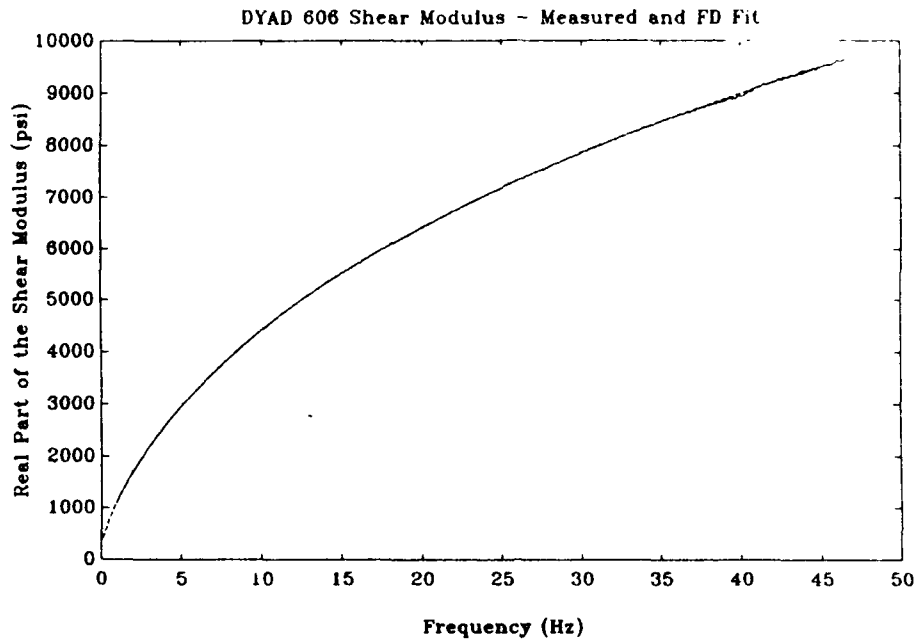


Figure 1 - Experimental DYAD - 606 Shear Modulus and Fractional Derivative Fit

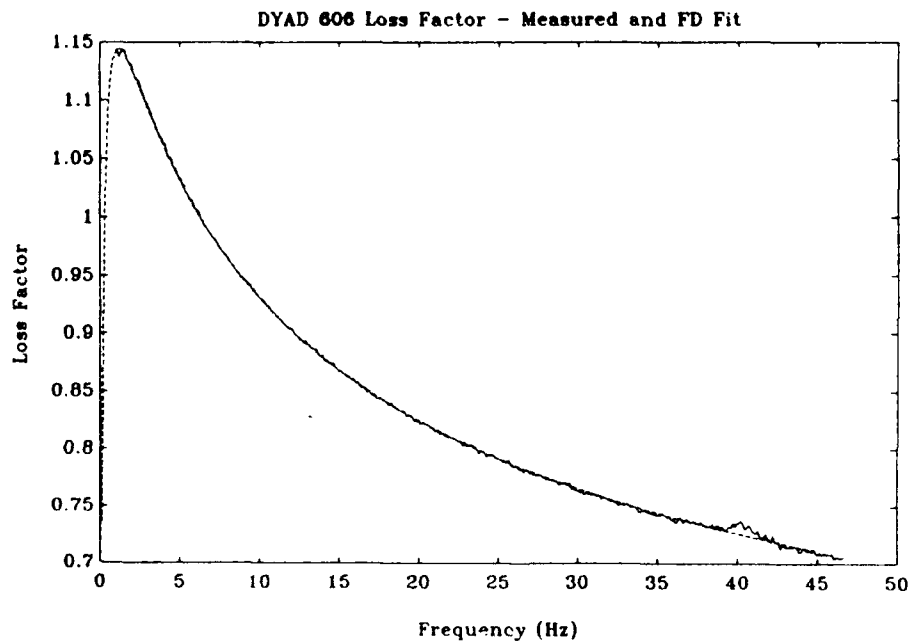


Figure 2 - Experimental DYAD - 606 Loss Factor and Fractional Derivative Fit

$$\mathbf{K}(\mathbf{s}) = \mathbf{K}_e + \sum_{i=1}^{nvm} \mathbf{G}_i(\mathbf{s}) \cdot \mathbf{K}_{vi} \quad (3)$$

where:

$\mathbf{K}(\mathbf{s})$ = the complex impedance matrix as a function of the Laplace variable

\mathbf{K}_e = the frequency independent stiffness matrix associated with all elastic elements

$\mathbf{G}_i(\mathbf{s})$ = the frequency-dependent complex shear modulus of the i^{th} viscoelastic material

\mathbf{K}_{vi} = the stiffness matrix associated with all elements made of the i^{th} viscoelastic material, assembled with a unit shear modulus

nvm = the number of viscoelastic material types in the system

The MSE method then assumes that if the modes of the system are found using the real part of the complex stiffness matrix which is assembled using viscoelastic material properties on the imaginary axis (at $\mathbf{s} = i\omega$), that these vectors are sufficiently "close" to the actual system eigenvectors, and that these approximate vectors are uncoupled through both the real and imaginary parts of the stiffness matrix.

Therefore, the typical sequence of steps in an MSE analysis are:

- 1) Form the real part of $\mathbf{K}(\mathbf{s})$ using an appropriate approximate value of the eigenvalue taken along the imaginary axis.
- 2) Using the real part of $\mathbf{K}(\mathbf{s})$ and the system mass matrix, calculate the real eigenvalues and eigenvectors.
- 3) Store those eigenvectors which are in the neighborhood of the approximate frequency value assumed in step 1.
- 4) Repeat steps 1 through 3 until all approximate eigenvectors in the frequency range of interest have been found.
- 5) Determine the approximate modal damping ratios using the MSE distribution.
- 6) Construct the state-space form of the MSE model of the plant.

This procedure provides a set of \mathbf{q} approximate mode shapes, frequencies, and damping ratios found using the MSE analysis procedure. The damping ratios of the system are usually computed using the formula:

$$\zeta_j = \frac{1}{2} \sum_{i=1}^{NE} \mathbf{S} \mathbf{E}_{ij} \cdot \eta_i \quad (4)$$

where:

- ζ_j = the approximate modal damping ratio of the j^{th} mode
- SE_{ij} = the percentage of modal strain energy in the i^{th} element in the j^{th} mode
- η_i = the loss factor of the i^{th} element in the neighborhood of the j^{th} modal frequency
- NE = the number of system finite elements

This MSE procedure is equivalent to the following matrix operations:

- 1) Using an approximate eigenvalue on the imaginary axis, construct the stiffness matrix $K(s)$ using equation (3) and the system mass matrix.
- 2) Decompose the stiffness matrix into its real and imaginary parts, K_I and K_R .
- 3) Solve the real eigenvalue problem $(K_R - \omega^2 \cdot M) \Phi = 0$ for the q lowest eigenvalues and eigenvectors.
- 4) Mass normalize the eigenvectors from step 3.
- 5) Using the modes which are near the approximate frequency, construct the matrix products:

$$\begin{aligned}\Phi^T \cdot M \cdot \Phi &= I \\ \Phi^T \cdot K_R \cdot \Phi &= \omega^2 \\ \Phi^T \cdot K_I \cdot \Phi &= K_{ml}\end{aligned}\tag{5}$$

- 6) Form the second-order modal equations:

$$\ddot{p} + I \cdot K_{ml} \cdot p + \omega^2 \cdot p = \Phi^T \cdot f\tag{6}$$

- 7) Assume that the generalized velocities are equal to $i\omega$ times the generalized displacements, and neglect the off-diagonal terms in K_{ml} :

$$\ddot{p} + D_{vl} \cdot \dot{p} + \omega^2 \cdot p = \Phi^T \cdot f\tag{7}$$

where:

$$D_{vl}(j,j) = K_{ml}(j,j) / \omega(j,j)$$

- 8) Under the above assumptions, the terms in the diagonal matrix D_{vl} are $2 \cdot \zeta_j \cdot \omega_j$.
- 9) Construct the state-space form of the plant using an assemblage of the appropriate modes, natural frequencies, and damping ratios:

$$\begin{aligned}\dot{\mathbf{x}} &= \mathbf{A} \cdot \mathbf{x} + \mathbf{B} \cdot \mathbf{u} \\ \mathbf{y} &= \mathbf{C} \cdot \mathbf{x}\end{aligned}$$

or:

$$\begin{aligned}\begin{bmatrix} \ddot{\mathbf{p}} \\ \dot{\mathbf{p}} \\ \mathbf{p} \end{bmatrix} &= \begin{bmatrix} -2\zeta\omega & -\omega^2 \\ \mathbf{I} & 0 \end{bmatrix} \cdot \begin{bmatrix} \dot{\mathbf{p}} \\ \mathbf{p} \end{bmatrix} + \begin{bmatrix} \Phi^T \\ 0 \end{bmatrix} \cdot \mathbf{f} \\ \begin{bmatrix} \dot{\mathbf{x}} \\ \mathbf{x} \end{bmatrix} &= \begin{bmatrix} \Phi & 0 \\ 0 & \Phi \end{bmatrix} \cdot \begin{bmatrix} \dot{\mathbf{p}} \\ \mathbf{p} \end{bmatrix}\end{aligned}\quad (8)$$

This state-space form of the open-loop system can be used to design a control system to provide desired closed-loop performance characteristics of the MSE plant. However, as numerous assumptions are used in the computation of the open-loop plant, the quality of the state-space model cannot be assessed. It will be demonstrated through an example problem that the effects of these assumptions can result in significant errors in the behavior of the closed-loop system, if the MSE plant is used in control design and performance evaluation.

4.0 The Eigenstructure of the Fractional Derivative Eigenvalue Problem

It is necessary to develop the definition of the eigenvalues and eigenvectors of systems which include viscoelastics modeled using fractional derivatives, to allow a comparison with the approximate values derived from the MSE method and their improvement. The transformed equations of motion for the system can, in general, be written in the Laplace domain as:

$$[\mathbf{M} \cdot \mathbf{s}^2 + \mathbf{K}(\mathbf{s})] \cdot \mathbf{X}(\mathbf{s}) = \mathbf{F}(\mathbf{s}) \quad (9)$$

where:

- \mathbf{M} = the system mass matrix
- $\mathbf{K}(\mathbf{s})$ = the complex frequency-dependent impedance matrix of equation (3)
- $\mathbf{X}(\mathbf{s})$ = the Laplace transform of the system displacements
- $\mathbf{F}(\mathbf{s})$ = the Laplace transform of the applied forces

The system dynamical matrix can now be defined as a function of the Laplace variable. This matrix is:

$$\mathbf{Z}(\mathbf{s}) = \mathbf{M} \cdot \mathbf{s}^2 + \mathbf{K}(\mathbf{s}) \quad (10)$$

For non-trivial solutions of the homogeneous differential equations, the dynamical matrix must become singular. Therefore, similar to the definition for classical undamped or viscously damped systems, the definition of an eigenvalue λ of the system with fractional derivative materials is:

$$\left| \mathbf{M} s^2 + \mathbf{K}(s) \right|_{s=\lambda} = 0 \quad (11)$$

The eigenvalues can be determined by expanding the determinant of the dynamical matrix and finding zeros of the characteristic polynomial. However, the matrix $\mathbf{K}(s)$ involves the Laplace variable raised to fractional powers. Therefore, the roots of this complex fractional-order characteristic equation are generally difficult to obtain. A surprising result of this development is that there are, in general, infinitely many roots to this equation for a finite number of degrees of freedom, if the fractional powers cannot be expressed as a rational fraction. If the fractional powers can be expressed as a rational fraction r/m , then there are $N(2m+r)$ eigenvalues where N is the number of system degrees of freedom. The additional eigenvalues are located on branches of the multi-valued fractional power function and contribute to response of the system by an integral term along a branch cut [3].

All the eigenvalues of the system can be found by expanding the equations of motion to clear the fractional powers [3,4,5], if the powers are expressible as rational fractions and all viscoelastic materials in the system have the same denominator m . A state-space model of the expanded system equations of motion may then be constructed in either physical or generalized coordinates [6].

The associated eigenvector for any known eigenvalue can be found by solving the homogeneous form of equation (9) for the mode shapes. To find a selected eigenvalue and eigenvector, a procedure which will be termed spectral iteration may be used. In this procedure, an approximate value for an eigenvalue is used to construct the complex impedance matrix, and a complex eigenvalue problem is solved. This procedure is given in equation (12).

Solve equation (7) for Φ and λ_{new} using an assumed value of λ :

$$\left[\mathbf{M} \cdot \lambda_{\text{new}}^2 + \mathbf{K}(\lambda) \right] \cdot \Phi = 0 \quad (12)$$

A simple method of obtaining a selected eigenpair is to iterate using equation (12). Using an approximate eigenvalue λ , the matrix function $\mathbf{K}(\lambda)$ is evaluated, and the eigenvalues using this complex matrix are found. If λ is a good approximate value, then one of the eigenvalues found will be "close" to the initial guess. This new guess is then used to recalculate the complex stiffness matrix. By performing this process iteratively, the procedure will converge to an exact eigenvalue and eigenvector of the system.

This is similar to the inverse power method developed in [7] for the solution of the fractional derivative eigenproblem, where a solution procedure based on the inverse power method with spectral shifting is used to evaluate the eigenpairs of the system. This procedure of spectral iteration can be further developed and improved to provide computationally inexpensive solutions. It will be shown that the MSE method is a form of the spectral iteration procedure, and further improvements to the MSE solution are possible at minimal computational expense.

For the solution of large-scale dynamic systems with fractional derivative materials, the major objective is to construct a reduced-order state-space model of the structure from its finite element representation. Typically, only a small subset of the system eigenvalues and eigenvectors will be required; and the solution of the expanded fractional derivative equations of motion for a system with many degrees of freedom would be computationally infeasible or even impossible if several materials are used. Therefore, for a typical structural application, the concern is to locate eigenvalues and eigenvectors of the system within a selected spectral radius from the origin of the Laplace domain (i.e., the q smallest eigenvalues). Expansion of the ideas of the MSE method and spectral iteration into a procedure consistent with subspace iteration allows the evaluation of the desired eigenpairs in an efficient manner.

5.0 The MSE Method and Standard Subspace Iteration

The MSE method provides an approximation to the q lowest eigenvalues of a damped system. In the solution of the fractional derivative equations, it is advantageous to consider the mathematical basis of the MSE method and means to improve the accuracy of the approximations. Therefore, consider the form of the stiffness matrix developed in equation (3), and the reduction of the mass and stiffness matrices in equation (5) using a set of q MSE approximate vectors as a vector basis (subspace):

$$\left[\Phi^T \cdot M \cdot \Phi \cdot s^2 + \Phi^T \cdot K(s) \cdot \Phi \right] \cdot P(s) = \Phi^T \cdot F(s) \quad (13)$$

These reduced equations can be written:

$$\left[M^R \cdot s^2 + K_{\bullet 1}^R + \sum_{i=1}^{nvm} G_i(s) \cdot K_{v_i}^R \right] \cdot P(s) = F^R(s) \quad (14)$$

where the reduced matrices are of size $q \times q$ and are formed by matrix triple products, and the forcing vector is a $q \times 1$ generalized forcing vector:

$$\begin{aligned} M^R &= \Phi^T \cdot M \cdot \Phi \\ K_{\bullet 1}^R &= \Phi^T \cdot K_{\bullet 1} \cdot \Phi \\ K_{v_i}^R &= \Phi^T \cdot K_{v_i} \cdot \Phi \\ F^R(s) &= \Phi^T \cdot F(s) \end{aligned} \quad (15)$$

It is obvious that since the eigenvectors computed using the MSE method will generally be computed using several real stiffness matrices, the reduced mass matrix will not be an identity matrix, and the real part of the reduced stiffness matrix will not be

diagonal. However, these matrix equations are similar in form to those in equation (12) and can be solved using spectral iteration in a similar manner,

i.e., solve:

$$\left[\mathbf{M}^R \cdot \lambda_{\text{new}}^2 + \mathbf{K}^R(\lambda) \right] \cdot \Psi = 0 \quad (16)$$

for the solution vectors Ψ and the eigenvalues λ using spectral iteration.

This iteration process is a Ritz analysis with the MSE method approximate MSE vectors Φ_{MSE} as the solution space [8]. The approximate eigenvalues of the full system are the eigenvalues λ of the reduced system, and the approximate eigenvectors are the complex vectors:

$$\Phi_C = \Phi_{\text{MSE}} \cdot \Psi \quad (17)$$

If the range of the approximate MSE vectors spans the solution space of the exact eigenvectors, the eigenpairs generated in this manner are exact solutions for the system. Notable cases where this will occur are when the damping in the modes is negligible, or if the entire system is composed of damped elements with an identical fractional derivative representation (i.e., proportional damping). In these cases, a set of real vectors can be found which provides an invariant subspace of the fractional derivative eigenvalue problem. The MSE approximation for the natural frequency and damping will be in error, however, even for a system of all damped elements.

In this manner, the MSE method can be shown to be an uncoupled Ritz analysis with the MSE vectors as a subspace. In fact, it is a Ritz analysis using uncoupled vectors (the Rayleigh Quotient) which was first used to derive the modal strain energy method [9]. It is assumed in the MSE method that these vectors are uncoupled in equation (16); therefore, the assumed reduced basis eigenvectors form an identity matrix.

The improved solution of the eigenvalue problem with a single spectral iteration is an inexpensive means of improving the quality of the solution, as it merely requires the generation of a real reduced mass matrix, a real reduced elastic stiffness matrix, and as many real reduced viscoelastic matrices as there are types of viscoelastic materials. The reduced complex impedance matrix is then formed by simply adding the reduced elastic stiffness matrix and the reduced viscoelastic matrices multiplied by their respective complex shear moduli. Therefore, to generate the initial reduced problem, products which involve only real matrices and real vectors must be formed. The solution of the $q \times q$ reduced-order problem by spectral iteration will be inexpensive due to the small order of the system.

In general, the real MSE vectors will not provide an invariant subspace of the fractional derivative problem. Therefore, a method is required to improve the subspace and allow a more accurate representation of the solution. To examine

methods of subspace improvement, consider the subspace iteration eigensolution method for real, constant stiffness and mass matrices.

Subspace Iteration Steps:

- 1) Select an initial subspace of vectors Φ_k of size $N \times p$ where N is the system order, and p is larger than the number of desired vectors, q .
- 2) Decompose the stiffness matrix into its $L D L^T$ factorization
- 3) Perform a simultaneous power iteration on the approximate vectors using forward elimination and back substitution,
i.e., solve for Φ_{k+1} using:

$$K \cdot \Phi_{k+1} = M \cdot \Phi_k \cdot \lambda_k^2 \quad (18)$$

- 4) Create reduced mass and stiffness matrices:

$$\begin{aligned} M_{k+1}^R &= \Phi_{k+1}^T \cdot M \cdot \Phi_{k+1} \\ K_{k+1}^R &= \Phi_{k+1}^T \cdot K \cdot \Phi_{k+1} \end{aligned} \quad (19)$$

- 5) Solve the reduced eigenproblem for λ_{k+1} and Ψ_{k+1} .

$$\left[M_{k+1}^R \cdot \lambda_{k+1}^2 + K_{k+1}^R \right] \cdot \Psi_{k+1} = 0 \quad (20)$$

- 6) Orthogonalize the current subspace:

$$\Phi_{k+1} = \Phi_{k+1} \cdot \Psi_{k+1} \quad (21)$$

- 7) Return to step 3 with Φ_{k+1} as new subspace, and iterate until convergence.
- 8) Perform a Sturm sequence check to determine if all desired eigenvalues and eigenvectors have been found.

This procedure may be used for the fractional derivative eigenvalue problem, with spectral iteration performed at step 5 for each major iteration. The greatest expense of this procedure, however, would be the computation which improves the subspace at step 3. For the fractional derivative eigenvalue problem, the "stiffness" matrix is complex and a function of the eigenvalue; and it is infeasible to factor the full-system size complex matrix and perform several complex matrix/complex vector products at each iteration. This is the major deficiency of the inverse power method with spectral shifting presented in [7], as a complex factorization was used for each power iteration.

To alleviate these difficulties, a method of accelerated subspace iteration which does not include the inversion of a matrix was developed for use in the solution of the fractional derivative eigenvalue problem. This procedure allows the improvement of the subspace with a minimum computational burden, and rapid convergence to the q smallest system eigenvalues.

5.0 Accelerated Subspace iteration for the Solution of the Open-Loop Eigenvalue Problem

Subspace iteration was first developed by Bathe in the early 1970s [10]. Further advances in the technique were subsequently developed and were designated accelerated subspace iteration [11]. In this procedure, Lanczos vectors are used to generate the initial subspace, and spectral shifting during the power iterations is performed using the approximate inversion method of successive overrelaxation. This method allows fewer than q vectors to be used as the p size subspace, while in the standard subspace iteration method usually the minimum of $2 \cdot q$ or $q+8$ vectors are selected as a subspace. Using several of the ideas of the accelerated subspace iteration, along with the spectral iteration technique and several new developments, an accelerated subspace iteration procedure for the fractional derivative eigenvalue problem was developed.

The basis of this technique is a preconditioned conjugate gradient procedure developed specifically to allow the iterative solution of linear equations with a symmetric coefficient matrix which is complex,

i.e., the solution technique was developed to solve the linear equations:

$$\mathbf{A} \cdot \mathbf{x} = \mathbf{b} \quad (22)$$

where the matrix \mathbf{A} is an $\mathbf{N} \times \mathbf{N}$ symmetric complex matrix, and the complex vectors \mathbf{x} and \mathbf{b} are of size \mathbf{N} . The derivation and the numerical algorithm will not be discussed here, however, the use of the technique will be described. The technique splits a shifted dynamical matrix into two components: \mathbf{K}_0 and $\Delta\mathbf{K} + (2\alpha\mu + \mu^2)\mathbf{M}$, where μ is an appropriate spectral shift at each step selected to allow rapid convergence to a particular eigenvalue, and α is a shift used in the generation of the matrix \mathbf{K}_0 . The updating procedure which is used to replace step 3 in the standard subspace iteration is then the formula:

$$\mathbf{K}_0 \cdot \Phi_{j+1} = -(\Delta\mathbf{K} + 2\alpha\mu_j\mathbf{M} + \mu_j^2\mathbf{M}) \cdot \Phi_j \quad (23)$$

where the residual error after j iterations is defined as:

$$\mathbf{r}_j = \mathbf{K}_0 \cdot \Phi_{j+1} + (\Delta\mathbf{K} + 2\alpha\mu_{j+1}\mathbf{M} + \mu_{j+1}^2\mathbf{M}) \cdot \Phi_{j+1} \quad (24)$$

The search directions are generated by conjugate gradients, and are selected to minimize the residual while being orthogonal through the dynamical matrix to all previous residuals and approximate modal vectors. This method is, therefore, similar

to the preconditioned method of conjugate gradients [12].; however, it was designed to allow complex matrices. The search vectors can be interpreted as Lanczos vectors selected to provide the greatest reduction in the norm of the residual vector on each step. With a proper selection of the matrix \mathbf{K}_0 , this procedure will converge in few iterations to an eigenvector which is closest to the shift point $\alpha + \mu$. An excellent selection of the preconditioner is the shifted real stiffness matrix (shifted by a value of α) computed during the modal strain energy procedure (it can be assumed that a shifted real stiffness matrix $(\mathbf{K}_{\text{MSE}} + \alpha \cdot \mathbf{M})$ was factored during the solution of the MSE real eigenvalue problem):

$$\mathbf{K}_0^{-1} = (\mathbf{K}_{\text{MSE}} + \alpha \cdot \mathbf{M})^{-1} \quad (25)$$

This selection results in low rank of the $\Delta \mathbf{K}$ matrix, as this matrix contains only terms from viscoelastic elements and, therefore, has many zero rows and columns. The eigenvalues of the matrix $\mathbf{K}_0^{-1} \cdot \Delta \mathbf{K}$ will be small, as the MSE stiffness matrix is "close" to $\mathbf{K}(\mathbf{s})$. These properties of $\Delta \mathbf{K}$ and $\mathbf{K}_0^{-1} \cdot \Delta \mathbf{K}$ provide rapid convergence of the iterations [12].

Convergence of this conjugate gradient procedure results in an eigenvector/eigenvalue of the system. Very importantly, the iterations need not be performed until convergence in the accelerated subspace procedure, as the objective of step 3 in the standard method is simply to improve the subspace. The linear combination of Lanczos vectors generated as search vectors provide a good set of basis vectors with which the subspace can be improved, even though the iterations have not converged. Therefore, in the accelerated subspace procedure, the iterations implied by equation (23) are only performed once, and these vectors are used as a new vector basis. After orthogonalization, a further basis improvement is performed.

In summary, the steps which comprise the accelerated subspace iteration procedure for systems which include materials modeled with fractional derivatives are:

- 1) Select the MSE solution vectors as the initial subspace.
- 2) Create the reduced mass, elastic stiffness, and viscoelastic stiffness matrices as per equation (15). Store all matrix/vector products such as $\mathbf{K}_{01} \cdot \Phi_{k+1}$.
- 3) Perform spectral iteration within the subspace to compute new approximate eigenvalues and eigenvectors.
- 4) Update matrix products using reduced basis modal transformation.
- 5) Improve the basis vectors, and update matrix/vector products using the complex conjugate gradient procedure.
- 6) Return to step 3 using new basis vectors and updated matrix/vector products.
- 7) Iterate from steps 3 to 6 until convergence of the subspace.

Notice that the only matrix/vector products required in the solution procedure are contained in the conjugate gradient algorithm, with two plus the number of viscoelastic materials matrix/vector multiplications required for each basis vector per conjugate gradient iteration. Also, the total solution subspace need not be updated on

every iteration; and only the vectors which correspond to the eigenvalues which have not yet converged need be updated each time.

The above procedure can be considered a hybrid of several highly successful eigenvalue extraction methods: the power method with spectral shifting; Ritz analysis; and Lanczos methods, which are combined with spectral iteration to allow for the frequency dependence of the stiffness matrix. Experience on example problems shows that this method is very effective for solving the fractional derivative eigenvalue equations for the invariant subspace corresponding to the lowest system eigenvalues. A complex Sturm sequence check can be used to verify that all eigenvalues/vectors within a given spectral radius from the origin have been found by factoring a shifted impedance matrix; however, it may be assumed that the initial MSE solution provided approximations to all eigenvalues within the search region.

7.0 Generation of the State-Space Plant Model

After a selected number of modes of the open-loop system have been generated by the above procedure, an appropriate state-space description of the plant is required for performance evaluation and the generation of vibration control systems, if needed. This state-space model should allow the use of available modern control algorithms to be used to generate a compensator which will provide desired performance of the closed-loop system. Therefore, a complex modal formulation of the plant was developed to obtain this state-space description. This formulation finds a viscous representation of the plant which has identical eigenvectors and eigenvalues to the fractional derivative system. This is an approximation, however, it provides the most accurate viscous representation possible.

The generation of the modal state-space equations begins with the equations of motion of the full-size open-loop system in the Laplace domain. An appropriate general form of these equations is:

$$\begin{bmatrix} \mathbf{M} & 0 \\ 0 & -\mathbf{K}_R(s) \end{bmatrix} \cdot \begin{bmatrix} \mathbf{X}(s) \cdot s \\ \mathbf{X}(s) \end{bmatrix} \cdot s = \begin{bmatrix} -\mathbf{C}_R(s) & -\mathbf{K}_R(s) \\ -\mathbf{K}_R(s) & 0 \end{bmatrix} \cdot \begin{bmatrix} \mathbf{X}(s) \cdot s \\ \mathbf{X}(s) \end{bmatrix} + \begin{bmatrix} \mathbf{F}(s) \\ 0 \end{bmatrix} \quad (26)$$

$$\text{where: } \mathbf{K}_R(s) = \text{real}(\mathbf{K}(s)) - \frac{\text{real}(s)}{\text{imag}(s)} \cdot \text{imag}(\mathbf{K}(s))$$

$$\mathbf{C}_R(s) = \frac{\text{imag}(\mathbf{K}(s))}{\text{imag}(s)}$$

Notice that these equations provide an identical impedance matrix for the fractional derivative system and the viscous system. By solving the equations in the Laplace domain for a system eigenpair, a modal substitution which uncouples the equations with $\mathbf{K}(s)$ evaluated at an eigenvalue can be constructed. An appropriate modal substitution is:

$$\begin{bmatrix} \mathbf{X}(s) \cdot s \\ \mathbf{X}(s) \end{bmatrix} = \begin{bmatrix} \Phi \cdot \lambda \\ \Phi \end{bmatrix} \cdot \mathbf{P}(s) \quad (27)$$

$$\text{or } \chi = \psi P$$

where:

Φ = A system eigenvector found using spectral iteration

λ = A system eigenvalue

$P(s)$ = the Laplace transform of the generalized coordinate

With the substitution of the transformation as given in equation (27), the single coordinate which corresponds to an eigenvector of the fractional derivative system coordinate can be uncoupled from all other coordinates. This is achieved by noting that the matrix on the left-hand side is symmetric; and that if all the eigenvalues of the complex system were found using this constant value of $K(s)$, the full-size matrix ψ would be orthogonal to this matrix. Therefore, with the correct normalization, the left-hand side can be transformed to an identity matrix. This yields an uncoupled equation for a single generalized coordinate and also for its complex conjugate. The correct normalization for the individual eigenvectors is such that:

$$\Phi^T \cdot M \cdot \Phi \cdot \lambda^2 - \Phi^T \cdot K(\lambda) \cdot \Phi = 1 \quad (28)$$

where Φ is a single eigenvector, and λ is its associated eigenvalue.

Notice that the complex conjugate modes and natural frequencies and their normalization are found using this method. This is consistent with the fractional derivative material representation, as the fractional derivative description provides a complex conjugate shear modulus at a complex conjugate value of the Laplace variable:

$K(s)$ and $K(\tilde{s})$ are related by:

$$K(\tilde{s}) = \tilde{K}(s) \quad (29)$$

where \sim denotes complex conjugation.

Therefore, the complex conjugate eigenvalue and eigenvector of any solutions found in the accelerated subspace procedure are also eigenvectors/eigenvalues of the fractional derivative system. This is required to provide real, stable solutions in the time domain. An additional requirement on the complex impedance matrix $K(s)$ is that it must smoothly become a real matrix at the origin of the Laplace domain. This ensures causality of time domain solutions, and it is obvious from the 5-parameter model that this requirement is met.

Finally, a normalized modal matrix can then be assembled which provides the transformation of the equations into truncated modal form in the Laplace domain:

$$\bar{\Psi} = \begin{bmatrix} \Phi \cdot \lambda & \tilde{\Phi} \cdot \tilde{\lambda} \\ \Phi & \tilde{\Phi} \end{bmatrix} \quad (30)$$

where Φ is an $N \times q$ matrix of normalized eigenvectors, and λ is a $q \times q$ matrix of eigenvalues. Using this modal transformation and taking the inverse Laplace transform of these equations yields the final form of the state-space equations in the time domain:

$$\begin{bmatrix} \dot{\bar{p}} \\ \bar{p} \end{bmatrix} = \begin{bmatrix} \lambda & 0 \\ 0 & \tilde{\lambda} \end{bmatrix} \cdot \begin{bmatrix} \bar{p} \\ \tilde{p} \end{bmatrix} + \bar{\Psi}^T \cdot \begin{bmatrix} f \\ 0 \end{bmatrix}$$

$$\begin{bmatrix} \dot{x} \\ x \end{bmatrix} = \bar{\Psi} \cdot \begin{bmatrix} \bar{p} \\ \tilde{p} \end{bmatrix} \quad (31)$$

These equations are in standard first-order state-space form and, therefore, can be used in conjunction with modern control algorithms to design a control system or predict system performance.

6.0 Application of the Solution Procedure to the PACOSS Multi-Actuator Control Experiment

To show the applicability of the procedure to the solution of realistic dynamics and control problems which incorporate viscoelastic damping treatments, an example system was selected. This system was the PACOSS Multi-Actuator Control Experiment (MACE) shown in Figure 3. This structure was previously constructed under the PACOSS Program to verify the performance of the control system hardware using modern control algorithms in a multi-actuator digital control application.

The original MACE hardware consisted of three proof mass actuators mounted to a series of flat aluminum beams. The system was hung from steel cables at three points with 60.9-lb/in. springs located at the top of the suspension. Constrained layer damping treatments using DYAD-606 damping material with steel constraining layers were applied to six locations on the beam members. These damping treatments provided from 0.5% to 2% critical damping in the modes of the system below 15 Hz.

While the original design of the MACE was satisfactory for the purposes of validating the successful operation of the PACOSS control system hardware, the relatively low damping levels are not characteristic of those which can be achieved in damped systems. Therefore, several modifications to the original design of the MACE structure were made for this example problem. First, the thickness of the DYAD damping material was increased from 0.050 in. to 0.120 in. to increase the damping performance of the constrained layer treatments. Second, viscoelastic dampers were designed which were placed in parallel with the suspension springs. These dampers use 3M-966 material in a configuration such that the spring constants in units of lb/in.

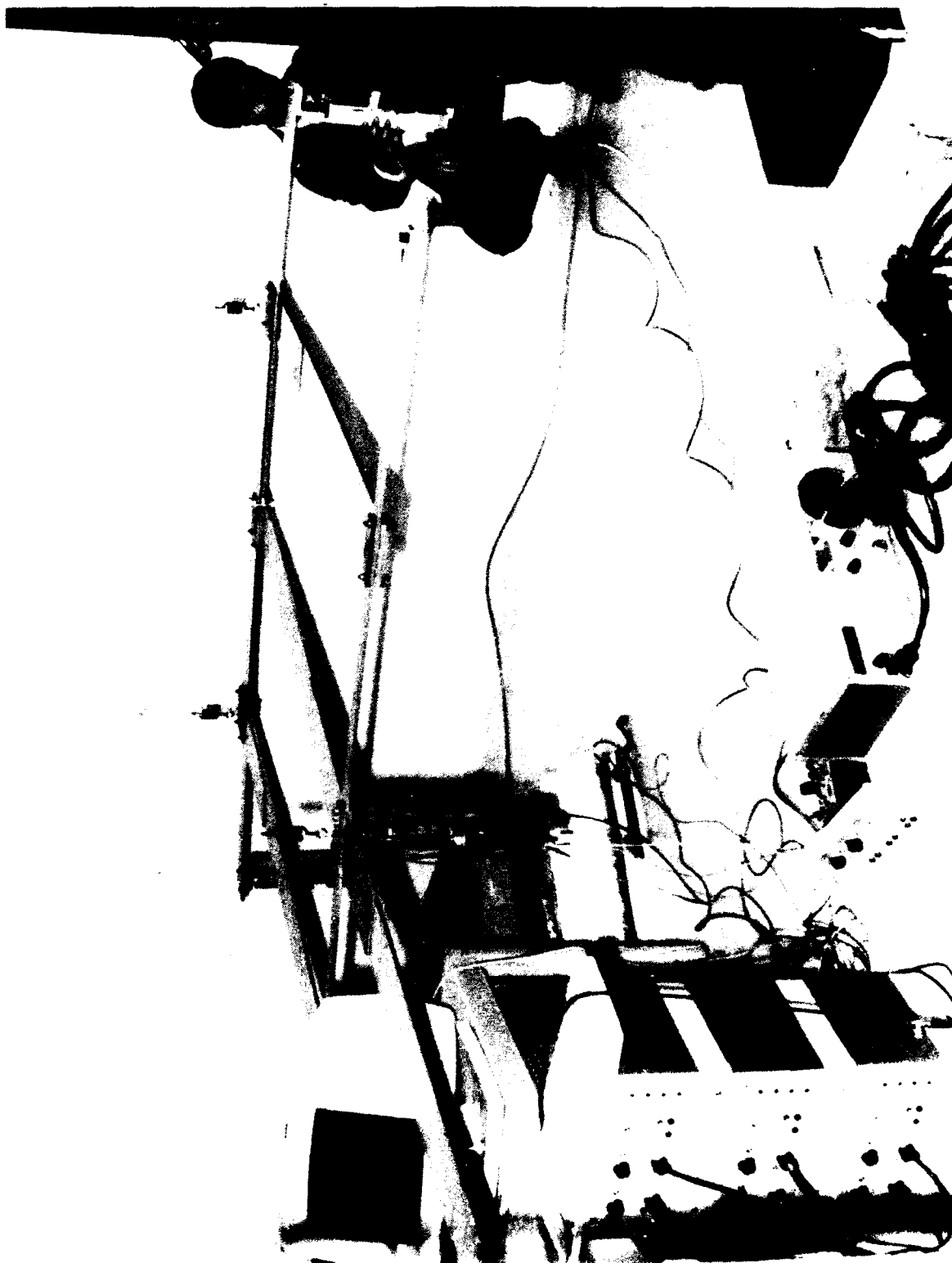


Figure 3 - Photograph of the PACOSS Multi-Actuator Control Experiment

were 0.25 multiplied by the material shear modulus in psi. Finally, four ideal actuators with ideal inertial velocity sensors were used instead of the three proof mass actuators used on the actual hardware. Four actuators were used to remove the actuator from the symmetric axis of the structure and to increase the control authority for anti-symmetric modes (Figure 4).

A finite element model of the damped structure was created using MSC/NASTRAN (Figure 5), which included the typical plate and solid element modeling of the constrained layer damping treatments as well as the pendulum behavior due to the suspension. The full-system mass matrix, the elastic/differential stiffness matrix excluding the damping materials, the stiffness matrix associated with the DYAD-606 material, and the stiffness matrix associated with the 3M-966 shear dampers were then assembled. Compatible stiffness matrices were easily formed by altering the material properties of the various components to be a small number. For example, to form the DYAD-606 stiffness matrix, the moduli of the main members and constraining layers, the suspension spring constants, and the 3M-966 moduli were set to extremely low values; and the modulus of the DYAD was set to unity. The full-stiffness matrix for any value of the Laplace variable could then be easily constructed by addition of the constitutive matrices, as per equation (3).

A performance metric was selected for the system, which was the vertical motion of a single point on the structure for noise inputs at the actuator locations. The objective to be achieved was a factor of 100 decrease in root mean square (RMS) motion of the performance point for white noise inputs from 0 to 30 Hz, as compared to a system without added damping treatments or active controls.

A modal strain energy analysis was performed on the system to approximate the open-loop modes, natural frequencies, and damping ratios in the frequency range from 0 to 30 Hz. The real stiffness matrix was assembled at six selected frequencies which were known to be "close" to system eigenvalues. The standard MSE method was used, with the modes nearest the corresponding frequency used to construct a state-space model of the plant as detailed in Section 6.0. Table 1 provides the open-loop frequencies and damping of the system computed using the MSE method.

Figure 6 provides the frequency response of the performance point motion for inputs at actuator #2, for both the MSE system and also for the system with 0.2% critical damping in the modes. Notice that the system has high modal density in the 0 to 30-Hz frequency range. The addition of passive damping treatments to the system lowers the RMS response by approximately a factor 5, so that active control is required to further reduce the system RMS response by a factor of 20.

Two active control algorithms were considered for the MACE example problem: local velocity feedback, and Linear Quadratic Gaussian with Loop Transfer Recovery (LQG/LTR). For local velocity feedback, a feedback gain of 0.25 lb-sec/in. was used for the inertial velocity at each of the actuators. The closed-loop response of the system was generated using the MSE state-space model, and compared with the open-loop system and the exact frequency response of the closed-loop fractional derivative model (Figure 7). Notice from the Figure that the agreement between the exact solution and the MSE solution is relatively good, differing only in some frequency

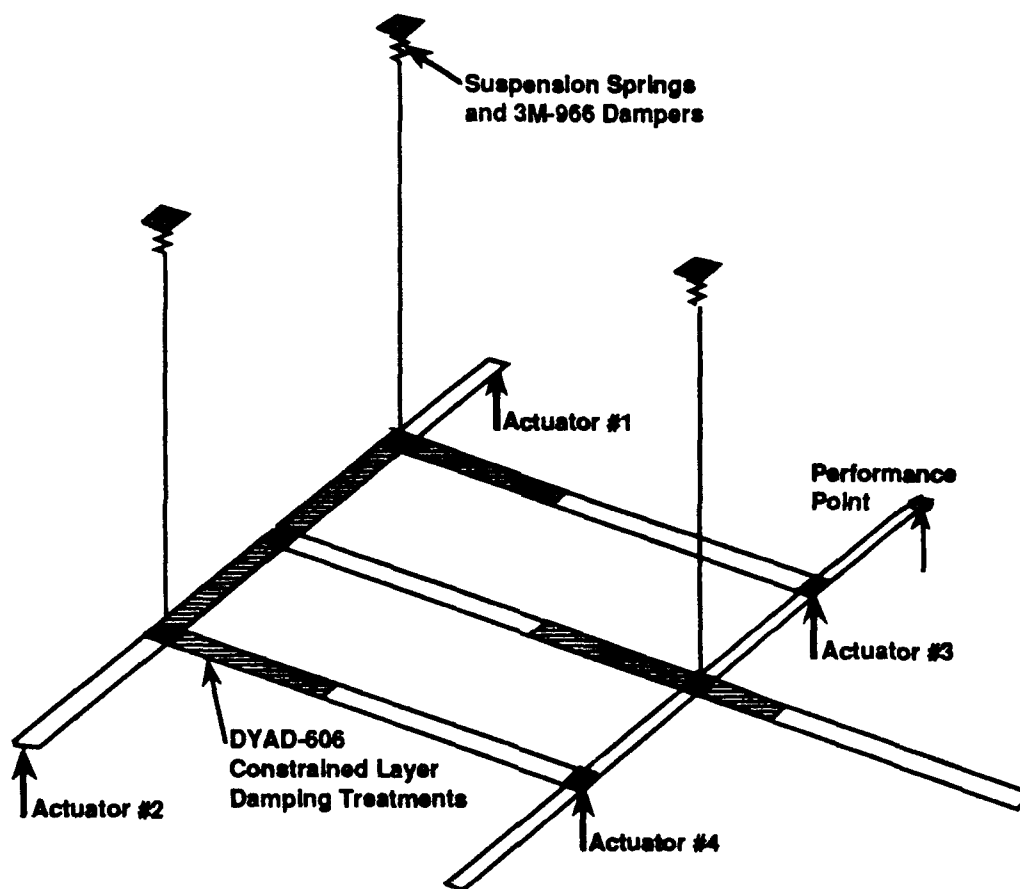


Figure 4 - Schematic of MACE Example Problem

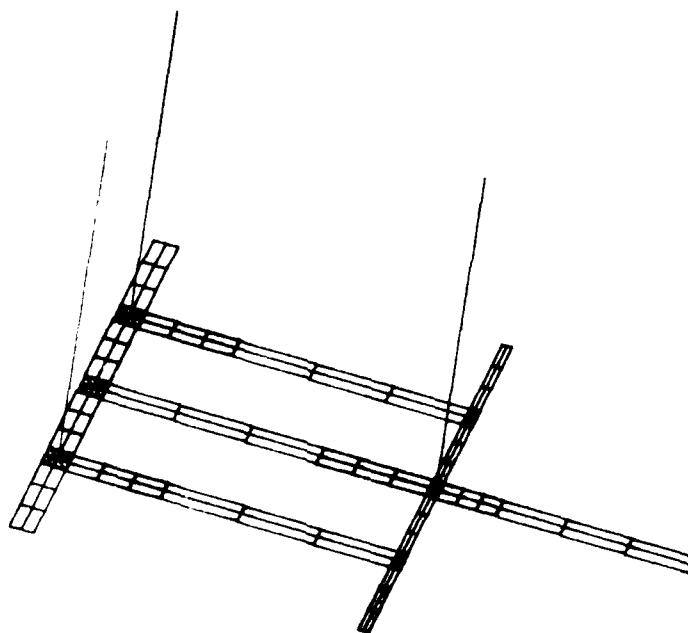
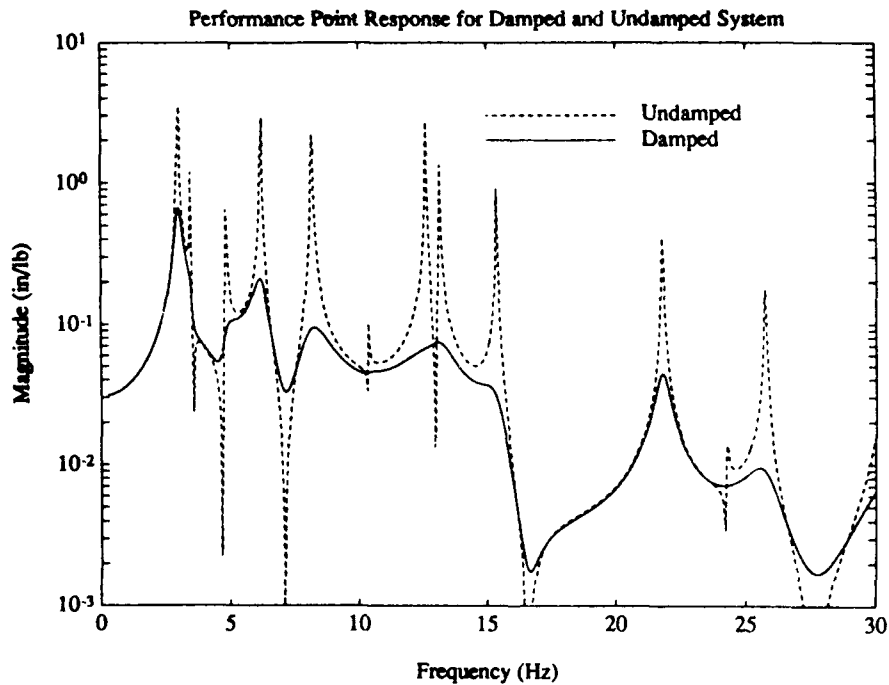


Figure 5 - NASTRAN Model of the MACE Example Problem

**Table 1 - Natural Frequencies and Damping Ratios of the MACE
Computed Using MSE**

Mode #	Frequency (Hz)	Damping Ratio (%)	Mode #	Frequency (Hz)	Damping Ratio (%)
1	0.28	0.0	11	12.6	7.9
2	0.28	0.0	12	13.1	4.1
3	0.28	0.0	13	15.4	3.3
4	2.83	5.0	14	21.8	1.2
5	2.98	4.0	15	24.3	5.1
6	3.46	3.8	16	25.7	2.5
7	4.82	5.4	17	30.5	3.9
8	6.18	4.2	18	34.3	3.3
9	8.17	7.0	19	37.1	3.8
10	10.3	2.7	20	37.8	3.7



**Figure 6 - Performance Point Frequency Response for Undamped System
and MSE Damped Solution**

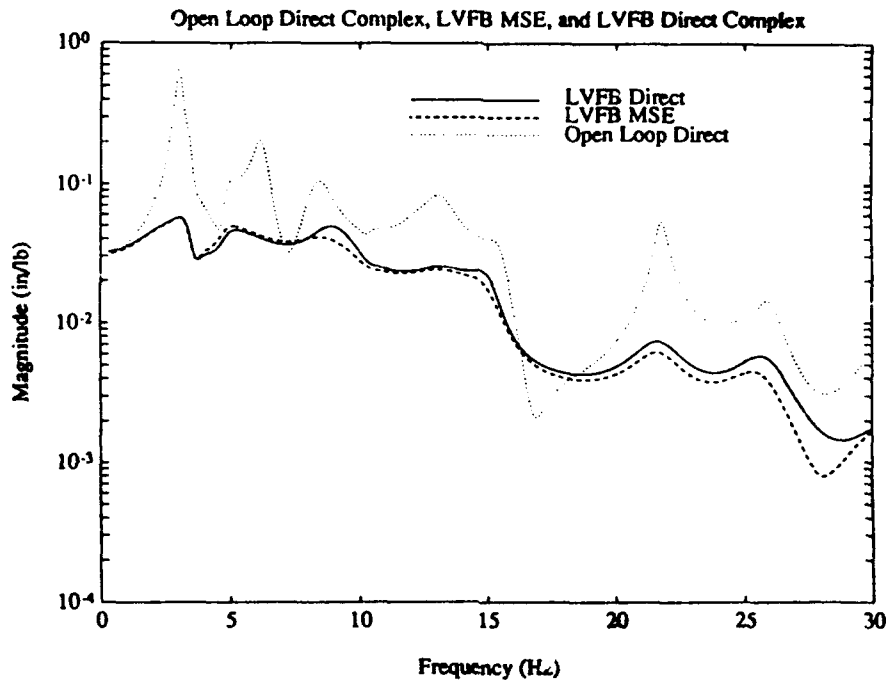


**Figure 7 - Local Velocity Feedback Closed-Loop Response
Exact and MSE Solutions**

ranges. The reduction in RMS response in this case is a factor of 3, when compared to the passively damped system. This agreement is consistent with PACOSS experience on the Dynamic Test Article [13], which used the MSE method to accurately predict the closed-loop response of a damped system with a local velocity feedback controller.

The exact frequency response of the closed-loop system was generated, using direct inversion of the closed-loop impedance matrix at each frequency point. This can be accomplished for an arbitrary controller by converting the compensator into an equivalent $N \times N$ frequency-dependent impedance matrix and adding it to the open-loop impedance matrix,

i.e., determine the $N \times N$ frequency-dependent matrix $G(s)$ which describes the Laplace transform of the control forces in terms of the motion of the structure. Then the Laplace transform of the closed-loop structural motion is:

$$\begin{aligned} X_{cl}(s) &= H_{cl}(s) \cdot F(s) \\ H_{cl}(s) &= [M \cdot s^2 + K(s) - G(s)]^{-1} \end{aligned} \quad (32)$$

Using this relationship, the closed-loop frequency response between applied noise at the actuators to the performance point motion can be computed at $s = i\omega$ by direct matrix inversion.

A compensator was also designed to control the MSE state-space model using the LQG/LTR algorithm. In this algorithm, a linear quadratic regulator is designed which provides the desired performance characteristics using full-state feedback. A linear quadratic estimator is then designed which approaches the full-state feedback performance by increasing a loop-transfer recovery parameter in the estimator design process. The regulator was designed so that the desired factor of 20 reduction in RMS response over the damped open-loop plant was obtained, and the loop-transfer recovery parameter was selected to the minimum value which provided acceptable performance of the estimator.

The exact closed-loop frequency response of the system was then generated using the LQG/LTR compensator designed for the MSE plant. A comparison of the open-loop response, the MSE prediction, and the exact closed-loop frequency response are given in Figure 8. Notice that there are large variations between the frequency responses predicted using the MSE plant and those found using direct inversion of the closed-loop impedance matrix. Although the closed-loop system does perform better than the open-loop system, in the 20-Hz region the closed-loop performance is actually amplified over the open-loop response. Furthermore, the reduction in RMS response is only a factor of 11, whereas the MSE plant predicts a reduction of a factor of nearly 21. This large discrepancy shows that for sophisticated active control algorithms, the MSE state-space model does not adequately describe the dynamic characteristics of the relatively simple MACE plant. A more accurate description of the open-loop system is required for a control design model.

A state-space model of the open-loop system was then generated using the accelerated subspace iteration procedure as described in the previous sections. This model was then used to design an LQG/LTR compensator to reduce the RMS response by a factor of 20, similar to the MSE design. The closed-loop frequency response predicted using this state-space model was then compared with the exact closed-loop solution. Figure 9 shows a comparison of the damped open-loop system frequency response, the exact open-loop frequency response, and the modal closed-loop response generated using the exact method and the reduced-order state-space model. Notice that there is good agreement between the open-loop performance predicted using the 40-state modal plant model and the exact response found by direct inversion.

Most important for the closed-loop system, the reduction in RMS response using the exact method is a factor of 21, which is the predicted reduction. The closed-loop performance predicted with the state-space model agrees well with the exact solution, although there are some differences in the frequency response. While the open-loop plant model accurately predicts the closed-loop response in this case, it may not in general. This is due to the assumption that the plant has viscous damping, which provides a plant which is locally accurate but may not be accurate if the poles are significantly altered by the controller. This is to be expected, as in the formation of the open-loop plant, the poles which describe the variation of the viscoelastic properties with frequency have been truncated. The introduction of the controller alters the eigenvalues of the plant and, therefore, a closed-loop eigenvalue problem must be solved with spectral iteration to achieve the best agreement with a modal model. However, the closed-loop performance shows that the described procedure provides

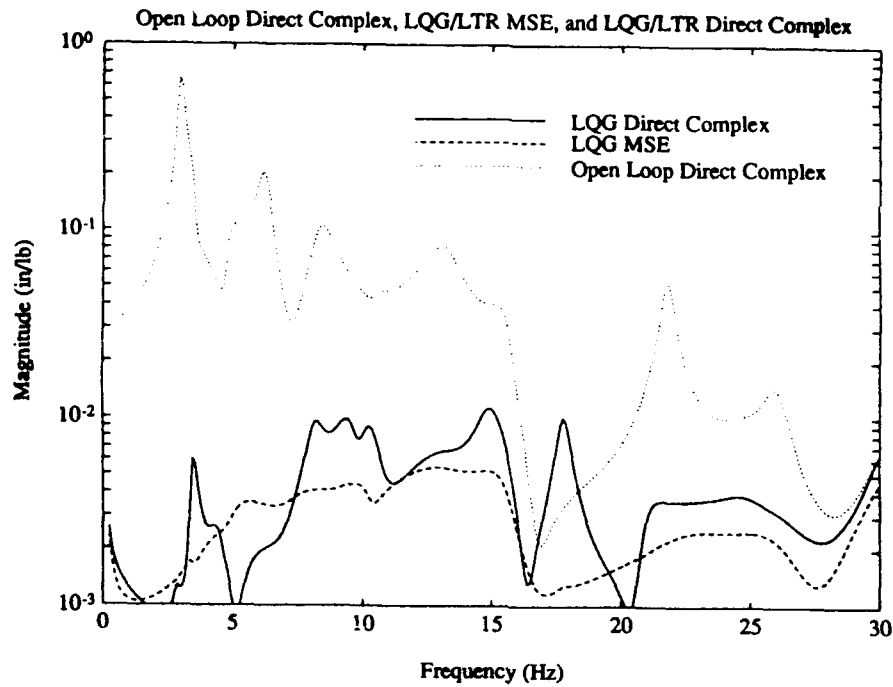


**Figure 8 - LQG/LTR Closed-Loop Frequency Response
Exact and MSE Solutions**

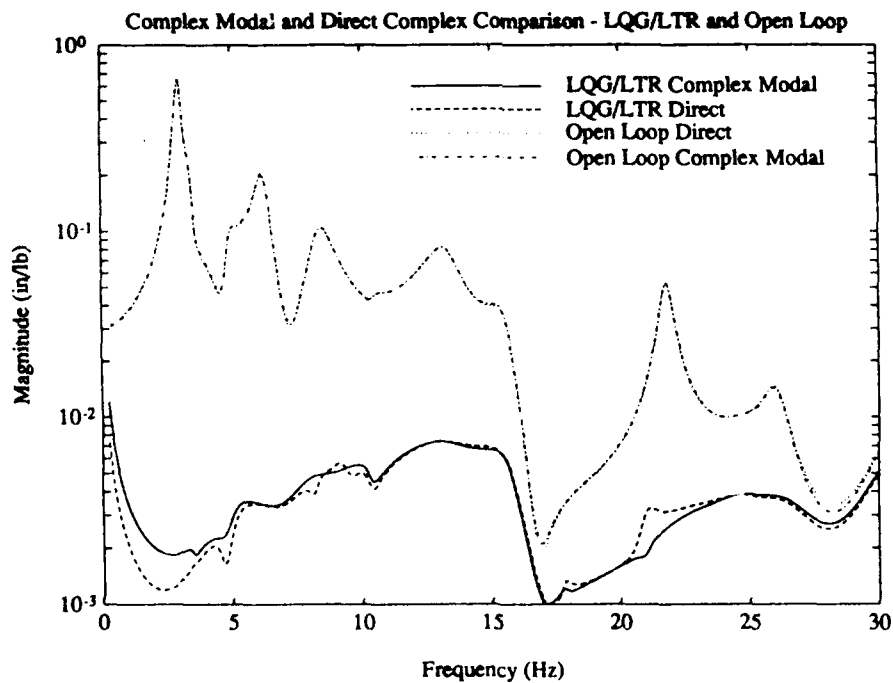


**Figure 9 - LQG/LTR Closed-Loop Frequency Response
Exact and Truncated Modal Solutions**

an accurate reduced-order plant model which allows the design of a controller which provides the desired closed-loop performance.

The variation between the MSE and complex modal open-loop plant models can also be seen in the comparison of the open-loop frequency responses. The greatest variation between the models is typically in the phase of the frequency response. As an example, consider the comparison of the phase of the frequency response of the MSE model, the complex modal model, and the exact solution given in Figure 10. Notice that there is nearly exact agreement between the complex modal model and the exact solution, but there is a large discrepancy between the phase of the MSE frequency response and the exact frequency response in several frequency ranges. At a frequency of 25 Hz, the phase of the MSE frequency response is actually 180° out of phase with the exact solution. This phase difference can cause significant performance degradation or even instabilities of the closed-loop system.

For the accelerated subspace procedure to be used for the analysis of actual systems, the cost of the procedure must not be excessive. Therefore, a comparison of the computer requirements for the MSE solution and for the improvement of the MSE solution using accelerated subspace iteration was made. Table 2 provides a comparison of the solution times for the two methods.

These computations were performed on a SUN 3/50 workstation, with the plant model having 279 degrees of freedom. The computer times represent elapsed time in seconds. To facilitate these computations, the full-size system matrices were reduced from nearly 1100 degrees of freedom by a Guyan reduction using viscoelastic properties in the middle of the desired bandwidth. This reduced model was then considered the exact model description. The MSE solution was generated using standard subspace iteration, and the MSE method to find the modes, natural frequencies, and damping ratios of the real system. Six frequency values were used to compute the MSE modes with the appropriate viscoelastic shear moduli. The complex subspace iteration procedure was applied using the inverse of the shifted MSE stiffness matrix with properties in the middle of the frequency band.

Notice that the accelerated subspace procedure is not excessive in terms of computer time, requiring only 125% of the MSE solution time, no matrix inversions, and 973 real matrix/complex vector multiplications. Therefore, the improvement of the MSE solution using the procedure defined in this paper can be used economically on large-scale structural systems, and will provide an accurate model for damped systems with minimal additional computational expense.

7.0 Conclusions

The above development and example problem allows several conclusions to be made in connection with the modeling of damped structural systems and active controls. The most important of these are:

- 1) The MSE method provides a tool which is very effective for use in the design of damped structures; however, it may not have sufficient accuracy for use in the final design of modern control systems for damped structures.

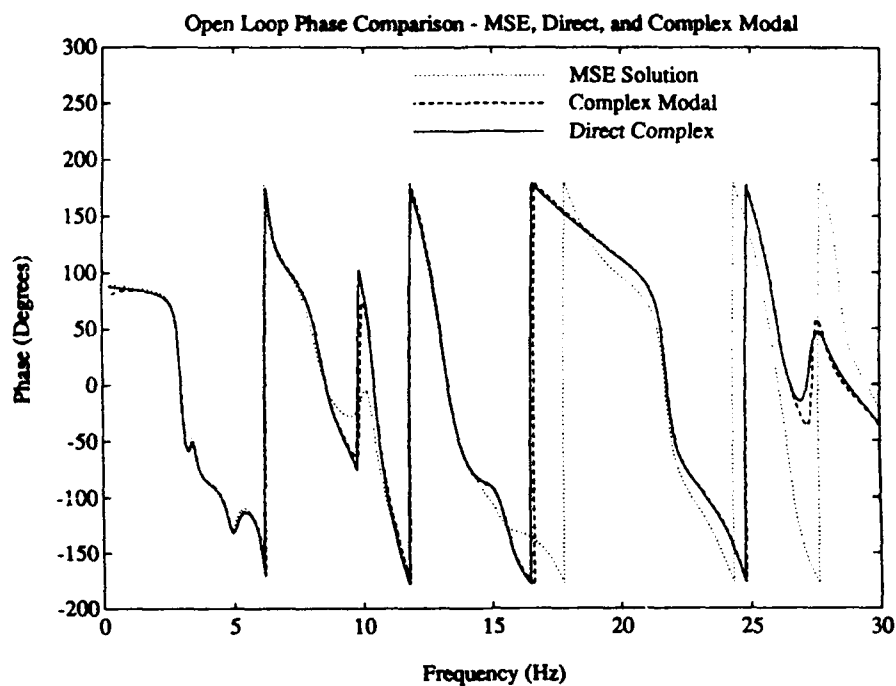


Figure 10 - Open-Loop Phase of MSE and Truncated Modal Solution Compared to Exact Solution

Table 2 - Solution Times for MSE Analyses and Accelerated Subspace Iteration with MSE Starting Vectors

Analysis Type	Number of Analyses	Number of Matrix Decomps	Number of Matrix/Vector Products	Total Elapsed Solution Time (sec)
MSE Using Subspace Iteration	7	7	1108	2815
Accelerated Complex Subspace Iteration	1	0	973	3530

- 2) The MSE method can be shown to be a low-cost approximation to a subspace/spectral iteration. Therefore, the developed procedure can be used in concert with the MSE method to improve the solution accuracy as a design cycle progresses.
- 3) The developed design and analysis procedure can be used efficiently in the solution of large-scale dynamics problems with viscoelastic damping treatments and active controls.
- 4) Although not shown here, the technique of subspace/spectral iteration can be used for the solution of problems with viscous damping or combined viscous/viscoelastic damping, and for closed-loop damped systems. The method is at least as efficient as the techniques for solving complex eigenvalue problems currently available in many finite element codes. In fact, the conjugate gradient inverse power iterations are very similar to those performed in MSC/NASTRAN [14], but convergence is accelerated using the subspace procedure and conjugate gradients.
- 5) The solution procedure obviates the necessity for the description of viscoelastic materials or members using networks of springs and dashpots (Maxwell elements), as the solution using these descriptions will inevitably be more expensive and less accurate than using the fractional derivative representation. These methods typically add a number of degrees of freedom to the system matrices and increase solution costs; and the method of solution of these eigenvalue problems in most finite element codes can be shown to be similar to the eigenvalue procedure developed here for systems with fractional derivative material representations. Damping element properties can be written as a function of frequency using the fractional derivative representation, and the solution to the equations can efficiently be solved as developed previously. This frequency-dependent reduction can be considered the equivalent of static condensation for systems which contain damped elements that have negligible internal mass effects.
- 6) The cost of the eigenvalue solution procedure is independent of the description of the damping phenomenon in the system elements, as long as the element impedance properties can be described as a function of the Laplace variable. Therefore, if a higher-order fractional derivative representation is appropriate for a particular material, the solution procedure is unaltered, and the cost is effectively unchanged.
- 7) The accelerated subspace solution method can be used for eigenvalue problems which contain combinations of viscous dampers, viscoelastic dampers, and even for closed-loop systems. This facilitates an accurate modal representation of actively controlled damped systems.

References

- 1) Bagley, R.L., and Torvik, P.J., "Generalized Derivative Model for an Elastomer Damper," Shock and Vibration Bulletin, No. 49, Part 2, pp 135-143, 1979.
- 2) Bagley, R.L., and Torvik, P.J., "A Theoretical Basis for the Application of Fractional Calculus to Viscoelasticity," J. of Rheology, Vol 27, No. 3, pp 918-925, 1985.
- 3) Bagley, R.L., and Torvik, P.J., "On the Fractional Calculus Model of Viscoelastic Behavior," Journal of Rheology, Vol 30, No. 1, pp 133-135, 1986.
- 4) Torvik, P.J., and Bagley, R.L., "Fractional Derivatives in the Description of Damping Materials and Phenomena," The Role of Damping in Vibration and Noise Control, ASME Publication, pp 125-135, 1987.
- 5) Koeller, R.C., "Application of Fractional Calculus to the Theory of Viscoelasticity," Journal of Applied Mechanics, Vol 51, pp 299-307, 1984.
- 6) Bagley, R.L., and Calico, R.A., "The Fractional Order State Equations for the Control of Viscoelastically Damped Structures," Proceedings of Damping '89, Vol I, pp DAB-1 to DAB-26, 1989.
- 7) Gaudreault, M., and Bagley, R.L., "Improved Solution Techniques for the Eigenstructure of Fractional Order Systems," Proceedings of Damping '89, Vol I, pp DAC-1 to DAC-19, 1989.
- 8) Craig, R.R., Structural Dynamics - An Introduction to Computer Methods, John Wiley and Sons Publishers, pp 313-317, 1981.
- 9) Johnson, C.D., and Kienholz, D.A., "Finite Element Prediction of Damping in Structures with Constrained Viscoelastic Layers," AIAA Journal, Vol 20, No. 9, pp 1284-1290, 1982.
- 10) Bathe, K.J., "Solution Methods of Large Generalized Eigenvalue Problems in Structural Engineering," Report UC SESM 71-20, University of California at Berkley, 1971.
- 11) Bathe, K.J., and Ramaswamy, S., "An Accelerated Subspace Iteration Method," Journal of Computer Methods in Applied Mechanics and Engineering, Vol 23, pp 313-331, 1980.
- 12) Golub, G.H., and Van Loan, C.F., Matrix Computations, The Johns Hopkins University Press Publishers, pp 352-379, 1983.
- 13) Gehling, R.N., "Modal Survey of the PACOSS DTA," Presented at Damping '89, West Palm Beach, Florida, 1989.
- 14) MSC/NASTRAN Theoretical Manual, The MacNeal-Schwendler Corporation, pp 10.4-24 to 10.4-35, 1972.

AN IMPLICIT FOURIER TRANSFORM METHOD
FOR NONLINEAR DYNAMIC ANALYSIS
WITH FREQUENCY DEPENDENT DAMPING

F. Venancio-Filho*

Rutgers, The State University of New Jersey, NJ, USA

A. M. Claret

School of Mines, Federal University of Ouro Preto, MG, Brazil

ABSTRACT

The SILFD (Step-by-step Incremental Linearization Frequency Domain) method for the frequency domain analysis of nonlinear structural systems with frequency dependent damping, described in Venancio-Filho and Claret [1989] is implemented in this work through the IFT (Implicit Fourier Transform) algorithm, Venancio-Filho and Claret [1991]. A new and more efficient process for the consideration of the initial conditions in the SILFD method is presented. Numerical examples are presented which show the applicability of the proposed method.

.

Department of Civil Engineering
COPPE/UFRJ, The Federal University of Rio de Janeiro
Caixa Postal 68506
21945 Rio de Janeiro RJ
BRAZIL

INTRODUCTION

A very efficient and accurate method for the treatment of structural dynamics engineering problems with frequency dependent damping is based in the frequency domain solution of the motion equations. Physical and geometrical nonlinearities, when present, should be considered in these problems. Only recently methods of nonlinear dynamic structural analysis in the frequency domain have been addressed. Several researchers have presented contributions in this subject. Kawamoto [1983] described a method called Hybrid Frequency-Time Domain, abbreviated HFTD, for nonlinear analysis in frequency domain. Wolf and Darbre [1986] presented the segmenting approach of HFTD method and obtained its convergence properties. Hilmer and Schmid [1988] describe a technique similar to the segmenting approach using Laplace Transform which computationally differs from Fourier Transform only in the treatment of initial conditions.

All these methods present some problems related to its applicability to real situations in structural engineering. Two problems are addressed in this work. The first refers to the computational effort in nonlinear analysis in the frequency domain where the conventional process needs numerous executions of direct and inverse Fourier transforms of complex series with a great number of terms. Consequently, the memory allocation and the computational effort is normally very high. The second problem is the treatment of initial conditions by a segmenting approach. Hilmer and Schmid [1988] state that the treatment of non null initial conditions through Fourier Transforms is numerically unfavorable because, in general, step functions cause great errors in transformed functions.

The SILFD method, described by Venancio-Filho and Claret [1989], combined with the Implicit Fourier Transform Algorithm for dynamic response in frequency domain, Venancio-Filho and Claret [1991], solves efficiently the first problem. The second problem is treated here using the physical significance of initial conditions and transforming the original problem in another with null initial conditions.

THE IMPLICIT FOURIER TRANSFORM ALGORITHM

The dynamic response of a SDOF system in the frequency domain can be expressed by the following equations, Clough and Penzien [1982]:

$$v(t_n) = \frac{\Delta\bar{\omega}}{2\pi} \sum_{m=0}^{N-1} H(\bar{\omega}_m) P(\bar{\omega}_m) e^{i2\pi \frac{mn}{N}} \quad (1)$$

and

$$P(\bar{\omega}_m) = \Delta t \sum_{n=0}^{N-1} p(t_n) e^{-i2\pi \frac{mn}{N}}. \quad (2)$$

The total time interval T_p in which the response is to be calculated is divided into N equal time intervals given by

$$\Delta t = \frac{T_p}{N} \quad (3)$$

and the discrete times in which the load is defined are given by

$$t_n = n \Delta t = n \frac{T_p}{N} \quad (0 \leq n \leq N-1). \quad (4)$$

The frequency range is likewise divided into N equal intervals $\Delta\bar{\omega}$ expressed as

$$\Delta\bar{\omega} = \frac{2\pi}{T_p} \quad (5)$$

and the discrete frequencies $\bar{\omega}_m$ are taken according to Table I (see Appendix 1).

In equation (2), $P(\bar{\omega}_m)$ is the discrete Fourier transform of the load; in equation (1), $H(\bar{\omega}_m) P(\bar{\omega}_m)$ is the discrete Fourier transform of the response (or the response in the frequency domain) and $v(t_n)$ is the inverse discrete Fourier transform of the response (or the response in the time

domain).

The dynamic response expressed by equations (1) and (2) can be numerically determined by the Fast Fourier Transform algorithm.

Let now

$$\{p\} = \{ p(t_0), p(t_1), p(t_2), \dots, p(t_n), \dots, p(t_{N-1}) \} \quad (6)$$

and

$$\{v\} = \{ v(t_0), v(t_1), v(t_2), \dots, v(t_n), \dots, v(t_{N-1}) \} \quad (7)$$

be, respectively, the vectors of the load and the response at the discrete times

$$t_n = n\Delta t, \quad n = 0, 1, 2, \dots, N-1, \quad (8)$$

and let

$$\{P\} = \{ P(\omega_0), P(\omega_1), P(\omega_2), \dots, P(\omega_m), \dots, P(\omega_{N-1}) \} \quad (9)$$

be the vector of the discrete Fourier transform of the load defined at the discrete frequencies ω_m interpreted according to Table I.

With the definition of equations (6) and (9), equation (2) can be casted in matrix form as

$$\{P\} = \Delta t [E^*] \{p\} \quad (10)$$

where the $(N \times N)$ matrix $[E^*]$ is defined as the matrix whose generic term E_{mn}^* is

$$E_{mn}^* = e^{-imn\alpha} \quad (11)$$

or, explicitly,

$$\tilde{E}^* = \begin{bmatrix} e^0 & e^0 & e^0 & \dots e^0 & \dots e^0 \\ & e^{-1\alpha} & e^{-12\alpha} & \dots e^{-1n\alpha} & \dots e^{-1(N-1)\alpha} \\ & & e^{-14\alpha} & \dots e^{-12n\alpha} & \dots e^{-12(N-1)\alpha} \\ & & & \ddots & \\ & & & & e^{-1m\alpha} & \dots e^{-1m(N-1)\alpha} \\ \text{Symmetric} & & & & & \ddots \\ & & & & & & e^{-1(N-1)\alpha} \end{bmatrix} \quad (12)$$

where $\alpha = (2\pi/N)$. By the same token, the response from equation (2) is written in matrix form as

$$\{v\} = \frac{\Delta\bar{\omega}}{2\pi} [E] [H] \{p\} \quad (13)$$

where $[E]$ is the matrix defined in equation (11) with positive signs in the exponentials instead of negative ones, and $[H]$ is the diagonal matrix formed with the complex frequency response functions calculated at the discrete frequencies of Table I. The typical term of $[H]$ is given by

$$H(\bar{\omega}_m) = (k - m\bar{\omega}_m^2 + i\bar{\omega}_m c)^{-1}, \quad (0 \leq m \leq m-1) \quad (14)$$

where k , m , and c are the stiffness, mass, and damping of the SDOF system, respectively. Substituting now $\{P\}$ from equation (10) into equation (13), the following equation is obtained:

$$\{v\} = \frac{1}{N} [E] [H] [E^*] \{p\} \quad (15)$$

Equation (15) expresses the matrix formulation of the dynamic analysis of SDOF systems in the frequency domain. The

calculation of the structural response in the frequency domain through this equation is the IFT algorithm.

THE SILFD METHOD

Consider the SDOF system of Fig. 1 submitted to an arbitrary excitation $p(t)$. The spring stiffness k depends on the displacements v due to the system non-linearity and the damping coefficient depends on the frequency of the excitation, $\bar{\omega}$. The problem is then to integrate the dynamic equilibrium equation

$$m\ddot{v} + c(\omega)\dot{v} + k(v)v = p(t). \quad (16)$$

As the damping coefficient is ω dependent a frequency-domain analysis has to be performed and, as the stiffness depends on the displacement, a linearization technique must be employed. Consequently the present method is a Step-by-step Incremental Linearization in the Frequency Domain (SILFD) method. In each linearized step a secant stiffness is considered.

In order to calculate the response of the system governed by Eq. 1 two approximations are made. The first one is the approximation of the given load by piecewise linear segments. The total time interval in which the response is to be calculated is divided in intervals $\Delta t_j = t_j - t_{j-1}$; p_j and p_{j-1} are the values of $p(t)$ in the times t_j and t_{j-1} , respectively, and $\Delta p_j = p_j - p_{j-1}$, Fig. 2a. The load variation in time interval Δt_j is given by, Fig. 2a,

$$p(\tau) = p_{j-1} + \frac{\Delta p_j}{\Delta t_j} \tau \quad (17)$$

where τ is the current time in Δt_j ($0 \leq \tau \leq \Delta t_j$). The second approximation refers to the spring force versus displacement curve. This curve is also approximated by piecewise linear segments as indicated in Fig. 2c. The levels of these two approximations depend on the accuracy with which the load and the stiffness variation can have a good representation.

The response of the system is calculated through the linearized steps along the time intervals Δt_j in which the spring is considered linear with stiffness k_j , Fig. 2b. the linearized dynamic equilibrium equation in time interval Δt_j

is

$$m\ddot{v} + c(\bar{\omega})\dot{v} + k_j v = p(\tau) \quad (18)$$

with the initial conditions v_{j-1} and \dot{v}_{j-1} , Fig. 2a. Herein the treatment of the initial conditions departs from Venancio-Filho and Claret [1989] in order to circumvent the errors in the transformed functions to the step functions.

The displacement response in time interval Δt_j due to the applied load obtained through the IFT algorithm is

$$\{v_j\}_L = \frac{\Delta\bar{\omega}}{2\pi} [E] [H] [E^*] \{p_j\}_L \quad (19)$$

where $\{p_j\}_L$ is the load vector in the time interval Δt_j .

The displacement response due to the initial displacement is equivalent to the response due to a constant force, in the time interval Δt_j , given by

$$\{p_j\}_I = -k_j v_{j-1} \{1\} \quad (20)$$

where $\{1\}$ is a vector with all elements equal to 1. Consequently the response is obtained from Eq. 19 as

$$\{v_j\}_{v_{j-1}} = - \frac{\Delta\bar{\omega}}{2\pi} [E] [H] [E^*] k_j v_{j-1} \{1\}. \quad (21)$$

The displacement response due to the initial velocity \dot{v}_{j-1} is the response to an impulse $m \dot{v}_{j-1}$ which is obtained from the unit impulse response function as

$$v_j = m \dot{v}_{j-1} h(t). \quad (22)$$

$h(t)$ is the inverse Fourier Transform of the complex frequency response function $H(\bar{\omega})$ and is given by

$$h(t) = \frac{1}{2\pi} \int_{-\infty}^{+\infty} H(\bar{\omega}) e^{i\bar{\omega}t} d\bar{\omega}. \quad (23)$$

Considering Eqs. 23, 22, and 15, the response due to $j-1$ is obtained as

$$\{v_j\}_{v_{j-1}} = \frac{m \dot{v}_{j-1} \Delta \bar{\omega}}{2\pi} [E] [H] \{1\}. \quad (24)$$

The total response in time interval Δt_j is the given by the sum of the responses in Eqs. 19, 21, and 24. The result is

$$\{v_j\} = \frac{\Delta \bar{\omega}}{2\pi} [E] [H] \left[[E^*] (\{p_j\}_L - k_j v_{j-1}) - m \dot{v}_{j-1} \{1\} \right]. \quad (25)$$

EXAMPLES

A SDOF system formed by a mass $m = 1$ kg and by a bilinear spring with constants $K_1 = 10000$ N/mm and $K_2 = 10$ N/mm was analysed by Kawamoto [1983] considering undamped vibrations. The same system is now analysed considering the following cases: I)- undamped system; II)- frequency-dependent damping according to the function $c(\bar{\omega})$ shown in Fig. 3; III)- frequency-dependent damping according to the function $c(\bar{\omega})$ shown in Fig. 4. The load function is

$$p(t) = 50 \sin(1.5t) + 100 \sin 0.005t \quad (26)$$

which is pictured in Fig. 5. The natural period of vibration is $T = 0.063$ sec. Kawamoto [1983] considered $\Delta t = 1$ sec to perform the analysis of system's response through the HFTD method, and $\Delta t = 0.02$ sec using direct integration of equilibrium equations.

In case I, using the SILFD method with the IFT, a time interval $\Delta t = 25$ sec is used, and the system's response is shown in Fig. 6. Comparing this response with Kawamoto's one (Kawamoto [1983], Figure 6.94, page 341), it is evident that the proposed method is efficient in predicting the maximum and minimum response of the system. Furthermore, the proposed method is better than HFTD in describing the "true" response of the system, particularly if we consider the accentuated

spring softening.

The responses of Cases II and III, Figs. 7 and 8, respectively, show that frequency-dependent damping is treated conveniently by the proposed method. Others types of $c(\omega)$ functions can be considered with no changes in the algorithm. A very small differences in the moduli of maxima displacements are observed from Case I to Cases II and III. One reason is predominant for this fact: the steady-state response is calculated and the static amplitude $p(t)/K_2$, for such a small value of K_2 , is predominant in the system's response.

CONCLUSIONS

The proposed method is efficient for treatment of dynamic nonlinear systems with frequency-dependent damping. In a future work, the computational effort needed will be measured and compared with the cpu time of others methods. However, it is very apparent that the SILFD method combined with the IFTalgorithm is well suited for nonlinear analysis in frequency domain, optimizing computational effort and memory allocation.

REFERENCES

- Venancio-Filho, F. and A. M. Claret [1989], "Non Linear Dynamic Analysis With Frequency-Dependent Damping", FDD-1, Damping 89 Conference, West Palm Beach, Florida, USA.
- Venancio-Filho, F. and A. M. Claret [1991], "Matrix Formulation of the Dyanmic Analysis of a SDOF System in Frequency Daomain", Braziliam Journal of Mechanical Sciences (to be published).
- Kawamoto, J. D. [1983], "Solution of Nonlinear Dynamic Structural Systems by a Hybrid Frequency-Time Domain Approach", PhD Thesis, Department of Civil Engineering, MIT.
- Darbre, G. R. and Wolf, J. P. [1987], "Criterion of Stability and Implementation Issues of Hybrid Frequency-Time Domain Procedure for Nonlinear Dynamic Analysis", Transactions of the International Conference on Structural Mechanics in Reactor Thecnology, Lausanne.
- Hilmer, P. and Schmid, G. [1988], "Calculation of Foundation

Uplift Effects Using a Numerical Laplace Transform",
Earthquake Engineering and Structural Dynamics, 16,
789-801.

APPENDIX

The discrete frequencies employed in this formulation must be interpreted according Table I. Taking into account the frequencies $\bar{\omega}_m$ from Table I, $H(\bar{\omega}_m)$ and $H(\bar{\omega}_{N-m})$, Eq. 14, are complex conjugate.

Table I. Discrete frequencies (N odd)

m	m or (N-m)	$\bar{\omega}_m$
0	0	0
1	1	$\Delta\bar{\omega}$
2	2	$2\Delta\bar{\omega}$
...
$(N/2-1)$	$(N/2-1)$	$(N/2-1)\Delta\bar{\omega}$
$N/2$	$N/2$	$(N/2)\Delta\bar{\omega}$
$(N/2+1)$	$(N/2+1)$	$[-(N/2+1)]\Delta\bar{\omega}$
...
$N-2$	2	$-2\Delta\bar{\omega}$
$N-1$	1	$-\Delta\bar{\omega}$

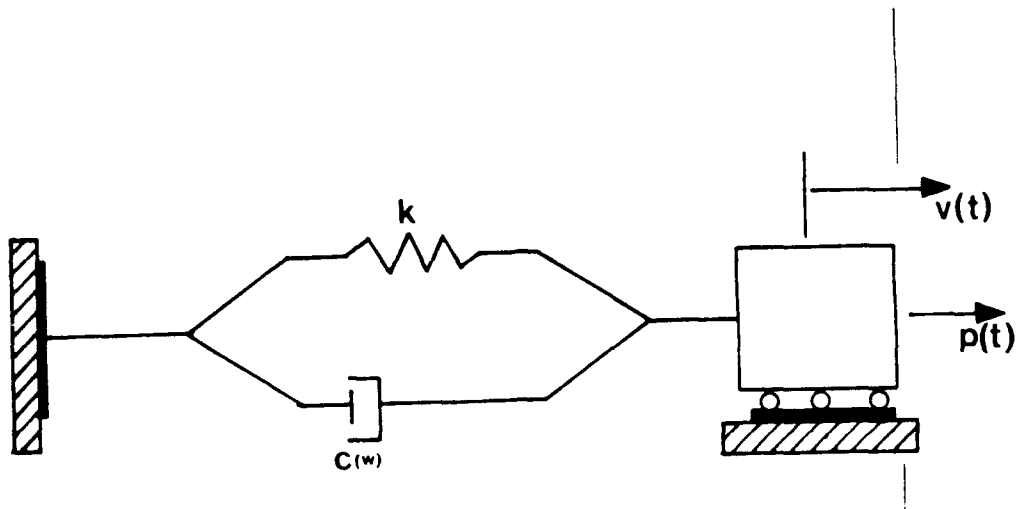
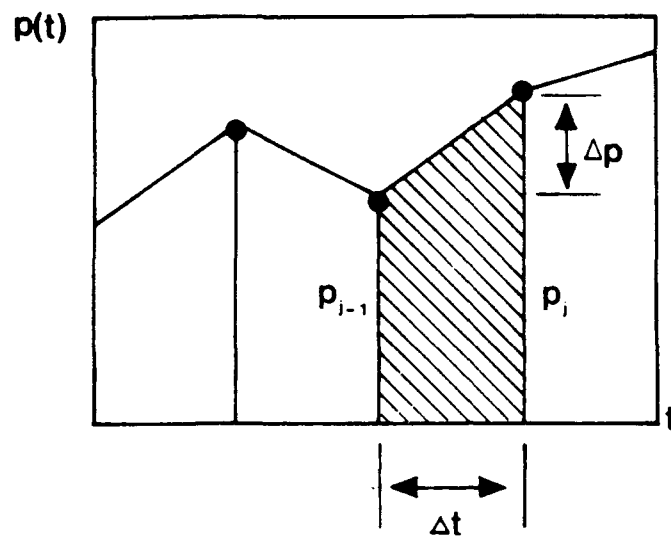
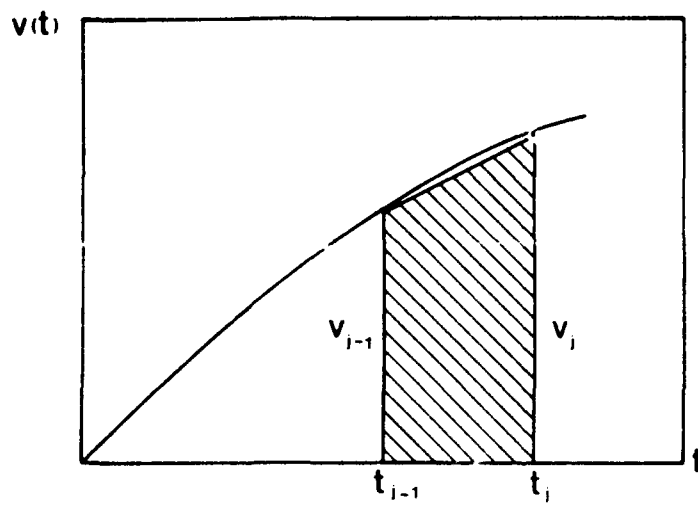


Fig. 1- SDOF system.



(a)



(b)

Fig. 2- (a) Load variation; (b)- displacement response.

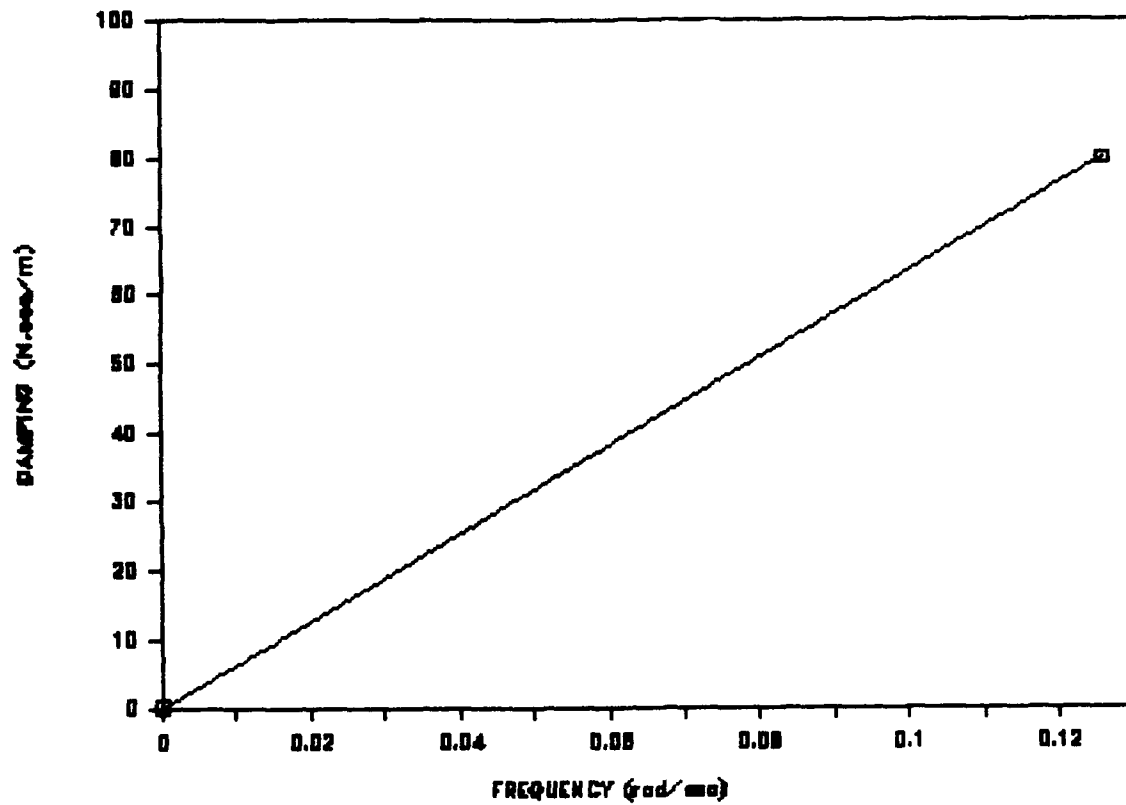


Fig. 3- Frequency-dependent damping in case II.

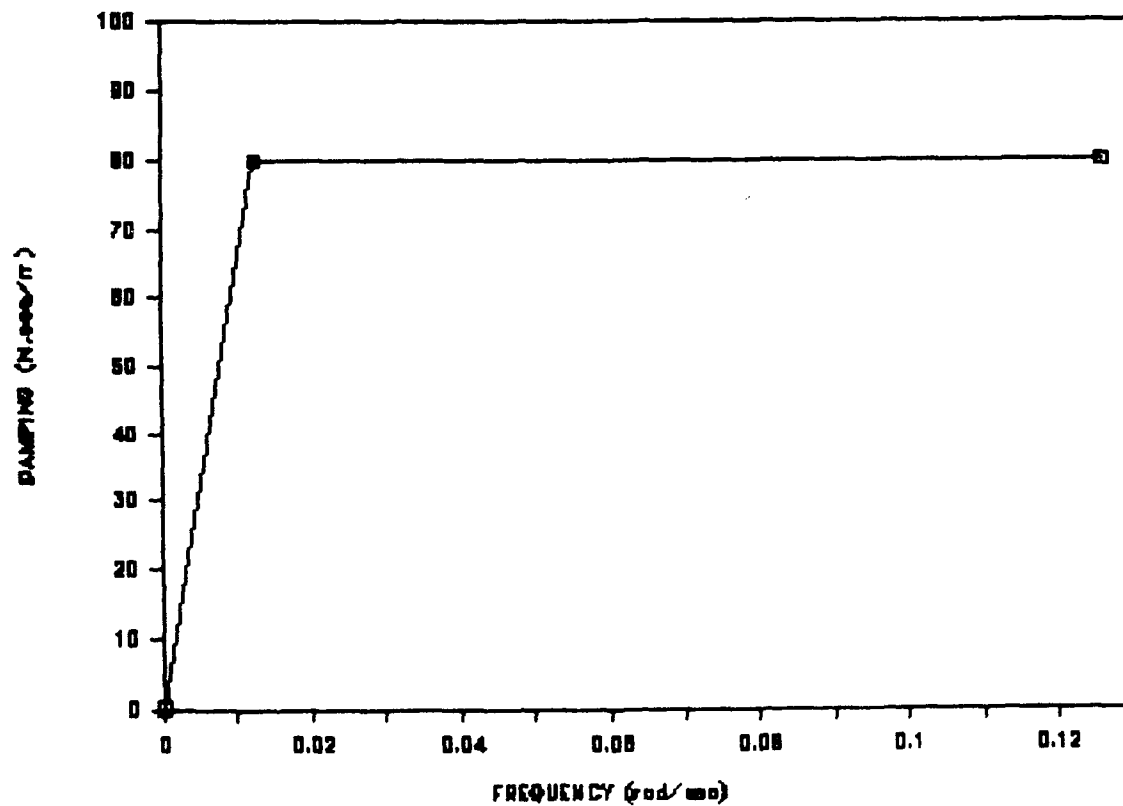


Fig. 4- Frequency-dependent damping in case III.

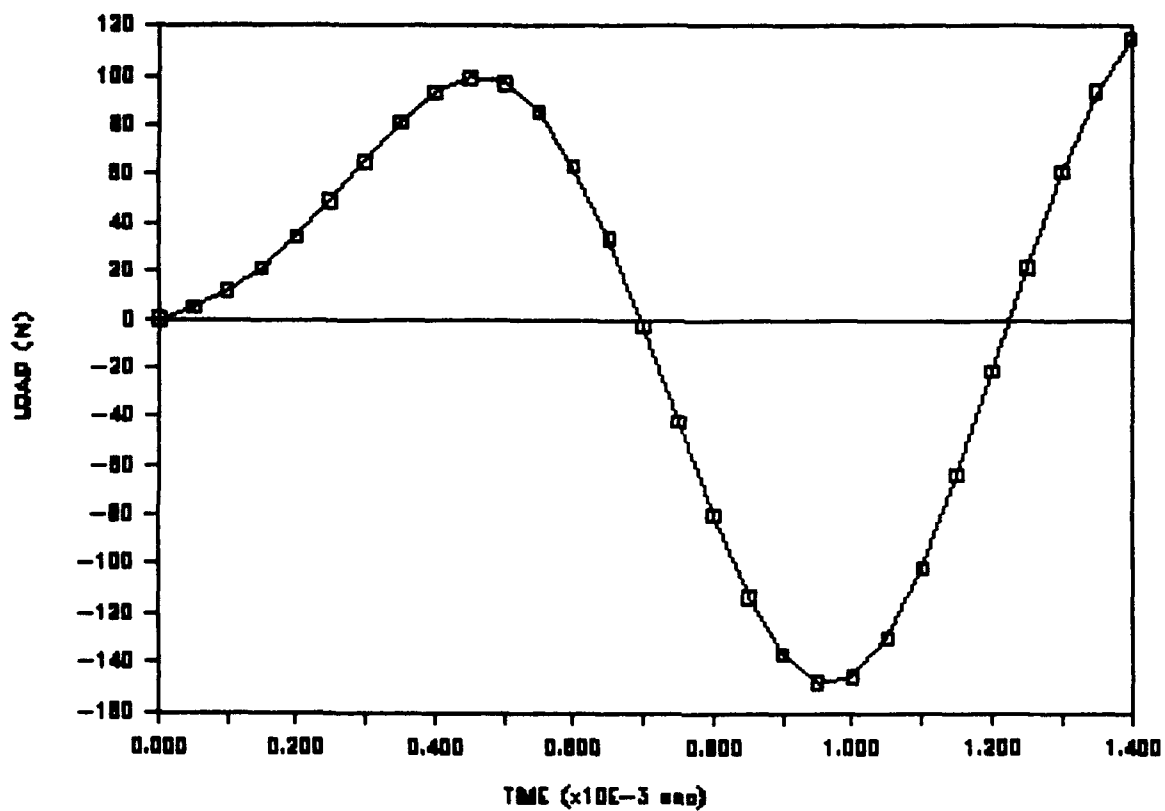


Fig. 5- Load function.

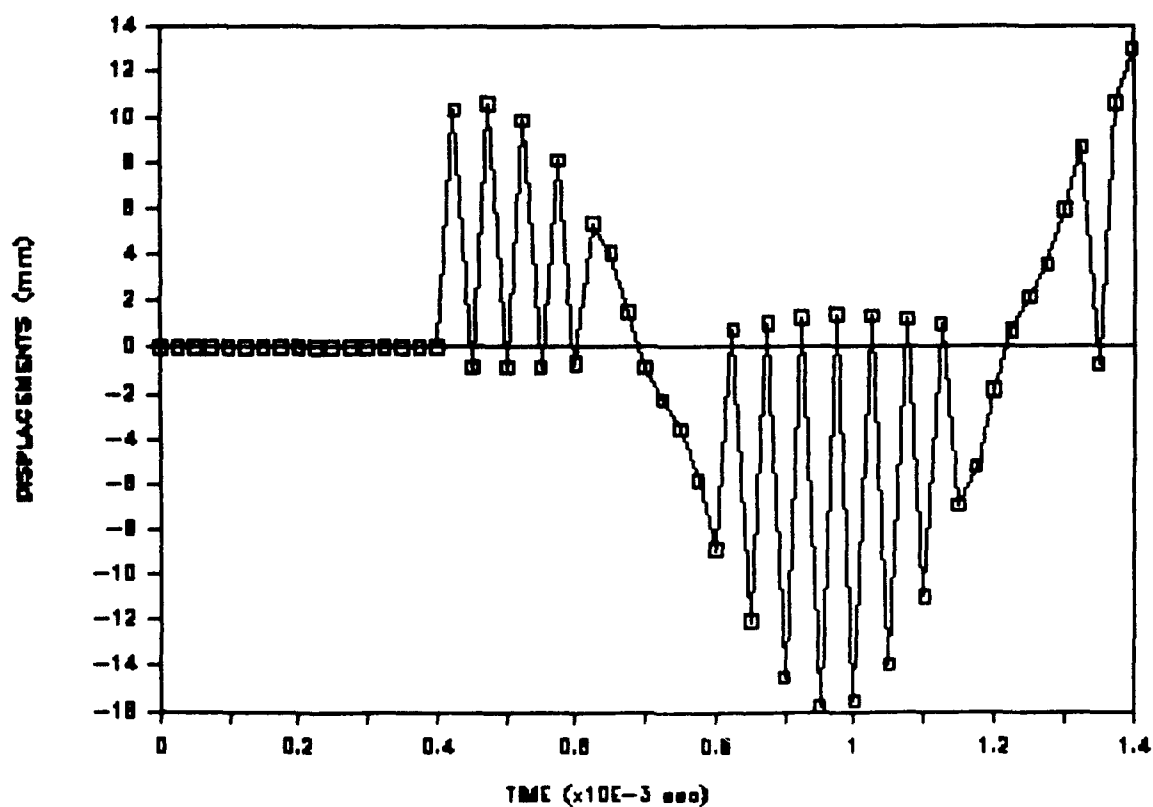


Fig. 6- System response in case I.

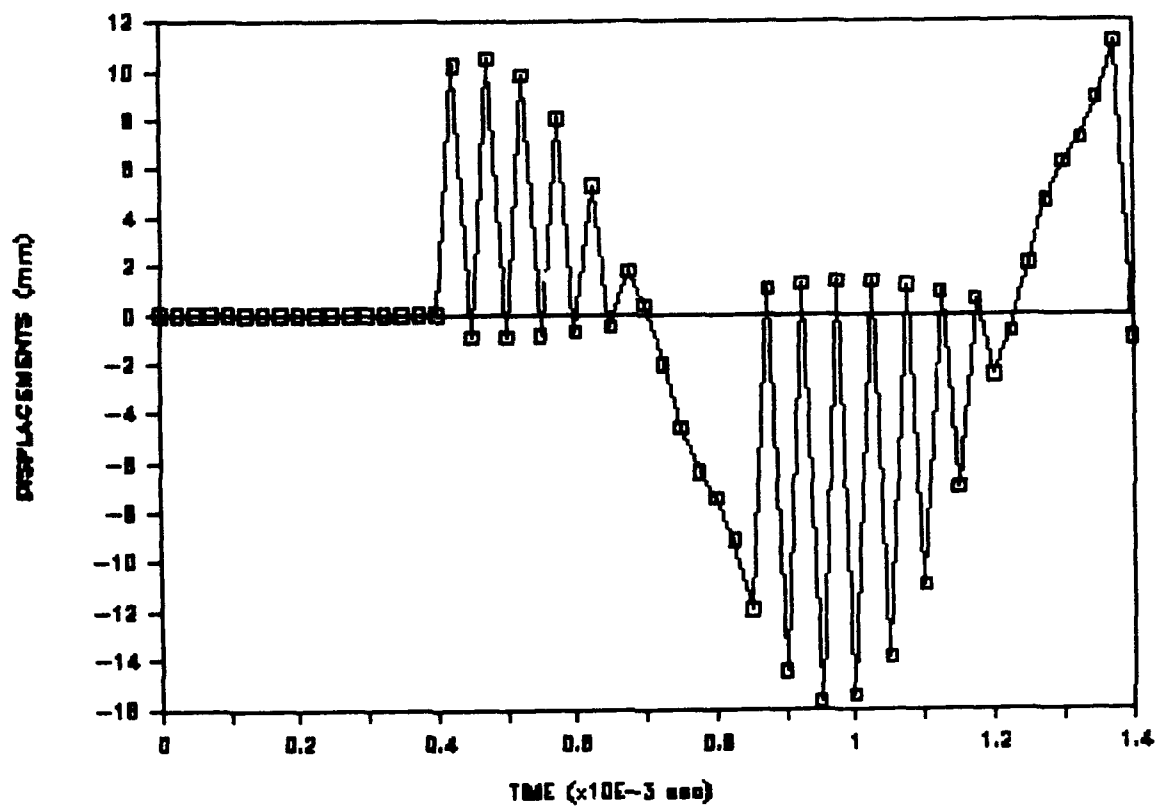


Fig. 7- System response in case II.

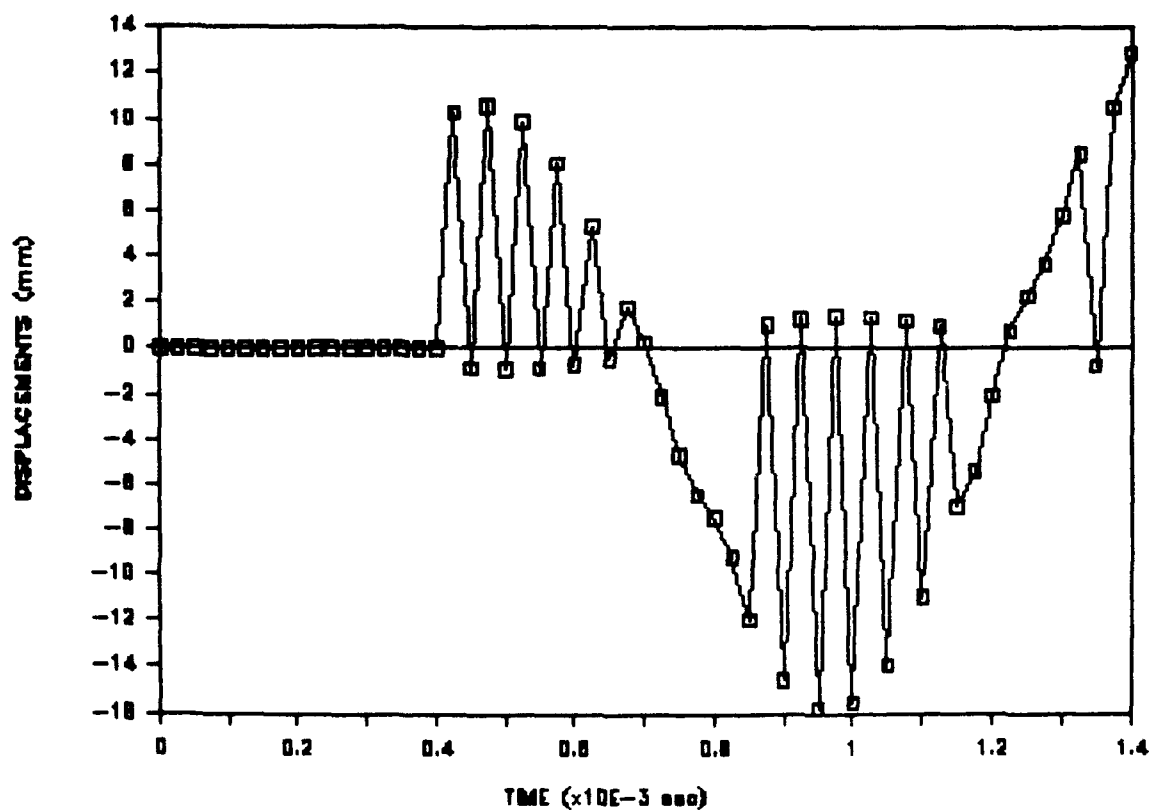


Fig. 8- System response in case III.

ON A LINEAR PROPERTY OF LIGHTLY DAMPED SYSTEMS

Z. Liang, G. C. Lee, and M. Tong

412 Bonner Hall
State University of New York at Buffalo
Amherst, NY 14260
Tel. (716) 636-2771

ABSTRACT

As one of the direct applications of complex damping theory, a useful property of structural damping is presented in this paper. If a structure is linear and lightly damped, (i.e. the maximum damping ratio < 0.3), then increased damping of the structure will result in proportional change in each modal damping ratio of the system. This property is particularly useful in damping re-design and damping measurement. A number of experimental and numerical examples are also presented.

INTRODUCTION

Quantities such as $\sqrt{1-\xi^2}$ and $\exp(-\xi\omega)$, where ξ is the damping ratio and ω is the undamped natural frequency, are often seen in the studies of dynamic systems. Direct treatments of these quantities are difficult. Furthermore, they are too complicated to be used in practice. Most engineering applications typically use approximated values for these quantities. In Table 1 some possible approximations of ξ and $\sqrt{1-\xi^2}$ together with the associated errors are given.

Table 1 Damping ratios and the approximations

approximation of ξ		approximation of $\sqrt{1-\xi^2}$		
ξ	sh(ξ) & error	$\sqrt{1-\xi^2}$	1 & error	$1-\xi^2/2$ & error
.001	1.0000005 0.0%	0.9999995	1 5e- 5%	.9999995 0.0%
.01	.0100001 1.6e-5%	0.99995	1 5e- 3%	.999995 0.0%
.05	.0500208 .042%	0.9987492	1 0.125%	.99875 -8e-5%
.1	.1001667 .167%	0.9949874	1 0.501%	.995 .00126%
.2	.201336 .668%	0.9797959	1 2.020%	.98 .0204%
.25	.2526123 1.04%	0.9682458	1 3.175%	.96875 .0504%
.3	.3045202 1.51%	0.9539392	1 6.060%	.955 .106%

In this Table, the largest error appears when $\sqrt{1-\xi^2}$ is approximated by unity. If the value of ξ is less than 10%, then the error is no more than 0.5%. If the value of ξ is less than 30%, then this error is less than 5%. If we approximate $1 - \xi^2/2$ by unity, then the error is no more than 0.106%. These errors are tolerable in most engineering applications. We define a structural system to be *lightly damped* if the absolute value of the damping ratio for the system is less than 30%. The damping of most civil engineering structures such as buildings, bridges, dams and towers is usually less than 10%. Metal structures have even less damping. Theoretically speaking, for lightly damped systems, we have the following equations

$$\sqrt{1-\xi^2} \approx 1$$

$$\begin{aligned}
\sqrt{1-\xi^2} &\approx 1 - \xi^2/2 \\
\exp(\xi) &\approx 1 + \xi + \xi^2/2 \\
\text{ch}(\xi) &\approx 1 \\
\text{sh}(\xi) &\approx \xi
\end{aligned} \tag{1}$$

This paper is limited to the discussion to such systems.

COMPLEX DAMPING OF LIGHTLY DAMPED STRUCTURES

We first describe the complex damping ratios of lightly damped systems. Consider an MDOF system. For each virtual mode of the system, we can have an equation

$$\ddot{u} + (a + jb) \dot{u} + \omega_n^2 u = 0 \tag{2}$$

The characteristic equation of (2) is given by

$$\lambda^2 + (a + jb) \lambda + \omega_n^2 = 0$$

with

$$\begin{aligned}
\lambda &= \frac{1}{2} [-(a+jb) \pm ((a+jb)^2 - 4\omega_n^2)^{1/2}] \\
&= \omega_n \left[-\left(\frac{a+jb}{2\omega_n}\right) \pm \left(\left(\frac{a+jb}{2\omega_n}\right)^2 - 1\right)^{1/2} \right] \\
&= j \omega_n \left[\left(\frac{a+jb}{2\omega_n} j\right) \pm \left(1 + \left(\frac{a+jb}{2\omega_n} j\right)^2\right)^{1/2} \right]
\end{aligned} \tag{3}$$

Using (1) for lightly damped systems, we have

$$\left| \left(\frac{a+jb}{2\omega_n} j \right) \right| \ll 1 \tag{4}$$

and

$$\left(1 + \left(\frac{a+jb}{2\omega_n} j \right)^2 \right)^{1/2} \approx 1 + \frac{1}{2} \left(\frac{a+jb}{2\omega_n} j \right)^2 \tag{5}$$

Without loss of generality, let us first take the positive sign of

$$\left(1 + \left(\frac{a+jb}{2\omega_n} j \right)^2 \right)^{1/2}$$

in Equation (3). Then we have

$$\lambda = j \omega_n \left[\left(\frac{a+jb}{2\omega_n} j \right) + 1 + \frac{1}{2} \left(\frac{a+jb}{2\omega_n} j \right)^2 \right] \tag{6}$$

By using (1), we have

$$\begin{aligned}
\left(\frac{a+jb}{2\omega_n} j \right) + 1 + \frac{1}{2} \left(\frac{a+jb}{2\omega_n} j \right)^2 &\approx \exp\left(\frac{ja-b}{2\omega_n}\right) \\
&= \exp\left(j\frac{a}{2\omega_n}\right) \exp\left(\frac{-b}{2\omega_n}\right) \\
&\approx \left[1 + j\frac{a}{2\omega_n} - \frac{1}{2}\left(\frac{a}{2\omega_n}\right)^2 \right] \exp\left(\frac{-b}{2\omega_n}\right) \\
&\approx \left[j\frac{a}{2\omega_n} + \left(1 - \left(\frac{a}{2\omega_n} j\right)^2 \right)^{1/2} \right] \exp\left(\frac{-b}{2\omega_n}\right)
\end{aligned}$$

It follows that

$$\begin{aligned}
\lambda &= j\omega_n \left[j\frac{a}{2\omega_n} + \left(1 - \left(\frac{a}{2\omega_n} j\right)^2 \right)^{1/2} \right] \exp\left(\frac{-b}{2\omega_n}\right) \\
&= -\frac{a}{2\omega_n} \exp\left(\frac{-b}{2\omega_n}\right) \omega_n + j \left(1 - \left(\frac{a}{2\omega_n} j\right)^2 \right)^{1/2} \exp\left(\frac{-b}{2\omega_n}\right) \omega_n \quad (7)
\end{aligned}$$

Now take the negative sign

$$- \left(1 + \left(\frac{a+jb}{2\omega_n} j \right)^2 \right)^{1/2}$$

In Equation (3), we have

$$\lambda = -\frac{a}{2\omega_n} \exp\left(\frac{b}{2\omega_n}\right) \omega_n - j \left(1 - \left(\frac{a}{2\omega_n} j\right)^2 \right)^{1/2} \exp\left(\frac{b}{2\omega_n}\right) \omega_n \quad (8)$$

Combining Equations (7) and (8), we have

$$\lambda = -\frac{a}{2\omega_n} \exp\left(\frac{\mp b}{2\omega_n}\right) \omega_n \pm j \left(1 - \left(\frac{a}{2\omega_n} j\right)^2 \right)^{1/2} \exp\left(\frac{\mp b}{2\omega_n}\right) \omega_n \quad (9)$$

By comparing the Equation (9) with the standard form of λ ,

$$\lambda = -\xi\omega \pm j\sqrt{1-\xi^2}\omega$$

we have

$$\frac{a}{2\omega_n} = \xi \quad (a = 2\xi\omega_n) \quad (10)$$

and

$$\exp\left(\frac{\mp b}{2\omega_n}\right) \omega_n = \omega$$

By using (1)

$$\exp\left(\frac{\mp b}{2\omega_n}\right) \approx 1 \pm \left(1 \mp \left(\frac{b}{2\omega_n}\right)^2 \right)^{1/2}$$

Then

$$\frac{b}{2\omega_n} = \zeta \quad (b = 2\zeta\omega_n) \quad (11)$$

In Equations (10) and (11), a and b are associated with the i^{th} virtual mode of the system. By assigning to a and b some proper subscripts, we have, for the i^{th} virtual mode of the system,

$$\begin{aligned} a_1 &= 2 \xi_1 \omega_{n1} \\ b_1 &= 2 \zeta_1 \omega_{n1} \end{aligned} \quad (12)$$

and

$$\lambda_1 = -\xi_1 \exp(\mp \zeta_1) \omega_{n1} \pm j \sqrt{1-\xi_1^2} \exp(\mp \zeta_1) \omega_{n1} \quad (13a)$$

Sometimes, it is convenient to approximate λ_1 by

$$\lambda_1 = j \omega_n \exp(\xi \pm j \zeta) \quad (13b)$$

If we define the i^{th} complex damping ratio of a lightly damped system by

$$\phi_1 = \frac{d_1}{2\omega_{n1}} = \xi_1 \pm j \zeta_1 \quad (14)$$

then we can make the following statements.

Theorem 1. For lightly damped MDOF system, The complex damping coefficient of the i^{th} virtual mode is

$$d_1 = 2 (\xi_1 + j \zeta_1) \omega_{n1}$$

where the real part of the complex damping ratio, ξ_1 , is the traditionally defined "damping ratio", ξ_1 , i.e.

$$\xi_1 = \frac{\text{real}(d_1)}{2 \omega_{n1}} = \xi_1,$$

the imaginary part of the complex damping ratio, ζ_1 , is associated with the change of undamped natural frequency ω_1 from the zero-damping frequency ω_{n1} , i.e.

$$\omega_1 = \exp(\zeta_1) \omega_{n1}.$$

Theorem 1 indicates that, for a lightly damped system, we can treat the real and imaginary parts of the complex damping ratio (or complex damping coefficient) separately. The Theorem is useful in energy analysis of real damping and imaginary damping.

THE LINEAR PROPERTY OF LIGHTLY DAMPED SYSTEMS

For lightly damped systems, the damped natural frequencies are approximately equal to the undamped natural frequencies. That is, if the value ζ_1 is sufficiently small, then

$$\exp(\zeta_1) \approx 1$$

$$\text{and} \quad \omega_1 = \exp(\zeta_1) \omega_{n1} \approx \omega_{n1} \quad (15)$$

Equation (15) says that, if two lightly damped systems, H_1 and H_2 , have the same mass and stiffness distribution, then

$$\Lambda_{Im}^{(1)} \approx \Lambda_{Im}^{(2)} \quad (16)$$

and

$$\lambda_{iIm}^{(1)} \approx \lambda_{iIm}^{(2)}, \quad i = 1, \dots, 2n \quad (17)$$

To simplify the notations, we arrange the system eigenvalues in the following order

$$\lambda_1, \lambda_2, \dots, \lambda_n$$

so that their corresponding natural frequencies satisfy

$$\omega_1 \leq \omega_2 \leq \dots \leq \omega_n.$$

For proportional systems, we now have the following lemma.

Lemma 1. If a lightly damped system H has proportional damping C_c which can be represented as the sum of two proportional damping C_{1c} and C_{2c} , i.e.

$$C_c = C_{1c} + C_{2c}$$

then, for the subsystem H_{1c} and H_{2c} , we have

$$\Lambda_{Re} = \Lambda_{Re}^{(1c)} + \Lambda_{Re}^{(2c)}$$

i.e.

$$\lambda_{iRe} = \lambda_{iRe}^{(1c)} + \lambda_{iRe}^{(2c)} \quad i = 1, \dots, 2n \quad (18)$$

and

$$\Lambda_{Im} \approx \Lambda_{Im}^{(1c)} \approx \Lambda_{Im}^{(2c)}$$

i.e.

$$\lambda_{iIm} \approx \lambda_{iIm}^{(1)} \approx \lambda_{iIm}^{(2)}, \quad i = 1, \dots, 2n \quad (19)$$

Lemma 1 says that, for a system with proportional damping, if it can be split into two subsystems both with proportional damping, then the imaginary part of the eigenvalues of the original system is the sum of the corresponding imaginary parts of the two subsystems. In other word, the damping ratios possess the following relationship

$$\xi_i^{(c)} = \xi_i^{(1c)} + \xi_i^{(2c)}, \quad i = 1, \dots, 2n \quad (20)$$

where the superscript (.) stands for the corresponding system (.).

Lemma 1 can be used in damping identification. When dampers are added to a structure, the damping ratio of the structure is changed. By using

equations (18) and (19), we can determine the damping ratio of the modified structure. In a later section, some examples will be given.

Lemma 1 can be extended to systems with general non-proportional damping. This is described in the following Lemma.

Lemma 2: For any lightly damped system with damping C , let H be the state matrix. If we separate the system into two subsystems H_P and H_N , then we have

$$\begin{aligned} \Lambda_{Re} &\approx \Lambda_{Re}^{(P)} \\ \text{i.e. } \lambda_{iRe} &\approx \lambda_{iRe}^{(P)}, \quad i = 1, 2, \dots, 2n \end{aligned} \quad (21)$$

$$\begin{aligned} \text{and } \Lambda_{Im} &\approx \Lambda_{Im}^{(P)} \approx \Lambda_{Im}^{(N)} \\ \text{i.e. } \lambda_{iIm} &\approx \lambda_{iIm}^{(P)} \approx \lambda_{iIm}^{(N)}, \quad i = 1, 2, \dots, 2n \end{aligned} \quad (22)$$

This lemma is easily understood by noting that systems H and H_P have the identical damping ratios for their modes, and almost the same natural frequencies per each mode.

Theorem 2. If the damping matrix C of a lightly damped system H can be represented by the sum of two matrices C_1 and C_2 , i.e. $C = C_1 + C_2$ then, for subsystems H_1 and H_2 , we have

$$\begin{aligned} \Lambda_{Re} &\approx \Lambda_{Re}^{(1)} + \Lambda_{Re}^{(2)} \\ \text{i.e. } \lambda_{iRe} &\approx \lambda_{iRe}^{(1)} + \lambda_{iRe}^{(2)}, \quad i = 1, 2, \dots, 2n. \end{aligned} \quad (23)$$

$$\begin{aligned} \text{and } \Lambda_{Im} &\approx \Lambda_{Im}^{(1)} \approx \Lambda_{Im}^{(2)} \\ \text{i.e. } \lambda_{iIm} &\approx \lambda_{iIm}^{(1)} \approx \lambda_{iIm}^{(2)}, \quad i = 1, 2, \dots, 2n \end{aligned} \quad (24)$$

PROOF.

Let $C_1 = C_{1P} + C_{1N}$ and $C_2 = C_{2P} + C_{2N}$. Then we have

$$C = C_1 + C_2 = (C_{1P} + C_{2P}) + (C_{1N} + C_{2N})$$

According to Lemma 2,

$$\begin{aligned} \Lambda_{Re} &\approx \Lambda_{Re}^{(1P+2P)} = \Lambda_{Re}^{(1P)} + \Lambda_{Re}^{(2P)} \\ &\approx \Lambda_{Re}^{(1)} + \Lambda_{Re}^{(2)} \end{aligned}$$

The second half of the theorem is obvious.

Corollary 1. If lightly damped systems H_1 and H_2 have same mass and stiffness distribution and damping matrix C_2 of H_2 is β times of C_1 of H_1 , (i.e. $C_2 = \beta C_1$), then, for H_1 and H_2 , we have

$$\begin{aligned} \Lambda^{(1)} &\approx \Lambda^{(2)} \\ \text{i.e. } \lambda_{iIm}^{(1)} &\approx \lambda_{iIm}^{(2)}, \quad i = 1, 2, \dots, 2n. \end{aligned} \quad (25)$$

$$\begin{aligned} \text{and } \Lambda_{Re}^{(2)} &\approx \beta \Lambda_{Re}^{(1)} \\ \text{i.e. } \lambda_{iRe}^{(2)} &\approx \beta \lambda_{iRe}^{(1)}, \quad i = 1, 2, \dots, 2n. \end{aligned} \quad (26)$$

APPLICATIONS AND EXAMPLES

Example I

Figure 1 shows a structure with 3 DOF. Before dampers are added, the system has the following damping ratios

Table 2 Damping Ratios of the Base Structure

Mode	I	II	III
damping ratio	.0102	.0087	.0079

By adding dampers to the base structure, the damping ratios are changed. Since the damping ratio of a damper is directly related to the physical parameters (such as the loss modulus and the volume of damping material), the ratio can be calculated when these parameters are given. Suppose we have already obtained the corresponding damping ratios contributed by the dampers (first row of Table 3). Now we would like to have the damping ratios of the structure after the dampers are incorporated. It is easy to see that the system is still lightly damped. So from Theorem 2 we can calculate the damping ratios using the linear property. The results are shown in the third row of Table 3. The last row in Table 3 gives of the experimental data to be directly compared with the calculated results.

Table 3 Calculation of damping ratio

mode	I	II	III
ξ_{add}	.275	.1010	.0744
ξ_{base}	.0102	.0087	.0079
calculated ξ	.2852	.1097	.07519
tested ξ	.2970	.0877	.06200

Example II

The second example is concerned with the damping matrix decompositions. Thus far, there are three popular damping matrix decompositions. (1). The Clough-Penzien decomposition

$$C = C_p + C_n$$

This decomposition gives a proportional damping matrix C_p . Consequently all the damping ratios of the system can be calculated.

(2). The pure proportional and non-proportional decomposition

$$C = C_d + C_o$$

This decomposition gives the pure non-proportional damping matrix C_o .

(3). The real-imaginary decomposition:

$$C = C_r + C_i$$

This decomposition gives the matrix C_r and the matrix C_i which provide the real part and the imaginary part of the complex damping ratio respectively.

Although decomposition (3) is in great use when dealing with energy analysis, its computations are intensive. With the help of Theorem 2 we can use the formula

$$C = C_d + C_n$$

to approximate $C = C_r + C_i$. This is a simple approach to obtain C

matrix.

Suppose we have the following M-C-K system,

$$M = I, \quad C = \begin{bmatrix} 2 & -1 & -1 & 0 \\ -1 & 3 & -1 & -1 \\ -1 & -1 & 4 & -2 \\ 0 & -1 & -2 & 5 \end{bmatrix} \quad \text{and} \quad K = \begin{bmatrix} 180 & -48 & 0 & 0 \\ -48 & 136 & -88 & 0 \\ 0 & -88 & 130 & -92 \\ 0 & 0 & -92 & 92 \end{bmatrix}.$$

Since

$$C K = \begin{bmatrix} 408 & -144 & -92 & 92 \\ -324 & 544 & -352 & 0 \\ -132 & -440 & 992 & -552 \\ 48 & 40 & -732 & 644 \end{bmatrix}$$

we know that the system is non-proportionally damped. Using the pure proportional decomposition, we have

$$C_d = \begin{bmatrix} 3.8507 & -.2994 & .0301 & -.3307 \\ -.2944 & 3.6314 & -1.1827 & -.5486 \\ .0301 & -1.1827 & 3.6328 & -1.3303 \\ -.3307 & -.5486 & -1.3303 & 2.8851 \end{bmatrix}$$

and

$$C_o = \begin{bmatrix} -1.8507 & -.7006 & -1.0301 & .3307 \\ -.7006 & -.6314 & .1827 & -.4514 \\ -1.0301 & .1827 & .3672 & -.6697 \\ .3307 & -.4514 & -.6697 & 2.1149 \end{bmatrix}$$

The eigenvalues of the system are given by

$$\begin{aligned} & -2.5182 \pm 16.5207j \\ & -1.8893 \pm 13.6937j \\ & -1.9617 \pm 9.8809j \\ & -0.6307 \pm 3.0123j \end{aligned}$$

their corresponding complex damping ratios are

$$\begin{aligned} & .1507 \pm .0098j \\ & .1367 \pm .0066j \\ & .1947 \pm .0063j \\ & .2050 \pm .0100j \end{aligned}$$

The maximum damping ratio is about 21%. According to Corollary 1, if the damping matrix is reduced to one tenth of the original value, then the damping ratios will be approximately decreased to ten times smaller. Therefore the maximum damping ratio is about 2%.

In Table 4 we listed the results of $\lambda(H_{C_o})$ and $\theta(H_{C_o})$ from $C_d - C_o$ decomposition as well as the results from the system of $C/10$ damping.

Table 4 $\lambda(H_{co})$ and $\phi(H_{co})$

	Original system	System with C/10
λ	$.0179 \pm 16.7148j$	$.0000 \pm 16.8771j$
	$-.0323 \pm 13.8242j$	$.0000 \pm 13.9147j$
	$.0148 \pm 10.0737j$	$.0000 \pm 10.0098j$
	$-.0004 \pm 3.0769j$	$.0000 \pm 3.0468j$
ϕ	$1 \times$	$1e-4 \times$
	$.1507 \pm .0098j$	$-.0100 \pm .9811j$
	$.1367 \pm .0066j$	$.0216 \pm .6170j$
	$.1947 \pm .0063j$	$-.0136 \pm .6156j$
	$.2050 \pm .0100j$	$.0012 \pm .9824j$

The numerical results in Table 4 show that the approximation is satisfactory. This is particularly obvious for the small damping ratios.

CONCLUDING REMARKS

Most engineering structures can be classified as lightly damped systems. Dynamic analyses of these structures could be different from and simpler than those of heavily damped systems. The nice linear property of the lightly damped systems presented in this paper is such an example. A further application of this property can be found in damper utilization design (see Liang et al 1991).

ACKNOWLEDGEMENT

Funding for the research reported in this paper has been provided jointly by the State University of New York at Buffalo and The National Science Foundation through the National Center for Earthquake Engineering Research under master contract number ECE86-07591.

REFERENCES

Caughey, T.K. and O'Kelly, M.M.J. "Classical Normal Mode in Damped Linear Dynamic Systems" J. of Appl. Mech. ASME Vol 32, pp.583-588, 1965.

- Clough, R. W. and Penzien, "Dynamics of Structures," McGraw-Hill, New York, 1975.
- Ewins, D.J "Modal Testing, Theory and Practice" Research Studies Press LTD. England (1986).
- Inman, D. "Vibration with Control, Measurement and Stability", Prentice-Hall, Englewood Cliffs, 1989.
- Juang, J-N.; Pappa, R.S. " An Eigensystem Realization Algorithm (ERA) for Modal Parameter Identification and Model Reduction" presented at NASA/JPL workshop on identification and control of flexible space structures, J. of Guidance, Control and Dynamics, Vol. 8, No. 5, Sept-Oct. 1985, pp.620-627.
- Kozin, F. and Natke, H.G. (1986). "System Identification Techniques", Structural Safety, Vol.#, pp.269-316.
- Lancaster, P. "Lambda-Matrices and Vibrating Systems" (1966) Pergamon Press.
- Liang, Z. and Lee, G.C. "On Complex Damping of MDOF Systems" Proc. of IMAC-8, 1990, pp.1048-1055.
- Liang, Z. and Lee, G.C. "Representation of Damping Matrix", J. of Eng. Mech. ASCE., May 1991 (to appear).
- Liang, Z., Lee, G.C. and Tong, M. (1991) "On A Theory of Complex Damping" Proc. of Damping '91, Feb. 13-15 1991, San Diego, CA., Sponsored by Wright Laboratory, Flight Dynamics Directorate, Wright-Patterson Air force Base.
- Liang, Z., Lee, G.C. and Tong, M. (1991) "A Strong Criterion For Testing Proportionally Damped Systems" Proc. of Damping '91, Feb. 13-15 1991, San Diego, CA., Sponsored by Wright Laboratory, Flight Dynamics Directorate, Wright-Patterson Air force Base.
- Lin, R.C., Liang, Z., Soong, T.T. and Zhang, R.H. "An Experimental Study of Seismic Structural Response With Added Viscoelastic Dampers", Technical report NCEER-88-0023. 1988.
- Natke, H.G., Yao, J.T-P. (1986). "System Identification Approach in Structural Damage Evaluation", ASCE Structures Congress '86, Preprint 17-1.
- Natke, H.G. "Updating Computational Models in the Frequency Domain Based on Measured Data: A Survey", Probabilistic Engineering Mech. Vol. 3, No.1 1988.
- Shinozuka, M., Yun, C-B. and Imai, H. (1982). "Identification of Linear Structural Dynamic Systems", J. of Structural Engineering,

ASCE, Vol. 108, No. EM6, pp.1371-1390.

Singh, M. D. and Ghafory-Ashtiani, M. (1986) "Modal Time History of Non-classically Damped Structures For Seismic Motions". Earthquake Engineering and Structural Dynamics, Vol 13. pp133-146.

Tong, M., Liang, Z. and Lee, G. C. (1991) "On an Application of Complex Damping Coefficients" Proc. of Damping '91, Feb. 13-15 1991, San Diego, CA., Sponsored by Wright Laboratory, Flight Dynamics Directorate, Wright-Patterson Air force Base.

Tong, M. Liang, Z, and Lee, G.C.(1991) "Techniques in Design and Using VE Dampers" Proc. of Damping '91, Feb. 13-15 1991, San Diego, CA., Sponsored by Wright Laboratory, Flight Dynamics Directorate, Wright-Patterson Air force Base.

Vold, H; Rocklin, G. " The Numerical Implementation of a Multi-Input Modal Estimation Method for Mini-Computer," Proc. of IMAC-1, 1982, pp.542-548.

**Active Vibration Suppression via LQG/LTR;
Analytic and Experimental Results for the
PACOSS Dynamic Test Article**

Russeli N. Gehling ‡
Martin Marietta Astronautics Group

ABSTRACT

Future large space systems (LSS) will possess high modal density at low frequencies, and mission performance requirements will necessitate control bandwidths encompassing these modal frequencies. This situation has potential for adverse controls/structure interaction (CSI) detrimental to system performance.

The Passive and Active Control of Space Structures (PACOSS) program has investigated the design, analysis, and verification of passive and active damping strategies applied to LSS. This paper discusses the results of an experiment in which a Linear Quadratic Gaussian with Loop Transfer Recovery (LQG/LTR) design technique was applied to the PACOSS Dynamic Test Article (DTA) for the purpose of high authority vibration suppression.

In general, the LQG/LTR control demonstrated high sensitivity to design model accuracy. Actual performance was significantly less than predicted, even though the control design utilized an accurate test-verified model.

The results of this experiment indicate that analytic LSS models which are quite accurate by structural dynamics standards may be insufficient for use as design models in modern control algorithms. However, passive damping designed into LSS flexible modes will simplify the active control design and implementation in terms of sensor/actuator requirements, design model order, real time computing requirements, and overall system robustness.

‡ P.O. Box 179, Denver, CO. 80201, Mail Stop H4330, phone: (303) 971-9388.

INTRODUCTION

Future large space systems (LSS) will possess high modal density at low frequencies. Some missions envisioned for these systems require rapid retargeting and precision pointing which lead to control bandwidths overlapping many closely spaced structural modes. Therefore, some means of structural vibration control will be necessary to avoid excessive excitation of the flexible modes. Passive/active vibration control is the most realistic and efficient approach for vibration suppression in such dynamically challenging systems.

The Passive and Active Control of Space Structures (PACOSS) program investigated the design and implementation of passive and active vibration suppression on structures typical of many LSS configurations. This involved design and fabrication of the passively damped dynamic test article (DTA) possessing high modal density between 1 and 10 Hz (Fig 1). Also, an active vibration control system was designed and implemented. A brief description of the DTA hardware and test setup is presented in this paper, while a detailed description of the DTA is given in Reference 1.

Previous investigations with the DTA demonstrated good agreement between measured and predicted performance of the passive damping design acting in concert with local direct velocity feedback (LDVFB) as discussed in Reference 2. However, the LDVFB was a relatively low authority active damping approach which did not dramatically improve the DTA line of sight (LOS) performance. Optimal control in the form of a Linear Quadratic Regulator (LQR) approach allows for efficient use of actuator capability in the design of high authority vibration control. The loop transfer recovery (LTR) technique allows for estimator design which recovers the desirable characteristics of the LQR full state feedback design. These characteristics make the LQG/LTR design algorithm attractive for designing a multi-input multi-output vibration controller for the DTA.

This paper discusses the application of the LQG/LTR control design algorithm to the DTA LOS vibration suppression problem. Analytic and measured results are presented to show the degree of agreement between analytic predictions and actual performance. Conclusions regarding the practical application of LQG control for vibration suppression and the role of passive damping are drawn from the test results and analytic studies.

HARDWARE DESCRIPTION AND MODELING

The PACOSS DTA is a laboratory testbed for passive and active structural vibration control implementation and testing. The DTA possesses 23 major structural modes between 1 and 10 Hz, many of which are global in nature. Using the method described in Reference 3, passive damping levels between 5% and 10% (modal viscous) were designed into the flexible modes which contribute to LOS error. The analytic model was then verified through a comprehensive modal survey (Reference 4). The DTA is suspended from three pneumatic suspension devices which have very low stiffness and virtually no friction. The suspension arrangement gives the DTA six rigid body modes below 0.3 Hz. The overall test setup is shown in Figure 2.

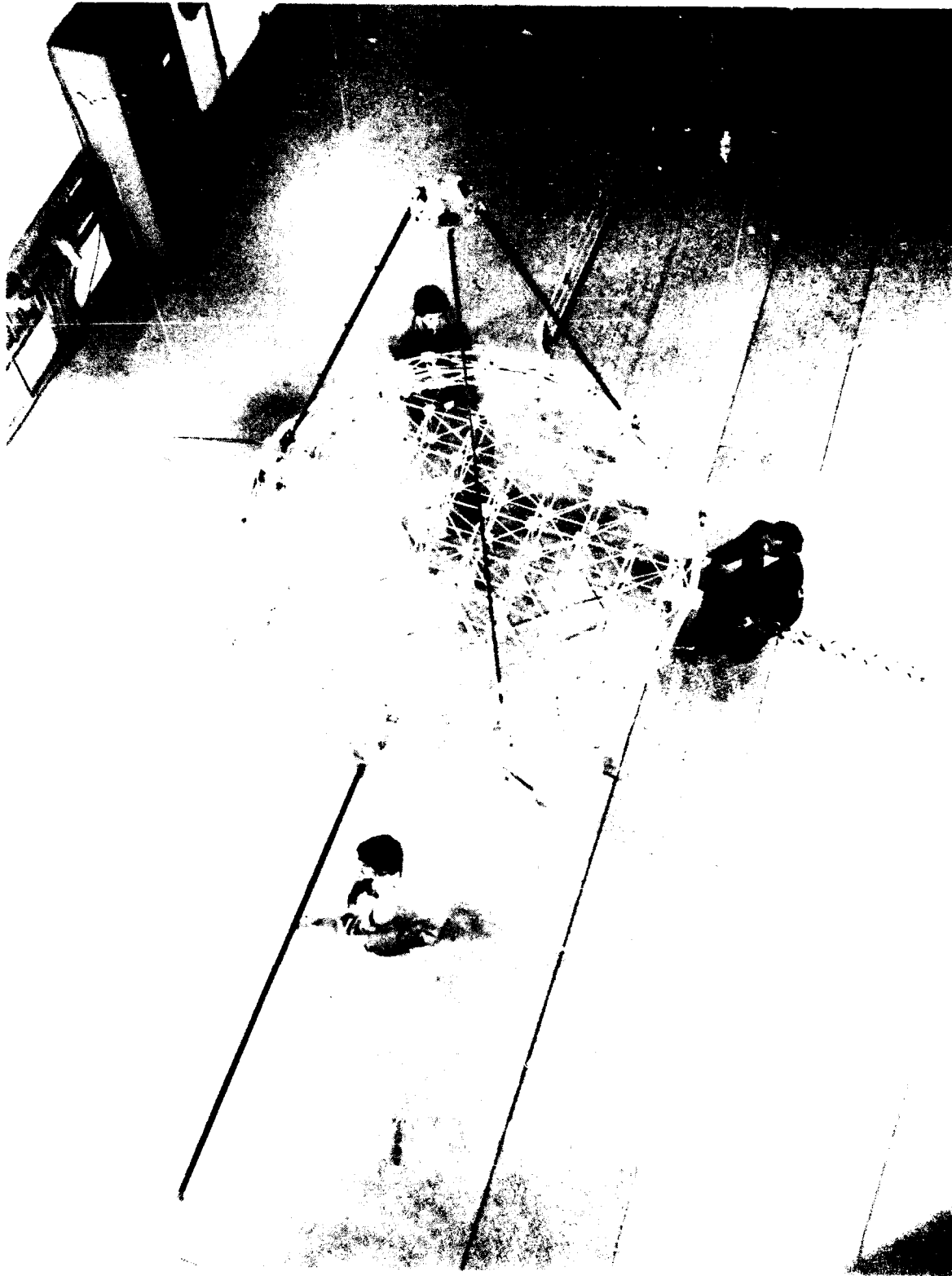


Figure 1 PACOSS Dynamic Test Article

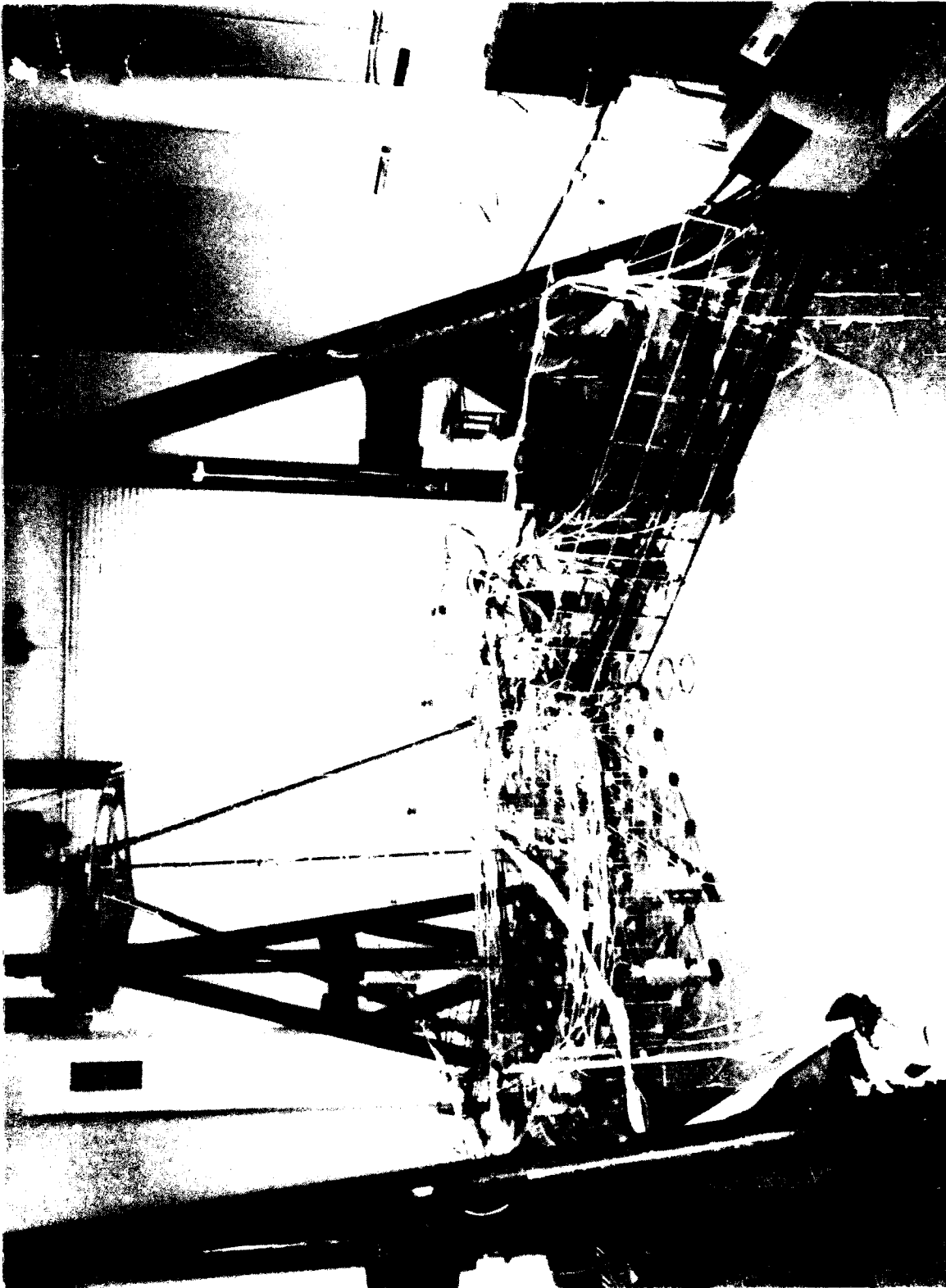


Figure 2 DTA Test Setup

The active control system includes reaction mass actuators (RMA), inertial velocity measurements, and a digital control processor. Ten RMAs with collocated Sundstrand QA-1400 accelerometers and linear velocity transducers are mounted at the locations shown in Figure 3. Also identified in Figure 3 are the locations of three additional non-collocated QA-1400 accelerometers. Inertial velocity is obtained from the 13 accelerometers by integrating the signals with bi-quad filters as discussed in Reference 5. Thus, the control system involves 23 inputs (10 collocated inertial velocities, 10 collocated relative velocities between the reaction masses and DTA, and 3 non-collocated inertial velocities), and 10 outputs. Control laws are implemented via an Optima/3 digital controller capable of handling up to 32 inputs and 32 outputs. In the PACOSS experiment, the processor ran the LQG/LTR control law (36 states, 23 inputs and 10 outputs) at a 400-Hz sample rate.

Due to their 1.5-Hz natural frequency, the RMAs cannot control the low frequency rigid body dynamics of the DTA. Therefore, a relative LOS was defined to exclude rigid body modes from the control system. Thus, the controller acts strictly as a vibration suppression system. Figure 3 identifies four disturbance input points on the DTA. These disturbances could be from maneuvering thrusters or onboard equipment. The relative LOS response to these disturbance inputs was taken as the performance metric to be minimized by the controller.

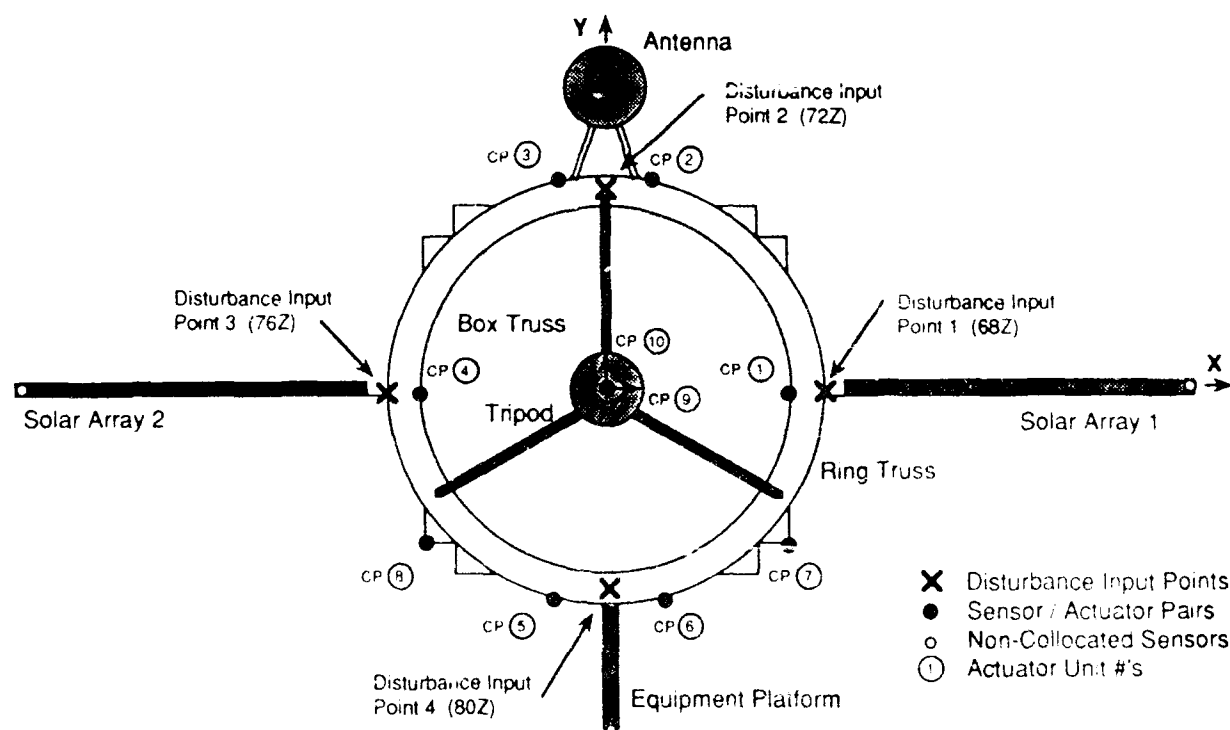


Figure 3. DTA Control Locations

In addition to the active control instrumentation, 182 Kistler model 8632 accelerometers were installed on the DTA for acquiring modal survey data. The large number of cables seen in Figure 2 are primarily from these modal accelerometers.

Tests with and without the majority of cables attached showed that the instrumentation cables had no effect on the flexible modes of the DTA. The LOS measurement was synthesized as a linear combination of selected measurements from the Kistler accelerometers.

A detailed finite element model of the DTA with over 10,000 degrees of freedom (DOF) was developed and test verified during the first phase of the PACOSS program. The detailed model was reduced (via a Guyan reduction) to 357 DOFs, and the modes determined from this reduced model. Table 1 compares the analytic and measured natural frequencies and damping ratios and lists the diagonal term of the orthogonality product between the predicted and identified modes up to 10 Hz. The modes retained in the control design model (CDM) were those possessing significant observability or controllability when the control points, sensor points, disturbance input points, and LOS were considered. Essentially, the CDM includes all global modes and a few appendage modes with frequencies below 10 Hz.

Table 1 Identified and Predicted Modes from DTA Modal Survey 3

Mode #	Measured		Analytic		X-orth diag.	Retained in control design model
	f_n (Hz)	ζ (%)	f_n (Hz)	ζ (%)		
1	1.03	2.9	1.04	4.8	0.97	
2	1.11	3.4	1.06	4.9	0.98	
3	2.59	3.9	2.68	2.8	0.98	X
4	3.03	7.4	3.17	5.9	0.51	
5	3.13	6.5	3.22	5.0	0.40	
6	3.30	5.1	3.37	5.3	0.71	X
7	3.45	8.7	3.54	7.4	0.74	X
8	3.73	6.3	3.75	4.9	0.98	X
9	4.12	7.4	3.85	10.1	0.98	
10	4.56	5.8	4.43	6.1	0.84	X
11	4.79	1.7	4.46	3.4	0.89	
12	4.82	1.6	4.46	3.0	0.89	
13	5.08	12.0	4.86	11.9	0.97	X
14	5.13	5.4	5.02	7.1	1.00	
15	5.78	1.6	5.85	2.6	0.94	X
16	5.82	2.1	5.85	2.5	0.98	X
17	6.49	5.0	6.00	3.3	0.96	
18	6.55	9.5	6.25	9.7	0.98	X
19	6.87	7.2	7.26	6.0	0.67	X
20	8.20	7.0	9.35	7.2	0.99	X
21	9.61	5.4	9.55	7.1	0.93	X
22	10.41	1.5	10.11	1.4	0.96	
23	10.48	1.4	10.11	1.4	0.94	

Note: Analytic damping ratios for modes 1 through 18 computed using VEM properties at 4 Hz, modes 19 through 23 computed using VEM properties at 9 Hz.

The correlation of the analytic and measured results was excellent in terms of frequency and damping ratios. The orthogonality diagonal term indicates agreement in terms of mode shape and should be greater than 0.9. As listed in Table 1, the mode shape correlation is quite good for most of the flexible modes retained in the CDM with the exception of modes 6, 7, 10, and 19. Modes 6 and 7 are antisymmetric global modes which involve the box truss, tripod, and solar arrays. Modes 10 and 19 are more local in nature, mainly involving the antenna.

Review of component modal surveys (Ref 6) indicated that the fundamental constrained interface mode of the box truss was about 6% higher in natural frequency than predicted. In an effort to evaluate the effect on the DTA system modes of matching the box truss constrained interface fundamental frequency, the 1/8-in. diameter x 0.014-in. wall box truss members were stiffened by 20%. This increased the box truss constrained interface fundamental frequency by the desired 6% to match the component test results. In this case, the fundamental mode shape of the box remained essentially unchanged. The DTA model was recoupled with the stiffened box model, and the system modes computed.

Table 2 lists the results for the updated model CDM modes. Note the negligible differences in natural frequencies and damping ratios between the two analytic models for all but modes 6 and 7 (see Table 1). These modes show a small shift in frequency but a relatively large change in damping ratio. Agreement with the measured values, while remaining quite good, improves somewhat for mode 7 but degrades slightly for mode 6. The orthogonality product diagonals for modes 6 and 7 between the measured and updated analytic modes are greatly improved as compared with the original DTA model. These results indicate that accurate prediction of closely spaced modes can be quite difficult. Here, a 6% change in a substructure modal frequency produced a major change in two very closely spaced system mode shapes. The task of predicting and identifying closely spaced modes in dynamically complex structures indeed requires extremely accurate finite element models.

Table 2 Measured and Analytic f_n and ζ for DTA Modes Retained in CDM

Mode #	Measured		Updated		X-orth diagonal
	f_n (Hz)	ζ (%)	f_n (Hz)	ζ (%)	
3	2.59	3.9	2.66	2.8	0.99
6	3.30	5.1	3.47	4.2	0.93
7	3.45	8.7	3.51	8.6	0.95
8	3.73	6.3	3.70	4.8	0.98
10	4.56	5.8	4.43	6.0	0.82
13	5.08	12.0	4.86	12.1	0.97
15	5.78	1.6	5.85	2.6	0.94
16	5.82	2.1	5.85	2.5	0.98
18	6.55	9.5	6.41	9.9	0.99
19	8.87	7.2	7.27	6.0	0.67
20	9.20	7.0	3.41	7.1	0.99
21	9.61	6.4	9.58	7.2	0.93

These observations indicate that DTA modes in the 3 to 4-Hz range are very sensitive to the relative stiffnesses of the box truss, tripod, and solar arrays. Stiffening the box truss seems to have improved correlation, but altering the tripod or solar array models may have similar effects. The DTA model with the stiffened box truss was used as the evaluation model for control performance evaluation. However, the original DTA model was used to design the LQG/LTR control since it was the best available model before conducting the final open loop modal survey in the 10 actuator DTA configuration.

LQG/LTR DESIGN APPROACH

Modern state-space control design techniques allow the analyst to conveniently model and analyze high-order, multi-input, multi-output (MIMO) systems. One branch of modern control theory well suited to the DTA vibration suppression problem is optimal LQG control. The LQG approach provides a framework in which LOS jitter suppression may be traded against active control effort to determine the most efficient compensator design for the required performance. The complete LQG/LTR design algorithm utilizes standard LQG design techniques (optimal regulator or estimator design, depending on the problem), and then computes the companion estimator or regulator design such that the singular values of the system loop-transfer matrix approach those of the full-state design case. This is known as "recovery" of loop-transfer functions (LTF).

The LQG control structure is shown in Figure 4. It consists of a Kalman-Bucy filter (KBF) with gains, K_f , designed to estimate the states of a nominal plant model, $G(s)$, and a full-state, linear-quadratic regulator, K_c . Figure 4 and the nomenclature used here were taken from Reference 7. Referring to Figure 4, the following properties for the LQG control structure may be stated:

- 1) The LTF obtained by breaking the LQG loop at point (i)' is the KBF LTF $C\Phi K_f$.
- 2) The LTF obtained by breaking the LQG loop at point (i) is GK . It can be made to approach $C\Phi K_f$ pointwise in s by designing the LQR in accordance with a "sensitivity recovery" procedure due to Kwakernaak (Ref 8). This assumes $G(s)$ is minimum phase and that $m \geq r$.
- 3) The LTF obtained by breaking the LQG loop at point (ii)' is the LQR LTF $K_c\Phi B$.
- 4) The LTF obtained by breaking the LQG loop at point (ii) is KG . It can be made to approach $K_c\Phi B$ pointwise in s by designing the KBF in accordance with a "robustness recovery" procedure due to Doyle and Stein (Ref 9). This assumes $G(s)$ is minimum phase and that $m \leq r$.

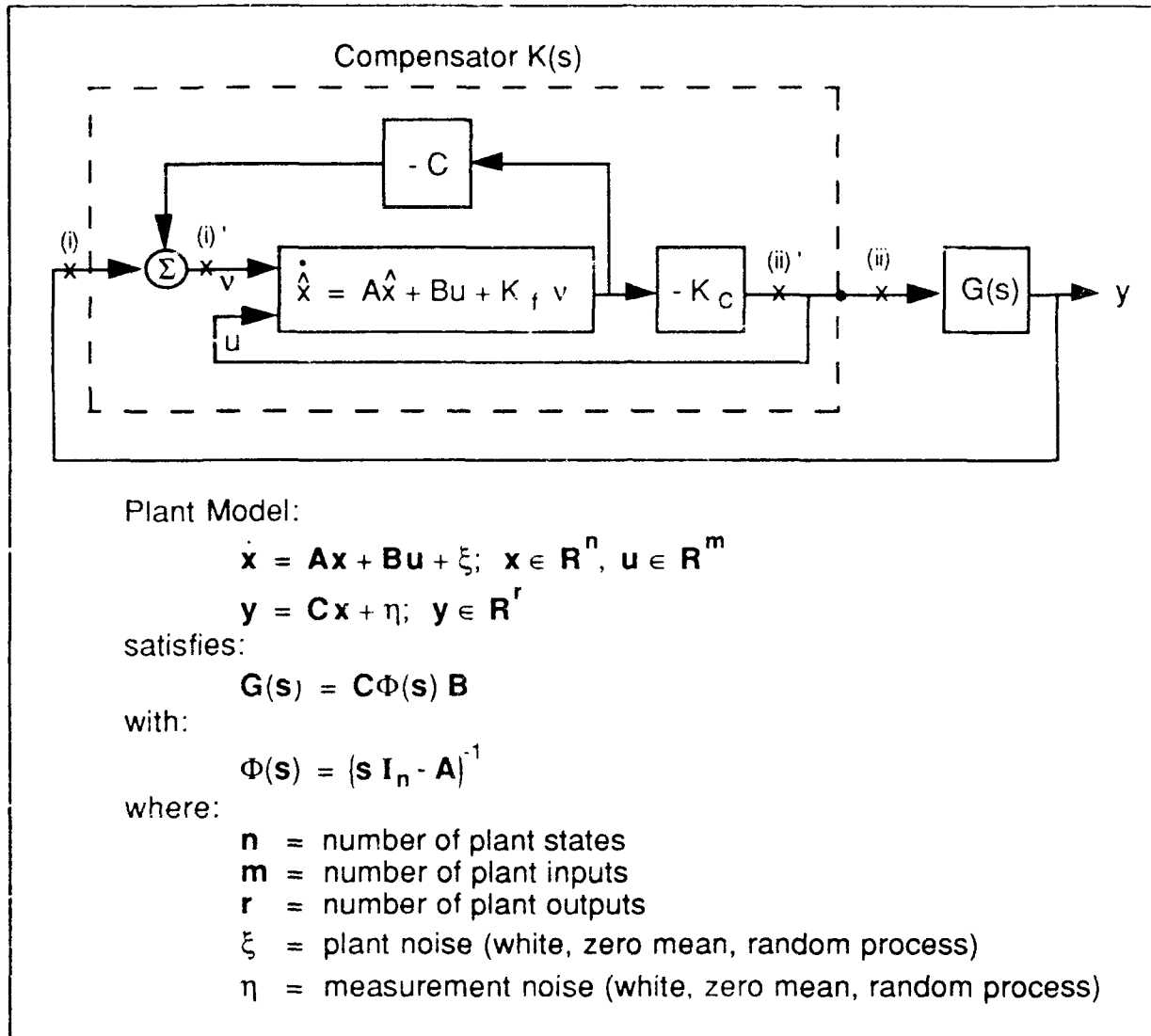


Figure 4. LQG Control Structure

As stated in Reference 7, "The significance of these four facts is that we can design LQG loop-transfer functions on a full-state feedback basis and then approximate them adequately with a recovery procedure."

The appropriate approach for the DTA is to design \mathbf{K}_C via the LQR technique and then compute \mathbf{K}_f to cause the singular values of the loop-transfer matrix, $\mathbf{K}\mathbf{G}$, to approach those of the full-state feedback case, $\mathbf{K}_C\Phi\mathbf{B}$. The procedure for computing the KBF gains is described in Reference 7 and summarized below:

- 1) Append dummy columns to \mathbf{B} and zero rows to \mathbf{K}_C to make $\mathbf{C}\Phi\mathbf{B}$ and $\mathbf{K}_C\Phi\mathbf{B}$ square ($r \times r$). $\mathbf{C}\Phi\mathbf{B}$ must remain minimum phase.

2) Design the KBF with modified noise intensity matrices:

$$E(\xi\xi^T) = [M_0 + q^2 B B^T] \delta(t - \tau)$$

$$E(\eta\eta^T) = N_0 \delta(t - \tau)$$

where M_0 , N_0 are the nominal noise intensity matrices and q is a scalar parameter.

Under these conditions (Ref 9):

$$(1/q)K_f \rightarrow B W N_0^{-1/2} \text{ as } q \rightarrow \infty$$

where W is an orthonormal matrix.

This calculation of K_f results in:

$$K(s) G(s) \rightarrow K_c \Phi B \text{ as } q \rightarrow \infty$$

The design procedure for a MIMO system involves calculation of K_f with successively increasing values of the fictitious plant noise, q . As q approaches infinity, the singular values of KG will approach those of $K_c \Phi B$. However, the gains in K_f will become quite large, which is generally undesirable. Thus, a designer will wish to use the smallest q for which the LTF of KG acceptably matches that of $K_c \Phi B$ in the bandwidth of interest.

An extension of the single-input, single-output Bode plot for MIMO systems is the singular value (SV) Bode plot. Comparison of SV Bode plots for KG and $K_c \Phi B$ is a good indicator of the loop-transfer recovery achieved for a given value of q . Therefore, SV Bode plots may be used to determine the convergence of KG to $K_c \Phi B$ over the bandwidth of interest.

The design goal of the LQG/LTR control algorithm for the DTA was to minimize the LOS response to slew commands and noise disturbances at known input points. The approach taken for application to the DTA was to design an optimal regulator based on full-state feedback and then recover the loop-transfer functions at the disturbance and slew command input points. Thus, as discussed in Reference 10, the desirable characteristics of the LQR full-state feedback design are recovered by the estimator.

Calculation of the LQR gain matrix involves selection of state and control weighting matrices, Q and R . These required matrices were determined as follows:

$$LOS = \begin{bmatrix} LOS-X \\ LOS-Y \end{bmatrix} = \begin{bmatrix} \text{philosx} & 0 \\ \text{philosy} & 0 \end{bmatrix} \begin{Bmatrix} \eta \\ \dot{\eta} \end{Bmatrix} = [TLOS] x$$

where:

philosx = mode shape coefficients defining LOS about X-axis
 philosy = mode shape coefficients defining LOS about Y-axis
 η = generalized modal coordinates

Minimize:

$$\mathbf{LOS}^T [\bar{\mathbf{Q}}] \mathbf{LOS} + \mathbf{u}^T [\mathbf{R} \mathbf{u}] = \mathbf{x}^T [\mathbf{TLOS}^T] [\bar{\mathbf{Q}}] [\mathbf{TLOS}] \mathbf{x} + \mathbf{u}^T [\mathbf{R}] \mathbf{u}$$

Let:

$$\mathbf{R} = \mathbf{I} \text{ (10 x 10)}$$

$$\bar{\mathbf{Q}} = [\mathbf{TLOS}^T] [\mathbf{TLOS}] \bar{\mathbf{Q}}$$

The magnitude of the scalar $\bar{\mathbf{Q}}$ is then varied to achieve the desired performance. Once the desired LOS response is achieved, representative disturbances and maneuvers are input to the full-state feedback closed-loop simulation to check if actuator stroke or force constraints are exceeded. If such limits are violated, the magnitude of $\bar{\mathbf{Q}}$ must be reduced, and \mathbf{K}_C recomputed.

After an acceptable LQR design is obtained, the KBF gain matrix is computed using the LTR method previously described. The input matrix, \mathbf{B} , used in the loop-transfer recovery procedure includes the control and disturbance input points. Note that the number of points used (number of columns in \mathbf{B}) must be less than or equal to the number of sensor measurements (number of rows in \mathbf{C}). After each computation with a given value of $\bar{\mathbf{q}}$, the SV Bode plots of $\mathbf{K}\mathbf{G}$ and $\mathbf{K}_C\Phi\mathbf{B}$ are compared. Once convergence (in a qualitative sense) is apparent, the control design is complete.

Following several iterations, good performance was achieved with a state-weighting parameter, $\bar{\mathbf{q}}$, of 10^9 . The LTR procedure was then performed for varying $\bar{\mathbf{q}}$. This process was conducted using the matrix algebra software package, PRO-MATLAB, and the Robust Control Toolbox function "ltru" (Ref 11). Figure 5 shows the convergence of the SV Bode plot for three values of $\bar{\mathbf{q}}$. The plots show nearly perfect agreement for $\bar{\mathbf{q}} = 10^9$. Using this value, the largest gain in the KBF matrix was 9600, which is large but proved to be acceptable.

The closed-loop frequencies and damping ratios for the initial LQG/LTR design coupled to the DTA CDM are listed in Table 3. Note that the LTR procedure resulted in several overdamped (real) poles far in the left half plane as well as several very low frequency real poles.

It was necessary to remove the high-frequency poles from the design to avoid aliasing problems when running the controller at 400 to 500 Hz. Also, since the 0.05-Hz bi-quad integrator poles were not included in the CDM, the low-frequency compensator poles could couple with the analog integrators used for the inertial velocity measurements and cause stability problems. Therefore, the compensator poles less than 0.5 Hz also had to be removed from the controller design.

In attempting to reduce the controller order, it was found that the low-frequency poles could not be removed from the compensator without causing instabilities when coupled with the DTA structural model. Therefore, the LQG/LTR design was repeated, but with a spectral shift applied to the Kalman filter design such

that the filter poles were required to be greater than 0.5 Hz. This procedure resulted in a compensator which indeed possessed no poles below 0.5 Hz, yet had performance nearly equivalent to the original design.

A reduced-order compensator was then obtained from the full-order design by removing compensator modes which had relatively small observability and controllability as determined from a balanced realization of the compensator formed using the PRO-MATLAB Robust Control Toolbox function, "obalreal" (Ref 11). This reduction removed most of the high-frequency compensator poles and several other relatively unimportant poles. A few remaining poles in the 100 to 400-Hz range were removed via a modal truncation, and the final compensator order was cut to 30 states, with a maximum frequency near 11 Hz. Figure 6 shows the SV Bode plot for full-state feedback, full-order compensator, and reduced-order compensator designs. Note that the maximum singular values agree nearly identically across the three cases.

In addition to the 30-state LQG/LTR compensator, three second-order bi-quad integrators were appended to the controller to derive inertial velocity from the non-collocated QA-1400 accelerometer measurements. Thus, the controller implemented in the Optima-3 involved 36 states with 23 inputs and 10 outputs. The Optima-3 was able to run the problem at a sample rate of 400 Hz.

Table 3 Initial DTA LQG/LTR Design Results

Complex Poles						Real Poles	
f_n (Hz)	ζ (%)	Type	f_n (Hz)	ζ (%)	Type	(rad/s)	
0.16	10.00	S	3.43	7.12	E	-1.92×10^{-4}	-2.27×10^3
0.16	10.00	S	3.54	7.38	F	-1.97×10^{-4}	-2.67×10^3
0.17	10.00	S	3.78	6.25	F	-2.00×10^{-4}	-3.17×10^3
0.26	10.00	S	3.90	15.40	E	-3.22×10^{-4}	-3.51×10^3
0.26	10.00	S	4.44	6.05	E	-3.84×10^{-4}	-8.85×10^4
0.29	1.00	S	4.45	6.46	F	-9.99×10^{-4}	-8.86×10^4
0.29	1.33	E	4.71	16.99	F	-9.99×10^{-4}	-8.88×10^4
0.29	1.07	E	4.82	32.12	E	-9.99×10^{-4}	-8.97×10^4
0.29	1.00	E	5.25	29.92	F	-9.99×10^{-4}	-8.97×10^4
0.56	83.90	A	5.84	2.52	F	-9.99×10^{-4}	-9.12×10^4
0.73	26.66	A	5.85	2.55	F	-9.99×10^{-4}	-9.43×10^4
1.00	37.09	A	5.85	2.70	E	-1.00×10^{-3}	-9.46×10^4
1.38	61.22	A	5.86	2.88	E	-1.00×10^{-3}	-9.53×10^4
1.50	5.03	A	6.73	45.26	E	-1.00×10^{-3}	-9.63×10^4
1.50	5.03	A	7.34	6.42	F	-7.96×10^{-2}	
1.50	5.03	A	7.39	6.23	E		
1.51	5.09	A	8.94	13.87	F	NOTE: S = Suspension Mode A = Actuator Mode F = DTA Flexible Mode E = Estimator Mode	
1.51	5.03	A	8.98	7.79	E		
1.53	5.00	A	10.06	22.51	F		
2.78	18.60	F	10.43	56.10	F		
3.21	6.99	E	10.61	44.63	E		

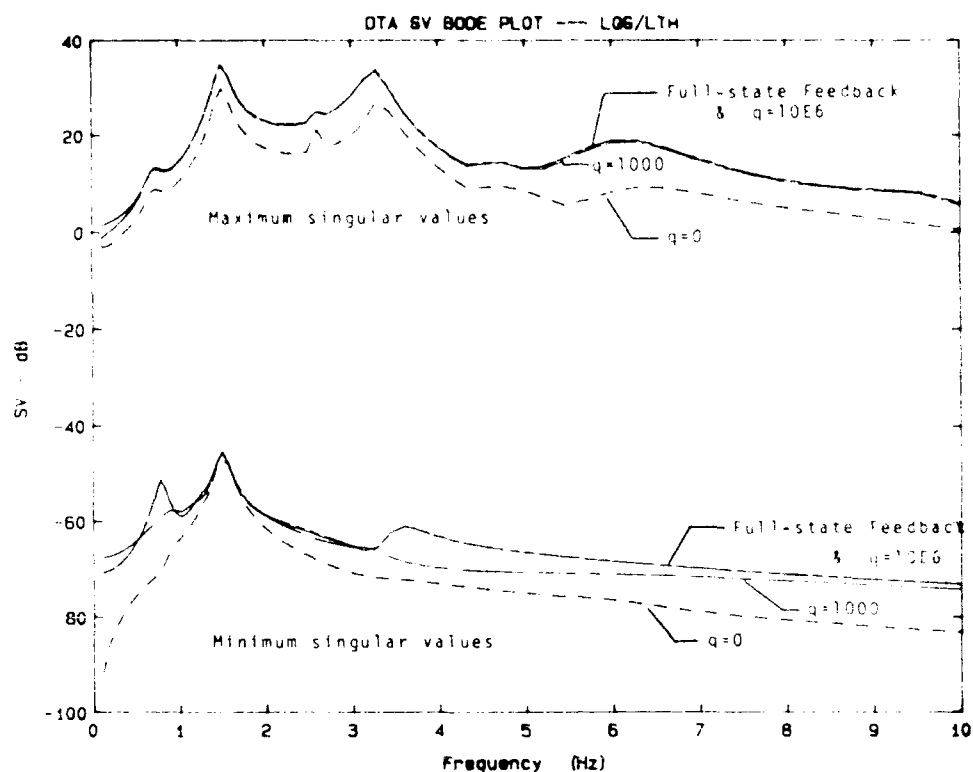


Figure 5. DTA SV Bode Plot, LQG/LTR

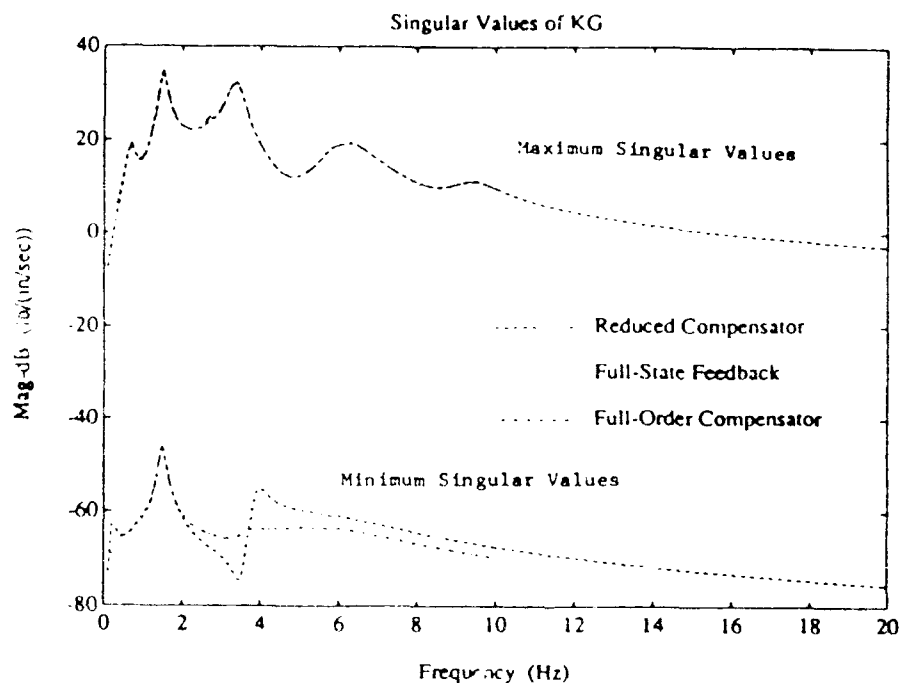


Figure 5. SV Bode Plot Comparing Full-State Feedback, Full-Order Compensator, and Reduced-Order Compensator for LQG/LTR Control

The analytic LOS frequency response function (FRF) for a slew command about the Y-axis is shown in Figure 7. The four traces show open-loop, closed-loop full-state feedback, closed-loop with the reduced-order state estimator designed using LTR coupled to the CDM, and the same reduced order compensator coupled to the full DTA model. The performance of the reduced-order compensator design on the CDM is very near that of the full-state feedback case, thereby showing the success of the LTR and reduction design process. The FRFs shown in Figure 7 indicate a 70 to 80% reduction in the root mean square (RMS) LOS jitter level based on response to white noise between 2 and 10 Hz. Another demonstration of the predicted control effectiveness is seen in the simulated slew response shown in Figure 8. Note that due to the passive damping designed into the DTA, only a few modes are significant in the open loop slew response. The active control system serves as a high authority control to virtually eliminate the response of these modes. Together, these FRFs and time response show the dramatic vibration suppression achieved by the modern optimal regulator design approach, and the effectiveness of combined passive/active control.

A drawback to the LQR method is sensitivity to modeling errors. While the design can be evaluated for stability robustness and bandwidth, actual performance can be seriously degraded by differences between the analytic design model and the actual structure. Recall that two DTA models were used in this study: the pretest model upon which the CDM was created, and the evaluation model, consisting of all modes below 20 Hz of the updated (stiffened box truss) model. The following section discusses analytic results for both these models and presents corresponding measured data.

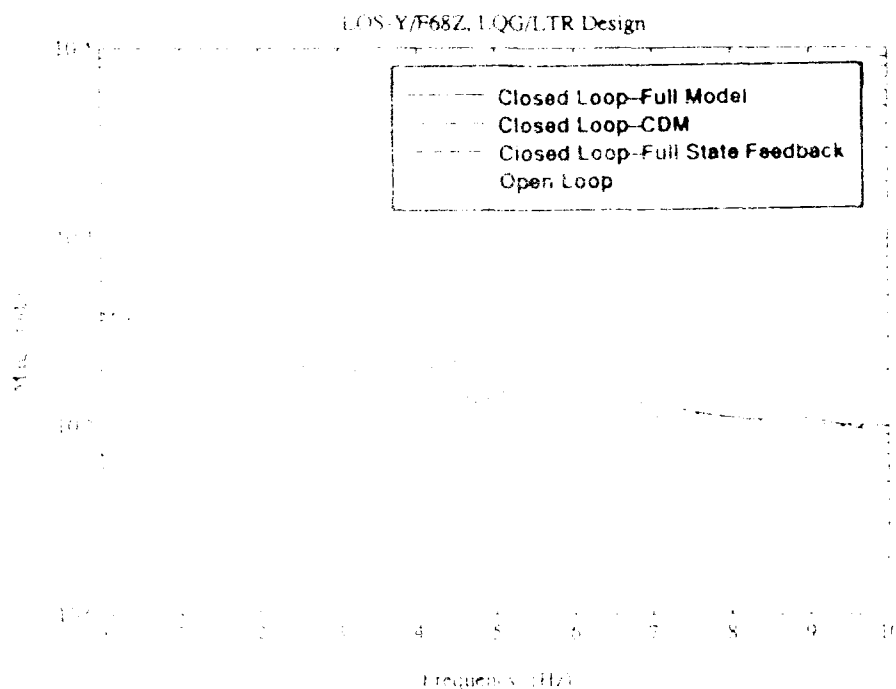


Figure 7. Analytic DTA LOS About Y-Axis

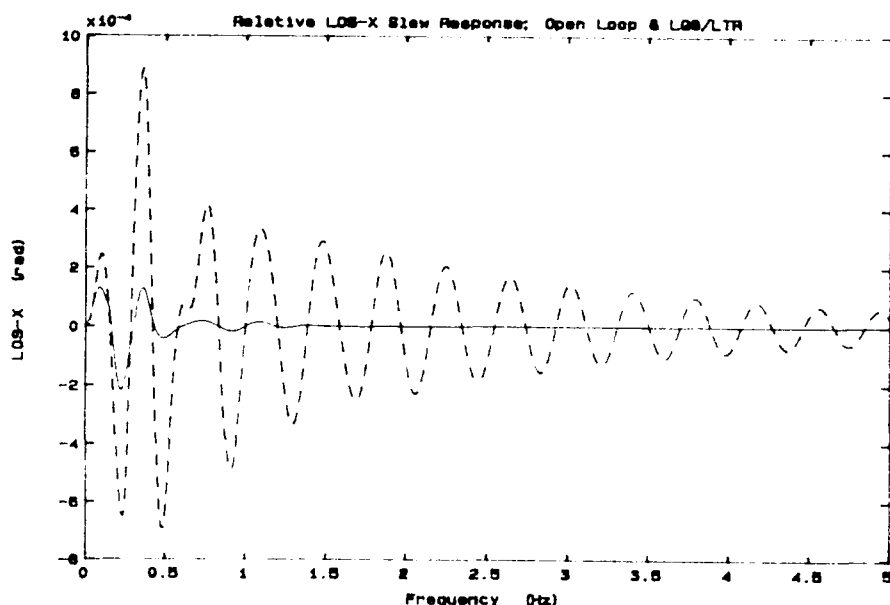


Figure 8. Relative LOS Slew Response, X-Axis

RESULTS

Open and closed loop FRFs were measured using burst random excitation at disturbance input points 68Z and 72Z (see Figure 3). Measurements were made for all the points which participate in the LOS, and the experimental LOS FRFs were computed as a linear combination of the actual measurements. Figure 9 shows the experimental open and closed loop FRFs for the LOS about the Y-axis due to excitation at point 68Z. The somewhat noisy closed loop response is a result of very low amplitude measurements being scaled by relatively large terms in the LOS computation. The corresponding analytic predictions, based on the original DTA model including all modes to 20 Hz, are shown in Figure 10. Note that while there is good qualitative agreement between the actual measurement and prediction for the open loop DTA, the LQG/LTR closed loop LOS measurement deviates significantly from predicted between 3 and 5 Hz. The cause of this error was, in part, due to the box truss component model. When the compensator was coupled to the updated DTA model, the FRF shown in Figure 11 resulted. This FRF shows a behavior very similar to that observed in the 3 to 5-Hz range. However, the overall response suppression is still less than predicted. A rough calculation of the actual RMS jitter reduction achieved by the control gives 63% versus 74% predicted using the updated DTA model.

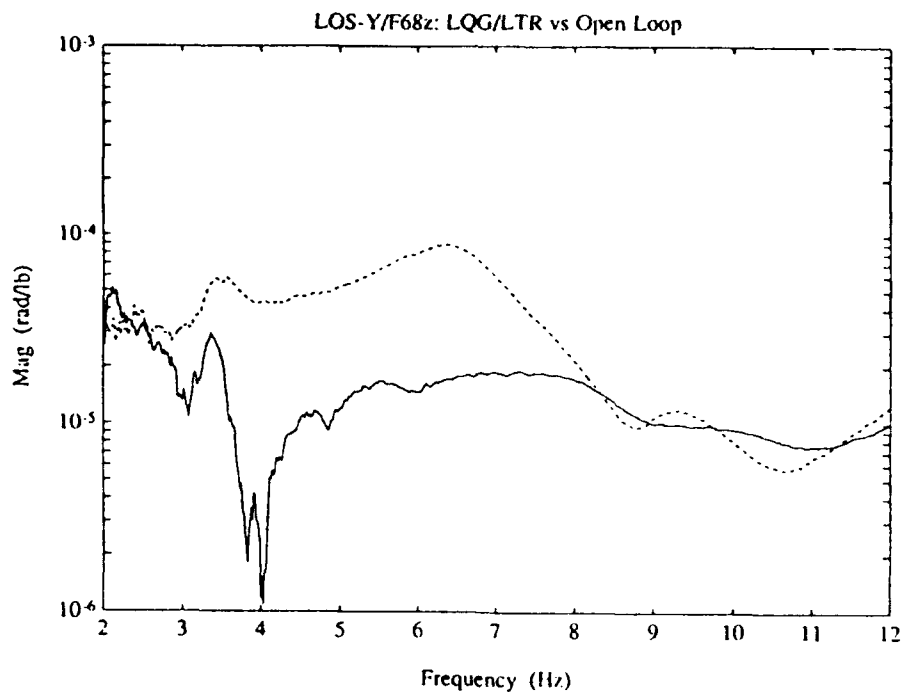


Figure 9 Experimental LOS FRF; LOS-Y/F68Z

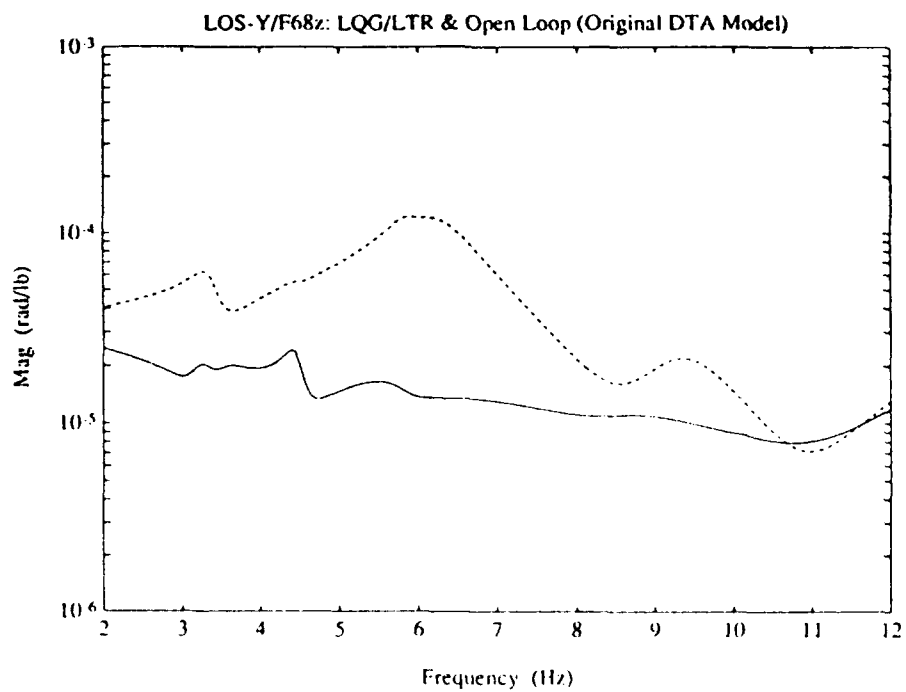


Figure 10 Predicted LOS-Y/F68Z; Original DTA Model

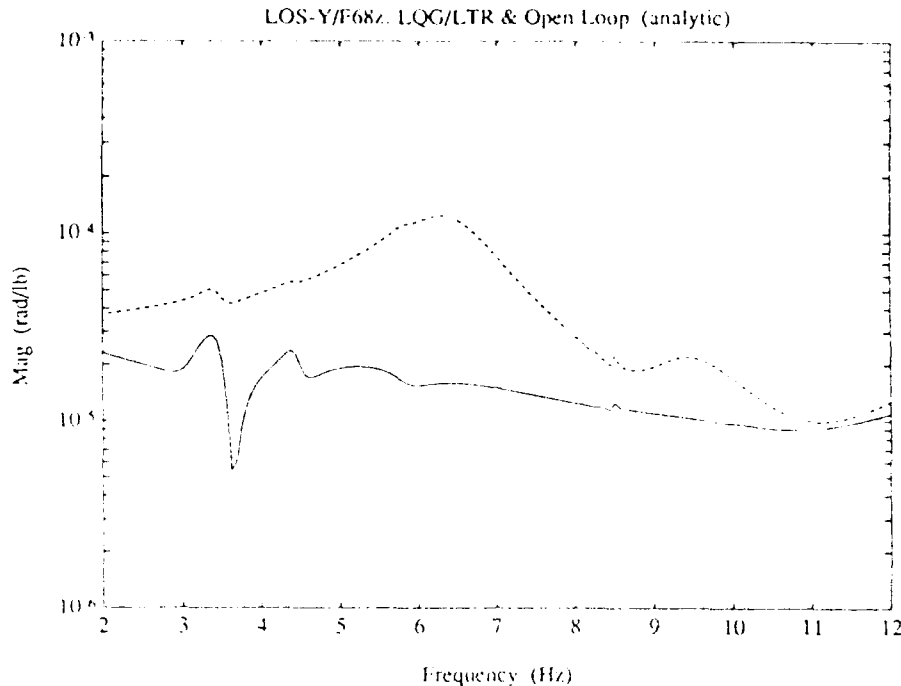


Figure 11 Predicted LOS-Y/F68Z; Updated DTA Model

The FRFs at selected control points demonstrated additional problems with the LQG/LTR design. Figure 12 shows the FRF between 72Z and CP2, and Figures 13 and 14 show the corresponding analytic FRFs using the original and updated DTA models respectively. Note the amplification of the closed loop FRF near 6 Hz. Apparently, a DTA mode near 6 Hz is being destabilized even though the open loop modal survey results indicated that the DTA flexible modes in this frequency range were accurate. As shown by the analytic FRFs, this is not predicted by either DTA model. Also, the control effectiveness at 3 Hz is much less than predicted. These observations indicate that the LQG/LTR design is quite sensitive to small differences between the CDM and actual structure.

Finally, Figure 15 shows a measured free decay for open and closed loop operation. This trace was produced by purely exciting the 2.6-Hz mode; perhaps the most accurately predicted mode of the DTA. The LQG/LTR control law did successfully apply a great amount of damping (on the order of 20% modal viscous) to this mode.

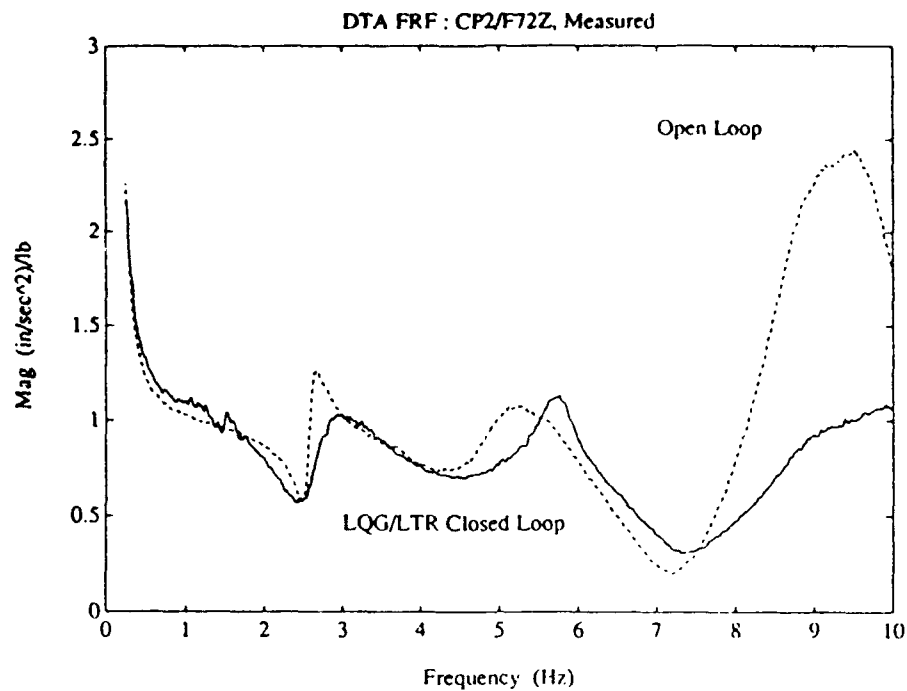


Figure 12 Measured DTA FRF; CP2/F72Z

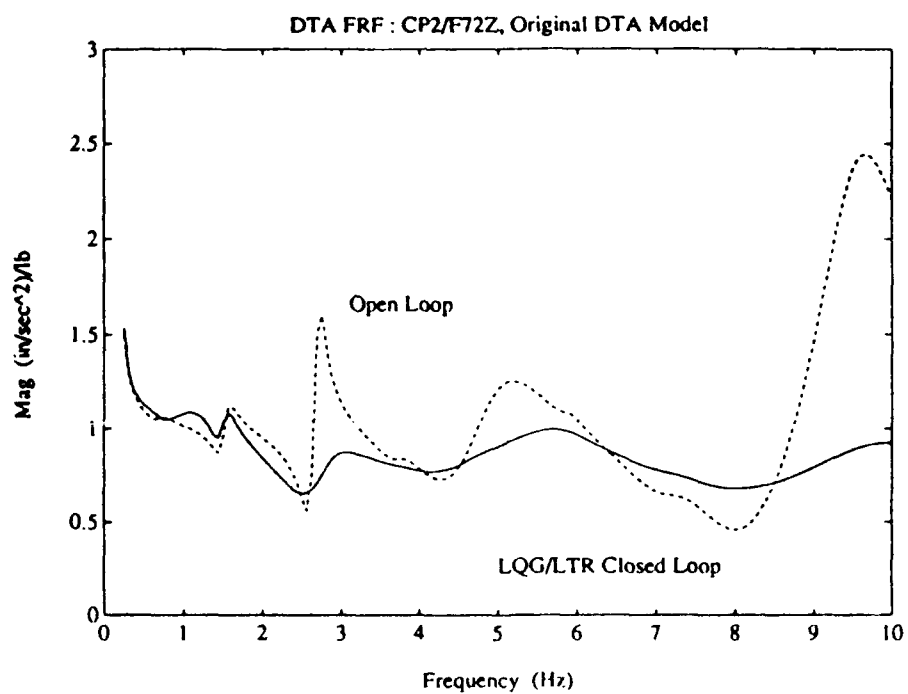


Figure 13 Predicted DTA FRF; CP2/F72Z, Original DTA Model

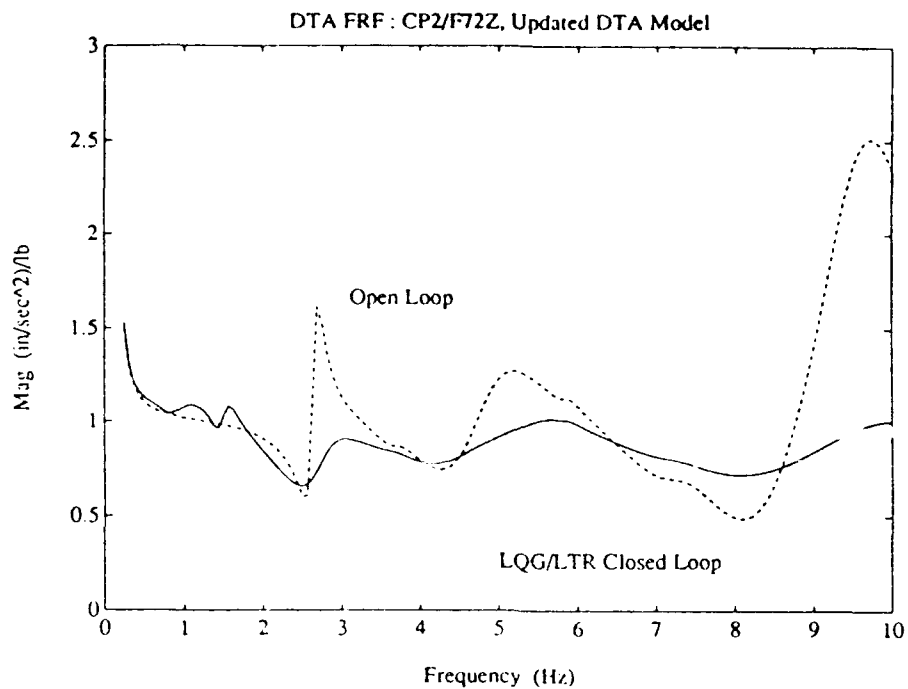


Figure 14 Predicted DTA FRF; CP2/F72Z, Updated DTA Model

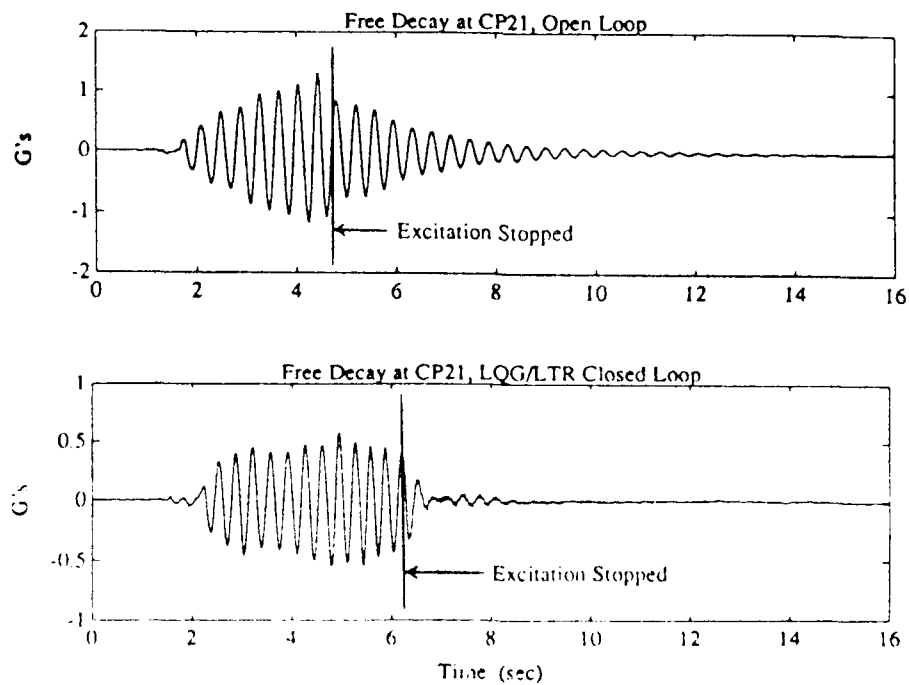


Figure 15 Free Decay of 2.6-Hz Mode

CONCLUSIONS

The open and closed loop results discussed above demonstrate that closely spaced flexible modes can be very difficult to accurately predict without resorting to empirically based model tuning. It is not surprising that the greatest degree of disagreement between predicted and measured results occurs in bands with closely spaced modes. While one source of error was identified (box truss frequency 6% low), there are undoubtedly many small differences between the DTA model and actual structure. While these discrepancies would typically be considered insignificant by a structural dynamicist, they lead to somewhat less than predicted performance of a sophisticated high authority control design such as LQG/LTR. In fact, the control law amplified the response of even well modeled modes, such as those in the 5 to 7-Hz range. It must be noted that the correlation between the pretest DTA model and the measured modes is probably much better than could be expected with an actual LSS which would not be tested until being assembled in orbit. Yet the DTA model still fails to predict critical performance problems when coupled to a modern controller. In fact, the results indicate that the control would probably have been unstable without the passive damping designed into the DTA.

The qualitative analysis/test agreement demonstrated by Figures 9 through 11 serves to validate the analysis. A natural question is; what if no passive damping were designed into the DTA? To answer this, an LQG/LTR design was performed for the original DTA model with only 0.2% modal viscous damping in all modes. As demonstrated by the DTA ring truss component modal survey (Ref 5), and the PACOSS D-Strut truss discussed in Reference 12, this level of damping would be expected from a tight, precision structure with no intentional damping designed in. The results of this design are shown in Figure 16. Note that the full-state feedback design achieves performance equivalent to that of the damped DTA closed loop performance. However, when the remaining plant modes are included in the plant model, a sharp peak near 4.5 Hz is evident. This demonstrates that without passive control, more modes must be considered in the control design, leading to higher order controllers requiring more control hardware (actuators, sensors) with greater capability. Also, a higher order plant makes the entire control design process more difficult since it is iterative in nature, requiring much insight from the analyst.

When coupled to the stiffened box truss DTA model, an unstable pole at 3.5 Hz was present. So, with passive damping, the LQG/LTR control was marginally successful, and with iterations and empirical tuning, could probably be made very effective. But without significant levels of passive damping designed into the structure, the sensitivity of LQG/LTR to parameter variations would have lead to closed loop instabilities and been very difficult to tune. These problems will be present whenever the controller bandwidth overlaps closely spaced flexible modes.

In summary, an LQG/LTR vibration suppression control design was conducted for a dynamically complex, passively damped system. Passive damping allowed many structural modes to be removed from the plant model in forming the CDM, thereby greatly simplifying the design process. Although only about 80% of the predicted closed loop performance was achieved, the design was stable and did significantly suppress LOS vibrations. Some structural modes were amplified, but the relatively

high passive damping designed into the structure maintained stability. The results of this experiment demonstrate that if high bandwidth, high authority modern control algorithms are to be successfully applied to LSS, passive damping must be designed into the LSS from the start.

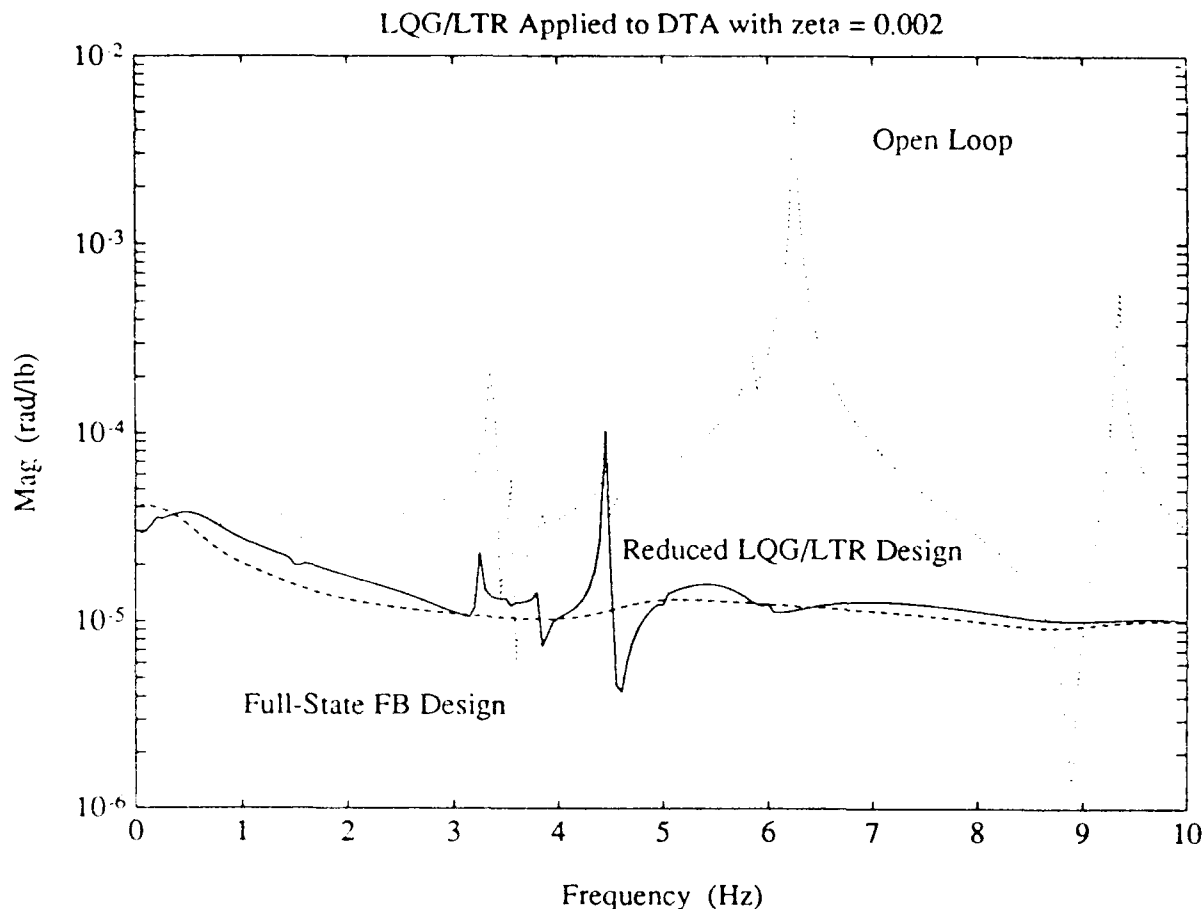


Figure 16 LQG/LTR Design with Nominally Damped DTA ($\zeta = 0.002$)

ACKNOWLEDGEMENT

This work was supported by the Air Force Flight Dynamics Laboratory Wright Research and Development Center under the Passive and Active Control of Space Structures (PACOSS) Program, Contract Number F33615-82-C-3222.

REFERENCES

1. Russell N. Gehling, *PACOSS Dynamic Test Article*, Proceedings of Damping '91, San Diego, CA, 13-15 February 1991.
2. PACOSS Final Report, Volume 2, Dynamic Test Article Modal Survey: Test and Analysis Results, (WRDC-TR-90-3044), September, 1990.
3. D. R. Morgenthaler, *Design and Analysis of Passively Damped Large Space Structures*, 11th Biennial Conference on Mechanical Vibration and Noise, Boston, MA, 27-30 September, 1987, (DE-Vol. 5), pp. 1-8.
4. Russell N. Gehling, *Modal Survey of the PACOSS DTA*, Proceedings of Damping '89, 8-10 February, 1989, (WRDC-TR-89-3116, Vol. III), pp. KCC-1 - KCC-31.
5. K. E. Richards, Jr., *PACOSS Program Status and Results*, NASA/DOD Control/Structures Interaction Technology 1989 Proceedings, February 1989, (NASA CP-3041), pp. 31-65.
6. Russell N. Gehling, *Large Space Structure Damping Treatment Performance: Analytic and Test Results*, 11th Biennial Conference on Mechanical Vibration and Noise, Boston, MA, 27-30 September, 1987, (DE-Vol. 5), pp. 93-100.
7. John C. Doyle and Gunter Stein, *Multivariable Feedback Design: Concepts for a Classical/Modern Synthesis*, IEEE Transactions on Automatic Control, Vol. AC-26, No. 1, February 1981.
8. H. Kwakernaak and R. Sivan, Linear Optimal Control Systems, New York, Wiley-Interscience, 1972.
9. John C. Doyle and Gunter Stein, *Robustness with Observers*, IEEE Transactions on Automatic Control, August 1979.
10. D. Brett Ridgely and Siva S. Banda, Introduction to Robust Multivariable Control, AFWAL-TR-85-3102, February, 1986.
11. Richard Y. Chiang and Michael Safonov, Robust Control Toolbox Users Guide, The MathWorks, Inc., South Natick, MA, June 1988.
12. D. R. Morgenthaler, *Design, Analysis, and Testing of the PACOSS D-Strut Truss*, Proceedings of Damping '91, San Diego, CA, 13-15 February 1991.

\mathcal{H}_∞ Control for the PACOSS DTA*

Christopher T. Voth[†] and R. Michael Stoughton

Research and Technology Department
Martin Marietta Civil Space Company

Abstract

This paper presents an application of an \mathcal{H}_∞ design technique to the active control of a passively damped large space structure test article. An active vibration suppression compensator was designed for the Passive and Active Control of Space Structures (PACOSS) Dynamic Test Article (DTA) using the \mathcal{H}_∞ technique. Analytic studies indicate passive damping of the structure results in reduced sensitivity to variations in plant structural modes for a given level of performance.

The control problem was to reduce the X and Y Line-of-Sight (LOS) pointing errors caused by deformation of the structure due to vibration. External disturbances at four locations along the DTA excite the vibrational modes of the structure, resulting in LOS errors. Passive damping elements designed into the structure result in open-loop damping ratios ranging from 0.12 to 0.02. Active suppression of structural modes is accomplished using 10 proof-mass actuators located on the structure. Sensors for active control provide 20 colocated inertial and relative velocity measurements as well as 3 noncolocated inertial velocity measurements at locations along the structure.

The \mathcal{H}_∞ approach allowed the integration of performance requirements, robustness requirements, and other design constraints into the design problem. Explicit presentation of model uncertainties was important in achieving a closed-loop system insensitive to plant variations typical of flight hardware.

Implementation of the resulting controller on the DTA structure provided experimental verification of closed-loop system stability and performance in the presence of model errors typical of test verified structures possessing high modal density.

An investigation of the relationship between the active control and passive damping indicated that passive damping was instrumental in achieving performance and reduced sensitivity to structural mode uncertainty. Passive damping of the structure also aided in reduction of the controller order for hardware implementation.

*Performed under Air-Force contract F33615-82-C-3222

[†]P.O. Box 179, Denver, Colorado 80201, (303) 977-4164

1 Introduction

Future scientific, commercial and military objectives in space will require construction of Large Space Systems (LSS). Proposed operational performance objectives for these large structures include stringent pointing accuracies, fast repositioning and short settling times. LSS will necessarily be lightweight and exhibit a dense, low-frequency modal spectrum with significant content within the control bandwidth.

Passive and active control methods will likely play important roles in achieving performance requirements for future LSS missions. The complexity of LSS structural dynamics often result in significant model inaccuracies. Attempts to control similar large systems through purely active means have often produced disappointing results.

The Dynamic Test Article (DTA) is a ground test experiment designed and built as part of the Passive and Active Control of Space Structures (PACOSS) program. The PACOSS program was initiated to investigate solutions to control-structure interaction problems by combining passive damping approaches, designed into the structure, with active control. The DTA was designed as a hardware validation experiment to simulate a large pointing system and contains seven substructures representative of future LSS.

This report describes the application of the \mathcal{H}_∞ design method to the active control of the DTA large space structure experiment. Passive damping elements designed into the structure provide increased open-loop structural damping and vibration suppression. Active control is used to further reduce pointing errors due to vibrations present in the passively damped DTA structure.

The \mathcal{H}_∞ approach allowed integration of performance requirements, robustness requirements, and other design constraints into the design problem. Representations of model uncertainty are used to reduce the sensitivity of the closed-loop design to model inaccuracies. Uncertainties within the control bandwidth prevent the cancellation of plant dynamics by compensator zeros, resulting in a design which is less sensitive to model errors. The resulting design is less sensitive to model errors typical of flight hardware.

Implementation of the active controller on the DTA structure provided experimental verification of closed-loop system stability and performance in the presence of model errors typical of test verified structures with high modal density. Tests results are given in the form of frequency responses and time response functions and show good agreement to analytic predictions for the final design.

An analytical study was performed to investigate the relationship between the active control and passive damping. Results indicate that passive damping was instrumental in achieving performance and reduced sensitivity to structural mode uncertainty. Passive damping of the structure also aided in reduction of the controller order for hardware implementation.

The algorithm used to solve the \mathcal{H}_∞ control problem is from the MATLAB *Robust Control Toolbox* and is described in Reference [4]. An excellent tutorial description and overview of \mathcal{H}_∞ based control design is provided by Maciejowski [3].

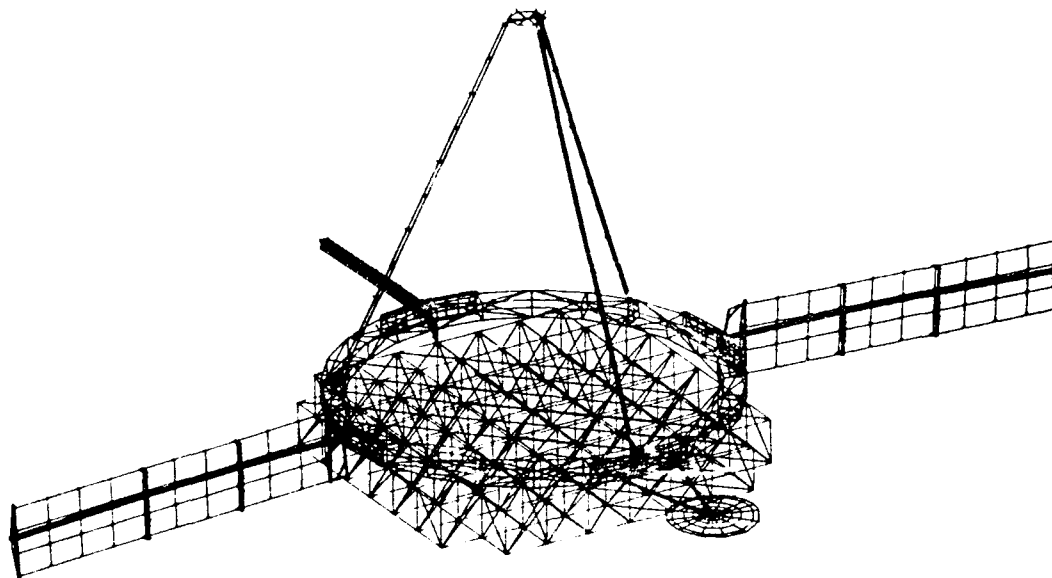


Figure 1: Dynamic Test Article

2 PACOSS Dynamic Test Article (DTA)

Figure 1 is a picture of the DTA. The DTA is a ground based structure for experimental validation of control design approaches applicable to LSS. The DTA is designed to simulate a large pointing system. The control objective is to minimize the effect of disturbances on the pointing accuracy of the structure. The pointing accuracy is defined in terms of the relative alignment of selected points on the lower truss structure and the secondary mirror structure on top of the tripod. The DTA is composed of 7 substructures which represent the following real structures: the lower ring truss represents a structural 'hardback' for the system. The lower box truss structure is a support structure intended for a large primary optical surface. The tripod system is intended to support a secondary mirror. The dish antenna is a communications antenna and the linear truss is to support sensitive equipment. Large side-panels represent two solar arrays.

2.1 Dynamic Description of DTA

The structure is symmetric about an axis running between the dish antenna and the linear truss and contains 39 modes below 10 Hz. Of these modes 6 are associated with the suspension mechanism for supporting the structure, 10 are associated with the actuators (each actuator is modeled as a 2nd order system), and 23 are structural modes. Many higher frequency structural modes exist in the system which are not included in the model. The structure was designed with passive damping elements to provide increased damping of the structural modes. Damping ratios of the structural modes range from 0.01 to 0.12. Similar large structures without passive damping have damping ratios less than 0.01.

The 10 actuators are proof-mass actuators, with a ± 1.0 inch stroke. Two actuators are located on the tripod, six on the lower ring truss structure and two on the box truss structure. These actuators work well for vibration suppression; however since they rely on the acceleration of a sliding mass to generate actuation force, they are only effective within a bandpass frequency range.

Each actuator has two sensors colocated with it. One is an accelerometer, filtered to measure inertial velocity, and the other measures relative velocity between the structure and the proof-mass of the actuator. In addition to the 20 colocated sensors, there are three noncolocated accelerometers with output filtering to measure inertial velocities, one located on each of the two solar arrays, and one on the linear truss.

2.2 Linear Model of DTA

A Linear Time-Invariant (LTI) model of the DTA was developed from a finite element analysis and verified with extensive modal testing of the assembled structure. The model formed the basis for the controller design and is more accurate than would typically be available for flight hardware.

The DTA structure contains modes beyond 10 Hz which have been truncated from the model. In addition to the sensor outputs, the model has two design outputs. The design outputs are X and Y axis Line-of-Sight (LOS) pointing errors. The LOS outputs are measurements of the relative alignment between the lower optical surface and the secondary mirror structure. The Y axis error is measured along an axis aligned with the axis of symmetry of the structure. The X axis error is measured relative to an axis perpendicular to the Y axis and passing through the center of the solar array panels.

Vibrational modes of system are excited by 4 disturbance inputs located on the box truss structure. Of the 23 structural modes, only 12 affect the sensor measurement outputs or the LOS outputs. The model used in the active control design contained only 12 structural modes and had a total of 28 dynamic modes.

Figure 2 shows the maximum singular value of the DTA model frequency response from the 4 disturbance inputs to each of the X and Y LOS errors. The effect of passive damping elements on vibration suppression is apparent from these plots. Few sharp resonant peaks characteristic of the response of an undamped structure are present.

3 Design Problem

The design problem facing the control engineer can be described as achieving the best trade-off between a set of performance requirements, design constraints, and sensitivity of the system to model uncertainties. The primary performance requirement for the closed-loop system is to minimize the relative LOS error in both the X and Y axes resulting from disturbances. Disturbances acting on the structure are in the frequency range from 1-10 Hz.

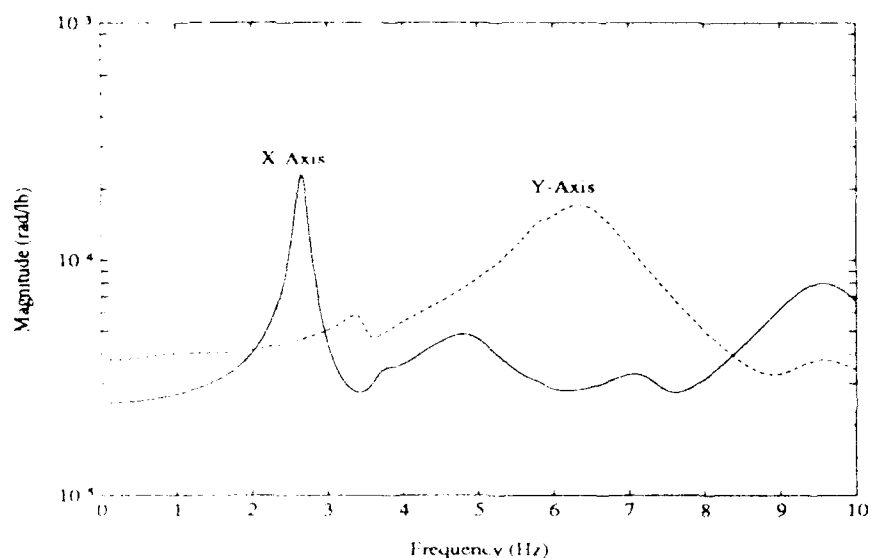


Figure 2: Maximum Singular Values of the Response from the Disturbance Inputs to the X and Y Axis LOS Errors for the DTA Model.

Design constraints and model uncertainties are:

- actuator displacement limited to ± 1.0 inches,
- unmodeled high frequency modes above 10 Hz,
- 5% uncertainty in structural mode frequency,
- 20% uncertainty in structural mode damping,

Additional constraints are related to the implementation of the controller. The controller must be digitally implemented at a sample rate of 280 Hz. The maximum size of the compensator is limited to 58 states.

4 Synthesis Model

Multivariable control design with modern techniques involves formulation of design performance objectives and other requirements in the form of a *synthesis model*. The synthesis model includes the model of the plant dynamics with control inputs and sensor outputs along with additional inputs and outputs which are important in the design. Design weighting functions on selected plant inputs and outputs are augmented with the plant model to form the synthesis model.

With \mathcal{H}_∞ design, performance requirements, design constraints and representations of model uncertainties must be included in the synthesis model. Model uncertainties may be represented as \mathcal{H}_∞ -norm criteria based on the small gain theorem. Development of the synthesis model for \mathcal{H}_∞ design is discussed by Boyd [1].

The \mathcal{H}_∞ synthesis model for the DTA control design is a transfer matrix represented by $P(s)$. Inputs to $P(s)$ are separated into a vector of control inputs, $u(s)$, and the exogenous input vector, $w(s)$. The vector $w(s)$ includes disturbances, and fictitious design inputs for representing model uncertainty. Outputs of the synthesis model are separated into a vector of measured feedback signals, $y(s)$, and the regulated output vector, $z(s)$. The vector $z(s)$ contains the performance criteria outputs and outputs which define constraints on the closed-loop system.

4.1 Performance Objectives and Constraints

The primary performance requirement for the DTA is to minimize the LOS error resulting from the external disturbances. This can be expressed as minimizing

$$\bar{\sigma}[H_{c_{LOS} d}(j\omega)], \quad (1)$$

where:

- $H(s)$ is the closed-loop transfer matrix of the plant and controller,
- c_{LOS} is an output vector containing X and Y LOS errors,
- d is a vector of disturbance inputs,
- $\bar{\sigma}[\]$ signifies the maximum singular value.

The performance criteria may be represented as a weighting function $W_S(s)$ on the design output $c_{LOS}(s)$. Let $W_S(s)$ be a diagonal transfer function matrix:

$$W_S(s) = \begin{bmatrix} w_{sx}(s) & 0 \\ 0 & w_{sy}(s) \end{bmatrix} \quad (2)$$

where:

- $w_{sx}(s)$ is a transfer function weighting for X axis LOS error,
- $w_{sy}(s)$ is a transfer function weighting for Y axis LOS error.

The \mathcal{H}_∞ design criteria for performance is to find a controller such that:

$$\|W_S(s)H_{c_{LOS} d}(s)\|_\infty < 1, \quad (3)$$

which implies:

$$\bar{\sigma}[H_{c_{LOS} d}(j\omega)] < [w_{sx}^{-1}(j\omega)] \quad (4)$$

$$\bar{\sigma}[H_{c_{LOS} d}(j\omega)] < [w_{sy}^{-1}(j\omega)] \quad (5)$$

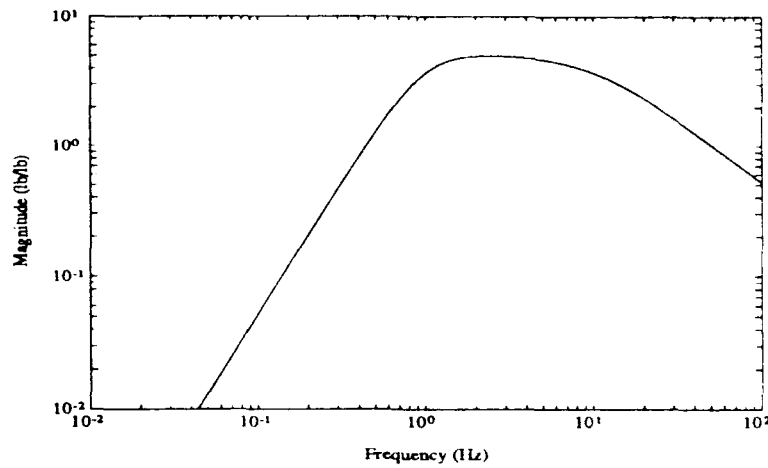


Figure 3: Magnitude plot of $w_{r_i}^{-1}$ weighting functions.

where:

e_{LOS_X} is the X axis LOS error,

e_{LOS_Y} is the Y axis LOS error.

By reducing $|w_{s_x}^{-1}(s)|$ and $|w_{s_y}^{-1}(s)|$ one can find the controller which minimizes the LOS error.

A constraint on actuator control activity is included in the synthesis model by limiting the closed-loop response from disturbances $d(s)$ to the controller output $u(s)$. The proof-mass actuators are only capable of providing force over a limited bandwidth. To account for this physical constraint, the closed-loop response is restricted to be 'band-pass' over the effective frequency range of the actuators. This is accomplished through the weighting function $W_R(s)$ on the closed-loop control vector $u(s)$.

$$W_R(s) = \begin{bmatrix} w_{r_1}(s) & & 0 \\ & \ddots & \\ 0 & & w_{r_{10}}(s) \end{bmatrix} \quad (6)$$

where:

$w_{r_i}(s)$ is a transfer function weighting on the i^{th} controller output.

In theory each of the controller outputs could be individually weighted. As a simplification an identical weighting is used on each of the outputs. Figure 3 is a plot of the magnitude of the $w_{r_i}^{-1}$ transfer functions.

The \mathcal{H}_∞ design constraint is to find a controller such that:

$$\|W_R(s)H_{ud}(s)\|_\infty < 1. \quad (7)$$

where:

$H_{ud}(s)$ is the closed loop transfer matrix from the disturbance input vector d , to the controller output vector u .

The disturbances $d(s)$ form the design criteria input vector $w_c(s)$ which is included in the exogenous input vector $w(s)$. The outputs of $W_S(s)$ and $W_R(s)$ form the design criteria output vector $z_c(s)$ which is included in the design output vector $z(s)$ of the synthesis model.

4.2 Representation of Model Uncertainty

The block diagram in Figure 4 shows the DTA model separated into a ladder structure. Model uncertainties are represented by Δ blocks at several locations in the nominal model. The block Δ_{add} represents unmodeled high frequency (>10 Hz) structural dynamics in the form of an additive uncertainty across the plant. The legend of Figure 4 indicates the types of uncertainties represented by each of the Δ blocks.

DTA model uncertainties shown in Figure 4 must be represented in the synthesis model. Model uncertainties may be represented as \mathcal{H}_∞ -norm criteria based on the small gain theorem. Uncertainties shown in Figure 4 may be grouped into a single block diagonal structure represented by $\underline{\Delta}(s)$. The uncertainty block $\underline{\Delta}(s)$ is normalized by scaling gains at the plant inputs and outputs such that

$$\|\underline{\Delta}(s)\|_\infty < 1. \quad (8)$$

Figure 5 is a block diagram showing the relationship between the synthesis model $P(s)$, the block-diagonal uncertainty matrix, $\underline{\Delta}(s)$ and the controller $F(s)$. The input vector z_Δ to $\underline{\Delta}$ is included in the z vector of regulated outputs of the synthesis model. The output vector w_Δ to $\underline{\Delta}$ is part of the exogenous input vector, w , of the synthesis model. From the 'small gain theorem' if a controller is found such that

$$\|H_{zw}(s)\|_\infty < 1, \quad (9)$$

where:

H_{zw} is the closed-loop transfer matrix from w to z ,

then the closed loop system will be stable for all possible plant variations represented by $\underline{\Delta}$. Maciejowski [3] and Doyle [2] provide more detail in modeling of uncertainty and representation by the small gain theorem.

The synthesis model for the DTA contains a simpler set of plant uncertainties than shown in Figure 4. This simplification is motivated by the overconstrained nature of the complete \mathcal{H}_∞ design problem. The \mathcal{H}_∞ problem results in a closed-loop system with

$$\|H_{zw}(s)\|_\infty < 1. \quad (10)$$

By using the \mathcal{H}_∞ norm from w to z as the design criteria, the diagonal structure of $\underline{\Delta}$ is ignored. The uncertainty $\underline{\Delta}$ is taken to be a fully coupled matrix. As the size of

Legend: Plant Model		Legend: Uncertainties	
$\{A_i, B_i, C_i\}$:	state-space representation of i^{th} structural mode	Δ_{add} :	unmodeled structural modes
e_{LOS} :	X and Y LOS errors	Δ_{A_i} :	actuator modal displacement for i^{th} mode
y :	sensor output vector	Δ_{S_i} :	sensor modal displacement for i^{th} mode
u :	controller output vector	Δ_{F_i} :	pole locations for i^{th} mode
d :	disturbance input vector		

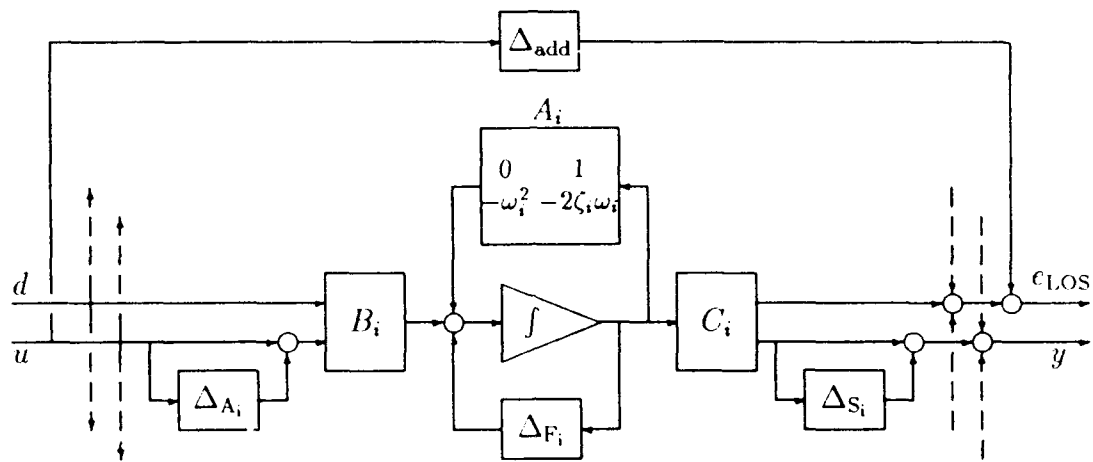


Figure 4: Block Diagram of the DTA Plant Model Showing Representation of Uncertainty.

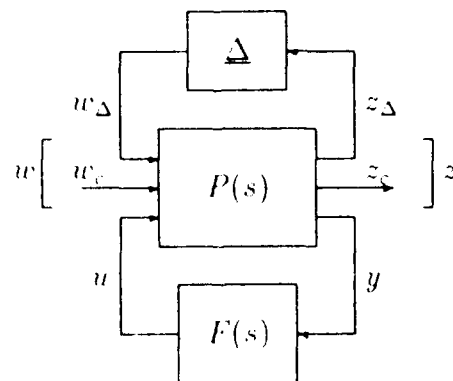


Figure 5: Closed-loop system of synthesis model and controller.

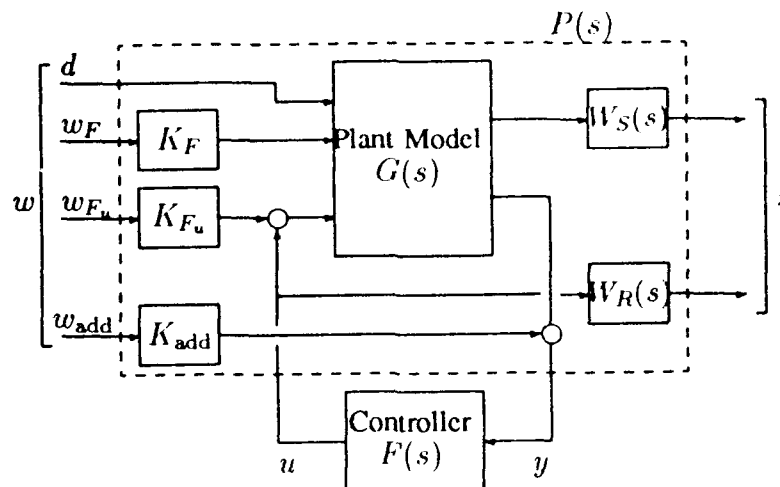


Figure 6: Complete Synthesis Model for Final \mathcal{H}_∞ Design

the matrix Δ increases, the potential for introducing conservativeness into the design increases.

An initial control design for the DTA used a synthesis model which did not include the plant model pole uncertainties represented by Δ_{F_i} . This initial design was found to be sensitive to variations in the plant dynamics. The initial control design was particularly sensitive to the 18th and 19th design model structural mode pole locations. Addition of a feedback uncertainty representation Δ_{F_u} from the LOS error outputs to the control inputs reduced the sensitivity of the closed-loop design to the plant dynamics.

Additional insensitivity to the 18th and 19th design model modes at 3.47 Hz and 3.51 Hz was obtained by including uncertainty representations for these modes as shown in Figure 4. The final uncertainty representation resulted in a controller with sufficient insensitivity to plant variations.

4.3 Final Design Synthesis Model

Figure 6 is a block diagram of the final synthesis model containing the design model, performance objectives, design constraints and uncertainty representations. Weighting functions $w_{s_x}(s)$ and $w_{s_y}(s)$ are constant gains. The weighting functions $w_{r_i}(s)$ are 3rd order transfer functions with magnitude gain shown in Figure 3.

The gain block K_{add} is a diagonal scaling block on the input associated with the additive uncertainty. K_F is a diagonal scaling matrix associated with the uncertainties $\Delta_{F_{18}}$ and $\Delta_{F_{19}}$ on the 18th and 19th mode pole locations. K_{F_u} is a diagonal scaling block

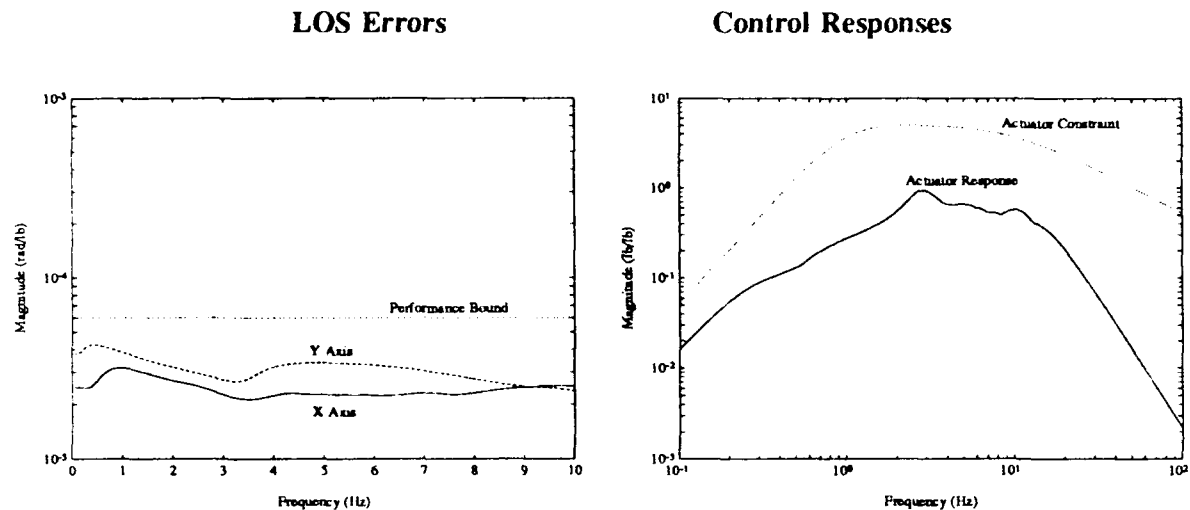


Figure 7: Singular Values of the Closed-Loop Responses to Disturbances.

associated with the feedback uncertainty block Δ_{F_u} .

The design process involves iterating on the selection of the design weightings and scaling gains to obtain a satisfactory trade-off between performance requirements, design constraints and sensitivity to model uncertainties.

The final synthesis model was 86th order, with a w input vector of dimension of 39 and z output vector dimension of 12. The resulting controller was also 86th order. The size of the controller was reduced to the maximum allowable of 58th order using balanced-truncation model reduction.

5 Analysis and Experimental Implementation

Figure 7 shows the closed-loop LOS errors for the X and Y axes and the control responses to disturbances. Vibration suppression is improved over the open-loop system by a factor of 8 in the X axis LOS error and a factor of 5 in Y axis LOS error. The original goal was to achieve a factor of 10 improvement over the open-loop structure. However the initial controller designs were sensitive to the 18th and 19th design model mode locations. The design objective was relaxed to obtain a factor of 5 improvement in LOS error, and to reduce the sensitivity of the closed-loop system to variations in the 18th and 19th modes. Table 1 is a table showing the sensitivity of the closed-loop system to variations in the 18th and 19th mode frequencies for the final design.

The \mathcal{H}_∞ designed controller was discretized using a zero-order-hold approximation, and implemented on a real-time controller running at 280 hz. The closed loop system was excited through the disturbance inputs and the sensor output data recorded. This data was used to reconstruct, off-line, an estimate of the magnitude response from a

Table 1: Allowable Range in Frequency of 18th and 19th Mode For Closed-Loop Stability.

Allowable Variation	18 th Mode	19 th Mode
% increase	69.5 %	∞
% decrease	78.4 %	90.4 %

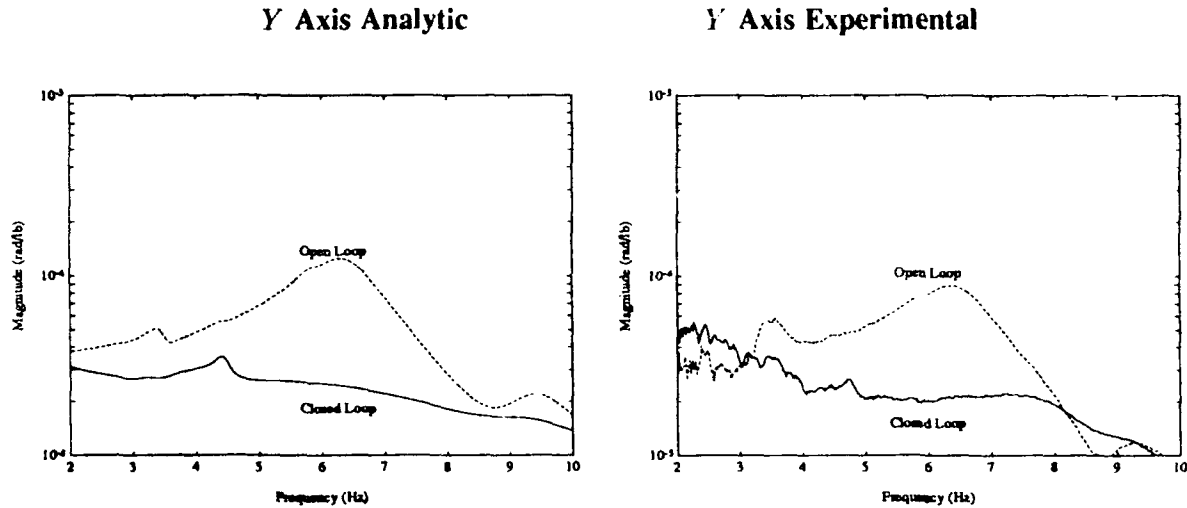


Figure 8: Comparison of Analytic Prediction of Y Axis LOS Error to Experimental Reconstruction.

single disturbance input to the X and Y LOS outputs. Figure 8 compares the analytic prediction and the experimentally reconstructed Y axis LOS error response to a single disturbance. At low frequencies the experimental reconstruction is corrupted by noise due to low amplitude signals with large relative contributions to the LOS error. However from about 3–10 Hz the analytic and experimental results show good agreement. A factor of 5 improvement in LOS error attenuation is seen for the dominant open-loop peak at 6 Hz.

Figure 9 compares the open and closed loop time response of an accelerometer on the structure to a disturbance input. Here the effectiveness of the controller in attenuating disturbances is clearly evident. A low frequency suspension mode (not controlled) is visible in the time response of Figure 9.

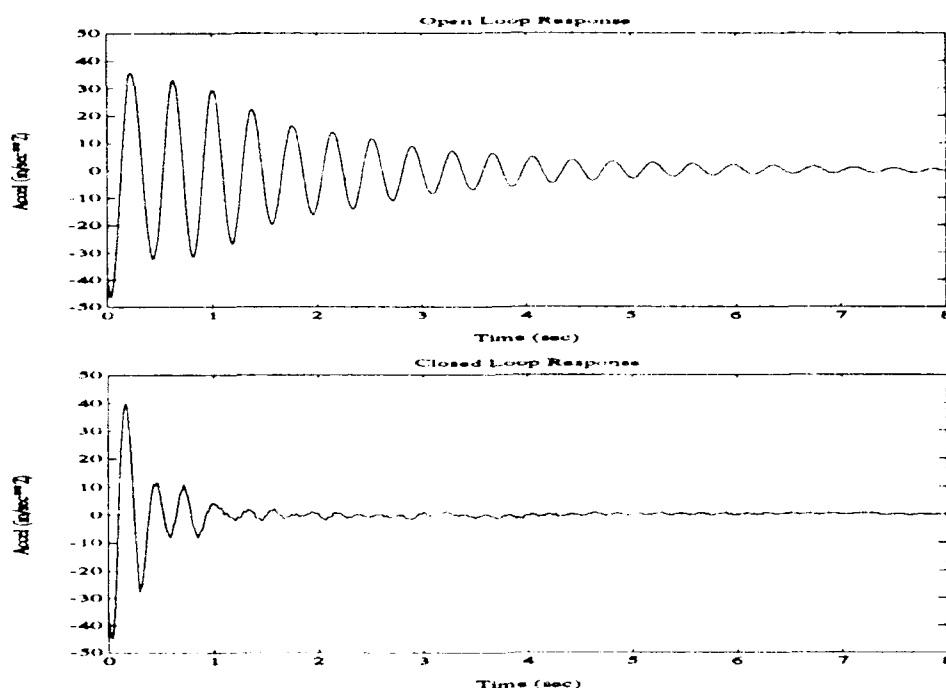


Figure 9: Open and Closed-Loop Time Response of an Accelerometer Output on the DTA Structure to an Impulse Disturbance Input.

6 Contribution of Passive Damping to Control

The DTA structure was designed and constructed with passive damping elements for vibration suppression. Typical LSS designed without passive damping have modal damping ratios significantly less than for the DTA. An analytic study on the contribution of passive damping to the performance of the active control is described in this section.

A representative 'undamped' model of the DTA structure without passive damping was developed based on typical modal damping present in LSS. The active controller was redesigned for the undamped structure using the same design criteria as for the passively damped structure. Comparisons of the passively damped and undamped designs provide a basis for evaluating the importance of passive damping.

6.1 Representative Undamped Structural Model

Modal damping ratios for the DTA structure with passive damping range from 0.023 to 0.121. An analytic model of a DTA structure without passive damping was obtained by reducing the structural mode damping ratios to 0.002, a value determined from measurements of the undamped ring truss component. Modal displacements and frequencies were not changed for the undamped model. Figure 10 is a plot of the maximum singular values of the frequency response from the disturbance inputs to each of the X and Y LOS error outputs.

The frequency response for the undamped model is significantly different from the

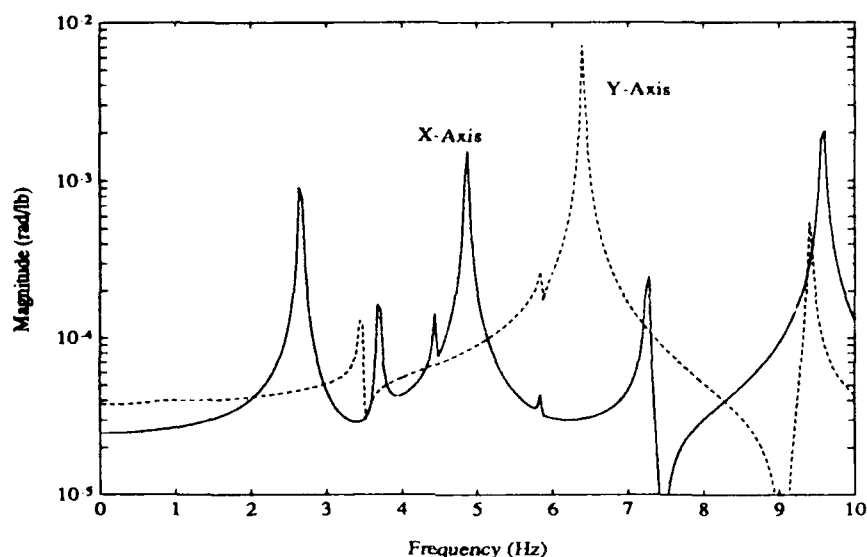


Figure 10: Maximum Singular Values of the Response from Disturbance Inputs to X and Y LOS Error Outputs for the Undamped DTA Model.

DTA model with passive damping (Fig. 2). The undamped model frequency response has many sharp resonance and anti-resonance peaks resulting from the decreased structural damping. In addition, the undamped model shows significant structural response up to 10 Hz whereas the passively damped DTA shows less response at these higher structural frequencies.

6.2 Control Redesign for Undamped Structure

The analytic DTA model without passive damping was used to redesign the \mathcal{H}_∞ controller. With the exception of the DTA plant model, the synthesis model was unchanged from the final \mathcal{H}_∞ control design. Synthesis model weighting functions were the same as in the final design for the passively damped structure.

A sensitivity analysis of the redesigned compensator revealed significantly greater sensitivity to the 18th and 19th design model mode pole locations than for the passively damped system. Table 2 gives a comparison of the allowable independent variations in frequencies for the passively damped system versus the system without passive damping. The passively damped system can tolerate a large increase in the frequency of the 19th mode, while a variation of less than +1.0% in frequency of the same mode will result in an unstable design for the undamped system.

The \mathcal{H}_∞ compensator resulting from the undamped model had two unstable modes which could not be reduced. Unstable compensators are generally undesirable due to the difficulties in implementation.

Table 2: Mode Frequency Tolerances for Control Designs

Allowable Frequency Variation	18 th mode	19 th mode
Passively Damped System	+69.5%, -78.4%	$+\infty$, -90.4%
Undamped System	+48.8% - 77.6%	+0.5%, -42.0%

Controller order reduction for the \mathcal{H}_∞ active controller was affected by the absence of passive damping in the analytic plant model. Balanced model truncation of the \mathcal{H}_∞ control designs to 58 states resulted in a total magnitude error bound of 0.1628 for the compensator with passive damping compared to 0.2968 for the compensator without passive damping. Reduction of the undamped system compensator to approximately the same total error resulted in a controller with 61 states.

To evaluate the influence of passive damping on controller performance, the \mathcal{H}_∞ controller for the undamped model was redesigned to recover, in part, the sensitivity margins of the \mathcal{H}_∞ controller for the passively damped system. The LOS error performance bound (i.e. $W_S^{-1}(s)$) was relaxed by a factor of two for the undamped DTA model. The uncertainty input gains were increased uniformly to minimize the sensitivity of the undamped closed-loop system to the mode pole locations of the model.

The full-order \mathcal{H}_∞ compensator was 86 states for both the passively damped and undamped DTA models. Figure 11 shows frequency responses to the LOS errors and control feedback from the disturbance inputs for the closed loop full-order design without passive damping. Both the LOS performance and control activities are similar to those of the passively damped system.

The structural mode frequencies of the passively damped and undamped models were perturbed by equal amounts of less than 10% of their nominal values. Figures 12 and 13 show a comparison of the LOS error response to disturbances for both the passively damped and undamped closed-loop systems. Clearly, from Figure 12, the sensitivity of the undamped system is still greater than for the passively damped system. For the same frequency perturbations the passively damped design meets the original performance bound while the undamped design violates even the relaxed performance requirement. The peak response of the LOS error is roughly two orders of magnitude greater for the undamped system as for the passively damped system.

7 Conclusions

An \mathcal{H}_∞ design approach was applied to the active control of a passively damped large space structure test article. Performance objectives, design constraints, and model uncertainties are directly included in the design process. Representation of model uncertainties was used to achieve designs which were insensitive to plant model variations.

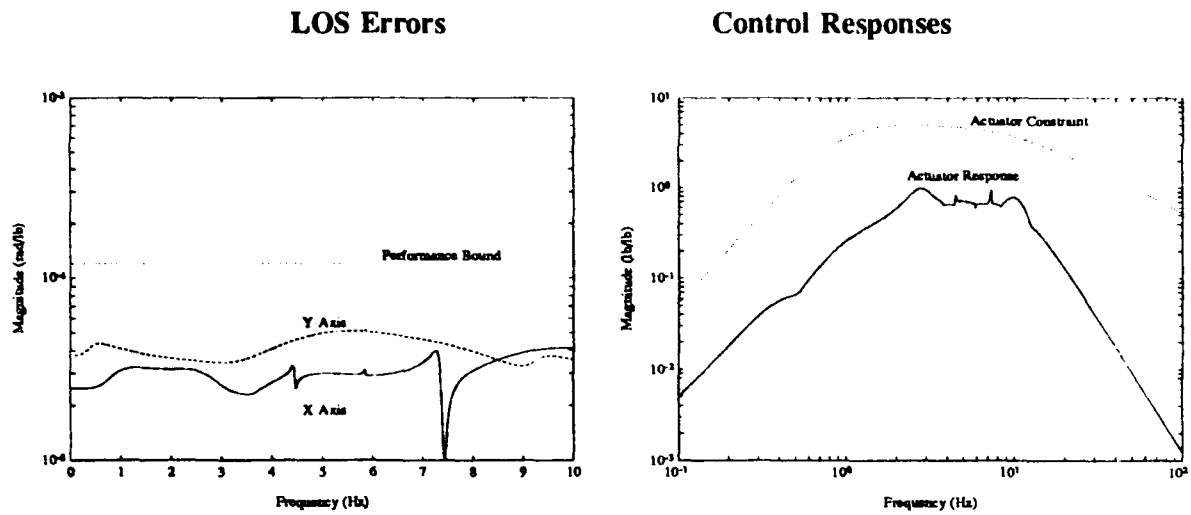


Figure 11: Singular Values of the Closed-Loop Responses to Disturbances for the Undamped \mathcal{H}_∞ Design.

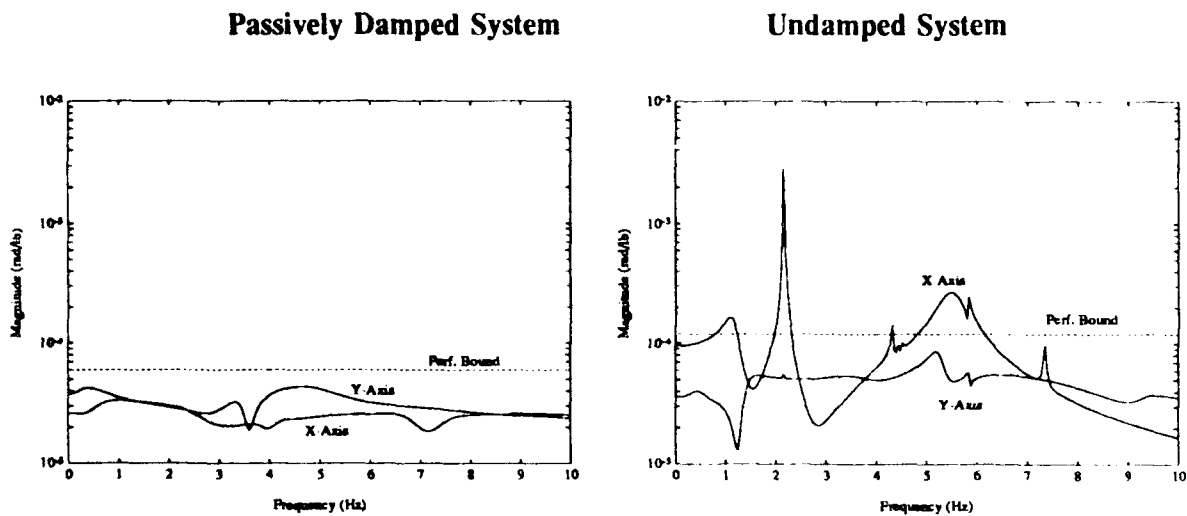


Figure 12: Singular Values of the Closed-Loop Responses to Disturbances for the Passively Damped and Undamped \mathcal{H}_∞ Designs with Perturbed Models.

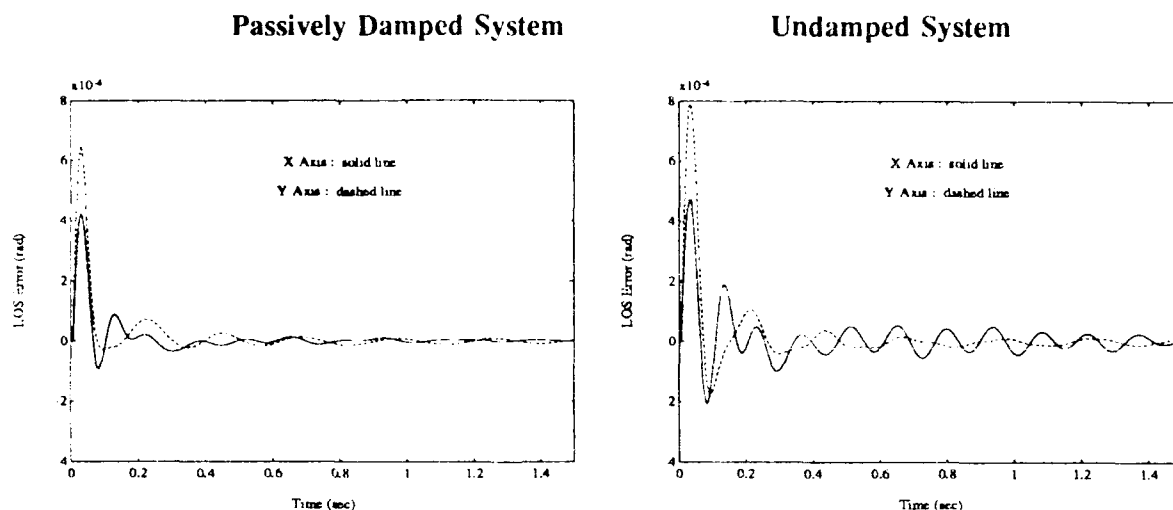


Figure 13: Closed-Loop Time Responses to Disturbances for the Passively Damped and Undamped \mathcal{H}_∞ Designs with Perturbed Model.

Analytical studies into the effects of the passive damping on the active control design reveal that the presense of passive damping decreases the sensitivity of the active controller to model errors and allows for improved performance. Furthermore, active control designs for the passively damped structure were found to be easier to reduce as compared to designs for the model without passive damping.

Hardware implementation of the active control design provided experimental verification of the design results. Analytical prediction showed good agreement to results from the test data.

References

- [1] S. Boyd, C. Barratt, and S. Norman. Linear controller design: limits of performance via convex optimization. In *Proc. IEEE*, 78(3), March 1990.
- [2] J.C. Doyle. Structured uncertainty in control system design. In *Proc. 24th IEEE Conference on Decision and Control*, December 1985.
- [3] J.M. Maciejowski. *Multivariable Feedback Design*. Addison Wesley, New York, 1989.
- [4] M.G. Safonov and D.J.N. Limebeer. Simplifying the \mathcal{H}_∞ theory via loop shifting. In *Proc. 27th Conference on Decision and Control*, December 1988.

ACTIVE DAMPING OF A CANTILEVER BEAM SYSTEM

H. V. Vu and S. E. Husher
Department of Mechanical Engineering

D. E. Zimmerman
Department of Engineering and Industrial Technology

California State University, Long Beach
Long Beach, CA 90840

Abstract

The control-structure interaction of a flexible structure, namely a cantilever beam, and a reaction mass actuator (RMA) is investigated. Mathematical model, in the form of differential equations and transfer functions, is obtained. The study is broken into two steps: (1) open loop and (2) closed loop. Within the open loop part, the RMA is broken into two sub-steps: (a) dead RMA and (b) passive RMA. In the closed loop part, negative feedback of the beam tip velocity is used for active RMA. Transient responses and root loci are given.

Introduction

The system under consideration is a cantilever beam with a RMA (reaction mass actuator), also called PMA (proof mass actuator) attached to the tip of the beam (Figure 1). The RMA consists of two mechanical components: the magnet-shaft assembly of mass m and the housing of mass m_h . When the magnet-shaft assembly is fixed to the housing, the RMA is called "dead RMA," and when the assembly is free, it is called "passive RMA." When the control loop is closed, the RMA is called "active RMA." The control-structure interaction (CSI) of this electromechanical system will be analyzed in the following steps:

1) Open loop

- a) Dead RMA. The simplest model is a single-degree-of-freedom (SDOF) system. The undamped natural frequency is determined, and the beam tip response, which is obtained experimentally, is presented.
- b) Passive RMA. The simplest model is a two-degree-of-freedom (TDOF) system. The undamped natural frequencies are determined, and the beam tip response which is obtained experimentally, is presented.

2) Closed loop

Active RMA. The velocity of the beam tip is used for negative feedback. The control-structure interaction is investigated. The transient responses and root loci are shown.

System Dynamics

1) Open Loop

The governing differential equation of the beam, using Euler-Bernoulli model, can be shown as

$$EI \frac{\partial^4 y}{\partial x^4} + \rho A \frac{\partial^2 y}{\partial t^2} = f(x, t) \quad 0 < x < l \quad (1)$$

where E , I , ρ , A , l are the Young's modulus, area-moment of inertia, density, cross-sectional area, and length, respectively.

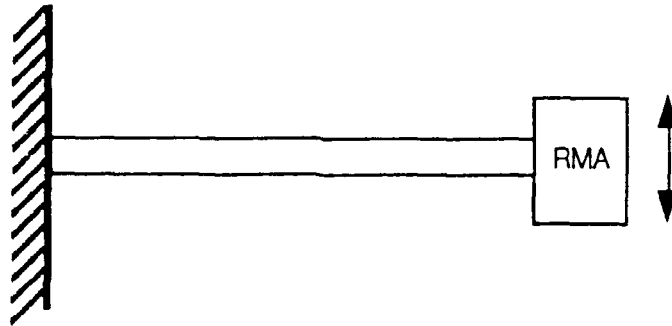


Figure 1 Cantilever beam system with RMA (Reaction Mass Actuator)

a) Dead RMA

The system consists of a cantilever beam with a concentrated mass at the beam tip. The frequency equation of the system can be shown, see [1] for example, as

$$1 + \frac{1}{\cos \lambda L \cosh \lambda L} - \frac{M}{\rho A L} \lambda L (\tan \lambda L - \tanh \lambda L) = 0 \quad (2)$$

The transcendental equation (2) must be solved numerically to yield the eigenvalues λ_i , then the natural frequencies are given as

$$\omega_i = \sqrt{\frac{EI}{\rho A L}} \lambda_i^2 \quad i = 1, 2, \dots, \infty \quad (3)$$

Since the beam model given by Eq. (1) yields infinite degrees of freedom, the control-structure interaction of the beam and the RMA is difficult to analyze. The problem is more tractable if the system with dead RMA is modeled as SDOF for the fundamental mode. Figure 2 shows this model with K , M , and b are the equivalent stiffness, equivalent mass, and equivalent damper, respectively. The mass and stiffness can be calculated from physical properties, but the damping must be determined experimentally.

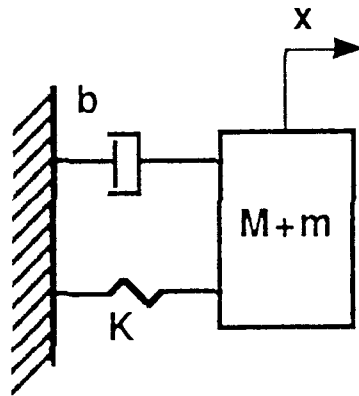


Figure 2 A simple model of the system with dead RMA

It can be found in vibration texts, see [2] for example, that

$$K = \frac{3EI}{L^3} \quad M = m_h + 0.236\rho A L \quad (4)$$

(m_h and m are the masses of the RMA magnet-shaft assembly and housing, respectively.)

An experiment was performed, where the physical parameters of the tested beam (Aluminum 6061-T6) are

$$L = 30.75 \text{ in.} \quad A = 3 \text{ in.} \times 0.25 \text{ in.} \quad E = 10 \times 10^6 \text{ psi} \quad \rho = 0.2588 \frac{\text{lb}_f \text{ s}^2}{\text{in}^4}$$

Thus, the equivalent stiffness and equivalent mass are calculated to be

$$K = 4.03 \frac{\text{lb}}{\text{in}} \quad M = 6.33 \times 10^{-2} \frac{\text{lb}_f \text{ s}^2}{\text{in}} \quad m = 6.47 \times 10^{-4} \frac{\text{lb}_f \text{ s}^2}{\text{in}}$$

The natural frequency is calculated and observed to be 3.8 Hz and 3.5 Hz, respectively. The response at the beam tip of the system with dead RMA is shown in Figure 3.

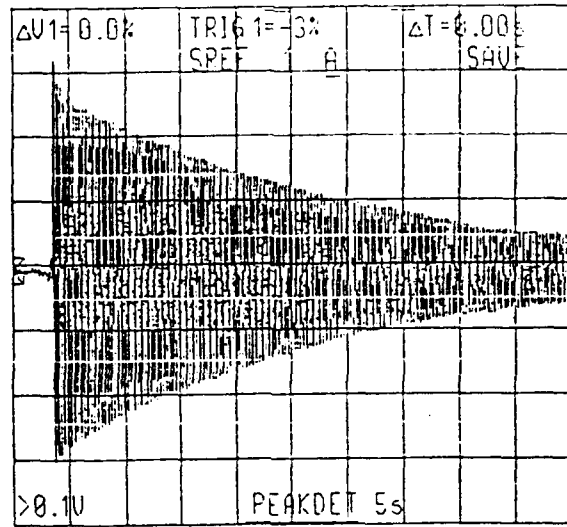


Figure 3 Response at the beam tip with dead RMA

b) Passive RMA

When the moving part of the RMA is released, the RMA acts as a passive vibration absorber (Figure 4). When $b = 0$, the system becomes the classical Den Hartog's vibration absorber problem [3].

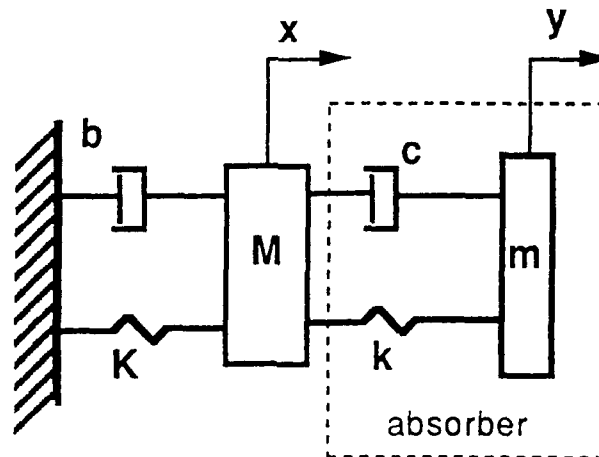


Figure 4 System with vibration absorber (passive RMA)

The differential equations are

$$\begin{bmatrix} M & 0 \\ 0 & m \end{bmatrix} \begin{Bmatrix} \ddot{x} \\ \ddot{y} \end{Bmatrix} + \begin{bmatrix} b+c & -c \\ -c & c \end{bmatrix} \begin{Bmatrix} \dot{x} \\ \dot{y} \end{Bmatrix} + \begin{bmatrix} K+k & -k \\ -k & k \end{bmatrix} \begin{Bmatrix} x \\ y \end{Bmatrix} = \begin{Bmatrix} 0 \\ 0 \end{Bmatrix} \quad (5)$$

where the undamped natural frequencies can be obtained as

$$\omega_1^2 = \frac{(M+m)k + mK}{2Mm} - \sqrt{\left(\frac{(M+m)k + mK}{2Mm}\right)^2 - \frac{Kk}{Mm}}$$

$$\omega_2^2 = \frac{(M+m)k + mK}{2Mm} + \sqrt{\left(\frac{(M+m)k + mK}{2Mm}\right)^2 - \frac{Kk}{Mm}}$$
(6)

The response at the beam tip with passive RMA is shown in Figure 5.

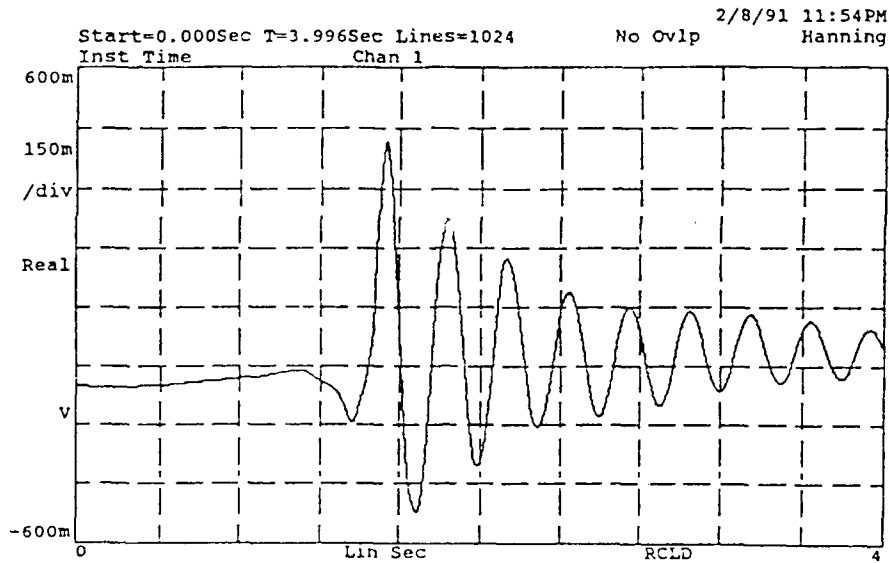


Figure 5 Response at the beam tip with passive RMA

2) Closed Loop - Active RMA

The closed loop control utilizes the beam tip velocity \dot{x} for negative feedback and the system can be *conceptualized* as shown in Figure 6.

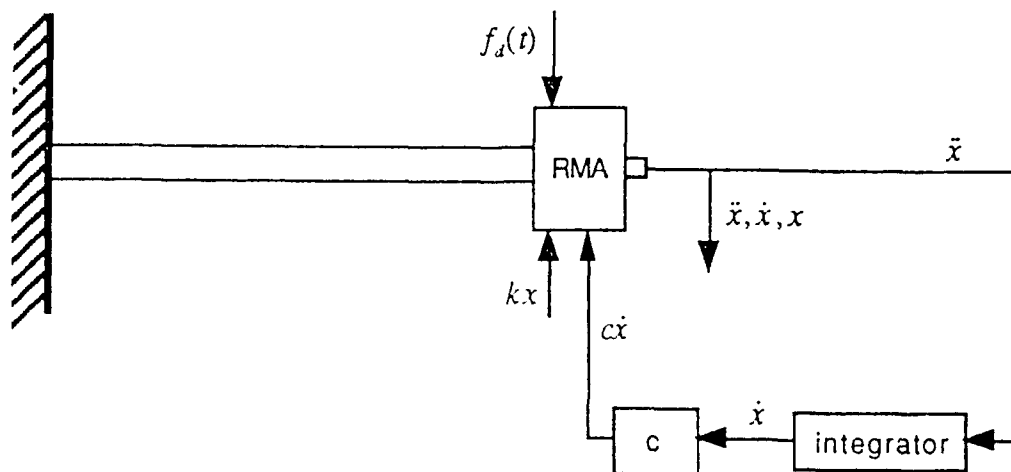


Figure 6 Conceptualized control scheme

For physical implementation, an *actual* system can be shown as in Figure 7.

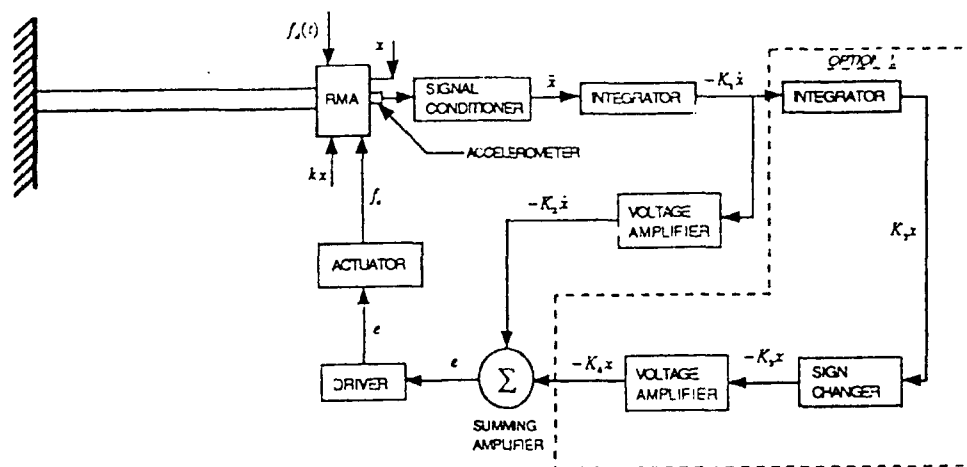


Figure 7 Implementation of the control system

When closed loop control is applied, the structure-RMA system shown in Figure 7 can be modeled as an electromechanical system (Figure 8).

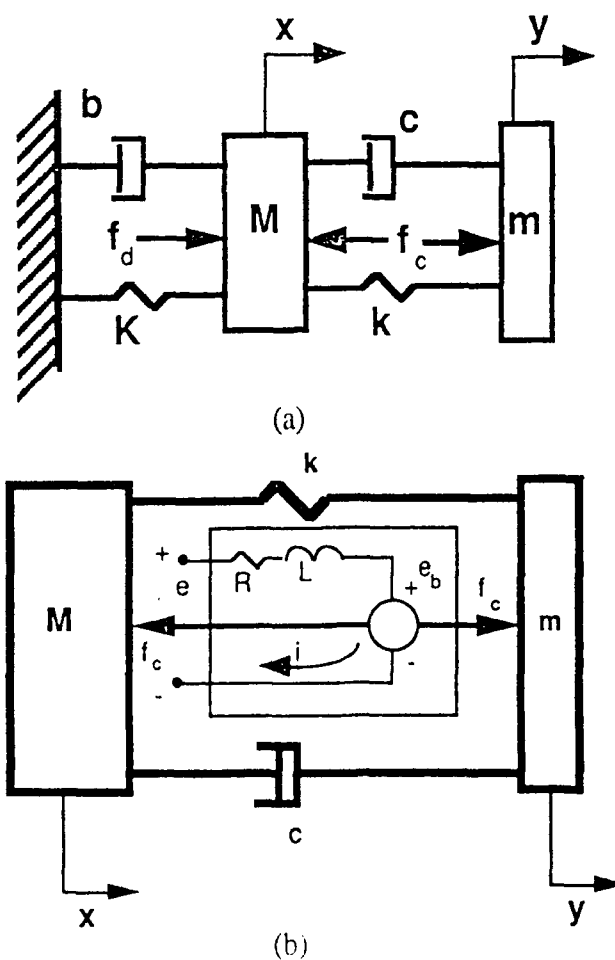


Figure 8 Electromechanical system: (a) mechanical and (b) electrical

The governing differential equations for the mechanical part can be obtained as

$$\begin{bmatrix} M & 0 \\ 0 & m \end{bmatrix} \begin{Bmatrix} \ddot{x} \\ \ddot{y} \end{Bmatrix} + \begin{bmatrix} b+c & -c \\ -c & c \end{bmatrix} \begin{Bmatrix} \dot{x} \\ \dot{y} \end{Bmatrix} + \begin{bmatrix} K+k & -k \\ -k & k \end{bmatrix} \begin{Bmatrix} x \\ y \end{Bmatrix} = \begin{Bmatrix} f_d - f_c \\ f_c \end{Bmatrix} \quad (7a)$$

where f_d and f_c are the disturbance force and control force, respectively. The differential equation for the electrical part is

$$e = Ri + L \frac{di}{dt} + e_b \quad (7b)$$

The electromechanical coupling is given by

$$f_c = k_m i \quad e_b = k_m (\dot{y} - \dot{x}) \quad (8)$$

If the beam tip velocity is used as negative feedback for the active RMA,

$$e = k_g \dot{x} \quad (9)$$

where k_g is the gain. Then, combining Eqs. (7-9) yields the closed-loop system equations as

$$\begin{bmatrix} M & 0 & 0 \\ 0 & m & 0 \\ 0 & 0 & 0 \end{bmatrix} \begin{Bmatrix} \ddot{x} \\ \ddot{y} \\ \ddot{i} \end{Bmatrix} + \begin{bmatrix} b+c & -c & 0 \\ -c & c & 0 \\ -(k_g + k_m) & k_m & L \end{bmatrix} \begin{Bmatrix} \dot{x} \\ \dot{y} \\ i \end{Bmatrix} + \begin{bmatrix} K+k & -k & k_m \\ -k & k & -k_m \\ 0 & 0 & R \end{bmatrix} \begin{Bmatrix} x \\ y \\ i \end{Bmatrix} = \begin{Bmatrix} f_d \\ 0 \\ 0 \end{Bmatrix} \quad (10)$$

Taking the Laplace transform,

$$\begin{bmatrix} Ms^2 + (b+c)s + K+k & -(cs+k) & k_m \\ -(cs+k) & ms^2 + cs + k & -k_m \\ -(k_g + k_m)s & k_ms & Ls + R \end{bmatrix} \begin{Bmatrix} X(s) \\ Y(s) \\ I(s) \end{Bmatrix} = \begin{Bmatrix} F_d(s) \\ 0 \\ 0 \end{Bmatrix} \quad (11)$$

The transfer functions relating x , y , i , and f_d are given by

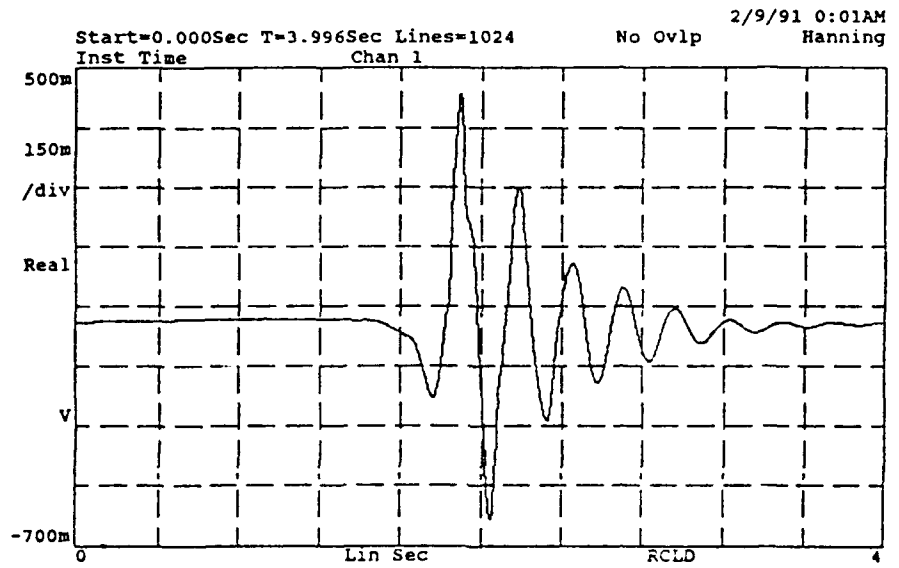
$$\begin{Bmatrix} X(s) \\ Y(s) \\ I(s) \end{Bmatrix} = \begin{Bmatrix} H_1(s) \\ H_2(s) \\ H_3(s) \end{Bmatrix} F_d(s) \quad (12)$$

where the following are obtained with the aid of Mathematica [4]

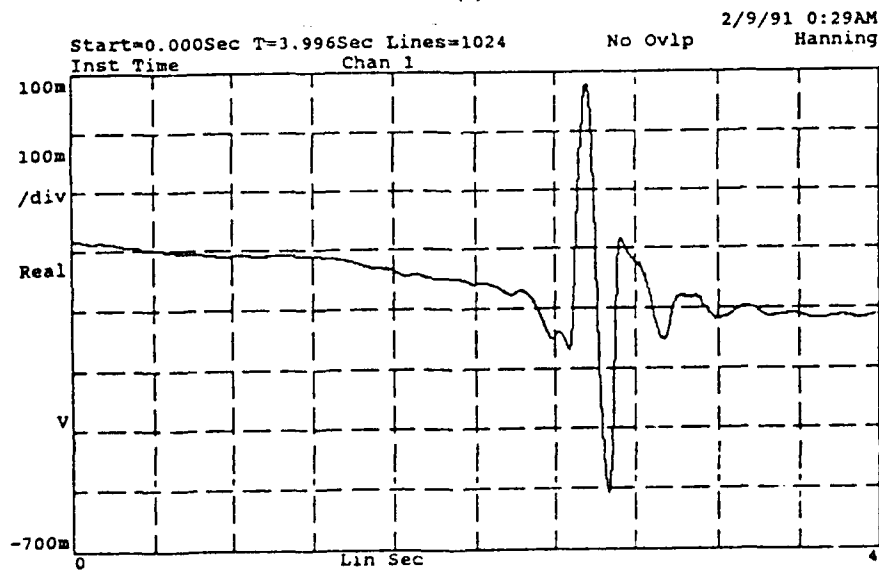
$$\begin{aligned} H_1(s) &= \frac{X(s)}{F_d(s)} = \frac{mLs^3 + (mR + cL)s^2 + (cR + kL + k_m^2)s + kR}{\Delta(s)} \\ H_2(s) &= \frac{Y(s)}{F_d(s)} = \frac{cLs^2 + (cR + kL + k_mk_g + k_m^2)s + kR}{\Delta(s)} \\ H_3(s) &= \frac{I(s)}{F_d(s)} = \frac{s[(k_m + k_g)ms^2 + ck_ms + kk_g]}{\Delta(s)} \end{aligned} \quad (13)$$

$$\begin{aligned}
\Delta(s) = & \{MmL\}s^5 \\
& + \{(MR + Lb)m + (M + m)cL\}s^4 \\
& + \{(M + m)cR + (Mk + mK + mk + bc)L + (M + m)k_m^2 + (Rb + k_g k_m)m\}s^3 \\
& + \{(Mk + mK + mk + bc)R + (Kc + bk)L + bk_m^2\}s^2 \\
& + \{(cR + Lk + k_m^2)K + Rbk\}s \\
& + \{KkR\}
\end{aligned} \tag{14}$$

The response at the beam tip, with active RMA, for different values of gain is shown in Figure 9.



(a)



(b)

Figure 9 System response with the active RMA: (a) moderate gain and (b) high gain

It is interesting to note that, for an otherwise stable control system, by simply switching the electrical leads of the RMA, the system becomes unstable or self-excited vibration is induced (Figure 10).

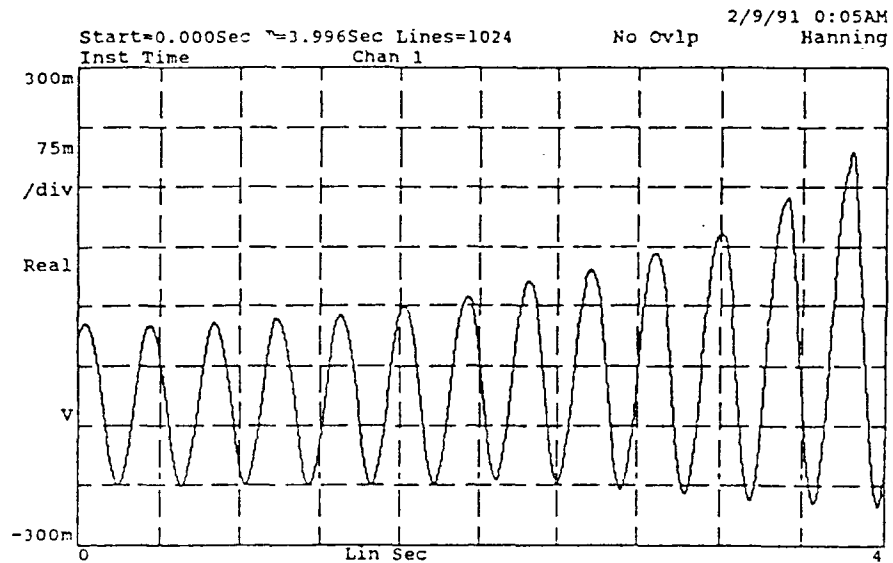


Figure 10 System response to positive feedback

The stability behavior of the controlled system, as k and c of the RMA are varied, can be seen in Figure 11.

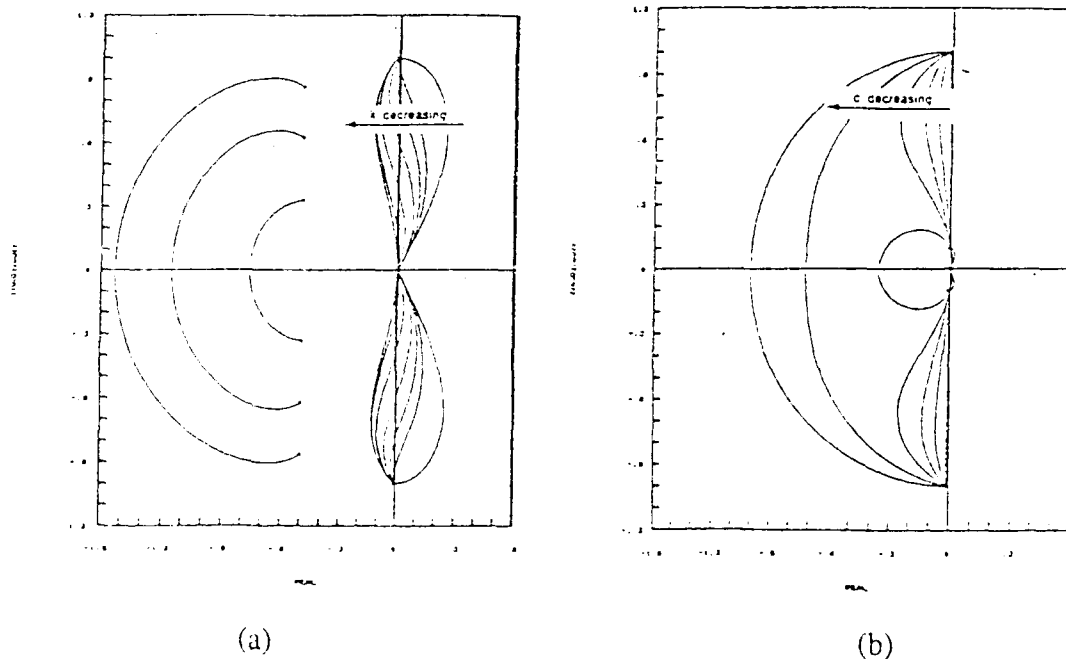


Figure 11 Root loci: (a) decreasing k and (b) decreasing c

Discussion

From the experimental results it can be seen that for the uncontrolled system (with dead RMA), the beam tip vibrates in excess of 45 seconds (Figure 3). The system's ability to dampen out vibration is improved by the use of passive RMA. It is about 4 seconds or 10 times faster (Figure 5). The system is further improved by the use of active RMA where the settling time is anywhere from 2 seconds to less than 1 second depending upon the values of control gain used (Figure 9).

Concluding Remarks

Active control applied to structures provides a powerful means of suppressing vibrations, but it also incurs some "costs." These costs are mainly: more expense; more complexity in electronics, hardware and software; and less reliability. With negative velocity feedback for the configuration under consideration, the control system is less reliable because it may become unstable, for certain values of physical parameters and control gain. This fact is also discussed by Inman [5].

Acknowledgements

We wish to thank the following organizations for supporting this research:

- US Air Force Office of Scientific Research (AFOSR) and Universal Energy Systems (UES), Inc.
- Frank J. Seiler Research Laboratory

References

1. Shaw, O.G. and H. V. Vu, "Modal Analysis and Active Vibration Control of a System of a Cantilever Beam and a Reaction-Mass Actuator," *Proceedings of the AIAA Guidance, Navigation, and Control Conference*, 1990, pp. 73-78.
2. Steidel, R.F., *An Introduction to Mechanical Vibrations*. New York: John Wiley & Sons, 1989.
3. Den Hartog, J. P., *Mechanical Vibrations*. New York: Dover Publications, Inc., 1985
4. Wolfram, S., *Mathematica: A System for Doing Mathematics by Computer*. Redwood City, CA: Addison-Wesley Publishing Company, Inc., 1991.
5. Inman, D., "Control/Structure Interaction: Effects of Actuator Dynamics," *Proceedings of the AIAA Dynamics Specialist Conference*, 1990, pp. 311-321.

THE INVESTIGATION OF LARGE SPACE STRUCTURE PASSIVE ELECTRODYNAMIC DAMPERS

by

Roger Stettner, Ph.D
Advanced Scientific Concepts, Inc.*

and

Paul Mlakar, Ph.D., P.E.
Jaycor

ABSTRACT

The focus of this study was on computationally verifying that passive electrodynamic damping was competitive or superior to current damping technologies recommended for Large Space Structures (LSS). Electrodynamic damping is linear and is characterized by a dash pot dissipative force which is proportional the relative velocity of the damper components. The constant of proportionality is c . The study investigated the maximum ratio of c to the mass of the damping system as well as the frequency dependence of c . Both analytic and ADINA models of an LSS-like structure, the Air Force Wright Aeronautical Laboratory 12 Meter Truss (TMT) were used, together with TMT data, to understand and verify Passive Electrodynamic Damper (PED) performance.

The study results indicate that the Auxiliary Mass PED (AM-PED) is competitive or superior to active dampers, in damping TMT bending modes, when the AM-PED weight is comparable to that of active damping actuators. This is important because of the enhanced reliability and cost savings of a passive damping system. An AM-PED does not require sensors, a power source or a computer control system. Although a detailed comparison was not made, it appears that equivalent weight strut PED systems may also be superior to viscoelastic-material strut dampers. This is important because PED systems do not outgas and are stable with respect to environmental temperature variations. In addition PED system performance is easily calculable, c is independent of frequency and of amplitude for the low modal frequencies characteristic of LSS.

* 2241 Foothill Lane, Santa Barbara, CA 93105, (805) 966-3331

1.0 INTRODUCTION

This paper describes research that was supported by the Strategic Defense Initiative Organization (SDIO). The object of the study was to investigate the feasibility of specially-designed, spacecraft vibration-damping-devices, known as a Passive Electrodynamic Dampers (PEDs). PEDs absorb mechanical energy, by means ohmic heating, when there is motion relative to the field of a permanent-magnet. Future military and non-military spacecraft are expected to be large and flexible, with many low frequency modes. Damping these modes is critical to the operation of some on-board sensors and equipment. A successful PED would therefore be applicable to military non-military space programs.

The goal of the study was to verify PED damping effectiveness by mathematically modeling and evaluating PED electrodynamic characteristics, as they relate to Large Space Structures (LSS), and computationally simulating the mechanical effect of PED configurations on LSS. The approach taken was to focus on one LSS test bed, called a model LSS (MLSS), since there was time to consider only one LSS simulation in the project. The electrodynamic modeling was more general, showing how the key PED design parameters - weight for example - varied as a function of LSS and space environment characteristics - frequency and temperature for example. The idea was to design a PED for the MLSS using the general PED design equations that evolved from the research. The MLSS modal damping was first approximated analytically so that the key parameters and their relationship to the damping could be identified. PED caused, LSS modal-damping was then compared to MLSS data obtained using other damping systems. Because the analytically calculated damping was satisfactory the PED was incorporated into an ADINA (Reference 1) code model of the MLSS. The ADINA model gave the most accurate PED modal damping effectiveness calculation and allowed the most accurate comparison with other damping methods.

After much consideration and discussion with the appropriate government agencies the MLSS chosen for the study was the AFWAL twelve meter truss (TMT, References 2 and 3). The reason for this choice was that the TMT was the simplest, technically acceptable structure for which adequate data was available.

Much of the research presented in this paper is an evaluation of the damping characteristics of a particular PED configuration called the Auxiliary Mass Passive Electrodynamic Damper (AM-PED). Both analytic and computer simulation results show the AM-PED is competitive with active damping systems anticipated for spacecraft use. Substitution of the AM-PED for active damping could mean large increases in space platform damper reliability, weight reduction and a lower cost damping system. The AM-PED is expected to be a very important addition to the technologies used for LSS damping. Other PED configurations are expected to also be important but they have not been studied in as much detail. The Strut Passive Electrodynamic Damper (S-PED) appears to be a particularly promising substitute for viscoelastic materials (VEM) in damping structural truss modes. PED damping concepts, electrodynamics and space environment characteristics are discussed in Section 2. Sections 2 - 4 discuss the results and analysis of this study. Section 5 presents the conclusions and recommendations. In the next subsection the rationale for studying low frequency dampers, in particular PEDs, is discussed

1.1 LARGE SPACE STRUCTURES (LSS) AND DAMPING

Increasingly greater roles are anticipated for satellites in the civilian economy, in government research and in military planning. Planned space structures are therefore becoming larger with more complex missions and increasing power requirements (References 4 and 5). The fiscal and complex-mission, space-structure requirements, for these planned systems, result in lightweight, flexible, loaded, LSS design concepts with very low modal frequencies. In combination with the lack of gravity these requirements also mean that there will be small frictional energy dissipation and modes will be poorly damped.

One proposed solution to the LSS structural requirements has been the use of trusses as the basic support structure. Trusses are both lightweight and rigid and have been designed in beam configurations. The plan is to mount sensors, equipment and solar panels on these lightweight frames. The resulting LSS are truss-type structures connecting a variety of flexible components. Predictions indicate that these flexible components will likely have natural frequencies in the same range as the dominant truss modes (Reference 5).

A number of groups have developed experimental LSS structural models to verify their structural dynamic computational tool predictions, as well as verify proposed damping concepts. The PACOSS (Passive and Active Control of Space Structures, Reference 6) dynamic test object and Twelve Meter Truss (TMT, References 2 and 3) supported by the Air Force and the Dynamic Scale Model Technology (DSMT, Reference 5) program supported by NASA are examples. The PACOSS program is particularly advanced and experimental results appear to support the current LSS damper design philosophy (Reference 7):

- (1) Damp as many modes as possible passively, using VEM.
- (2) Damp all remaining modes (assumed to be only a few) by means of active damping.

The TMT approximates a twelve meter beam and experiments have been performed in both a cantilevered and a free-free configuration. The cantilevered configuration is not "realistic" for a complete LSS¹ and is a compromise so that experiments can be performed with low-frequency structural modes (2.25 Hz). TMT cantilever experiments have been performed and analyzed with and without VEM struts. Free-free TMT experiments have been performed with and without VEM struts but the results have not been analyzed in detail. Active-damper, cantilevered-TMT NASTRAN experimental pretest predictions are also available.

Not only damper development but LSS designs and structural dynamic testing are still in the research and development stage. At the present time VEM is the passive damper of choice and for the most part, in practice, it has been used in strut configurations (References 3 and 6). However, there are some shortcomings to the use of this material. The full temperature variation for an exterior spacecraft component could be 150°C, from about -50°C to about 100°C. Some VEM materials have a useful range of only 20 - 30 °C. It is recognized that one material will not suffice for every application and that active heating elements will have to be used in conjunction with VEM to maintain constant damping (Reference 8), for some applications. In addition VEM is nonlinear and its damping characteristics are not easily predicted.

¹ There are structures that are expected to be cantilevered off the truss. The solar paddles in Reference 5 are an example.

These shortcomings imply uncertainties and expense in damper design as well as possible reliability problems in actual practice. In addition there is the question of the VEM damper effectiveness with respect to its weight. In the TMT experiments the final VEM passive damper configuration weighed about 50% more than the undamped truss. Not all of this damping material was effective in damping the modes, however, and future TMT studies may investigate the elimination of the least effective struts.

At the present time a common active damping system uses a coil and permanent-magnet actuator system. A current is generated in the coil and exerts a force on a moving magnet corresponding to a predetermined algorithm. One such algorithm is to make the force proportional to the velocity of the attachment point for example. The system is very convenient in its application: the actuator is attached at a position of maximum modal amplitude, consistent with dynamic stability requirements. In addition, because it is made of metals, its performance is very stable with respect to expected environmental temperature variations. There are some shortcomings, however. One of these appears to be that the force exerted is limited by the maximum current that can flow through the coil. Too high a current will melt the coil. Most of the power dissipated in the coil appears to result in a restoring force which changes direction as a function of time. Only a small portion of the force actually damps the motion of the LSS modes. Additionally the actuator system requires motion sensors, a computer control system and a power supply. All these system components add weight and contribute to system reliability issues.

If the objective of the active damping system is to damp only a few modes, replacing the electrical-power generated restoring force with a spring and a permanent-magnet system may be the most efficient and cost effective design. The AM-PED herein is a passive damping device which does just that. It has all the advantages of this active damping system but apparently none of its disadvantages. In addition it may be more effective in damping LSS modes than an active damping system.

2.0 THE PED

In this section the PED concept is first discussed from a general point of view. In Section 2.1 the AM-PED is discussed and then in Section 2.2 the design constraints imposed by the electromagnetics is examined. Finally in Section 2.3 the effect of the space environment on the PED is discussed.

The basic PED concept is to mechanically couple LSS vibrations to relative motion between an armature and a magnet. The relative motion gives rise to a dissipative force F which is proportional to the relative velocity of the two PED components. That is

$$F = cv, \quad (1)$$

where v is the armature/magnet relative velocity and c is the constant of proportionality. Figure 1 illustrates the principle. The relative motion generates a current in the armature and vibrational energy is absorbed via ohmic heating. This kind of damping - electromagnetic damping - has been considered in the past for other kinds of systems (Reference 9) and so the concept is not new. What is new is the application of the concept to LSS and the particular LSS PED structural and magnetic configurations. Because of the low LSS frequencies electromagnetic damping, as

manifested in the PED design, is a very weight efficient LSS vibration damper. This will be demonstrated in Sections 3 and 4. Because of superior PED, spacecraft-environment, material-properties and its simplicity it is a very desirable damper system.

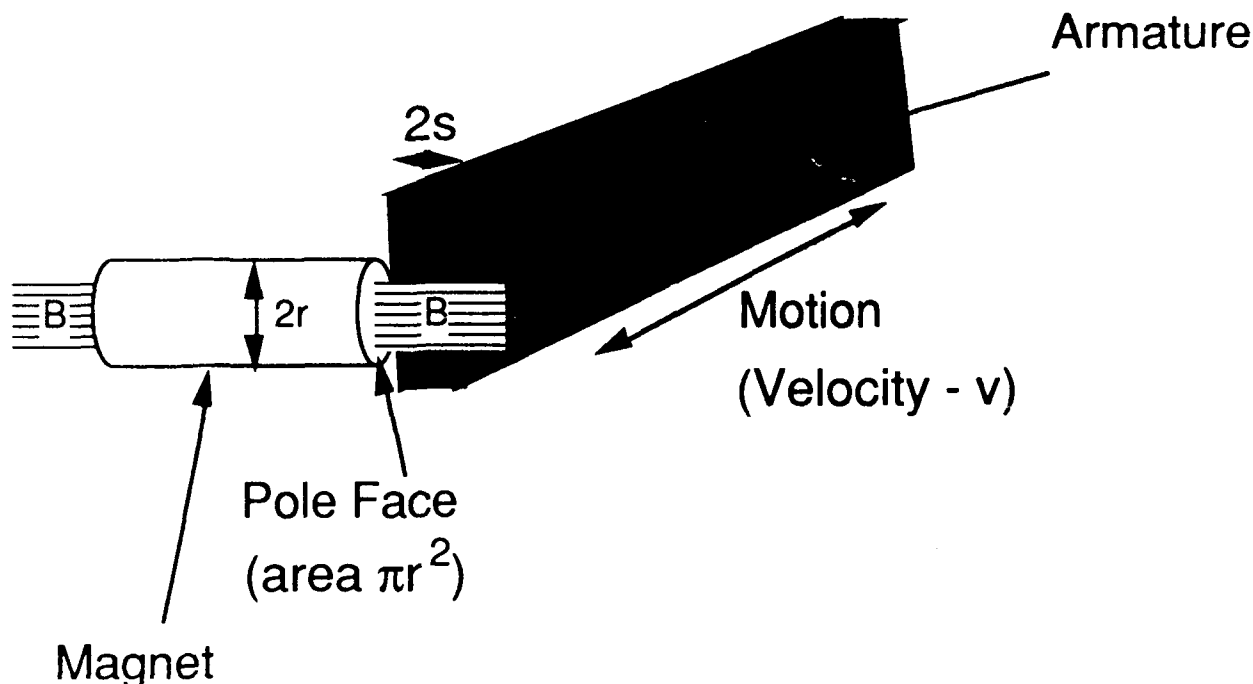


Figure 1. Generic PED Components

The PED is essentially a dash pot, for all LSS vibrational amplitudes of concern, and the mechanical analysis is relatively straight forward. Difficulties lie in efficiently designing the magnetic circuit and in coupling the dissipative force to the complex multi-modal mechanical motion. Two coupling configurations were studied: (1) the Auxiliary Mass Passive Electromagnetic Damper (AM-PED), and the (2) Strut PED (S-PED). The idea behind the AM-PED is to transfer the LSS vibrational energy to a proof mass and then dissipate the the proof mass energy via ohmic heating. The AM-PED can theoretically be attached anywhere on the LSS the vibration amplitude is large. The S-PED is used mainly as a component of the LSS truss support structure to dissipate truss vibrations.

For most coupling the PED is designed to have its own restoring force proportional to displacement and consequently its own resonant frequency ω_0 . The PED has, of course, its own mass, m , as well. One design problem is choosing the PED parameters, c , ω_0 , and m to optimize the damping over the LSS frequency range of interest. For a given m , we are actually optimizing the damping by appropriately choosing the parameters c/m and ω_0 .

One of the advantages of the PED is that it is a simple, linear, mechanical system and its effect can be calculated. However, coupling to a complex LSS means the analysis is more complex than for a one dimensional system. In general the PED

damping of a given LSS of mass M and frequency Ω_{0n} ($n = 0, 1, 2, 3, \dots$) will not be the same as for a one dimensional system of mass M with a damping force proportional to velocity. That is the percent of critical damping, γ_n , of the particular LSS mode will not be simply $c/(2M\Omega_{0n})$. We can expect that γ_n will be related to the effective mass of the LSS, for the particular modal vibration of concern (the total LSS mass is not necessarily effective in the vibrations of a particular mode), and to the PED parameters. These latter comments are particularly relevant to the AM-PED configuration.

We now consider how the PED parameter c (equation 1) is related to the PED design parameters. As expressed in equation 1, the force is cv , v is the relative velocity (m/sec), and

$$c \approx \sigma \pi r^2 (2s) B^2 \quad (\text{kg/sec}), \quad (3)$$

where B is the flux density field (Weber/m²), σ is the conductivity (mhos/m) r is the magnet radius (m) and $2s$ the thickness (m) of the armature. Reference should be made to Figure 1. Equation 3 assumes that none of the magnetic leakage flux is effective in damping the system and is thus a lower bound on c : the armature will be wide enough to cut most of the leakage flux lines.

Equation 3 is not valid for all frequencies and although an arbitrarily large c can be developed simply by making the magnet large enough the important ratio c/m cannot be made arbitrarily large. Equation 3 is valid so long as current can be generated throughout the thickness, $2s$, of the armature. If the frequency of oscillation is very large the current will only exist on the surface of the armature and $2s$ in equation 3 will be replaced by a smaller number. Therefore at high frequency c is smaller than expressed by equation 3. The depth of penetration of the current into the armature is controlled by a parameter called the "skin depth", δ , which has the dimensions of length. Roughly speaking when $\delta > 2s$ equation 3 is valid. As we will see in Section 2.2 we can expect equation 3 to be valid below about 50 Hz. This frequency is far above expected LSS frequencies.

Equation 3 shows that the dimensions of the magnetic system (Figure 1) enter the calculation of c (the area, πr^2 , of the permanent-magnet for example). What is not obvious from equation 3 is that the magnetic field B is also dependent upon the dimensions of the magnetic system as well as the type of magnetic material used. Optimized designs have a maximum c/m value which is dependent upon the magnetic system design. The maximum practical LSS c/m ratio, for an aluminium armature, is about 500 sec⁻¹. We will see in the next section that the c/m ratio is relevant when designing a AM-PED to damp more than one LSS mode. It is also important when comparing the equivalent weight of alternative passive damping concepts. In Section 3.2 we roughly compare the S-PED to VEM struts.

2.1 THE AUXILIARY MASS PASSIVE ELECTROMAGNETIC DAMPER (AM-PED)

The AM-PED concept is straight forward and very simply applied to a LSS. The idea is to continuously transfer LSS vibrational energy to a proof mass and dissipate the proof mass kinetic energy. In the case of the AM-PED the proof mass is essentially

the magnetic system and the dissipative force is described by equations 1 and 3. The AM-PED is made lightweight and springs act as a linear restoring force. Relative motion causes currents to flow in the armature resulting in energy dissipation. For the present discussion it is only necessary to know that the dominant weight of the device arises from the magnetic system taken to be the mass m . For reference the amplitude of magnet motion will be about an inch (maximum LSS vibration amplitudes are fractions of an inch), the overall dimensions of the AM-PED designed for the TM1 will be about 10 cm x 10 cm x 10 cm with a mass roughly equal to 4 lbs. This is a very compact device which is attached externally to the LSS (in this case the TM1) at positions of maximum vibration amplitude. (Note that many AM-PED designs are possible using different dimensions and magnetic materials.) As we will see AM-PED damping is expected to exceed 5% for very reasonable AM-PED masses and compared with active damping systems, 5% damping is approximately the requirement for many systems (Reference 7).

2.2 ELECTRODYNAMIC PED CONSIDERATIONS

As discussed in Section 2.0, the damping constant, c , depends upon the value of the current in the AM-PED armature and the magnetic field. The flow of current in the armature is affected by the development of electric fields which oppose the flow of current. These electric fields are manifested through the skin depth introduced in Section 2.0. The armature current flow also generates a magnetic field which may oppose the magnetic field of the magnet. An opposing magnetic field might reduce the force on the armature and demagnetize the magnet, so it must be considered in the analysis. If either the opposing electric field or the opposing magnetic field effects were substantial they could reduce the damping constant below that expected from equation 3. In the detailed analysis we find, as expected, that the parameter of greatest importance is the electrodynamic skin depth δ (meters)

$$\delta = (\mu_0 \sigma \omega / 2)^{-1/2} \quad , \quad (4)$$

where μ_0 is the permeability of free space (the armature is made of non-magnetic material and equal to $4\pi \times 10^{-7}$ h/m, σ is the armature conductivity (mho/m), and ω is the angular frequency of motion. In order that the current in the armature reach its maximum value, δ must be larger than about twice the thickness of the armature. For proposed PED armature dimensions, skin depth should not be a problem for frequencies less than about 50 Hz.

In order that the dimensions of the armature not affect the design of the system, the above calculations suggest a minimum armature width to magnet diameter ratio of 3. The required coding length of the armature is determined by other design requirements. Large vibration amplitudes can affect the high frequency content of the armature-current and the magnetic field, however, if designed properly the damping system will be independent of amplitude.

2.3 PED SPACE ENVIRONMENT CONSIDERATIONS

Carbon fiber composites (VEM) are the recommended passive damping material for use within structural components of truss structures (diagonal

for example). However, large temperature variations in space make designing passive VEM damping treatments difficult (Reference 8). The full temperature variation for an exterior spacecraft component could be 150°C, from about -50°C to about 100°C. Some VEM materials have a useful range of only 20 - 30 °C, making many materials and, depending upon the specific problem, temperature control elements necessary. One of the virtues of the PED designs is that, because they are made of metals, they are extremely stable with respect to temperature variations.

The Curie point (temperature at which magnetic properties change - Reference 10) of all common magnetic materials is many hundred degrees C, far above the highest expected space environment temperature. The most temperature dependent parameter in the damping constant "c" (equation 1) is the conductivity. "c" is proportional to the conductivity (equation 3). For temperatures near and above the Debye temperature (Reference 11) of the material, the conductivity varies directly with absolute temperature. -50°C is 223 °K and many metals have a Debye temperature near this value. The Debye temperature of silver, the armature material giving the largest c/m value is 226°K, for example. The ratio of absolute temperatures over the expected temperature range is $373/223 = 1.67$ and so "c" is expected to vary by less than a factor of 2 over the full temperature range. A look at tables of material data supports this expectation. If a PED experienced the full temperature variation (an AM-PED at the end of a solar paddle, for example) it could be designed to operate most effectively at the mid temperature range (about room temperature) and then the expected variation in "c" would be less than $\pm 30\%$.

Because the coefficient of thermal expansion for the materials under consideration is about $10\text{-}20 \times 10^{-6}$ per degree C, the expected length or gap changes are only about .3%, too little to effect PED operation.

The effects of environmental temperature variation on the spring of the AM-PED are also expected to be manageable. Considerable information exists about the effects of temperature on the mechanical properties of metals (Reference 12). This information suggests that strength may change by $\pm 10\%$ over the applicable range. This can easily be addressed in the detailed design of the spring. The small displacements, $\pm .17\%$ imposed by thermal expansions can be considered similarly. Finally, the stiffness may vary by $\pm 5\%$ which should not significantly detune the device.

3.0 PRELIMINARY DESIGN OF PED SYSTEMS

In this section we will be concerned with analytic evaluations of PED performance and the impact of performance upon design parameters. The major focus is upon the AM-PED, considered in Section 3.1. The analytic approximations and discussion in Section 3.1 are a background to the consideration of another PED configuration, the Strut-PED (S-PED). Preliminary estimates do suggest that the S-PED may be very competitive in performance with VEM damping strut configurations. In addition the S-PED does not have any of the VEM temperature dependence, outgassing, nonlinearity and frequency dependence problems.

3.1 AM-PED PRELIMINARY DESIGN FOR THE 12 METER TRUSS (TMT)

One of the objectives of this section is to compare the predicted performance of an AM-PED with that of an equal-weight actuator, active-damping system. Active-damping computer predictions have been made for the TMT in its low frequency

cantilevered position (References 2 and 3). These predictions are compared with an analytic, continuous-beam model of the AM-PED/TMT combination. In Section 4 AM-PED performance is compared with the active damping calculations utilizing a ADINA computer model of the TMT. This later comparison is important because the actual TMT is not continuous and the beam-model resonant frequencies differs from the experimentally measured TMT frequencies. The measured ratio of the second bending to the first bending, TMT mode frequency is $10.72/2.26 = 4.74$. The frequency ratio of a one end clamped beam is 6.27 so the analytic model is reasonable but differences should be expected between the analytic model predictions and the more accurate ADINA model. As we will see in Section 4, AM-PED damping is actually more effective with the ADINA truss model. This is in part due to the fact that the truss does not adjust its modal shape to external forces in the same manner as the continuous beam. The analytical modeling provides a framework for understanding how to design an AM-PED and is used to make preliminary estimates of AM-PED performance. (In the original study AM-PED effectiveness on a free-free TMT was also computationally simulated. The analysis is not presented in this paper. The damping was found to be 23% less than the cantilevered beam, for equivalent weight AM-PEDs.) The general dynamical problem is considered first.

What is required is to solve the dynamical equations of motion of the AM-PED system coupled to the LSS. The design requirements are that the percent of LSS modal damping should be about 5% so the damping can be solved for by a perturbation analysis. In addition the mass of the LSS, M , is much greater than m so m/M can be treated as a small parameter. As the detailed analysis shows, if $F_s(\omega, x)$ is an expression for the force exerted on the AM-PED by the LSS, where x is the amplitude of motion for the frequency ω , then the frequencies of the system can be obtained from the equation

$$F_s(\omega, x)/M = \beta \omega^2 g(\omega) x, \quad (5)$$

where

$$\beta \equiv m/M, \quad (6)$$

$$g(\omega) \equiv (-2r + W^2(W^2 - 1) + 4r^2)/(4r^2 + (W^2 - 1)^2), \quad (7)$$

$$r(\omega) \equiv c/2m\omega, \quad (8)$$

$$W(\omega) \equiv \omega_0/\omega, \quad (9)$$

$$\omega_0^2 \equiv k/m, \quad (10)$$

and k is the AM-PED spring constant. In the limit that the new LSS/AM-PED modal frequencies are very near the old frequencies, Ω_{0n} , (that is β is small) we find that percent of critical damping, γ_n , given for each of the LSS modes is

$$\gamma_n \approx -\text{Imag}\{\beta \Omega_{0n} g(\Omega_{0n}) x / (M^{-1} \partial F_s(\Omega_{0n}, x) / \partial \omega)\}. \quad (11)$$

Assuming the TMT can be modeled as continuous cantilevered beam and the AM-PED is mounted on its free end, F_s can be analytically defined and the operations required by equation 11 performed. The result is

$$\gamma_n = \{2\beta\} [2r(\Omega_{0n})] [4r(\Omega_{0n})^2 + (W(\Omega_{0n})^2 - 1)^2]^{-1} \equiv 2\beta d_n, \quad (12)$$

where reference is to be made to equations 8 and 9. Assuming the mass m is fixed at the value of the active damping actuator, we can choose the AM-PED parameters c/m and ω_0 to either maximize the damping for a particular mode or damp more than one mode. We also note that if the LSS were a one dimensional system of mass M , the factor in curly brackets would be $1/4$ of the equation 12 result. This means, at least in the limit of small frequency changes, that the effective mass of the cantilevered beam is $1/4$ of its actual mass, for all modes when an AM-PED is attached to its free end.

The active damper is effective for both the first and second bending modes (Ω_{00} and Ω_{01}) respectively so we design the AM-PED to compete with it and also damp the first and second bending modes. We are interested in obtaining the best damping we can for the lowest mode and still obtain reasonable damping for the higher modes. As the detailed analysis shows, for a given r and Ω_{00} in equation 12 the numerator can be minimized by choosing

$$W(\Omega_{00}) = 1, \text{ or } \omega_0 = \Omega_{00}.$$

The damping of Ω_{00} is then maximized with the choice

$$c/m = \Omega_{00}. \quad (13)$$

As discussed in Section 2 this c/m ratio is easily achievable with the magnetic system. The choice of AM-PED parameters defined by equations 12 and 13 imply that for $\Omega_{0n} \gg \Omega_{00}$

$$\gamma_n \approx \gamma_0 [\Omega_{00}/\Omega_{0n}], \quad (14)$$

when

$$\gamma_0 = 2\beta. \quad (15)$$

The TMT active damper predictions were actually made with two 4 lb dampers at the free end and two additional 4 lb dampers, one at the center and one one-quarter of the length from the free end. A worst case comparison is made by using only one 8 lb AM-PED (equivalent to two 4 lb dampers) at the free end. Since the TMT is 220 lbs and the ratio of $\Omega_{00}/\Omega_{01} = 4.74$, as stated above, we find for the TMT that

$$\gamma_0 \approx 2 \times 8 / 220 = 7.3\%, \text{ and } \gamma_1 \approx 7.3\% / 4.74 = 1.5\%. \quad (16)$$

Table 1 shows the TMT active damper predictions as a function of four velocity feed back schemes. The AM-PED is therefore expected to be very competitive with active damping systems. In Section 4 we will see that there is reason to suspect that the AM-PED may, in some circumstances, be a better damper than the active system. (The

overall damping ratio with an 8 lb AM-PED is 11% for the computer simulated TMT, 50% greater than the analytic, continuous beam result.)

**Table 1 TMT Active Vibration Control
(From Reference 2, x Bending)
Closed-Loop Modal Damping Predictions**

	Open-Loop	LQG, LTR output Feedback	MEOP	Overlapping Decomp	Component Synthesis
1st Bending	.80	9.36	4.49	8.02	7.24
2nd Bending	.16	1.45	1.38	3.19	2.97

One can also estimate the TMT modal damping by using a one dimensional analog. For driven, single degree of freedom system the damping is $(2T)^{-1}$, where T is the transmissibility. Using this relationship, where the cantilever is base driven, we obtain, 6.6% damping for the first mode and 1.4% damping for the second. These numbers are consistent with the results in equations 16. But again, we have here used a continuous beam model for the TMT and differences are expected for the real structure.

3.2. STRUT-PED (S-PED) CONFIGURATION

A S-PED would be used very much like VEM damper struts used in LSS truss structures. For example, experiments were performed with the TMT using VEM diagonal strut dampers (Reference 2 and 3) in all bays (see Figure 2). The resulting damping was 4.2% for the first bending mode and 7.0 % for the second bending mode but the weight of the TMT was increased by more than 100 lbs (45 kg). It is clear that the struts could be removed from those bays experiencing the lowest modal strain energy and the damper weight would be reduced. However, the damping would be reduced somewhat as well. The TMT with strut dampers in all bays probably represents the maximum TMT damping possible with VEM.

A rough comparison of what is possible with a S-PED can be made by employing two diagonal S-PEDs in the first TMT bay (see Figure 2) and choosing a c to maximize damping for the first mode. A transmissibility analysis is then used to evaluate the damping for the second mode. The detailed analysis indicates that under these circumstances the strut dampers operate very much like the Isolator-PED of Reference 13. The Reference 13 analysis showed that the damping of the first cantilever mode was maximized at about 30% when

$$c/m = 1.5 \Omega_{00}. \quad (17)$$

This equation is very similar to the AM-PED design equation (equation 13) except that in the case of equation 17 the mass is the effective mass of the TMT in its first mode and not the mass of the AM-PED. As discussed in Section 3.1 the effective mass of the

TMT is 1/4 the total mass or 55 lbs (25 kg). We saw that about 7% damping was expected with two 4 lb AM-PED masses, larger masses producing greater damping. In the S-PED design the moving mass is the system itself. The larger mass implies greater damping.

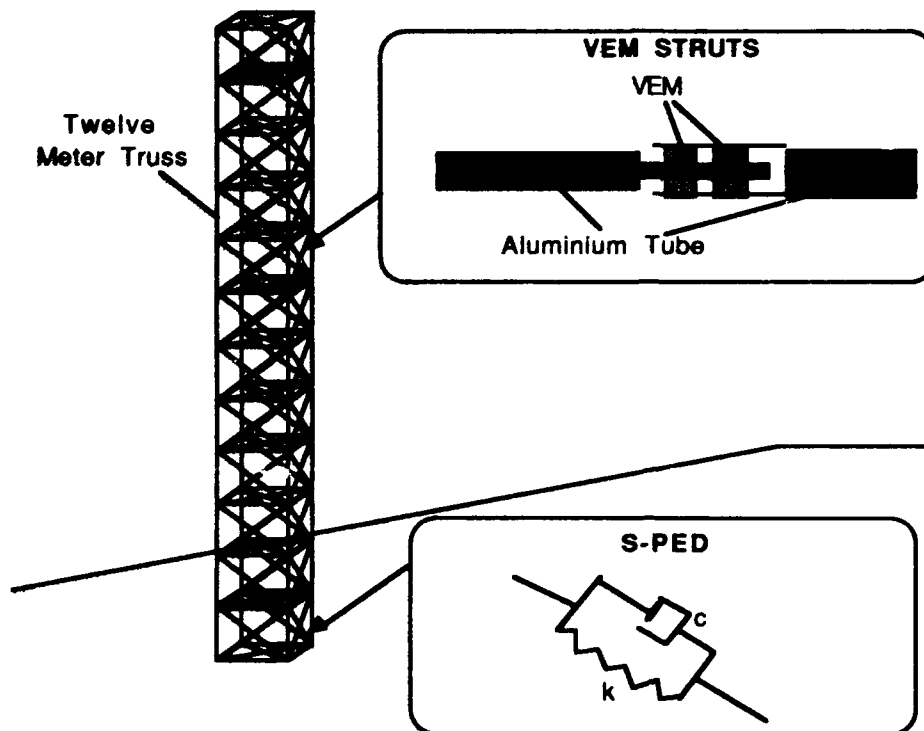


Figure 2. Twelve-Meter-Truss, Damper Strut Configurations.

The c that we need in order to obtain this large damping is given by inserting the correct parameters into equation 17. We need

$$c = 25 \times 1.5 \times 2\pi \times 2.25 = 530 \text{ kg/sec}, \quad (18)$$

or if two struts are used per bay $c = 265 \text{ kg/sec}$ for each strut. For a particular design we can achieve the required c with a total magnet mass of 2.1 kg (4.6 lbs). With this S-PED system the expected damping, predicted from a base driven transmissibility analysis of a continuous cantilever beam, is 19% for the first bending mode and 2.5% for the second bending mode. We have tuned the S-PED system for the first bending mode and it is most effective for that mode. The 19% damping of the first mode differs from the 30% expected from the single degree of freedom Reference 13 analog, but given the difference in the approximation methods numerical differences are expected. In addition, experience with comparing the AM-PED, continuous beam, analytic results with the TMT computer simulations suggests that the analytic damping estimates are a conservative lower bound.

It is difficult to directly compare the analytical S-PED analysis with the TMT VEM damping data. Theoretically, with a factor of 22 less weight (excluding the weight of the struts and armature) we have a factor of 4.5 more damping in the first bending mode. This seems to be a definite advantage. The S-PED damping in the second mode is, however, about a factor of 3 less than the VEM system. It is clear that by detuning the

S-PED the second mode damping could be increased at the expense of the first mode, if that were desirable. Although the analysis has not been performed, the expectation is that the S-PED would be superior to the VEM damping strut system. Replacing the VEM system with an S-PED would have a number of advantages: (1) there would be no outgassing problems, (2) designing a damping treatment would be simpler since the PED system is linear with respect to amplitude and c does not depend upon frequency, (3) heating coils would be avoided because the PED system performance changes very little with temperature, (4) the same PED system could be used anywhere on the LSS because of the near temperature independence of the PED.

4.0 STRUCTURAL DYNAMICS

In Section 1, it was noted that the AFWAL 12m Truss (TMT) dynamically represents large space structures of generic interest. To suppress the vibration of such systems, the application of the PED as an auxiliary mass damper was discussed to be very promising. In Section 3, a preliminary design AM-PED for the cantilevered 12m Truss was discussed. It was observed that its effectiveness, reliability, and weight compare favorably to actively controlled and mechanical passive damping alternatives.

The structural dynamics of the TMT with AM-PED is now comprehensively analyzed to further investigate these promising possibilities. The modal analysis is considered first to gain insight and then realistic transient excitations are considered. Next, the effect of AM-PED parameters on performance is examined.

4.1 MODAL CHARACTERISTICS

The study begins with the natural frequencies and mode shapes of the system. These were obtained through the ADINA finite element model of Figure 3 (Reference 1). This describes each of the 16 bays of the TMT with a 2-noded beam element. Complete restraint against translation and rotation is assumed at the support. The AM-PED is modeled as a lumped mass connected to the free end through a general element having concentrated damping and stiffness. In all, 33 degrees of freedom describe the planar flexural vibration of this system. The modal characteristics of this response were found through a determinant search algorithm.

The undamped TMT was first considered without the AM-PED. The total length was taken to be 471 in. and the total weight 220 lbs in accordance with published data. The stiffness parameters of the beam elements are adjusted to match the first two frequencies measured by the AFWAL. These are given in Table 2 and reflect the influence of shear as well as flexural deformation. The corresponding shapes, Figures 4 and 5, contain one and two lobes in the first and second modes, respectively, as one would expect.

Next, the influence of the AM-PED on these characteristics was studied. For this, the parameters of the preliminary design are considered which are reported in the first row of Table 3. The AM-PED design causes the system to have two natural frequencies close to the undamped fundamental mode of the cantilever. These frequencies and shapes appear in Table 2 and Figure 4, respectively. The first of these modes has a slightly lower frequency than the undamped fundamental and is characterized by auxiliary mass motion in phase with the beam. The second mode frequency is only higher than the fundamental and an auxiliary mass counteracts

opposition to the beam. In both modes, the large amplitude of the auxiliary mass motion will be effective in dissipating the beam's vibration. Note in Table 2 that the second flexural frequency of the beam is minimally influenced by the design. Neither is the corresponding mode shape, Figure 5, in which the auxiliary mass experiences little displacement.

4.2 TRANSIENT RESPONSE

With the benefit of the foregoing modal insight, the response of the system to a transient excitation is considered. A uniform, unit, initial velocity of the beam is specifically chosen. This approximates the excitation of an impulsive maneuver by the spacecraft from which it would be cantilevered. It may also represent the loading produced by the fluence of a hostile impulsive laser attack on the platform. The response to this initial disturbance was calculated using the ADINA model through a direct time integration with a step of 0.010 sec.

The resulting tip deflection for the undamped case is shown in Figure 6. This is dominated by the fundamental mode at 2.26 Hz. With no dissipative mechanism in the system, the oscillations continue indefinitely. Such behavior is not consistent with the precise stability requirements for many space platforms.

Fortunately, the situation improves dramatically in the response with the preliminary AM-PED design which is superimposed in Figure 6. This response is initially dominated by the fundamental bending modes. However, these are effectively damped in a few cycles. A least squares fit of the response indicates that it decays with an exponential envelope corresponding to 6.2% damping. This is almost twice as large as predicted in Section 3.1 for the continuous beam. (Note that in Section 3.1 we considered an 8 lb AM-PED, here the simulation was for a 4 lb AM-PED. Equations 6 and 12 show that damping is expected to be linearly proportional to AM-PED mass.)

4.3 PARAMETRIC ANALYSIS

The above transient analyses indicate that the preliminary AM-PED design should be quite effective in suppressing the vibration of large space structures. Accordingly, the influence of its design parameters on this effectiveness is studied. Auxiliary mass and frequency tuning is specifically addressed.

To examine the effect of auxiliary mass, this parameter is doubled above the 4 lb preliminary design. In accordance with the preliminary design procedure, we also double the stiffness and damping values to maintain the same tuning relative to the cantilever's fundamental mode. The response with this 8 lb device is compared to that previously calculated for the 4 lb design in Figure 7. With the additional mass, the vibration is suppressed even more rapidly. The equivalent damping, Table 3, is now 10.9 %. Thus the damping effectiveness increases almost linearly with the size of the auxiliary mass, as suggested by our first order perturbation analysis.

To examine the influence of AM-PED tuning, the auxiliary mass is returned to the initial value of 4 lb. In lieu of the preliminary design of Section 3, an alternative exists which attempts to limit the response of the primary system over a range of frequencies in the neighborhood of its fundamental mode (Reference 14). The parameters of this "optimal" design for the cantilevered TMT are given in the third row of Table 3. The response of this system is compared to that previously calculated for

our preliminary design in Figure 8. The effectiveness of the AM-PED is seen to be a function of frequency tuning. For the uniform initial excitation imposed, the "optimal" design achieves 3.6 % damping and is less effective than the preliminary concept.

TABLE 2 NATURAL MODES OF 12M TRUSS

Beam Character	Undamped Frequency Hz	AM-PED Frequency, Hz
Fundamental	2.26	1.98 2.56
Second	10.70	10.71

TABLE 3 AM-PED EFFECTIVENESS

12m Truss Configuration	mg lb	c lb-sec/in	k lb/in	Damping ratio
Cantilevered	4	0.1464	2.069	0.062
Cantilevered	8	0.2928	4.138	0.109
Cantilevered	4	0.0487	1.577	0.036
Free	2*	0.422*	34.4*	0.048

*Values for each of two AM-PEDs. Free-Free analysis not presented.

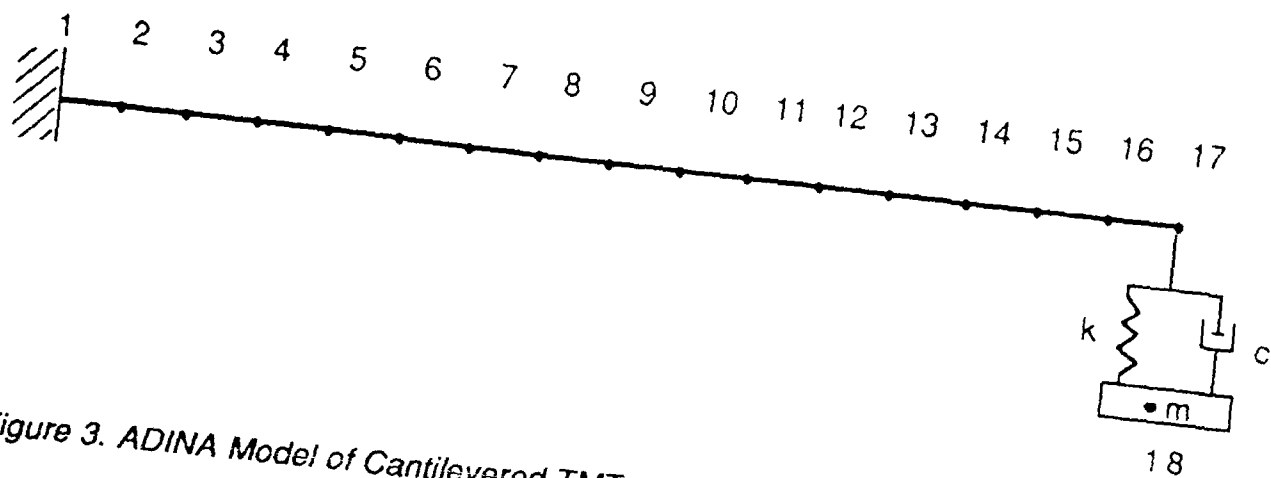


Figure 3. ADINA Model of Cantilevered TMT

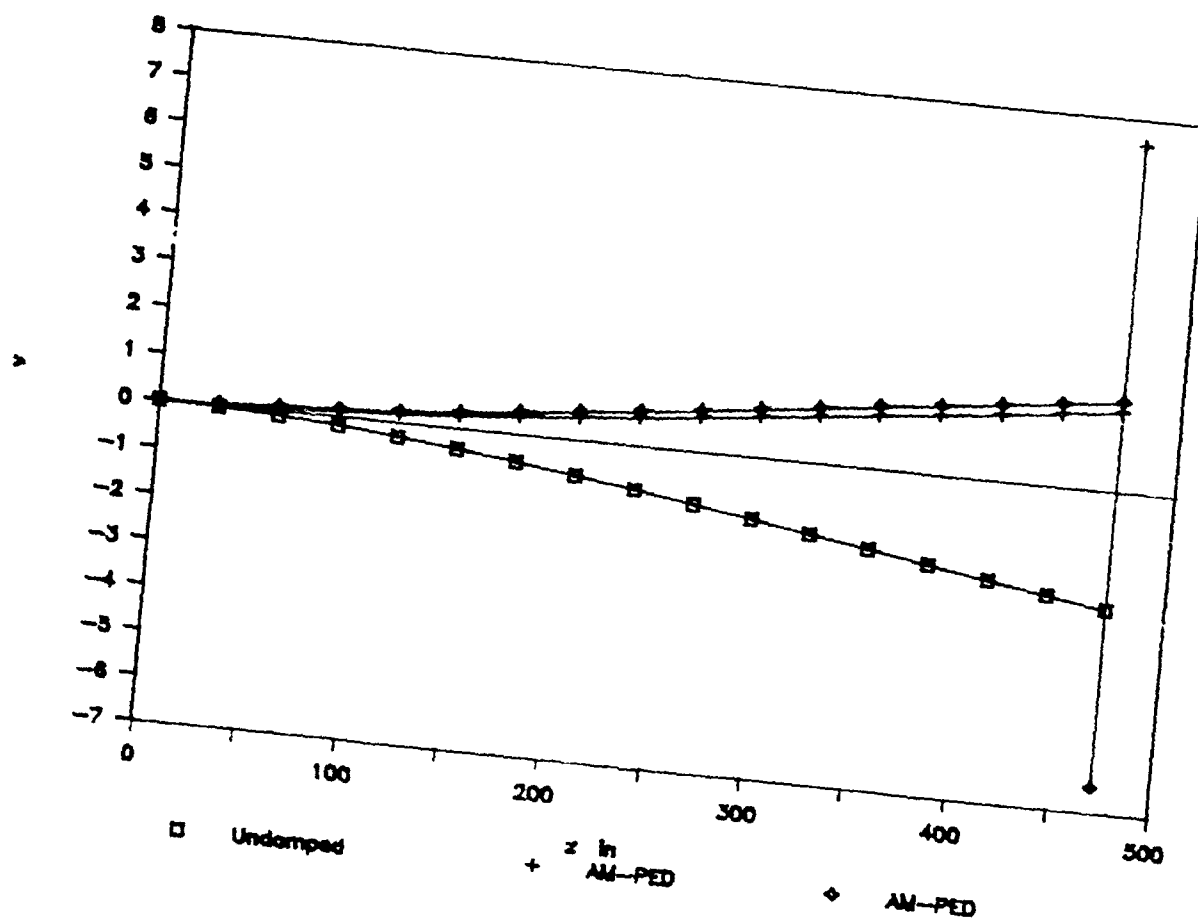


Figure 4. Fundamental Mode of TMT

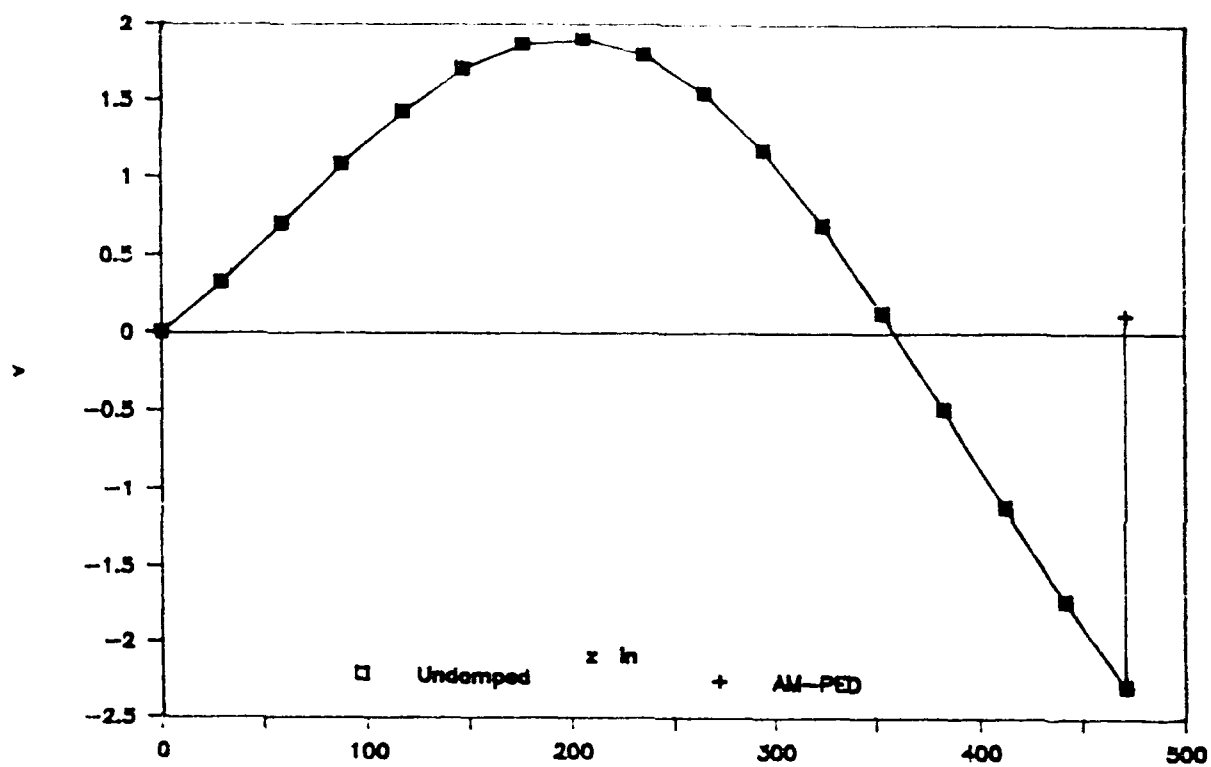


Figure 5. Second Mode of TMT

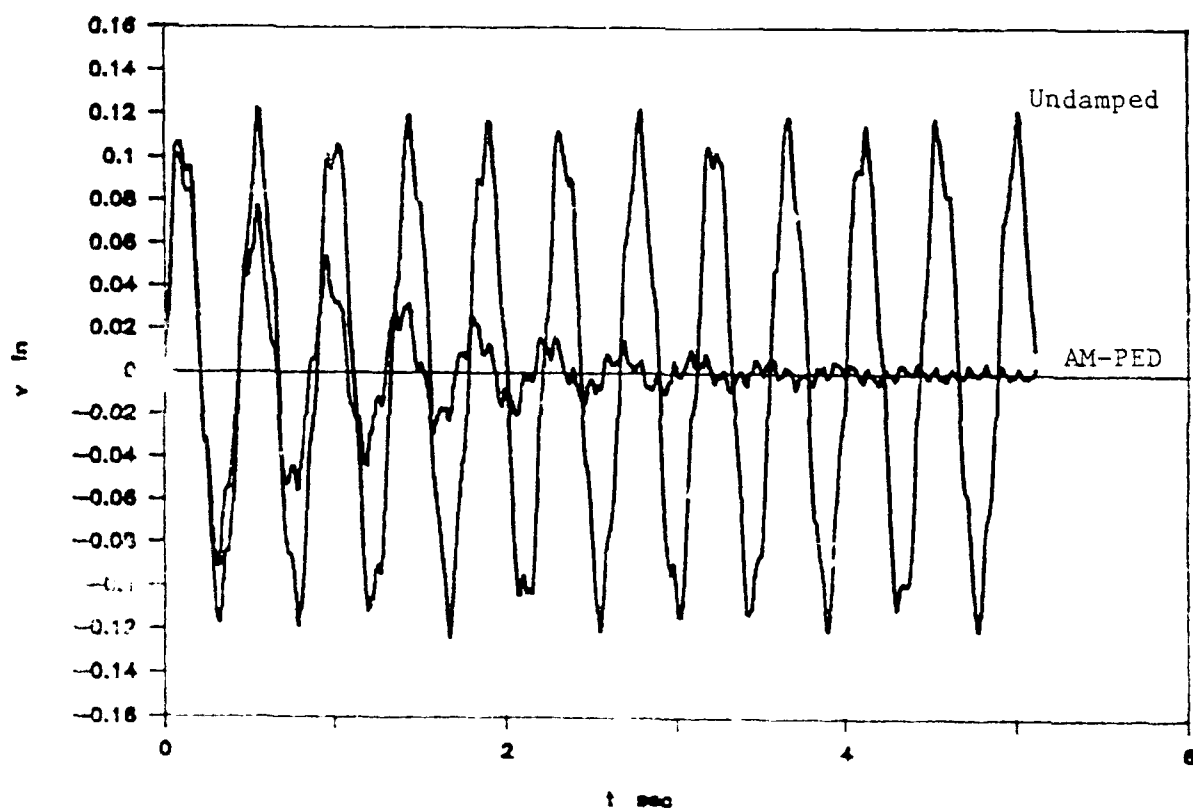


Figure 6. Transient Response of TMT

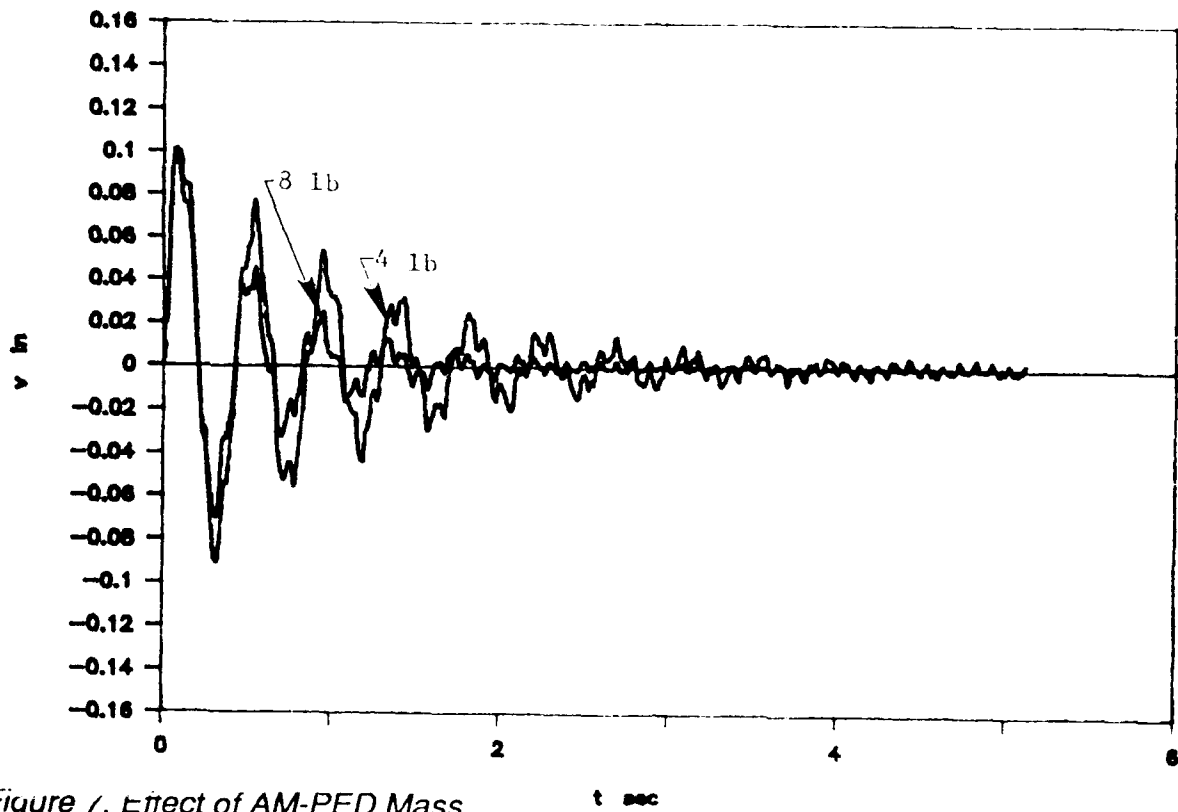


Figure 7. Effect of AM-PED Mass

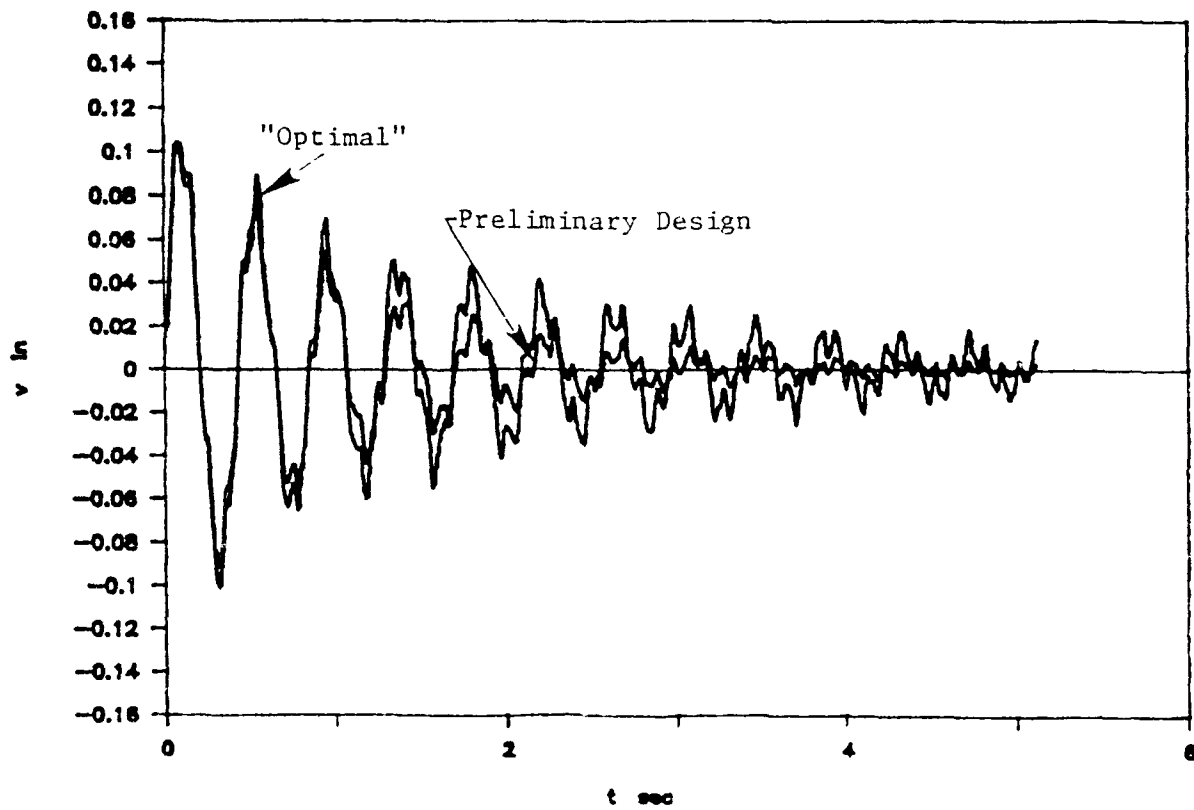


Figure 8. Effect of AM-PED Tuning

5.0. CONCLUSIONS AND RECOMMENDATIONS

In this study the feasibility of Passive Electrodynamic Dampers (PEDs) for Large Space Structures (LSS) has been investigated. The overall conclusion is that preliminary PED designs appear very promising, being competitive and in many ways superior to current active damping and passive damping LSS technologies. The overall recommendation is that a detailed design and experimental test program be undertaken to verify the conclusions of the study. The detailed conclusions of this study are presented below.

The AM-PED operates by converting LSS vibrational energy to the kinetic energy of the magnetic-system mass. This energy is then dissipated through ohmic heating in the armature. Mechanical springs are used as a restoring force and the system is "tuned" to damp over a range of LSS modal frequencies. Because of the simple PED force relationship, analytic LSS damping estimates can be made when analytic LSS modal solutions exist. Computational solutions are required for realistic LSS truss structures which only roughly approximate continuous, analytically-tractable systems.

Besides computationally evaluating the effectiveness of the PEDs it was considered important to compare PED effectiveness with experimental data and pretest predictions for other damping systems. The AFWAL 12 Meter Truss (TMT) experiments were chosen for comparison. The majority of analyzed TMT data is for the low-frequency cantilevered position. The AM-PED, designed according to the analytic analysis, and the TMT were ADINA modeled.

The conclusions of the study are the following:

- (1) The maximum practical LSS c/m ratio is about 500 sec^{-1} in mks units.
- (2) The maximum c/m ratio depends on magnetic system size.
- (3) The dominant effect which reduces c is the dependence of skin depth on the frequency. PED designs should be independent of frequency below 50 Hz.
- (4) PED damping should be independent of amplitude for expected LSS vibrational amplitudes.
- (5) PED damping should vary by only about $\pm 30\%$ over the full 150°C space environment temperature variation.
- (6) Compared to TMT bending-mode, active-damping predictions, for a roughly equivalent weight damping system (8 lbs - actually the total active damping actuator weight was twice the AM-PED weight), the AM-PED is more effective than active damping. The PED damping is expected to be about 11%. The largest active damping is expected to be 9.4% for the first bending mode. The AM-PED is not only expected to be superior to active damping in performance but more reliable and cost effective. The AM-PED doesn't require a power supply, motion sensors or a computer control system.
- (7) The mass efficiency of the AM-PED damper is only slightly decreased (23%) below that of the TMT, for the free TMT (analysis not presented in this paper).
- (8) The AM-PED system is expected to be comparable or superior to VEM strut dampers. VEM systems, in performance, should weigh less and be far superior with respect to reliability, outgassing, and calculability.

REFERENCES

1. ADINA Engineering, Inc., "A Finite Element Program for Automatic Dynamic Incremental Nonlinear Analysis," Users Manual, Vol 1, Report ARD 87-1, Watertown, MA, December 1987.
2. Inhouse Experiments in Large Space Structures Air Force Wright Aeronautical Laboratories Flight Dynamics Laboratory, View Graph Presentation, R. W. Gordon AFWAL/FDSGC, Umit Ozguner and Steven Yurkovich, The Ohio State University.
3. CPT. Michael L. Zeigler, Modal Test Results of a Passively Damped Large Space Structure, Wright Research and Development Center, WRDC/FIBAA, WPAFB, OH 45433, Oct. 1989.
4. Strategic Defense Initiative, 1989 Report to Congress, March 1989, Prepared by SDIO
5. Paul E. McGowan, Harold H. Edighoffer, and John W. Wallace, Development of an Experimental Space Station Model for Structural Dynamics Research, NASA Langley Research Center, Hampton VA, October 1989.
6. Workshop on Advanced Structural Materials for SDI Spacecraft Applications, Session: Vibration Suppression in Spacecraft Applications, Paper: Passive and Active Control of Space Structures, Ken Richards (Martin Marietta)
7. Workshop on Advanced Structural Materials for SDI Spacecraft Applications, Session: Vibration Suppression in Spacecraft Applications, Paper: Overview of L502 Vibration Suppression Program, Lynn Rogers (WRDC/FIBA); Working Group on Vibration Suppression in Advanced Space Structures, Lynn Rogers.
8. Workshop on Advanced Structural Materials for SDI Spacecraft Applications, Session: Vibration Suppression in Spacecraft Applications, Paper: Passive Damping Methods and Applications, Conor Johnson (CSA Engineering); discussions between R. Stettner and Conor Johnson.
9. "Design of Electromagnetic Damping Apparatus", David Taylor U.S. Model Basin, Navy Yard, Washington, DC., Nov. 1930.
10. "Ferromagnetism", R. M. Bozorth, D. Van Nostrand Company, Inc., 1964.
11. "Introduction to Solid State Physics", C. Kittel, John Wiley and Sons, Inc., 1966.
12. The Design of A Passive Electromagnetic Damper of Large Space Structure Vibrations, Advanced Scientific Concepts, Inc., Proposal to SDIO P 100 - 11.3, 12/28/88.
13. US Government Printing Office, "Metallic Materials and Elements for Flight Vehicle Structures," MIL-HNBK 5, Washington, DC, 1962
14. Shock and Vibration Handbook, C.M. Harris and C.E. Crede ed., 2nd Edition 1976, Dynamic Vibration Absorbers and Auxiliary Mass Dampers (F.E Reed Chapter Author).

A METHOD FOR THE MEASUREMENT OF THE COMPLEX COMPRESSIONAL MODULUS OF THIN LAYERS

J. D. Rogers¹
Sandia National Laboratories
Albuquerque, NM

ABSTRACT

A method has been developed for the direct measurement of the complex compressional modulus of thin layers at low frequencies. The test method utilizes an electrodynamic shaker and a special test fixture which maintains the plane strain state of the thin layer. Preliminary tests have been performed on high damping materials with good results. An improved version of the test fixture is being designed to improve the infinitely distant boundary condition simulation.

**FULL PAPER NOT AVAILABLE FOR
PUBLICATION**

¹Sandia National Laboratories, Division 7544, P.O. Box 5800, Albuquerque, NM 87185. (705) 844-7700

THE EVALUATION OF YOUNG'S COMPLEX MODULUS OF VISCOELASTIC MATERIALS

G. OST GUY and M. TARDIF

Ecole Polytechnique, Montreal, Quebec, Canada

The motion of a root-excited cantilever beam coated on both sides with a vibration-damping viscoelastic material is investigated.

Measurements of relative amplitudes and phase lag between the free and driven ends of the beam are used to characterize the variation of the viscoelastic material's complex young's modulus with frequency. Effects of other parameters such as temperature or humidity on the complex modulus can be evaluated provided that tests are done in an environmental chamber.

The method is readily applicable to beams with coatings of viscoelastic material of equal thickness on both sides and also to any beam manufactured out of a single self-supporting material. It is efficient, fast and accurate. It is a valuable alternative to the ASTM E756-83 "Standard Method for Measuring Vibration-Damping Properties of Materials".

Key words: vibration, viscoelastic, damping, complex, modulus
experimental, measurement

INTRODUCTION

Over the years, numerous methods were developed to measure and/or evaluate the damping characteristics of non-linear and/or viscoelastic material. A large share of those methods were used to evaluate experimentally damping properties with the young's complex modulus approach. This is

explained by the fact that simpler analytical developments and experimental rigs are required.

Van Oort [1] and Oberst and Frankenfeld [2,3] first studied the behaviour of thin fixed-free beams coated with viscoelastic materials on one, or both sides (Van Oort only). The relationships derived by Van Oort, because of their assumptions, are not used for the investigation of vibration damping materials having a high loss factor. The work by Oberst and Frankenfeld was aimed at vibration damping materials having a low elastic modulus E and a high loss factor η . The so-called *Oberst beam method* has since been generally accepted and is now standardized by the DIN [4] and the ASTM [5].

Schwarzl analyzed, in a more rigorous manner, vibrations of beams made up of two viscoelastic materials [6]. He concluded that Van Oort and Oberst and Frankenfeld theories were simplified versions of his own approach because, in their assumptions, they had neglected the effects of coupling between flexural and extensional motions. He also pointed out that, for an asymmetric beam made of two materials having different loss factors, the neutral fibre was moving through the cross-section at a frequency twice that of lateral vibrations.

Ross, Kerwin and Ungar's [7] analysis was developed for a three-layer system and included extensional and shear type damping treatments for plates as well as for beams. In the special case of unconstrained damping treatment of a beam (zero thickness of third layer), RKU equations simplify to those reported by Oberst and Frankenfeld.

Nashif [8] developed a method using the Oberst apparatus [9] with a metal supporting beam coated on both sides with equals thicknesses of a viscoelastic material. Bending problems at high -or low- temperature caused by the large difference between thermal coefficient of expansion of viscoelastic materials and metals were eliminated. Surprisingly, no mention to Schwarzl's [6] neutral fibre movement conclusion was made by Nashif to further justify the use of symmetric specimens.

The ASTM has published a "Standard Method for Measuring Vibration-Damping Properties of Materials" [5] which is based on the equations proposed by Oberst and Frankenfeld, Nashif and Ross, Kerwin and Ungar. Unfortunately, these methods contain a number of assumptions that prevent them from being generally applicable.

- The damping effects of the supporting material are neglected;
- Eigenvalues equations are derived without considering the effects of damping (added stiffness, phase lag, etc.);
- The global loss factor is calculated with methods that were developed for lightly damped, single degree of freedom systems (half power bandwidth or logarithmic decrement).

To eliminate the restrictions of existing methods, an approach based on the study of lateral vibrations of root-excited cantilever beams is proposed. It is an extension of the work on damping properties of rigid polymers by Ostiguy and Evar, Iwanowski [10], Horro and Brinson [11], Blau and Lee [12] and Strella [13].

THEORETICAL ANALYSIS

The use of a root-excited beam enables one to use both amplitude and phase lag measurements for the characterization of damping. The viscoelastic material's elastic modulus and loss factor can be determined from experimental measurements, without using any approximations or assumptions. This proves valuable particularly for materials having high loss factors. Symmetric test sections are used so that the neutral fibre is remains in the geometric center of the cross-section and that no thermally induced bending occurs.

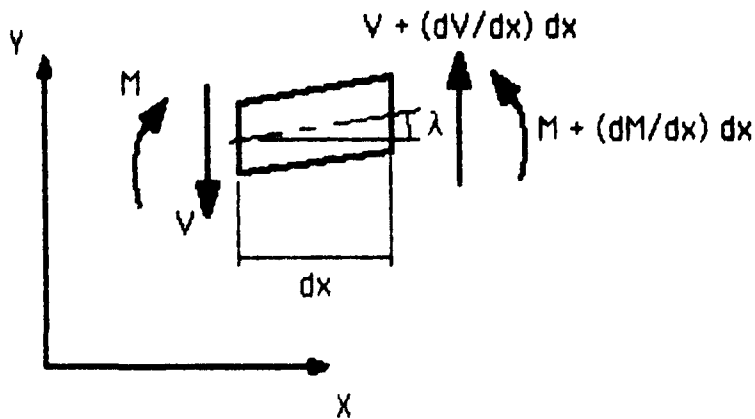


Figure 1: Free body diagram of differential element

A free body diagram of a differential element of length dx of a beam is shown in figure 1. By equating the forces in the Y direction to the corresponding inertia force and by summing the moments about the

element's center of gravity, we obtain the standard equation of motion for Euler beams (shear and rotatory inertia effects neglected)

$$m \frac{\partial^2 y}{\partial t^2} + \frac{\partial^2 M}{\partial x^2} = 0 \quad (1)$$

where m is the mass per unit length. From the classical theory of pure bending of beams, the bending moment is related to the lateral motion through the flexural rigidity term. This equation can be applied to viscoelastic materials by replacing the standard elastic Young's modulus E by the complex modulus E^* . We then have

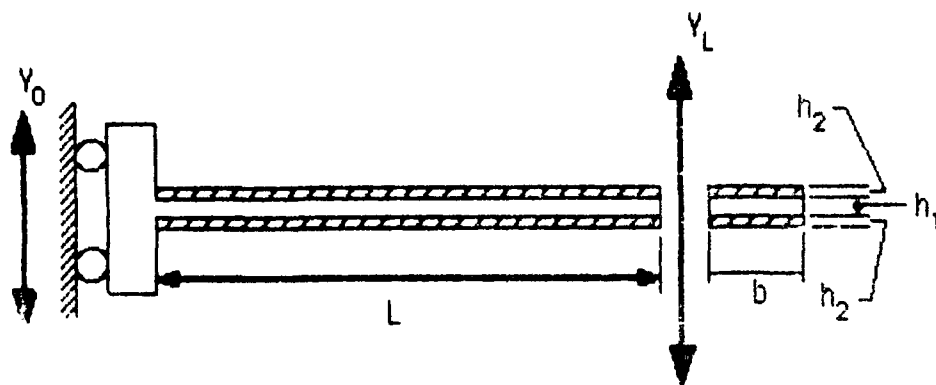


Figure 2: Test beam geometry and test layout

$$M = E^* I \partial^2 y / \partial x^2 \quad (2)$$

Combining equations (1) and (2) we get

$$m \partial^2 y / \partial t^2 + (E^* I) \partial^4 y / \partial x^4 = 0 \quad (3)$$

For the beam shown in the test section schematic view (figure 2), mass, stiffness and inertia properties are

$$m = \rho_1 S_1 + \rho_2 S_2 = \rho_1 b h_1 + 2 \rho_2 b h_2 \quad (4)$$

$$E^* I = E_1 (1 + \eta_1) I_1 + E_2 (1 + \eta_2) I_2 \quad (5)$$

$$I_1 = b h_1^3 / 12 \quad (6)$$

$$I_2 = \rho h_1^2 h_2 / 2 + b h_1 h_2^2 + 2 b h_2^3 / 3 \quad (7)$$

with the use of the following parameters

$$H = h_2 / h_1 \quad (8)$$

$$K_H = 6H + 12H^2 + 8H^3 \quad (9)$$

equations (3) to (7) give

$$12 (\rho_1 + 2\rho_2 H) \partial^2 y / \partial t^2 + h_1^2 [E_1(1+i\eta_1) + K_H E_2(1+i\eta_2)] \partial^4 y / \partial x^4 = 0 \quad (10)$$

By separating space and time solutions and by defining the q parameter as

$$q^4 = \frac{12 (\rho_1 + 2\rho_2 H) \omega^2}{h_1^2 [(E_1 + K_H E_2) + i(\eta_1 E_1 + K_H \eta_2 E_2)]} \quad (11)$$

we have

$$d^4 Y / dx^4 - q^4 Y = 0 \quad (12)$$

For the beam shown in figure 2, the boundary conditions are

$$\begin{aligned} Y &= Y_0 & dY/dx &= 0 & \text{at } x &= 0; \\ d^2 Y / dx^2 &= 0 & d^3 Y / dx^3 &= 0 & \text{at } x &= L. \end{aligned} \quad (13)$$

Only the motion at the free end is of interest. It is found by solving equation (12) with the above boundary conditions and then putting $x=L$. Dividing by the motion at the driven end gives the ratio of amplitude AR and the phase lag θ between the free and driven ends

$$AR e^{-i\theta} = \frac{\cos \Psi + \cosh \Psi}{1 + \cos \Psi + \cosh \Psi} \quad (14)$$

where

$$\Psi = \left[\frac{12 (\rho_1 + 2\rho_2 H) \omega^2 L^4}{h_1^2 ((E_1 + K_H E_2) + i(\eta_1 E_1 + K_H \eta_2 E_2))} \right]^{1/4} = qL = \alpha + i\beta \quad (15)$$

Equation (14) can be transformed into two functions of unknown parameters α and β by equating the real and imaginary parts on both sides of the equation. Once simplified, these two functions are

$$\begin{aligned} AR (1 + \cos \alpha \cos \beta \cosh \alpha \cosh \beta + \sin \alpha \sin \beta \sinh \alpha \sinh \beta) \\ - \cos \theta (\cos \alpha \cosh \beta + \cosh \alpha \cos \beta) \\ - \sin \theta (\sin \alpha \sinh \beta - \sinh \alpha \sin \beta) = 0 \end{aligned} \quad (16)$$

and

$$\begin{aligned} AR (\cos \alpha \sin \beta \sinh \alpha \cosh \beta - \sin \alpha \cos \beta \cosh \alpha \sinh \beta) \\ + \cos \theta (\sin \alpha \sinh \beta - \sinh \alpha \sin \beta) \\ - \sin \theta (\cos \alpha \cosh \beta + \cosh \alpha \cos \beta) = 0 \end{aligned} \quad (17)$$

These non-linear equations are solved numerically by a Newton-Raphson scheme [14]. Reasonably close starting values (α_0, β_0) are required. For that purpose, we define the following two parameters

$$A = \frac{h_1^2 (E_1 + K_H E_2)}{12 (\rho_1 + 2\rho_2 H)} \quad (18)$$

and

$$B = \frac{h_1^2 (\eta_1 E_1 + K_H \eta_2 E_2)}{12 \omega (\rho_1 + 2\rho_2 H)} \quad (19)$$

Equation (12) then becomes

$$(A + i\omega B) d^4 Y/dx^4 - \omega^2 Y = 0 \quad (20)$$

which is identical to equation (10) in Strella's paper [13]. With the current symbols, equations (30), (31) and (32) of Strella become

$$A = \left[\frac{(16 \omega_r L^2)}{(16 a_0^2 - F^2)} \right]^2 \quad (21)$$

$$B = \frac{F L^2}{a_0^3} \frac{(16 \omega_r L^2)}{(16 a_0^2 - F^2)} \quad (22)$$

$$F = \frac{-5.478 + 2 \sqrt{7.502 + 6.15 AR^2}}{1.689 AR^2} \quad (23)$$

where ω_r is a resonant frequency, a_0 is the eigenvalue of the equivalent mode number for a fixed-free beam ($a_0 = 1.875, 4.694, 7.855$, etc.) and AR is as previously defined. Approximate values for E_2 and η_2 are found with equations (18) and (19). These approximations are given by

$$E_{02} = \frac{12(\rho_1 + 2\rho_2 H)A}{K_H h_1^2} - \frac{E_1}{K_H} \quad (24)$$

and

$$\eta_{02} = \frac{12(\rho_1 + 2\rho_2 H)\omega_r B}{K_H h_1^2 E_{02}} - \frac{\eta_1 E_1}{K_H E_{02}} \quad (25)$$

We then obtain from equation (15)

$$\begin{aligned} \alpha_0 &= \sqrt[4]{R} \cos(\phi/4) \\ \beta_0 &= \sqrt[4]{R} \sin(\phi/4) \end{aligned} \quad (26)$$

where

$$R = \frac{12(\rho_1 + 2\rho_2 H)\omega_r^2 L^4}{h_1^2 \sqrt{((E_1 + K_H E_{02})^2 + (\eta_1 E_1 + K_H \eta_{02} E_{02})^2)}} \quad (27)$$

and

$$\phi = \tan^{-1} \frac{(\eta_1 E_1 + K_H \eta_{02} E_{02})}{(E_1 + K_H E_{02})} \quad (28)$$

These starting values α_0 and β_0 are now used to iterate to the final solution for α and β with the Newton-Raphson method. The numerical value of the complex angle $\Psi = (\alpha + i\beta)$ is now known. Again rearranging equation (15), we obtain

$$(E_1 + K_H E_2) + i(\eta_1 E_1 + K_H \eta_2 E_2) = \frac{12 (\rho_1 + 2\rho_2 H) \omega^2 L^4}{h_1^2 (\alpha + i\beta)^4} \quad (29)$$

The numerical values of elastic modulus E_2 and loss factor η_2 of the viscoelastic coating are found by equating the real and imaginary parts on both sides of equation (29). After simplifications, we have

$$E_2 = \frac{12 (\rho_1 + 2\rho_2 H) \omega^2 L^4}{K_H h_1^2} \left[\frac{\alpha^4 + \beta^4 - 6\alpha^2\beta^2}{\alpha^8 + \beta^8 - 6\alpha^4\beta^4 - 4\alpha^2\beta^2(\alpha^4 + \beta^4)} \right] - \frac{E_1}{K_H} \quad (30)$$

and

$$\eta_2 = \frac{12 (\rho_1 + 2\rho_2 H) \omega^2 L^4}{K_H h_1^2} \left[\frac{4\alpha\beta(\beta^2 - \alpha^2)}{\alpha^8 + \beta^8 - 6\alpha^4\beta^4 - 4\alpha^2\beta^2(\alpha^4 + \beta^4)} \right] - \frac{\eta_1 E_1}{K_H E_2} \quad (31)$$

To evaluate the complex modulus $E^*_2(i\omega)$ of a non-self-supporting viscoelastic material, the procedures outlined below must be followed.

- 1- record the following parameters, with appropriate units: L , ρ_1 , h_1 , E_1 , η_1 , ρ_2 and h_2 ,
- 2- evaluate H and K_H with equations (8) and (9),
- 3- record amplification AR , phase lag θ , resonant frequency ω_r and mode number so that Strella's approximate method can be used as a first approximation,
- 4- evaluate A , B and F as per equations (21), (22) and (23) with appropriate resonant frequency ω_r and eigenvalue a_0 .

- 5- evaluate E_{02} and η_{02} with equations (24) and (25);
- 6- find starting values α_0 and β_0 with equations (26), (27) and (28),
- 7- iterate toward final values α and β ;
- 8- evaluate elastic modulus E_2 and loss factor η_2 with equations (30) and (31).

CONCLUSIONS AND RECOMMENDATIONS

When testing a non-self-supporting material, the support beam can be manufactured out of a viscoelastic material because its own damping characteristics were carried throughout the derivation of the equations. For self supporting materials that can be shaped as a beam, the equations defined in this paper are simplified by eliminating all terms containing 2 as a subscript. The equations then become identical as those derived by Ostiguy and Evan-Iwanowski [10].

An experimental setup similar to those used by Ostiguy and Evan-Iwanowski [10] or Strella [13] is recommended. Strella's setup is particularly useful because it allows quick free length changes to be made. The length/thickness ratio should remain greater than 50 so that shear and inertia effects can be neglected. Non-contacting electro-optical or laser instrumentation should be used for amplitude and phase lag measurements. Tests should be done inside an environmental chamber to evaluate the effects of temperature, humidity, vacuum, etc. Frequency and temperature effects can be combined, with the use of a reduced frequency nomogram

[15, 16], to provide a complete description of damping properties of a material on a single chart

The approach proposed in this paper allows one to evaluate quickly and precisely the Young's complex modulus of viscoelastic materials. Additional work is being done to adapt this method for complex shear modulus evaluation. The method can be used for any material, without any restriction. It is fast, accurate and its repeatability has been demonstrated [10]. It brings significant improvements over existing test methods

NOMENCLATURE

a_0	eigenvalues for a clamped-free beam
A, B	parameters defined by equations (18) and (19)
AR	amplitude ratio of free vs driven end
b	beam width (m)
E	elastic modulus, real part of E^* (N/m ²)
E_0	approximate value of E (N/m ²)
E^*	Young's complex modulus (N/m ²)
F	parameter defined in reference [13]
G^*	complex shear modulus (N/m ²)
h	thickness (m)
H	thickness ratio
i	unit imaginary number ($i^2 = -1$)
I	area moment of inertia (m ⁴)
K_H	$= 6H + 12H^2 + 8H^3$
L	free length of beam (m)
m	mass per unit length (kg/m)
M	bending moment (N m)
qL	complex frequency parameter
R	parameter defined by equation (27)
S	cross-section (m ²)
t	time (s)
V	shear force (N)
x	station along beam (m)

$y(x,t)$	transverse displacement of beam (m)
$Y(x)$	vibration amplitude (m)
Y_0	vibration amplitude at driven end (m)
Y_L	vibration amplitude at free end (m)
α, β	real and imaginary parts of Ψ
α_0, β_0	approximate values of α and β
η	loss factor
η_0	approximate value of η
λ	angular deformation (rad)
θ	phase lag between free and driven ends (rad)
ρ	density (kg/m ³)
ϕ	angle defined by equation (28) (rad)
Ψ	complex angle (rad)
ω	circular frequency of vibration (rad/s)
ω_r	resonant frequency (rad/s)
i, j	subscript for beam materials

REFERENCES

1. W.P. Van Oort, "Eine Methode zur Messung der Dynamisch-mechanischen Eigenschaften kleiner plastischer Stoffe," *Microtechnik*, Vol. 7, pp. 246-255, 1953
2. H. Oberst und K. Frankenfeld, "Über die Dämpfung der Biegeschwingungen dünner Bleche durch fest haftende Beläge," *Acustica*, Vol. 2, Beiheft 4, pp. AB 181-194, 1952.
3. H. Oberst, G.W. Becker und K. Frankenfeld, "Über die Dämpfung der Biegeschwingungen dünner Bleche durch fest haftende Beläge II," *Acustica*, Vol. 4, pp. 433-444, 1954
4. DIN, "Biegeschwingungsversuch. Bestimmung von Kengrossen schwingungsgedämpfter Mehrschichtsysteme," DIN 53 440, Blatt 3, 1971
5. ASTM, "Standard Method for Measuring Vibration-Damping Properties of Materials," ASTM E756-83, Annual Book of ASTM Standards, Vol. 04.06, 1989.
6. F. Schwarzl, "Forced Bending and Extensional Vibrations of a Two-Layer Compound Linear Viscoelastic Beam," *Acustica*, Vol. 8, pp. 164-172, 1958.
7. D. Ross, E.E. Ungar and E.M. Kerwin, Jr., "Damping of Plate Flexural Vibrations by Means of Viscoelastic Laminate," *Structural Damping*, ASME, New York, pp. 49-88, 1959
8. A.D. Nashif, "New Method for Determining Damping Properties of Viscoelastic Materials," *The Shock and Vibration Bulletin*, Vol. 36, pp. 37-47, 1967
9. Bruel & Kjaer, Complex Modulus Apparatus, Bruel & Kjaer Type 3930 Instructions and Applications, Bruel & Kjaer, Lyngby, Denmark, 1968.
10. G.L. Ostiguy and R.M. Evan-Iwanowski, On Viscoelasticity and Methods of Measuring Dynamic Mechanical Properties of Linear Viscoelastic Solids, Technical Report No. EP77-R-13, Syracuse University, 1977
11. H. Horio and S. Onogi, "Forced Vibration of Reed as a Method of Determining Viscoelasticity," *Journal of Applied Physics*, Vol. 22, pp. 977-981, 1951
12. C.R. Brand and E.H. Lee, "Calculation of the Complex Modulus of Linear Viscoelastic Materials from Vibrating Reed Measurements," *Journal of Applied Physics*, Vol. 26, pp. 1492-1503, 1955
13. S. Strella, "Vibrating Reed Test for Plastics," *ASTM Bulletin*, May 1956, pp. 47-50

- 14 C.F. Gerald, P.O. Wheatley, Applied Numerical Analysis, third edition, Addison-Wesley, Reading Massachusetts, 1984
- 15 A.D. Nashif, D.I.G. Jones and J.P. Henderson, Vibration Damping, Wiley-Interscience, New York, 1985
- 16 D.I.G. Jones, "Viscoelastic Materials for Damping Applications," AMD-Vol. 38, Damping Applications for Vibration Control, ASTM, New York, pp 27-51, 1980.

ROLE OF MORPHOLOGY IN DAMPING EFFICIENCY

L. H. Sperling¹
Lehigh University
Bethlehem, PA

J. J. Fay
Lehigh University
Bethlehem, PA

D. A. Thomas
Lehigh University
Bethlehem, PA

ABSTRACT

The role of multiphase morphology in damping was explored using interpenetrating polymer networks and latex blends. Several polymer combinations were employed as model materials. These included acrylics and methacrylics, styrenics, polybutadiene, and poly(vinyl methyl ether). The loss area, LA, under the E'' -temperature curves was measured on a Rheovibron at 110 Hz. The results were compared to one-phased statistical copolymers.

Several IPN compositions were found which damp more than expected, based on the group contribution analysis found to hold for homopolymers and one-phased statistical copolymers. The damping increases are interpreted in terms of phase continuity and stiffness. In general, high $\tan\delta$ values would be expected in morphologies where the lower glass transition polymer forms the continuous phase, and the higher glass transition polymer forms the discontinuous phase.

**FULL PAPER NOT AVAILABLE FOR
PUBLICATION**

¹Lehigh University, Whitaker Laboratory #5, MRC, Bethlehem, PA 18015, (215) 758-3845

THE THERMORHEOLOGICALLY COMPLEX MATERIAL

Ronald L. Bagley¹
Air Force Institute of Technology
Wright-Patterson Air Force Base, OH

ABSTRACT

An approximate quantum mechanical description of molecular energy transitions leads to fractional order time derivative descriptions of linear viscoelastic stress relaxation in polymers. The resulting fractional calculus stress-strain constitutive laws are mathematically compact and suitable for rheological and engineering analyses. The mathematical form of the models suggests a modification to the thermorheologically simple material that enables the description of temperature-dependent changes to the shape of curves representing a material's modulus in the transition region. The fractional calculus models are seen to be extensions of the traditional exponential models of stress relaxation.

ACCEPTED FOR PUBLICATION IN THE
International Journal of Engineering Science, 1991

¹Professor of Mechanics, Department of Aeronautics and Astronautics, Air Force Institute of Technology, Wright-Patterson AFB, OH 45433, (513) 270-3517

METHODS OF REDUCTION OF WIND INDUCED DYNAMIC RESPONSE IN SOLAR CONCENTRATORS AND OTHER SMALL LIGHTWEIGHT STRUCTURES

Monte A. McGlaun
LaJet Energy Company

ABSTRACT:

Wind tunnel studies indicate that solar concentrator structures with low damping properties are susceptible to dynamic wind loading characteristic of the earth's boundary layer. Solar concentrators are sensitive to deflections in optical systems and can be costly when required to have minimal deflections. The cost and performance characteristics can be improved through structural design approaches to reduce dynamic response. This study evaluates the benefits of various methods to control dynamic response: passive damping, multiple supports, friction connections, mass alterations, and beam length modifications.

The Modal Strain Energy Method (MSEM) is an efficient analysis tool for evaluating overall structural damping on complex structures. Modal strain energies were found using a finite element analysis structural program. The MSEM was used to analyze the complex structure of the LaJet Energy LEC 1900 Solar Concentrator. MSEM methodologies are described in-depth.

Viscoelastic (passive) damping and bracing were found most efficient at reducing dynamic response in the structure. Braces were located to develop large modal strain energies. When bracing and damping were located to develop high modal strain energy for particular modes, system loss factors were notably improved. Damping was effective when radial girders were dynamically involved in the mode shape definition.

Monte A. McGlaun, P.E.
Director of R & D
LaJet Energy Company
3130 Antilley Road
Abilene, TX 79606
(915) 698-8800

1.0 INTRODUCTION

1.1. PROJECT OBJECTIVE: *To apply the modal strain energy method (MSEM) to design damping and bracing to achieve greater dynamic stability in a large solar concentrator dish.*

1.2. FUNDING OF STUDY: SBIR Program, DOE Contract No. DE-AC05-87/ER80519
DOE Report No. DOE/ER/80519-1

1.3. BACKGROUND

LaJet Energy has designed, built, tested, and marketed solar concentrators since 1978. In 1983 and with internal dollars and private funding LaJet Energy designed and built SOLARPLANT 1, a solar thermal electric-generating power plant at Warner Springs, California with 700 LEC 460 solar concentrators.

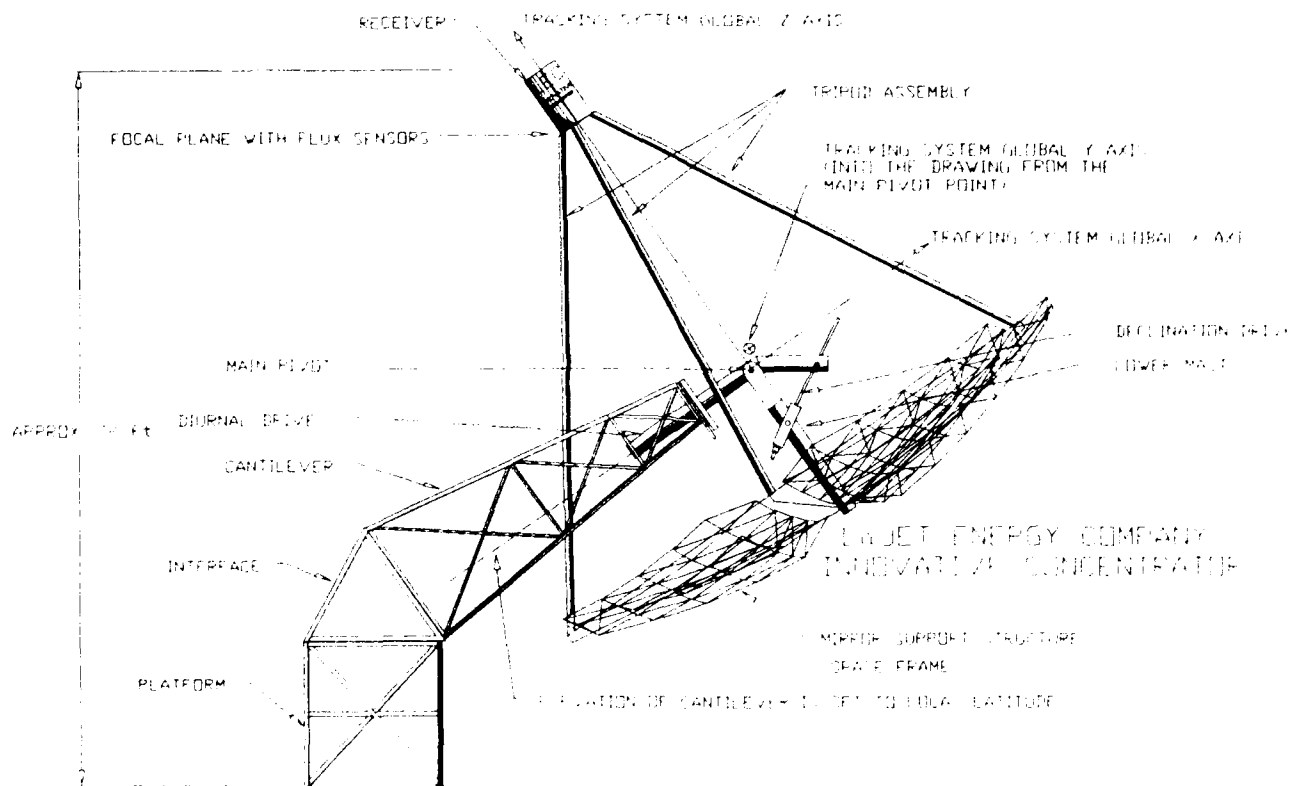


Figure 1 - LaJet Energy's DOE Innovative Concentrator Overall Side View
(from the east)

LaJet Energy's solar concentrator technology is licensed to Cummins Power Generation (a wholly owned subsidiary of Cummins Engine Company) for worldwide sales for electrical production. Cummins is funding the commercialization of a free-piston Stirling engine - solar concentrator electrical production system. The project is in the second year of a five year program.

The structural design used in this study is designated the *Large Scale Innovative Concentrator* (IC). LaJet Energy designed the IC under U. S. Department of Energy (DOE) cost-share agreement (DE-FC04-85 ET30171).

The *IC* accommodates 95 silver polymer film mirrors to reflect 135kw_{th} through a 20 inch diameter aperture. Figure 1 shows the *IC* at solar noon and at the vernal or autumnal equinox. The structure is comprised of a stationary support system and a tracking support system. The platform, interface, and cantilever are the stationary structure. The lower mast, girders, space frames, mirror facets, tripods, and receiver are the tracking assembly.

The tracking functions are performed under microprocessor control that operates one or both of the two drive motors to keep the optical axis (global z axis) pointed to the sun. The array of concave mirrors reflects and focuses the incoming solar radiation into an opening in the bottom of the receiver. The receiver can be any device designed to accept concentrated solar radiation for a purpose such as creating steam, generating electricity, or high temperature materials processing.

2.0 STRUCTURAL LOADING

2.1. GRAVITY

The LaJet Energy solar concentrator structures have high strength-to-weight ratios; therefore, gravity loading is usually secondary to wind loading. Ice and snow loading in the northern tier locations may be large and require special design situations (*solar devices are more likely to be located in warmer climates*).

2.2. WIND

Wind is characterized as a spectral loading, and the majority of energy imparted occurs at excitation frequencies up to 30 Hz. Since solar dishes have very large surface areas, wind is the primary loading. Wind forces near the earth have a turbulent boundary layer with characteristics that depend on the roughness of the surrounding terrain. A model of the structure under study was tested in the boundary layer wind tunnel at Colorado State University to determine the loads at the main pivots of the tracking array but not the distributed loads [19].

2.3. APPLICATIONS

For example free piston Stirling engines are currently being tested on the LaJet Energy Concentrators by Cummins Power Generation. The engine operates at 60 Hz and a .5 mm amplitude. The mass of the associated engine mounting components on the solar concentrator reduce the amplitude by the inverse ratio of the masses. The concentrators have not exhibited destructive modes in the region of 60 Hz. Application dynamic loading is less of a design issue than gravity considerations.

2.4. SEISMIC

The primary destructive mode of seismic activity is through the application of lateral forces. Since the dish is designed for wind acting as a large lateral load and since the dish has a high strength-to-weight ratio, seismic loading is always evaluated by is typically a secondary factor of design.

3.0 ANALYTICAL MODEL DEVELOPMENT

3.1. FINITE ELEMENT ANALYSIS (IMAGES 3D)

IMAGES3D Finite Element Analysis Program is a copyright of Celestial Software, Inc., 125 University Avenue, Berkeley, CA 94710, telephone (415) 420-0300 [13]. The distribution of the components of the finite element model of the tracking portion of the *IC* is shown. All materials used in the *As-Designed* model were steel. The components of the *IC* have been sized, modeled, and constructed as shown in the tables following:

696 node points to describe the geometry	
986 beam elements drawn from 20 different cross-sections	
290 plate elements to describe the 18 inch diameter, 3/4 inch wall Lower Mast.	
Girders	5.56" O.D. x .188" wall
Tripods	8.625" O.D. x .188" wall
Space Frame Beams	a. 1.00" O.D. x .035" wall b. 1.25" O.D. x .035" wall c. 1.163" O.D. x .057" wall d. 1.510" O.D. x .065" wall
Lower Mast	18" O.D. x .75" wall
Simulated Engine Weight	4,400 lb _f at z = 509 inches

Table 1 - Structural & FEM Components for the *As-Designed IC*

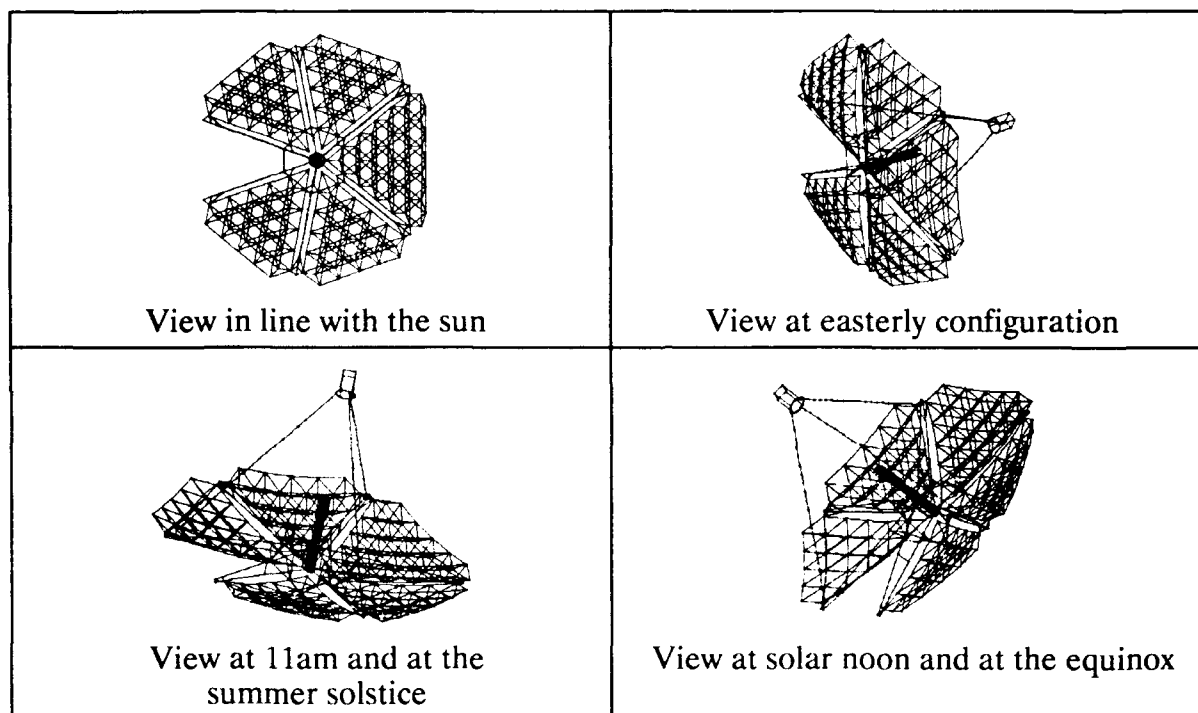


FIGURE 2 - IMAGES3D Plots of the *IC* Tracking System

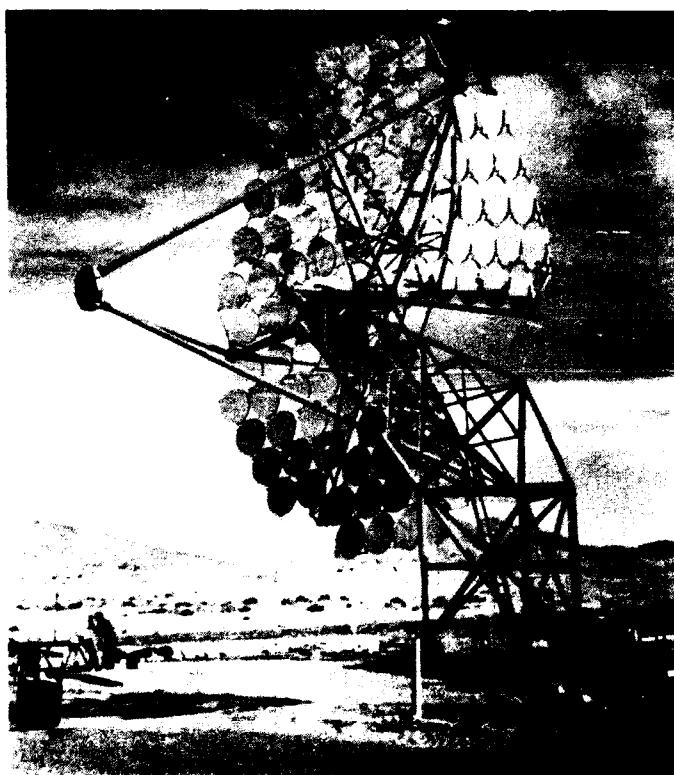


FIGURE 3 - PHOTO OF *IC* IN THE ORIGINAL CONFIGURATION IN WESTERLY CONFIGURATIONS

3.2. MODAL STRAIN ENERGY COMPUTATION

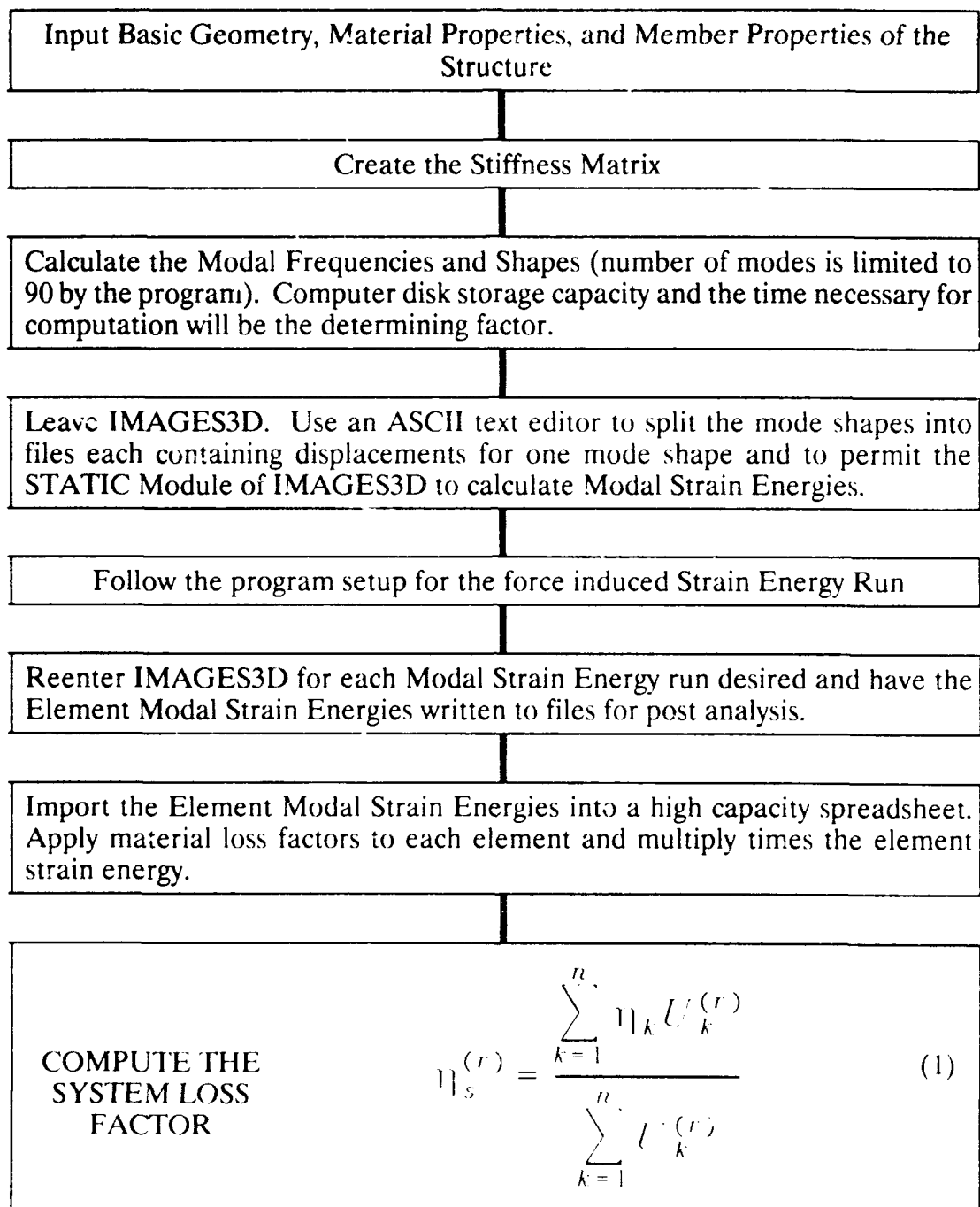


TABLE 2 - Modal Strain Energy Analysis Flow Chart

In the following tables, successive derived mode shapes are presented graphically. The center panel is the undeformed geometry, the left panel subtracts 100 times the modal deflections, and the right panel adds 100 times the modal deflection. Therefore, a sense of the computer mode shape animation can be derived from looking left to right. For the *As-Built* analysis the material loss factor, η , is taken at a very low value of .001 since all materials are metal.

3.3. AS-DESIGNED MODAL ANALYSIS

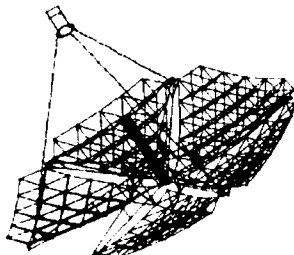
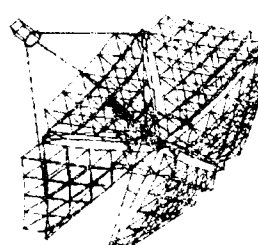
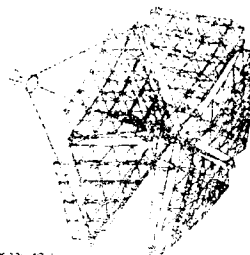
MODE 1					
					
System Loss Factor, $\sum \eta_k$				0.001	Modal Frequency = 0.24052 Hz
System Strain Energy, $\sum U_k^{(1)}$				0.226287	
System Loss Product, $\sum \eta_k U_k^{(1)}$				9.000226	
Element				Description	
No.	Strain Energy, $U_k^{(1)}$	η_k	Descending Sort of Component Loss Factors, $\eta_k U_k^{(1)}$	Component	Portion of Component
711	3.77028E-06	0.001	3.77028E-09	GIRDER 1	Top
769	1.64302E-06	0.001	1.64302E-09	GIRDER 3	Top
721	1.48344E-06	0.001	1.48344E-09	GIRDER 1	Mid Vert Tie
719	1.45392E-06	0.001	1.45392E-09	GIRDER 1	Bottom
712	1.28791E-06	0.001	1.28791E-09	GIRDER 1	Top
710	1.26862E-06	0.001	1.26862E-09	GIRDER 1	Top
722	1.26787E-06	0.001	1.26787E-09	GIRDER 1	Outboard Vert Tie
718	1.23123E-06	0.001	1.23123E-09	GIRDER 1	Bottom
776	9.42109E-07	0.001	9.42109E-10	GIRDER 3	Bottom
708	9.02250E-07	0.001	9.02250E-10	GIRDER 1	Top
768	8.78665E-07	0.001	8.78665E-10	GIRDER 3	Top
766	7.76672E-07	0.001	7.76672E-10	GIRDER 3	Top
715	7.38142E-07	0.001	7.38142E-10	GIRDER 1	Bottom
779	6.75916E-07	0.001	6.75916E-10	GIRDER 3	Mid Vert Tie
717	6.18575E-07	0.001	6.18575E-10	GIRDER 1	Bottom
709	5.61057E-07	0.001	5.61057E-10	GIRDER 1	Top
773	5.00326E-07	0.001	5.00326E-10	GIRDER 3	Bottom
767	4.43813E-07	0.001	4.43813E-10	GIRDER 3	Top
775	3.82166E-07	0.001	3.82166E-10	GIRDER 3	Bottom
777	3.66264E-07	0.001	3.66264E-10	GIRDER 3	Bottom

Figure 4 - Undamped Mode Shape 1 of As-Designed IC

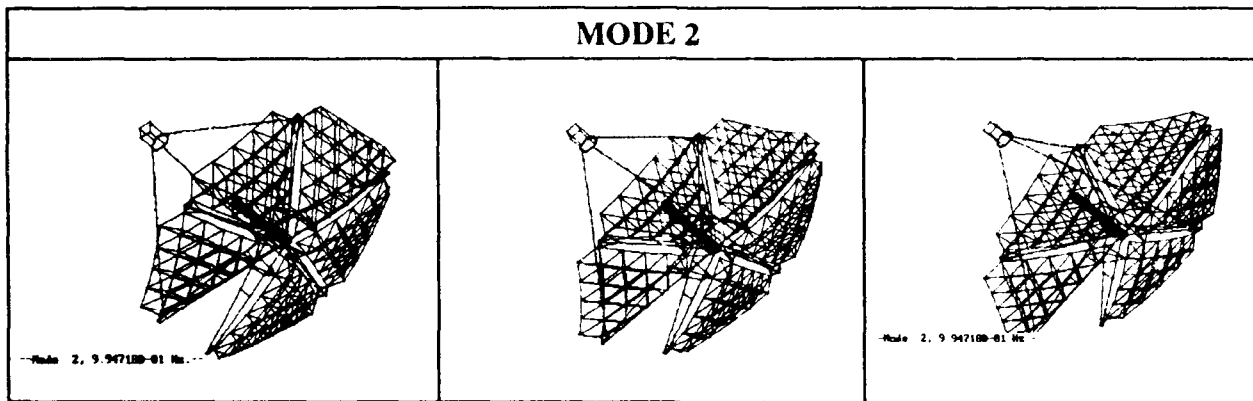


Figure 5 - Undamped Mode Shape 2 of *As-Designed IC*

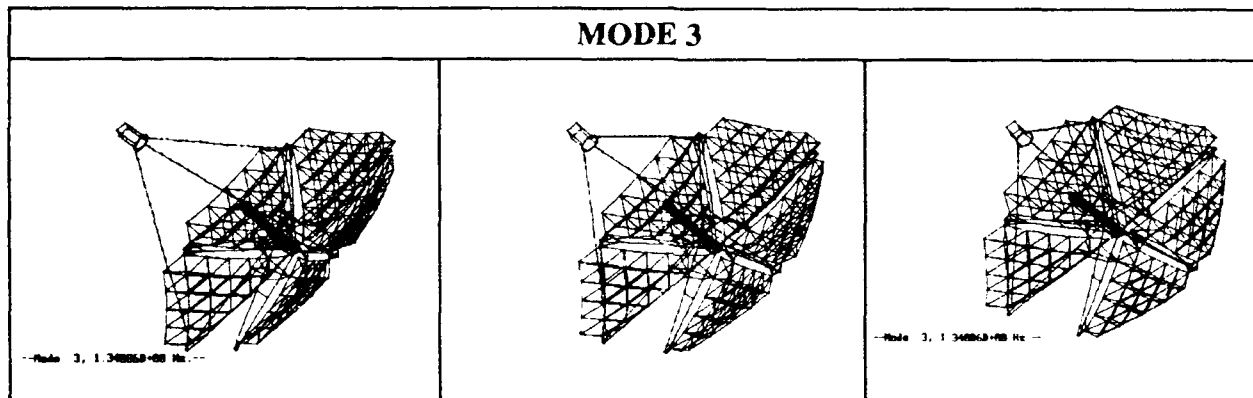


Figure 6 - Undamped Mode Shape 3 of *As-Designed IC*

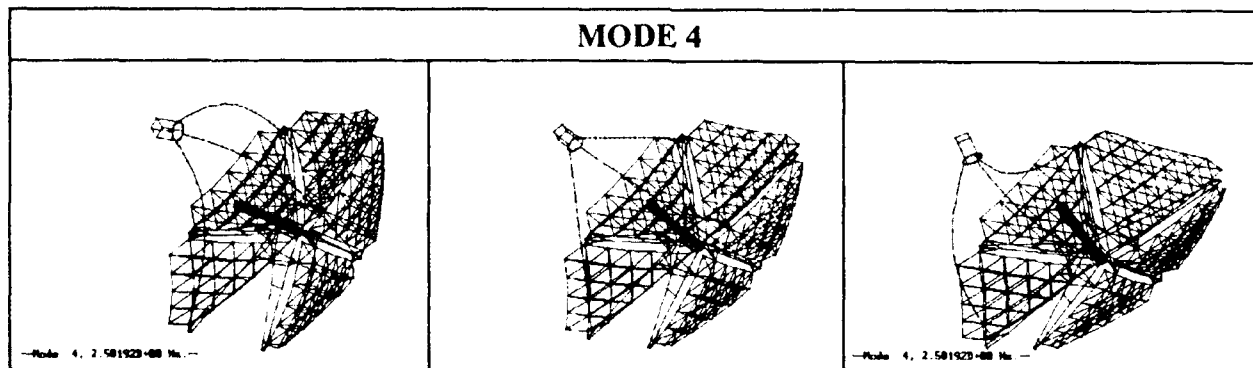


Figure 7 - Undamped Mode Shape 4 of *As-Designed IC*

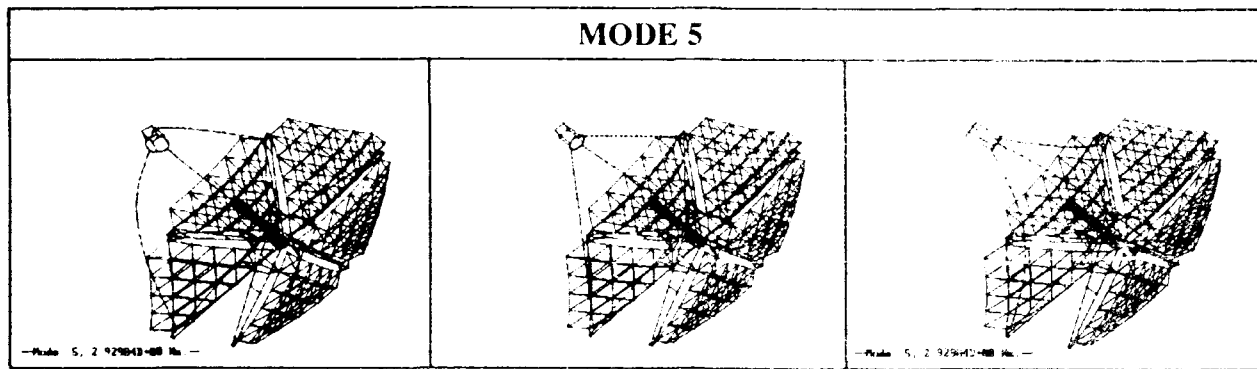


Figure 8 - Undamped Mode Shape 5 of As-Designed IC

4.0 STRUCTURAL BRACING AND DAMPING

Figures show stiffeners and dampers for the Girders and Tripods on the Innovative Concentrator. Two options were analyzed: *stiffeners only* and *stiffeners with dampers*. A choice was made based on experience with the IC structure to install stiffeners and dampers sized as shown in the Table.

Stiffeners	3" O.D. with .086" wall, $A = .7854 \text{ in}^2$, $I = .8345 \text{ in}^4$
Viscoelastic Dampers	6" O.D. with $A = 28.3 \text{ in}^2$, $I = 3.98 \text{ in}^4$, thickness = .25" of $\eta = 1.0$ material, Two .375" steel plates

Table 3 - Stiffener and Damper Selections

Young's Modulus, linear elastic	$E = 1.0833 \text{ ksi}$
Weight density	$\rho_f = .001 \text{ lb}_f/\text{in}^3$
Poisson's Ratio	$\nu = .3$
Shear Modulus, linear elastic	$G = .4117 \text{ ksi}$
Coeff. of Thermal Expansion	Not Used

Table 4 - Viscoelastic Material Properties Used in FEA

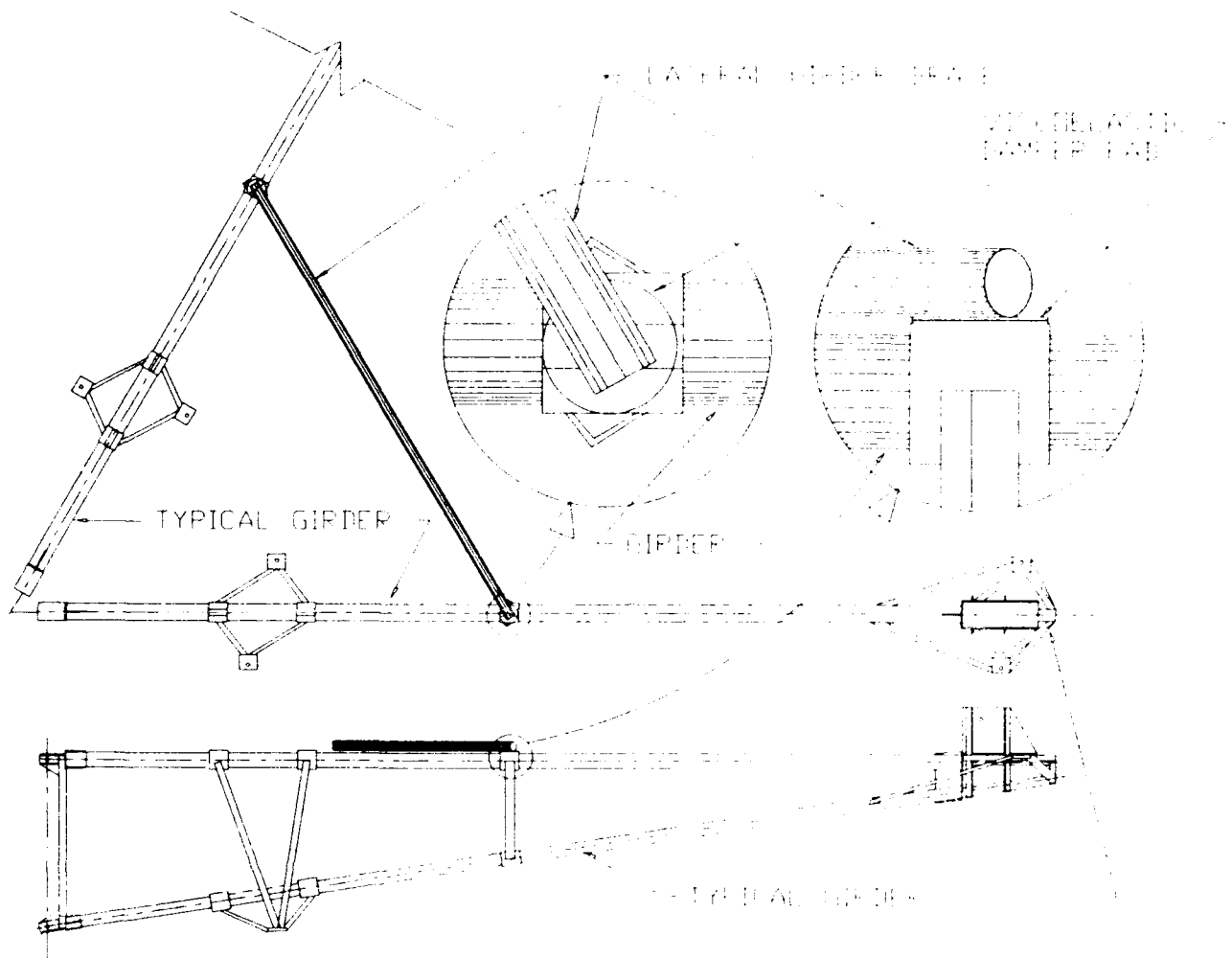


Figure 9 - Stiffening & Damping of Lateral Modes in the Girders

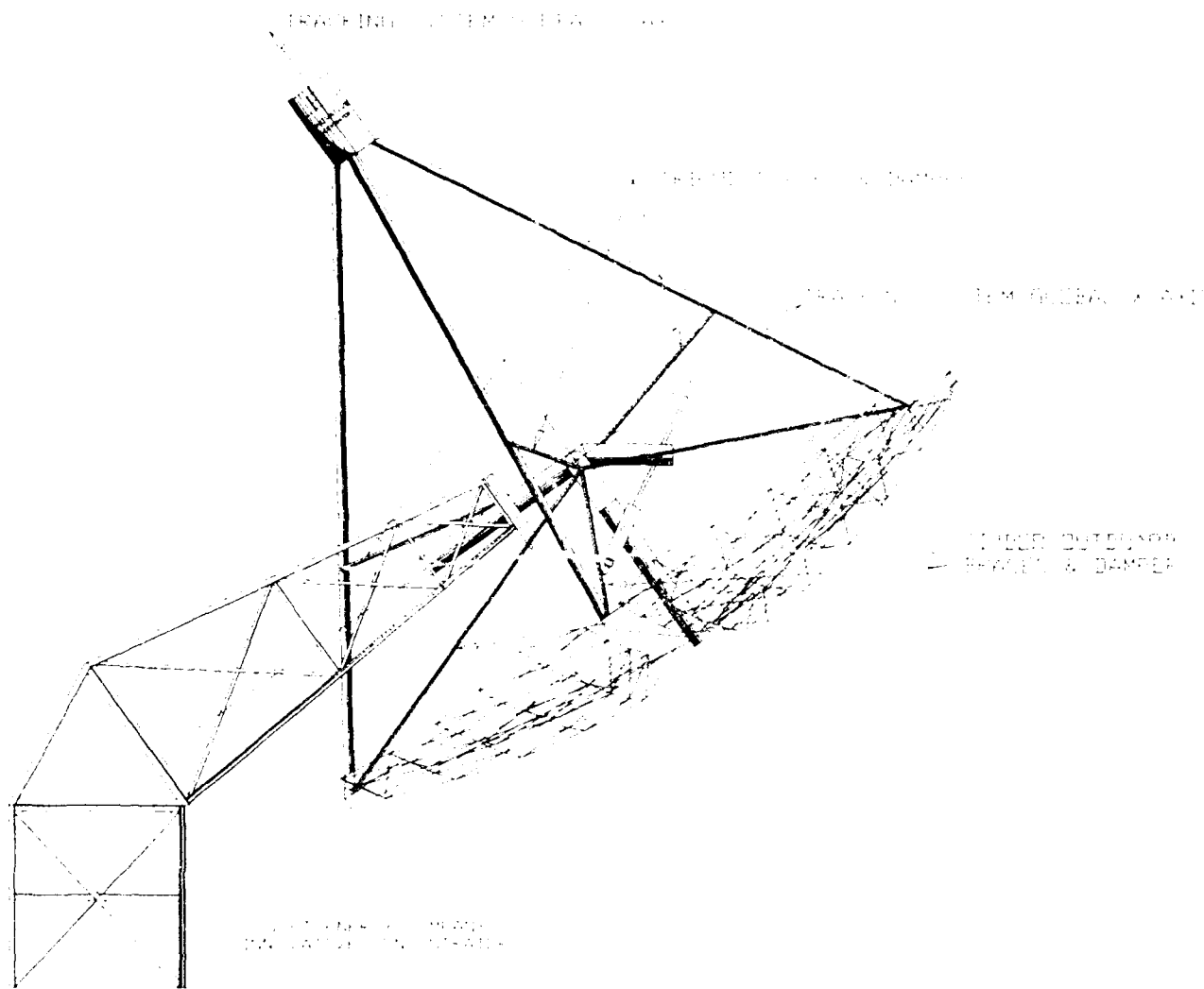


Figure 10 - Tripod In-Plane & Girder Vertical Stiffeners & Dampers

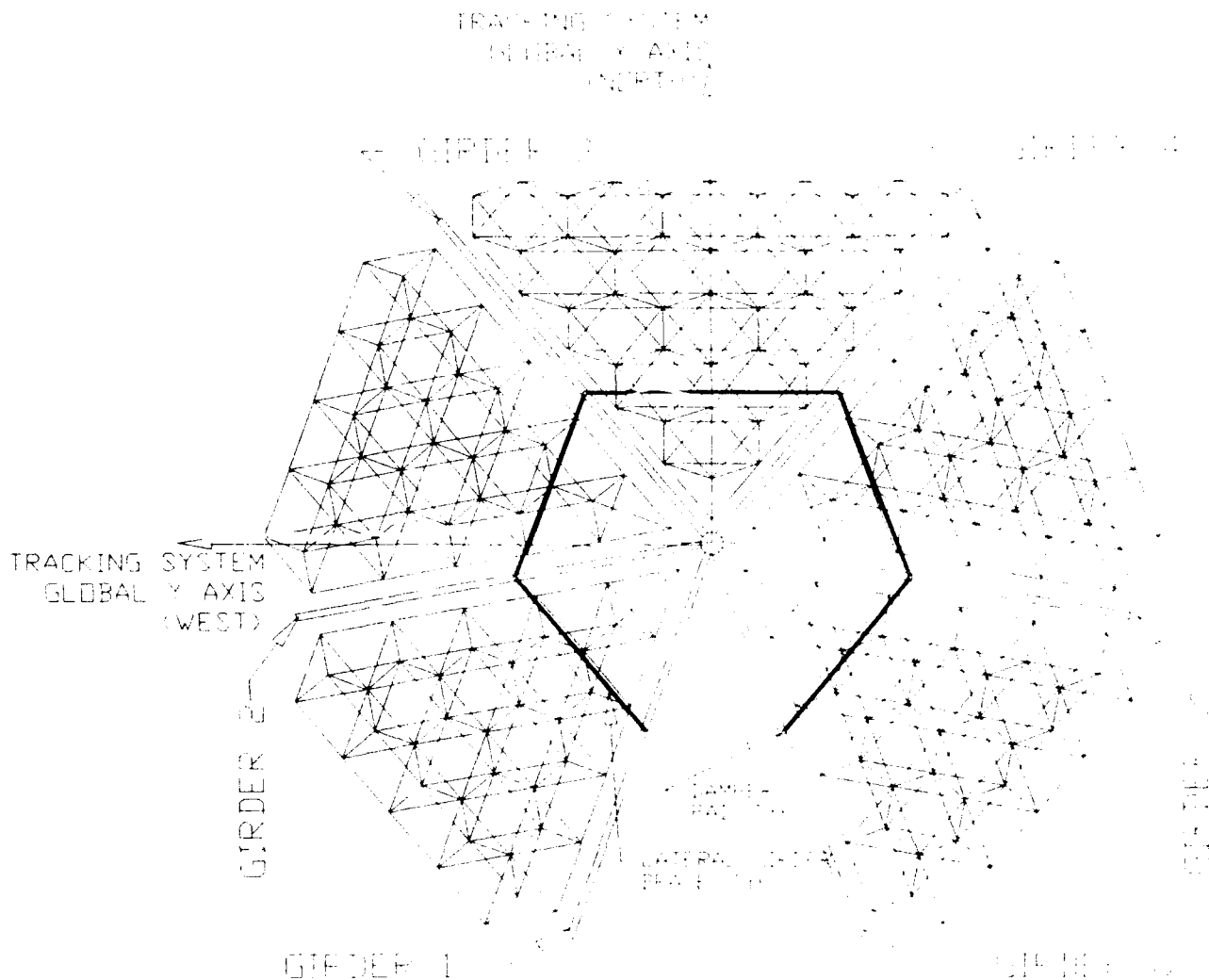


Figure 11 - Girder Lateral Stiffener Positions

5.0 DAMPED AND STIFFENED RESULTS

The following mode is a typical indication that the damper location was selected correctly to develop largest strain energies. With the high loss factors of a viscoelastic damper, the loss product sum for the structure is much larger than for the undamped structure. Note that the system loss factor is dramatically increased with the addition of a dampers in relatively few locations.

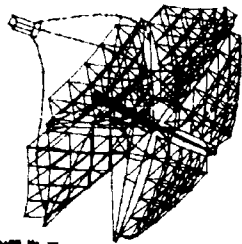
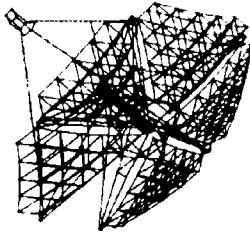
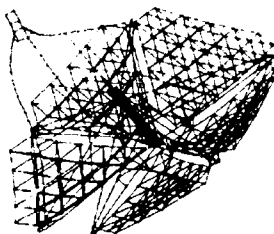
MODE 5					
					
System Loss Factor, $\sum \eta_k$			0.16739	Modal Frequency	
				3.68319 Hz	
System Strain Energy $\sum U_k^{(r)}$			1.774E+03		
System Loss Product, $\sum \eta_k U_k^{(r)}$			2.970E+02		
Element				Description	
No.	Strain Energy, $U_k^{(r)}$	η_k	Descending Sort of Component Loss Factors, $\eta_k U_k^{(r)}$	Component	Portion of Component
982	2.20234E+02	1	2.20234E+02	DAMPER	Girder 3 Outbrd Active
988	1.56167E+02	0.001	1.56167E-01	BRACES	Girder 3 Outbrd
766	5.80972E+01	0.001	5.80972E-02	GIRDER 3	Top
980	5.07246E+01	1	5.07246E+01	DAMPER	Girder 1 Outbrd Active
773	3.83241E+01	0.001	3.83241E-02	GIRDER 3	Bottom
986	3.65928E+01	0.001	3.65928E-02	BRACES	Girder 1 Outbrd
776	3.48538E+01	0.001	3.48538E-02	GIRDER 3	Mid Vert Tie
907	2.92025E+01	0.001	2.92025E-02	POD 1	
906	2.39679E+01	0.001	2.39679E-02	POD 1	
765	2.21329E+01	0.001	2.21329E-02	GIRDER 3	Top

Figure 12 - MODE SHAPE 5 OF DAMPED AND STIFFENED IC

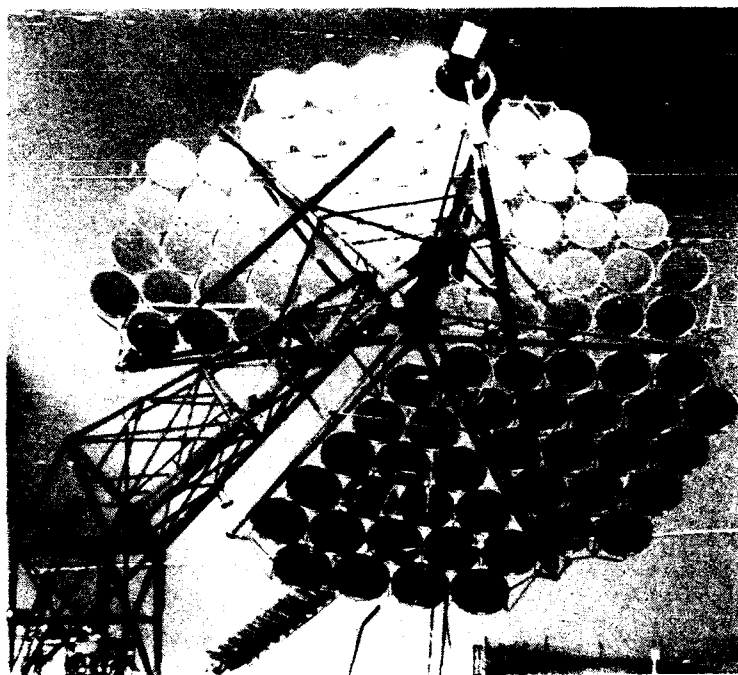


FIGURE 13 - PHOTO OF IC IN THE STIFFENED CONFIGURATION

The modal frequency of a single degree-of-freedom mass-spring-damper system is $\omega = (k/m)^{1/2}$. Therefore, it is to be expected that the addition of bracing to the Innovative Concentrator structure will raise the modal frequencies. Since hysteretic damping is modeled as a very low stiffness element within the finite element model, damping should reduce the modal frequencies below the *stiffened only* model. The Figure below is a plot of the modal frequencies for the three cases analyzed and for the first fifteen modes, and shows that the expected trends in modal frequency occur as expected. The frequencies follow the same general tendency until Mode 10 where the Tripod excitation dominates the response. In the *stiffened only* and *damped and stiffened* runs, the Tripod members are braced which raises the resonant frequency.

Modes 1 and 2 are essentially the same for all the structural cases explored. Mode 1 has a 41.7 second period which is accompanied by low excitation energy. Mode 2 is readily observed on both the LEC 460 and the IC and is a gross rotation about the z-axis (optical axis) of the dish. The z-rotation results in a widely distributed low stress level.

Dampers on the *in-plane* Tripod braces did not develop large strain energies for any of the modes. Consequently, where the mode shapes involved large modal activity of the Girders, the system loss factor was high. Conversely, if the Tripod modal strain energies dominated the mode shape summary, then the system loss factor was low. The graph in Figure below shows the system loss factor for each Mode. Note that Modes 3, 5, 6, 7, 9, and 10 have large Girder related modal strain energies and, as a result, have larger system loss factors.

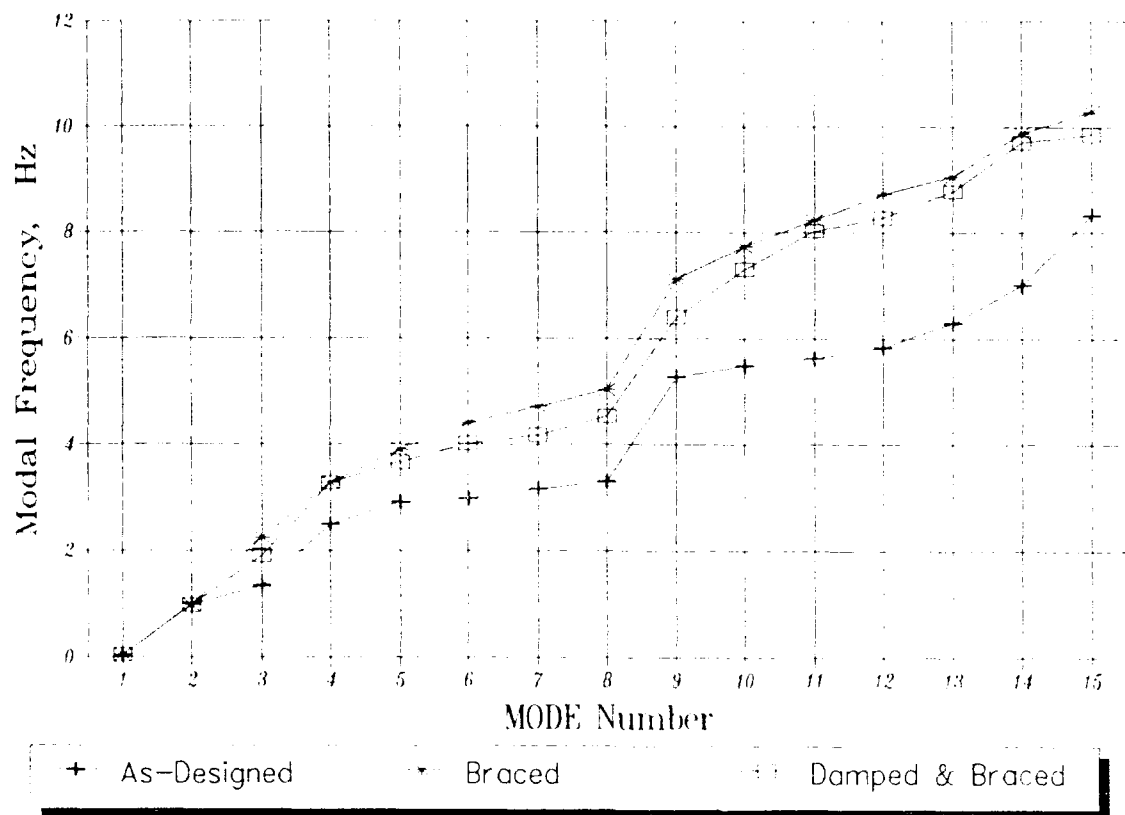


Figure 14 - Modal Frequencies

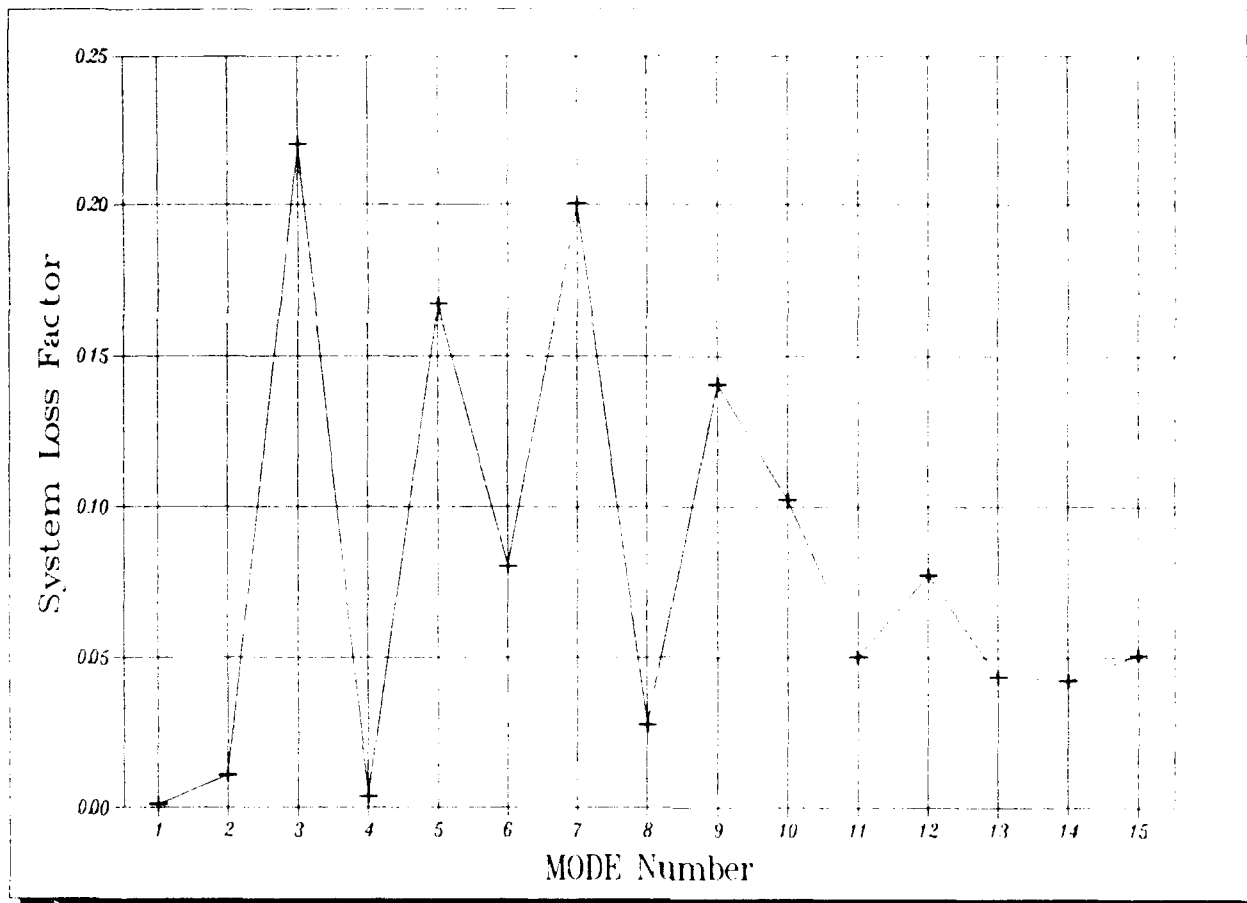


Figure 15 - System Loss Factors vs. Mode Numbers

Modal strain energy is developed in all portions of the structure. The Lower Mast was modeled with plate elements while the balance of the structure was modeled with beam elements. The strain energy associated with the Lower Mast was lower for all modes but Modes 1 and 2. Damping would be difficult to apply to the Lower Mast, and its lower modal strain energy values indicate that damping the Lower Mast would be marginally effective in increasing the system loss factor and reducing dynamic response. Therefore, damping was not considered for the Lower Mast in this study. The Figures below show the total modal strain energy by mode for both beam and plate elements for each analysis.

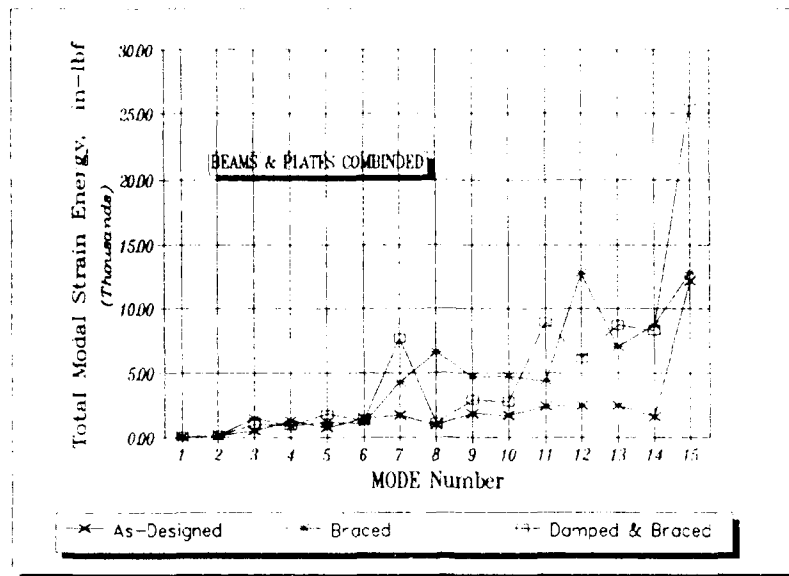


Figure 16 - Total Modal Strain Energy by Mode Number

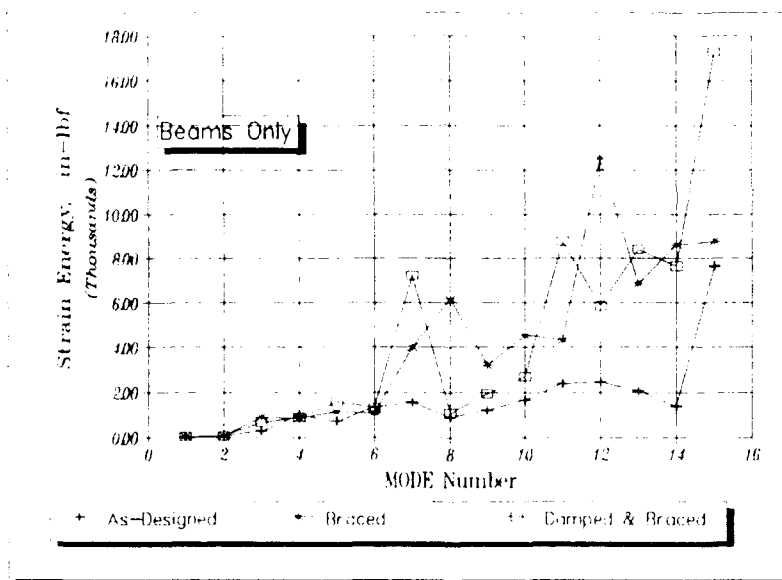


Figure 17 - Total Beam Modal Strain Energy by Mode Number

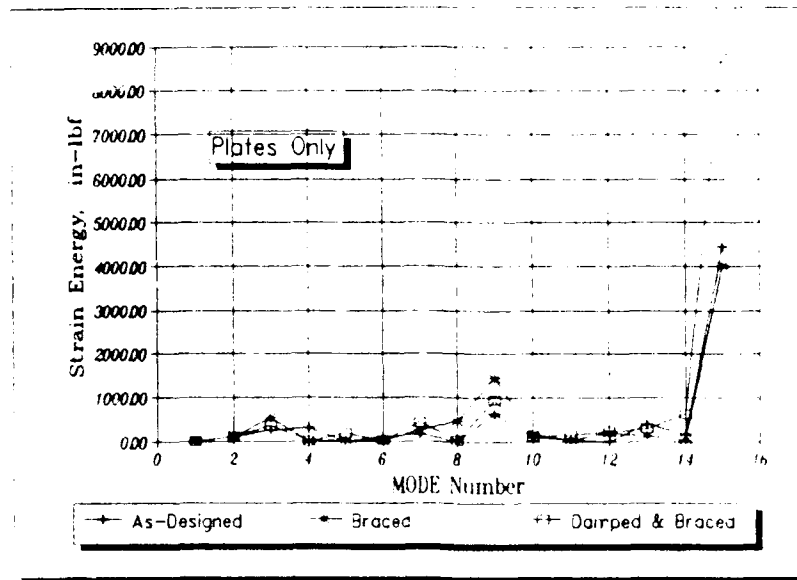


Figure 18 - Total Plate Modal Strain Energy by Mode Number

6.0 CONCLUSIONS & OBSERVATIONS

- The MSEM is efficient and easily implemented for complex structures.
- The MSEM is an effective means to identify wind induced modal deflections that can effect the optical stability of solar concentrators.
- Bracing to reduce modal deflections was identified by the MSEM was installed on the structure studied.
- As an added benefit, bracing to reduce modal deflections of long slender elements will provide lateral stability against elastic buckling.
- Damping has the potential of improving solar concentrator performance, survivability, durability, reliability, and cost.

7.0 REFERENCES

1. Cermak Peterka Peterson, Inc., *Analysis and Review of Field Test Data from the LaJet LEC-460 Collector*, April 1987, prepared for Sandia National Labs, Albuquerque, NM.
2. Chen, W.F., and Lui, E.M., *Structural Stability*, Elsevier Science Publishing Co., Inc., NY, 1987.
3. Clough, R.W. and Penzien, J., *Dynamics of Structures*, McGraw-Hill, Inc., NY, 1975.
4. Davenport, A.G., Isyumov, N., Rothman, H., and Tanaka, H., *Wind-Induced Response of Suspension Bridges - Wind Tunnel Model and Full Scale Observations*, *Wind Engineering*, Proceedings of the Fifth International Conference, Cermak, J.E. (ed.), Fort Collins, CO, July 1979, Pergamon Press, Oxford, 1980, Vol. 2, pp. 807-824.
5. Drake, M.L. and Bouchard, M.P., "On Damping Of Large Honeycomb Structure," *Journal Of Vibration, Stress, and Reliability in Design*, Vol. 107, 361-366.

6. Drake, M.L., and Kluesener, M.F., "Finite Element Methods For Passive Damping Design," presented at ASME Intl. Computers in Engineering Conference, Boston, MA, Aug. 1985, Vol. 2 (Bk. No. GO286B).
7. Dynamic Stability of Large Structures: Non-Structural Viscoelastic Dampers, Product Design and Selection Guide, 3M Company, Structural Products Department, Industrial Specialties Division/3M, 230-1F-02 3M Center, St. Paul, MN 55144-1000.
8. IMAGES3D, Finite Element Analysis Program Manual, Celestial Software, Inc., 125 University Avenue, Berkeley, CA 94710.
9. Johnson, C.D., and Kienholz, D.A. and Rogers, L.C., "Finite Element Prediction Of Damping In Beams With Constrained Viscoelastic Layers," *The Shock and Vibration Bulletin*, 51, Pt. 1, 71-81 (May 1981).
10. Johnson, C.D., and Kienholz, D.A., "Finite Element Prediction Of Damping In Structures With Constrained Viscoelastic Layers," *AIAA Journal*, 20(9), 1284-1290, (September 1982).
11. Kluesener, M.F., "Results Of Finite Element Analysis Of Damped Structures," presented at Vibration Damping Workshop, Long Beach, CA, Feb. 1984.
12. Kluesener, M.F., and Drake, M.L., "Damped Structure Design Using Finite Element Analysis," *The Shock and Vibration Bulletin*, 52, Pt. 5, 1-12 (May 1982).
13. Leung, W.H., IMAGES3D, Finite Element Analysis Program Technical Reference Manual, Version 1.4, Celestial Software, Inc., 125 University Avenue, Berkeley, CA 94710.
14. Mahmoodi, P., and Keel, C.J., "Performance Of Viscoelastic Structural Dampers for the Columbia Center Building", 3M Company, technical reference catalog titled *Effective Damping of Large Structures*.
15. Nashif, A.D., Jones, D.I.G., and Henderson, J.P., Vibration Damping, Wiley-Interscience, John Wiley & Sons, Inc., NY, 1985.
16. Soni, M.L., Kluesener, M.F. and Drake, M.L., "Damping and Control of Spacecraft Structures Using Synthesis and Damped Design for Flexible Spacecraft Structures," *Computers & Structures*, Pergamon Press Ltd., 1985, Vol. 20, No. 1-3, pp. 563-574.
17. Soni, M.L., "Finite Element Analysis of Viscoelastically Damped Sandwich Structures," *The Shock and Vibration Bulletin*, 51, Pt. 1, 97-108 (May 1981).
18. Strachan, J. W., *LaJet Wind Load Tests*, informal report, Solar Thermal Test Facility, Sandia National Laboratories, Albuquerque, NM (no date).
19. Throckmorton, S.T., Peterka, J.A., and Cermak, J.E., "Wind Tunnel Study of Wind Loads on LaJet Solar Collector Model", CSU Project 2-96350, November 1985, Fluid Dynamics and Diffusion Laboratory, Colorado State University, Fort Collins, CO 80523.
20. Ungar, E.E., and Kerwin, E.M., Jr., "Loss Factors of Viscoelastic Systems in Terms of Energy Concepts," *Journal of the Acoustic Society of America*, Vol. 34, July 1962, pp. 954-957.
21. Zienkiewicz, O.C., The Finite Element Method, 3/e, McGraw-Hill Book Company (UK) Limited, Maidenhead Berkshire, England, 1977.

Analysis of a Five-Layer Viscoelastic Constrained-Layer Beam

Michael Falugi
WEDC/RBAA
Wright-Patterson AFB, OH 45433
Formerly of Anamet Laboratories, Inc.

ABSTRACT

This paper documents the analysis and application of the five-layer beam damping system which consists of: undamped beam (layer 1), adhesive layer (layer 2), standard spacing (layer 3), viscoelastic damping material (layer 4) and nonstraining layer (layer 5). It includes the derivation of equations and development of the general-purpose computer program to compute and provide graphical plots of modal loss factor, modal frequency, RMS response and peak resonance, each as a function of temperature. Parametric results are presented for variation in thickness of each layer (except the undamped beam layer). This technology can be used by designers as a means of estimating damping in beam-like structures with viscoelastic constrained-layer damping.

TABLE OF CONTENTS

Section	Page
1.0 INTRODUCTION	1
2.0 DERIVATION OF GOVERNING EQUATION	4
3.0 COMPARISON OF RESPONSE	2
4.0 PROGRAM DEVELOPMENT AND COMPUTATIONS	15
5.0 GRAPHICS	21
6.0 AN EXAMPLE PARAMETRIC STUDY	25
7.0 CONCLUSIONS	25
REFERENCES	28

LIST OF FIGURES

Figure		Page
1	Schematic of Four-Layer Viscoelastic Constrained Layer Damping System	2
2	Schematic of Five-Layer Viscoelastic Constrained Layer Damping System	3
3	Schematic of Five-Layer Viscoelastic Constrained Layer Damping System Due to Bending	5
4	Output Plot for the Five-Layer Beam Computer Program Where Stand-Off (H3) and the Viscoelastic Layer (H4) are Set at Zero	13
5	Output Plot for the Four-Layer Beam Computer Program Where the Stand-off Layer (H2) is Set at Zero	14
6	Flow Diagram for the Five Layer Model Computer Program	16
7	Multiple Layer Temperature Broadening Effect	17
8	Damping Properties of Material LT1MP for Layers 2 and 4	18
9	Damping Properties of Material 3M-468 for Layers 2 and 4	19

LIST OF FIGURES

Figure		Page
10	Combined Effect of the Two Materials. 3M-468 (for Layer 2) and LT1MP (for Layer 4)	20
11	Combined Effect of the Two Materials. LT1MP (for Layer 2) and 3M-468 (for Layer 4)	22
12	Carpet Plot of Maximum Modal Loss Factor vs. Temperature (Degrees Fahrenheit)	23
13	Carpet Plot for Maximum RMS Ratio vs Temperature (Degrees Fahrenheit)	24

LIST OF TABLES

Table		Page
1	Parametric Results	27

1.0 INTRODUCTION

A traditional design approach to reduce resonant vibration in aircraft structures is to either stiffen the structure - increasing the natural frequencies - or add mass - both approaches typically result in an increase in weight penalty. These approaches are not viable in today's design environment because demanding mission requirements dictate a need for lighter-weight structures. Two alternatives are to either properly integrate damping technology into the structure during design and manufacturing, or if necessary use add-on damping treatments to reduce resonant response and increase structural fatigue life without significant weight increases. In either case, simplified analytical equations are prerequisite to good structural designs.

A practical stand-off damping treatment for a beam structural element which is one variation of constrained-layer damping [1 - 4], has been recently devised [5 - 8]. This treatment consists of a stand-off layer, the viscoelastic material layer, and a constraining layer attached to the base beam structure (Figure 1). The damping system considered in this report consist of the same treatment with another layer - an adhesive layer added between the base beam and the stand-off layer (Figure 2). The purpose of this report is to document the analysis and application of this five-layer-beam damping system.

The report includes the derivation of equations and a description of a general purpose computer program V5LBD (viscoelastic five-layer beam damping) to compute results and provide parametric analysis. V5LBD computes and provides graphical plots of modal loss factor, modal frequency, RMS response, and peak response, each as a function of temperature over the range of -50 to 250°F [9].

Sections 2.0 and 3.0 of this report present theory and derivation of the governing equations. Section 4.0 discusses the development of V5LBD which calculates results from the governing equations. Graphics capabilities - of a plot plotting program are presented in section 5.0. Parametric analysis is provided in section 6.0, and conclusions in section 7.0.

This technology can be used by designers to predict damping characteristics of structures to that viscoelastic constrained layer damping concept and the effect of use. It can also be used by engineers to design add-on treatments to damping structures that must overcome vibration problems in service.

LAYERS

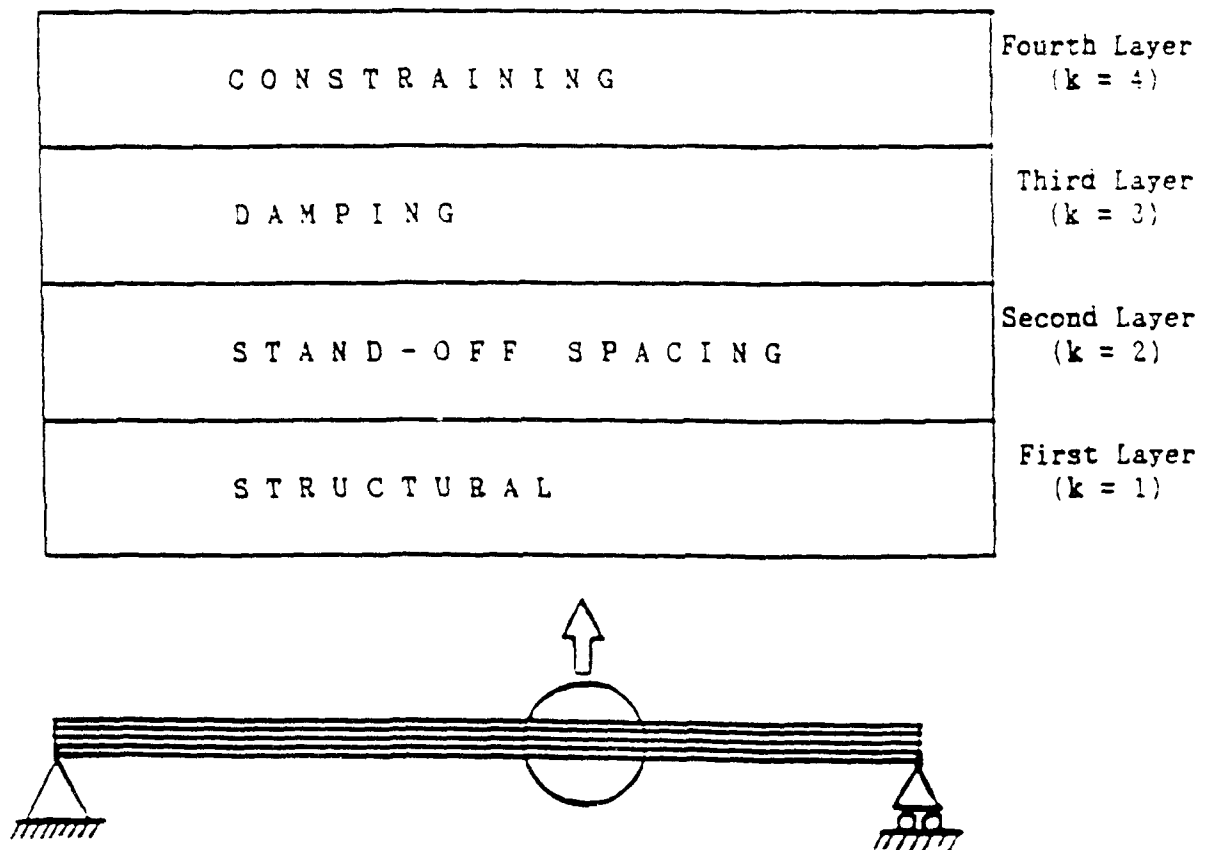


FIGURE 1 - SCHEMATIC OF FOUR-LAYER VISCOELASTIC
CONSTRAINED LAYER DAMPING SYSTEM

LAYERS

CONSTRAINING	Fifth Layer ($k = 5$)
VISCOELASTIC DAMPING	Fourth Layer ($k = 4$)
STAND-OFF SPACING	Third Layer ($k = 3$)
ADHESIVE	Second Layer ($k = 2$)
STRUCTURES	First Layer ($k = 1$)

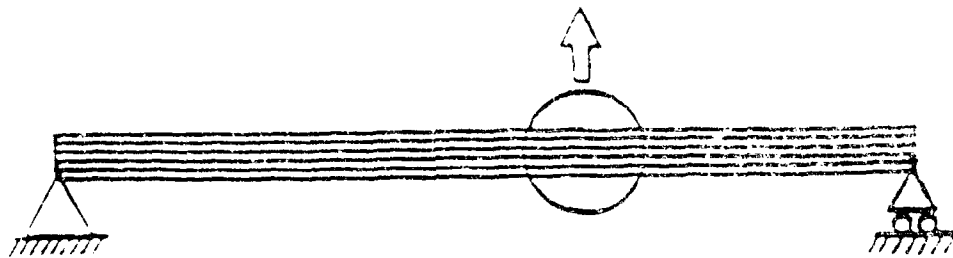


FIGURE 2 - SCHEMATIC OF FIVE-LAYER VISCOELASTIC
CONSTRAINED LAYER DAMPING SYSTEM

2.0 DERIVATION OF GOVERNING EQUATIONS

The five-layer simply-supported beam model is depicted in Figure 2. The principal assumptions used to derive the governing equations are:

1. Only bending and shear deformations are considered. In-plane extensional strains are assumed to be small and negligible.
2. Bending deformations are governed by classical Euler-Bernoulli beam theory [10].
3. Shear deformations of the base structure and constraining layer (Figure 3) are identical. The principal shearing-energy dissipation mechanism occurs in the viscoelastic damping layers (layers 2 and 4) since the shear stiffnesses of these layers are much lower than those of the other layers.

It is implicitly assumed that the structural and constraining layers are made of metallic materials, whereas the spacing and damping layers are made of polymeric compounds. Additional assumptions required to complete the development are presented as required.

The extensional stress (σ) in each layer is given by the following equation:

$$\sigma_k = E_k \epsilon_k, \quad k = 1, \dots, 5 \quad (1)$$

where E_k and ϵ_k are The Youngs modulus of elasticity and strain respectively.

The general equation for the extensional forces (F) can be written in the form:

$$F_k = E_k \epsilon_k A_k, \quad k = 1, \dots, 5 \quad (2)$$

where A_k is the cross sectional area in k^{th} layer.

For the simplified, one-dimensional analysis described below the sectional properties, namely, centroid location, Z_d , and flexural rigidity, \overline{EI} , are needed. As shown in Figure 3, Z_d is defined to be the distance from the mid-plane of the structural layer to the sectional centroid. The strain-displacement relations for the layers are:

$$\epsilon_1 = Z_d \phi' \quad (3)$$

$$\epsilon_2 = (H_{21} - Z_d) \phi' - \frac{H_2}{2} \psi_1' \quad (4)$$

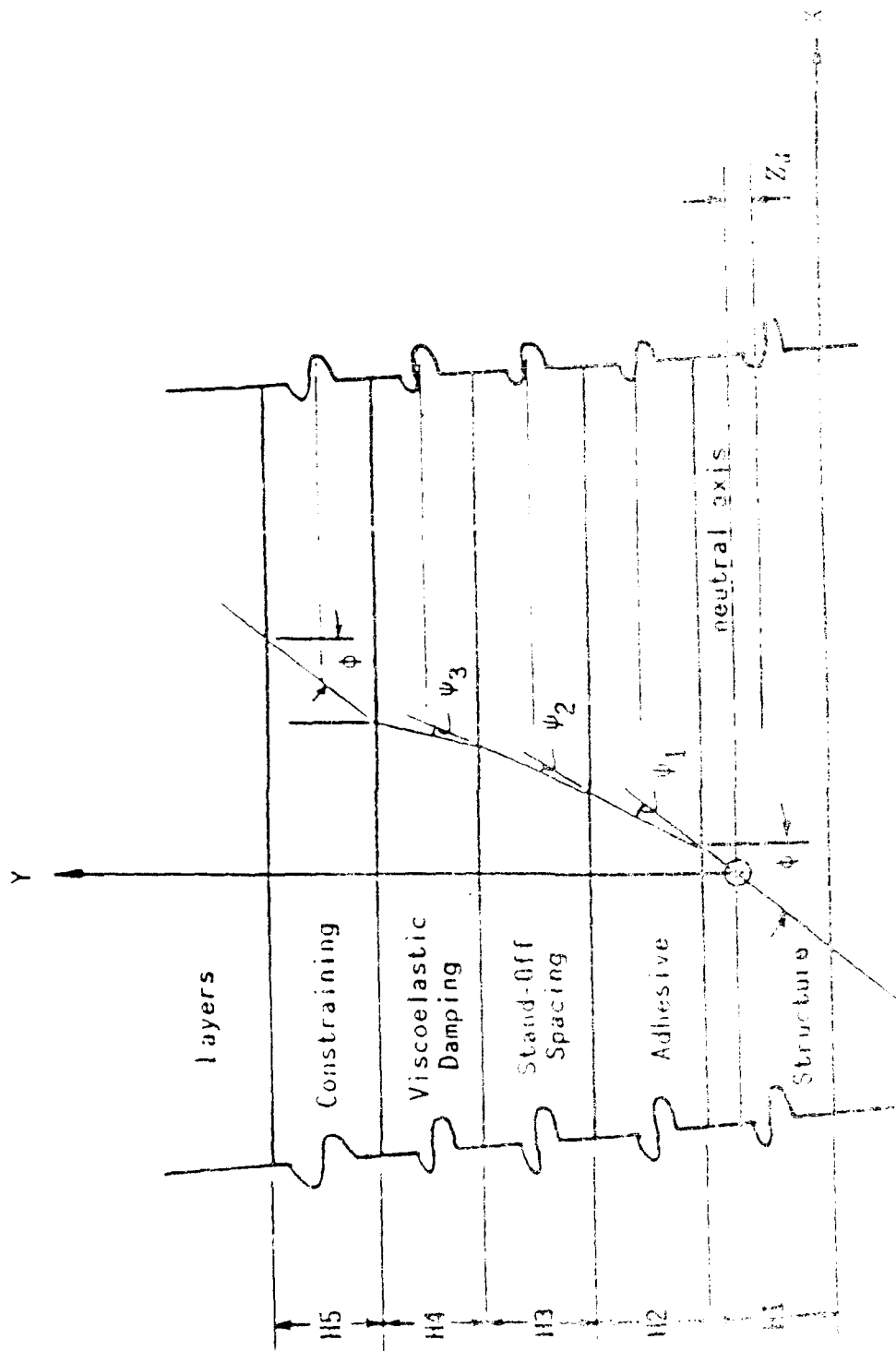


Figure 3 - Schematic of Five-layer Viscoelastic Constrained Layer Damping System Due to Bending

$$\epsilon_3 = (H_{31} - Z_d)\phi' - (H_2 + \frac{H_3}{2})\psi'_1 - \frac{H_3}{2}\psi'_2 \quad (5)$$

$$\epsilon_4 = (H_{41} - Z_d)\phi' - (H_2 + H_3 + \frac{H_4}{2})\psi'_1 - (H_3 + \frac{H_4}{2})\psi'_2 - \frac{H_4}{2}\psi'_3 \quad (6)$$

$$\epsilon_5 = (H_{51} - Z_d)\phi' - (H_2 + H_3 + H_4)\psi'_1 - (H_3 + H_4)\psi'_2 - H_4\psi'_3 \quad (7)$$

where

$$H_{21} = \frac{1}{2}(H_1 + H_2)$$

$$H_{31} = H_2 + \frac{1}{2}(H_1 + H_3)$$

$$H_{41} = H_2 + H_3 + \frac{1}{2}(H_1 + H_4)$$

$$H_{51} = H_2 + H_3 + H_4 + \frac{1}{2}(H_1 + H_5)$$

The prime represents differentiation with respect to x .

By substituting the strain equations (3) through (7) into (2) we get the force equations:

$$F_1 = X_1 Z_d \phi' \quad (8)$$

$$F_2 = X_2 \left[(H_{21} - Z_d)\phi' - \frac{H_2}{2}\psi'_1 \right] \quad (9)$$

$$F_3 = X_3 \left[(H_{31} - Z_d)\phi' - (H_2 + \frac{H_3}{2})\psi'_1 - \frac{H_3}{2}\psi'_2 \right] \quad (10)$$

$$F_4 = X_4 \left[(H_{41} - Z_d)\phi' - (H_2 + H_3 + \frac{H_4}{2})\psi'_1 - (H_3 + \frac{H_4}{2})\psi'_2 - \frac{H_4}{2}\psi'_3 \right] \quad (11)$$

$$F_5 = X_5 \left[(H_{51} - Z_d)\phi' - (H_2 + H_3 + H_4)\psi'_1 - (H_3 + H_4)\psi'_2 - H_4\psi'_3 \right] \quad (12)$$

where

$$X_k = E_k H_k \quad k = 1, \dots, 5 \quad (13)$$

Applying the requirement for equilibrium of in-plane forces, i.e.,

$$\sum_{k=1}^5 F_k = 0 \quad (14)$$

and simplifying produces the equation

$$\begin{aligned} & - \left[X_1 + X_2 + X_3 + X_4 + X_5 \right] Z_d \phi' \\ & + \left[X_2 H_{21} + X_3 H_{31} + X_4 H_{41} + X_5 H_{51} \right] \phi' \\ & - \left[X_2 \frac{H_2}{2} + X_3 \left(H_2 + \frac{H_3}{2} \right) + X_4 \left(H_2 + H_3 + \frac{H_4}{2} \right) + X_5 (H_2 + H_3 + H_4) \right] \psi'_1 \\ & - \left[X_3 \frac{H_3}{2} + X_4 \left(H_3 + \frac{H_4}{2} \right) + X_5 (H_3 + H_4) \right] \psi'_2 \\ & - H_4 \left[\frac{X_4}{2} + X_5 \right] \psi'_3 = 0 \end{aligned} \quad (15)$$

Equation (15) is rearranged to give:

$$\begin{aligned} & \left[X_2 H_{21} + X_3 H_{31} + X_4 H_{41} + X_5 H_{51} \right] = \\ & + \left[X_1 + X_2 + X_3 + X_4 + X_5 \right] Z_d \\ & + \left[X_2 \frac{H_2}{2} + X_3 \left(H_2 + \frac{H_3}{2} \right) + X_4 \left(H_2 + H_3 + \frac{H_4}{2} \right) + X_5 (H_2 + H_3 + H_4) \right] \frac{\psi'_1}{\phi'} \\ & + \left[X_3 \frac{H_3}{2} + X_4 \left(H_3 + \frac{H_4}{2} \right) + X_5 (H_3 + H_4) \right] \frac{\psi'_2}{\phi'} \\ & + H_4 \left[\frac{X_4}{2} + X_5 \right] \frac{\psi'_3}{\phi'} \end{aligned} \quad (16)$$

The equilibrium equations for the shear forces (τ) in the X-direction are:

$$\tau_3 = -G_2 \psi_1 = F'_5 + F'_4 + F'_3 \quad (17)$$

$$\tau_4 = -G_3 \psi_2 = F'_5 + F'_4 \quad (18)$$

$$\tau_5 = -G_4 \psi_3 = F'_5 \quad (19)$$

where G_k is the shear modulus and ψ_k the angle of deformation in the k^{th} layer (see Figure 3). The quantities F_3' , F_4' and F_5' are easily obtained by differentiation of equations (10) through (12).

At this point in the derivation it is necessary to assume a sinusoidal mode shape (which satisfies the boundary conditions for a simply-supported beam) in order to determine ψ_1 , ψ_2 and ψ_3 consistent with the definition of loss factor presented in [12]. Assuming for simplicity that

$$w = \sin Kx \quad (20)$$

then

$$\phi = w' = K \cos Kx \quad (21)$$

$$\phi' = w'' = -K^2 \sin Kx \quad (22)$$

and

$$\phi'' = w''' = -K^3 \cos Kx \quad (23)$$

Substituting equation (21) into (23) provides

$$\phi'' = -K^2 \phi \quad (24)$$

Assuming that ψ_1 , ψ_2 and ψ_3 have the same distribution as w , ψ_1 , ψ_2 , and ψ_3 are related to ϕ by

$$\psi_1 = \alpha_1 \phi \quad (25)$$

$$\psi_2 = \alpha_2 \phi \quad (26)$$

and

$$\psi_3 = \alpha_3 \phi \quad (27)$$

where the α 's are coefficients of proportionality. Subsequent differentiations of Equations (25) through (27) give

$$\alpha_1 = \frac{\psi_1'}{\phi'} = \frac{\psi_1''}{\phi''} \quad (28)$$

$$\alpha_2 = \frac{\psi_2'}{\phi'} = \frac{\psi_2''}{\phi''} \quad (29)$$

and

$$\alpha_3 = \frac{\psi_3'}{\phi'} = \frac{\psi_3''}{\phi''} \quad (30)$$

Returning to equation (24) and using the relations in equations (25) through (30), equation (17) can be written as

$$\begin{aligned} -G_2\psi_1 &= \frac{G_2\psi_1''}{K^2} = \left[X_5(H_{51} - Z_d) + X_4(H_{41} - Z_d) + X_3(H_{31} - Z_d) \right] \phi'' \\ &\quad - \left[X_5(H_2 + H_3 + H_4) + X_4(H_2 + H_3 + \frac{H_4}{2}) + X_3(H_2 + \frac{H_3}{2}) \right] \psi_1'' \\ &\quad - \left[X_5(H_3 + H_4) + X_4(H_3 + \frac{H_4}{2}) + X_3\frac{H_3}{2} \right] \psi_2'' \\ &\quad - \left[X_5H_4 + X_4\frac{H_4}{2} + X_3\frac{H_3}{2} \right] \psi_3'' \end{aligned} \quad (31)$$

Finally, equation (31) can be written in the form:

$$\begin{aligned} &\left[X_5(H_{51} - Z_d) + X_4(H_{41} - Z_d) + X_3(H_{31} - Z_d) \right] = \\ &\quad + \left[\frac{G_2}{K^2} + X_5(H_2 + H_3 + H_4) + X_4(H_2 + H_3 + \frac{H_4}{2}) + X_3(H_2 + \frac{H_3}{2}) \right] \frac{\psi_1''}{\phi''} \\ &\quad + \left[X_5(H_3 + H_4) + X_4(H_3 + \frac{H_4}{2}) + X_3\frac{H_3}{2} \right] \frac{\psi_2''}{\phi''} \\ &\quad + \left[X_5H_4 + X_4\frac{H_4}{2} + X_3\frac{H_3}{2} \right] \frac{\psi_3''}{\phi''} \end{aligned} \quad (32)$$

Similarly, equation (18) is written as

$$\begin{aligned} -G_3\psi_2 &= \frac{G_3\psi_2''}{K^2} = \left[X_5(H_{51} - Z_d) + X_4(H_{41} - Z_d) \right] \phi'' \\ &\quad - \left[X_5(H_2 + H_3 + H_4) + X_4(H_2 + H_3 + \frac{H_4}{2}) \right] \psi_1'' \\ &\quad - \left[X_5(H_3 + H_4) + X_4(H_3 + \frac{H_4}{2}) \right] \psi_2'' \\ &\quad - \left[X_5H_4 + X_4\frac{H_4}{2} \right] \psi_3'' \end{aligned} \quad (33)$$

Rearranging equation (33) gives

$$\begin{aligned} -G_4\psi_3 &= \frac{G_4\psi_3''}{K^2} = \left[X_5(H_{51} - Z_d) \right] \phi'' - \left[X_5(H_2 + H_3 + H_4) \right] \psi_1'' \\ &\quad - \left[X_5(H_3 + H_4) \right] \psi_2'' - \left[X_5H_4 \right] \psi_3'' \end{aligned} \quad (34)$$

Also equation (19) can be written as

$$-G_4 \psi_3 = \frac{G_4 \psi_2''}{K^2} = \left[X_5 (H_{51} - Z_d) \right] \phi'' - \left[X_5 (H_2 + H_3 + H_4) \right] \psi_1'' - \left[X_5 (H_3 + H_4) \right] \psi_2'' - \left[X_5 H_4 \right] \psi_3'' \quad (35)$$

Rearranging equation (35) gives

$$\left[X_5 (H_{51} - Z_d) \right] = \left[X_5 (H_2 + H_3 + H_4) \right] \frac{\psi_1''}{\phi''} + \left[X_5 (H_3 + H_4) \right] \frac{\psi_2''}{\phi''} + \left[\frac{G_4}{K^2} + X_5 H_4 \right] \frac{\psi_3''}{\phi''} \quad (36)$$

Thus equations (17), (18), and (19) are replaced by equations (32), (34), and (36) respectively.

Since the assumption that plane sections remain plane is being used, the bending moment M can be related to deflection by

$$\overline{EI} \phi' = M \quad (37)$$

where \overline{EI} is the flexural rigidity. The total bending moment is expressed by

$$M = \sum_{k=1}^5 M_{kk} + \sum_{k=1}^5 F_k (H_{k1} - Z_d) \quad (38)$$

where M_{kk} is the bending moment of the k^{th} layer given by

$$M_{kk} = \phi' E_k I_k \quad (39)$$

Equations (37) and (38) define the flexural rigidity as follows:

$$\begin{aligned} \overline{EI} = & \left[E_1 I_1 + E_2 I_2 + E_3 I_3 + E_4 I_4 + E_5 I_5 \right. \\ & + X_1 Z_d^2 + X_2 (H_{21} - Z_d)^2 + X_3 (H_{31} - Z_d)^2 + X_4 (H_{41} - Z_d)^2 + X_5 (H_{51} - Z_d)^2 \\ & - \left[E_2 I_2 + E_3 I_3 - E_4 I_4 + \frac{X_2 H_2}{2} (H_{21} - Z_d) + X_3 (H_{31} - Z_d) (H_2 + \frac{H_3}{2}) \right. \\ & + X_4 (H_{41} - Z_d) (H_2 + H_3 + \frac{H_4}{2}) + X_5 (H_{51} - Z_d) (H_2 + H_3 + H_4) \left. \right] \frac{\psi_1'}{\phi'} \\ & - \left[E_3 I_3 + E_4 I_4 + X_3 (H_{31} - Z_d) \frac{H_3}{2} + X_4 (H_{41} - Z_d) (H_3 + \frac{H_4}{2}) + X_5 (H_{51} - Z_d) (H_3 + H_4) \right] \frac{\psi_2'}{\phi'} \\ & - \left[X_4 (H_{41} - Z_d) \frac{H_4}{2} + X_5 (H_{51} - Z_d) H_4 + E_4 I_4 \right] \frac{\psi_3'}{\phi'} \end{aligned} \quad (40)$$

To compute the loss factor η ($\eta = 2\beta$, the fraction of critical damping) for the five-layer system, it is necessary to replace the elastic (E_1, E_2) and shear (G_1, G_2) of the viscoelastic layers by the following complex moduli:

$$E_1^* = E_1(1 - i\eta_1) \quad (41)$$

$$G_2^* = G_2(1 - i\eta_2) \quad (42)$$

and

$$E_2^* = E_2(1 - i\eta_3) \quad (43)$$

$$G_1^* = G_1(1 - i\eta_4) \quad (44)$$

where $i = \sqrt{-1}$.

The complex natural rigidity $\bar{E}T^*$ can be found by substituting equations (35) through (38) and equations (41), (42), (43) and (44) and solving for β_1 , α_1 , α_2 , and α_3 . By substituting these values into equation (40) and replacing the moduli with equations (41) through (44),

$$\bar{E}T^* = \bar{E}L_{\text{eq}} + \bar{G}L_{\text{eq}} \quad (45)$$

The terms L_{eq} and L_{eq} are used to determine $\bar{E}L_{\text{eq}}$ and $\bar{G}L_{\text{eq}}$ are used to determine $\bar{G}L_{\text{eq}}$. These terms are not dimensionless. The system moduli E_1, E_2, G_1 and G_2 are

$$E_1 = \frac{E_1^*}{1 - i\eta_1} \quad (46)$$

It is important to note that the complex modulus E_1^* is the equivalent of the modulus E_1 in the case of a single layer. If we let $\eta_1 = 0$, then $E_1^* = E_1$ and $E_1 = E_1$.

The modal frequency ω_n for the n th mode of vibration is calculated from

$$\omega_n = \frac{1}{L} \sqrt{\frac{E_1^*}{\rho} \left(\frac{1}{1 - i\eta_1} \right) + \frac{G_2^*}{\rho} \left(\frac{1}{1 - i\eta_2} \right)} \quad (47)$$

where:

H_k = k^{th} layer thickness;

ρ_k = k^{th} layer density, mass/unit volume;

N = mode number; and

g = acceleration of gravity.

In practice the complex modulus is evaluated for a given temperature and an estimated modal frequency, f_e . The modal frequency is calculated from f_N and compared to the convergence criteria

$$1 - \frac{f_e}{f_N} \leq \epsilon_{FREQ} = 0.01 \quad (48)$$

If this condition is not met, the new estimated frequency is taken as the old calculated frequency and the process repeated.

First-order verification of the equations derived for the five-layer beam damping system was made by comparing predictions with those for a degenerate case. This comparison was made by setting the four-layer beam system thicknesses for layers three and four equal to zero (stand-off and viscoelastic layers) in the five-layer program and thickness for layer two equal to zero (stand-off layer) in the four-layer program. Predicted outputs for modal loss factor, modal frequency ratio, RMS response and peak resonance were compared and found to be identical (See Figures 4 and 5). This comparison partially validates the five-layer equations, but other extensive comparisons beyond the scope of this study could be made to totally validate them.

3.0 COMPARISON OF RESPONSE

The undamped/damped amplitude ratio for a single-degree-of-freedom system undergoing sinusoidal excitation is

$$\frac{A_{peakundamp}}{A_{peakdamp}} = \frac{\eta_u}{\eta_d} \times \left(\frac{f_d}{f_u} \right)^2 \times \frac{\eta_d}{\eta_u} \quad (49)$$

where m is the weight density of the structure. The subscript "u" refers to the undamped base structure and the subscript "d" the response with damping treatment.

The root-mean-square amplitude response W_{rms} , is obtained by using the equation

FIVE LAYER BEAM MODEL

MODULUS OF ELASTICITY = 30E6 lb/in² by 1
 DENSITY = 0.00078 lb/in³ by 1
 INITIAL TEMPERATURE = 70.0 F by 1
 YOUNG'S MODULUS = 30E6
 (1) BAY RATE 30.000 in 30.000 sec/mil 1.000E+06 sec
 0.000 in 0.000 sec/mil
 (2) ALUMINUM 30.000 in 30.000 sec/mil 1.000E+06 sec
 (3) STEEL 30.000 in 30.000 sec/mil 1.000E+06 sec
 (4) COPPER 30.000 in 30.000 sec/mil 1.000E+06 sec
 (5) COAT LAYER 30.000 in 30.000 sec/mil 1.000E+06 sec

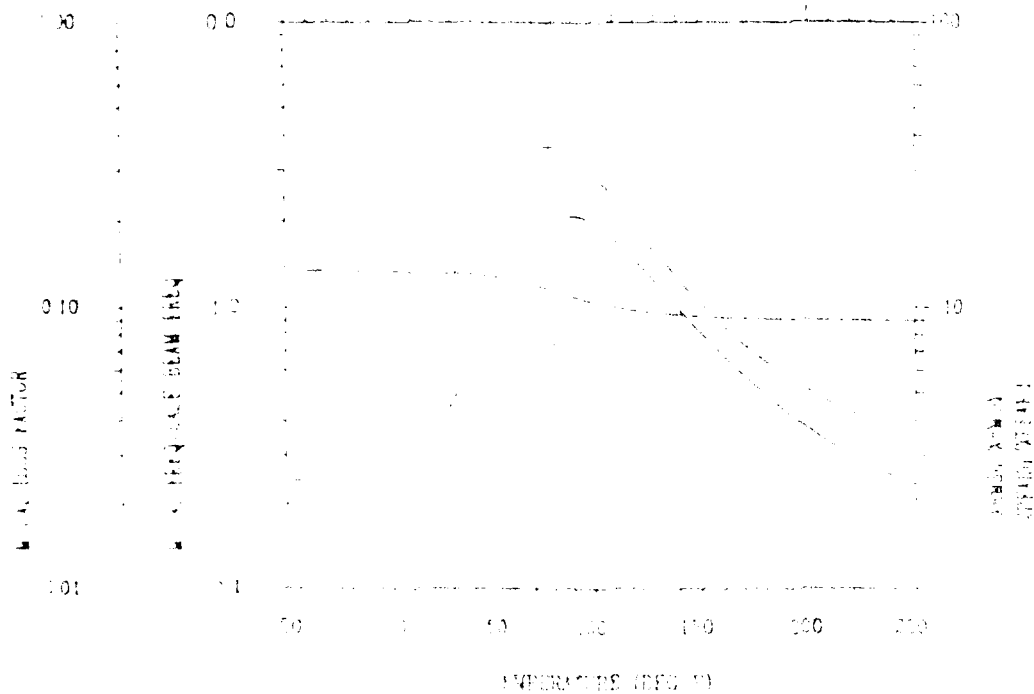


Figure 1 - Output of the Five-Layer Beam Computer Program
 Where: Modulus (H) and the Thermal Expansion Coefficient (H)

FOUR-LAYER BEAM, MODE 1

(MODAL LOSS FACTOR)MAX= 0.21, AT T= 90. Deg F

(XRMSu/XRMSd)MAX= 7.54, AT T= 75. Deg F

(XPEAKu/XPEAKd)MAX= 36.40, AT T= 80. Deg F

(W/LAYER/XBASE)= 1.31

(1) BASE BEAM H1=0.070 in. R01=098 lb/in3, E=0.100E+08 psi
L= 5.00 in. Freq= 252. hz

(2) SPACER H2=0.000 in. R02= .000 lb/in3, G=0.200E+06 psi

(3) YEM H3=0.005 in. R03=035 lb/in3, 3M-468

(4) CONST. LAYER H4=0.020 in. R04=098 lb/in3, E=0.100E+08 psi

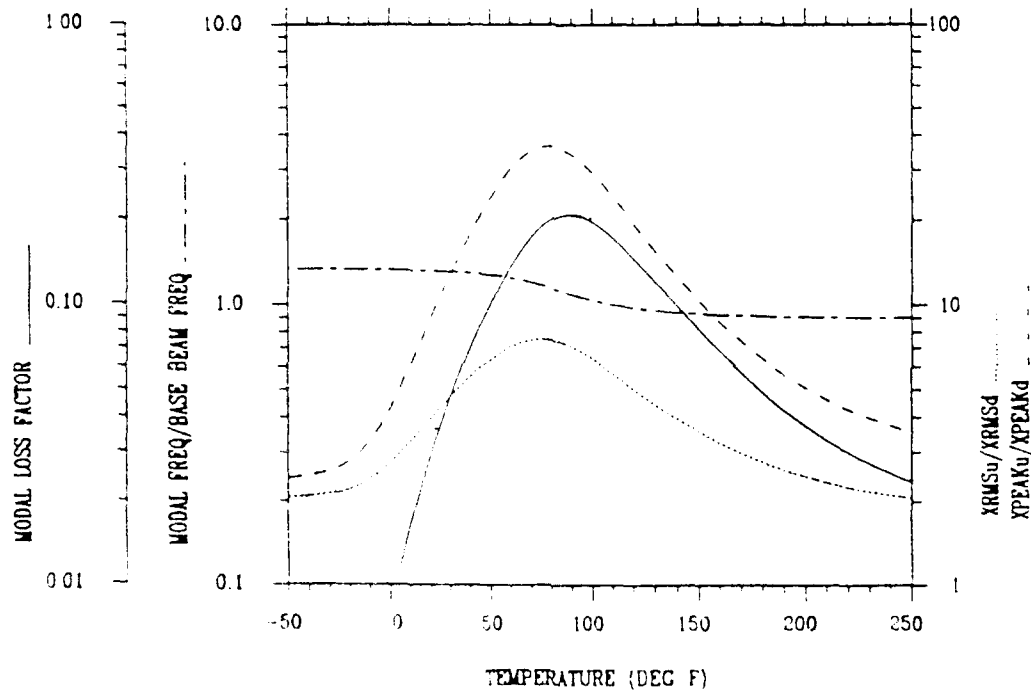


Figure 5 - Output Plot for the Four-Layer Beam Computer Program
Where the Stand-Off Layer (H2) is Set at Zero

derived in [13]; which is

$$W_{rms} = \frac{\pi \bar{F}(w)}{2\sqrt{2}m^{1/4}K^{3/4}\eta^{1/2}} \times \frac{(1 + \sqrt{1 + \eta^2})}{\sqrt{1 + \eta^2}} \quad (50)$$

Noting that

$$K = mw^2 = m(2\pi f)^2 \quad (51)$$

The undamped/damped response ratio is given by

$$R_{rms} = \frac{(W_{rms}/\bar{F}(w))_u}{(W_{rms}/\bar{F}(w))_d} = \frac{m_d}{m_u} \times \frac{\sqrt{1 + \eta_d^2}}{\sqrt{1 + \eta_u^2}} \times \frac{[1 + \sqrt{1 + \eta_u^2}]}{[1 + \sqrt{1 + \eta_d^2}]} \times \sqrt{\frac{\eta_d}{\eta_u}} \times \left(\frac{f_d}{f_u}\right)^{\frac{3}{2}} \quad (52)$$

the response with damping treatment.

In summary the four main governing equations derived are: modal loss factor equation which results by solving equation (45) and calculating the response ratio (46), modal frequency equation (47), peak amplitude equation (49), and RMS response equation (52).

4.0 PROGRAM DEVELOPMENT AND COMPUTATIONS

An overview of the computer program V5LBD computations scheme is presented in the flow diagram shown in Figure 6. The geometry of the base beam, thickness and material properties for each layer, and the viscoelastic damping parameters are input variables. The following quantities are calculated for a specified temperature: frequency estimate (approximate frequency), temperature shift function, reduced frequency, shear modulus, and the material damping of the viscoelastic layer. Next, modal damping and frequency are calculated. The calculated modal frequency is then compared to the estimated frequency using the convergence criterion. If the convergence criterion is not satisfied, the calculation is iterated for an improved value of the frequency estimate. Once convergence is achieved, the RMS and peak response values are calculated.

The five-layer damping system analyzed in this report includes two different viscoelastic materials for one damping application. When using only one viscoelastic material the effective temperature range of that material may be narrower than the re-

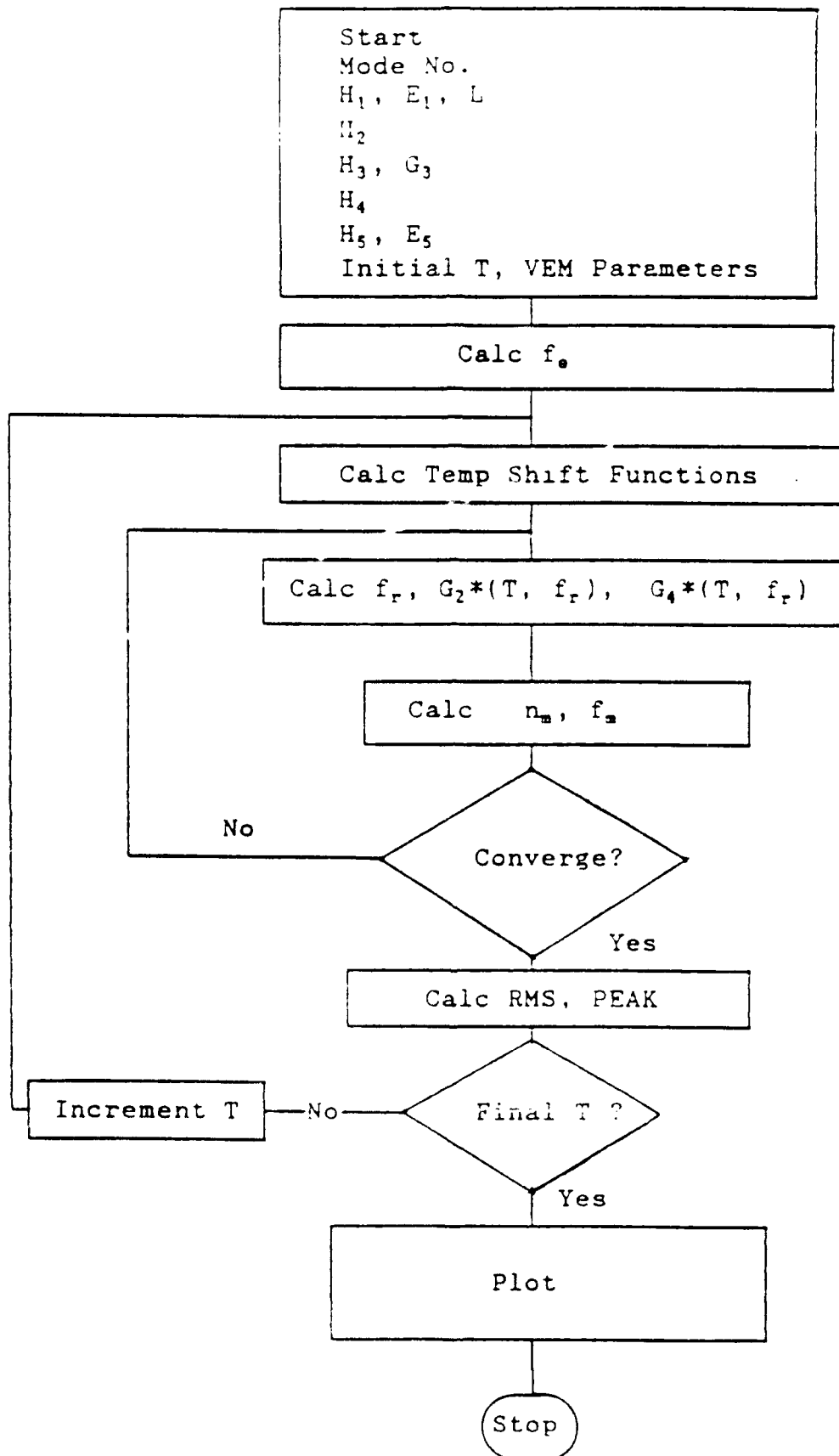


Figure 6 - Flow Diagram for the Five-Layer Model Computer Program

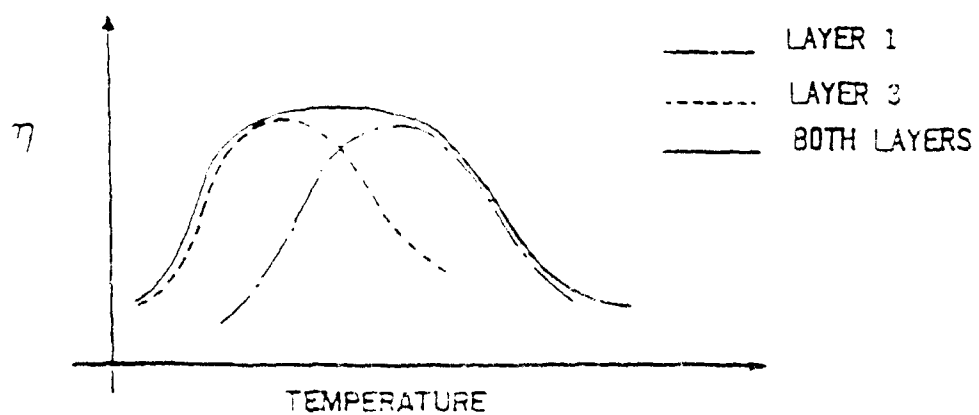
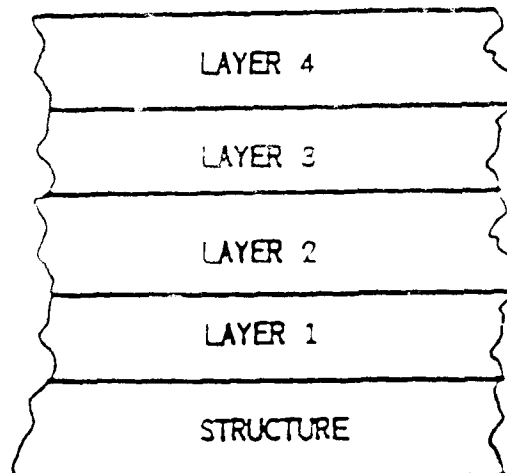


Figure 7 - Multiple Layer Temperature Broadening Effect

FIVE-LAYER BEAM MODE 1

(MODAL LOSS FACTOR)MAX = 0.49, AT T = -25 Deg F
 (XRMSu/XRMSd)MAX = 29.77, AT T = -25 Deg F
 (XPEAKu/XPEAKd)MAX = 268.05, AT T = -25 Deg F
 (MASSd/MASSu) = 1.40
 (1) PLY 1 H1=0.055 in. E01=0.08 lb/in. L=0.100E+06 psi
 L=5.00 in. Freq= 198. Hz
 (2) ADHESIVE H2=0.006 in. E02=0.05 lb/in. LTIMP
 (3) SPACER H3=0.100 in. E03=0.08 lb/in. G=0.200E+06 psi
 (4) PLY H4=0.005 in. E04=0.05 lb/in. LTIMP
 (5) CONST. LAYER H5=0.010 in. E05=0.08 lb/in. L=0.100E+06 psi

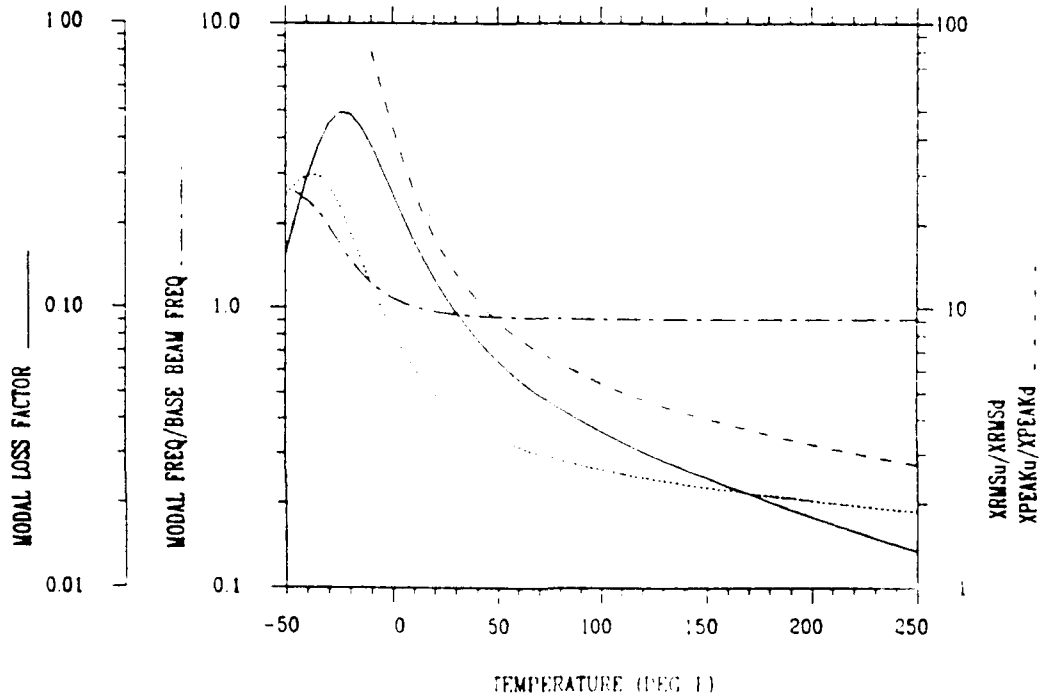


Figure 8 - Damping Properties of Material
 LTIMP for Layers 2 and 4

FIVE-LAYER BEAM, MODE 1

(MODAL LOSS FACTOR)MAX = 0.37, AT T = 55. Deg F

(XRMSu/XRMSd)MAX = 11.87, AT T = 40. Deg F

(XPEAKu/XPEAKd)MAX = 79.59, AT T = 45. Deg F

(MASSu/MASSd) = 1.17

(1) BASE BEAM H1=0.000 in. B01=0.98 lb/in. E=0.119E+09 psi
L=5.00 in. Freq= 236 Hz

(2) ADHESIVE H2=0.005 in. B02=0.05 lb/in. G=468

(3) SPACER H3=0.000 in. B03=0.05 lb/in. G=0.200E+06 psi

(4) VEM H4=0.005 in. B04=0.05 lb/in. G=468

(5) CONST. LAYER H5=0.005 in. B05=0.98 lb/in. E=0.960E+07 psi

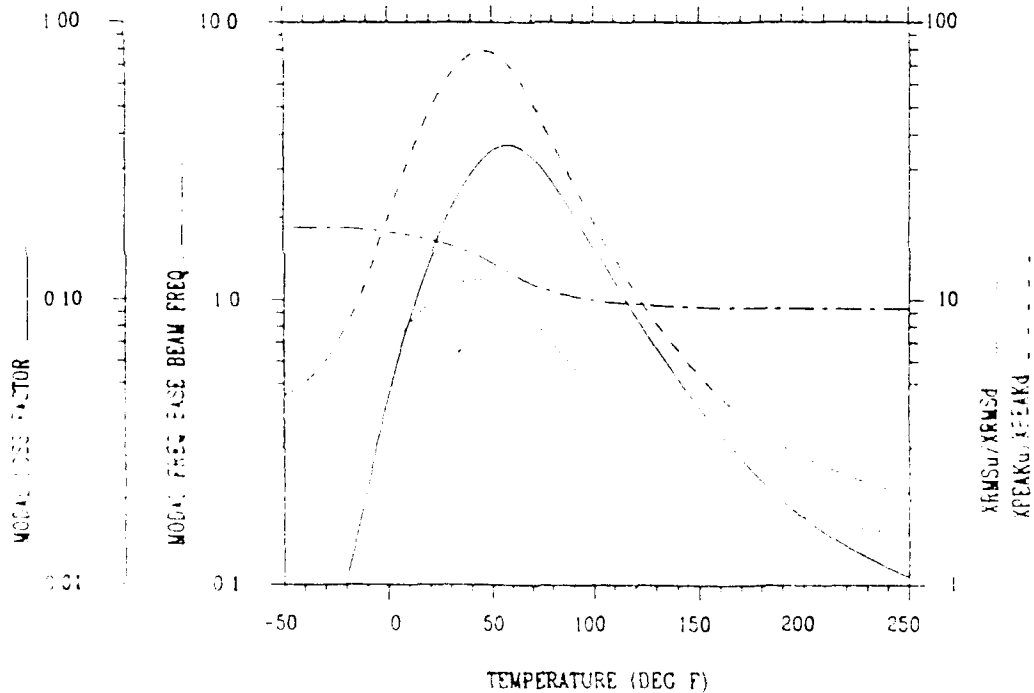


Figure 9 - Damping Properties of Material 3M-468 for Layers 2 and 4

FIVE-LAYER BEAM, MODE 1

(MODAL LOSS FACTOR)MAX= 0.45, AT T= 50 Deg F
 (XRMSu/XRMSd)MAX= 24.60, AT T= 5 Deg F
 (XPEAKu/XPEAKd)MAX= 188.73, AT T= 10 Deg F
 (MASSu/MASSd)= 1.40
 (1) BASE BEAM H1=0.055 in. B01=0.08 lb/in. E=0.100E+08 psi
 L=5.00 in. Freq= 198 Hz
 (2) ADHESIVE H2=0.006 in. B02=0.05 lb/in. JN=168
 (3) SPACER H3=0.108 in. B03=0.08 lb/in. C=0.200E+08 psi
 (4) FIBER H4=0.005 in. B04=0.05 lb/in. LTIMP
 (5) CONST. LAYER H5=0.010 in. B05=0.08 lb/in. E=0.100E+08 psi

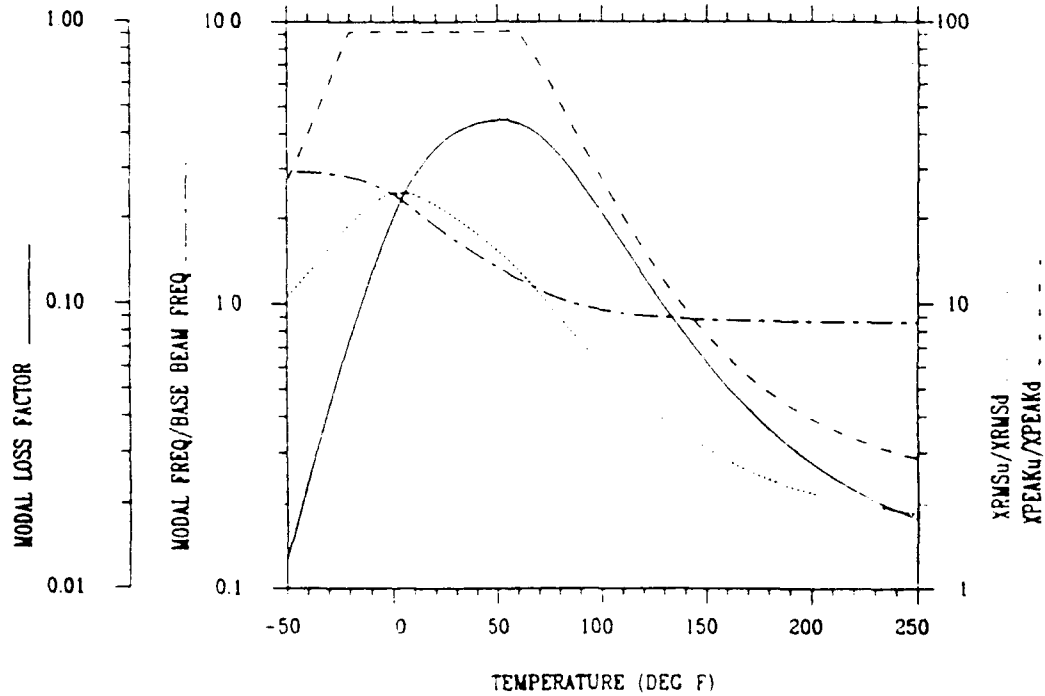


Figure 10 - Combined Effect of the Two Materials, 3M-468
 (for Layer 2) and LTIMP (for Layer 4)

quired temperature range for an effective damping design. One way of broadening the temperature range over which maximum damping can be achieved is to use multiple viscoelastic materials with peaks in loss factor occurring at different temperatures (see Figure 7). As an example, suppose the temperature range for which the damping design has to operate is from 0 to 150° F. Using the analysis procedure in section 2.0, two materials are selected: LT1MP and 3M-468. The first material has its peak damping at -25° F (Figure 8) the second at 55° F (Figure 9). By placing the two materials in the order shown in Figure 10 the combined effect gives the desired results over a broader temperature range than provided by either material used separately.

The order in which the viscoelastic layers are applied is also important. Analysis has shown that the layer nearest the structure has to have the higher temperature damping properties to get a wider range of damping performance. To illustrate this concept consider two cases. In the first case, 3M-468 was used as the second layer and LT1MP as a fourth layer. In the second case these materials were reversed. It was found for a loss factor of $\eta \geq 0.1$, that the first case gave a wider temperature coverage -20 through 130° F (see Figure 10), while the second case resulted in a more narrow temperature coverage, -60 through 34° F. (see Figure 11).

5.0 GRAPHICS

Graphical plotting capability was built into the program using DI3000 software. The software allows users to plot the following four curves on the same graph: modal loss factor, modal frequency, RMS response ratio, and peak resonance ratio, each as a function of temperature. Users also have the option of inputting the required range of temperatures and choosing whether to plot results on the printer or only display them on the screen.

A general purpose computer program CP5LD (carpet plot for five layer beam) to generate carpet plots for the five-layer damping system was also developed [2]. The first part of the program consists of developing carpet plots of maximum modal loss factor values versus temperature (Figure 12). The second part of the program generates carpet plots of maximum RMS response ratios versus temperature for different combinations of layer thicknesses of viscoelastic (H1) and constraining (H5) layers (Figure 13). The input data for the program consists of the material properties, geometry

FIVE-LAYER BEAM, MODE 1

(MODAL LOSS FACTOR)MAX = 0.49, AT T = -25 Deg F
 (XRMScu/XRMSd)MAX = 29.90, AT T = -25 Deg F
 (XPEAKu/XPEAKd)MAX = 253.69, AT T = -25 Deg F
 (MASSu/MASSd) = 1.40
 (1) BASE BEAM R1=0.055 in. R01=0.98 lb/inch. E=0.100E+08 psi
 L=5.00 in. Freq= 198 Hz
 (2) ADHESIVE R2=0.005 in. R02=0.05 lb/inch. LT1MP
 (3) SPACER R3=0.100 in. R03=0.08 lb/inch. G=0.200E+08 psi
 (4) FIBER R4=0.005 in. R04=0.05 lb/inch. 3M-468
 (5) CONST. LAYER R5=0.010 in. R05=0.98 lb/inch. E=0.100E+08 psi

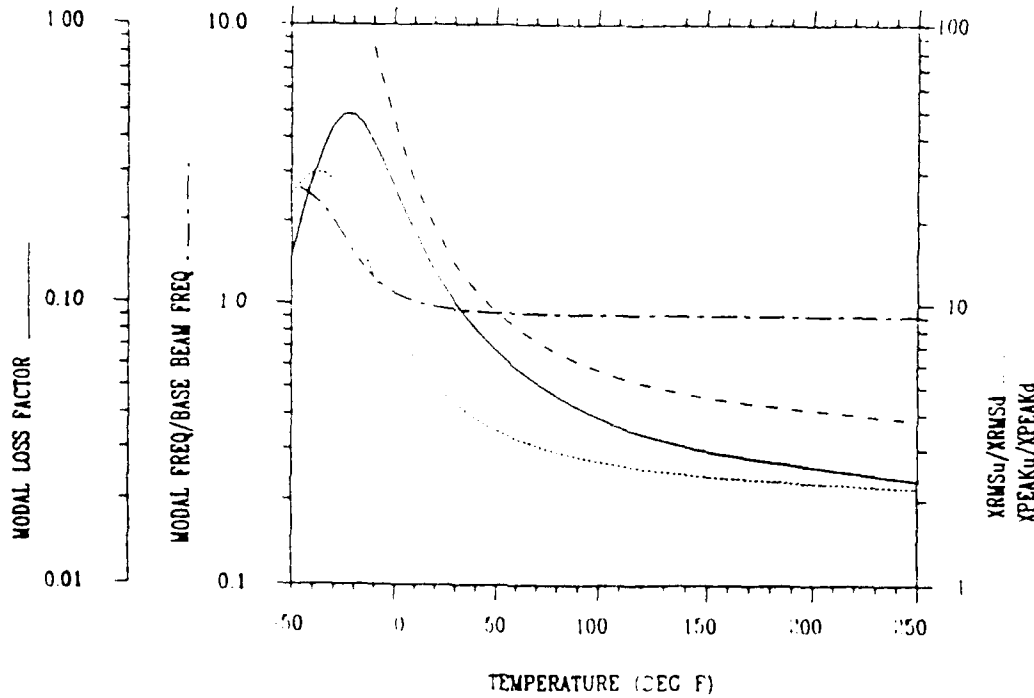


Figure 11 - Combined Effect of the Two Materials, LT1MP
 (for Layer 2) and 3M-468 (for Layer 4)

CARPET PLOT FOR FIVE-LAYER BEAM, MODE 1

1st CASE

- (1) BASE BEAM H1=0.065 in. R01=0.98 lb/in³, E=0.100E+08 psi
L=5.00 in. Freq= 198 Hz
(2) ADHESIVE H2=0.005 in. R02=0.35 lb/in³, G=0.168
(3) SPACER H3=0.100 in. R03=0.08 lb/in³, G=0.200E+06 psi
(4) VEM R04=0.35 lb/in³, LTIMP
(5) CONST LAYER R05=0.98 lb/in³, E=0.100E+08 psi

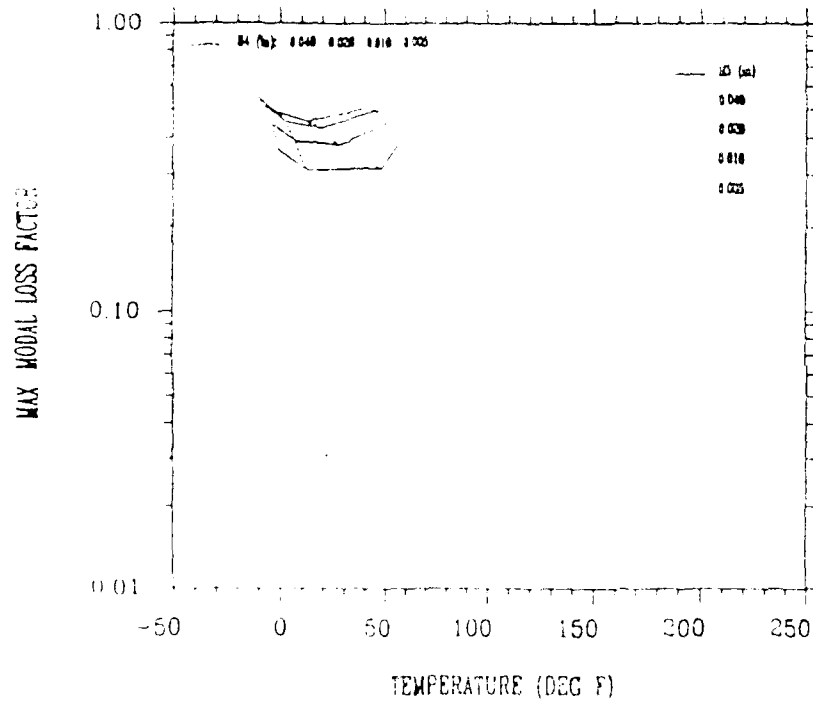


Figure 12 - Carpet Plot of Maximum Modal Loss Factor vs. Temperature (Degrees Fahrenheit)

CARPET PLOT FOR FIVE-LAYER BEAM, MODE 1

1st CASE

- (1) BASE BEAM H1=0.055 in. R01= 098 lb/in3, E=0.100E+08 psi
L=5.00 in. Freq= 198. hz
- (2) ADHESIVE H2=0.005 in. R02= 035 lb/in3, 3M-468
- (3) SPACER H3=0.100 in. R03= 008 lb/in3, C=0.200E+06 psi
- (4) VEM R04= 035 lb/in3, LTIMP
- (5) CONST LAYER R05= 098 lb/in3, E=0.100E+08 psi

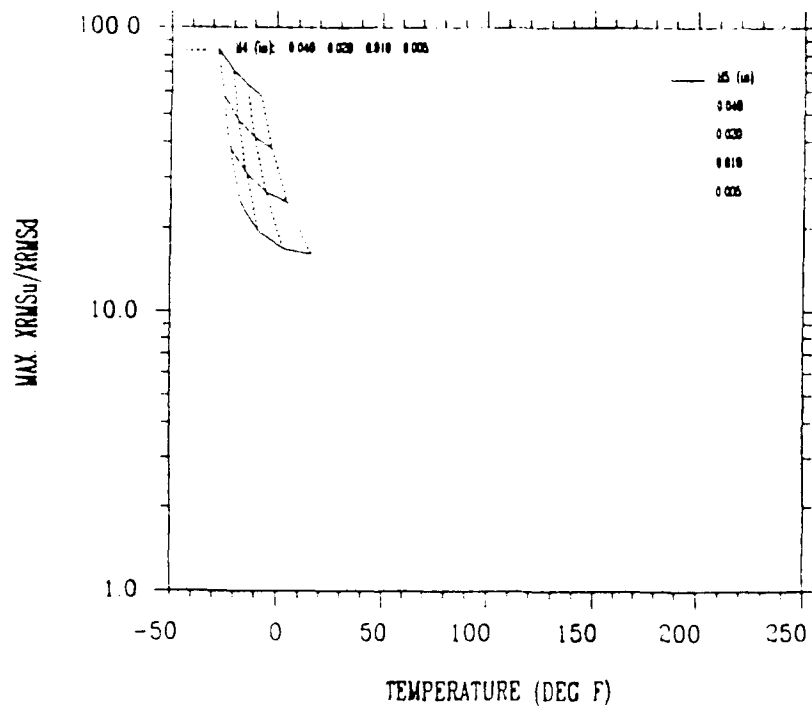


Figure 13 - Carpet Plot for Maximum RMS Ratio
vs. Temperature (Degrees Fahrenheit)

of the undamped beam structure, the adhesive layer, and stand-off layer and desired thickness values for H_1 and H_2 . Four different thicknesses for each of H_1 and H_2 are used, see figure 12. The program calculates the maximum modal loss factor at different combinations of H_1 and H_2 and uses an IMSL routine to fit a quadratic function to the data which forms the carpet plot curves. These carpet plots can then be used to choose optimum damping configurations for the five-layer systems. This shows the effect on damping properties created by different combinations of system layer thicknesses.

The computer program, CP5LB which generates carpet plots, can provide a convenient way to show trends in the maximum values of modal damping and RMS response ratio as functions of temperature.

6.0 AN EXAMPLE PARAMETRIC STUDY

To obtain an understanding of the behavior of the five-layer beam damping system, an example parametric study was conducted by varying the thickness of each layer (except the base beam) by 20 %. The baseline model consists of a base beam 0.006 inches thick and 5.0 inches long; 0.005 inches of 3M-468 adhesive; a 0.10 inches stand-off layer; 0.005 inches of LT1MP viscoelastic material; and an aluminum constraining layer 0.01 inches thick. The results of the example parametric study are shown in Table 1. These results indicate that the stand-off layer is the most significant parameter to effect damping. It decreased the damped response by 19.18 % compared to 0.89 % for the other variables.

7.0 CONCLUSIONS

This damping technology is very effective in helping designers predict damping characteristics for beam-like structures. The temperature range can be broadened over which maximum damping is achieved by applying two different viscoelastic materials with peak in loss factors occurring at different temperatures. By using the computer program U5LBD, which utilizes the developed governing equations, it was shown that the order in which the viscoelastic layers are applied is not important. The viscoelastic layer closest to the structure must be the layer that has a peak in loss at the higher temperature in order to achieve maximum damping over the entire temperature range.

range.

The carpet plotting program, CP5LB is an effective tool to show trends in damping characteristics as a function of temperature for parametric changes in the geometry of applied layers. It was demonstrated by conducting parametric studies for the five-layer system by varying the thickness of each layer (except the base beam) by 20 % that the stand-off layer had the most significant damping effect on response, decreasing RMS response by 19.18 % compared to 0.89 % for the adhesive-layer. Additional verifications of V5LBD need to be done as well as a comparison of the program output with actual test data. The five-layer system presented can be a very effective technique in helping the designer to select proper damping treatments for reducing resonant vibrations.

TABLE 1 - Parametric

H2 (in.)	H3 (in.)	H4 (in.)	H5 (in.)	E5 (psi)	XRMSu/XRMSd (MAX)	TEMP (°F.)	% CHANGE
0.005	0.10	0.005	0.010	10E6	24.66	5	BASE
0.006	0.10	0.005	0.010	10E6	24.88	5	0.89
0.005	0.12	0.005	0.010	10E6	29.39	5	19.18
0.005	0.10	0.006	0.010	10E6	24.98	0	1.30
0.005	0.10	0.005	0.012	10E6	27.52	0	11.60
0.005	0.10	0.005	0.010	12E6	27.06	0	9.73

REFERENCES

1. Ross, D., Ungar, E. E., and Kerwin, E. M., "Structural Damping", J. E. Ruzicka, Ed., American Society of Mechanical Engineers, 1959.
2. Snowdon, J. C., "Vibration and Shock in Damped Mechanical Systems", John Wiley & Sons, 1968.
3. Rogers, L., Notes from Vibration Damping Short Course, University of Dayton Research Institute, Sections 6 and 7, November 1987.
4. Miles, R. N., "The Prediction of the Damping Effectiveness of Multiple Constrained Layer Damping Treatments", Presented at Acoustical Society of America, Massachusetts Institute of Technology, June 11-15, 1979.
5. Ross, D., E.E. Ungar, and E.M. Kerwin, Jr., "Damping of Plate Flexural Vibrations by Means of Viscoelastic Laminae", Section III of Structural Damping, ASME, 1959.
6. Henderson, J.P., "New Techniques and Materials for Damping", ASME paper paper 64-MD-22, 1964; design abstract in Machine Design, July 30, 1964.
7. Falugi, M., Moon Y. I., and Rocky R. Arnold, "Investigation of a Four-Layer Viscoelastic, Constrained Layer Damping System", ASIAC Report No. 189.1A, March 1989.
8. Parin M., Rogers L., Moon Y. I., Falugi, M., "Practical Stand Off Damping for Sheet Metal", Damping '89, February 1989.
9. Falugi, M., "Users Guide for Computer Program BVDS (Beam Viscoelastic Damped Structures)", ASIAC Report No. 1289.1E, December 1989.
10. Fung, Y. C., "A First Course In Continuum Mechanics", Second Edition, Prentice-Hall, Inc., Englewood Cliffs, New Jersey, 1977.
11. Byars, E. F., and Snyder, R. D., "Engineering Mechanics of Deformable Bodies", Second Edition, International Textbook Company, Scranton, Pennsylvania, 1969.
12. Ungar, E. E., and Kerwin, Jr., E. M., "Loss Factors of Viscoelastic Systems in Terms of Energy Concepts," The Journal of the Acoustical Society of America, Vol. 34, No. 7, pp. 954-957, July 1962.
13. Nashif, A., and Jones, D., Henderson, J. P., "Vibration Damping", John Wiley & Sons, 1985.

DYNAMICS OF A CLASS OF VISCOUSLY DAMPED STRUTS

Y. C. Yiu

Structural Dynamics, Space Systems Division, Dept. 62-18, B/104
Lockheed Missiles & Space Company, 1111 Lockheed Way, Sunnyvale, CA 94089
Telephone : 408-742-4048

S.D. Ginter

Honeywell Inc., Satellite Systems Operation
P.O. Box 52199, Phoenix, AR 85022
Telephone : 602-561-3244

ABSTRACT

The dynamics of a class of struts with one viscous chamber at one end of the strut is developed using formulation and methods consistent with finite element dynamic analysis of structural system. This technique is developed to enable consistent and systematic design and analysis of large truss structures passively damped by viscous struts. Modeling and model reduction methods for accurate analysis with a minimum number of design parameters are developed. Design parameters for optimum damping characteristic, and the associated dynamic stiffness and bandwidth characteristics are derived. A design procedure and design curves to size the struts for system level integration are presented.

INTRODUCTION

Large flexible structures are characterized by many flexible modes within the disturbance and control bandwidth. For most precision structures, the performance requirements are very stringent. However, this class of structures often has very low intrinsic damping, less than 0.1% equivalent viscous damping ratio¹, which results in significant dynamic responses. For truss type structures, a strut with good stiffness and damping characteristics will significantly enhance the structural performance.

Struts with viscoelastic materials have been designed, tested and implemented in demonstration test articles and structures². Modal Strain Energy method is often used in the design and analysis of this type of struts and structures³. The mathematical problem of struts and structures are posed in a frequency dependent form. Results from this approximate solution technique matched quite well with test data².

Viscous energy dissipation is a well understood damping mechanism. Incorporating a damping chamber in a strut can provide the necessary damping characteristics. An effective design of this type of viscously damped struts has been implemented by Honeywell⁴. In order to successfully integrate the viscous struts into a system level design, the dynamics of the struts must be totally understood. The same analysis method should be used to study the strut dynamics and system level dynamics so that the integrated design and analysis can be performed consistently and systematically⁵. Also, in order to understand the behavior of the struts as contributing members of a large structure, the problem must be simplified to a few key design parameters by applying engineering assumptions. Simplified design procedure with design curves are presented to compute the key strut design parameters. However, the details of the mechanical design is not the subject of this paper.

VISCOUS STRUT CONFIGURATION

The viscous strut is a mechanical device comprised of three basic elements: an outer tube, an inner tube and a small viscous damper. A typical strut configuration is shown in Figure 1⁴. The damper is placed in series with the inner tube. The outer tube is placed in parallel with the damper/inner tube. An axial displacement across the strut produces a displacement across the damper. The damper forces fluid through a small diameter orifice, thereby causing a shear flow in the fluid. For Newtonian viscous fluids, the fluid shear is actually proportional to the displacement rate across the damper and thus, a velocity dependent viscous damping force is obtained. Under quasi-static load, the fluid flows and provides no resistance and the outer tube provides the static stiffness to the strut. The stiffness of the inner tube is important to impart sufficient displacement/velocity to the damper. The damping coefficient of the damper is a function of the fluid material properties and the geometry of the viscous chamber. Since the strut has other small components, they will introduce additional flexibility to the strut and degrade the performance. It is important to account for these flexible elements accurately.

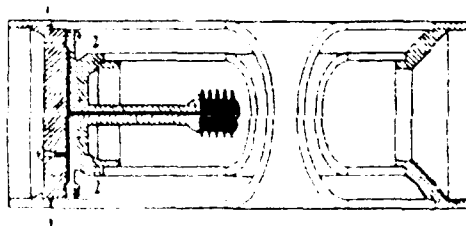


Figure 1 Configuration of Viscously Damped Strut⁴

The formulation presented here is applicable to a general class of viscously damped struts which are axially symmetric with the viscous chambers rigidly attached to one end of the struts. This considerably simplifies the mathematics and lead to a design model with a minimum number of key parameters.

STRUT ANALYTICAL MODEL

A viscous strut is a structural component which can be analyzed by standard structural analysis methods. As such, it can be analyzed using conventional structural analysis techniques and tools. For a complex strut design, a finite element model can be developed easily using a combination of beam, plate, solid and viscous elements. The analysis is quite straight forward except for the viscous element which is not often used in conventional structural analysis. In general, the governing differential equation for a strut can be expressed as:

$$\mathbf{M}\ddot{\mathbf{u}} + \mathbf{C}\dot{\mathbf{u}} + \mathbf{K}\mathbf{u} = \mathbf{p} g(t) \quad (1)$$

The damping matrix has contributions from two sources: the intrinsic material and joint damping, and damping from the viscous dashpot. The intrinsic damping is insignificant compared with the contribution from the viscous dashpot and hence ignored. Equation (1) is normally cast in the first order form for solution:

$$\begin{bmatrix} \mathbf{C} & \mathbf{M} \\ \mathbf{M} & \mathbf{0} \end{bmatrix} \begin{bmatrix} \dot{\mathbf{u}} \\ \mathbf{u} \end{bmatrix} + \begin{bmatrix} \mathbf{K} & \mathbf{0} \\ \mathbf{0} & -\mathbf{M} \end{bmatrix} \begin{bmatrix} \mathbf{u} \\ \dot{\mathbf{u}} \end{bmatrix} = \begin{bmatrix} \mathbf{p} \\ \mathbf{0} \end{bmatrix} g(t) \quad (2)$$

The strut can be modeled by many structural nodes to provide a general description of its dynamic behavior in 3 dimensional space. Let one end of the strut be fixed, the displacement vector of the end node be \mathbf{u}_1 , and the displacement vector at the viscous chamber be \mathbf{u}_2 . Many other interior structural nodes may be needed to model the stiffness distribution in the finite element model (see Figure 2).

$$\mathbf{u} = \begin{bmatrix} \mathbf{u}_1 \\ \mathbf{u}_2 \\ \vdots \\ \mathbf{u}_n \end{bmatrix} \quad (3)$$

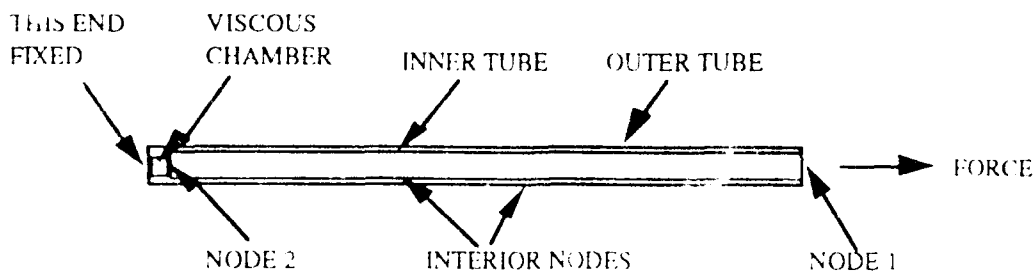


Figure 2 An Idealized Viscous Strut

The lumped mass matrix, damping matrix, and stiffness matrix can be expressed in the following form:

$$\mathbf{M} = \begin{bmatrix} \mathbf{M}_{11} & 0 & \dots & 0 \\ 0 & \mathbf{M}_{22} & \dots & 0 \\ \vdots & \vdots & \ddots & \vdots \\ 0 & 0 & \dots & \mathbf{M}_{nn} \end{bmatrix}, \quad \mathbf{C} = \begin{bmatrix} 0 & 0 & \dots & 0 \\ 0 & \mathbf{C}_{22} & \dots & 0 \\ \vdots & \vdots & \ddots & \vdots \\ 0 & 0 & \dots & 0 \end{bmatrix}, \quad \mathbf{K} = \begin{bmatrix} \mathbf{K}_{11} & \mathbf{K}_{12} & \dots & \mathbf{K}_{1n} \\ \mathbf{K}_{21} & \mathbf{K}_{22} & \dots & \mathbf{K}_{2n} \\ \vdots & \vdots & \ddots & \vdots \\ \mathbf{K}_{n1} & \mathbf{K}_{n2} & \dots & \mathbf{K}_{nn} \end{bmatrix} \quad (4)$$

Since there is no applied force at the interior nodes, the force vector is given by:

$$\mathbf{p} = \begin{bmatrix} \mathbf{p}_1 \\ 0 \\ \vdots \\ 0 \end{bmatrix} \quad (5)$$

This finite element model is capable of predicting all the details of the global and local strut behavior. However, the strut is normally designed to act only as an axial load carrying member providing strength, stiffness and damping to meet the design requirements. The analysis model in this form also does not explicitly express the relationship between the essential dynamic characteristics and the key parameters. It should only be used if the detailed local dynamics is important or as a verification model after the strut parameters are selected by other means.

STRUT MODEL REDUCTION

In order to understand the dynamic characteristics of the strut, the analytical model should be simplified to a small set of parameters. The reduction of the component level model will also significantly reduce the complexity of the system level model. For design purpose, only axial behavior of the struts are considered. Consequently, the analysis model is constrained to have displacement only in the axial direction. At each node, only the axial degree of freedom and two rotations are retained. For structural problem, the internal dynamics is generally not important and the internal inertial effect is ignored.

There are only two degrees of freedom necessary to characterize the strut: u_1 - the axial degree of freedom at the strut end for connectivity and u_2 - the axial degree of freedom at the dashpot for damping. The standard static condensation reduces the stiffness matrix to a symmetric 2x2 matrix with only 3 independent terms:

$$\mathbf{k} = \begin{bmatrix} k_{11} & k_{12} \\ k_{21} & k_{22} \end{bmatrix} \quad (6)$$

Therefore, any complex viscous strut design can be reduced to only 3 equivalent stiffness constants. For the same 3 stiffness constants, there can be many designs having the same condensed characteristics. Since for the class of struts of interest, the dashpot is at the supported end, the condensed damping matrix is very simple:

$$\mathbf{c} = \begin{bmatrix} 0 & 0 \\ 0 & c \end{bmatrix} \quad (7)$$

As for the mass matrix, normally a simple lumping procedure is sufficient since the inertia effect of the strut is considered not important.

STRUT DESIGN MODEL

Static condensation of a relatively complex strut design allows a simple equivalent mechanical modeling of the strut for understanding its dynamics. Due to the design details, many strut configurations also have an additional characteristic⁴ that $k_{12} = -k_{22}$. This allows a further simplification such that the abstract 2x2 stiffness matrix of Equation (6) can be represented by an equivalent lumped parameter model as shown in Figure 2. A viscously damped strut can now be represented by 3 frequency independent parameters, k_1 - the outer spring, k_2 - the inner spring and c - the dashpot.

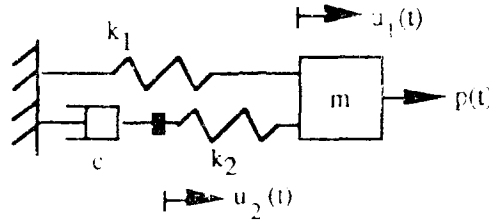


Figure 2 3-Parameter 2 DOFs Viscous Strut Model

The equation of motion of the 3-parameter viscous strut model can be written as:

$$m\ddot{u} + c\dot{u} + ku = p \quad g(t) \quad (8)$$

where,

$$m = \begin{bmatrix} m & 0 \\ 0 & 0 \end{bmatrix}, \quad k = \begin{bmatrix} k_1+k_2 & -k_2 \\ -k_2 & k_2 \end{bmatrix}, \quad c = \begin{bmatrix} 0 & 0 \\ 0 & c \end{bmatrix}, \quad p = \begin{bmatrix} p \\ 0 \end{bmatrix} \quad (9)$$

If the strut is used to support a rigid mass which is include in the mass matrix, the characteristics of this structural system is given by the free vibration problem:

$$m\ddot{u} + c\dot{u} + ku = 0 \quad (10)$$

or, in the first order form⁶:

$$\begin{bmatrix} c & m \\ m & 0 \end{bmatrix} \begin{bmatrix} \dot{u} \\ \ddot{u} \end{bmatrix} + \begin{bmatrix} k & 0 \\ 0 & -m \end{bmatrix} \begin{bmatrix} u \\ \dot{u} \end{bmatrix} = \begin{bmatrix} 0 \\ 0 \end{bmatrix} \quad (11)$$

For this three parameter model, Equation (11) can be written explicitly as:

$$\begin{bmatrix} 0 & 0 & m & 0 \\ 0 & c & 0 & 0 \\ m & 0 & 0 & 0 \\ 0 & 0 & 0 & 0 \end{bmatrix} \begin{bmatrix} \dot{u}_1 \\ \dot{u}_2 \\ \ddot{u}_1 \\ \ddot{u}_2 \end{bmatrix} + \begin{bmatrix} k_1+k_2 & -k_2 & 0 & 0 \\ -k_2 & k_2 & 0 & 0 \\ 0 & 0 & -m & 0 \\ 0 & 0 & 0 & 0 \end{bmatrix} \begin{bmatrix} u_1 \\ u_2 \\ \dot{u}_1 \\ \dot{u}_2 \end{bmatrix} = \begin{bmatrix} 0 \\ 0 \\ 0 \\ 0 \end{bmatrix} \quad (12a)$$

The eigenvalue problem is therefore given by:

$$\left\{ \lambda, \begin{bmatrix} 0 & 0 & m \\ 0 & c & 0 \\ m & 0 & 0 \end{bmatrix} + \begin{bmatrix} k_1+k_2 & -k_2 & 0 \\ k_2 & k_2 & 0 \\ 0 & 0 & m \end{bmatrix} \right\} \psi_1 = 0 \quad (12b)$$

The eigenvalues, λ_i , and eigenvectors, ψ_i , are generally complex. For a lightly damped system, there is one pair of complex eigenvalues which represent the under-damped modes and one real eigenvalue which represents the over-damped mode. Eigensolvers used in structural codes normally assume the structures to be lightly damped and solve for complex pairs only. However, solving the eigenvalue problem does not give any physical insight into the design of struts. Therefore, a simpler design approach is more appropriate.

APPROXIMATE ANALYSIS OF DAMPED STRUTS

When a strut is functioning as a member of a large structure or as an individual member under a harmonic force given by:

$$g(t) = e^{i\omega t} \quad (13)$$

the steady state solution takes the form:

$$\mathbf{u} = \begin{bmatrix} u_1 \\ u_2 \end{bmatrix} e^{i\omega t} \quad (14)$$

Assuming that the mass at the internal degree of freedom, u_2 , is small, and the internal dynamics of the strut is not important to the problem, the governing differential equation is given by:

$$\left\{ \begin{bmatrix} k_1+k_2 & -k_2 \\ -k_2 & k_2 \end{bmatrix} - \omega^2 \begin{bmatrix} m & 0 \\ 0 & 0 \end{bmatrix} + i \omega \begin{bmatrix} 0 & 0 \\ 0 & c \end{bmatrix} \right\} \begin{bmatrix} u_1 \\ u_2 \end{bmatrix} = \begin{bmatrix} p \\ 0 \end{bmatrix} \quad (15)$$

The equations of motion are described by frequency independent coefficient matrices. The internal degree of freedom, u_2 , is not subject to any external force. Again, the static condensation technique is used to reduce the internal degree of freedom by considering the second equation of Equation (15):

$$-k_2 u_1 + (k_2 + i\omega c) u_2 = 0 \quad (16a)$$

$$u_2 = \frac{k_2}{k_2 + i\omega c} u_1 \quad (16b)$$

Therefore, the effective strut dynamics is given by:

$$\left(-\omega^2 m + (k_1 + k_2) - \frac{k_2^2}{k_2 + i\omega c} \right) u_1 = p \quad (17a)$$

The term in parenthesis is the strut dynamic impedance which is frequency dependent. However it is more useful to describe the strut in terms of complex stiffness (i.e., $k(\omega) = k^R(\omega) + ik^I(\omega)$):

$$(-\omega^2 m + k^R + ik^I) u_1 = p \quad (17b)$$

where,

$$k^R = \frac{k_1 k_2^2 + (k_1 + k_2)(c\omega)^2}{k_2^2 + (c\omega)^2} \quad (18a)$$

$$k^I = \frac{k_2^2 (c\omega)}{k_2^2 + (c\omega)^2} \quad (18b)$$

The complex stiffness can further be expressed in a different form in terms of the real part of the stiffness and the loss factor as:

$$k = k^R (1 + i\eta) \quad (19a)$$

where,

$$\eta = \frac{k_2^2 (c\omega)}{k_1 k_2^2 + (k_1 + k_2)(c\omega)^2} \quad (19b)$$

These relationships can be presented in a more useful form for design purposes in terms of normalized parameters. Define the stiffness ratio as:

$$\kappa = \frac{k_2}{k_1} \quad (20a)$$

the strut frequency constant as:

$$\omega_c = \frac{k_1}{c} \quad (20b)$$

and the normalized excitation frequency as:

$$\beta = \frac{\omega}{\omega_c} \quad (20c)$$

Rewrite the strut real stiffness and loss factor in terms of the normalized ratios:

$$\frac{k^R}{k_1} = \left[\frac{\kappa^2 + (1 + \kappa)\beta^2}{\beta^2 + \kappa^2} \right] \quad (21a)$$

$$\eta = \frac{\kappa^2 \beta}{\kappa^2 + (1 + \kappa)\beta^2} \quad (21b)$$

In this normalized form, useful design curves can be generated to aid damping design. The damping and frequency relationships of a few selected stiffness ratios are shown in Figure 4. The loss factor has a slope of one and negative one at the low and high frequency range on the log-log scale and has a distinct maximum at the mid frequency range. The damping loss factor increases with the stiffness ratio.

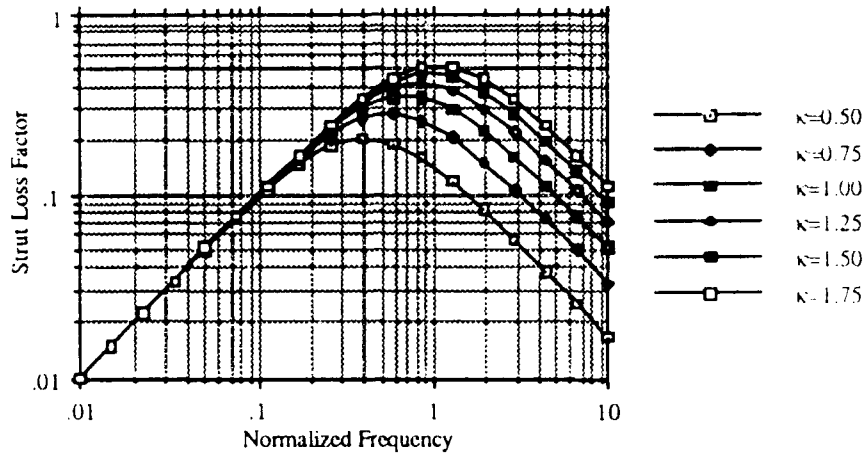


Figure 4 Normalized Design Curves

For design purposes, it is important to understand the frequency and damping characteristics of the damped strut in terms of an equivalent single degree of freedom (SDOF) system. This approximation bypasses the eigenvalue problem of Equation (12). An equivalent SDOF system is shown in Figure 5. The equation of motion of this system subject to steady state force is given by:

$$(-\omega^2 m + k + i\omega c) u = p \quad (22)$$

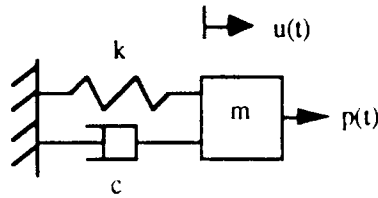


Figure 5 Equivalent Single Degree of Freedom System

Comparing Equation (22) to Equation (17), for lightly damped systems, say $\xi \leq 0.2$, the equivalent natural frequency of the damped strut system can be approximated by:

$$\omega_{eq} = \sqrt{\frac{k^R(\omega)}{m}} \quad (23)$$

The equivalent viscous damping ratio can be found by equating the energy loss of the strut to that of an equivalent SDOF viscous system. The energy dissipated per cycle of the strut as described by Equation (19) under a harmonic force is given by⁷:

$$D_\eta = \pi \eta k^R u_1^2 \quad (24)$$

The damping of an equivalent SDOF viscous system is given by:

$$D_\xi = \pi \xi_{eq} (2m\omega_{eq}) \omega u^2 \quad (25)$$

Equating the energy dissipation at resonance, $\omega = \omega_{eq}$:

$$\xi_{eq} = \frac{\eta(\omega_{eq})}{2} \quad (26)$$

OPTIMUM STRUT BEHAVIOR

For a given a design, i.e. k_1 , k_2 and c , the strut dynamic stiffness and damping can be computed using Equations (21a) and (21b). A typical plot of the stiffness and loss factor of a strut is shown in Figure 6.

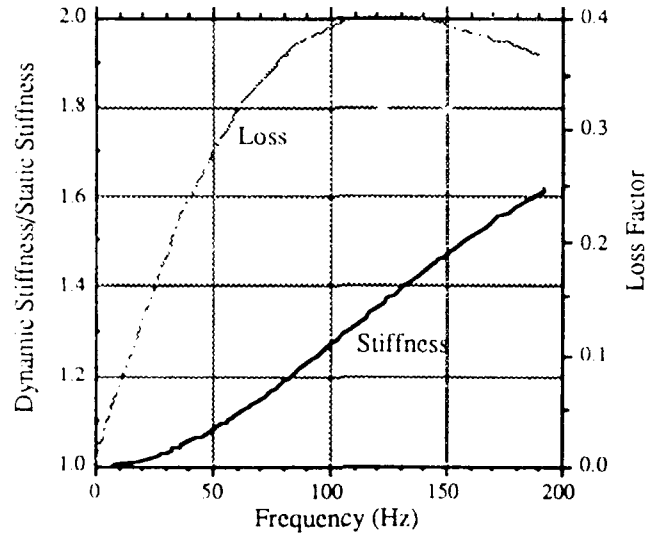


Figure 6 Typical Viscous Strut Stiffness and Loss Factor vs. Frequency

For design purposes, it is important to find the optimum performance region of the strut so that the strut can be designed to perform effectively, i.e. high damping at the desired frequency range. The maximum loss factor with respect to frequency can be found by setting the derivation of Equation (19b) to be zero:

$$\frac{\partial \eta}{\partial \omega} = 0 \quad (27)$$

The condition at which the damping is at maximum is denoted by the subscript op.

$$\eta_{op} = \frac{\kappa}{2\sqrt{1+\kappa}} \quad (28a)$$

$$k_{op}^R = \frac{2(1+\kappa)}{2+\kappa} k_1 \quad (28b)$$

$$\omega_{op} = \frac{\kappa}{\sqrt{1+\kappa}} \omega_c \quad (28c)$$

$$\beta_{op} = \frac{\kappa}{\sqrt{1+\kappa}} = 2 \eta_{op} \quad (28d)$$

It is important to note that the maximum loss factor is governed by κ , the ratio of the inner and outer stiffnesses. A flexible inner tube is not effective in providing force to the damper to activate energy dissipation. A stiff inner tube is very desirable for high damping but the strut will also be heavier. It is also important to note that there is not much damping at low and high frequency. The stiffness corresponding to maximum loss factor is at the transition between the static stiffness, k_1 , and asymptotic stiffness, k_1+k_2 . The frequency at which the maximum loss occurs is proportional to the damper non-dimensional frequency, ω_c . As a matter of fact, the normalized optimum frequency is twice the maximum loss factor. Using these relationships, frequency independent parameters can be computed easily to match the key points of test data in order to characterize the dynamic behavior. Comparisons between analytical and test data were excellent.

These relationships can easily be used to size the key strut parameters. For a desired level of damping, η_r , use Equation (28a) to find the required stiffness ratio, κ_r .

$$\kappa_r = 2 \eta_r^2 + 2 \eta_r \sqrt{\eta_r^2 + 1} \quad (29)$$

Then use Equation (28c) to compute the damping coefficient, c_r , required to locate the frequency, ω_r , where the maximum damping is required.

$$c_r = \frac{\kappa_r}{\sqrt{1+\kappa_r}} \frac{k_1}{\omega_r} \quad (30)$$

STRUT BANDWIDTH

Another important performance parameter is the bandwidth of the strut over which there is significant amount of damping. The effective bandwidth can influence the design of struts for a large structure with a wide range of natural frequencies.

The bandwidth of the strut can be defined as the frequency range over which the strut has a damping efficiency γ .

$$\gamma = \frac{\eta_1}{\eta_{op}} \quad (31)$$

The bandwidth can be found by solving Equation (21b). For a given damping efficiency, there are two frequency points:

$$\beta_{1,2} = \frac{\kappa}{\gamma} \frac{1 \pm \sqrt{1 - \gamma^2}}{\sqrt{1+\kappa}} \quad (32)$$

The corresponding normalized frequency bandwidth is given by:

$$\Delta\beta = \frac{2\kappa\sqrt{1 - \gamma^2}}{\gamma\sqrt{1+\kappa}} \quad (33)$$

The actual frequency bandwidth is given by:

$$\Delta\omega = \frac{2\kappa\sqrt{1-\gamma^2}}{\gamma\sqrt{1+\kappa}} \frac{k_1}{c} \quad (34)$$

The damping bandwidth is shown graphically in Figure 7. The damping within the bandwidth is guaranteed to be higher than the specified efficiency. The bandwidth concept can be used for many other design reasons. The reciprocal of damping efficiency can be interpreted as a safety factor for damping design. The bandwidth can be used to cover the uncertainty in the natural frequencies of a large structure.

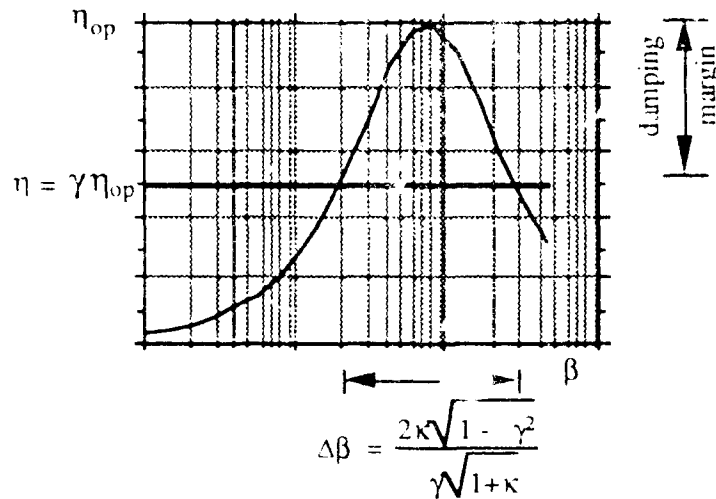


Figure 7 Strut Damping Bandwidth

DESIGN EXAMPLE

The method developed can be used to size the key parameters of a strut. Only simple algebraic equations are solved and an eigenvalue problem is totally avoided. Suppose a 20-pound weight is supported by a strut. The system is required to have 20 Hertz natural frequency and 5% viscous damping. By using the design equations, the strut parameters were computed to be: $k_1 = 758.8$ lb/in, $k_2 = 166.86$ lb/in, $c = 1.2$ lb-sec/in. The frequency and damping characteristic of the system with these parameters were checked with an exact eigensolution. The results compare favorably and are summarized in Table 1.

Table 1 Comparison of Results

Parameters	Design Goal	Eigensolution	Error
Frequency	20.0 Hz	20.2 Hz	1%
Damping	5%	5.25%	5%

CONCLUSION

The dynamics of a class of viscously damped struts is presented. The derivation is based on the principles of structural dynamics and governing equations of motion of a finite element model. This approach is consistent with the system level analysis methods. The use of condensation technique allows a complex strut design to be reduced to 3 stiffness parameters which are further reduced to 2 lumped stiffness parameters. The dynamics of the struts can be understood through non-dimensional design variables. Design curves can be used to facilitate component sizing. The bandwidth characteristics of the struts provide further insight into the performance of this class of struts. Results from using this method compared favorably with the exact solution from a complex eigenvalue problem. Therefore, a 3-parameter model can be used to characterize the performance of a viscously damped strut for system level design and analysis. The method can be used to derive component specification to meet system level design requirements⁵.

NOMENCLATURE

Symbols

C, c, c	=	viscous damping matrix or scalar
D	=	energy dissipation per cycle
g	=	forcing function
i	=	imaginary unit, $\sqrt{-1}$
K, k, k	=	stiffness stiffness or scalar
M, m, m	=	mass matrix or scalar
p	=	spatial force vector
u, u	=	displacement vector and axial displacement degree of freedom
β	=	non-dimensional forcing frequency
γ	=	damping efficiency factor
Δ	=	change/bandwidth
λ	=	complex eigenvalue
ψ	=	complex eigenvectors
η	=	loss factor
κ	=	stiffness ratio of inner spring to outer spring
ξ	=	damping ratio
ω	=	frequency, radian/second

Subscripts

eq	=	equivalent
c	=	pertaining to damping
i	=	for the i-th mode
op	=	condition at maximum loss factor
r	=	pertaining to the required conditions
ξ	=	pertaining to viscous damping
η	=	pertaining to viscoelastic (hysteretic) damping

Superscripts

I	=	Imaginary
R	=	Real
T	=	matrix transpose

REFERENCES

1. J.L. Fanson, G.H. Blackwood and C.-C. Chu, 'Active Member Control of Precision Structures', *AIAA/ASME,ASCE,AHS/ASC 30-th Structures, Structural Dynamics, and Materials (SDM) Conference*, 1989, Mobile, Alabama.
2. Johnson, C.D., and Kienholz, D.A., 'Design and Testing of a Sixty-Foot Damped Generic Space Truss', *Damping 1986*, AFWAL-TR-86-3059, Flight Dynamics Laboratory, Air Force Wight Aeronautical Laboratories (1986).
3. Johnson, C.D., and Kienholz, D.A., 'Finite Element Prediction of Damping in Structures with Constrained Viscoelastic Layers', *AIAA Journal* Vol 20, No. 9 (Sept. 1982).
4. E. Anderson, M. Trubert, J. Fanson, and P. Davis, 'Testing and Application of a Viscous Passive Damper for Use in Precision Truss Structure', *AIAA/ASME,ASCE,AHS/ASC 32-th Structures, Structural Dynamics, and Materials (SDM) Conference*, 1991, Baltimore, Maryland.
5. Y.C. Yiu, 'System Level Design and Analysis of Truss Structures Damped by Viscous Struts', *Damping '91 Conference*, February 1991, San Diego, California.
6. Hurty, W.C. and Rubinstein, M.F., *Dynamics of Structures*, Prentice-Hall, Inc., 1964.
7. Nashif, A.D., D.I.G. Jones, and J.P. Henderson, *Vibration Damping*, John Wiley & Sons (New York, 1985).

A Study of a Vibration Absorber to Control the
Vibration of Rectangular Plate

Akio SUGIMOTO / Mechanical Engineering Research
Laboratories, Kobe Steel Ltd.

Hideo UTSUNO,
Toshimitsu TANAKA / Mechanical Engineering Research
Laboratories, Kobe Steel Ltd.

ABSTRACT

A vibration absorber was studied to control the dynamic behavior of a rectangular plate. The absorber consists of a vibration damping composite steel beam and an additive mass. By evaluating the loss factor and the bending rigidity of the composite steel beam using the Ross-Kerwin-Ungar model, the length and the thickness of the composite steel beam and the additive mass were determined in order to tune the resonance frequency of the absorber to any resonance frequency of the rectangular plate. The dynamic behavior of the rectangular plate with the absorber was measured and compared with the calculation. The close agreement achieved suggests that the present method is sufficiently reliable to predict the dynamic behavior of the vibration absorber consisting of the vibration damping composite steel beam.

1-5-5 Takatsukadai Nishi-ku Kobe 651-22, Japan
Phone 078-991-5640 Fax 078-991-5605

INTRODUCTION

A vibration absorber is an effective method to solve vibration and noise problems in several industrial structures and machines. The absorber is a passive damping device to reduce the amplitude of vibration at resonance. The optimum design method for the single of degree system was already derived (1). Though many investigations of vibration absorbers have been reported (2)-(5), there is few reports to study the absorbers using a vibration damping composite steel beam as a spring and damping element.

In this paper, we propose a method to design the absorber consisting of the composite steel beam and an additive mass. By evaluating the loss factor and the bending rigidity of the beam using the Ross-Kerwin-Ungar model (6), (7), the thicknesses of the steel and viscoelastic resin layers and the length of the beam are determined to tune a resonance frequency and of a vibrating main body to be damped.

The vibration absorber was designed to control the first vibration mode of the rectangular aluminum plate using the above method. The frequency response curve of inertance of the plate with the absorber is calculated to be compared with the experimental results. The close agreement achieved suggests that this method is sufficiently reliable to predict the dynamic behavior of the absorber consisting of the composite steel beam.

1. CALCULATION METHOD OF DYNAMIC BEHAVIOR OF THE ABSORBER

1.1 CALCULATION MODEL

The vibration absorber is shown in Fig. 1. It consists of the vibration damping composite steel beam and the additive mass placed on the both ends. The beam is supported at the center and attached to the vibrating main body (a rectangular aluminum plate in this paper) to be controlled. As the shape of the absorber is symmetric, the calculation model is assumed to be the cantilever with an additive mass at the free end as depicted in Fig. 2.

1.2 CALCULATION OF THE DYNAMIC BEHAVIOR OF THE ABSORBER

The vibration damping composite steel beam is considered to be equivalent to the homogeneous beam with the structural damping. To incorporate the damping into the beam, it is necessary to replace a bending rigidity EI of the beam by a complex bending rigidity $EI(1+j\eta)$. The complex bending rigidity $EI(1+j\eta)$ can be calculated by using the Ross-Kerwin-Ungar model (referred to hereafter the RKU model) (8). Bending wave equation for the vibration absorber is given by

$$\rho A \frac{\partial^2 w}{\partial t^2} + EI(1+j\eta) \frac{\partial^4 w}{\partial x^4} = 0 \quad (1)$$

where w, ρ, A , and I are the displacement in Y-axis, the mass per unit length, the cross-sectional area, and the area moment of inertia of the composite steel beam, respectively. η is the loss factor. The general solution to Eq.(1) is given by

$$w = W \exp(j\omega t) \quad (2)$$

$$W = A_1 \exp(-jk_b x) + A_2 \exp(jk_b x) + A_3 \exp(-k_b x) + A_4 \exp(k_b x) \quad (3)$$

where W is the amplitude of displacement in Y-axis, A_1 - A_4 are undetermined constants, and k_b is a complex wave number defined by

$$k_b = \left[\frac{\rho A \omega^2}{EI(1+\eta^2)^{1/2}} \right]^{1/4} (\alpha - j\beta) \quad (4)$$

$$\alpha = \cos\left(\frac{1}{4} \tan^{-1} \eta\right) \quad (5)$$

$$\beta = \sin\left(\frac{1}{4} \tan^{-1} \eta\right) \quad (6)$$

The boundary conditions at the clamped end($X=0$) and the free end($X=L$) are given by

$$\text{Clamped end}(X=0) \quad W = 0 \quad (7)$$

$$\frac{dW}{dx} = 0 \quad (8)$$

$$\text{Free end}(X=L) \quad \frac{F_0}{EI(1+j\eta)} + \frac{m\omega^2 W}{EI(1+j\eta)} = \frac{d^3 W}{dx^3} \quad (9)$$

$$\frac{d^2 W}{dx^2} = 0 \quad (10)$$

where m is the additive mass and ω is the circular frequency. Substituting Eqs.(3)-(6) into Eqs.(7)-(10), we obtain

$$A_1 = j(\cos k_b L - \sin k_b L + \cosh k_b L - \sinh k_b L) F/D \quad (11)$$

$$A_2 = j(\cos k_b L + \sin k_b L + \cosh k_b L + \sinh k_b L) F/D \quad (12)$$

$$A_3 = [-\sin k_b L - \sinh k_b L - j(\cos k_b L + \cosh k_b L)] F/D \quad (13)$$

$$A_4 = [\sin k_b L + \sinh k_b L - j(\cos k_b L + \cosh k_b L)] F/D \quad (14)$$

where

$$F = F_0 k_b / \rho A \omega^2 \quad (15)$$

$$D = 4 [1 + \cos k_b L \cosh k_b L + H(\cos k_b L \sinh k_b L - \sinh k_b L \cosh k_b L)] \quad (16)$$

$$H = m k_b L / \rho A \quad (17)$$

Substituting Eqs.(11)-(17) into Eq.(2),(3), we can calculate the amplitude of the displacement. The frequency response curve of inertance of the absorber is found by differentiating the displacement $W \exp(j\omega t)$ twice with respect to time t and divided by the sinusoidal force $F_0 \exp(j\omega t)$ which acts on the free end.

1.3 RKU MODEL OF THE VIBRATION DAMPING COMPOSITE STEEL BEAM

The vibrating damping composite steel beam has three layers as shown in Fig. 3. The complex bending rigidity $EI(1+j\eta)$ of the beam can be calculated by substituting Young's moduli E_1, E_3 and the thicknesses t_1, t_3 of the steel, the complex shear modulus G_1+jG_2 and the thickness t_2 of the viscoelastic layer into Eqs.(18)-(20).

The value of G_1+jG_2 used in this calculation is the reduced data of the modulus over the frequency range 10.0Hz to 2.0kHz at +24°C obtained from the measured data over the frequency range 0.03 to 80.0 Hz and the temperature range -30 to +50°C by using the temperature-frequency superposition principle⁽¹⁾.

$$EI(1+j\eta) = \frac{E_1 b t_1^3}{12} + \frac{E_3 b t_3^3}{12} + DE_1 b t_1 \left(\frac{t_1+t_3}{2} + t_2 \right) \quad (18)$$

$$D = \frac{g E_3 t_3}{E_1 t_1 + g(E_1 t_1 + E_3 t_3)} \left(\frac{t_1+t_3}{2} + t_2 \right) \quad (19)$$

$$g = \frac{G_1+jG_2}{\omega E_3 t_3 t_2} \left[\frac{EI(1+j\eta)}{\rho A} \right]^{1/2} \quad (20)$$

2. OPTIMUM DESIGN OF THE ABSORBER

2.1 DETERMINATION OF THE OPTIMUM DIMENSIONS OF THE BEAM

The vibration absorber is applied to control the first mode of the rectangular aluminum plate(1000x1000x4mm) in this section. After measuring the resonance frequency f_0 and the equivalent mass M for the plate, The optimum values of the resonance frequency f_{opt} and loss factor η_{opt} of the absorber can be calculated using Eqs.(21)-(23)⁽¹⁹⁾.

$$\mu = 2m/M \quad (21)$$

$$f_{opt} = \frac{1}{1+\mu} f_0 \quad (22)$$

$$\eta_{opt} = [3\mu/2(1+\mu)]^{1/2} \quad (23)$$

The values of f_0 and M can be evaluated by applying the half-power bandwidth method⁽⁹⁾ to the frequency response curve of inertance, measured at the center of the plate where the maximum amplitude of the first vibration mode occurs. The frequency response curve measured is shown in Fig. 4. We obtain $f_0=24.5\text{Hz}$, $M=2.88\text{ kg}$, and $\eta=0.0171$. Assuming the additive mass $m=110\text{g}$ ($\mu=3.82\%$), we obtain $f_{opt}=23.7\text{Hz}$, $\eta_{opt}=0.235$.

To achieve these values, the frequency response curve of inertance for several dimensions of the absorber were calculated. The resonance frequency f and the loss factor η of the absorber were estimated by applying the half-power bandwidth method to the frequency response curve of inertance calculated by using Eqs.(3)-(20). The calculation of the frequency response curves of inertance was carried out for the cases of $t_2=30, 50, 70, 100\text{ }\mu\text{m}$ and $L=90, 100, 110, 120\text{ mm}$ under the condition that the both of t_1 and t_3 are fixed at 1.6mm . The calculated results for $t_2=70\text{ }\mu\text{m}$, $L=100, 110, 120\text{ mm}$ are shown in Fig. 5. The optimum values of t_2 and L are determined by choosing their optimum combination so that the calculated results of f and η equal f_{opt} and η_{opt} , respectively. The relation between f and η of the absorber for each values of t_2 and L is shown in Fig. 6. This shows that $f=24.9\text{Hz}$, $\eta=0.245$ can be achieved by setting $t_2=70\text{ }\mu\text{m}$, $L=110\text{mm}$.

2.2 CALCULATION OF THE REDUCTION OF VIBRATION AMPLITUDE

The frequency response curve of inertance of the rectangular aluminum plate with the absorber can be calculated from the values of the equivalent mass M , the spring constant K , and the loss factor η of the first vibration mode of the plate and that of the absorber as shown in Table 1.

The calculated results of the frequency response curve are shown in Fig. 7. The solid line represents a calculated result without the absorber. The dashed line represents a calculated one with the absorber setting $t_2=70\text{ }\mu\text{m}$. The broken line represents a calculated one with the absorber setting $t_2=30\text{ }\mu\text{m}$. The former is tuned to the optimum value, and it reduces the vibration amplitude by about 20 dB. On the other hand, the loss factor of the latter is about half of the optimum value, and it causes 3 dB inferiority in the reduction in the vibration amplitude of the absorber.

3. COMPARISON OF CALCULATIONS WITH EXPERIMENT

3.1 THE INERTANCE TRANSFER FUNCTION

The measuring system of the dynamic behavior of the absorber is shown in Fig. 8 (the temperature of the thermostatic oven is set at +24°C). An absorber is made to realize the optimum dimension and the frequency response curve of inertance of the absorber is measured. The result is shown in Fig. 9. The values of the equivalent mass m , the spring constant k , and the loss factor η of the absorber can be obtained from the measured frequency response curve, and compared with the calculated result as shown in Table 2. These results show the close agreement, and it can be concluded that the present method is sufficiently accurate to predict the dynamic behavior of the absorber.

3.2 THE EFFECT OF THE VIBRATION ABSORBER

Figure 10 shows the frequency response curve of inertance at a center of the aluminum plate with the absorber. The solid line represents the calculated result and the broken line represents the measured result. The close agreement of the measured and calculated results suggests that the present method is sufficiently reliable to predict the reduction in the vibration amplitude at resonance.

CONCLUSION

In this paper, the effective method to design the vibration absorber using the vibration damping composite steel beam was proposed to tune the resonance frequency and the loss factor of the absorber to the optimum value. The following results were obtained;

(1) We proposed a method to design the vibration absorber consisting of the composite steel beam and the additive mass. The optimum values of the thicknesses of the steel and viscoelastic layers and the length of the beam can be determined by using this method.

(2) The dynamic behavior of the rectangular aluminum plate with the absorber can be predicted with a practical accuracy by using this method.

(3) The remarkable reduction of 25dB in the amplitude of vibration can be achieved by applying the absorber to the rectangular aluminum plate.

REFERENCES

- (1) Den Hartog, J.P., Mechanical Vibrations, 1956, pp.108, McGraw-Hill.
- (2) K.Seto et al., Vibration Control of Multi-Degree-of-Freedom Systems by Dynamic Absorbers 1st Report, Trans. JSME, Vol.50, No.458, 1984, pp.1962.
- (3) K.Seto, Vibration Control of Multi-Degree-of-Freedom Systems by Dynamic Absorbers 2nd Report, Trans. JSME, Vol.50, No.458, C., 1984, pp.1970.
- (4) M.Ookuma et al., Vibration Control of Structures by Dynamic Absorbers 1st Report, Trans. JSME, Vol.52, No.484, 1986, pp.3184.
- (5) H.Yamaguchi, On Optimum Design of a Composite Beam Dynamic Vibration Absorber, Proc. 67th JSME Spring Ann. Meeting, No.900-14, 1990, pp.104.
- (6) L.Beranek, Noise & Vibration Control, 1971, pp.460, McGraw-Hill.
- (7) Nashif, A.D., VIBRATION DAMPING, 1985, pp.259, John Wiley & Sons, Inc.
- (8) H.Utsuno et al., Study of Dynamic Behavior of Viscoelastic Sandwich Materials, Proc. 249th JSME (Kansai), 1990, pp.139.
- (9) N.Ookubo, Modal Analysis of Mechanics, 1981, pp.85, Chuoo Univ. Press.

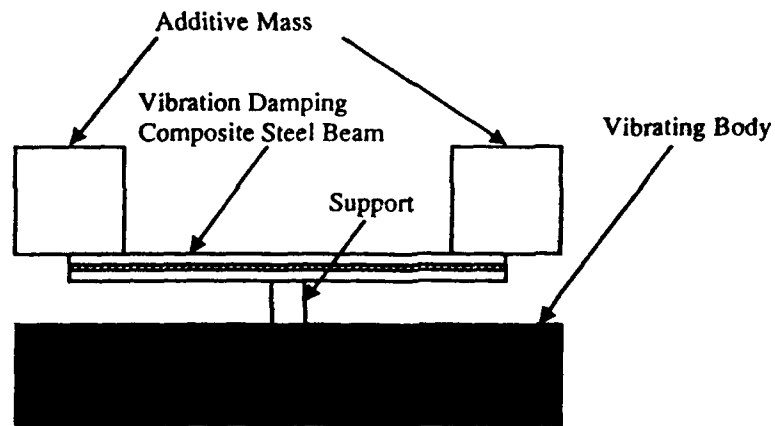


Fig. 1 Structure of Vibration Absorber

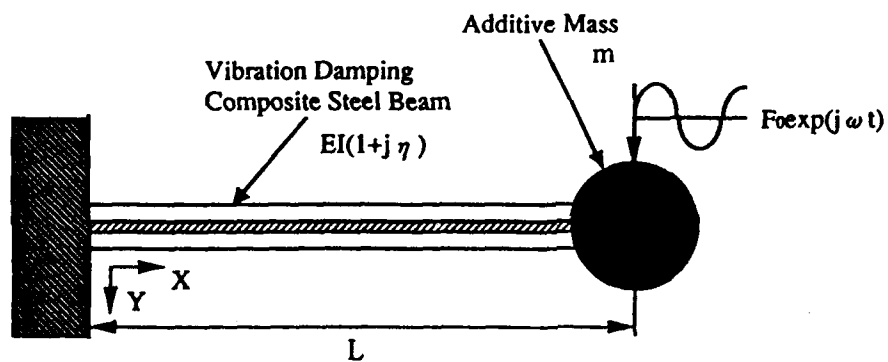


Fig. 2 Calculation Model of Absorber

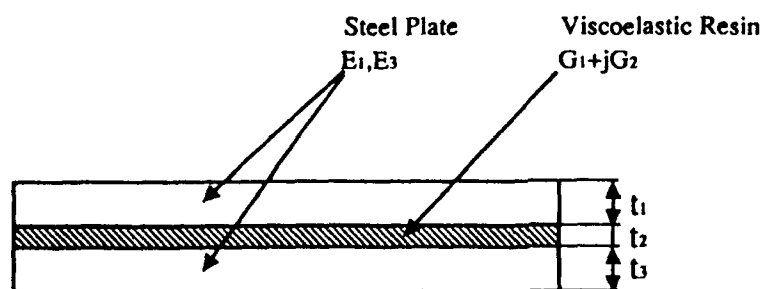


Fig. 3 Structure of Vibration Damping
Composite Steel Beam

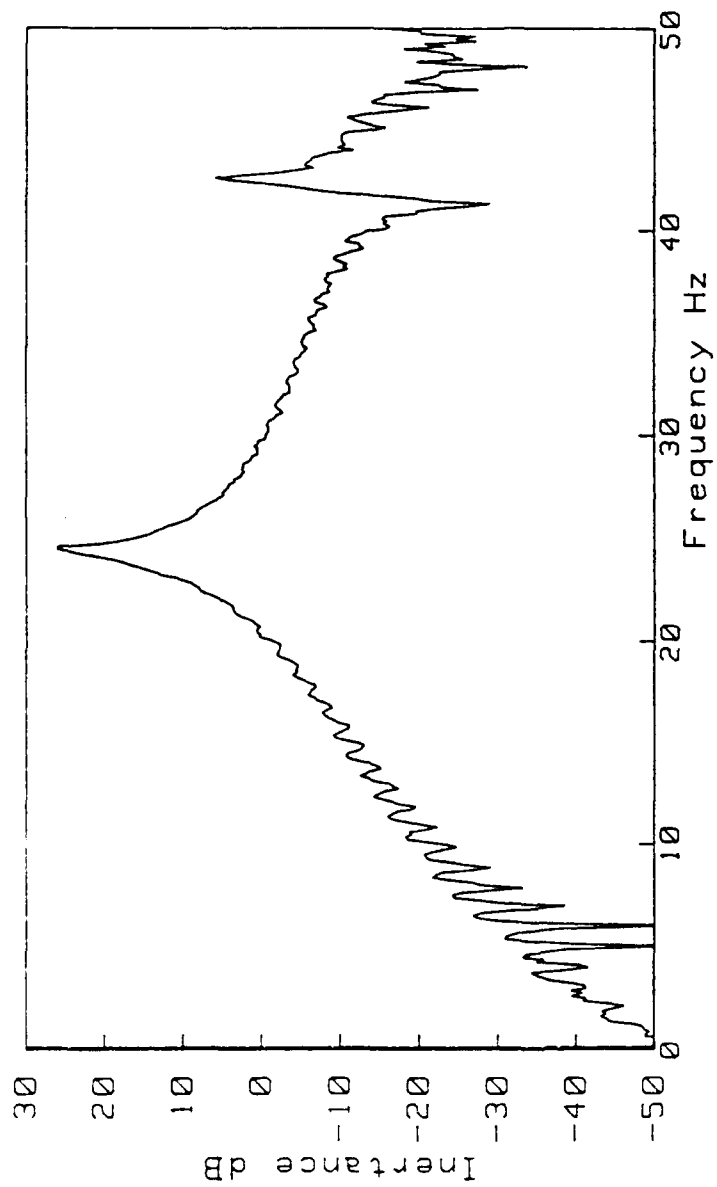


Fig.4 Measured Frequency Response Curve
of Aluminum Plate

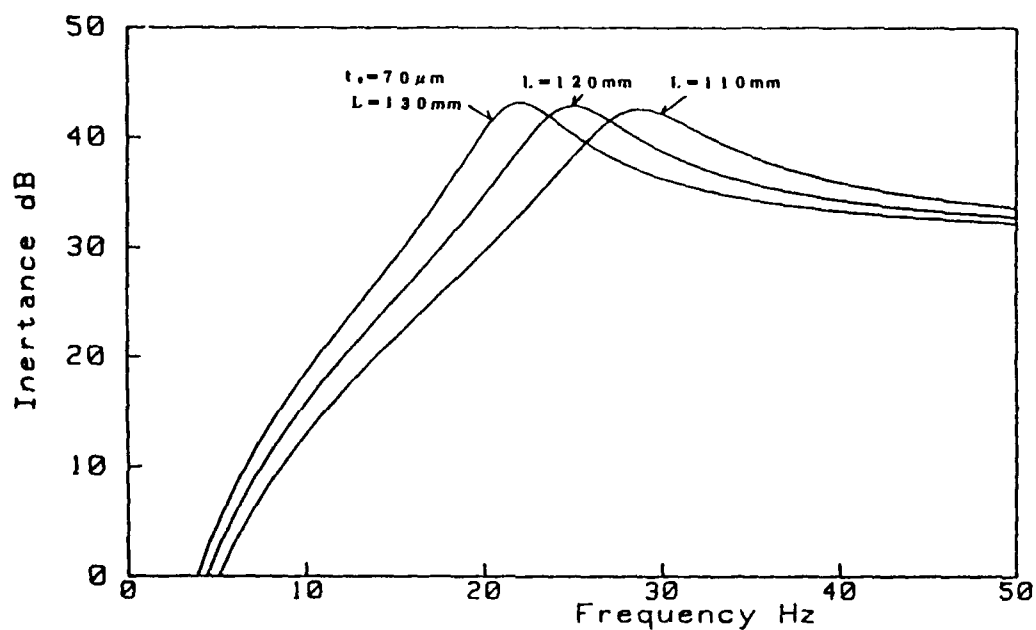


Fig. 5 Calculated Frequency Response Curve
of Absorber

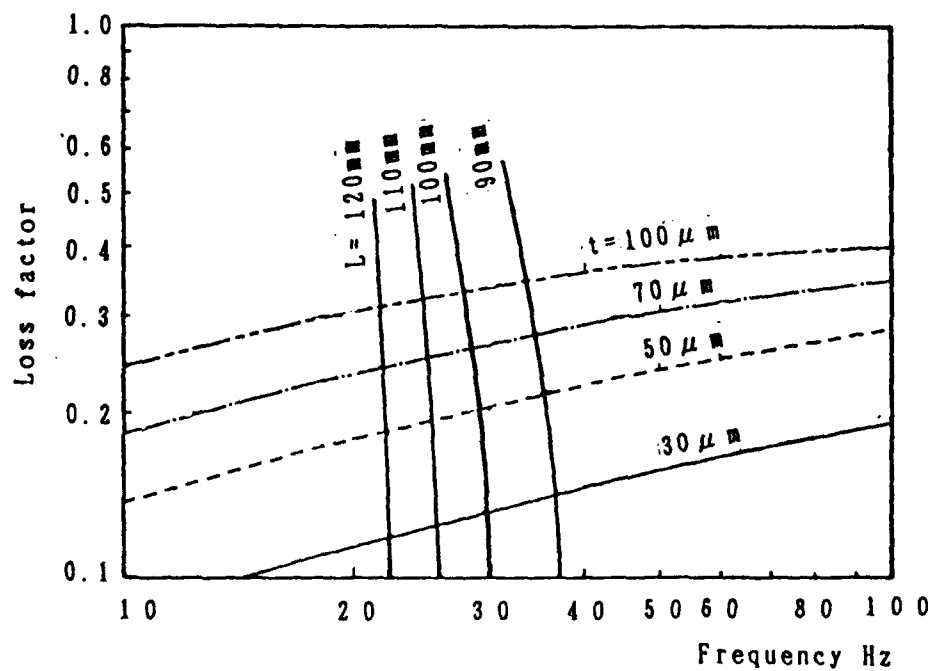


Fig. 6 Relation between Resonance Frequency
and Loss Factor of Absorber

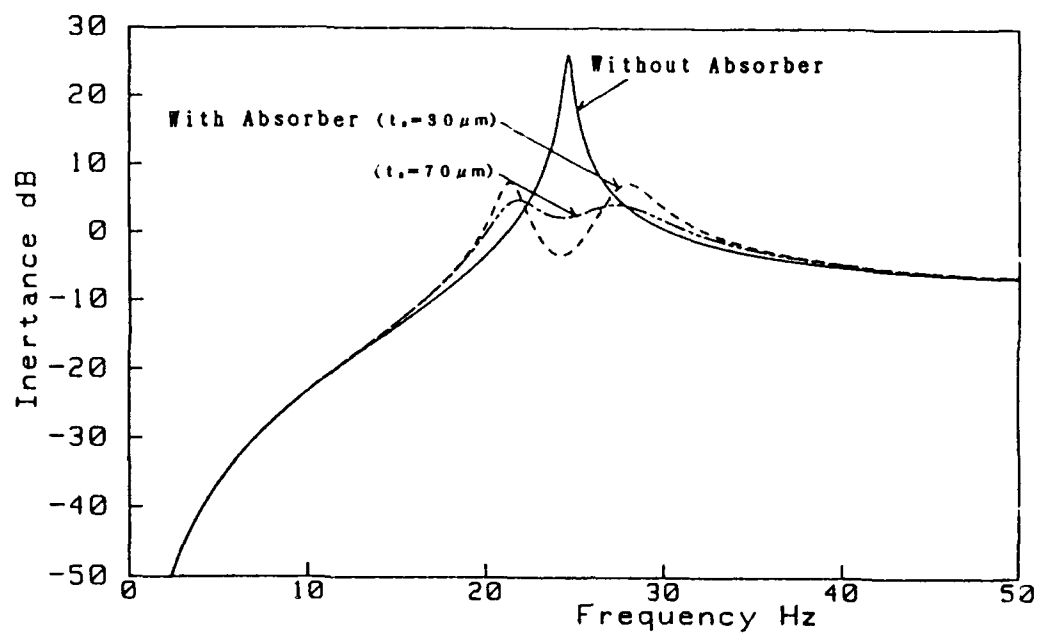


Fig. 7 Prediction of Reduction in Vibration
by Absorber

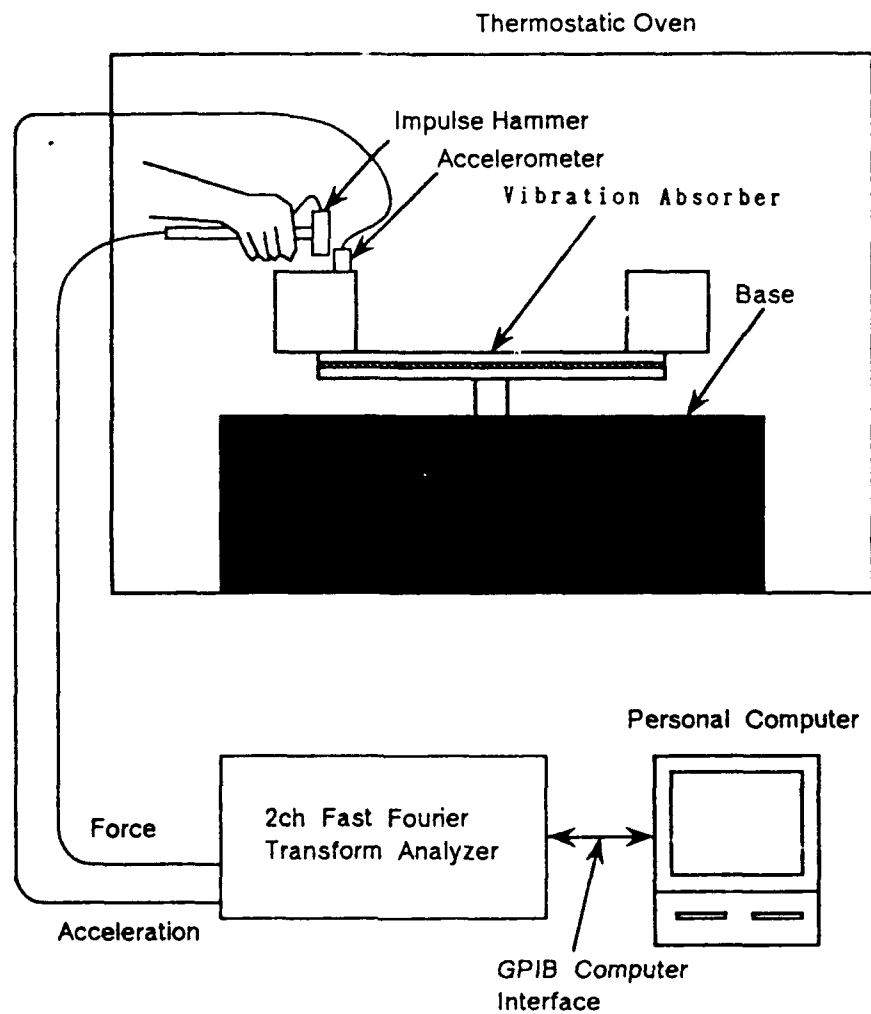


Fig.8 Measuring System of Dynamic Behavior of Absorber

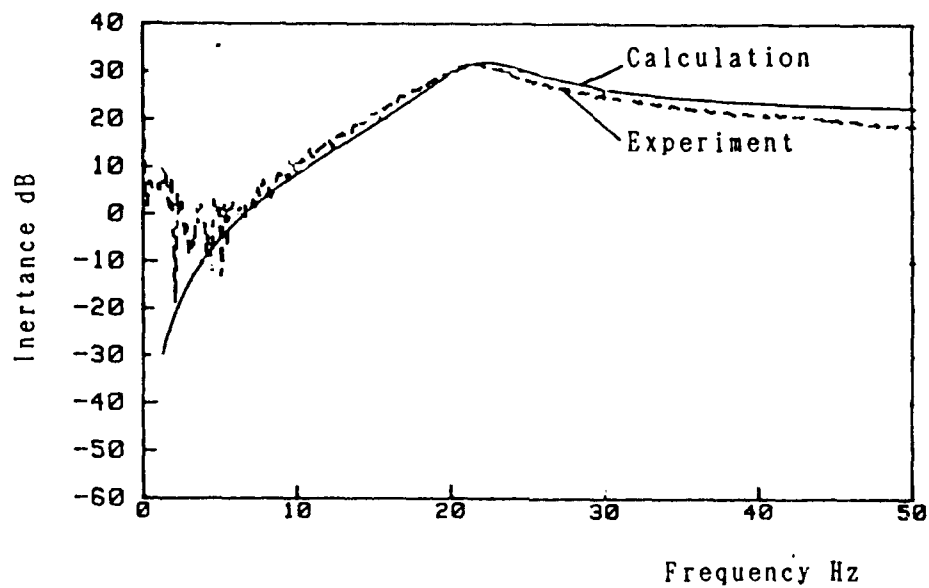


Fig. 9 Frequency Response of Vibration Absorber

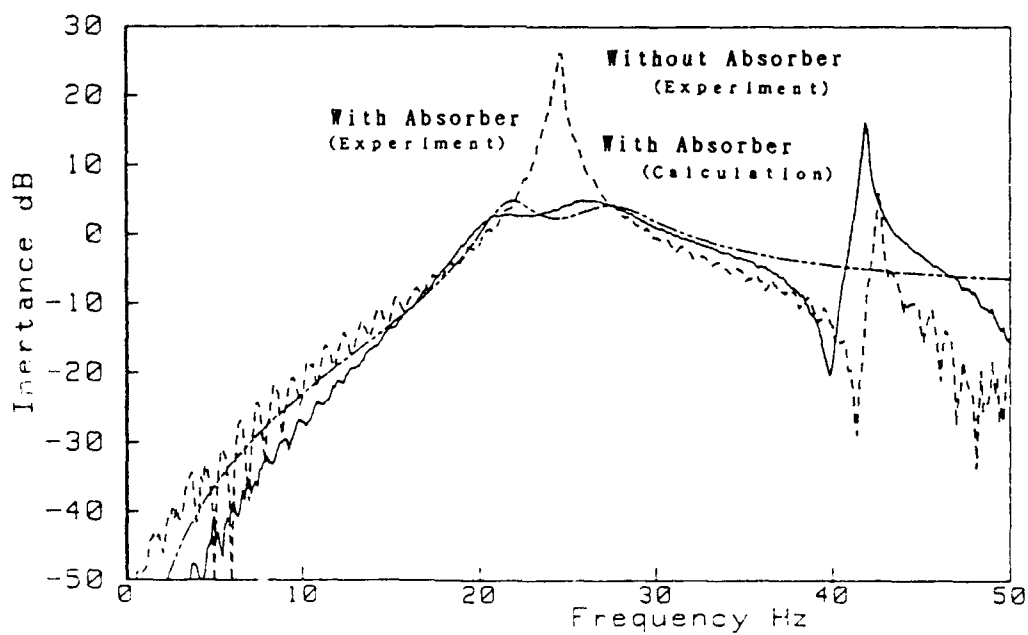


Fig. 10 Frequency Response of Aluminum Plate

Table.1 M, K, η of Aluminum Plate & Vibration Absorber

		M kg	K N/m	η
1st Mode of Plate		2.88	6.90×10^4	0.0171
Absorber	$t_s = 70 \mu m$.109	2.56×10^3	0.2450
	$t_s = 30 \mu m$.108	2.54×10^3	0.1204

Table.2 Comparison of Calculated & Measured Values of m, k, η of Absorber

	m kg	k N/m	η
Calculated	1.09×10^{-1}	2.56×10^3	0.2450
Measured	1.12×10^{-1}	2.74×10^3	0.2521

IMPEDANCE MATCHED MASS-DAMPERS: A NEW APPROACH FOR IMPROVING STRUCTURAL DAMPING

Craig Gardner, General Electric-Power Generation¹
Richard H. Lyon, MIT

ABSTRACT

Statistical Energy Analysis (SEA) techniques are used to analytically determine the damping effect achieved by attaching a quantity of mass-dampers to a damped flat plate. Mass-dampers are defined as SDOF oscillators which are over damped and have a resonant frequency below the frequency range of interest. The analysis has shown that the damping effect achieved by this approach is maximized when damper impedance is matched to a particular ratio of the average drive point impedance of the plate. The analysis indicates that the damping effect achieved is significant for mass-damper mass to plate mass ratios as low as 0.05 to 0.2.

A prototype mass-damper system was designed and tested to verify the analytical results. The experimental results showed that significant improvements in damping were achieved and that the amplitude of modal frequencies were reduced by as much as 10-15 dB over a wide frequency range.

This approach differs from visco-elastic techniques in that it does not share strain energy with base structure. This characteristic may make this approach effective for damping stiff structures at low frequencies.

¹ 1100 Western Ave., Lynn MA 01910, MS:GPNR7, Tel.(617) 594-6241

1.0 INTRODUCTION

The low frequency damping characteristics of many structures are critical to their performance. Among such structures are submarines, which must have low structureborne noise levels to remain undetected and tall buildings which need to minimize wind induced and seismic vibrations for comfort and safety considerations. Other applications may include reducing low frequency vibrations in aircraft and automobiles to improve passenger comfort.

Designing and implementing structural damping systems which perform well on stiff structures at low frequencies is a challenging task. Visco-elastic materials are often used in the design of such damping systems. In order for such designs to be effective, they must share a significant portion of the dynamic strain energy. This requirement can at times be difficult to obtain in practice.

Because of this difficulty, a damping system which did not rely on sharing strain energy with the base structure might have an advantage. Such a system would ideally function over a broad frequency range and not be tuned to a particular resonance of the base structure as is the case with tuned absorbers.

Our approach began by analyzing the effect of adding a quantity of masses and a dashpots combined in series on plate dynamics. Figure 1 shows a plate with 6 Mass-Dampers. It was felt that impedance matching of the Mass-Dampers to the plate could result in dissipating a significant amount of power and therefore increase the damping of the plate.

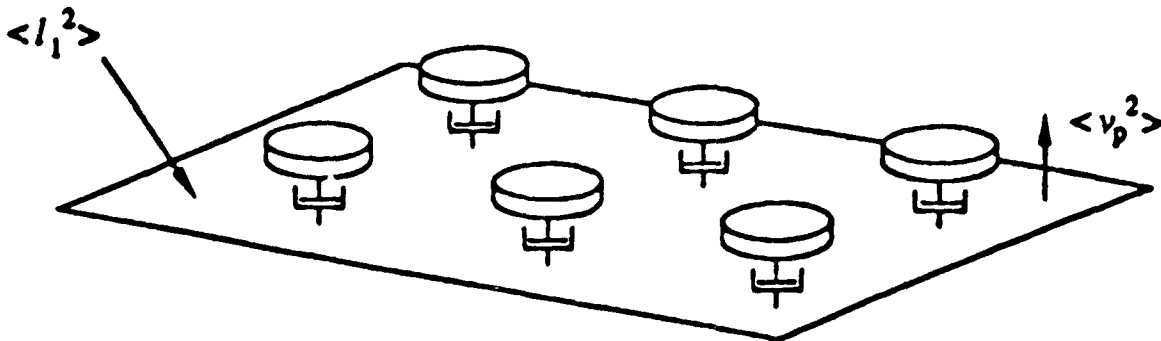


Figure 1 Plate with 6 Mass-Dampers.

Statistical Energy Analysis (SEA) techniques were used to analyze the effectiveness of these Impedance Matched Mass-Dampers. A prototype system of Mass-Dampers was designed based on squeeze film damping principles. The effectiveness of these dampers was experimentally verified and compared with analytical predictions.

2.0 SEA ANALYSIS OF A PLATE WITH MASS-DAMPERS



Figure 2 Rectangular plate with mean-square input force $\langle I_1^2 \rangle$, average m.s. velocity $\langle v_p^2 \rangle$, drive point conductance G_p , loss factor η_p , and mass M_p .

Lyon¹ has shown that for the plate shown on Fig. 2 the power input to the plate and dissipated by the plate are equal and therefore the average mean-square transfer function TF is given by eq. (1).

$$\frac{\langle v_p^2 \rangle}{\langle I_1^2 \rangle} = \frac{\overline{G_p}}{\omega \eta_p M_p} \quad (1)$$

where:

- $\langle v_p^2 \rangle$ = average mean square plate velocity
- $\langle I_1^2 \rangle$ = average mean square input force
- $\overline{G_p}$ = average plate drive point conductance = Real part of plate mobility
- $\omega \eta_p M_p = R_p$ = effective plate resistance
- $\eta_p M_p$ = plate loss factor and mass respectively

Note that the basic form for the plate TF is a ratio of the plate conductance to the plate resistance, R_p .

We expand on this concept to derive an expression for the plate TF with mass-dampers. Fig. 3 shows the system which we will analyze, a plate with two Mass-Dampers. The mass-dampers shown on Fig. 3 are basically SDOF systems that have the same components as a tuned damped absorber.

Our approach to using these elements will be different from the tuned damped absorber approach in two important aspects. First, these mass-dampers are designed to improve structural damping

at frequencies well above their undamped natural frequency by using an impedance matching approach. Tuned absorbers are frequency tuned to add damping for a particular structural mode.

Second, these mass-dampers are very much overdamped (typical $\zeta=1.2$) whereas tuned damped absorbers are typically underdamped. Because they are very much overdamped they could be accurately modeled as a simple mass and damper combination. The primary purpose of the spring is to support the static weight of the mass-damper mass.

We derive an equation for the mean square transfer function (TF) $\langle v_p^2 \rangle / \langle l_i^2 \rangle$ for this system where the number of Mass-Dampers, N is 2 but in general N can have any value. From the expression for the TF we will be able to derive an equation for the effective resistance, R_{eff} resulting from the mass-dampers.

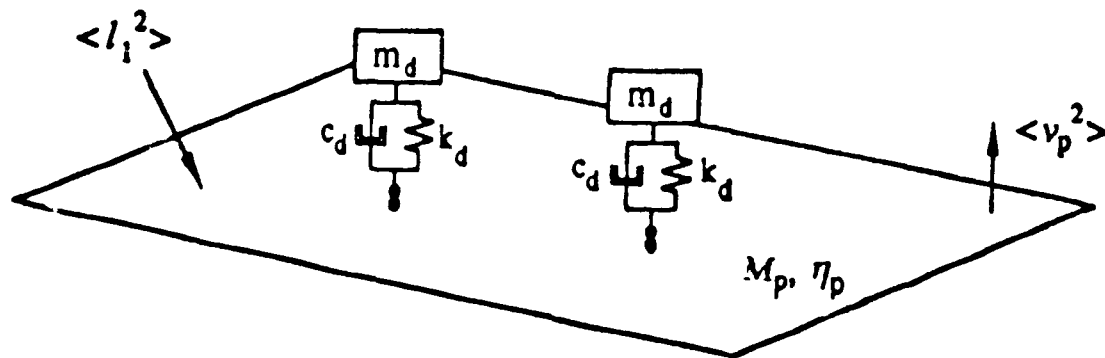


Figure 3 Plate with 2 Mass-Dampers.

We make the following assumptions in performing the analysis:

1. Points on the plate move independently, i.e. the attachment points are separated by a distance greater than half a bending wavelength.
2. The dynamic properties of the plate can be described by average parameters and mean square response.
- 3 The addition of passive discrete elements does not significantly affect the average drive point conductance of the plate, G_p .

We analyze this system by exercising two reciprocal analytical "experiments". In "experiment 1" as shown in Fig. 4 a mean-square force $\langle l_l^2 \rangle$ is applied to the plate and the points on the plate that attach to the two dampers are "blocked". Forces $\langle l_{bl3}^2 \rangle$ and $\langle l_{bl1}^2 \rangle$ are applied such that the mean square velocities, $\langle v_{l3}^2 \rangle$ and $\langle v_{l1}^2 \rangle$ at these points are zero. We assume that the system is linear and that locations 11 and 13 are typical and therefore the blocked forces applied at these points are equal.

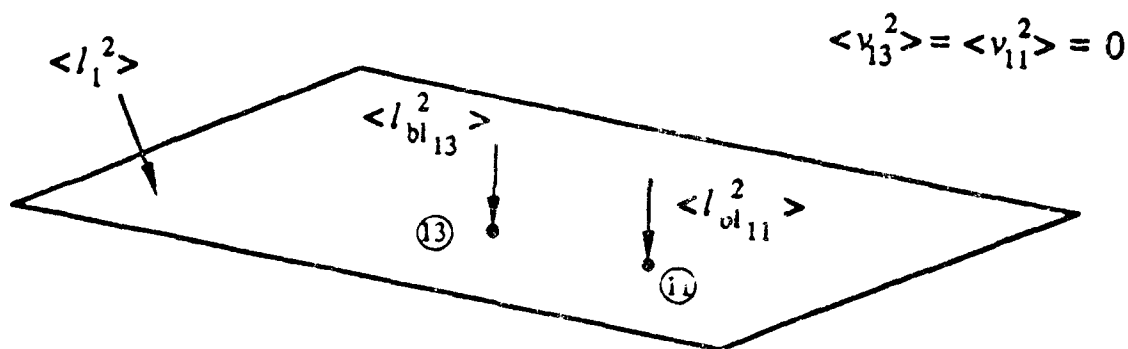


Figure 4 "Experiment 1" with input force $\langle l_l^2 \rangle$ and "blocked" forces $\langle l_{bl3}^2 \rangle$ and $\langle l_{bl1}^2 \rangle$.

We also assume linearity so, that the "blocked" force, $\langle l_{bl}^2 \rangle$ is proportional to the mean square plate velocity, $\langle v_p^2 \rangle$ as shown by eq. (2).

$$\langle l_{bl}^2 \rangle = \Gamma' \langle v_p^2 \rangle \quad (2)$$

Since the power input to the plate equals the power dissipated,

$$\Pi_{in} = \Pi_{dissipated} \quad (3)$$

$$\langle l_l^2 \rangle \overline{G_p} = \omega \eta_p M_p \langle v_p^2 \rangle \quad (4)$$

where:

- $\langle l_i^2 \rangle$ = mean square input force
- \overline{G}_p = Real Part of plate mobility $= (8\rho_s \kappa c_p)^{-1}$
- ρ_s = surface mass density
- κ = radius of gyration
- h = plate thickness
- c_l = longitudinal wave speed
- η_p = plate loss factor
- M_p = plate mass
- $\langle v_p^2 \rangle$ = average m.s. plate velocity over space and time

In "experiment 2" we prescribe 2 equal mean-square velocities $\langle v'_{11}{}^2 \rangle$ and $\langle v'_{13}{}^2 \rangle$ as shown on Figure 5. Relating the prescribed velocities to "blocked" forces from "experiment 1", i.e., $\langle v^2 \rangle = \langle l_b^2 \rangle / |Y_{eff}|^2$, we obtain (5).

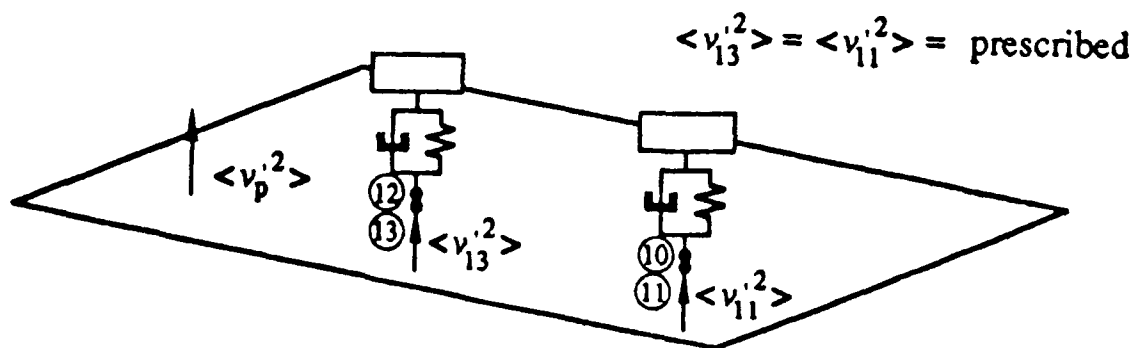


Figure 5 "Experiment 2" with prescribed velocity inputs.

$$\langle v'_{10}{}^2 \rangle = \langle v'_{11}{}^2 \rangle = \frac{\langle l_{b/11}{}^2 \rangle |Y_{10}|^2 |Y_{11}|^2}{|Y_{10} + Y_{11}|^2} \quad (5)$$

where:

The mean square plate mobility $|Y_{10}|^2$ is given by³ as shown in equation (6).

$\langle v'_{10} \rangle^2$ = prescribed velocity at plate-damper junction
 Y_{10} = drive point mobility of mass-damper
 Y_{11} = drive point mobility of plate

$$|Y_{11}|^2 = \overline{G_p}^2 + \sigma_{\overline{G_p}}^2 + \sigma_{B_p}^2 \quad (6)$$

where:

$\sigma_{\overline{G_p}}^2$ = input conductance variance = $9\overline{G_p}/8M$
 M = modal overlap = $\Pi f \eta_p / 2\delta f$
 $\sigma_{B_p}^2$ = input susceptance variance = $\sigma_{\overline{G_p}}^2$
 f = frequency (Hz)
 δf = average modal spacing

If we assume that the locations of the mass-dampers are typical and therefore the velocities at the mass-damper plate are the same, then each mass-damper will dissipate the same amount of power. Furthermore, in order for energy to be conserved the power input to a mass-damper must equal the power dissipated by it as shown by equation (7).

$$\langle v'^2_{10} \rangle R_{10} = C_d |v'_{10} - v'_d|^2 \quad (7)$$

where:

$R_{10} = G_{10} / |Y_{10}|^2$ = \Re part of mass-damper drive point impedance
 G_{10} = drive point conductance of mass-damper
 $|Y_{10}|^2$ = mean square drive point mobility of mass-damper
 v'_d = mass-damper mass velocity
 C_d = damper constant

The power input and dissipated by the plate is given by equation (8).

$$N \langle v'^2_{11} \rangle R_{11} = \omega \eta_p M_p \langle v'^2_p \rangle \quad (8)$$

By reciprocity² the ratio of the input force to the blocked force of "experiment 1" is equal to the ratio of the prescribed velocity to the mean square plate velocity of "experiment 2" as shown by equation (9).

$$\frac{\langle l_1^2 \rangle}{\langle l_{bl}^2 \rangle} = \frac{\langle v'^2_{10} \rangle}{\langle v'^2_p \rangle} \quad (9)$$

Substituting equations (2),(4) and (8) in (9) and we get (10).

$$\Gamma = \frac{R_{11}}{G_p} = \frac{1}{|Y_{11}|^2} \quad (10)$$

We can now get an expression for the plate velocity at the mass-damper plate junction, v'_{11} in terms of the "free" plate velocity, v_p by substituting (2), (5) and (8) in equation (10) which yields (11).

$$\frac{\langle v_{11}^2 \rangle}{\langle v_p^2 \rangle} = \frac{|Y_{10}|^2}{|Y_{10} + Y_{11}|^2} \quad (11)$$

It can be shown⁴ that by considering v_{10} to be a velocity source applied to the mass-damper oscillator then the relative velocity across the damper can be defined in terms of the mass-damper mobilities and the junction velocity as shown by equation (12).

$$v_{10} - v_d = v_{10} \left[\frac{Y_{kd} Y_{cd}}{(Y_{kd} Y_{cd}) + Y_{md} (Y_{kd} + Y_{cd})} \right] \quad (12)$$

where:

- v_{10} = velocity at plate, mass-damper junction
- v_d = mass-damper mass velocity
- Y_{cd} = mobility of mass-damper damper
- Y_{kd} = mobility of mass-damper spring
- Y_{md} = mobility of mass-damper mass

We will now use these results to determine the mean-square transfer mobility for a plate with N mass-dampers. Since the system is conservative,

$$\Pi_{input} = \Pi_{diss. \text{ plate}} + \Pi_{diss. \text{ mass-dampers}} \quad (13)$$

The input power is simply the product of the plate drive point conductance and the mean square input force as shown by eq. (14).

$$\Pi_{input} = \langle I_1^2 \rangle \overline{G_p} \quad (14)$$

The power dissipated by the plate is given by eq. (15) and is equal to the effective resistance of the plate times the mean-square plate velocity.

$$\Pi_{diss. \text{ plate}} = \omega \eta_p M_p \langle v_p^2 \rangle \quad (15)$$

The power dissipated by the mass-dampers is equal to the product of the number of mass-dampers, N the damper resistance and the relative mean-square velocity across the damper as shown by eq. (16).

$$\Pi_{\text{diss. mass-dampers}} = NC_d |v_{10} - v_d|^2 \quad (16)$$

If we can now combine the results from eqs. (11)-(16) to solve for the average mean-square transfer function for a plate with N mass-dampers which is given by eq. (17).

$$\frac{\langle v_p^2 \rangle}{\langle l_1^2 \rangle} = \frac{\overline{G_p}}{\omega \eta_p M_p + NC_d \left[\frac{|Y_{10}|^2 |Y_{kd}|^2 |Y_{cd}|^2}{|Y_{10} + Y_{11}|^2 |Y_{kd} Y_{cd} + Y_{md} (Y_{kd} + Y_{cd})|^2} \right]} \quad (17)$$

It can be seen from eq. (17) that the TF for a plate with mass-dampers has a similar form to that for the plate alone eq. (1), i.e. ratio of conductance to resistance, the only difference being the additional term in the denominator of (17) which is the effective resistance of the mass-dampers. Consequently, eq.(17) can be written in the form shown by eq. (18).

$$\frac{\langle v_p^2 \rangle}{\langle l_1^2 \rangle} = \frac{\overline{G_p}}{R_p + R_{\text{eff}}} \quad (18)$$

where:

$$R_p = \omega \eta_p M_p$$

$$R_{\text{eff}} = NC_d \left[\frac{|Y_{10}|^2 |Y_{kd}|^2 |Y_{cd}|^2}{|Y_{10} + Y_{11}|^2 |Y_{kd} Y_{cd} + Y_{md} (Y_{kd} + Y_{cd})|^2} \right]$$

We define the η_{eff} as shown in equation (19).

$$\eta_{\text{eff}} = \frac{R_{\text{eff}}}{\omega M_p} \quad (19)$$

Several FORTRAN programs were then written to evaluate the expressions derived here. The results are discussed in the following section.

3.0 DISCUSSION OF ANALYTICAL RESULTS

We will now look at some of the trends predicted by these analyses. More specifically we will analyze trends predicted for configurations for which we have experimental data.

The plate studied was 1/8 in. (3mm) thick aluminum 24 in. (.61m) wide by 30 in. (.76m) long. It was partially coated with a free layer viscoelastic damping treatment and had an initial average loss factor of .007 over a frequency range of 200-2500 Hz. We studied this plate with 0, 10, 25 and 35-70 gram mass-dampers.

The plate weighed approximately 4 kg. and the mass dampers added were from 5 to 20% of the plate mass. For the 35 mass-damper system we evaluated the effect of varying the damper constant, C_d on system performance. Because we were primarily interested in the 500-2500 Hz frequency range, the mass-damper natural frequency was set to 40 Hz.

Figure 6 shows the magnitude of the average acceleration/force TF versus the ratio of the mass-damper resistance, C_d to the Real part of the plate impedance, $Re\{Z_p\}$. These calculations are for frequencies ranging from 500 to 10,000 Hz.

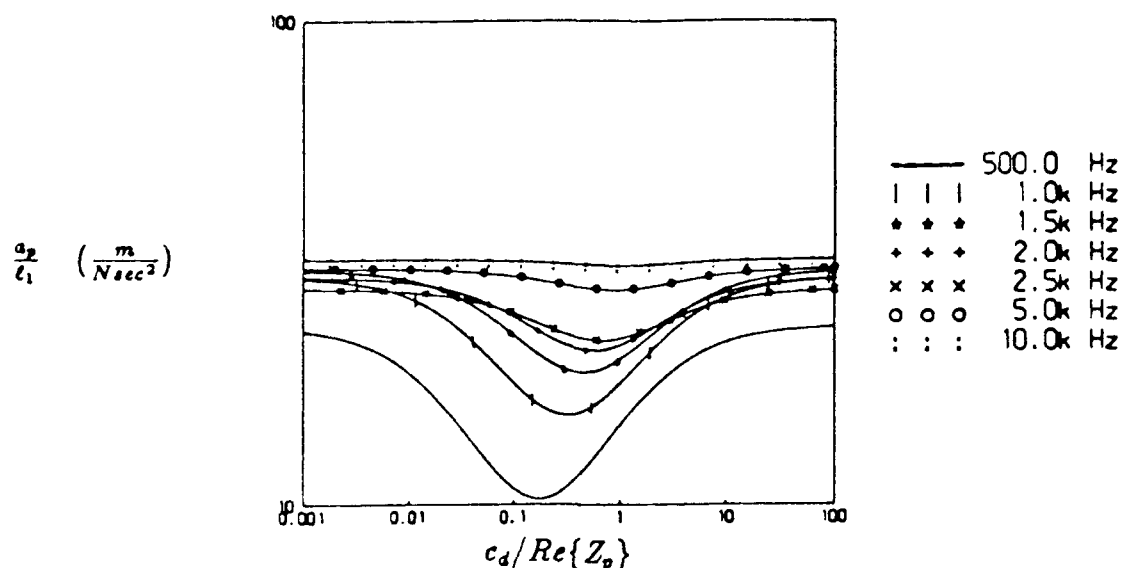


Figure 6 TF vs. $C_d/Re\{Z_p\}$ for plate with 10 mass-dampers evaluated at several frequencies.

It can be seen from Fig. 6 that there is an optimum ratio for which the transfer function response is minimized and that the optimum value increases with frequency. As one might expect with either too low or too high an impedance ratio, the reduction in response is minimal.

This makes sense if we take this concept to extremes. For example if $C_d=0$, there would be no power dissipated by the mass-dampers. On the other hand if $C_d=\infty$ the damper mass would essentially be rigidly attached to the plate and hence would only be adding mass, again with no power dissipation.

It can also be seen from Figure 6 that reduction in the transfer function is most significant at lower frequencies. This data shows that at 500 Hz the magnitude of the TF is reduced ≈ 6 dB when the impedance ratio is optimized. Calculations using eq. (17) showed that if we rigidly attach 10 mass-dampers (5% plate mass) we would only expect about a 0.2 dB decrease in the TF at 500 Hz.

Figures 7 and 8 show the TF magnitude vs. impedance ratio for 25 and 35 mass-dampers respectively. These curves show the same trends as the 10 mass-damper case but with a stronger effect as the number of mass-dampers is increased. With 35 mass-dampers the optimum

impedance ratio reduces the average TF by 10 dB. The optimum impedance ratio does not change significantly as the number of mass-dampers is increased.

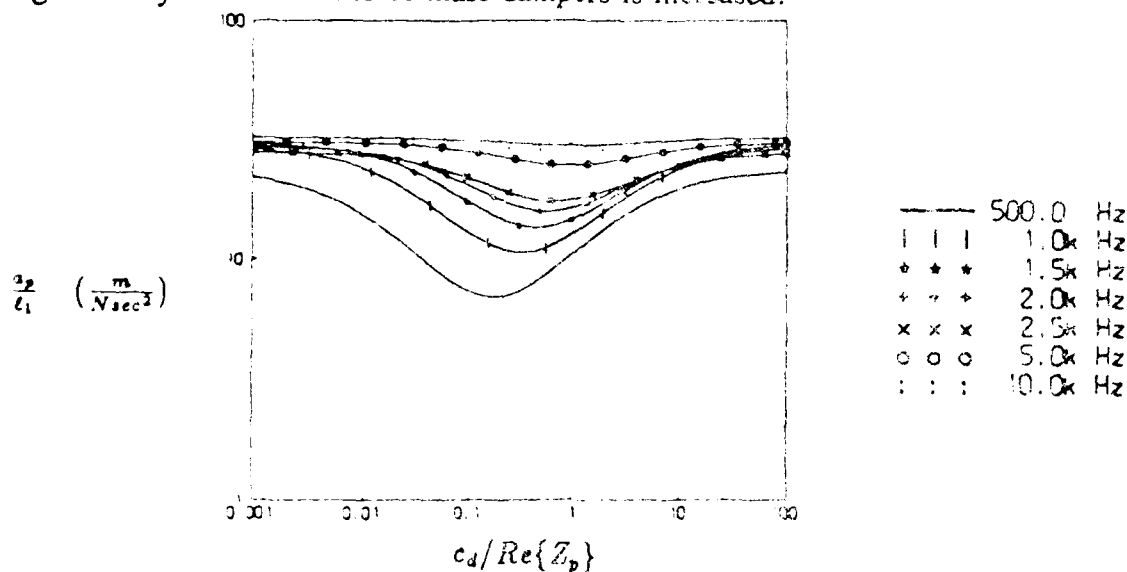


Figure 7 TF vs. $C_d/Re\{Z_p\}$ for plate with 25 mass-dampers evaluated at several frequencies.

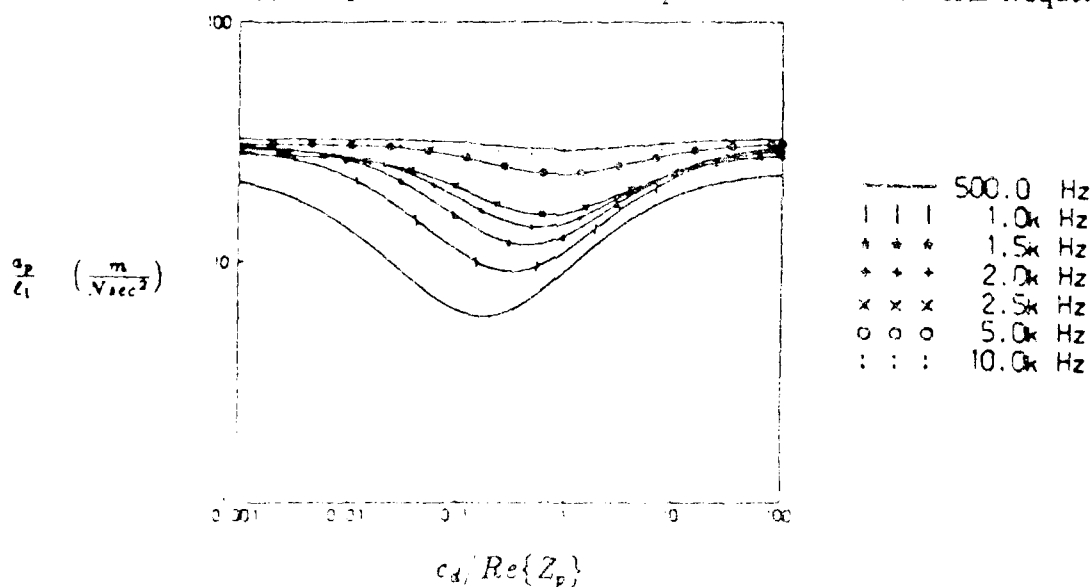


Figure 8 TF vs. $C_d/Re\{Z_p\}$ for plate with 35 mass-dampers evaluated at several frequencies.

Figure 9 shows η_{eff} as defined by eq. (19) as a function of the impedance ratio for 35 mass-dampers. These curves show that loss factors greater than 0.1 are achieved from 500-2000 Hz. It can also be seen from these curves that considering the log scale of the x axis, there is a fairly broad range of impedance ratios for which the η_{eff} is nearly maximized.

If we choose C_d so that the damping by the mass dampers is maximized at 1000 Hz and plot the TF for the plate with visco-elastic material alone, 10, 25 and 35 mass-dampers we obtain the TF curves shown on Figure 10. These curves show results similar to other additive damping treatments in that large improvements are made initially and then gradually smaller improvements are made by adding more mass-dampers. We should note however, that the plate had some damping to begin with and that the improvement in damping is attributable to the mass-dampers

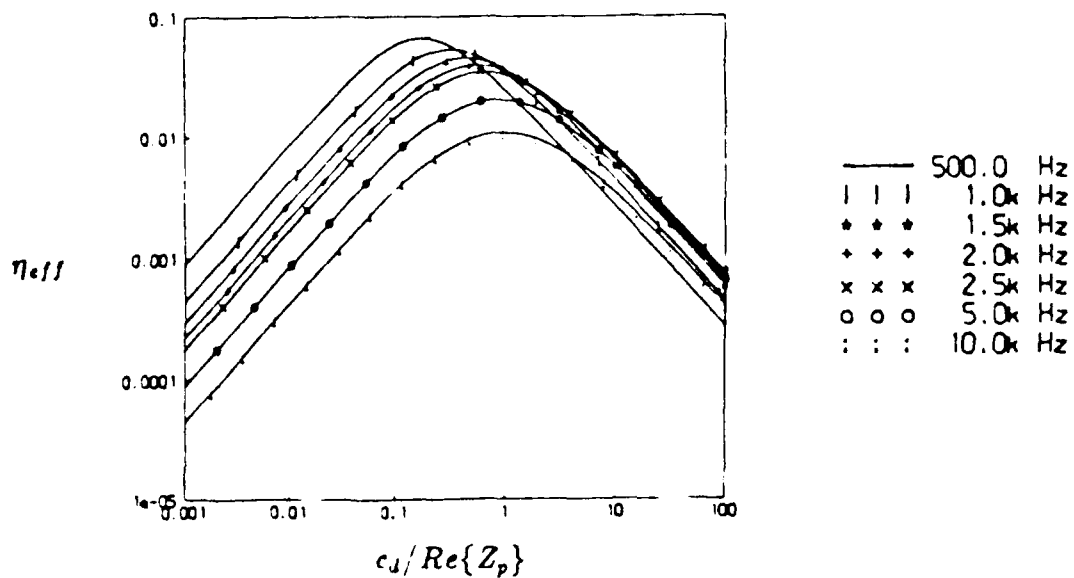


Figure 9 η_{eff} vs. $C_d/Re\{Z_p\}$ for plate with 35 mass-dampers evaluated at several frequencies.

further reduces the TF as much as 10 dB at the lower frequencies.

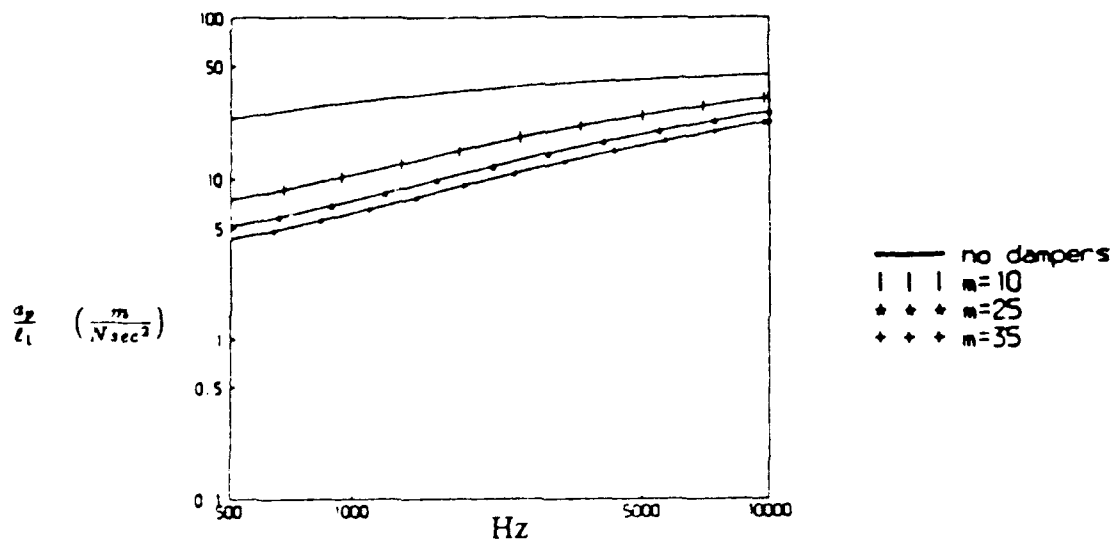


Figure 10 TFs for damped plate alone and with 10, 25, and 35 mass-dampers.

4.0 MASS-DAMPER DESIGN

Visco-elastic materials were originally considered for a prototype mass-damper system but, initial calculations showed that a material with a loss factor of at least 100 would be needed for such a system to work, while present materials have a maximum loss factor of ≈ 1 . A fluid film damper approach was chosen because of the simplicity of the design and the large damping constants that can be achieved. It can be shown⁵ that the damping resistance for a circular fluid film damper is governed by eq. (20).

$$C_d = \frac{3\pi\mu d^4}{32e^3} \quad (20)$$

where:

C_d = damper constant, $N\text{sec}/m$
 μ = dynamic viscosity, $N\text{sec}/m^2$
 d = damper diameter
 e = film thickness

On Figure 11 can be seen a sketch of the prototype mass-damper system. It consists of an aluminum disk which serves as both the damper mass and the fluid film damper area. The disk diameter was 34mm, chosen so that it is less than 1/2 a bending wavelength on the plate at 2500 Hz. The disk is supported by 3 small cylinders of polyurethane foam whose spring rate was such that the natural frequency of the system was 40 Hz. The polyurethane "springs" were bonded to set screws which were used to vary the film thickness, e and hence the damping constant, C_d . A bead of silicone sealant was used to contain the glycerol. Glycerol was chosen as the damping fluid because of its high dynamic viscosity.

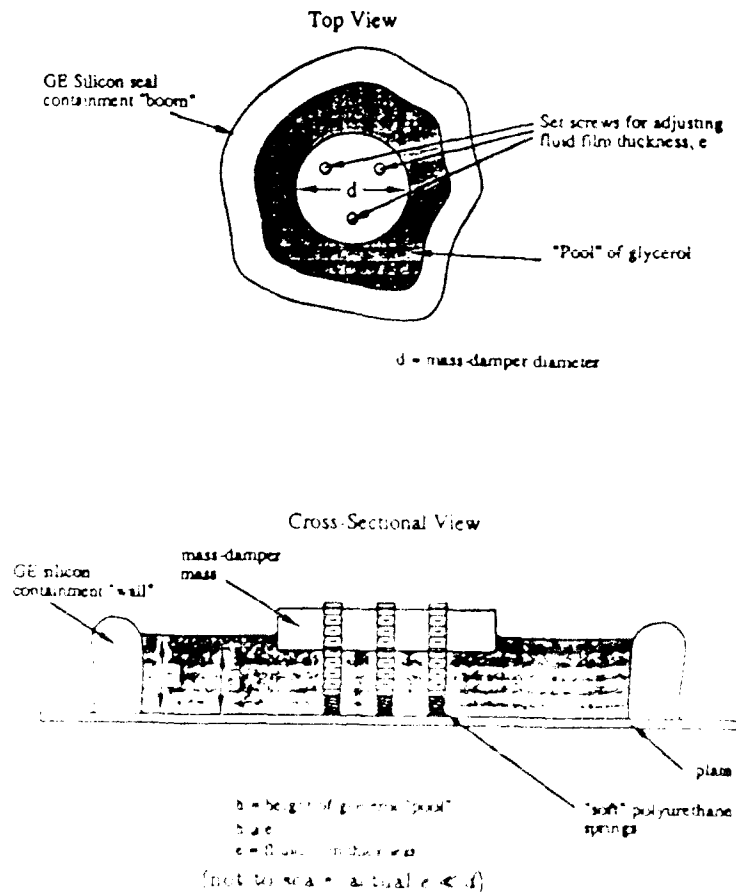


Figure 11 Sketch of fluid film mass damper design

5.0 EXPERIMENTAL APPROACH

The experiments were designed to measure the effect of varying the number of mass-dampers and their damping constant, C_d on the average TF and loss factor, η of the plate. A sketch of the experimental setup is shown on Figure 13. The plate was supported by foam rubber to simulate free-free boundary conditions. A 8 channel FFT analyzer was used to measure plate transfer functions for the locations shown on Figure 14 for the 3 different quantities of mass-dampers tested. Average TFs were calculated by averaging the magnitude of the 4 measured frequency response functions using the GenRad signal processing language TSL2. A frequency resolution of 0.25 Hz was used for all measurements. The average loss factor was measured for 4 frequency bands using the integrated impulse technique⁶.

6.0 EXPERIMENTAL RESULTS

6.1 EVALUATION OF MASS LOADING EFFECT OF MASS-DAMPERS ON PLATE VIBRATION

Figure 12 shows a comparison of the average TF of the plate with 10 mass-dampers and the average TF of the plate at the mass-damper locations. It can be seen from this figure that the

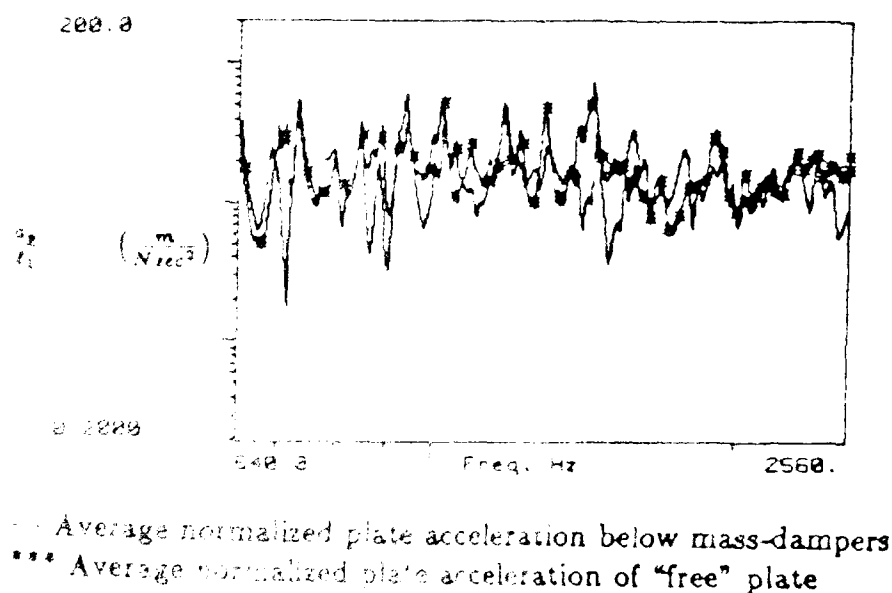


Figure 12 Comparison of the average "free" plate TF with average TF of the plate below the mass-dampers.

2 curves are quite similar. From this comparison we conclude that the mass-dampers are not mass loading the plate but are acting as a mass damper system as intended.

6.2 EFFECT OF MASS-DAMPERS ON PLATE η AND AVERAGE TF

The analytical data shown in Figure 8 showed that an impedance ratio of 0.32 should minimize the TF at 1000 Hz. This is approximately the mid point of the 0-2500 Hz frequency band of interest. On Table 1 can be seen the estimated plate loss factor, η for 0, 10, 25 and 35 mass-dampers tested with the impedance ratio equal to 0.32. It can be seen from Table 1 that there is a significant increase in the measured plate loss factor as the number of mass-dampers is increased. The increase is on the order of 200-500% and is evident over frequency span of almost 2000 Hz. It should be noted that due to the difficulty of measuring the fluid film thickness of this softly sprung system, the impedance ratios can only be considered approximate.

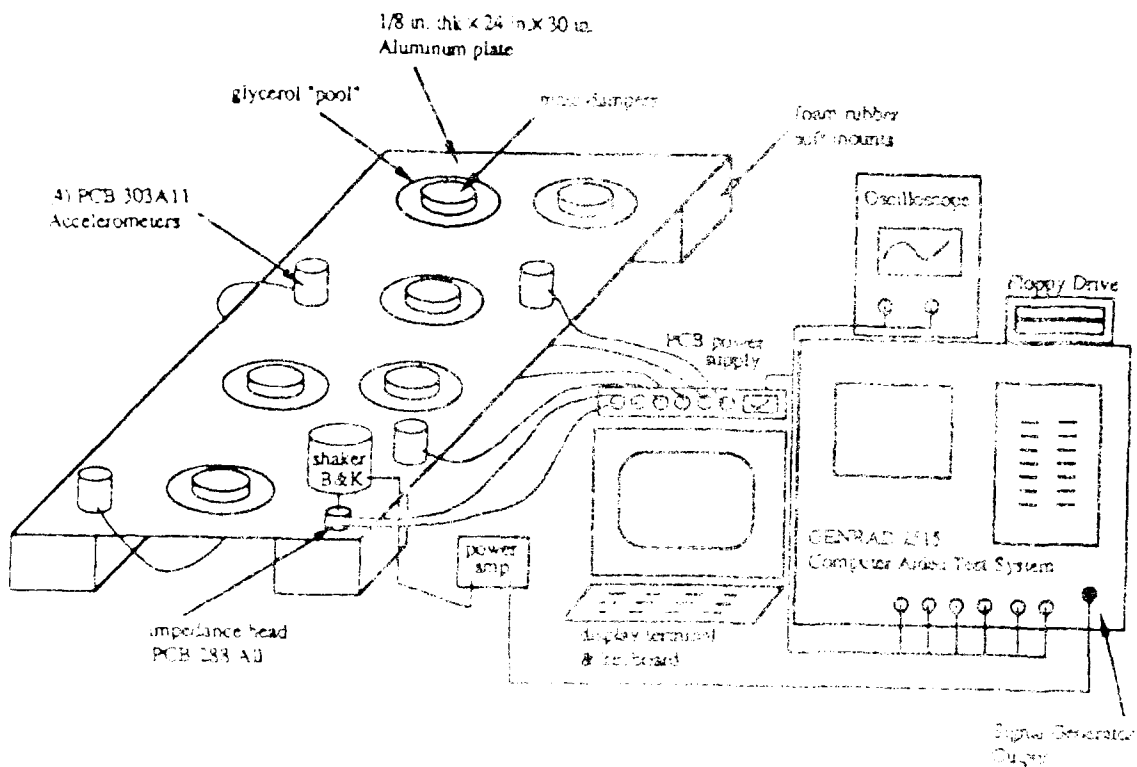


Figure 12 Experimental Setup for measuring η and η .

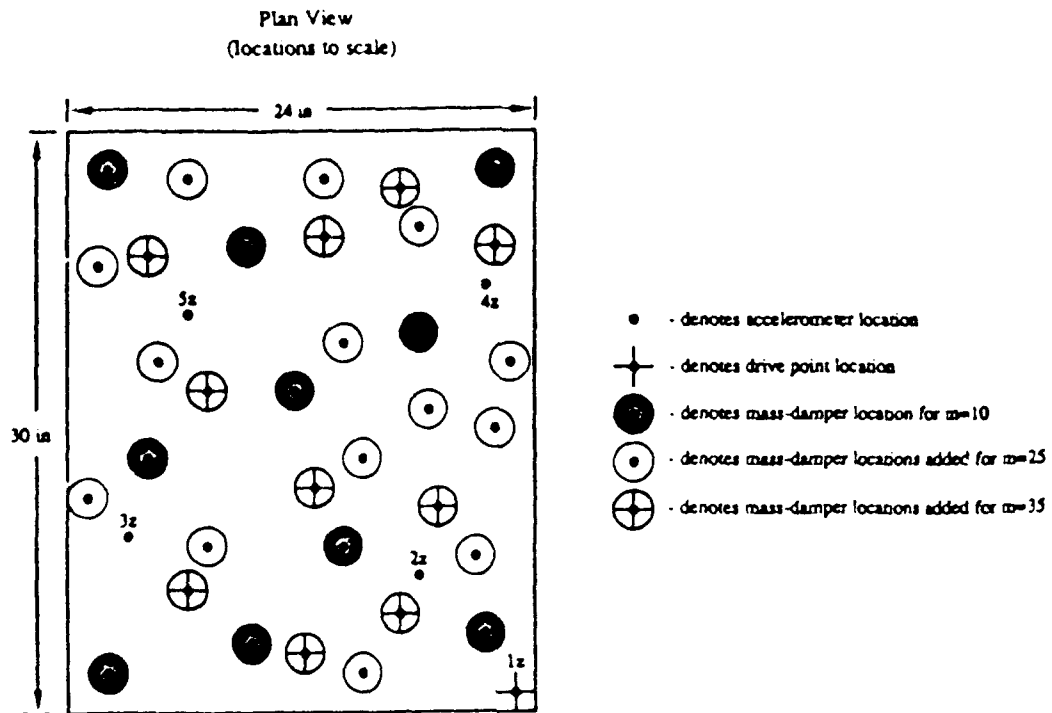


Figure 14 Accelerometer, shaker and mass-damper locations.

Table 1: Measured Plate Loss Factor η , for $N=0,10,25,35$						
# Mass-Dampers	Added Mass	Impedance Ratio	Center Freqs. of 320 Hz Wide Bands			
N	%	$C_d/\text{Re}\{Z_p\}$	320 Hz	960 Hz	1600 Hz	2240 Hz
None	0	N/A	0.007	0.0040	0.007	0.008
10	5	0.32	0.009	0.014	0.012	0.011
25	13	0.32	0.012	0.014	0.024	0.026
35	18	0.32	0.015	0.019	0.025	0.035

Table 2 shows the affect of large changes in the impedance ratio on the plate loss factor for a fixed quantity of mass-dampers. We would expect lower ratios to provide a larger loss factor at lower frequencies and higher ratios to provide larger loss factors at higher frequencies. In general that data on Table 2 show this trend except that we would have expected the largest impedance ratio to have the best performance in the 2240 Hz band.

Table 2: Measured Plate Loss Factor η , for $N=35$ $Cd/Re\{Z_p\} = .21, .32, .94$						
# Mass-Dampers	Added Mass	Impedance Ratio	Center Freqs. of 320 Hz Wide Bands			
N	%	$Cd/Re\{Z_p\}$	320 Hz	960 Hz	1600 Hz	2240 Hz
35	18	0.21	0.021	0.025	0.026	0.029
35	18	0.32	0.015	0.019	0.025	0.035
35	18	0.94	0.016	0.014	0.019	0.028

Figures 15 and 16 show the average TF for the damped plate alone and the same plate with 35 mass-dampers, over frequency ranges of 10-640 Hz and 640-2540 Hz respectively. It can be seen from these curves that above 300 Hz the magnitude of the TF is reduced by as much as 15 dB.

7.0 COMPARISON ON ANALYTICAL AND EXPERIMENTAL DATA

A comparison of experimental and analytical TFs can be found on Figure 17. It can be from these curves that the analysis overestimates the TF above 1000 Hz. We also find that although the experimental and analytical data have the same trend the analysis predicts a larger reduction in the TF due to the addition of the mass-dampers than was measured experimentally. On average a 9 dB reduction is predicted while a 6 dB reduction was measured. Recent data suggests that these differences may be influenced in part by mass loading effects of the silicone bead used to contain the glycerol.

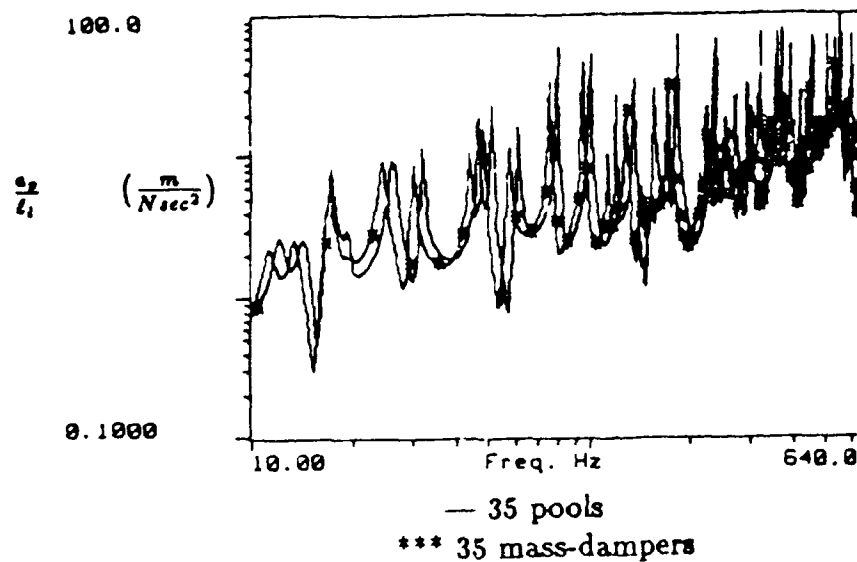


Figure 15 Comparison of average TF (10-640 Hz) for damped plate alone and damped plate with 35 mass-dampers, $C_d/Re\{Z_p\} = .32$.

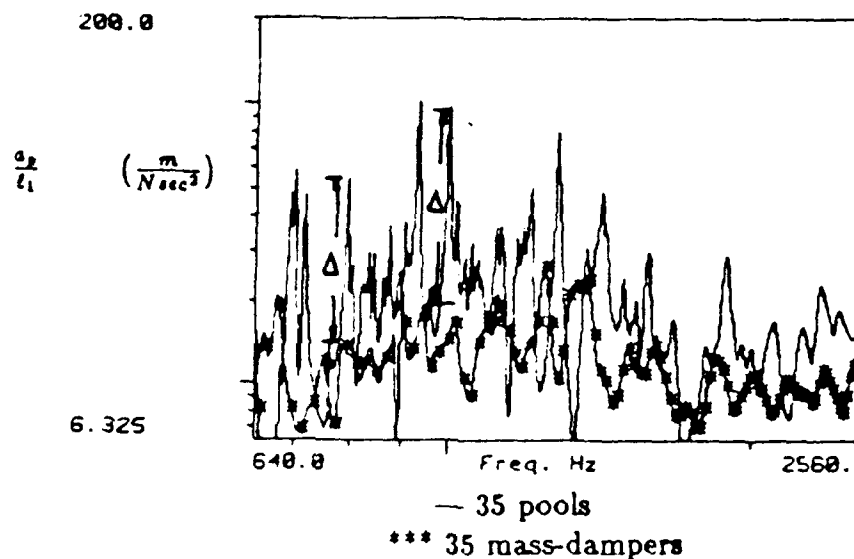


Figure 16 Comparison of average TF (640-2540 Hz) for damped plate alone and damped plate with 35 mass-dampers, $C_d/Re\{Z_p\} = .32$.

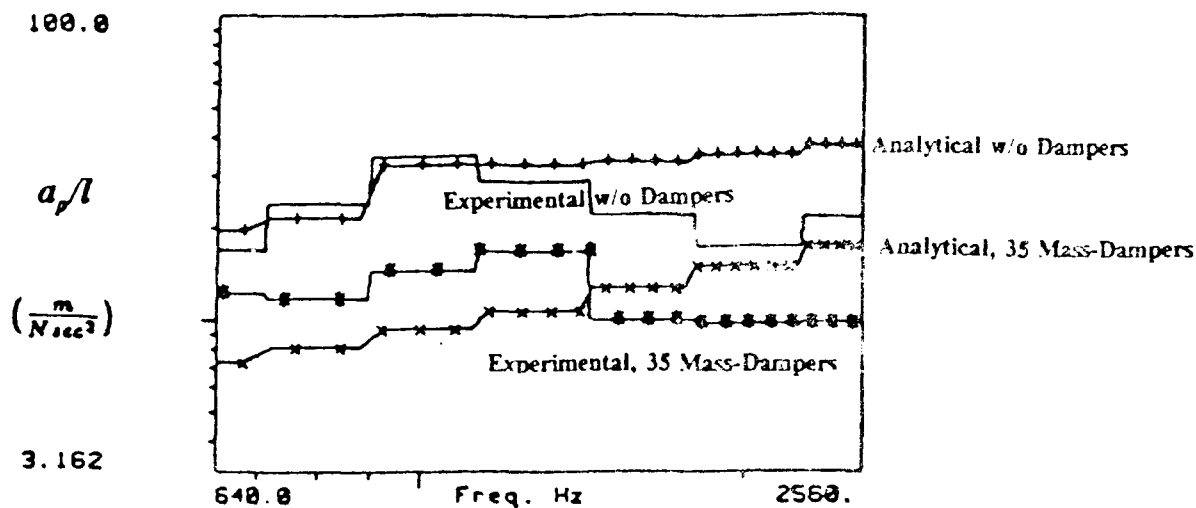


Figure 17 A Comparison of analytical and experimental average TFs with and without 35 mass-dampers.

8.0 CONCLUSIONS

SEA techniques have been used to predict the effect of impedance matched mass-dampers on the damping of a rectangular plate. This analysis indicates that plate damping can be significantly improved using this approach. The analysis also indicates that this method is most effective below 2500 Hz for the plate evaluated. Analytical work⁴ done to model 3 dimensional structures as 2 dimensional ones has indicated that this approach can even be effective below 50 Hz. It appears that theoretically, there is no lower limit to the frequency at which this approach is effective, although, more mass is required to get the same effect at lower frequencies and the damping effect at higher frequencies is lessened.

A prototype impedance matched mass-damper system which utilized fluid film damping principles was built and tested. Experimental data has shown that this approach can significantly improve the damping of a plate. Because this technique does not share strain energy with the base structure but, rather looks at the base structure as a velocity source, it may prove useful in damping structures where it is difficult to design a strain energy sharing visco-elastic system. Such applications would typically be the low frequency modes of structures which generally have lower bending strain energies. Typical applications might be in marine hardware to reduce structureborne noise levels, in buildings to reduce wind and seismically induced vibrations and in automobiles or aircraft to reduce low frequency vibrations and improve passenger comfort.

A conceptual sketch of one such design is shown on Figure 18. It consists of a housing which could be made of aluminum or plastic and a hockey puck shaped mass which is softly sprung from the housing in 3 orthogonal directions.

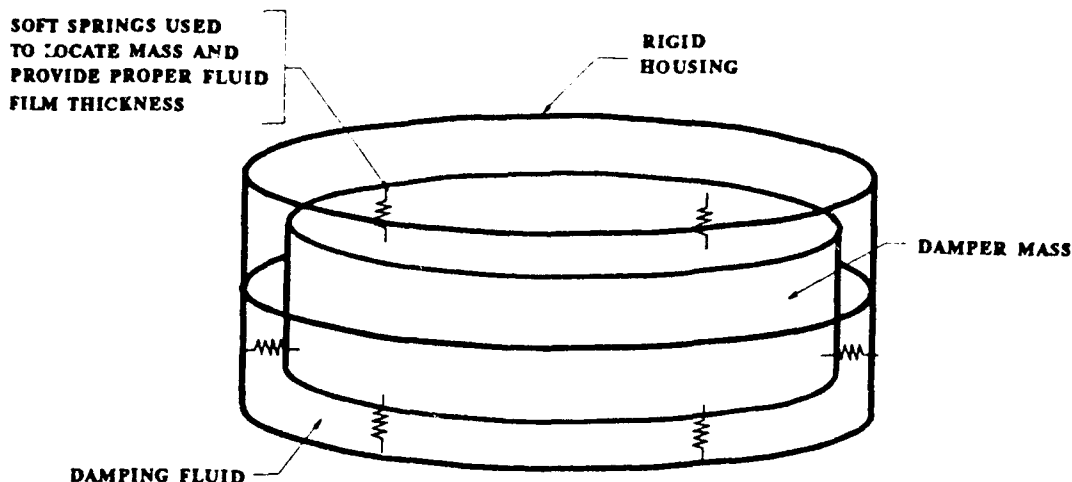


Figure 18 Conceptual sketch of a mass-damper design which provides damping in 3 orthogonal directions.

The fluid level and film thickness between the mass and housing are designed such that the system provides damping in 3 orthogonal directions, independent of its mounting orientation. This approach is the subject of a MIT patent application. Many other configurations are possible but, further work needs to be done to evaluate the design parameters required by particular applications.

REFERENCES

1. Lyon, Richard H., *Machinery Noise and Diagnostics*, Butterworths Publishers, Stoneham, MA, 1987.
2. Lyon, Richard H., *Statistical Energy Analysis of Dynamical Systems: Theory and Applications*, MIT Press, Cambridge, MA 1976.
3. Lyon, Richard H., "Statistical Analysis of Power Injection and Response in Structures and Rooms", *The Journal of the Acoustical Society of America*, 45, No. 3, 545-565.
4. Gardner, Craig M., "On the Design and Use of Impedance Matched Mass-Dampers to Reduce Structural Vibration", MIT Dept. of Mechanical Engineering, Masters Thesis, May, 1989.
5. Peters, J., and VanHerck, P., "Theory and Practice of Fluid Dampers in Machine Tools", *Advances in Machine Tool Design and Research, 1969. Proceeding of 10th International M.T.D.R. Conference*, September 1969, University of Manchester.
6. Schroeder, M. R., "New Method for Measuring Reverberation Time", *The Journal of the Acoustical Society of America*, 37, No. 3, 409-412, March, 1965.

ANALYTICAL AND EXPERIMENTAL MODAL ANALYSIS OF A TWO-TIERED STRUCTURE

H. V. Vu, T. K. Vuong, and W. C. Flynn, Jr.
Department of Mechanical Engineering
California State University, Long Beach
Long Beach, CA 90840

Abstract

A test structure, namely a two-tiered structure (TTS), was used as a physical model for obtaining modal parameters of flexible structures. These parameters, which were determined analytically and experimentally, are natural frequencies, mode shapes, and damping ratios. In the analytical portion, finite element method (FEM) was used with MSC/NASTRAN, MSC/pal 2, and MSC/MOD. In the experimental part, the structure was excited by random noise, and frequency-response function (FRF) plot and modal parameters were obtained. Both the HP 3566A/3567A (Hewlett Packard Spectrum/Network Analyzer) and STAR System (Structural Measurement Systems software) were utilized. An exact model-reduction technique was used to obtain a complete mathematical model of a reduced-order system, which includes the reduced-order *physical* mass, stiffness, and damping matrices.

Introduction

Analytical and experimental modal analysis can be used to determine dynamic properties or modal parameters of flexible structures. These modal parameters are natural frequencies, mode shapes, and damping ratios. The characteristics of flexible structures are low natural frequencies, low damping, and some of the modes are closely spaced.

In finite element analysis, it is necessary that the structure under consideration is modeled using a large number of degrees of freedom (DOF's) for accurate results. But if the number of DOF's is large, the results from finite element program become unmanageable for the purpose of design and analysis of vibration control or for subsequent studies. A model reduction technique [1] can be used to reduce a large-DOF model to a small-DOF model which exactly represents the first few modes.

In experimental modal analysis [2-4], also called *modal testing*, natural frequencies and damping ratios can be obtained from the frequency response function (FRF) plot. In modal testing it is important to have high-quality test setup, testing craftsmanship, and data processing, etc.

The equations of motion of a structure can be written in the *configuration-space form* [5] as

$$\mathbf{m}\ddot{\mathbf{x}} + \mathbf{c}\dot{\mathbf{x}} + \mathbf{k}\mathbf{x} = \mathbf{f} \quad (1)$$

where \mathbf{m} , \mathbf{k} , and \mathbf{c} are the *physical* mass, stiffness, and damping matrices, respectively; and \mathbf{f} is the applied forcing vector.

The physical mass and stiffness matrices of a structure under consideration can be obtained analytically by the given physical properties, dimensions, and boundary conditions; however, the physical damping matrix must be determined experimentally.

A complete mathematical model of a reduced-order system will be determined, which includes the reduced-order *physical* mass, stiffness, and damping matrices.

The Test Structure

The test structure, a two-tiered structure (TTS), shown in Fig. 1, is chosen so it can be used for studying vibration characteristics of flexible structures. It was designed specifically to possess the following characteristics:

- . low natural frequencies, light damping, and intuitive mode shapes for the first few modes
- . inexpensive and easy to build
- . instructive for analytical analysis and computer simulation, and experimental modal analysis

Finite Element Model

A finite element model of the structure is created using MSC/MOD (Fig. 2). The floors and the columns are modeled by plate elements and bar elements, respectively. The brackets connecting the plates and columns are modeled by concentrated mass elements. The model has 136 elements, 146 nodal points and 790 (active) degrees of freedoms ($n = 790$). It may appear that the number of plate elements is more than adequate; however, in this study, the model is relatively small and simple so that mesh optimization is ignored.

The finite element model is then analyzed by using two commercially available finite element analysis packages: MSC/NASTRAN (on main-frame computer), and MSC/MOD and MSC/pal 2

(on MS-DOS machine) [6]. The undamped natural frequencies obtained, using these packages, are given in Table 1, and the corresponding mode shapes (from MSC/pal 2) are shown in Figs. 3-8.

Exact Model Reduction

For the undamped free vibration or eigenvalue problem, Eq. (1) reduces to

$$\mathbf{m}\ddot{\mathbf{x}} + \mathbf{k}\mathbf{x} = \mathbf{0} \quad (2)$$

When the structure vibrates in its natural modes, we have

$$(\mathbf{k} - \omega_r^2 \mathbf{m})\phi_r = \mathbf{0} \quad r = 1, 2, \dots, n \quad (3)$$

where ω_r and ϕ_r are the undamped natural frequencies and the corresponding mode-shape vectors, respectively.

The orthogonality properties are *mass normalized* so that the *modal* mass and stiffness matrices are given as

$$\begin{aligned} \mathbf{M} &= \Phi^T \mathbf{m} \Phi = \mathbf{I} \\ \mathbf{K} &= \Phi^T \mathbf{k} \Phi = \text{diag}[\omega_r^2] \quad r = 1, 2, \dots, n \end{aligned} \quad (4)$$

where the full-order (mass-normalized) mode-shape matrix is given as

$$\Phi = [\phi_1 \quad \phi_2 \quad \dots \quad \phi_n] \quad (5)$$

The full-order physical mass and stiffness matrices can be written, from Eq. (4), as

$$\begin{aligned} \mathbf{m} &= \Phi^{-T} \Phi^{-1} \\ \mathbf{k} &= \Phi^{-T} \text{diag}[\omega_r^2] \Phi^{-1} \quad r = 1, 2, \dots, n \end{aligned} \quad (6)$$

The 790-DOF full-order model ($n = 790$) is reduced to a 6-DOF reduced-order model ($m = 6$) which exactly represents the first six modes using [1]. The reduced-order model is obtained by selecting the four translational DOF's located at the centers of the floors for the first four bending modes. For each of the first two torsional modes, the angular DOF is defined by a set of any two translational DOF's of a given floor. Using the numerical values of the full-order mode-shape matrix (from MSC/NASTRAN, not shown), the reduced-order mode-shape matrix can be selected as

$\Phi_R =$

$$\begin{bmatrix} \begin{Bmatrix} 4.175227 \\ 0 \\ 0 \\ 6.724909 \\ 0 \\ 0 \end{Bmatrix}_1 & \begin{Bmatrix} 0 \\ 4.195279 \\ 0 \\ 0 \\ 6.710377 \\ 0 \end{Bmatrix}_2 & \begin{Bmatrix} 0 \\ 0 \\ -0.500879 \\ 0 \\ 0 \\ -0.711376 \end{Bmatrix}_3 & \begin{Bmatrix} 6.274968 \\ 0 \\ 0 \\ -4.559574 \\ 0 \\ 0 \end{Bmatrix}_4 & \begin{Bmatrix} 0 \\ -6.261847 \\ 0 \\ 0 \\ 4.580626 \\ 0 \end{Bmatrix}_5 & \begin{Bmatrix} 0 \\ 0 \\ 0.657553 \\ 0 \\ 0 \\ -0.561635 \end{Bmatrix}_6 \end{bmatrix} \quad (7)$$

where the subscript R denotes reduced-order model.

The differential equations for undamped free vibration of the reduced-order model are given as

$$\mathbf{m}_R \ddot{\mathbf{x}}_R + \mathbf{k}_R \mathbf{x}_R = 0 \quad (8)$$

where

$$\mathbf{m}_R = \Phi_R^{-T} \Phi_R^{-1} \quad (9)$$

$$\mathbf{k}_R = \Phi_R^{-T} \text{diag}[\omega_r^2] \Phi_R^{-1} \quad r = 1, 2, \dots, m$$

$$\mathbf{x}_R = \{x_1 \quad y_1 \quad 1 \cdot \theta_1 \quad x_2 \quad y_2 \quad 1 \cdot \theta_2\}^T \quad (10)$$

The numerical value 1 in Eq. (10) has dimension of length so \mathbf{x}_R is dimensionally homogeneous, and the subscripts 1 and 2 denote the middle floor and the top floor, respectively (Fig. 1).

Introducing Φ_R from Eq. (7) and ω_r from Table 1 (MSC/NASTRAN) into Eq. (9), we have

$$\mathbf{m}_R = 10^{-2} \begin{bmatrix} 1.7605 & 0 & 0 & 0.0142 & 0 & 0 \\ 0 & 1.7604 & 0 & 0 & 0.0142 & 0 \\ 0 & 0 & \frac{146.40}{1^2} & 0 & 0 & \frac{2.3153}{1^2} \\ 0.0142 & 0 & 0 & 1.5149 & 0 & 0 \\ 0 & 0.0142 & 0 & 0 & 1.5150 & 0 \\ 0 & 0 & \frac{2.3153}{1^2} & 0 & 0 & \frac{121.77}{1^2} \end{bmatrix} \frac{lb_f s^2}{in} \quad (11)$$

$$\mathbf{k}_R = 10^3 \begin{bmatrix} 0.0171 & 0 & 0 & -0.0084 & 0 & 0 \\ 0 & 0.0171 & 0 & 0 & -0.0085 & 0 \\ 0 & 0 & \frac{2.0839}{1^2} & 0 & 0 & \frac{-1.1283}{1^2} \\ -0.0084 & 0 & 0 & 0.0082 & 0 & 0 \\ 0 & -0.0085 & 0 & 0 & 0.0083 & 0 \\ 0 & 0 & \frac{-1.1283}{1^2} & 0 & 0 & \frac{1.1921}{1^2} \end{bmatrix} \frac{lb_f}{in}$$

The numerical value 1^2 in Eq. (11) has dimension of length squared so the elements of \mathbf{m}_R and \mathbf{k}_R have proper dimensions.

Modal Testing

The experimental setup is shown in Fig. 9. Continuous random signal and Hanning window were used to obtain the FRF plot (Fig. 10). This plot includes the first six modes of the structure, of which the natural frequencies can be read directly. In the process of obtaining the *modal* damping ratios, the FRF data was first converted from the HP 3566A/3567A format to the STAR System format, then curve fitting methods were used. For widely spaced modes, the determination of damping ratios by curve fitting is straight forward; because in these modes, the structure behaves as if it were single degree of freedom (SDOF). However, for closely spaced modes, the damping ratios are difficult to obtained with great accuracy. The experimental results for natural frequencies ω_r and damping ratios ζ_r are given in Table 2.

Physical Damping Matrix

A physical damping matrix can be determined as

$$\mathbf{c}_R = \Phi_R^{-T} \text{diag}[2\zeta_r \omega_r] \Phi_R^{-1} \quad r = 1, 2, \dots, n \quad (12)$$

The modal damping matrix is given as

$$(\mathbf{C}_R)_e = \text{diag}[2\zeta_r \omega_r] = \text{diag}[0.4008 \quad 0.3314 \quad 0.1633 \quad 0.9068 \quad 0.8671 \quad 0.2771] \frac{\text{rad}}{s} \quad (13)$$

or

$$(\mathbf{C}_R)_a = \text{diag}[2\zeta_r \omega_r] = \text{diag}[0.4032 \quad 0.3191 \quad 0.1184 \quad 0.9392 \quad 0.8767 \quad 0.2205] \frac{\text{rad}}{s} \quad (14)$$

where ω_r in Eqs. (13) and (14) are the experimental and analytical (MSC/NASTRAN, Table 1) natural frequencies, respectively.

Introducing Eqs. (7, 13) into Eq. (12), we have

$$\mathbf{c}_R = \begin{bmatrix} 0.0132 & 0 & 0 & -0.0037 & 0 & 0 \\ 0 & 0.0123 & 0 & 0 & -0.0040 & 0 \\ 0 & 0 & \frac{0.3417}{1^2} & 0 & 0 & \frac{-0.0685}{1^2} \\ -0.0037 & 0 & 0 & 0.0084 & 0 & 0 \\ 0 & -0.0040 & 0 & 0 & 0.0075 & 0 \\ 0 & 0 & \frac{-0.0685}{1^2} & 0 & 0 & \frac{0.2497}{1^2} \end{bmatrix} \frac{\text{lb}_f s}{\text{in}} \quad (15)$$

The numerical value 1^2 in Eq. (15) has dimension of length squared so \mathbf{c}_R is dimensionally homogeneous.

Concluding Remarks

A complete mathematical model of the reduced order system has been determined, as given by

$$\mathbf{m}_R \ddot{\mathbf{x}}_R + \mathbf{c}_R \dot{\mathbf{x}}_R + \mathbf{k}_R \mathbf{x}_R = 0 \quad (16)$$

It should be noted that the physical damping matrix can be obtained using the experimental damping ratios and experimental/analytical natural frequencies and mode-shape matrix. If the physical damping matrix is *proportional*, the modal damping matrix is diagonal, or if the off-diagonal elements of the modal damping matrix are negligible, then the physical damping matrix can be approximated as proportional. Modal analysis can, then, be performed since the equations of motion can be decoupled via orthogonality properties [7].

Table 1 shows that the results obtained from the finite-element model agree very well with the experimental results in bending modes but not so well in torsional modes. Some explanation for these discrepancies is currently being sought.

References

1. Hallauer, W. and S. Lamberson, "Experimental Active Vibration Damping of a Plane Truss Using Hybrid Actuation," *Proceedings of the AIAA/ASME/ASCE/AHS 30th Structures, Structure Dynamics, and Material Conference*, 1989, pp. 80-90.
2. Ewins, D. J., *Modal Testing: Theory and Practice*. New York: John Wiley & Sons, 1988.
3. Inman, D. J., *Vibration with Control, Measurement, and Stability*. Englewood, NJ: Prentice-Hall, Inc., 1989.
4. Zaveri, K., *Modal Analysis of Large Structures - Multiple Exciter Systems*. Naerum: Bruel and Kjaer Publications, 1984.
5. Meirovitch, L., *Dynamics and Control of Structures*. New York: John Wiley & Sons, 1990.
6. MSC/pal 2 and MSC/NASTRAN *User's Manuals*, The MacNeal-Schwendler Corporation, Los Angeles.
7. Meirovitch, L., *Elements of Vibration Analysis*. McGraw-Hill Book Company, 1986.

Table 1 Comparison of Experimental and Analytical Natural Frequencies

Mode Number	Experimental (Hz)	MSC/pal 2 (Hz) (% Diff.)	MSC/NASTRAN (Hz) (% Diff.)
1	2.125	2.184 (+2.78)	2.228 (+4.85)
2	2.334	2.225 (-4.76)	2.247 (-3.73)
3	3.938	2.796 (-29.00)	2.854 (-27.53)
4	5.594	5.746 (+2.72)	5.794 (+2.77)
5	5.750	5.789 (+0.68)	5.814 (+1.11)
6	9.188	7.224 (-21.38)	7.311 (-20.43)

Table 2 Experimental Natural Frequencies and Damping Ratios

Mode Number	Frequency (Hz)	Damping Ratio (%)
1	2.125	1.44
2	2.334	1.13
3	3.938	0.33
4	5.594	1.29
5	5.750	1.20
6	9.188	0.24

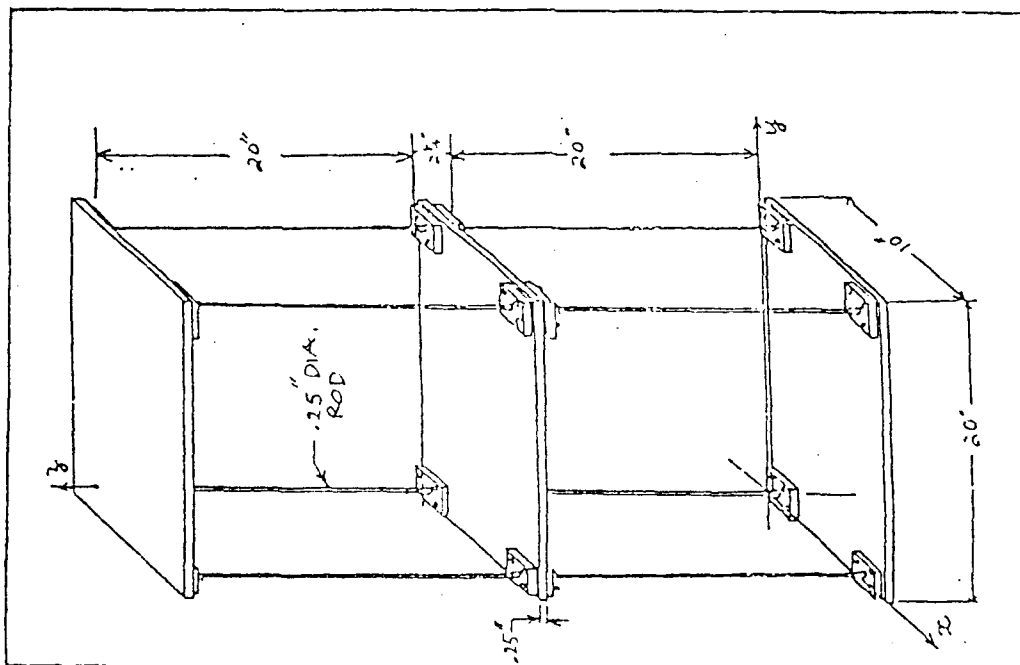


Fig. 1 The test structure (Aluminum 6061-T6)

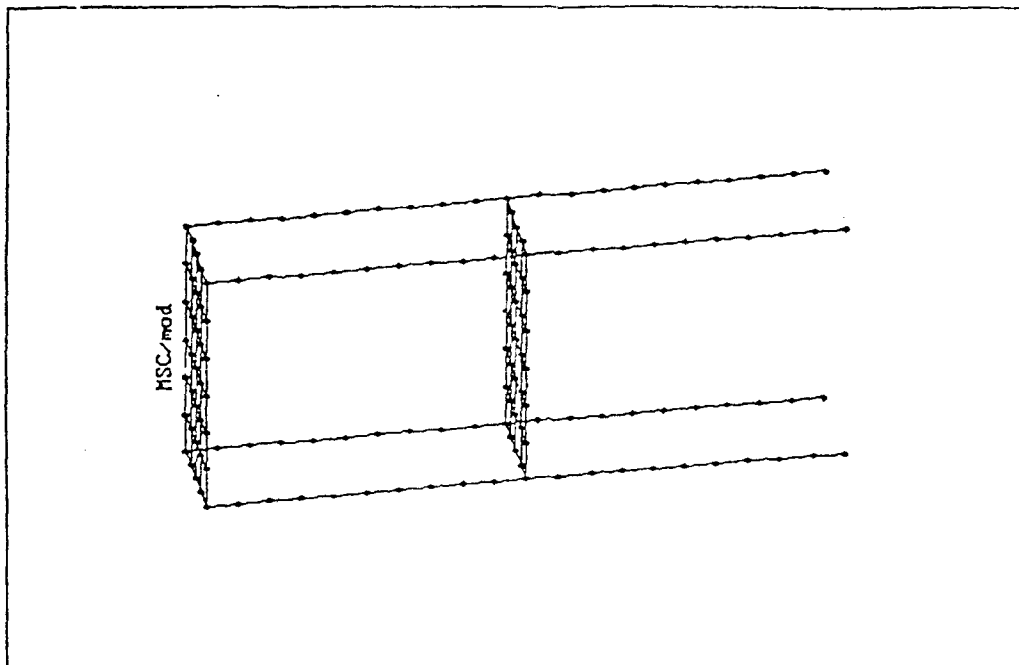


Fig. 2 Finite element model

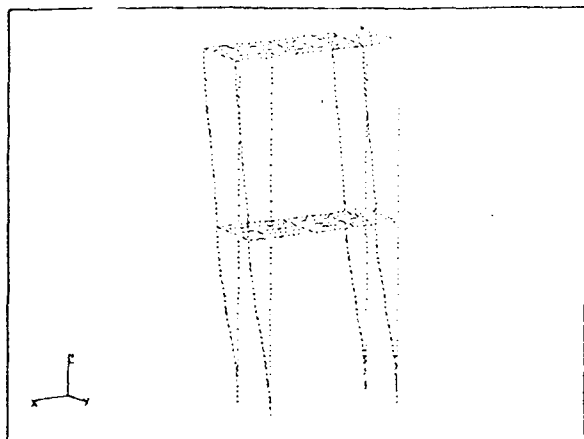


Fig. 3 First x-z bending, 2.184 Hz

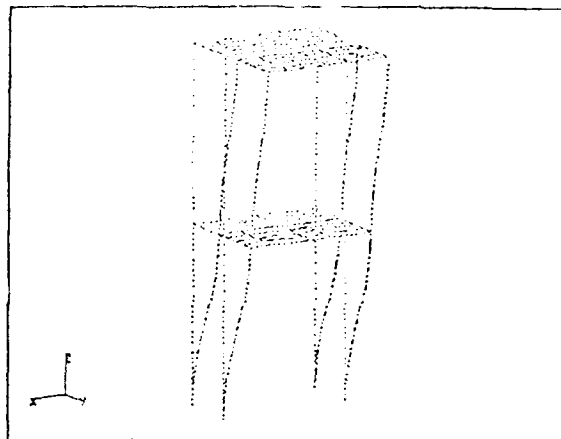


Fig. 4 First y-z bending, 2.225 Hz

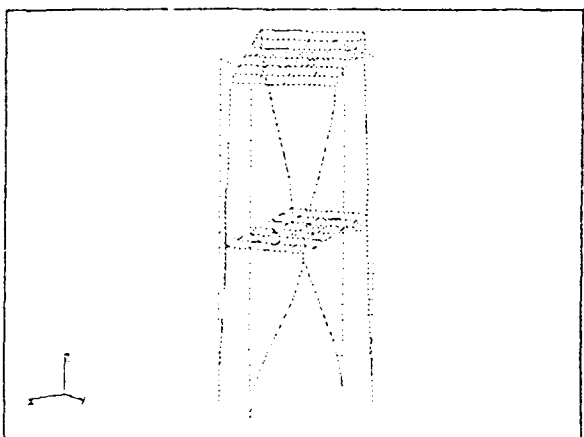


Fig. 5 First z torsion, 2.796 Hz

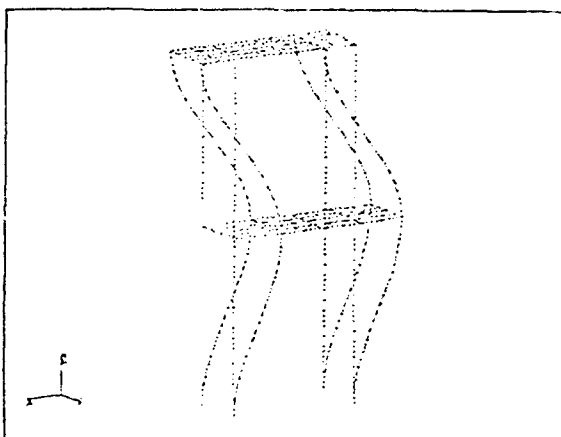


Fig. 6 Second x-z bending, 5.746 Hz

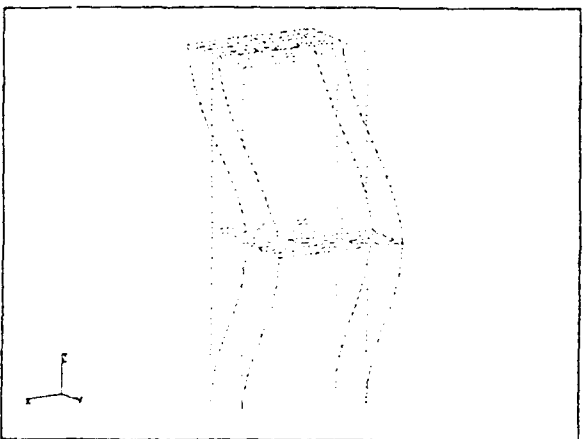


Fig. 7 Second y-z bending, 5.789 Hz

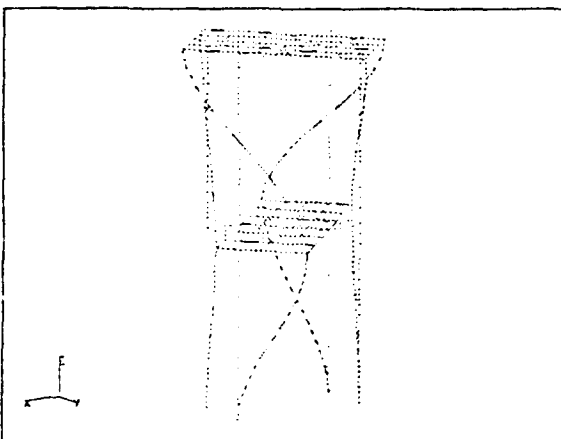


Fig. 8 Second z torsion, 7.224 Hz

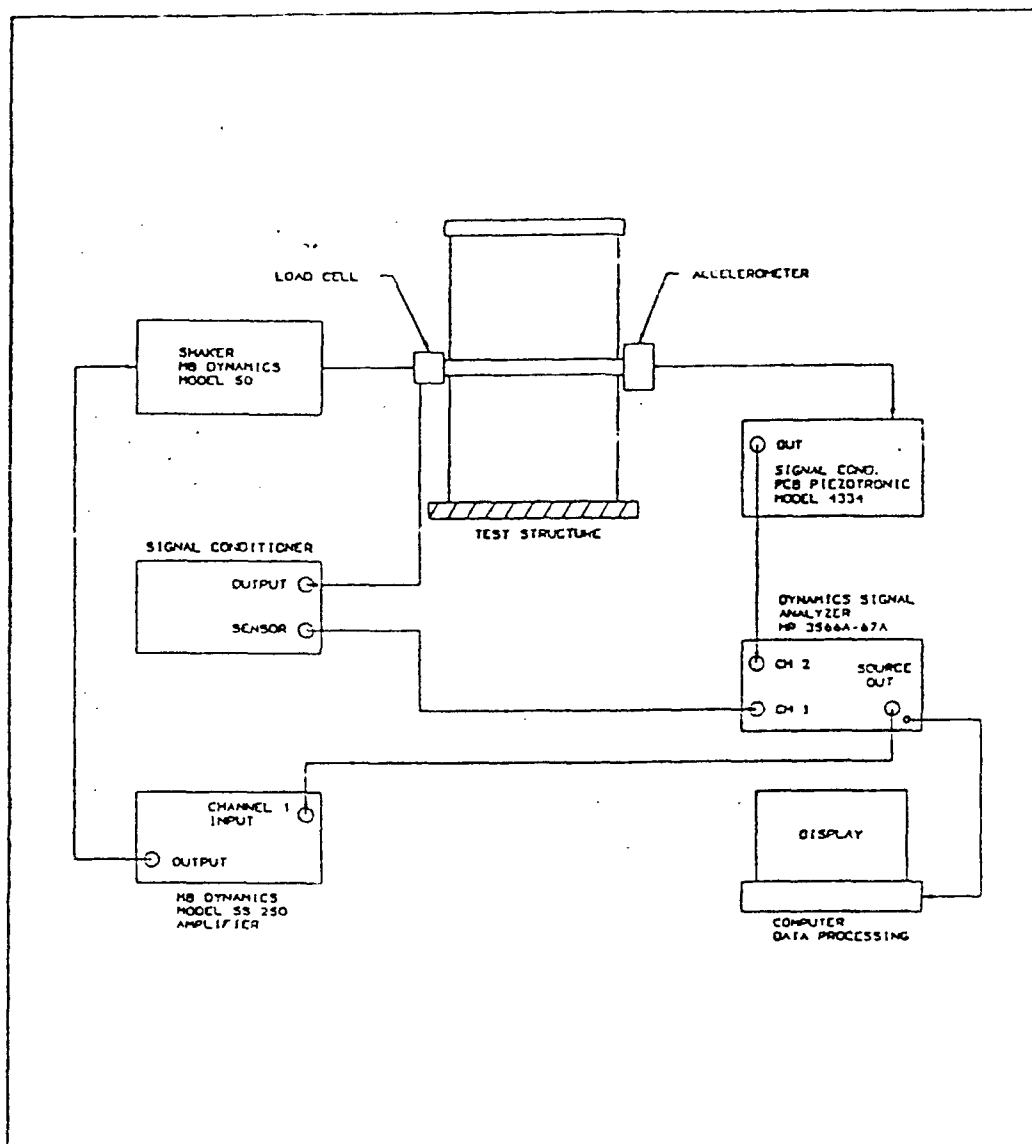


Fig. 9 Experiment setup

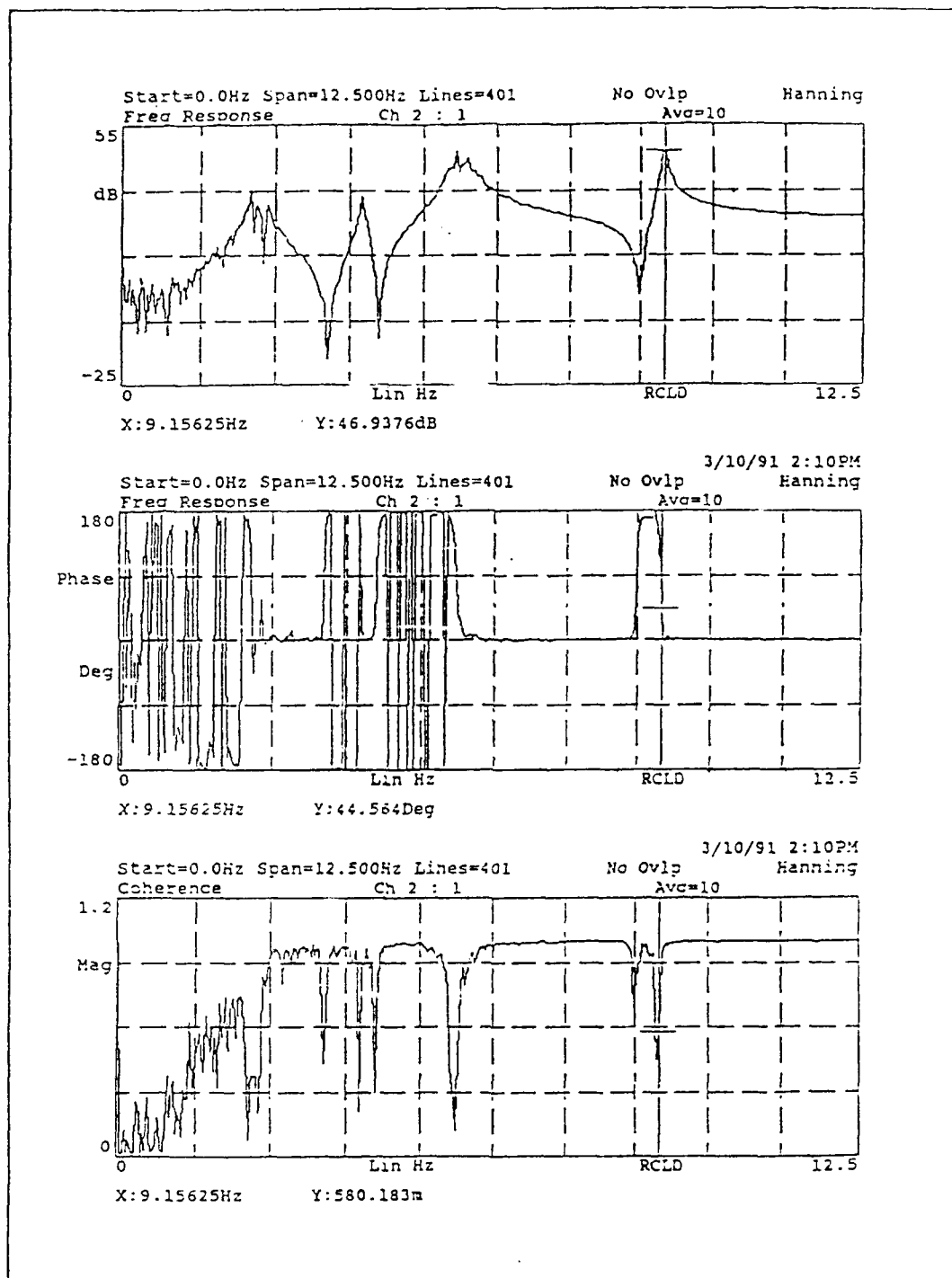


Fig. 10 Frequency Response spanning the first 6 modes

DEVELOPMENT OF A MAGNETIC SUSPENSION SYSTEM FOR RELIABLE VIBRATION DAMPING MEASUREMENT

Dantam K. Rao¹
Mechanical Technology, Inc.
Latham, NY

ABSTRACT

The damping properties of viscoelastic polymeric materials, as measured by different organizations and test techniques, often differ considerably. Sources for the discrepancy include parasitic energy dissipation at clamped supports of sandwich beam configurations, as well as imperfect simulation of a perfect clamped end condition. This uncertainty can be eliminated by magnetically suspending the test beam in a free configuration, without mechanical contact for pickup or excitation.

This paper will describe an approach to develop a proof-of-principle magnetic suspension system to levitate a typical test beam. The magnetic suspension system consists of an attraction electromagnet whose stiffness is controlled by closed loop feedback system.

Controllable stiffness of magnetic suspension will help eliminate measurement discrepancies attributable to the use of different fixtures by different organizations to clamp sandwich beams.

FULL PAPER NOT AVAILABLE FOR PUBLICATION

¹Mechanical Technology, Inc., 968 Albany-Shaker Road, Latham, NY 12110, (518) 785-2489

VEM CHARACTERIZATION PROGRAM

Bryce L. Fowler*
CSA Engineering, Inc.
Palo Alto, California

ABSTRACT

The development and use of an interactive computer program for the characterization of complex modulus data is described. The program uses the collocation process which accurately fits the real part of the complex modulus data and then uses the lack of fit of the loss factor to adjust the temperature shift function. This iterative method, which has converged when both the real modulus and the loss factor are fit simultaneously (the real directly and the loss factor indirectly), yields the most accurate estimate of the temperature shift function possible.

*CSA Engineering, 560 San Antonio Road, Suite 101, Palo Alto, CA 94306-4682, (415) 494-7351

1. Introduction

Successful design of passive damping treatments using viscoelastic materials (VEM's) such as elastomers depends upon several factors. One important factor is accurate knowledge of the sensitivity of VEM properties to variations in temperature and frequency. Since it is impossible to test a viscoelastic material at every combination of temperature and frequency, the material is tested at discrete temperatures and frequencies and a mathematical relationship is developed that characterizes the material at all other combinations of temperature and frequency. This process is referred to as characterization.

The equations used in characterization are parametric in nature. They are easily represented on computers. The difficulty lies in correctly choosing the equation parameters so that they accurately represent the VEM's. Interactive computer graphics have greatly improved the process of choosing and adjusting the correct parametric values.

This paper describes a recently developed computer program which implements the Collocation process [1] to accurately characterize viscoelastic materials.

2. VEMINT MAC

VEMINT MAC is a computer program developed to run on Apple Macintosh II computers. It fully utilizes the Macintosh windowing environment to allow point-and-click manipulation of complex modulus data. VEMINT MAC incorporates new characterization models as well as many of the models used in the past.

Five analytical representations of the temperature shift function (TSF, or α_T) are available. They are

1. Spline fit of slope
2. WLF equation
3. $\log(\alpha_T)$ is an exponential
4. $d(\log(\alpha_T))/dT$ is quadratic in $1/T$
5. Arrhenius equation

The "Spline fit of slope" model is discussed later in more detail. VEMINT MAC also has the capability to use the historical, discretized (tabulated for each experimental temperature) representation of α_T .

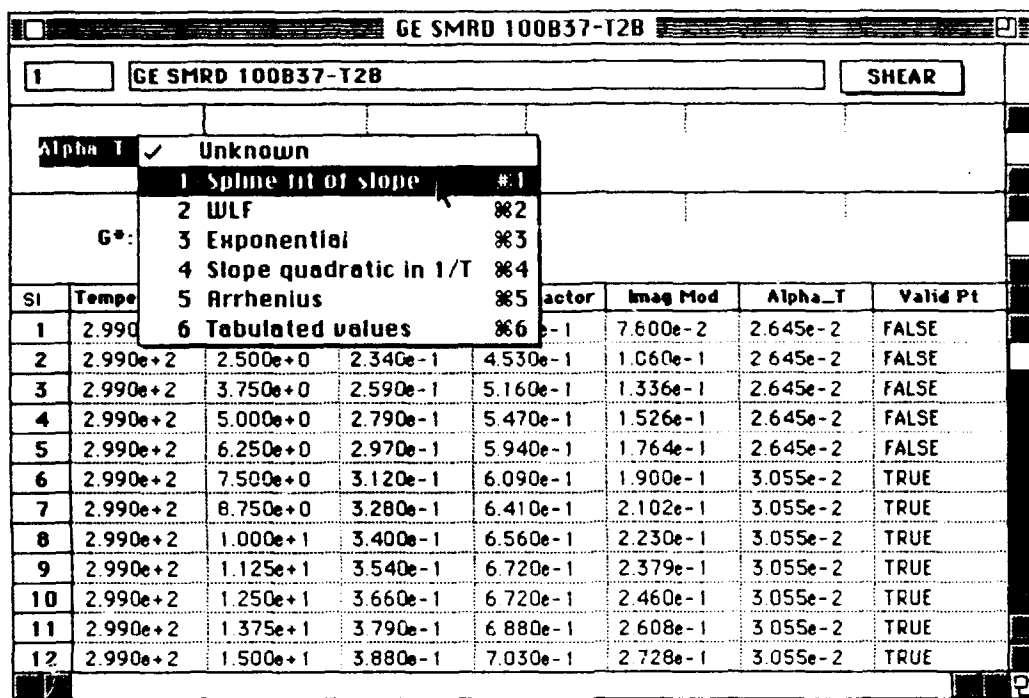


Figure 1. VEMINT MAC data window

Seven complex modulus equations are available in VEMINT MAC. They are

1. Ratio of factored polynomials
2. Rogers empirical
3. Bagley fractional
4. Huett fractional
5. Capps polynomial
6. Nashif 8 parameter
7. Nashif 15 parameter

Data and model parameters are displayed by VEMINT MAC in a spreadsheet-like window in which characterization models are chosen using popup menus (Figure 1). VEM data is read into VEMINT MAC in the form of ASCII text files with the format shown in Figure 2. Tab-delimited and English data formats are also supported. The data in Figure 2 has already been characterized. New uncharacterized data must have the same general format, but only the first four data fields are necessary, as shown in Figure 3.

001		3M ISD 113				SHEAR	
-----+-----+-----+-----+-----+-----+-----+-----							
ALFA-T MODEL							
NALF	NA	A(1)	A(2)	A(3)	A(4)	A(5)	A(6)
4	6	290.	220.	400.	5.016E-02	0.102	1.580E-03
-----+-----+-----+-----+-----+-----+-----+-----							
COMPLEX MODULUS MODEL							
NVEM	NB	B(1)	B(2)	B(3)	B(4)	B(5)	B(6)
4	6	4.190E-02	499.	4.640E+06	0.675	1.95	7.850E-02
-----+-----+-----+-----+-----+-----+-----+-----							
COMPLEX MODULUS DATA AS A FUNCTION OF TEMPERATURE AND FREQUENCY							
Temp	Freq	MReal	Eta	MImag	Alpha-t		
(DEG K)	(HZ)	(MPA)		(MPA)			
227.6	1861.	261.1	7.5670E-02	19.76	2.7260E+04	T	
227.6	3579.	289.1	7.3270E-02	21.18	2.7260E+04	T	
227.6	5788.	307.7	6.6440E-02	20.44	2.7260E+04	T	
241.5	1828.	170.1	0.2031	34.55	1576.	T	
241.5	3486.	179.8	0.2133	38.35	1576.	T	
241.5	5591.	188.0	0.2006	37.71	1576.	T	
255.4	638.0	29.06	0.9018	26.21	129.9	T	

Figure 2. VEMi data previously characterized

The Macintosh windowing interface is fully utilized to allow the user to simultaneously display multiple plots and data side-by-side. Erroneous points, as might be observed in the Wicket or the reduced frequency plots, may be double-clicked on and their corresponding values are displayed in the data window.

The Collocation method is used to characterize all new data. The method uses the "Spline fit of slope" temperature shift model in conjunction with the "Ratio of factored polynomials" complex modulus model. This is described in more detail below.

Once characterized, hardcopy of plots, such as the International and Wicket plots, as well as numerical data may be laser printed. VEMINT MAC provides all the plots and data described in the proposed ISO standard [4]. These are

1. An updated tabulated data file
2. Plots of $\log(\eta)$ vs. $\log(G^* M(f, T))$ in S.I. and English. (Wicket plot)
3. A plot of $\log(\alpha_T)$, $d(\log(\alpha_T))/dT$, and apparent activation energy vs. temperature

```

      1      3M ISD 113      SHEAR
-----+-----+-----+
                        ALFA-T MODEL
NALF  NA      A
  0    0
-----+-----+-----+
                        COMPLEX MODULUS MODEL
NVEM  NB      B
  0    0
-----+-----+-----+
COMPLEX MODULUS DATA AS A FUNCTION OF TEMPERATURE AND FREQUENCY
Temp      Freq      MReal      Eta
(DEG K)    (HZ)      (MPA)
227.6      1861.      261.1      7.5670E-02
227.6      3579.      289.1      7.3270E-02
227.6      5788.      307.7      6.6440E-02
241.5      1828.      170.1      0.2031
241.5      3486.      179.8      0.2133
241.5      5591.      188.0      0.2006
255.4      638.0      29.06      0.9018
.
.

```

Figure 3. Uncharacterized VEM data

4. A plot of $\log(\alpha_T)$ vs. $1/\text{temperature}$
5. Plots of $\log(\text{frequency})$ vs. temperature , (S.I. and English)
6. Plots of $\log(G^*_R(f, T))$, $\log(G^*_I(f, T))$, and $\log(\eta)$ vs. temperature , (S.I. and English)
7. Plots of $\log(\eta)$ vs. $\log(G^*_R(f, T))$ with constant temperature lines and an experimental frequency axis (Reduced Wicket plot) in both S.I. and English
8. Plots of $\log(G^*_R(f, T))$, $\log(G^*_I(f, T))$, and $\log(\eta)$ vs. reduced frequency with constant temperature lines and an experimental frequency axis (International plot) in both S.I. and English

3. Temperature Shift Function

Historically, the WLF equation [2] has been used to define the TSF. This, however, has not been able to shift all viscoelastic material data correctly outside the transition. A new approach is to use a spline fit of the slope of $\log \alpha_T$ for a relatively small number of temperature points (e.g., 7 points) to define the TSF. The temperature points are calculated such that the corresponding α_T values are equally spaced on the vertical log scale.

The Wicket plot (Figure 4) is used interactively to obtain values for the maximum loss factor (η_{\max}), the rubbery modulus asymptote (G_e), and the glassy modulus asymptote (G_g). The transition region is defined by η_{cutoff} , which is calculated as $0.7\eta_{\max}$.

The reference temperature, T_{ref} , is obtained in two steps, first as the average of the temperatures defining the transition region, $T_{\text{ref1}} = (T_{\text{cutoff_min}} + T_{\text{cutoff_max}})/2$. In [3] it was shown that the time-dependent stress-strain relations for a viscoelastic material in the transition region is described by

$$G^*(f_R) = \frac{G_e + G_g \left(\frac{1f_R}{f_{R0}} \right)^3}{1 + \left(\frac{1f_R}{f_{R0}} \right)^3} \quad (1)$$

where

$$\beta = \frac{2}{\pi} \arctan \left[\frac{\eta_{\max} \left[(1 - C^2) + 2(1 - C)C^{1/2}(1 + \eta_{\max}^2)^{1/2} \right]}{(1 - C)^2 - 4C\eta_{\max}^2} \right]$$

$$C = G_e/G_g$$

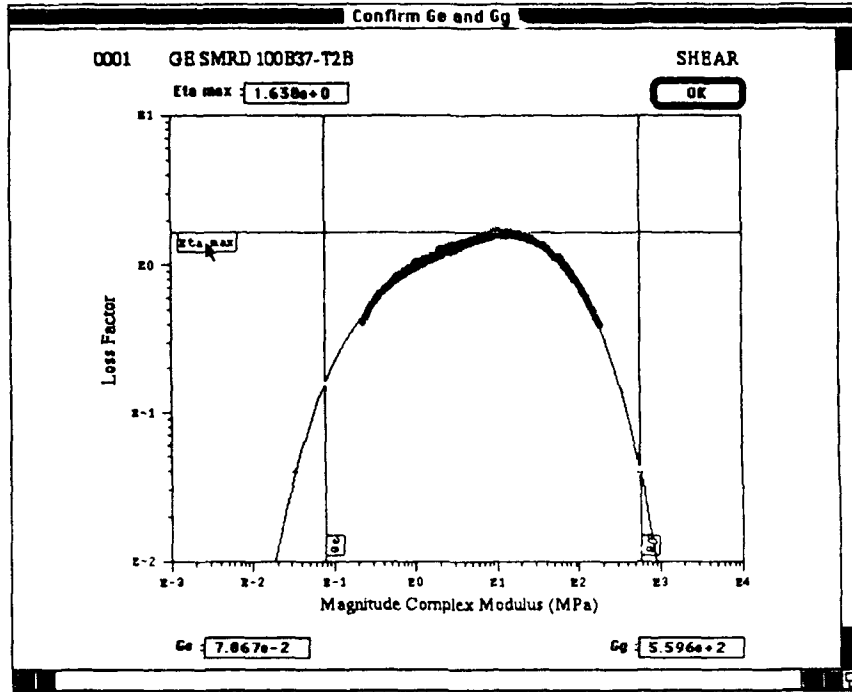


Figure 4. Wicket plot used to determine parameters

Solving for α_T/f_{R_0} gives

$$\frac{\alpha_T(T_i)}{f_{R_0}} = \frac{1}{j f_i} \left[\frac{G_i^* - G_e}{G_g - G_i^*} \right]^{\frac{1}{B}} \quad (2)$$

By fitting a quadratic through the data points defined within the transition by $\eta \geq \eta_{\text{cutoff}}$ an initial value for the slope of the log of α_T at T_{ref} is calculated. Next, a quadratic fit of $\log \eta$ versus reduced temperature, where the reduced temperature is given by

$$T_{\text{red}i} = \frac{T_{\text{exp}i}}{1 + \frac{\log(f_{\text{exp}i}/f_{\text{ref}})T_{\text{exp}i}}{S_{\text{ref}}T_{\text{ref}}^2}} \quad (3)$$

is used to calculate $T_{\text{ref}} = T_{\text{red}}$ evaluated at η_{max} . A value of 100 Hz is presently used for f_{ref} . The final reference slope, S_{ref} , is re-calculated from the quadratic through Equation 2.

A plot of $\log \alpha_T$ versus T is then displayed, where α_T is calculated from the " $d(\log(\alpha_T))/dT$ is quadratic in $1/T$ " equation. As shown in Figure 5, the user may adjust the temperature shift function outside the transition by changing the values of $d(\log(\alpha_T))/dT$ (designated as SAL and SAZ) at the endpoints. Finally, α_T is calculated as the integral of the spline of the slope, where the constant of integration is given by $\alpha_T \equiv 1.0$ at T_{ref} .

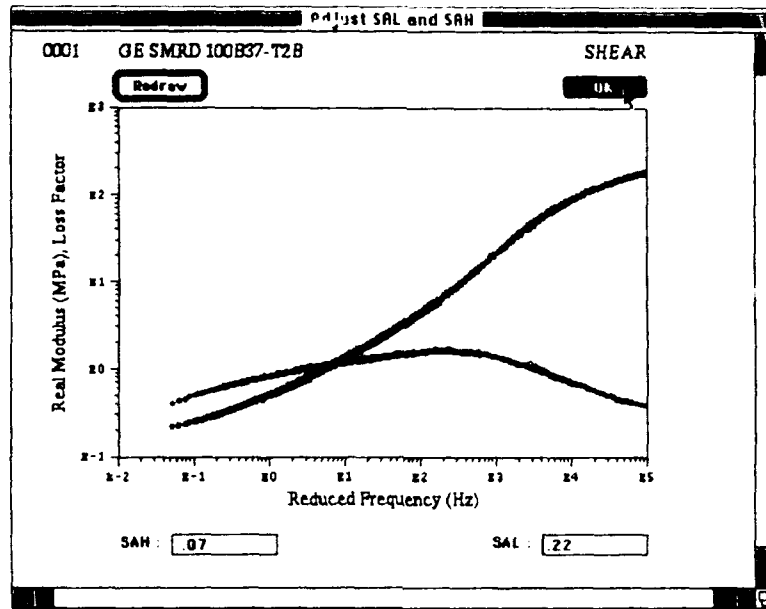


Figure 5. Adjust $d(\log(\alpha_T))/dT$ endpoints

The accuracy of the TSF parameters is checked by looking at a plot of the complex modulus data versus the reduced frequency. The spline knots may be interactively adjusted if any isotherm "shingles" are observed (Figures 6 and 7). Note, the reduced frequency at each temperature knot is calculated as

$$f_{Ri} = \alpha_T (T_{\text{knot}i}) f_{\text{ref}} \quad (4)$$

where f_{ref} here is calculated as the geometric mean of the experimental frequencies

$$\log(f_{\text{ref}}) = \left(\sum_{i=1}^n \log f_{\text{exp}i} \right) / n \quad (5)$$

4. Complex Modulus

The "Ratio of factored polynomials" model is given by

$$G(z) = G_e \prod_{i=1}^N \frac{1 + e \left(\frac{z}{r_i} \right)^{\beta_k}}{1 + \frac{1}{e} \left(\frac{z}{r_i} \right)^{\beta_k}} \quad (6)$$

where

$$\begin{aligned} z &= j2\pi f_R \\ e &= (G_g/G_e)^{1/2N} \end{aligned}$$

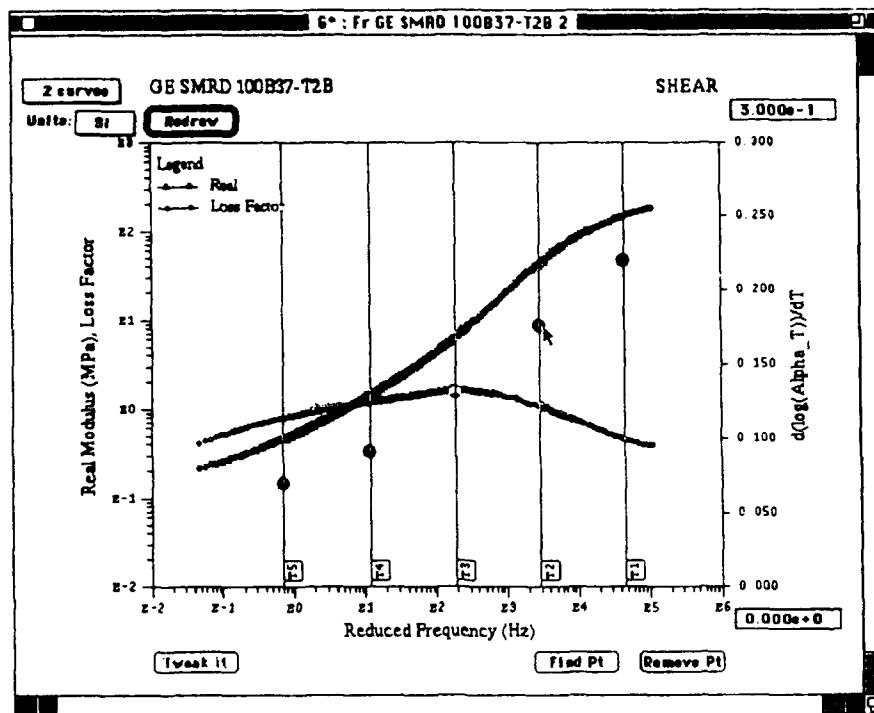


Figure 6. Spline knots may be interactively adjusted

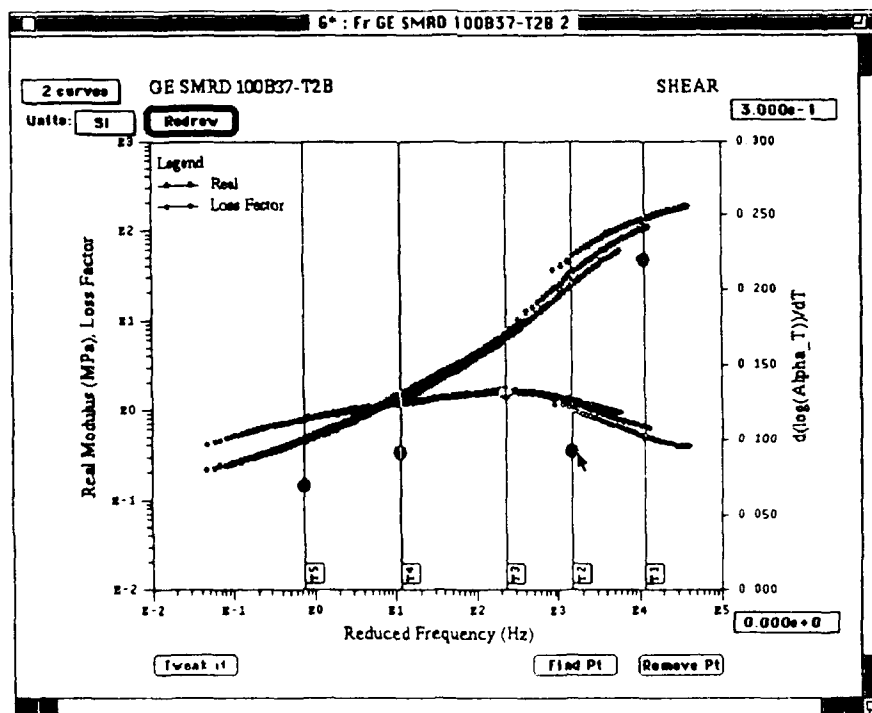


Figure 7. Reduced frequency after gross spline knot adjustment

In the present effort $\beta_k = 0.7$ although values from 0.5 to 1.0 have been used in the past.

Initial values of r_i are generated by first calculating logarithmically even spaced values between G_e and G_g with

$$\begin{aligned} G_{\text{fit}1} &= G_e e \\ G_{\text{fit}2} &= G_{\text{fit}1} e^2 \\ &\vdots \\ G_{\text{fit}n} &= G_{\text{fit}n-1} e^2 \end{aligned}$$

A smoothing spline is fit to the magnitude complex modulus versus the reduced frequency. To ensure full coverage from rubbery to glassy plateaus, the spline is extended six decades below and above the minimum and maximum experimental reduced frequencies respectively. Each r_i is initialized as the reduced frequency at each $G_{\text{fit}i}$ on the spline. The r_i values are then iteratively refined with

$$r_{i\text{new}} = r_{i\text{old}} \left(\frac{f_{R_{\text{fit}i}}}{f_{R_{\text{curve}i}}} \right)^\zeta \quad (7)$$

to fit Equation 6 to the magnitude modulus spline, where $f_{R_{\text{curve}i}}$ is the reduced frequency for Equation 6 which returns $G_{\text{fit}i}$. The exponent ζ is set less than unity to keep individual iterative steps from overshooting the spline. A value of 0.5 is presently used.

5. Collocation

In addition to the smoothing spline fit through the magnitude modulus versus reduced frequency, a smoothing spline is also fit through η versus the reduced frequency. This is assumed to be the best estimate of the experimental loss factor. Starting with the TSF knot closest to the reference temperature and alternately working out, the corresponding reduced frequency is calculated using Equation 4. The equation

$$S_{\text{new}i} = S_{\text{old}i} \frac{\arctan(\eta_{\text{curve}i})}{\arctan(\eta_{\text{exp}i})} \quad (8)$$

is then used to iteratively adjust the TSF based on the lack of fit of Equation 6. (Note, within the program, $S_{\text{new}i}$ is constrained to be within a user-defined percentage of $S_{\text{old}i}$.)

This is in contrast to [1] where the Wicket plot was used to make the comparison between η_{curve} and η_{exp} . The change to using η versus reduced frequency alleviates

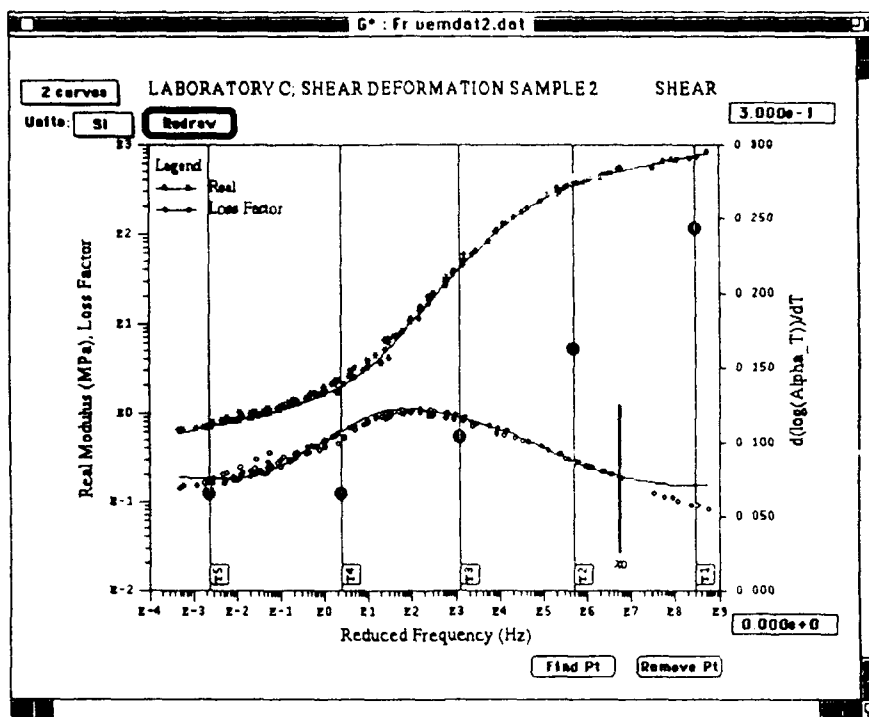


Figure 8. Loss factor divergence at x_0

possible problems encountered with numerical ill conditioning outside the transition where the slope of the Wicket typically gets steep. The plot of η versus reduced frequency is easily extended to allow the interactive adjustment of the TSF knots directly on the computer screen as seen in Figures 6 and 7.

After all the TSF knots have been adjusted, the smoothing splines are re-fit for both the magnitude modulus and the loss factor to the new reduced frequency and Equations 7 and 8 are repeated. The process stops when S_{new} is within 1% of S_{old} for every knot, or when a user specified number of iterations have taken place.

6. Observations

The need for good characterization has always been present. With advances in damping design tools the need has become even more critical.

The program VEMINT MAC has gone a long way toward more accurate characterization of VEMs; however, numerical difficulties still exist. It has been observed that outside the transition, η_{curve} and η_{exp} may begin to diverge at some reduced frequency. This may be especially true when coverage of experimental frequency is limited (Figure 10). A correction can be applied to the τ_i 's that does not change the modulus appreciably but does correctly adjust the loss factor and is the subject of further study.

VEMINT MAC, provides a great increase in the speed and accuracy with which damping material characterizations may be processed. The materials user may quickly find particular data points and set initial parameter values using the graphical interface.

The use of the Collocation method effectively allows the data to define the TSF, thus precluding possible errors due to operator bias. Numerical instabilities still need to be addressed, however.

References

- [1] L. Rogers, "An Accurate Temperature Shift Function and a New Approach to Modeling Complex Modulus," Presented at 60th Shock and Vibration Symposium, Virginia Beach, VA, November 14-16, 1989.
- [2] J. D. Ferry, *Viscoelastic Properties of Polymers*, John Wiley and Sons, 3rd ed., 1980.
- [3] L. C. Rogers, "Operators and Fractional Derivatives for Viscoelastic Constitutive Equations," *J. Rheology*, Vol. 27, No. 4, 1983, pp. 351-372.
- [4] L. Rogers, "Graphical Presentation of Damping Material Complex Modulus," *Proposed Standard*, ISO/TC108/WG13-N25, August 1987.

DATA BASE OF THE DYNAMIC PROPERTIES OF MATERIALS

Presenting Author

Ahid D. Nashif
Anatrol Corporation

Co-Author

Tom M. Lewis
Anatrol Corporation

ABSTRACT

Measurements of the damping properties of materials continues to be a major effort at Anatrol to provide the basis for using both the damping and isolation technologies. The current library of the damping properties at Anatrol contains over a thousand materials and is being expanded on a daily basis. Those materials have been completely characterized for their damping properties and are stored on the computer in terms of:

- * temperature and frequency
- * dynamic and static non-linearities
- * creep and relaxation behavior
- * aging, outgassing, etc.

The properties for most of these materials have been measured by more than one technique covering wide ranges of temperatures and frequencies to ensure their accuracies and to arrive at the appropriate shift factor reducing the data.

This paper will give examples of the properties for various families of materials currently on the data base and how they can be accessed by various users working in the damping and isolation areas.

Anatrol Corporation, 10895 Indeco Drive, Cincinnati, Ohio. 45241
Tel: (513) 793-8844

I. INTRODUCTION

Reducing noise and vibration levels in various products has been receiving more and more attention in recent years. This increased level of awareness has been caused not only by the need to build better, more efficient items, but also because products with low noise and vibrational response are now being perceived as having better quality. Products with low noise and vibrational characteristics can be designed by implementing both passive and active control systems. The approach for passive control systems consists of mainly using structural modifications, damping, and isolation. Before either the damping and/or the isolation technologies can be properly utilized, however, a good knowledge of the dynamic behavior of the materials as functions of different environments needs to be known. Without such properties on hand it becomes very difficult to perform the analysis and optimize the design for a given system.

Available information on the properties of materials, either from manufacturers or in the open literature, is limited, has considerable scatter, and covers only some environmental ranges. To overcome these limitations, Anatrol has undertaken the task of measuring and evaluating the dynamic properties of materials under various conditions. This information has been gathered to establish an extensive data base used to assist in the design and implementation of passive control systems. Over the past fourteen years, measurements have been made on several thousand different materials including structural adhesives, PSA's, plastics, enamels, rubber materials, foams, and composites.

The various techniques that have been used to measure the dynamic properties of materials at Anatrol, include those that are in the frequency domain, such as the impedance and beam techniques, and those that are in the time domain, such as the relaxation and creep techniques. From those measurements the properties of the specific material of interest is then generated in terms of temperature, frequency, static non-linearity, dynamic non-linearity, and time under load. Those properties are then curve fitted with analytical expressions and stored on the computer as analytical functions along with other information, such as their form of availability, resistance to solvents, outgassing, aging effects, and so on.

The purpose of this paper is to describe the current data base that is now available at Anatrol, and how it can be accessed by users to design various passive control systems. Specific details regarding the measurement techniques, presentation of the data, and the curve fitting analysis can be found in Reference [1].

II. MEASUREMENT TECHNIQUES

Different measurement techniques are needed to evaluate the dynamic properties of materials because such properties vary greatly with the different environments, and currently there is no one technique that is capable of covering such extreme ranges. Another important reason for generating the data by more than one technique is to cover wide temperature and frequency ranges for the measurements to establish confidence in using the temperature-frequency superposition principle. Without having measured the data over such wide temperature and frequency ranges and verified the accuracy of the shift factor, the use of the temperature-frequency superposition principle is likely to be questioned. Anatrol has put forth the extra effort to make the measurements by

several techniques and over wide temperature and frequency ranges to establish good confidence in the data base.

The various techniques that have been primarily used to generate the material properties in the data base include, the beam technique, the impedance technique, and the relaxation and creep techniques. Both the beam and impedance techniques are used to measure the dynamic properties of materials in the frequency domain at different temperatures and dynamic loading conditions. The creep and relaxation techniques are used to measure the relaxation modulus and the creep compliance as functions of time under different loading conditions.

II.1 BEAM TECHNIQUE

The beam technique is used to measure the dynamic properties of materials in either shear or tension/compression over wide temperature and frequency ranges, in the linear region of the material in terms of strain amplitude. The frequency range where this technique is typically used is between from about 50 to 5,000 Hz. The technique is based on combining the material of interest to a metal beam and making measurements on the composite system. By knowing the frequencies of the various modes of vibration and their damping values along with the geometry of the beam, the dynamic properties of the material under test can be computed independent of the geometry. Typical properties for a material measured in shear by the beam technique are given in Figure 1.

II.2 IMPEDANCE TECHNIQUE

The impedance technique consists of applying a known force into a sample and measuring the resultant displacement. The force and displacement signals and the phase angle between them are used to compute the dynamic properties of the materials. Loading is typically applied in either tension/compression or shear, depending on the geometry of the sample, to generate either Young's modulus or the shear modulus. The impedance technique can cover frequency ranges from as low as 10^{-3} Hz to 1000 Hz. It is difficult to use the impedance technique at higher frequencies because of fixture resonances. Also, it is difficult to use this technique for many materials when testing in the glassy region because the test specimen can approach the stiffness of the fixture. Even with such limitations however, the material properties can be generated over wide temperature and frequency ranges. Also, by using simple geometry and varying the force, the behavior of the material in terms of loading (static or dynamic) can be measured.

Figure 2 represents the results measured by the impedance technique in shear over a wide frequency range and at some selected temperatures.

II.3 RELAXATION AND CREEP TECHNIQUES

The relaxation and creep techniques are used to determine the response of the materials under load as a function of time. With the relaxation technique, a fixed displacement is applied to the sample and the resultant force is measured as a function of time. From such a measurement the relaxation modulus as a function of time can be computed. On the other hand, the creep technique is based upon applying a fixed force to the sample and measuring the resultant displacement as a function of time, which will yield the creep compliance as a function of time. The relaxation technique is usually used for soft materials

while the creep technique is used for stiff materials. Tension/compression or shear specimens could be used with either technique.

Not only the behavior of the material under load as a function of time can be determined from such measurements, but the results can also be used to compute the dynamic properties of the material at extremely low frequency, by transforming the measured data from the time domain into the frequency domain.

Figure 3 represents typical results for the relaxation modulus measured at different temperatures with time.

II.4 CORRELATION OF THE PROPERTIES

Figure 4 combines the results of Figure 1 and 2 together. It can be seen here that good correlation has been achieved between the two techniques even though those measured by the impedance technique are for low frequencies, while those for the beam technique are for high frequency. This kind of correlation gives confidence in the shift factor used to collapse all the data. Figure 4 is curve fitted with analytical expressions which are then stored on the computer for later use.

The correlation of the measured results by the impedance, beam, and relaxation techniques is shown in Figure 5 for several samples. The agreement between the various techniques illustrates that each technique is being well used within its limitation and no erroneous data is generated.

III. DESCRIPTION OF THE DATA BASE

III.1 MEASUREMENT CONDITIONS

All materials in the data base are measured either in tension/compression to generate the properties in extension (Young's modulus and loss factor) and/or in shear to generate the properties in shear (shear modulus and loss factor). If the properties are measured in both states of stress, then Poisson's ratio can be computed. If the properties are measured in one state of stress only, and the material has a rubber-like behavior, then Poisson's ratio can be assumed to be almost 0.5 and the properties in the other state of stress can be computed. Figure 6 represents the properties for the material of Figure 4 but for both states of stress.

All materials in the database are measured over wide temperature and frequency ranges to enable curve fitting of the data with analytical expressions as shown in Figure 4. Such analytical expressions are then stored on the computer for later analysis or literature search as necessary. In the following Figures, the analytical expressions are used to describe the material properties in terms of temperature for some discrete frequencies. Other frequencies could be generated from the stored curve fitted data as necessary.

In addition to the above conditions, many of the materials in the data base are also measured in terms of static non-linearity, dynamic non-linearity, aging, exposure to high temperatures, and exposure to fuel and oil, and others. Figures 7 through 10 represent the effects of such environments on the measured properties.

III.2 TYPES OF MATERIALS

Although it is difficult to classify all the materials in the data base, some classifications could be used as follows.

ELASTOMERS

This heading includes all materials with rubber-like behavior at room temperature. Specifically, such materials include the silicones, natural rubbers, vitons, butyls, nitriles, ABS, and so on. Figure 11 through 14 illustrate the properties of some of the materials in this category. Such materials are used in various isolation systems, tuned dampers, and some constrained and unconstrained layer damping treatments.

PRESSURE SENSITIVE ADHESIVES

Pressure sensitive adhesives are widely used as the damping materials in constrained layer damping treatments. Such materials could be of the acrylic, silicone or rubber base type. Figure 15 and 16 give the properties of some of these materials.

PLASTICS

Many plastics are used as structural materials and as damping materials at high temperatures. Those materials could include the various vinyls, styrenes, PMMA, PEEK, PVC, polypropylenes, polysulphones, nylons, and so on. Figure 17 and 18 contain the properties of some of the plastics from the data base.

FOAMS

Foams can be made from several materials such as acrylics, polyurethanes, silicones, etc. and therefore, can have varying properties, as shown in Figures 19 and 20.

SPRAYABLE MATERIALS

Materials in this category include those that could be sprayed on the structure, for ease of application. The use of such materials is to provide extensional damping over wide frequency ranges. Figures 21 and 22 illustrate the dynamic properties of only two of the materials.

AUTOMOTIVE BODY PANEL MATERIALS

The materials under this heading, which are called "Mastics", are usually applied to automotive body panels to provide damping. The materials can be either of the heat bondable type or the type that requires a pressure sensitive adhesive for application. These materials have good damping properties around room temperature as shown in Figures 23 and 24.

DAMPED LAMINATES

Laminates are now being used in various sheet metal applications in the automotive, aircraft, and appliance industries to provide high damping. Because such materials are sold in the laminate form (two layers of metal sandwiching a

very thin layer of damping material), the properties are given in Figure 21, in terms of the composite properties for the indicated configuration.

PRESSURE SENSITIVE FOAM TAPES

Pressure sensitive foam tapes have been used as damping materials in constrained layer surface damping treatments and in damping link configurations. These materials are generally acrylic, rubber, or urethane based, and are generally available in thicknesses on the order of 1mm thick. Figures 26 and 27 give sample properties of several of these materials.

COMMERCIAL FOIL BACK TAPES

These products are often utilized as off-the-shelf constrained layer damping systems. They combine acrylic or rubber based pressure sensitive adhesives with an aluminum constraining layer. These products are commonly utilized by the aircraft industry in fuselage skin damping applications. Figure 28 illustrates the damping performance of several foil back tape systems.

POLYMERIC STIFFENERS

These products are designed to provide reinforcement to automotive body panels. They generally consist of a thermosetting, resin impregnated glass fiber reinforced sheet stock, which is cured after application. Figures 29 and 30 show sample properties.

AIRCRAFT FUEL TANK SEALANTS

These materials generally consist of two parts, room temperature curing polysulphide, and elastomers. They are resistant to jet aviation fuels, hydraulic oils, salt water, and to some dilute acids. Figure 31 demonstrates properties for one of these materials.

ENAMELS

Enamels are used not only as protective and decorative coatings, but also as damping materials at high temperatures. This is because such materials exhibit good damping capabilities within their softening region before the meltdown. Enamels are typically used in a free-layer damping treatment and therefore the dynamic properties are usually measured in tension/compression and over wide temperatures and frequencies. Different materials have been identified to cover ranges up to 2000 F, and Figures 32 and 33 represent the properties of two such materials.

STRUCTURAL ADHESIVES (EPOXIES)

The dynamic properties of epoxies and/or structural adhesives have been evaluated for better understanding of their use. As a result of this evaluation a number of structural adhesives have been found to have good damping properties in addition to their high modulus, as can be seen in Figures 34 and 35.

III.6 COMPOSITES

The data base includes both metal matrix composites and resin reinforced composites. Those composites are usually measured assuming they are homogeneous materials, and such properties are shown in Figures 33 and 37.

IV. ACCESS OF THE DATA BASE

The data base at Anatrol can be accessed in two ways. The first is for Anatrol to perform a literature search for the customer on a job-by-job basis. This search will be based on the customer specifying to Anatrol, the material properties of interest, and the environmental factors to be considered in the search. The second is for Anatrol to install parts, or all of the data base on the customer's computer. For either case, Anatrol will discuss the specific requirements and scope of this service with the customer and quote it accordingly.

REFERENCE

1. A.D. Nashif, D.I.G. Jones and J.P. Henderson, Vibration Damping, Wiley Interscience, 1985.

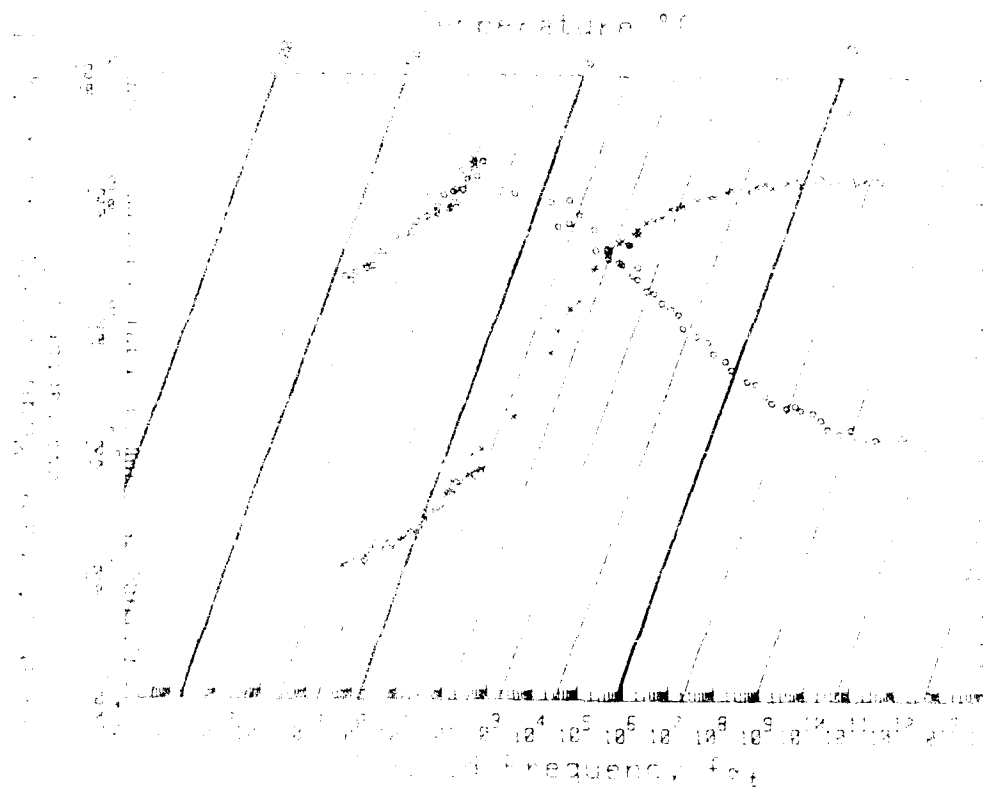


Figure 1: Reduced Frequency Nomogram for a Typical Material in Shear Using the Vibrating Beam Technique [Library #580 - Vinyl Rubber]

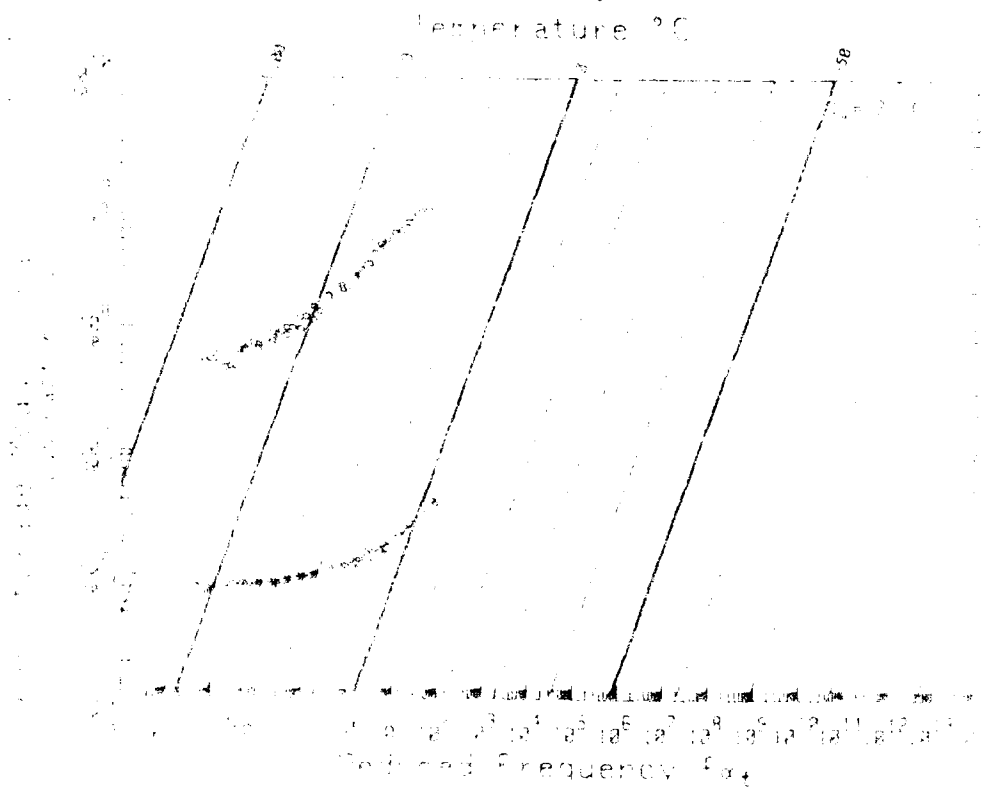


Figure 2: Reduced Frequency Nomogram for a Typical Material in Shear Using the Impedance Technique [Library #580 - Vinyl Rubber]

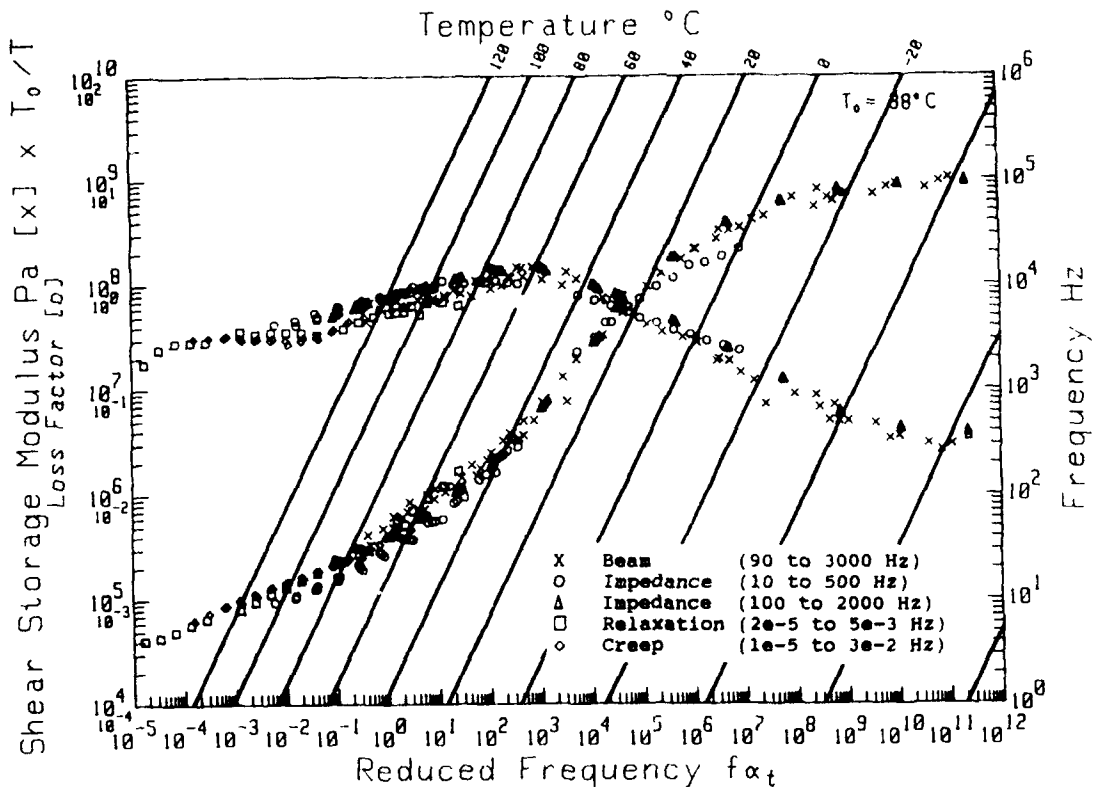


Figure 5: Reduced Frequency Nomogram for a Typical Material Using Various Measurement Techniques

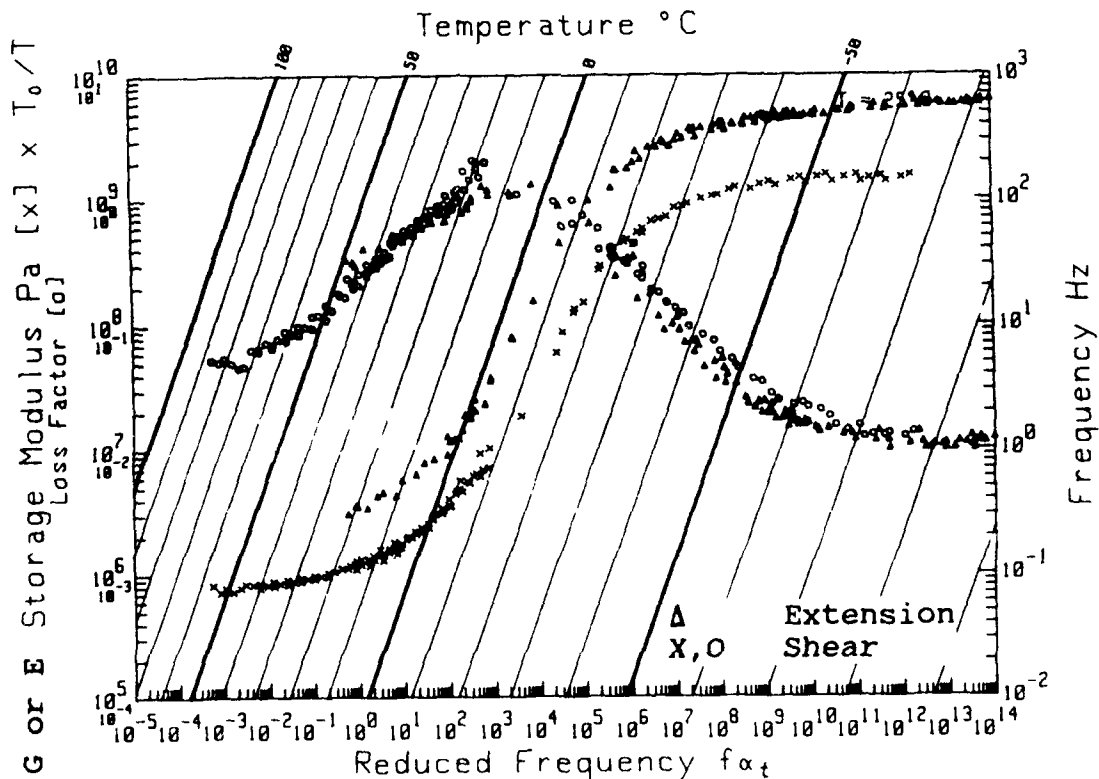


Figure 6: Material Properties for Shear and Extension Using the Vibrating Beam and Impedance Techniques [Library #580 - Vinyl Rubber]

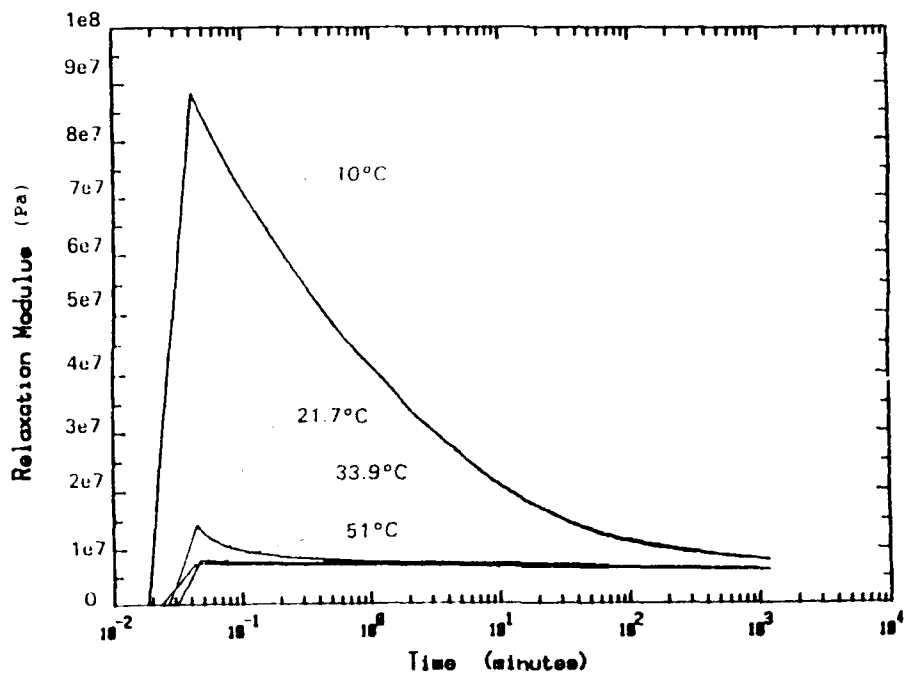


Figure 3: Relaxation Modulus Properties for a Typical Material at Various Temperatures over Time

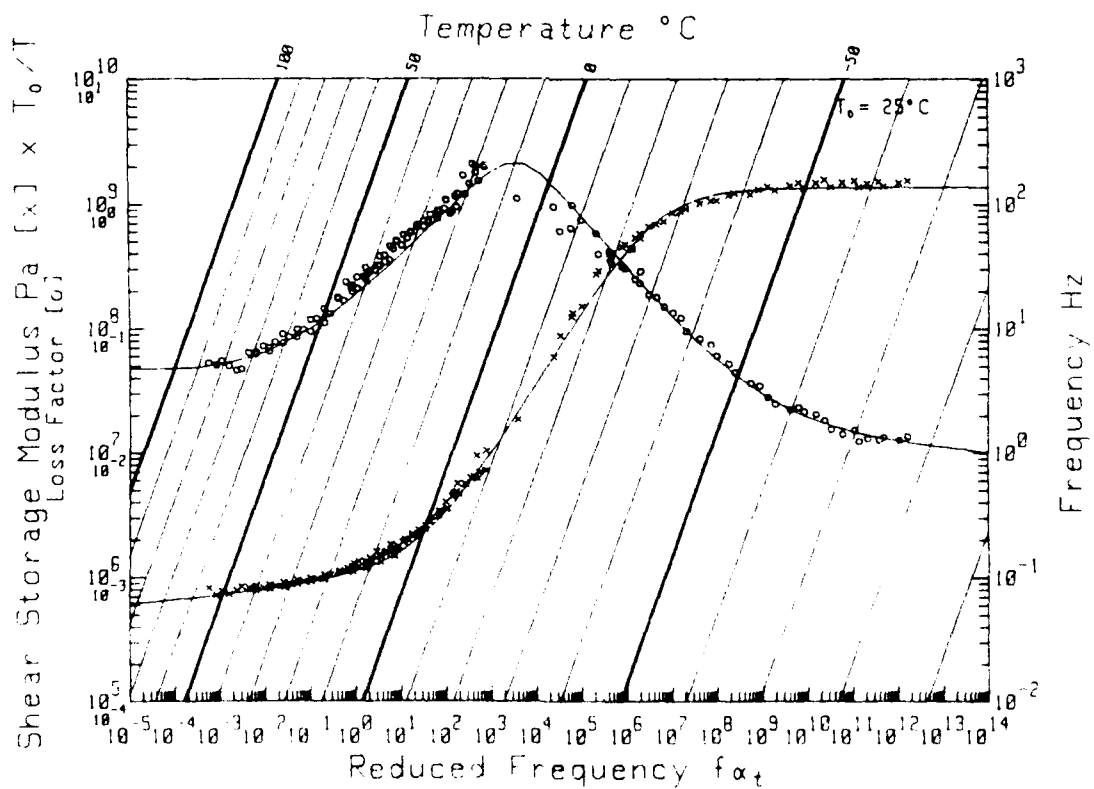


Figure 4: Reduced Frequency Nomogram for Both the Vibrating Beam and Impedance Techniques in Shear [Library #580 - Vinyl Rubber]

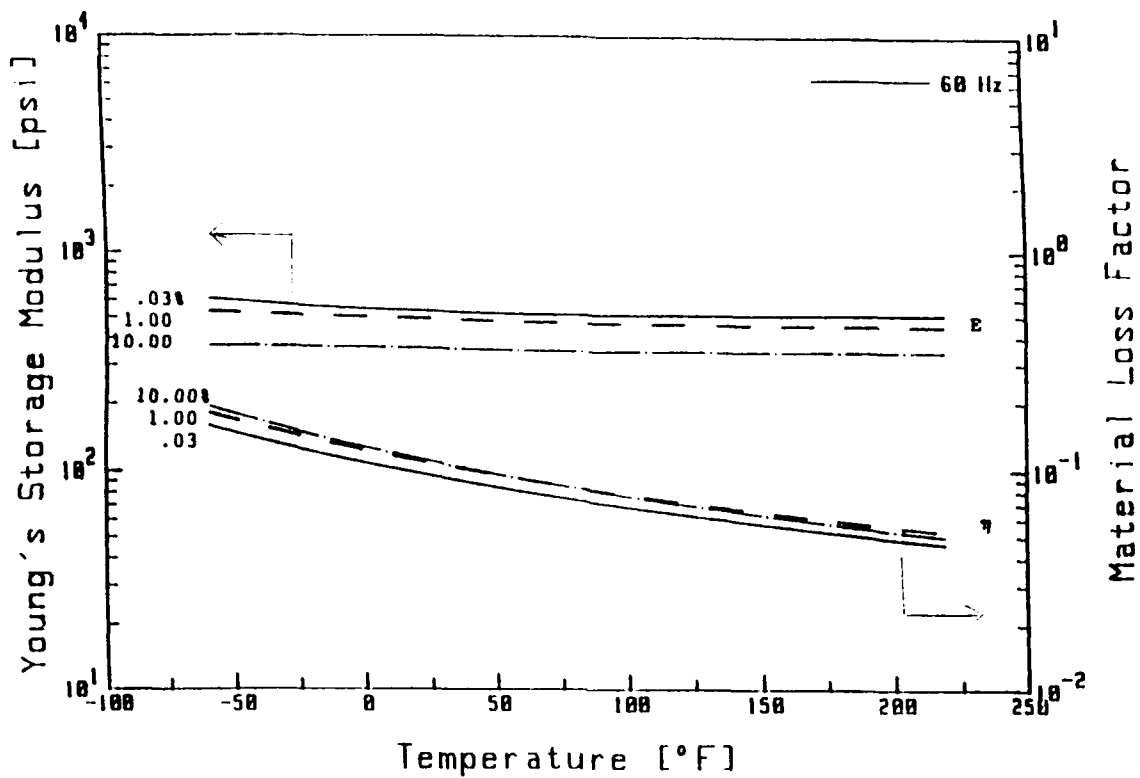


Figure 7: Variation of Material Properties with Strain Amplitude and Temperature for 60 Hz
[Library #380 - Silicone]

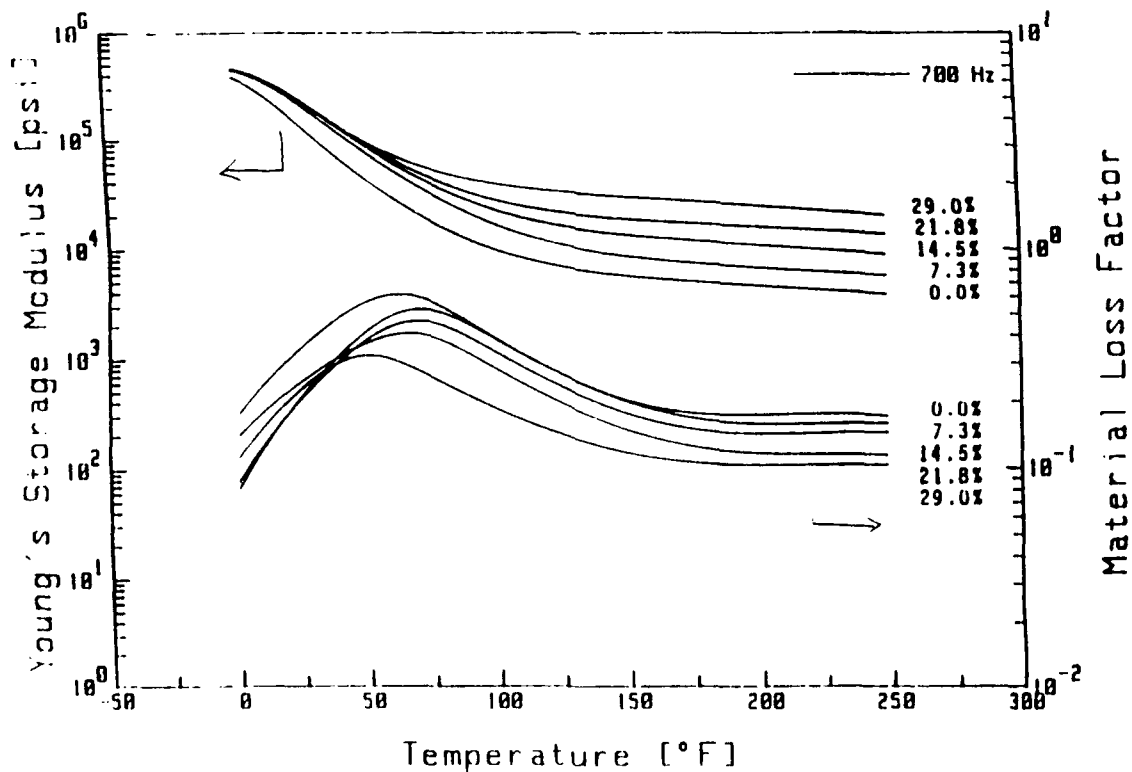


Figure 8: Variation of Material Properties with Static Preload and Temperature for 700 Hz
[Library #241 - Rubber Compound]

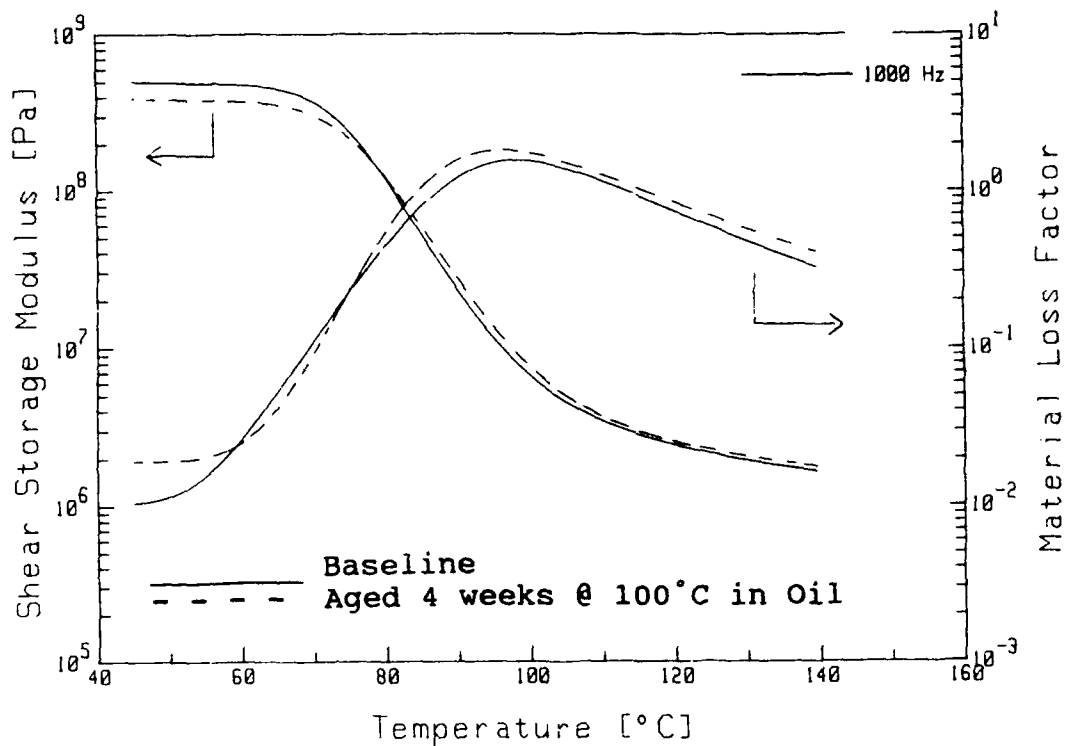


Figure 9: Effect of Heat Aging and Oil Exposure on the Properties of a Typical Material for 1000 Hz

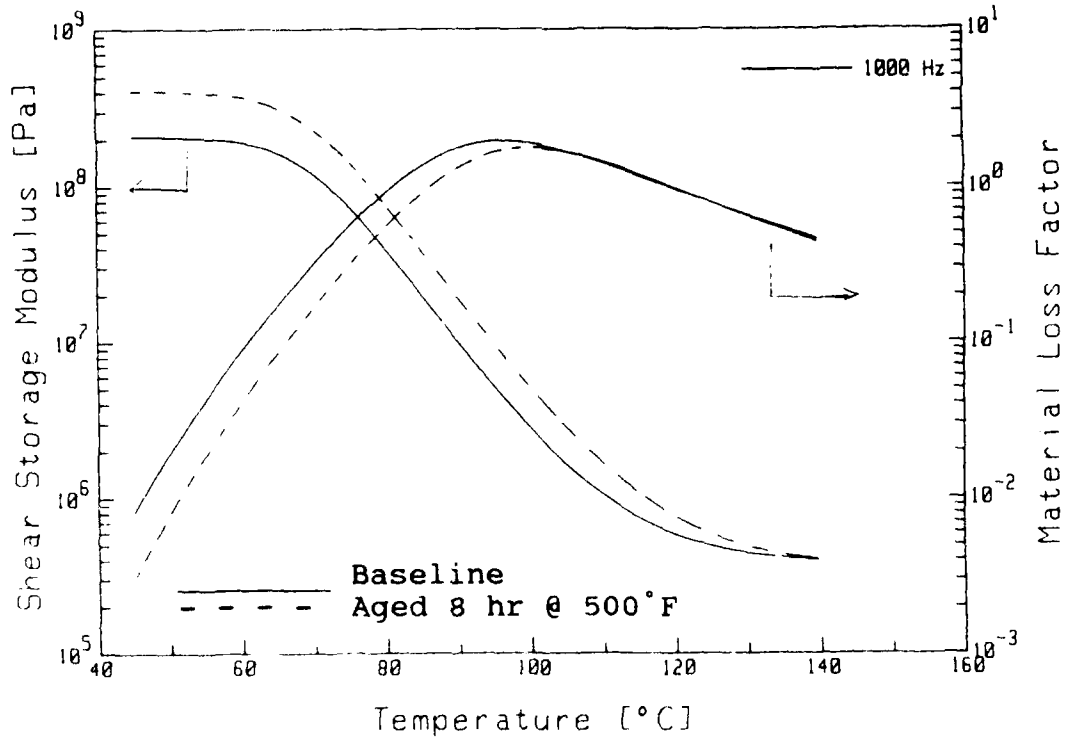


Figure 10: Effect of Heat Aging on the Properties of a Typical Material for 1000 Hz

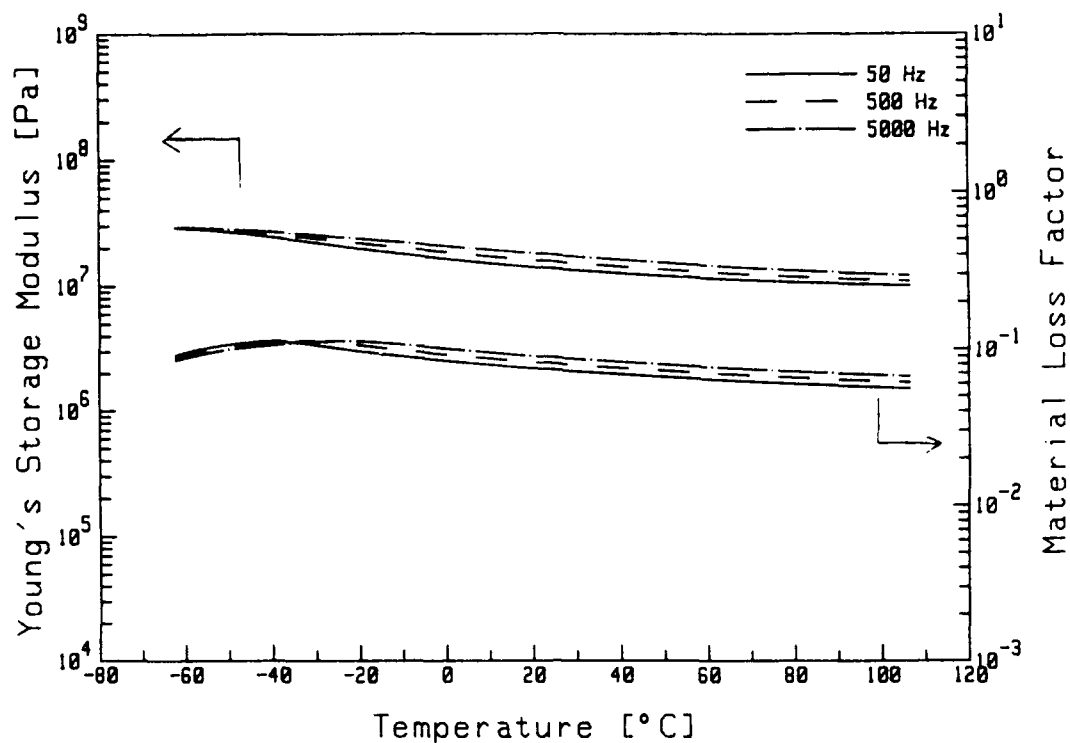


Figure 11: Variation of Material Properties with Temperature for Various Constant Frequencies [Library #743 - Silicone Elastomer]

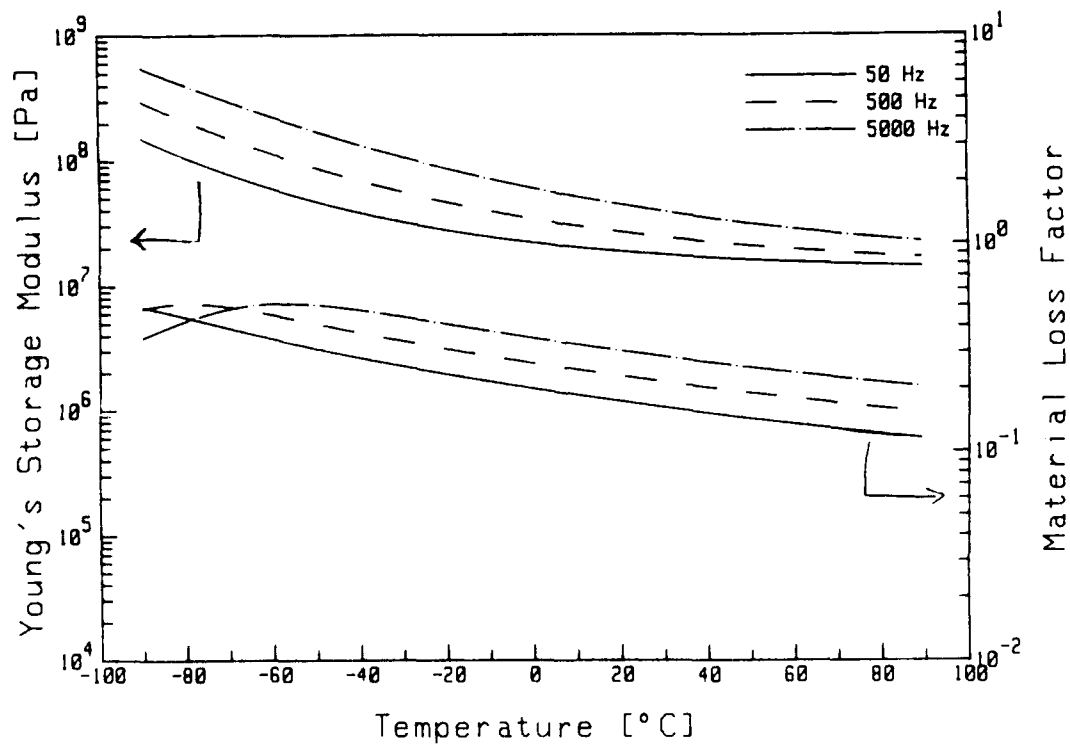


Figure 12: Variation of Material Properties with Temperature for Various Constant Frequencies [Library #351 - EPDM Elastomer]

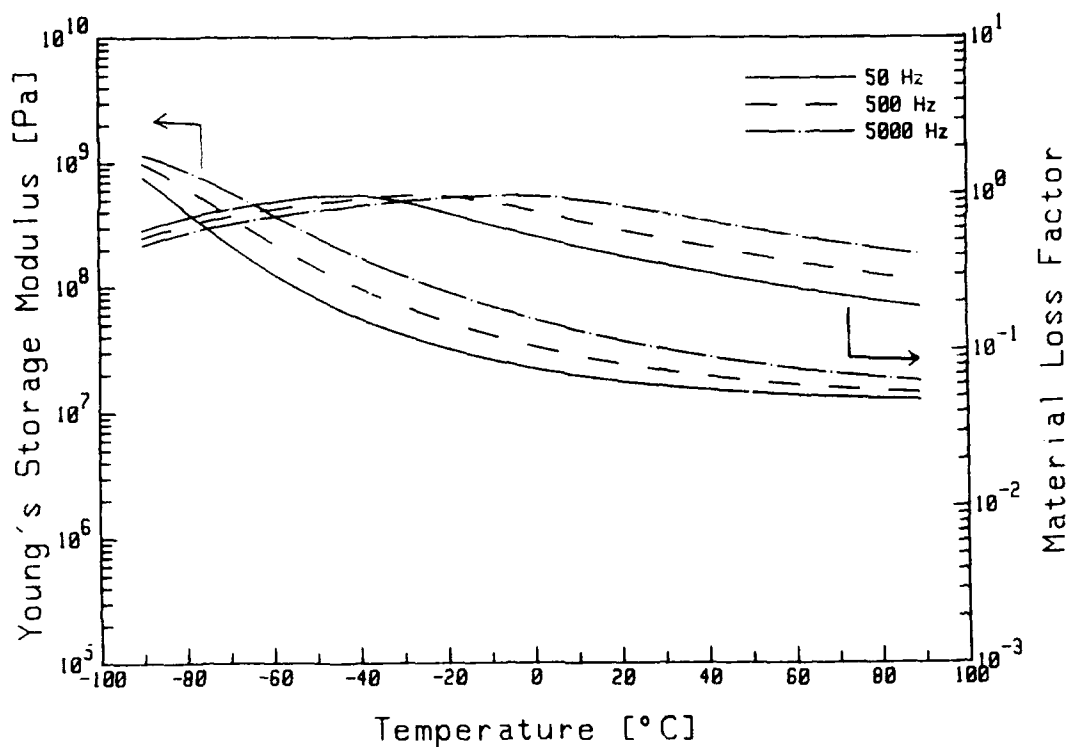


Figure 13: Variation of Material Properties with Temperature for Various Constant Frequencies [Library #496 - Butyl Elastomer]

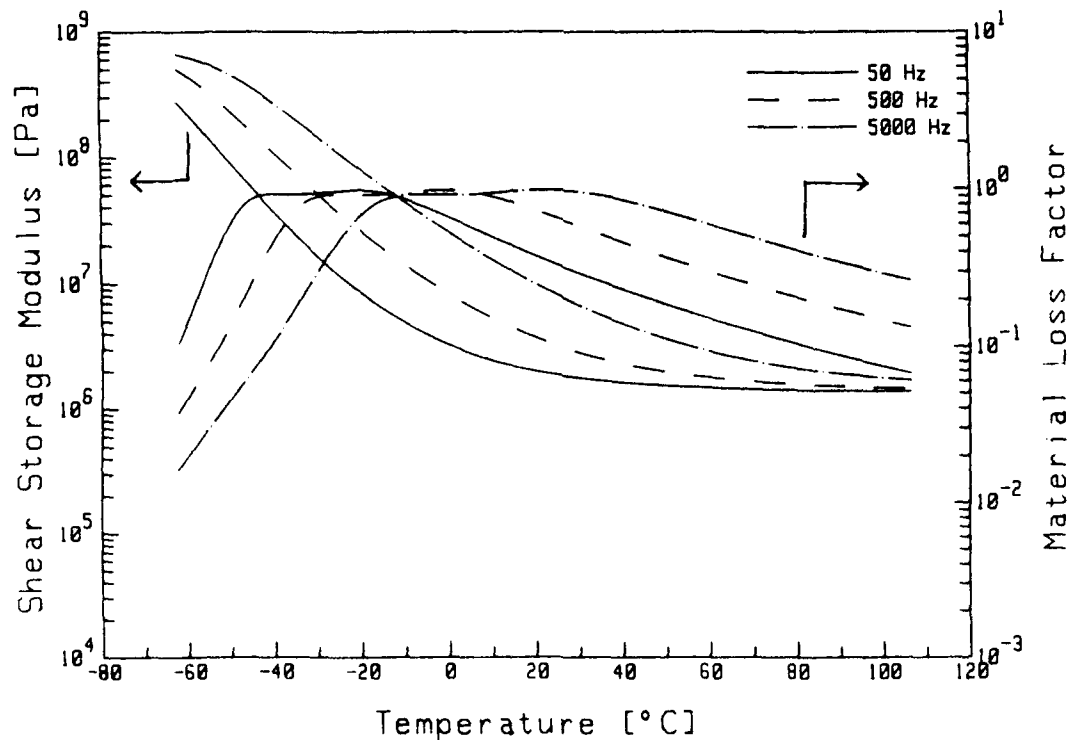


Figure 14: Variation of Material Properties with Temperature for Various Constant Frequencies [Library #519 - Polyphosphazene Elastomer]

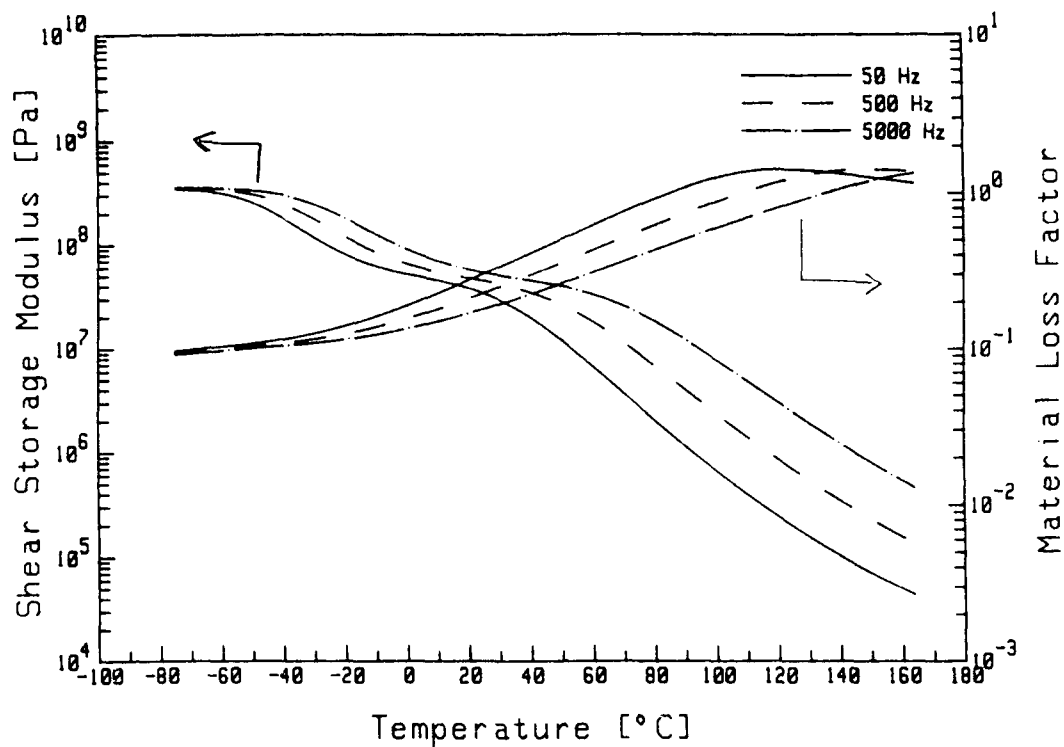


Figure 15: Variation of Material Properties with Temperature for Various Constant Frequencies
[Library #766 - Silicone Pressure Sensitive Adh.]

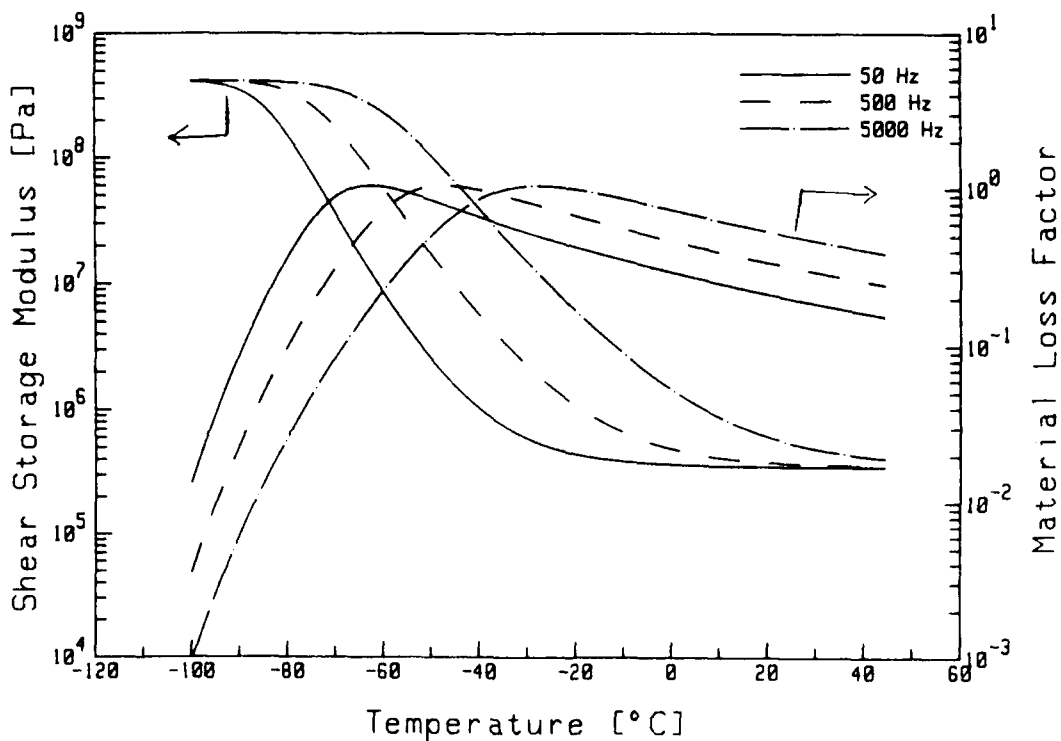


Figure 16: Variation of the Dynamic Material Properties with Temperature for the Indicated Constant Frequencies
[Library #14 - Rubber Base PSA]

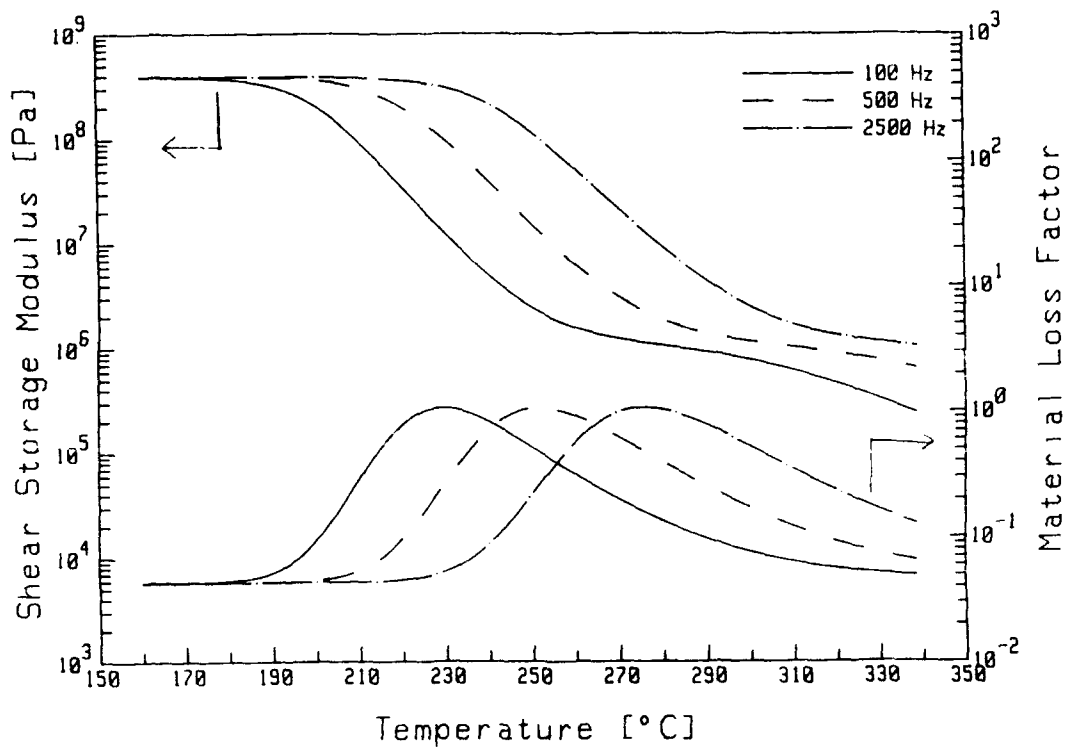


Figure 17: Variation of the Dynamic Material Properties with Temperature for the Indicated Constant Frequencies [Library #380 - Polyetherimide Plastic]

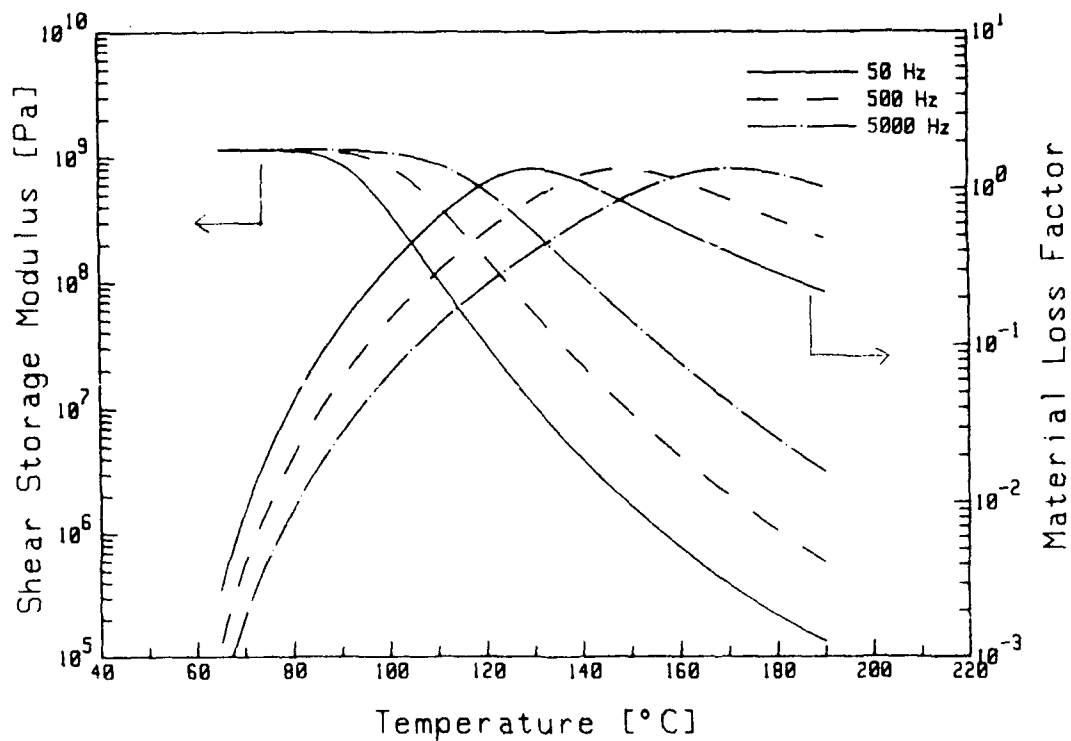


Figure 18: Variation of the Dynamic Material Properties with Temperature for the Indicated Constant Frequencies [Library #181 - Plexiglass Plastic]

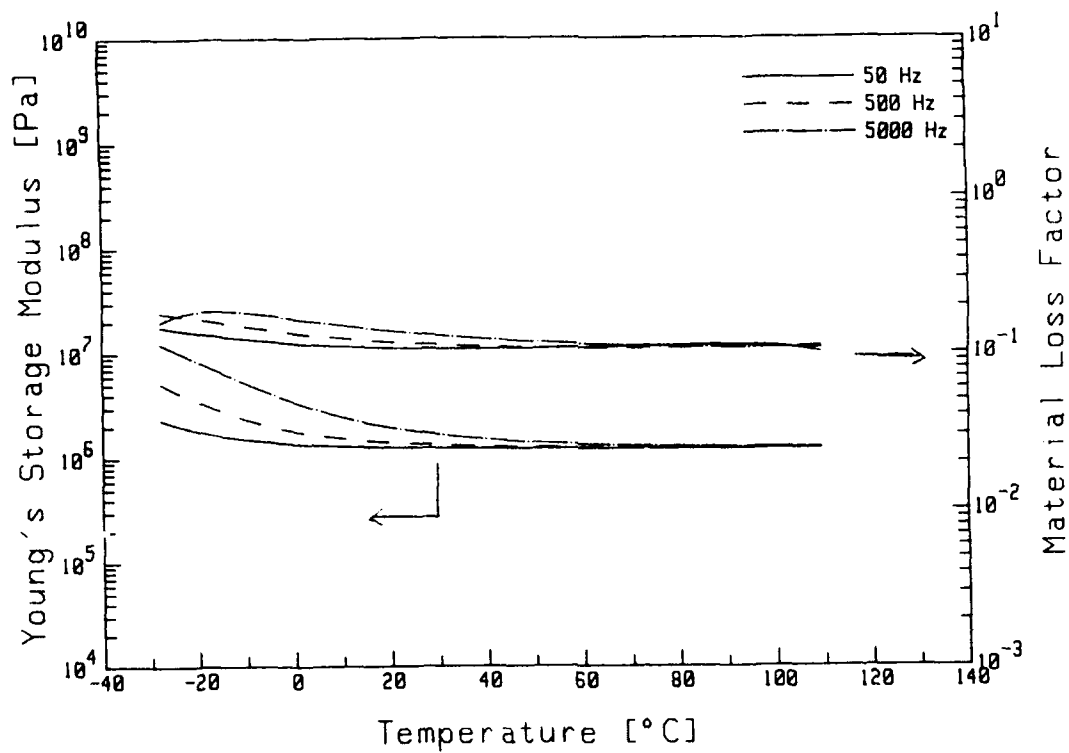


Figure 19: Variation of the Dynamic Material Properties with Temperature for the Indicated Constant Frequencies [Library #717 - Foam]

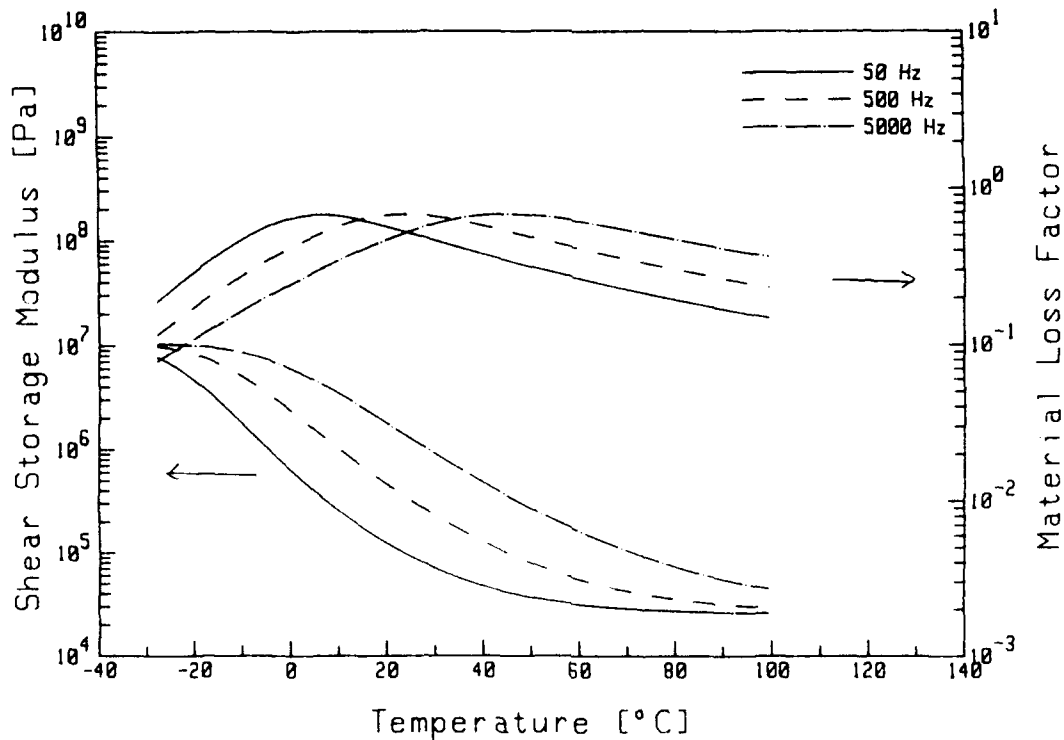


Figure 20: Variation of the Dynamic Material Properties with Temperature for the Indicated Constant Frequencies [Library #674 - Foam]

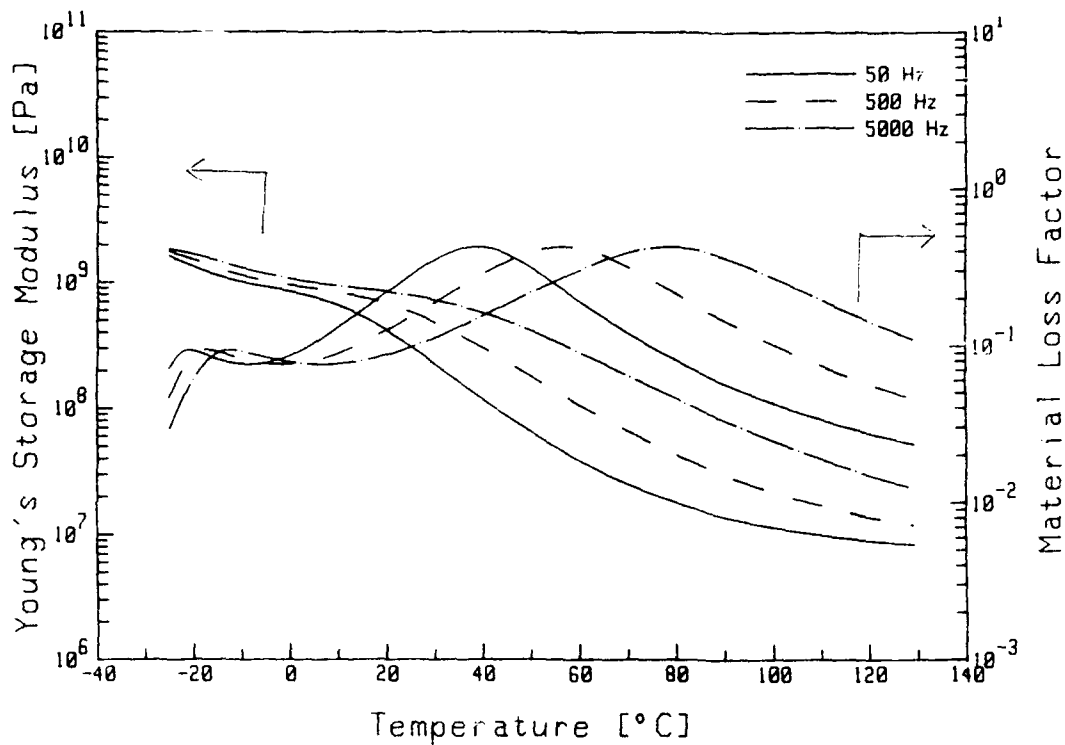


Figure 21: Variation of the Dynamic Material Properties with Temperature for the Indicated Constant Frequencies [Library #543 - Sprayable Free Layer Damping System]

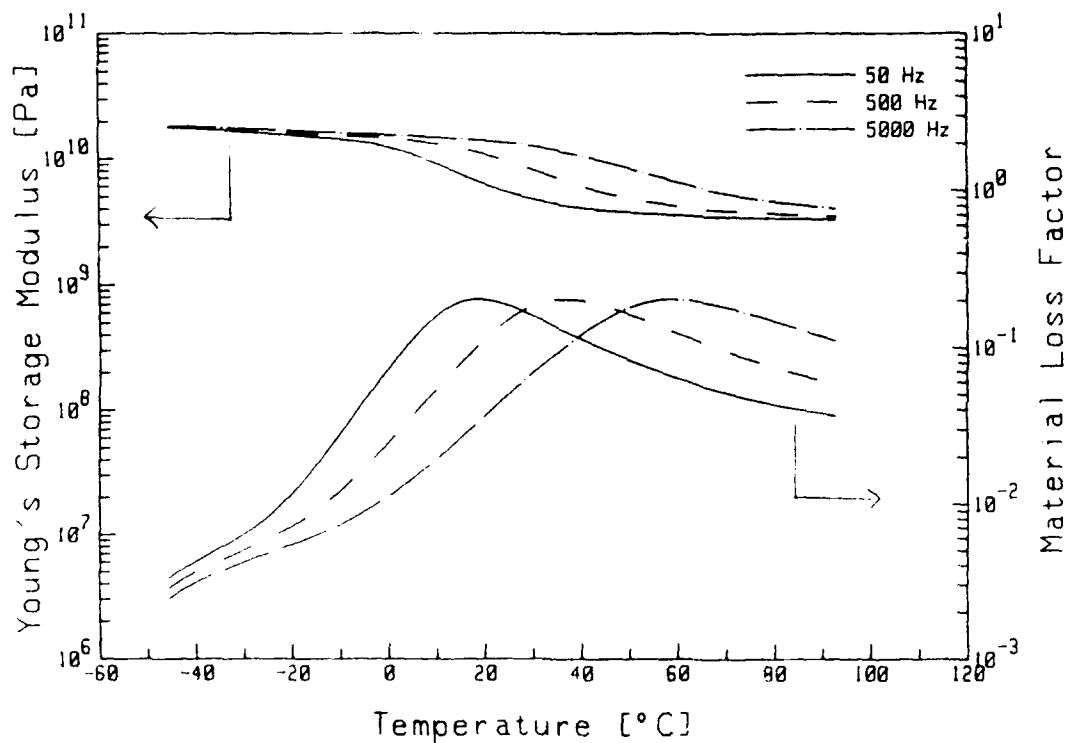


Figure 22: Variation of the Dynamic Material Properties with Temperature for the Indicated Constant Frequencies [Library #630 - Sprayable Free Layer Damping System]

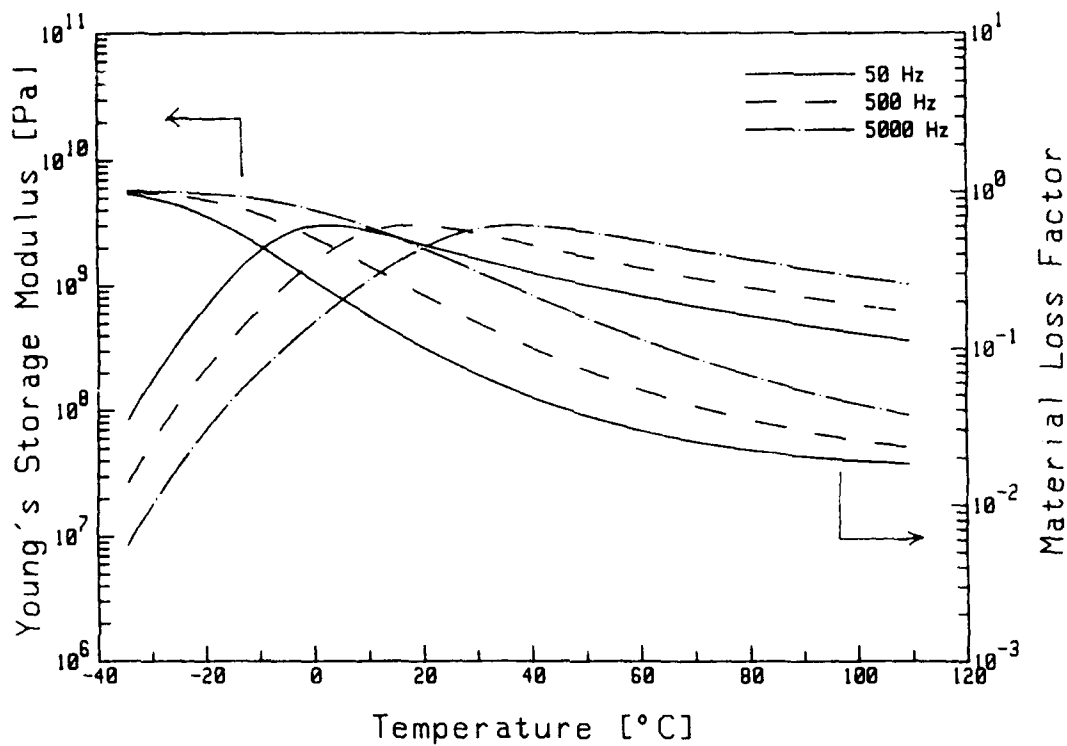


Figure 23: Variation of the Dynamic Material Properties with Temperature for the Indicated Constant Frequencies [Library #279 - Commercial Add-On Surface Treatment]

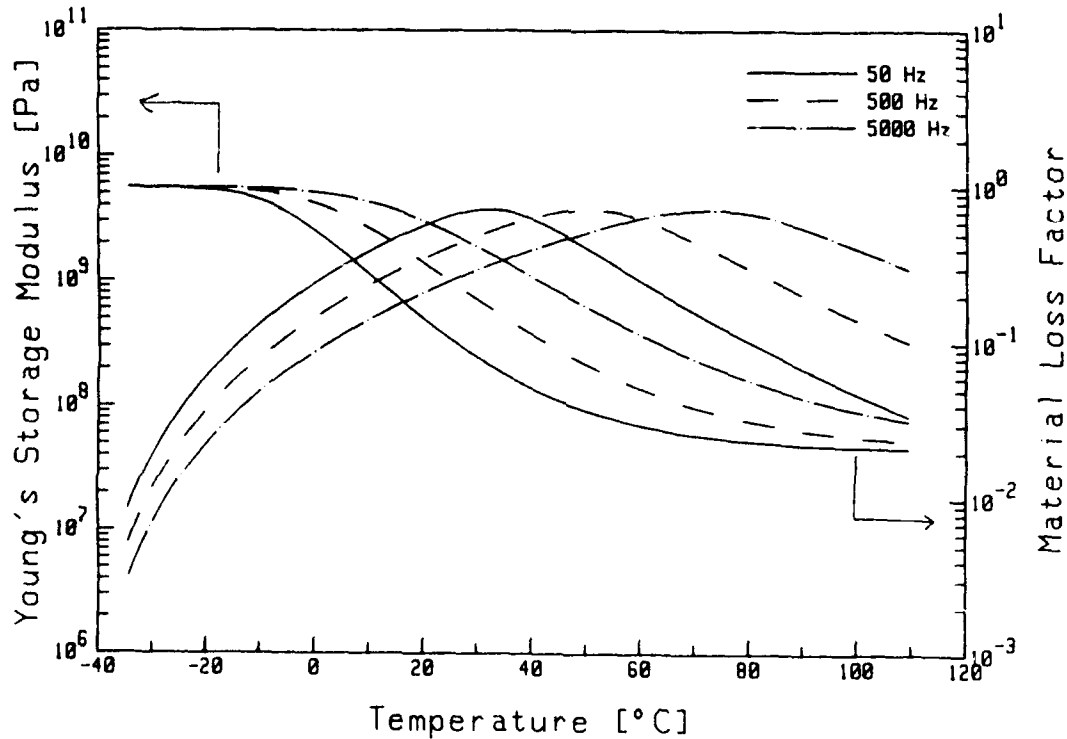


Figure 24: Variation of the Dynamic Material Properties with Temperature for the Indicated Constant Frequencies [Library #278 - Commercial Add-On Surface Treatment]

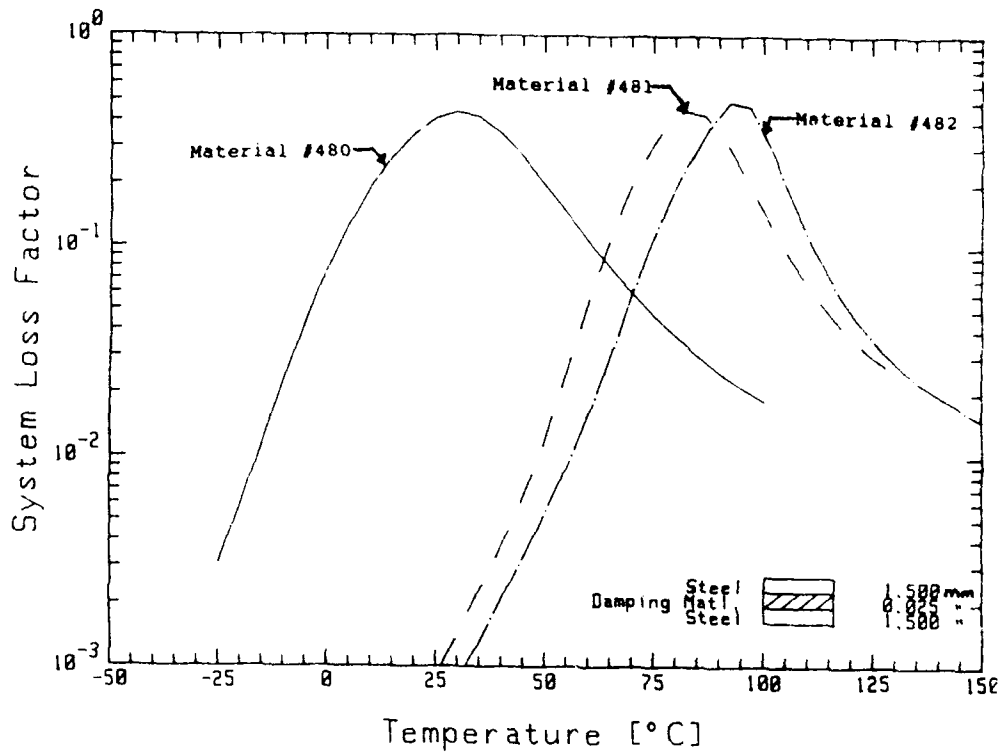


Figure 25: Loss Factor Properties of Various Laminates at 1000 Hz [Library #480, #481, #482]

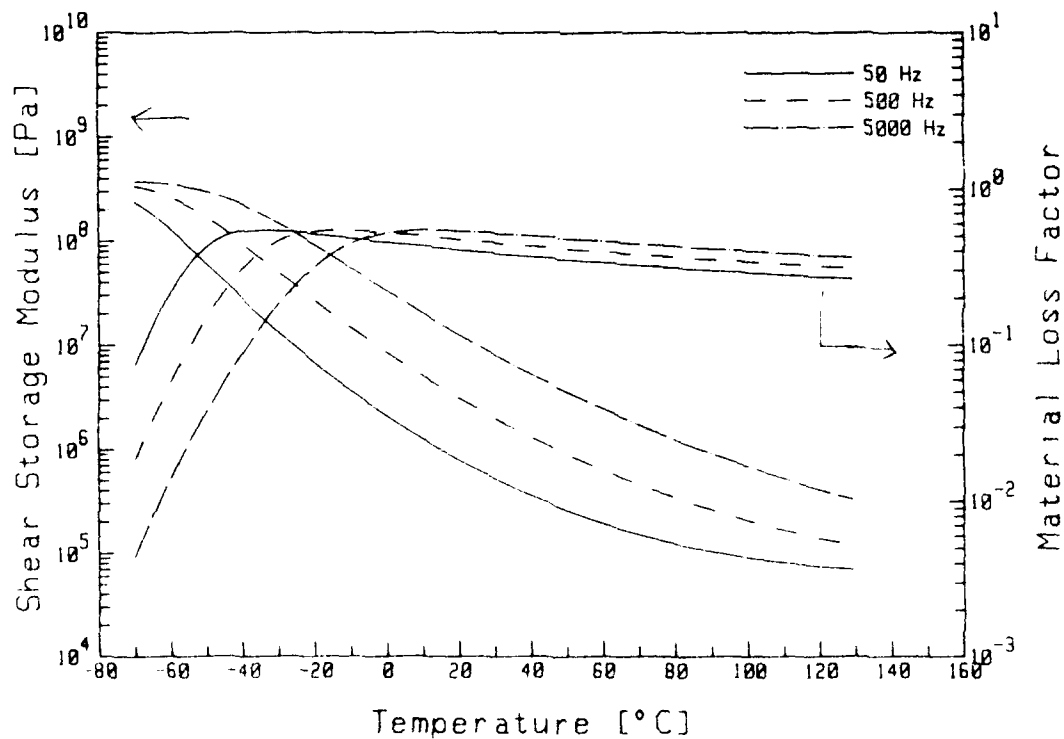


Figure 26: Variation of the Dynamic Material Properties with Temperature for the Indicated Constant Frequencies [Library #57 - Pressure Sensitive Foam Tape]

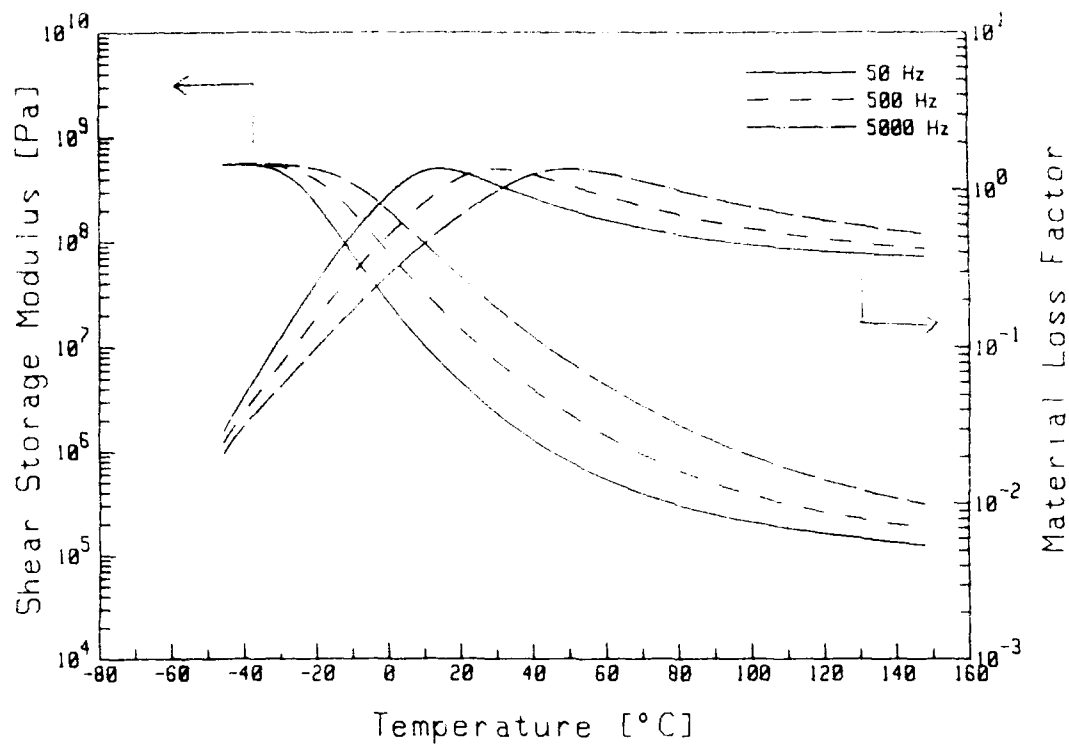


Figure 27: Variation of the Dynamic Material Properties with Temperature for the Indicated Constant Frequencies [Library #242 - Pressure Sensitive Foam Tape]

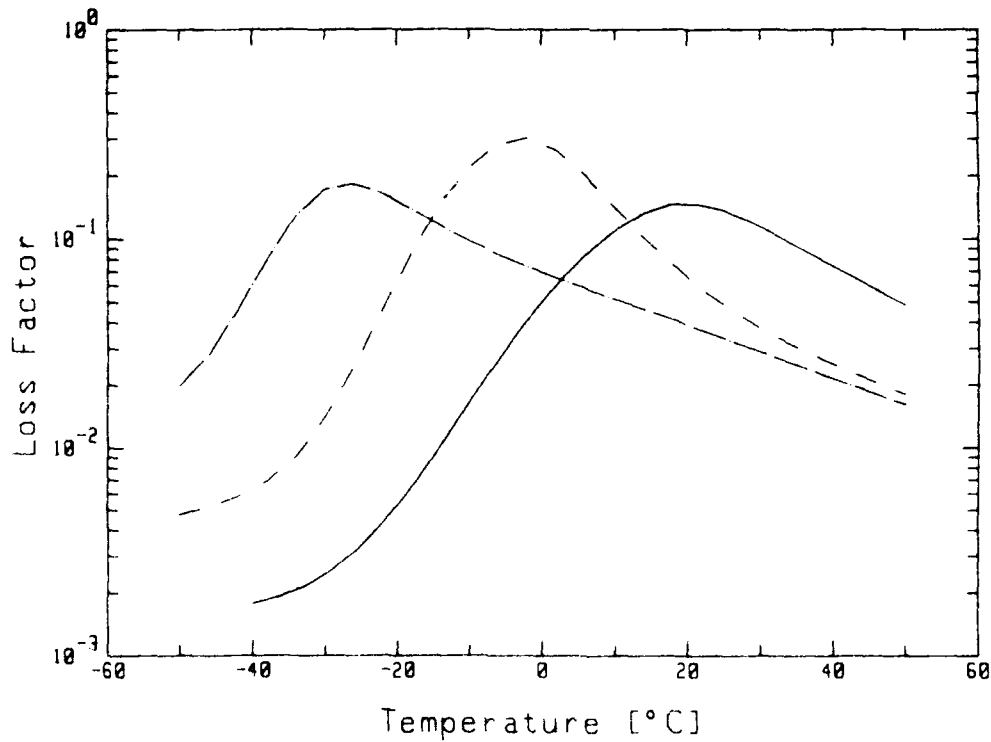


Figure 28: Damping Properties of Typical Commercial Foil Back Treatments

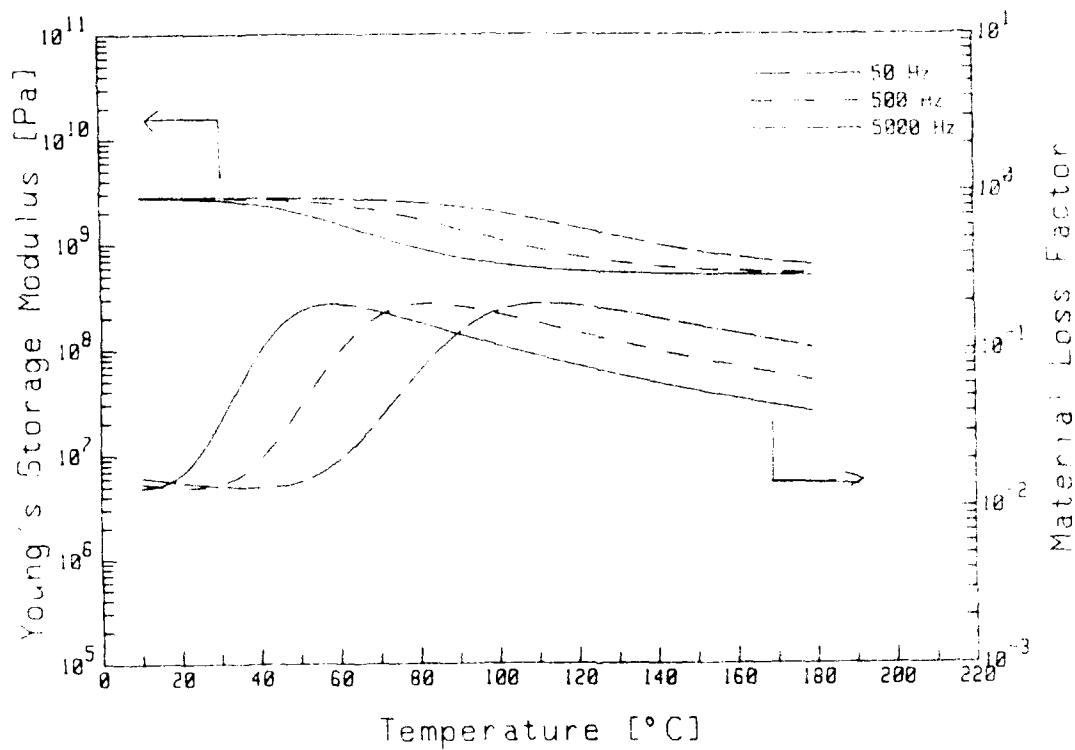


Figure 29: Variation of the Dynamic Material Properties with Temperature for the Indicated Constant Frequencies [Library #749 - Polymeric Reinforcement System]

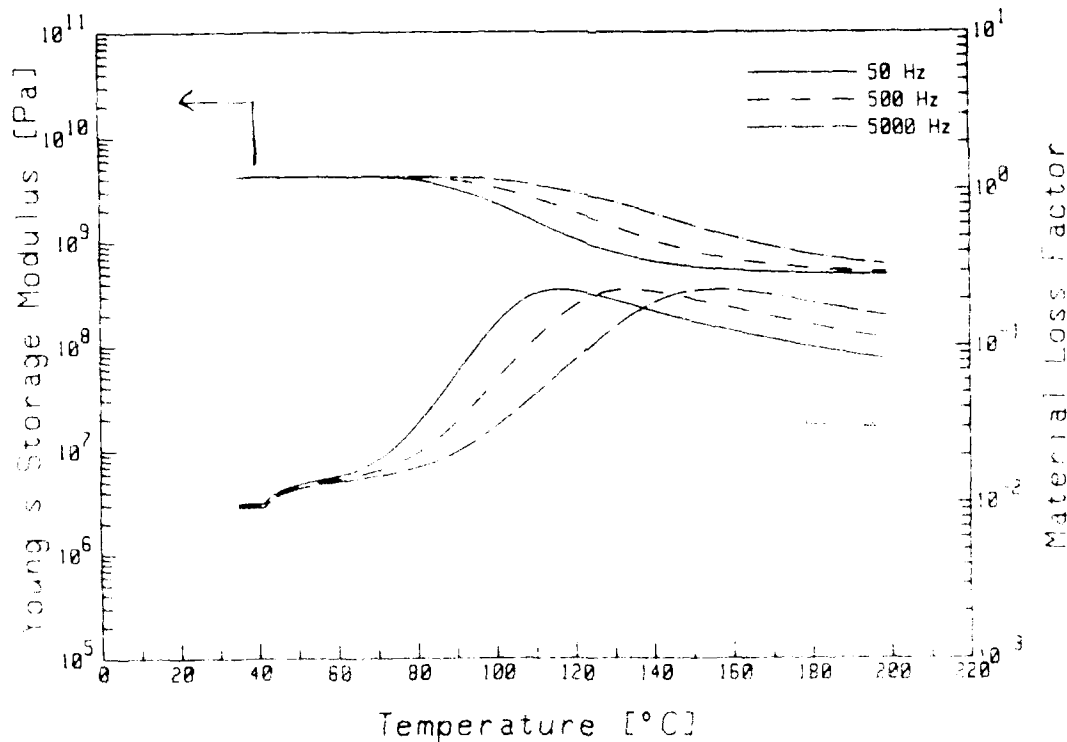


Figure 30: Variation of the Dynamic Material Properties with Temperature for the Indicated Constant Frequencies [Library #616 - Polymeric Reinforcement System]

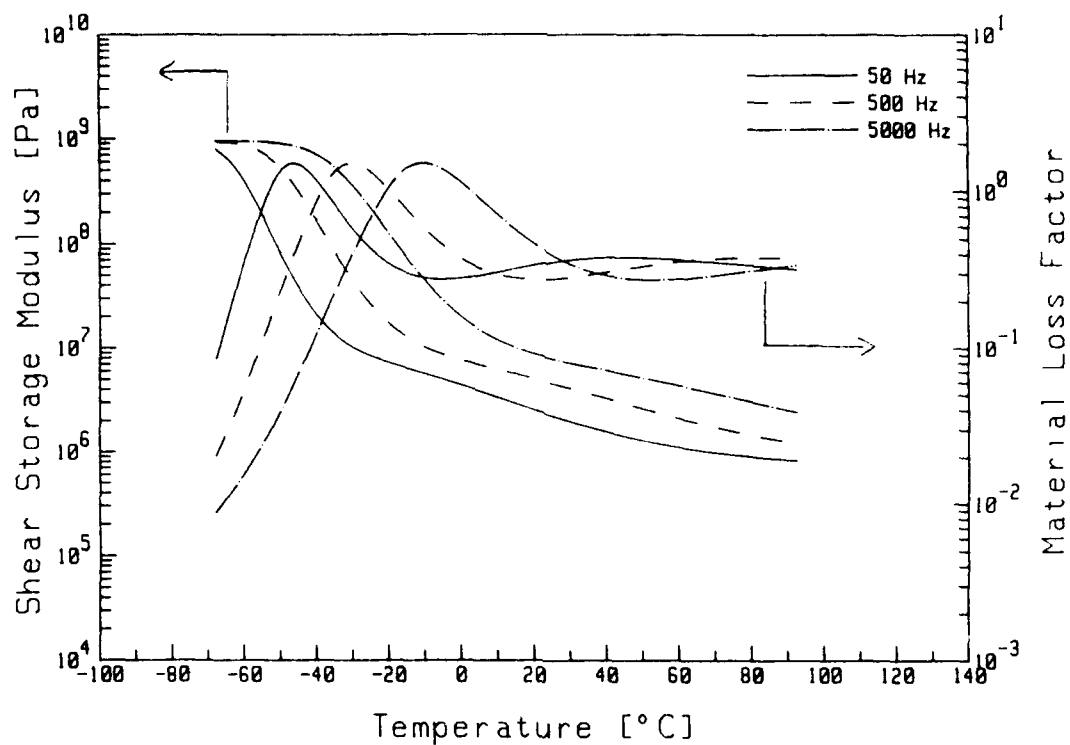


Figure 31: Variation of the Dynamic Material Properties with Temperature for the Indicated Constant Frequencies [Library #513 - Polysulfide Sealant]

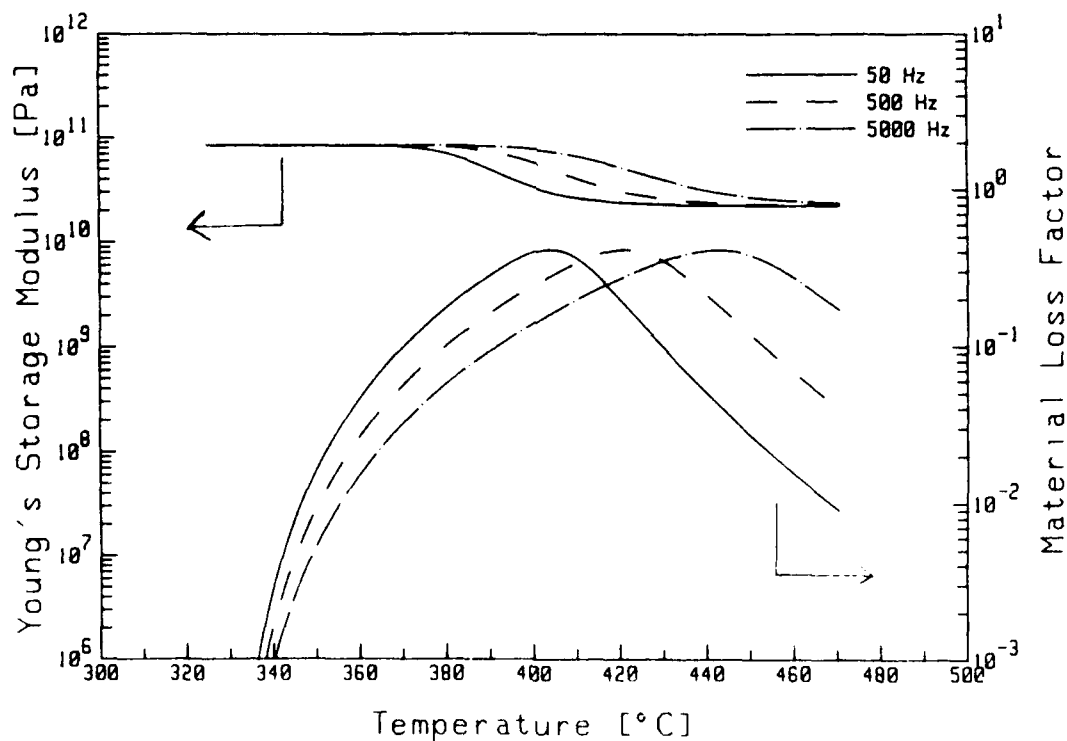


Figure 32: Variation of the Dynamic Material Properties with Temperature for the Indicated Constant Frequencies [Library #2 - Glass Enamel]

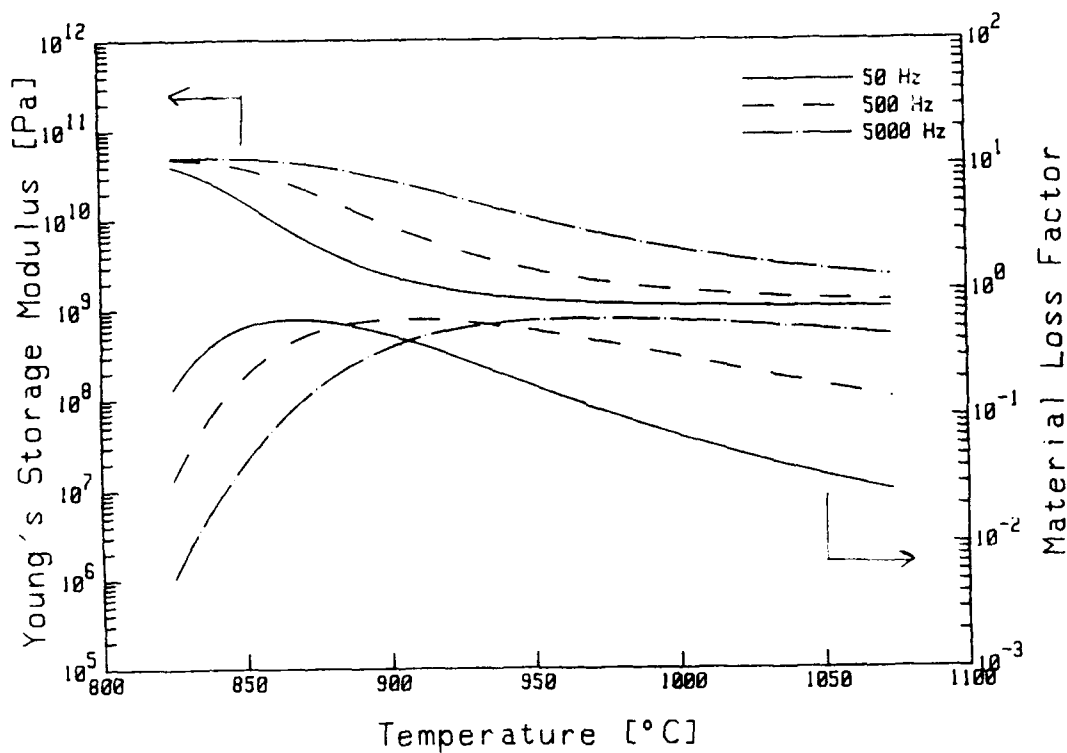


Figure 33: Variation of the Dynamic Material Properties with Temperature for the Indicated Constant Frequencies [Library #843 - Glass Enamel]

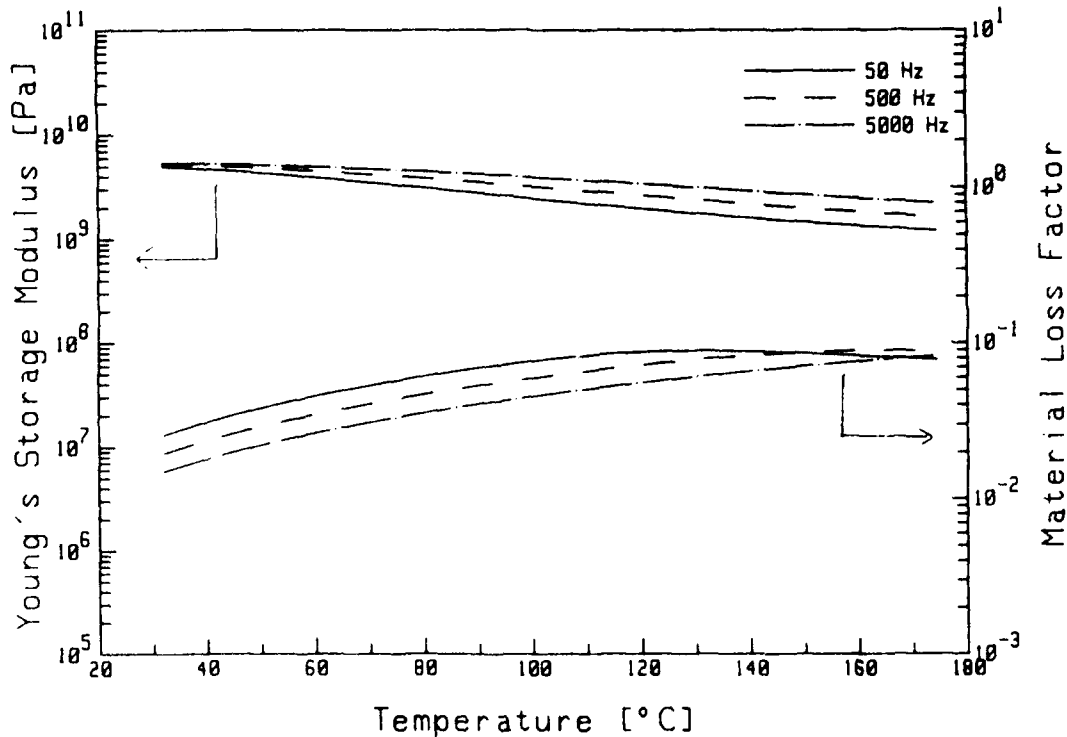


Figure 34: Variation of the Dynamic Material Properties with Temperature of the Indicated Constant Frequencies [Library #284 - 2 Part Structure Adhesive]

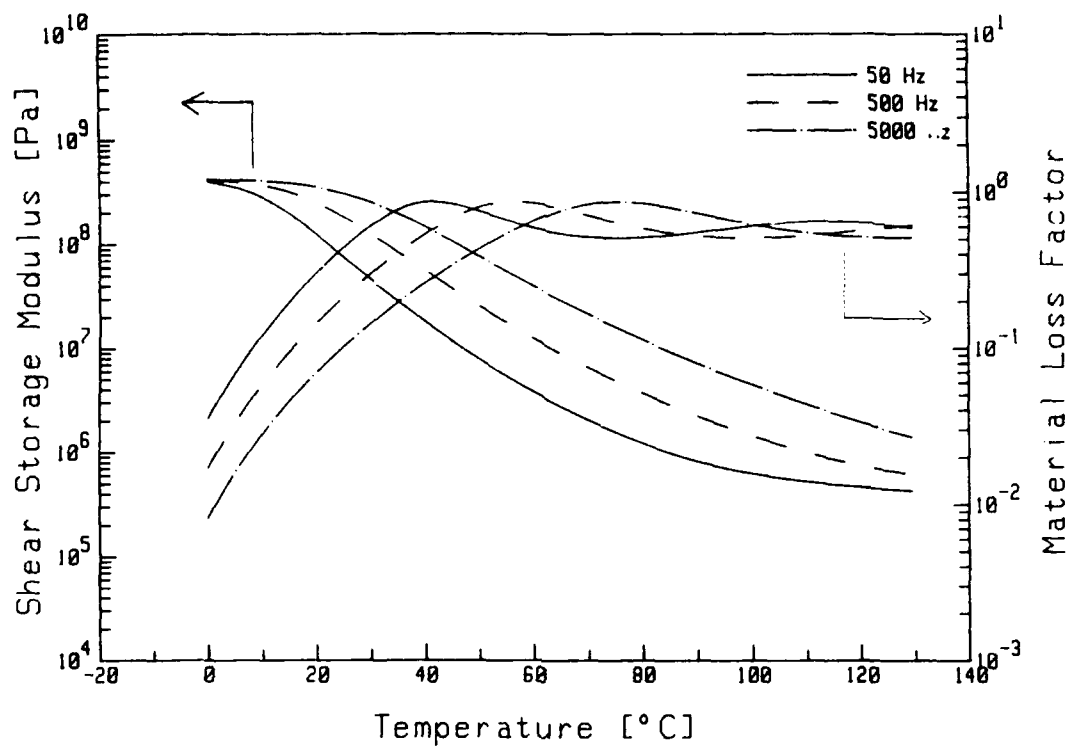


Figure 35: Variation of the Dynamic Material Properties with Temperature for the Indicated Constant Frequencies [Library #330 - Structural Adhesive Film]

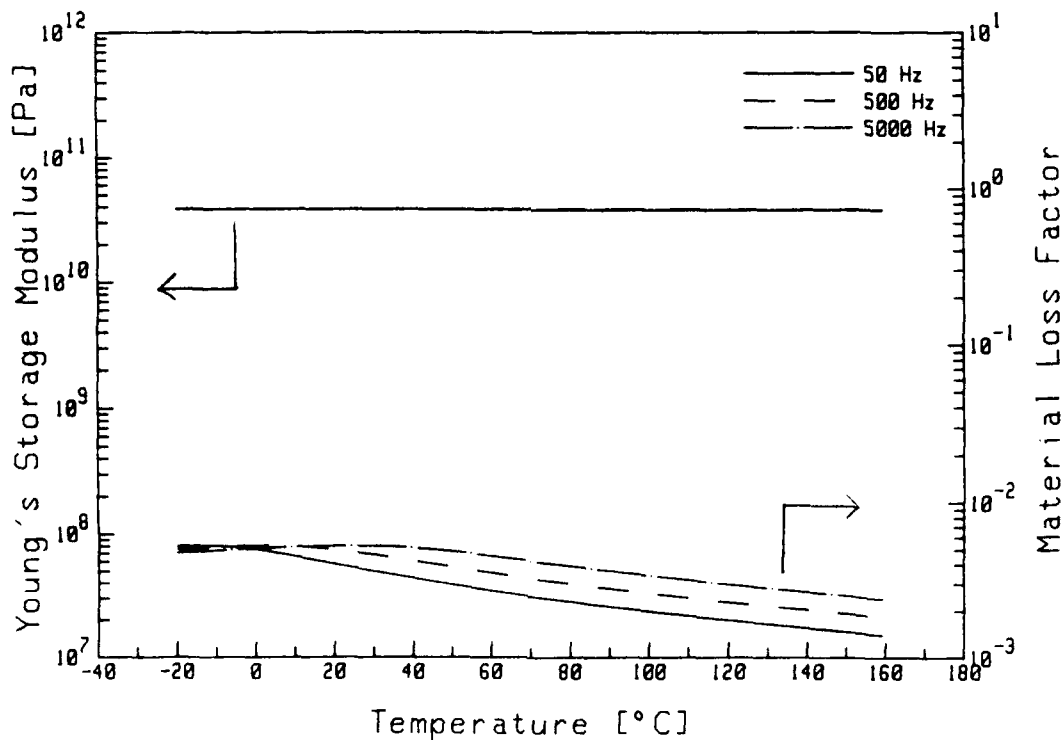


Figure 36: Variation of the Dynamic Material Properties with Temperature for the Indicated Constant Frequencies [Library #52 - Graphite Composite]

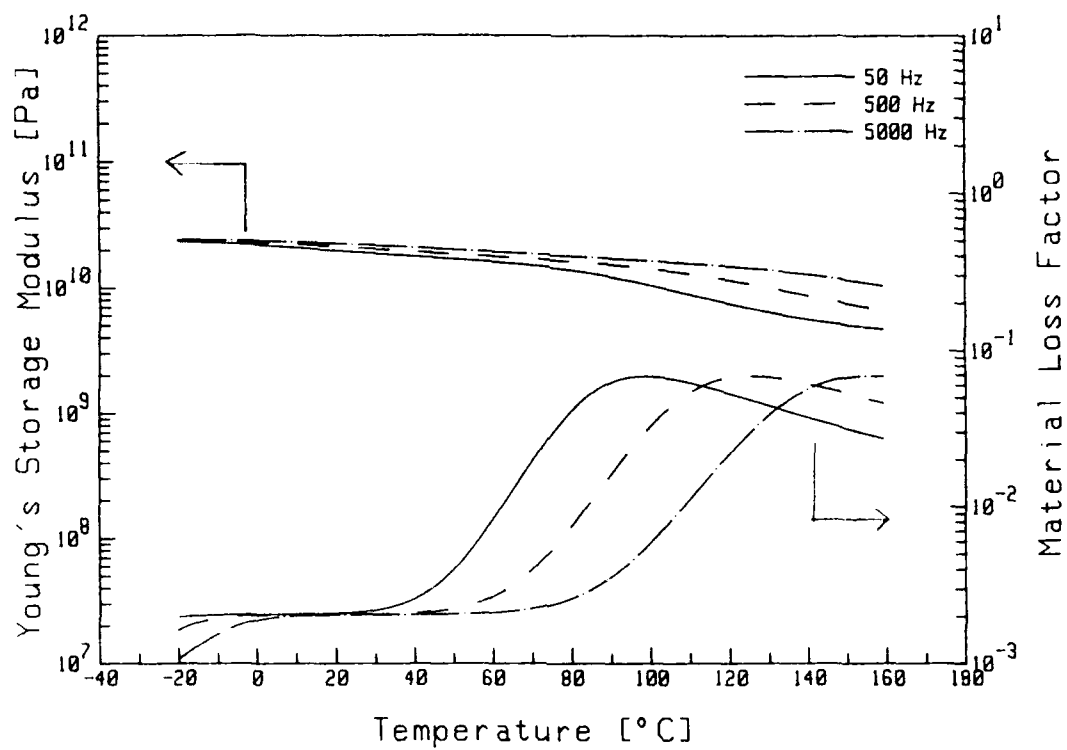


Figure 37: Variation of the Dynamic Material Properties with Temperature for the Indicated Constant Frequencies [Library #488 - PPS Plastic Composite]

ESTABLISHING THE VALIDITY OF THE MASTER CURVE TECHNIQUE FOR COMPLEX MODULUS DATA REDUCTION

S.O. OYADIJI and G.R. TOMLINSON

Dynamics and Control Research Group,
Department of Engineering,
University of Manchester,
Manchester, M13 9PL, U.K.
(061) 275 4437/8

ABSTRACT

The applicability of the master curve technique for the reduction of temperature- and frequency-dependent complex modulus data to a set of "master" complex modulus curves, which depend on only one variable, is validated for a polyisoprene rubber of shore hardness 55. Using the direct stiffness method, complex Young's modulus data was determined for a sample of the material over 2 narrow frequency bands of 2 octaves each and a wide temperature range of -60°C to 100°C . Small temperature intervals of 2°C at low temperatures rising to 20°C at high temperatures were used in the tests. This resulted in two sets of "temperature-dominated" complex modulus data from which smooth, continuous master curves were generated by the application of the master curve technique. The procedure was repeated for a wider test frequency range of 2 decades, the same temperature range but larger temperature increments of 10°C at low temperatures rising to 80°C at high temperature. This resulted in a "frequency-dominated" complex modulus data set from which master curves were again obtained. It is shown that the master curves obtained from the three data sets correlate quite well.

1. INTRODUCTION

The master curve technique is a well known tool for the reduction of temperature- and frequency-dependent complex modulus data to a set of master curves of modulus and loss factor which depend on a single variable called the reduced frequency or reduced temperature [1-3]. The technique, which is also called the method of reduced variables or the temperature-frequency superposition principle, exploits the inverse relationship of the dependence of complex modulus properties on temperature and frequency to produce a dependence of these properties on a single parameter, the reduced frequency or the reduced temperature, which combines the separate effects of frequency and temperature. Thus complex modulus data obtained over narrow frequency ranges and a wide temperature range, using a single test method, are reduced to sets of single curves of modulus and loss factor which cover several decades of frequency at a specified reference temperature. Similarly, using an appropriate test method or a combination of test methods, complex modulus data can be obtained over a wide frequency range and a small temperature-range or even at constant temperature. From this data, master curves can be again obtained. If, for the material under consideration, the temperature-frequency superposition principle is applicable then the two sets of master curves will be identical.

The use of the master curve technique started on an empirical basis. Subsequently, theoretical models were developed to correlate some of the experimental observations [1]. However, the development and application of the technique has tended to be more empirically orientated. The shift function, which is used for the data reduction process, was for a long time based on the William-Landel-Ferry (WLF) equation. Other forms of shift functions based on the Arrhenius model, statistical method and iterative approach are now in use [3, 4]. It is generally agreed that satisfactory data reduction depends on the use of an appropriate shift function.

Whenever the method of reduced variables is applied, one is confronted by the question of the uniqueness and validity of the generated master curves. Thus, it is often desirable to employ other means to validate the master curves produced. The most direct method of validation is to measure the complex modulus properties at a single temperature, e.g. room temperature, and over a very wide frequency range using a variety of test methods such as stress relaxation, direct stiffness, resonance and ultrasonic methods. However, this is not usually possible as one is often restricted by resources, to the use of one test method. Hence, a different approach is required.

The approach used in the present work for validating the master curve technique is based on an experimental application of a result of the temperature-frequency superposition or equivalence principle. If the principle holds for a given viscoelastic material, then the master curves produced from complex modulus data obtained at constant frequency and varying temperature should be identical to the master curves generated from complex modulus data obtained at constant temperature and varying frequency. The constant frequency data sets are said to be "temperature-dominated" while the constant temperature data sets are said to be "frequency-dominated". Relaxing these two extreme test conditions to become (i) narrow frequency band and many temperature steps, and (ii) wide frequency band and few temperature steps, the sets of complex modulus that will be obtained will still be relatively "temperature-dominated" and "frequency-dominated" respectively. It is shown that for the polyisoprene rubber investigated, the master curves of complex Young's modulus obtained from the temperature-dominated and frequency-dominated data sets are quite similar. The experimental test method employed is the direct stiffness technique.

2. EXPERIMENTAL DETERMINATION OF COMPLEX YOUNG'S MODULUS

2.1 Direct Stiffness Test Method

The direct stiffness method, which is a forced vibration, non-resonance technique for the determination of the complex Young's or shear modulus of polymeric materials [5-7], was used to determine the complex Young's modulus of the polyisoprene rubber investigated. Two samples of the material of 30 mm diameter by 5 mm and 30 mm thick were prepared and bonded to metal discs. Each sample assembly was placed in turn, between the vibration table of an electrodynamic exciter and a rigid termination of theoretically infinite impedance as shown in Figure 1 which also shows the associated measurement and control instrumentation for the experimental tests. The end of the sample connected to the exciter was subjected to controlled sinusoidal displacement excitations of the form $x(t) = X e^{j\omega t}$. The ratio of the output force $f(t) = F^* e^{j\omega t}$ to the input displacement gave the complex dynamic axial stiffness k^* at the excitation frequency ω . The magnitude k , phase (loss) angle θ , and loss factor η are related to k^* by

$$\begin{aligned} k &= |k^*| = |F^*/X| \\ \theta &= \arg k^* = \arg (F^*/X) \\ \eta &= \tan \theta \end{aligned} \quad (1)$$

Thus, the complex dynamic axial stiffness of the sample can be represented as

$$\begin{aligned} k^* &= k' + jk'' = k'(1 + j\eta) \\ k &= |k^*| = k'(1 + \eta^2)^{1/2} \end{aligned} \quad (2)$$

2.2 Derivation of Complex Young's Modulus

Due to the restraints imposed on the bonded ends of a sample, subjected to tension-compression deformation, multiplying the complex stiffness k^* by the factor L/A , where L is length and A is cross-sectional area of a prismatic sample gives an apparent complex Young's modulus, E_a^* . The true and apparent magnitudes E and E_a of the true and apparent complex Young's moduli are related by [2,8]

$$E_a = E(1 + \beta S^2) ; E_a = kL/A \quad (3)$$

where β is a numerical constant which has values of $1.5 \leq \beta \leq 2.0$ that depend on the filler content of the elastomer, and S is a shape factor defined as,

$$S = D/4L \quad (4)$$

for a solid cylindrical element of diameter D and length L .

Thus, the true complex Young's modulus E^* is related to the measured complex extensional stiffness k^* by

$$E^* = E_a^*/(1 + \beta S^2) = k^*L/(1 + \beta S^2)A \quad (5)$$

where

$$E = |E^*| = kL/(1 + BS^2)A \quad (6)$$

$$\eta_E = \eta$$

3. COMPLEX YOUNG'S MODULUS DATA AND MASTER CURVES.

Using the procedures described above, the complex Young's modulus of the polyisoprene rubber was determined under three test frequency conditions, namely;

- (1) Narrow band, low frequency tests (10 to 40 Hz)
- (2) Narrow band, intermediate frequency tests (100 to 400 Hz)
- (3) Wide frequency band tests (10 to 1000 Hz)

The complex Young's modulus data obtained under these test conditions and the resultant master curves are described in the following. In reducing the data to master curves, the modulus data was firstly shifted vertically using the relation

$$E_r = (T_r/T)E \quad (7)$$

where E is the Young's modulus at experimental temperature T , E_r is the reduced Young's modulus at the reference temperature T_r , and density variations are assumed to be negligible. The shift factors used were of the general form

$$\log \alpha_T = \varphi(T - T_r) \quad (8)$$

where the forms of the function φ were determined directly from the measured data.

3.1 Narrow Band, Low Frequency Data

For the narrow band, low frequency tests, the experimental frequency was from 10 to 40 Hz, that is 2 octaves, while the temperature range was from -60°C to 100°C . The temperature steps were 2°C between -60°C and -30°C , about 3°C between -30°C and -10°C , 10°C between -10°C and 20°C , and 20°C for test temperatures between 20°C and 100°C . This resulted in 30 test temperatures. The number of frequency points was 6 per data set. Thus, the total number of Young's modulus and loss factor pairs of data obtained was 180 as shown in Table 1. These data sets are certainly "temperature-dominated". Figure 2 shows the wicket plot of \log (loss factor) versus \log (modulus) for the data. The low temperature (below -50°C) data seems to be subject to relatively higher random errors whereas the high temperature data (above 20°C) seems to be affected by some systematic effects. Using the master curve technique, in its general empirical form, master curves of Young's modulus and loss factor were produced from this data at a reference temperature of -40°C . The shift function used for the data reduction process is shown in Figure 3. It was estimated numerically from the data using a computerized data shifting process. The resultant master curves are shown in Figure 4. It can be seen that the data scatter is low but it is significant for the loss factor curve at low temperatures.

3.2 Narrow Band, Intermediate Frequency Data

The test conditions for this case are quite similar to those of the previous case. The only difference is that the frequencies are ten times higher than those of the narrow band, low frequency data. Thus, the frequency range for the narrow band, intermediate frequency tests is 100 to 400 Hz (2 octaves) with unequal frequency increments resulting in a total of 6 frequency points per data set. The test temperatures and temperature steps are exactly identical to those of the previous case. Thus, 180 pairs of temperature-dominated data were again obtained as shown in Table 2. The wicket plot of the data is shown in Figure 5. It can be seen that the data scatter is generally small being higher for temperatures greater than 40C. By repeated data shifting process a "best" estimate of the shift factor curve was obtained at a reference temperature of -40C as shown in Figure 6. Using this curve the complex Young's modulus data was reduced to master curves as shown in Figure 7. It can be seen that the data scatter is quite small being relatively more pronounced for the loss factor data at higher temperatures.

3.3 Wide Frequency Band Data

The frequency range of the wide frequency band tests was wider than the previous cases being from 10 to 1000 Hz (2 decades). The frequency steps were about 12 per decade giving 23 frequency steps in total. The temperature range used for the tests was again from -60C to 100C but the temperature steps were higher being -10C at very low temperatures and rising to 80C at high temperature. The number of test temperatures used was 6. Thus, the total number of pairs of data was 138 as shown in Table 3. These data sets are relatively more "frequency-dominated" than in the previous cases. Figure 8 shows the wicket plot for these data sets. It can be seen that the data scatter due to random errors is small. However the 100C data set seems to be subjected to some systematic errors as it is somewhat removed from the general body of data. By means of the master curve technique, the data was reduced to master curves of Young's modulus and loss factor at a reference temperature of -40C. The shift factor curve used for the data reduction is shown in Figure 9. The master curves obtained are shown in Figure 10. It can be seen that random data scatter is small but there may be some systematic errors with the high temperature (low reduced frequency) data.

3.4 Comparison of Master Curves

The three sets of master curves of complex Young's modulus obtained are compared with one another as shown in Figure 11. Except for some slight discrepancies which occur in the loss factor master curves at high reduced frequencies, it can be seen that the master curves correlate reasonably well within the limits of data measurement and processing errors. This implies that whether temperature-dominated or frequency-dominated data is used, the master curves generated will be very similar and unique. Thus, it can be concluded that the temperature-frequency superposition is valid for the reduction of temperature- and frequency-dependent complex modulus data of polyisoprene rubber to master curves.

4. CONCLUSIONS

The master curve methodology is valid for the reduction of complex modulus data to master curves provided the material under consideration is thermorheologically simple. It has been demonstrated that the application of the master curve technique for the reduction of complex Young's modulus data of the polyisoprene rubber investigated is valid. Thus, it can be inferred that this material is thermorheologically simple. When it is uncertain whether a material is thermorheologically simple, such a validity test, as demonstrated in this paper, might prove useful.

5. ACKNOWLEDGEMENTS

This work is part of a research contract sponsored jointly by the Science and Engineering Research Council and Rolls-Royce plc, Derby.

6. REFERENCES

1. J.D. Ferry, *Viscoelastic Properties of Polymers*, John Wiley, New York, 1980.
2. A.D. Nashif, D.I.G. Jones and J.P. Henderson, *Vibration Damping*, John Wiley, New York, 1985.
3. D.I.G. Jones, On Temperature-Frequency Analysis of Polymer Dynamic Mechanical Behaviour, *Journal of Sound and Vibration*, 139(1), 1990.
4. L.C. Rogers, An Accurate Temperature Shift Function and A New Approach to Modelling Complex Modulus, *Proceedings of the 60th Shock and Vibration Symposium*, Virginia Beach, November 1989.
5. S.O. Oyadiji, *Vibration Transmissibility Characteristics of Reinforced Flexible Pipes*, Ph.D. Thesis, University of Manchester, 1983.
6. S.O. Oyadiji and G.R. Tomlinson, Determination of the Complex Moduli of Viscoelastic Structural Elements by Resonance and Non-Resonance Methods, *Journal of Sound and Vibration*, 101, pp. 277-298, 1985.
7. B.E. Read and G.D. Dean, *The Determination of Dynamic Properties of Polymers and Composites*, Adam Higler, Bristol, 1978.
8. P.K. Treakley and A.R. Payne, *Theory and Practise of Engineering with Rubber*, Applied Science Publishers Ltd, London, 1978.

TABLE 1 : COMPLEX YOUNG'S MODULUS DATA FOR POLYISOPRENE RUBBER
(NARROW BAND, LOW FREQUENCY DATA)

T(C)	f= 10Hz		f= 15Hz		f= 20Hz		f= 25Hz		f= 30Hz		f= 40Hz	
	E(MPa)		E(MPa)		E(MPa)		E(MPa)		E(MPa)		E(MPa)	
-60	2042.1	.30	2087.4	.27	2132.8	.25	2178.2	.24	2223.6	.21	2268.9	.21
-58	1769.5	.37	1821.6	.34	1873.6	.30	1925.7	.31	1977.7	.30	2029.8	.28
-56	1165.0	.53	1234.0	.45	1303.1	.50	1396.5	.39	1538.4	.43	1665.3	.36
-54	806.9	.75	851.8	.64	896.6	.63	956.4	.52	1050.6	.58	1333.0	.55
-52	485.4	1.16	516.7	.95	548.0	.93	620.0	.83	697.0	.82	828.7	.88
-50	270.1	1.52	331.8	1.42	374.5	1.31	415.9	1.28	457.9	1.24	523.7	1.17
-48	137.3	1.33	176.4	1.43	211.3	1.43	237.4	1.36	261.7	1.39	326.7	1.43
-46	100.6	1.39	113.5	1.38	146.9	1.31	169.0	1.39	198.3	1.48	230.5	1.53
-44	55.2	1.13	70.4	1.24	83.6	1.31	97.1	1.30	112.4	1.36	137.8	1.39
-42	38.5	1.06	48.6	1.17	58.7	1.25	67.4	1.31	75.1	1.31	85.6	1.40
-30	26.3	.99	33.5	1.08	39.4	1.17	45.4	1.22	50.6	1.27	61.2	1.30
-38	19.4	.87	23.7	.97	27.6	1.02	30.7	1.06	34.7	1.13	41.8	1.08
-36	14.9	.78	17.9	.86	20.6	.91	23.0	.95	25.5	.98	29.9	1.02
-34	11.5	.65	13.6	.73	15.5	.80	17.2	.84	19.0	.87	22.7	.91
-32	10.3	.60	12.1	.68	13.8	.73	15.4	.77	16.7	.81	19.6	.87
-30	8.9	.52	10.2	.59	11.5	.65	12.6	.69	13.6	.72	15.5	.78
-28	7.6	.41	8.5	.48	9.3	.52	10.0	.56	10.7	.58	12.0	.63
-25	6.9	.33	7.7	.40	8.3	.44	8.8	.48	9.4	.51	10.4	.57
-23	6.3	.28	6.8	.33	7.2	.37	7.6	.41	8.1	.42	8.8	.46
-20	6.2	.22	6.3	.25	6.8	.29	7.0	.32	7.3	.35	8.2	.40
-17	5.6	.17	5.8	.21	6.1	.24	6.3	.26	6.5	.28	6.9	.32
-13	5.4	.13	5.5	.16	5.8	.18	5.9	.20	6.0	.22	6.4	.24
-10	5.4	.10	5.6	.13	5.7	.13	5.8	.15	5.9	.17	6.1	.18
0	5.2	.07	5.2	.08	5.3	.08	5.4	.09	5.5	.10	5.6	.11
10	4.9	.06	5.0	.06	5.1	.06	5.1	.07	5.2	.08	5.2	.08
20	4.9	.05	4.9	.05	4.9	.05	5.0	.06	5.0	.06	5.2	.06
40	4.3	.06	4.4	.06	4.5	.06	4.6	.06	4.6	.06	4.7	.06
60	4.1	.06	4.2	.06	4.2	.06	4.3	.06	4.4	.06	4.5	.06
80	3.9	.06	4.0	.06	4.1	.06	4.2	.06	4.3	.06	4.3	.05
100	3.8	.06	3.9	.06	4.0	.06	4.1	.06	4.1	.05	4.2	.06

TABLE 2 : COMPLEX YOUNG'S MODULUS DATA FOR POLYISOPRENE RUBBER
(NARROW BAND, INTERMEDIATE FREQUENCY DATA)

T(C)	f=100Hz		f=150Hz		f=200Hz		f=250Hz		f=300Hz		f=400Hz	
	E(MPa)		E(MPa)		E(MPa)		E(MPa)		E(MPa)		E(MPa)	
-60	2495.8	.13	2413.3	.13	2565.5	.12	2526.0	.11	2525.1	.10	2678.4	.10
-58	2290.0	.18	2188.1	.15	2353.3	.16	2361.3	.14	2361.0	.14	2505.5	.14
-56	1866.4	.30	1960.5	.27	2111.2	.26	2133.3	.22	2164.0	.22	2251.9	.20
-54	1544.9	.38	1781.1	.35	1923.2	.32	1974.6	.28	2001.1	.27	2143.2	.25
-52	1164.8	.60	1375.4	.56	1530.4	.50	1609.4	.44	1660.2	.41	1814.8	.38
-50	848.1	.85	967.0	.80	1117.6	.71	1207.7	.66	1279.2	.62	1430.4	.56
-48	513.8	1.40	669.1	1.05	783.1	.97	875.9	.88	955.0	.83	1094.2	.75
-46	403.9	1.45	531.9	1.18	637.5	1.08	713.7	1.01	777.5	.95	896.4	.88
-44	236.1	1.56	313.1	1.42	380.8	1.35	431.5	1.29	481.6	1.23	571.7	1.17
-42	159.4	1.56	212.3	1.51	258.0	1.48	297.7	1.43	332.3	1.39	401.7	1.35
-30	99.4	1.45	131.2	1.50	158.8	1.52	183.4	1.53	207.1	1.51	253.3	1.49
-38	68.6	1.41	88.7	1.45	106.5	1.46	123.7	1.49	138.9	1.49	168.3	1.53
-36	48.9	1.27	62.6	1.33	75.2	1.40	85.7	1.42	96.5	1.44	116.2	1.48
-34	35.5	1.13	45.0	1.22	53.4	1.27	60.8	1.31	68.3	1.34	82.3	1.39
-32	29.3	1.07	36.9	1.15	43.3	1.21	49.1	1.25	54.6	1.28	65.0	1.32
-30	23.2	.96	28.6	1.04	33.1	1.10	37.5	1.14	41.7	1.16	49.6	1.22
-28	16.7	.81	20.3	.88	23.2	.92	26.1	.96	28.8	.99	34.0	1.05
-25	14.1	.73	16.7	.81	19.1	.86	21.5	.90	23.3	.93	27.4	.97
-23	11.4	.61	13.3	.68	14.9	.72	16.5	.76	17.8	.78	20.7	.84
-20	9.9	.55	11.5	.64	12.8	.69	14.2	.72	15.2	.75	17.7	.78
-17	8.4	.45	9.4	.52	10.5	.56	11.3	.60	12.2	.61	14.0	.68
-13	7.4	.36	8.1	.42	8.9	.45	9.6	.50	10.3	.52	11.9	.59
-10	6.8	.31	7.4	.38	8.0	.41	8.4	.45	8.8	.48	9.9	.49
0	5.9	.16	6.1	.19	6.5	.22	6.6	.23	7.0	.24	7.7	.28
10	5.6	.09	5.7	.12	5.9	.14	6.1	.14	6.3	.14	6.8	.15
20	5.4	.07	5.5	.07	5.6	.08	5.9	.08	5.8	.09	6.1	.11
40	4.9	.06	5.1	.06	5.1	.06	5.3	.06	5.5	.06	5.8	.06
60	4.7	.06	4.8	.06	5.0	.05	5.1	.06	5.3	.05	5.3	.06
80	4.5	.06	4.5	.07	4.7	.06	4.9	.05	5.1	.06	5.4	.06
100	4.4	.06	4.5	.06	4.6	.05	4.7	.06	4.9	.06	5.0	.06

TABLE 3 : COMPLEX YOUNG'S MODULUS DATA FOR POLYISOPRENE RUBBER
(WIDE FREQUENCY BAND DATA)

f (Hz)	T=-60C		T=-50C		T=-40C		T=-20C		T= 20C		T=100C	
	E (MPa)		E (MPa)		E (MPa)		E (MPa)		E (MPa)		E (MPa)	
10	2042.1	.30	270.1	1.52	26.3	.99	6.2	.22	4.9	.05	3.8	.06
15	2087.4	.27	331.8	1.42	33.5	1.08	6.3	.25	4.9	.05	3.9	.06
20	2132.8	.25	374.5	1.31	39.4	1.17	6.8	.29	4.9	.05	4.0	.06
25	2178.2	.24	415.9	1.28	45.4	1.22	7.0	.32	5.0	.06	4.1	.06
30	2223.6	.21	457.9	1.24	50.6	1.27	7.3	.35	5.0	.06	4.1	.05
40	2268.9	.21	523.7	1.17	61.2	1.30	8.2	.37	5.2	.06	4.2	.06
50	2314.3	.19	589.5	1.11	72.1	1.34	8.5	.41	5.2	.06	4.2	.06
60	2359.7	.16	659.5	1.05	78.8	1.36	8.9	.44	5.3	.07	4.3	.05
70	2405.1	.15	729.5	1.00	85.6	1.36	8.9	.45	5.3	.07	4.3	.06
80	2450.5	.15	749.2	.95	89.7	1.34	9.3	.46	5.3	.07	4.3	.06
90	2495.8	.15	769.0	.90	91.8	1.40	9.7	.49	5.3	.07	4.4	.06
100	2495.8	.13	848.1	.85	99.4	1.45	9.9	.54	5.4	.07	4.4	.06
150	2413.3	.13	967.0	.80	131.2	1.50	11.5	.59	5.5	.07	4.5	.06
200	2565.5	.12	1117.6	.71	158.8	1.52	12.8	.62	5.6	.08	4.6	.05
250	2526.0	.11	1207.7	.66	183.4	1.53	13.9	.67	5.6	.08	4.6	.06
300	2525.1	.10	1279.2	.62	207.1	1.51	14.7	.71	5.6	.09	4.9	.06
400	2678.4	.10	1430.4	.56	253.3	1.49	16.6	.76	5.7	.11	5.0	.06
500	2669.0	.10	1524.6	.52	294.2	1.44	18.2	.78	6.2	.12	5.2	.06
600	2779.1	.10	1610.1	.48	333.6	1.43	19.6	.82	6.3	.11	5.1	.06
700	2741.9	.10	1592.9	.47	375.6	1.37	21.1	.83	6.3	.12	5.7	.04
800	3055.3	.10	1740.0	.45	409.7	1.38	22.1	.87	6.1	.13	5.4	.06
900	2844.9	.08	1712.3	.43	448.6	1.30	23.1	.89	6.3	.15	5.7	.05
1000	3024.5	.07	1858.5	.41	493.1	1.28	24.2	.93	6.6	.16	5.9	.06

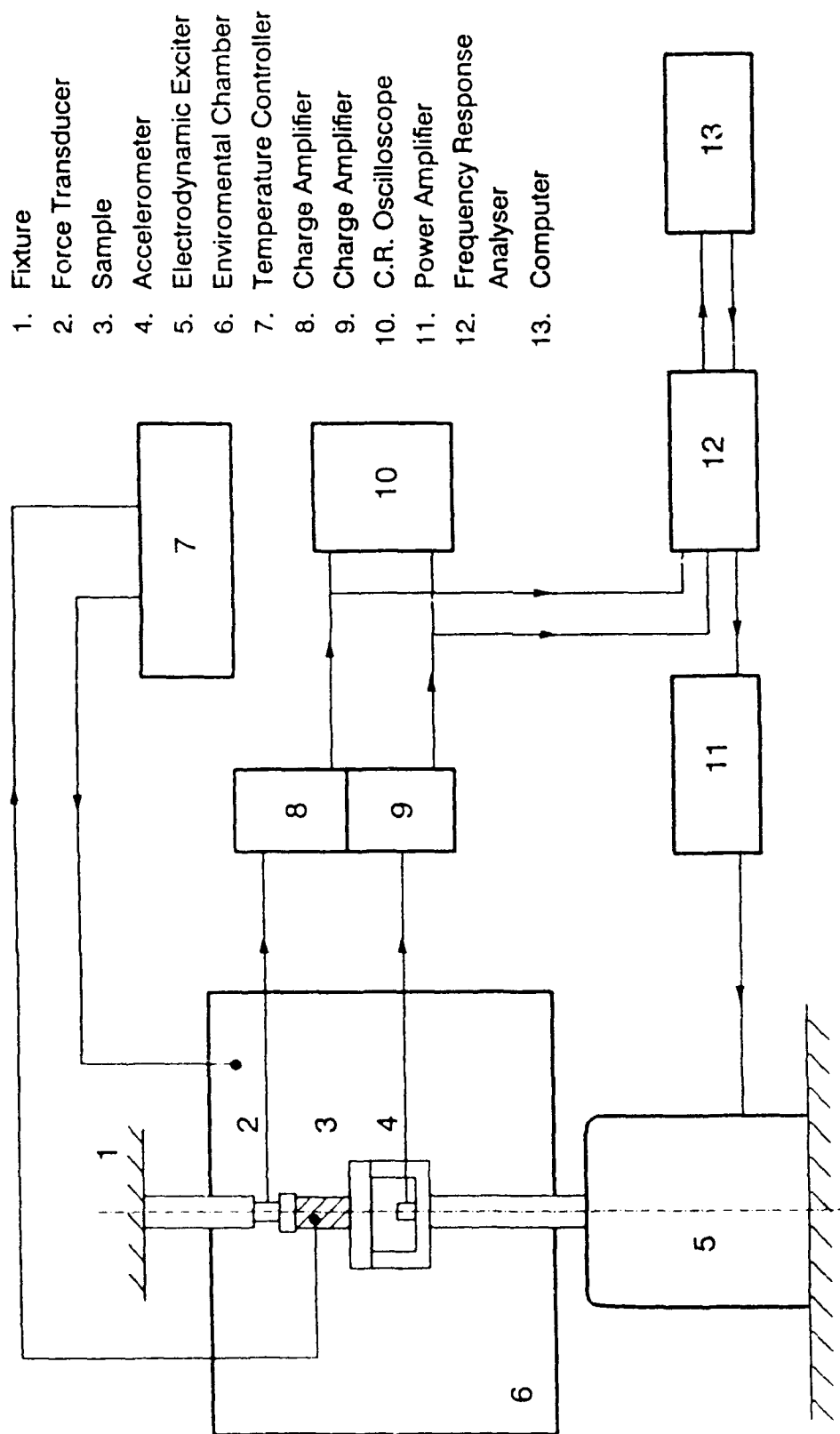


FIGURE 1 : SCHEMATIC DIAGRAM OF DIRECT COMPLEX STIFFNESS TEST CONFIGURATION

o < x v * > \$ a b c d e f g h k m n p q r s t u w y z £ % & 100C
 -60C -56C -54C -52C -50C -48C -46C -44C -42C -40C -38C -36C -34C -32C -30C -28C -25C -23C -20C -17C -13C -10C 0C 10C 20C 40C 60C 80C 100C

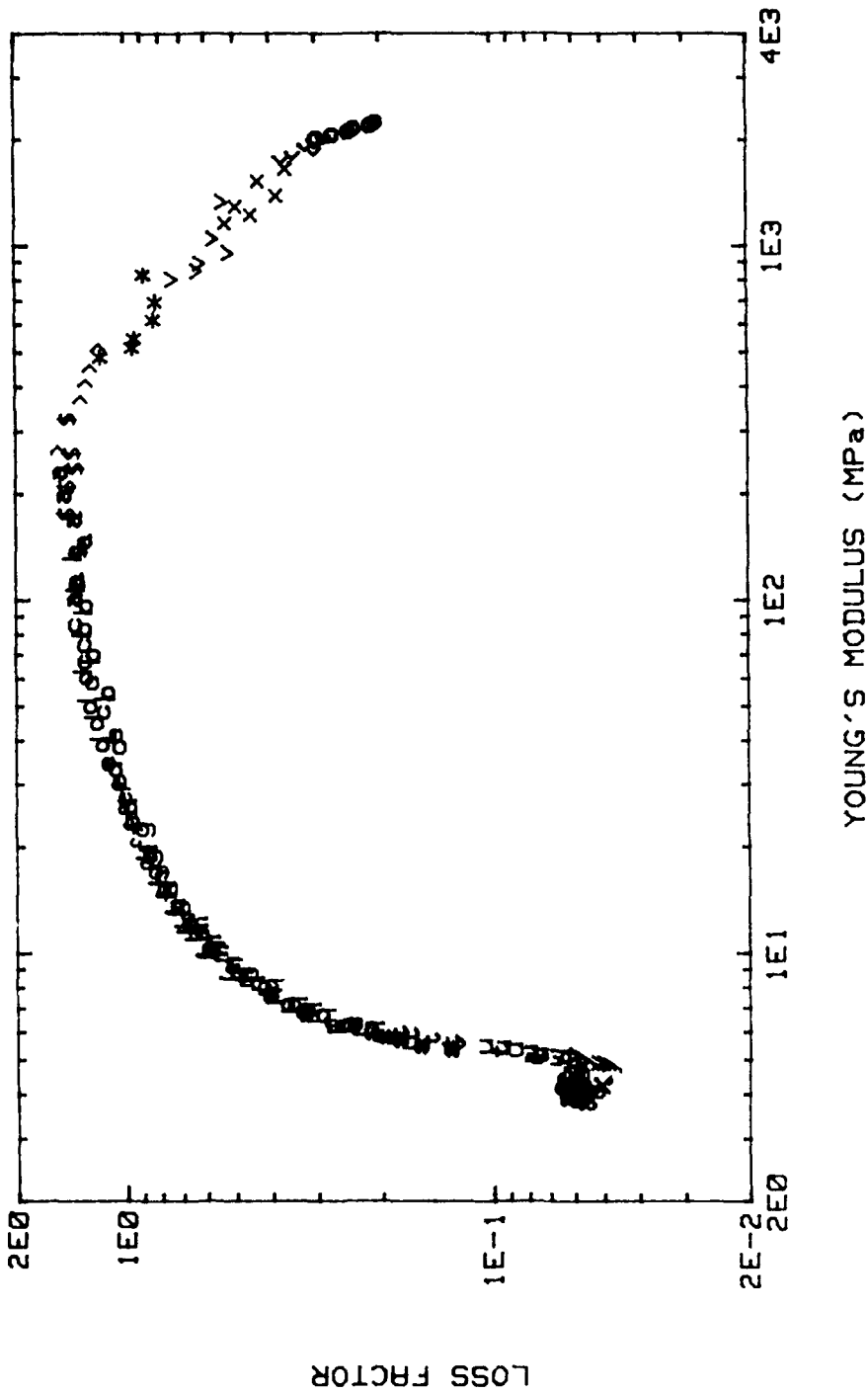


FIGURE 2 : LOSS FACTOR VS. MODULUS (WICKET PLOT) FOR POLYISOPRENE RUBBER
 (NARROW BAND, LOW FREQUENCY DATA)

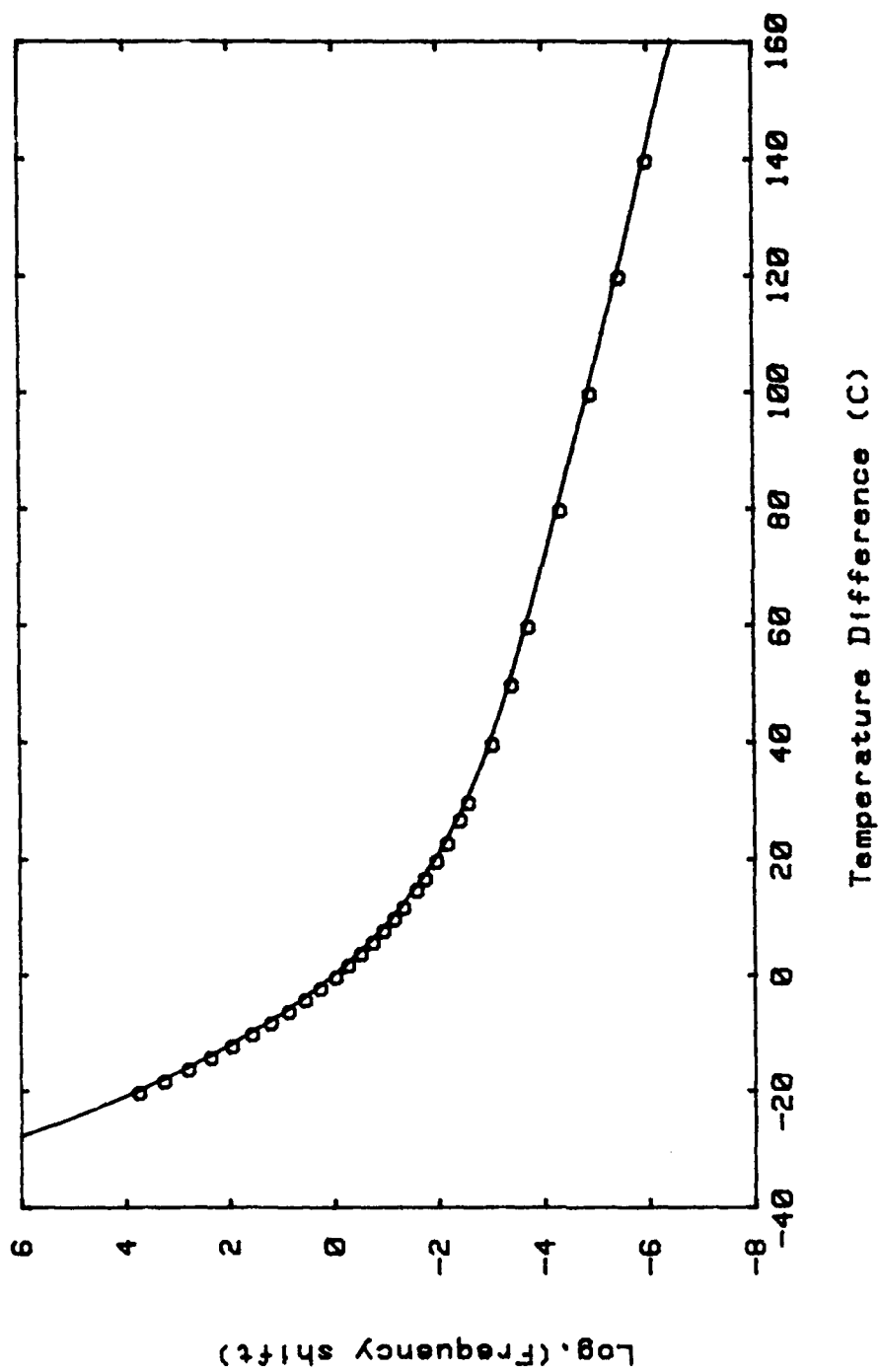


FIGURE 3 : SHIFT FACTOR CURVE FOR NARROW BAND, LOW FREQUENCY DATA

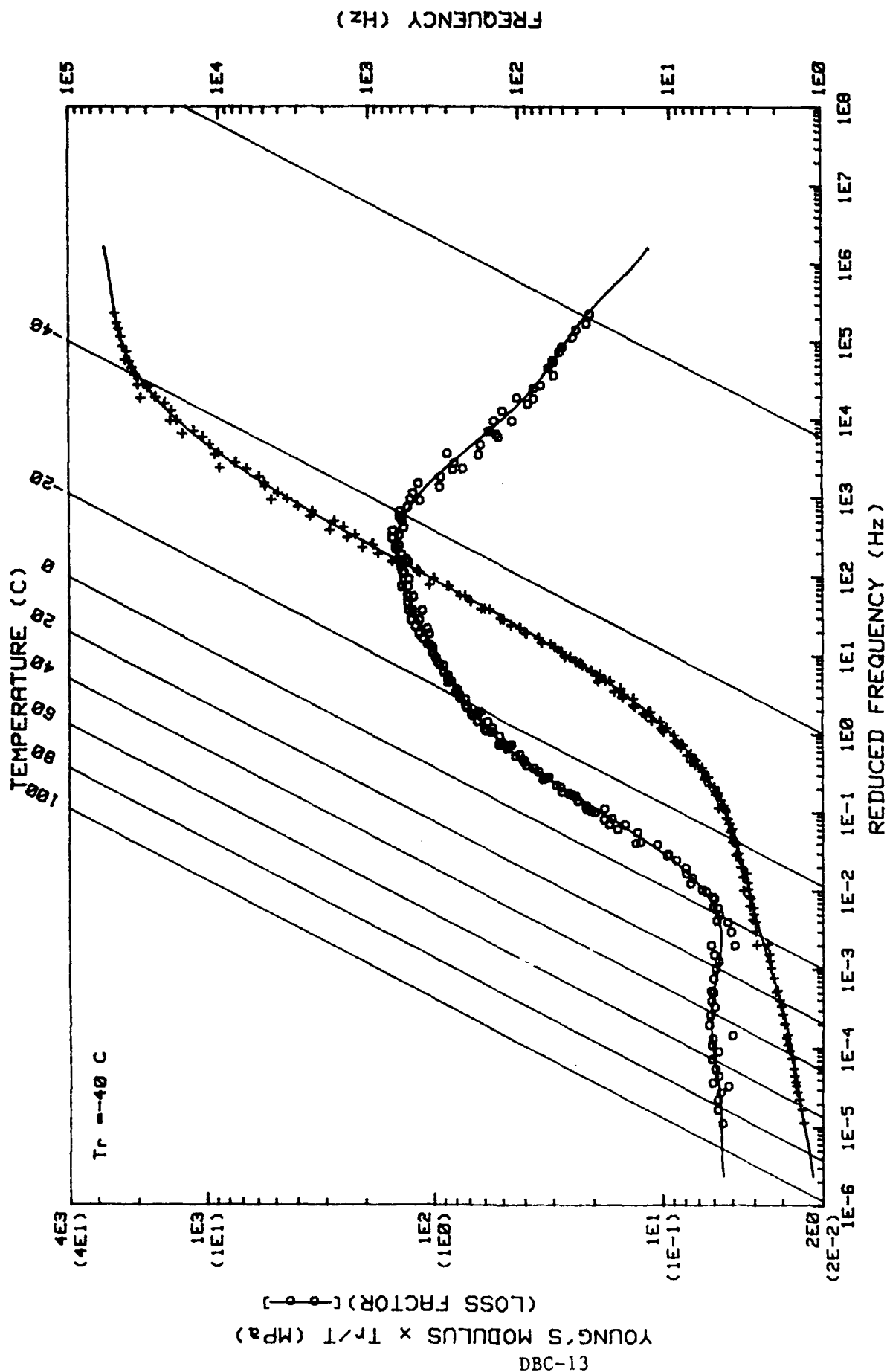


FIGURE 4 : INTERNATIONAL PLOT OF COMPLEX YOUNG'S MODULUS FOR POLYISOPRENE RUBBER
(NARROW BAND, LOW FREQUENCY DATA)

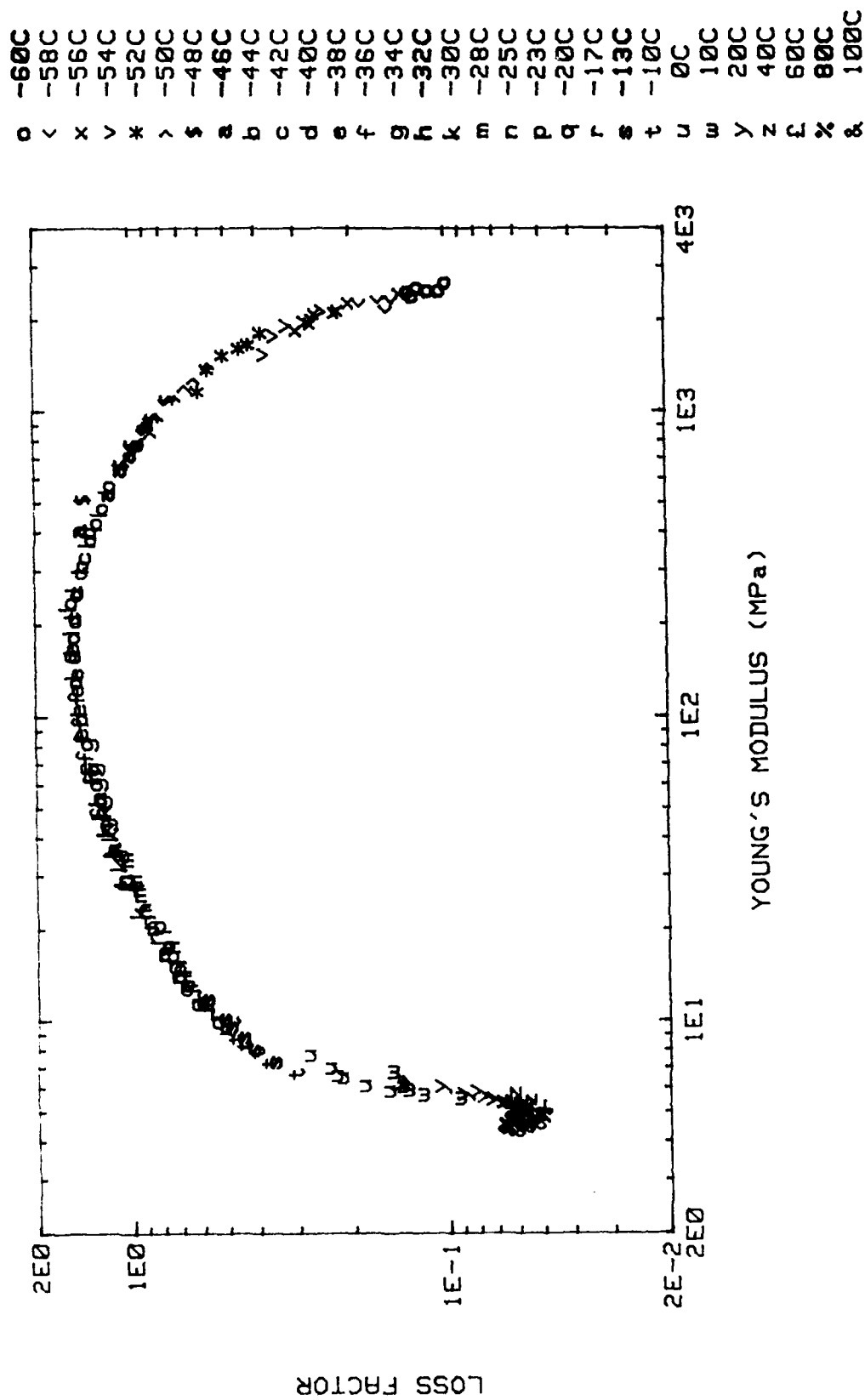


FIGURE 5 : LOSS FACTOR VS. MODULUS (WICKET PLOT) FOR POLYISOPRENE RUBBER
(NARROW BAND, INTERMEDIATE FREQUENCY DATA)

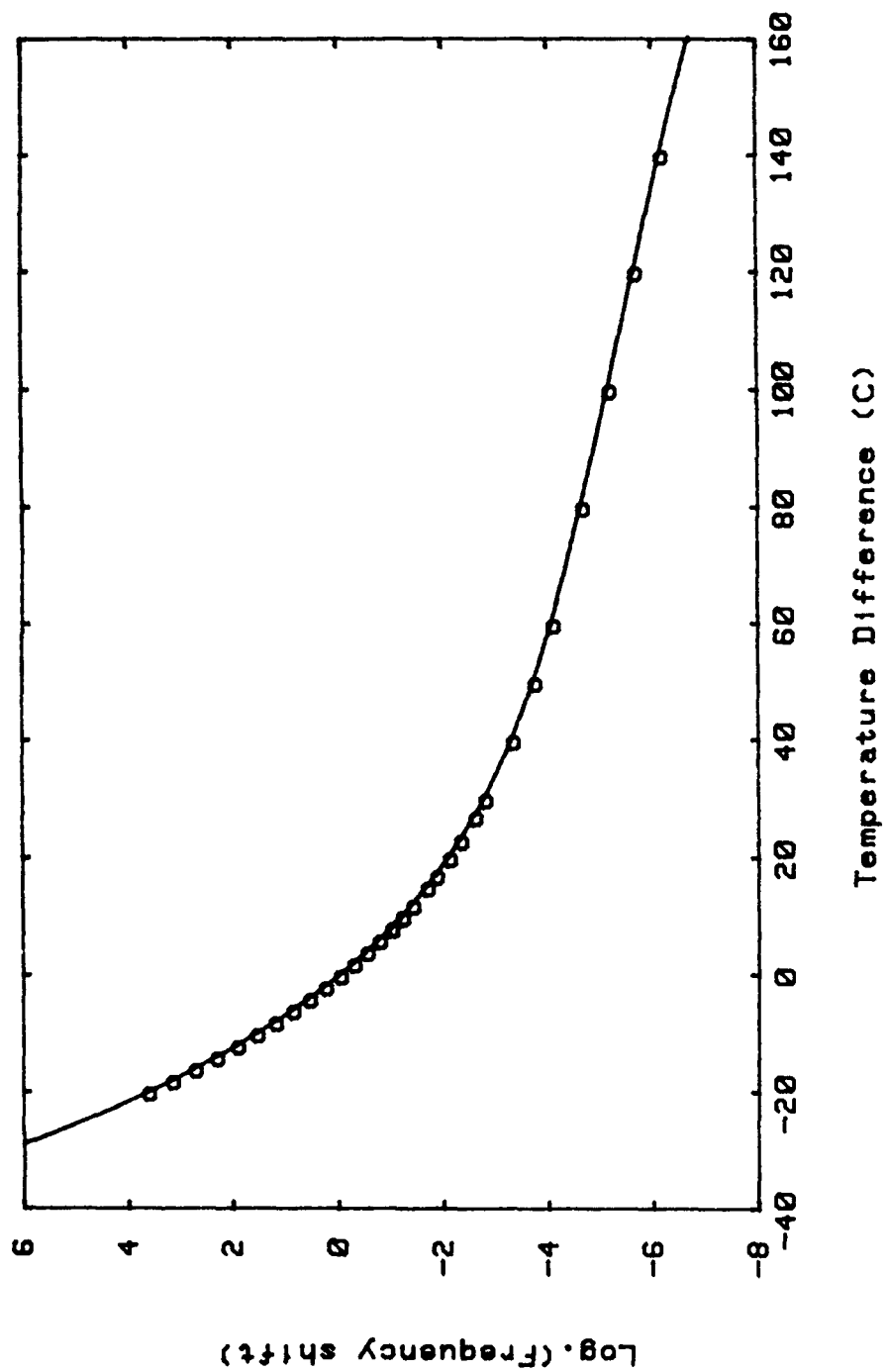


FIGURE 6 : SHIFT FACTOR CURVE FOR NARROW BAND, INTERMEDIATE FREQUENCY DATA

YOUNG'S MODULUS $\times T_r/T$ (MPa)

(LOSS FACTOR) [—○—]

DBC-16

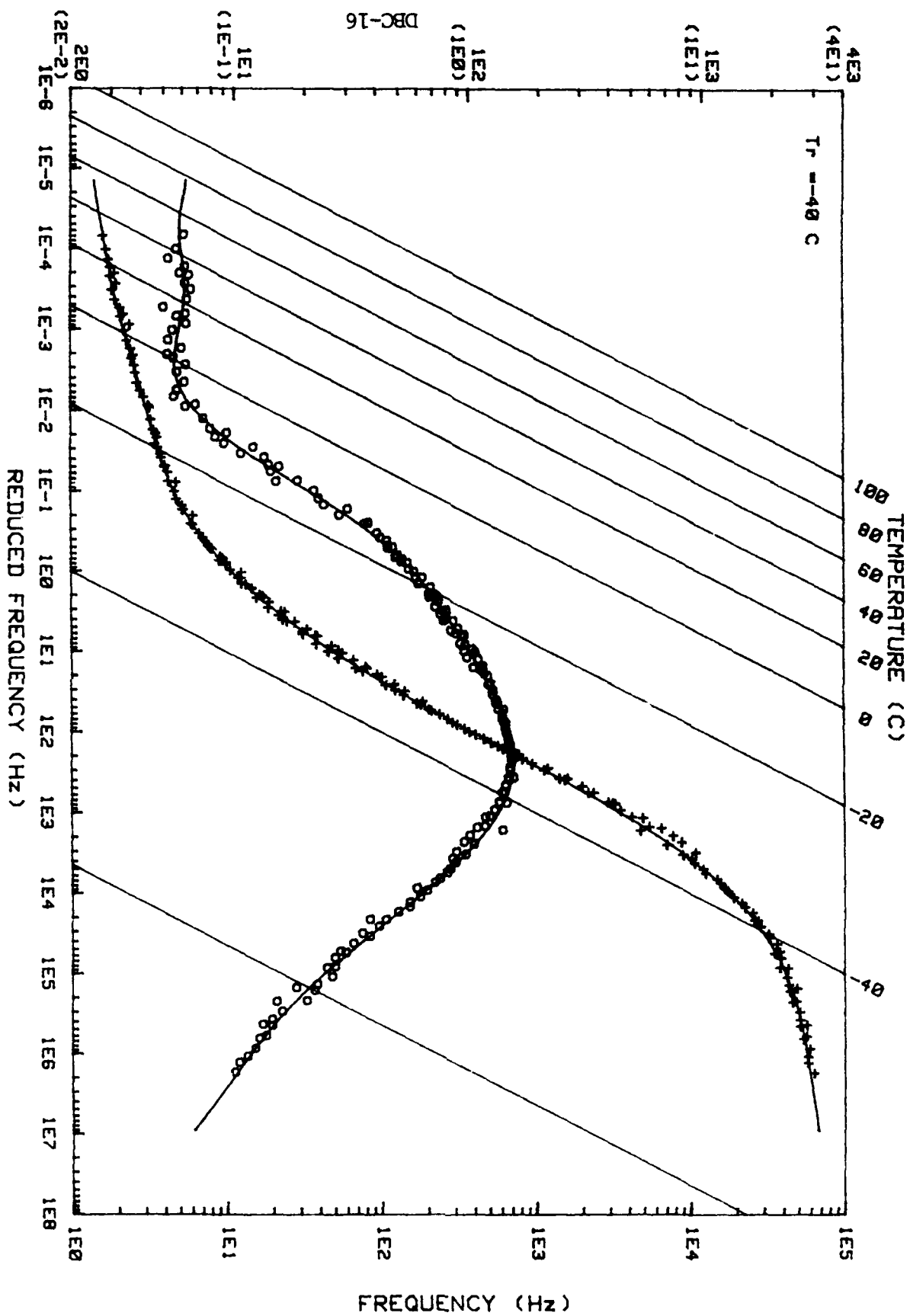


FIGURE 7 : INTERNATIONAL PLOT OF COMPLEX YOUNG'S MODULUS FOR POLYISOPRENE RUBBER
(NARROW BAND, INTERMEDIATE FREQUENCY DATA)

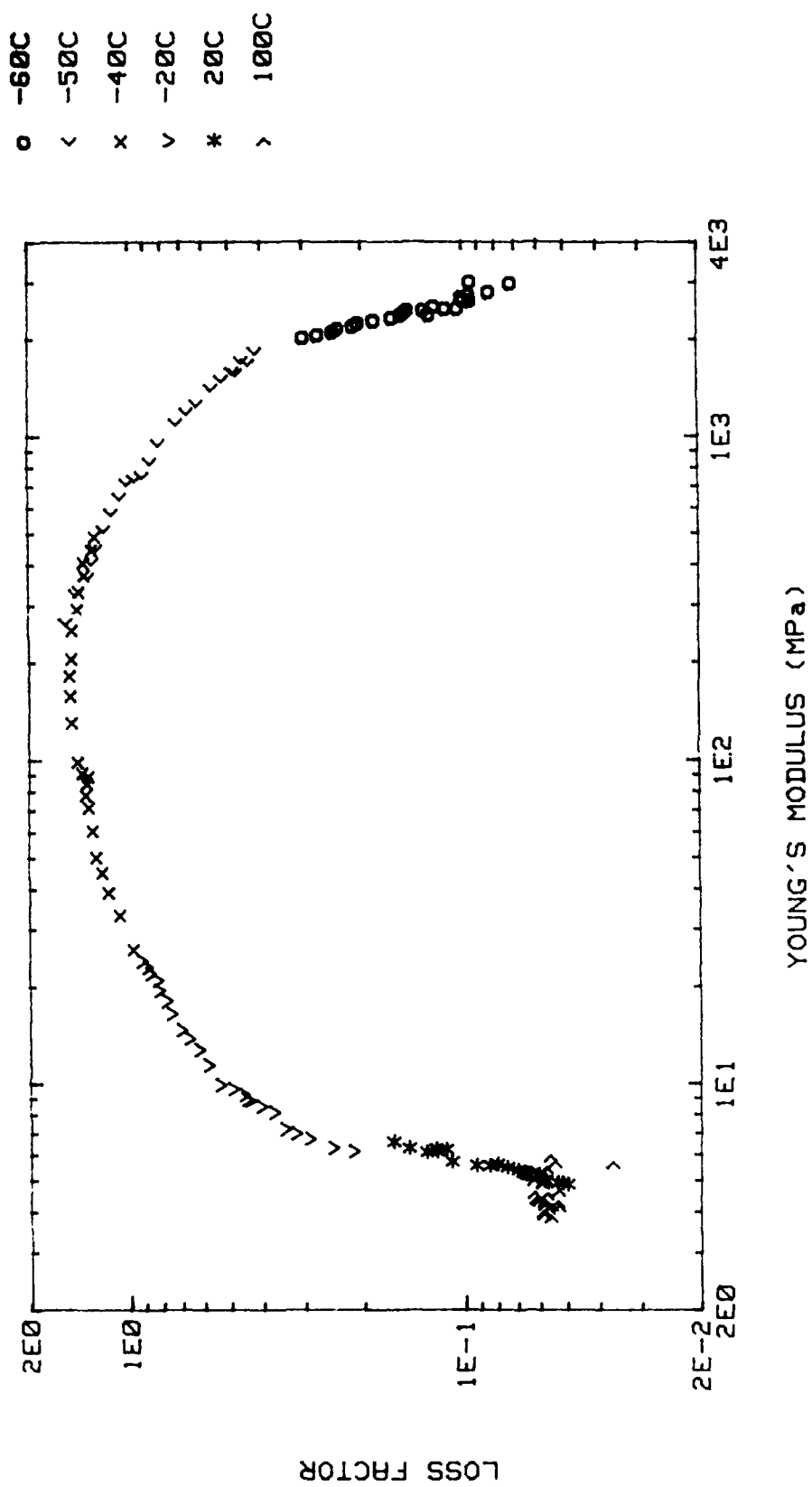


FIGURE 8 : LOSS FACTOR VS. MODULUS (WICKET PLOT) FOR POLYISOPRENE RUBBER
(WIDE FREQUENCY BAND DATA)

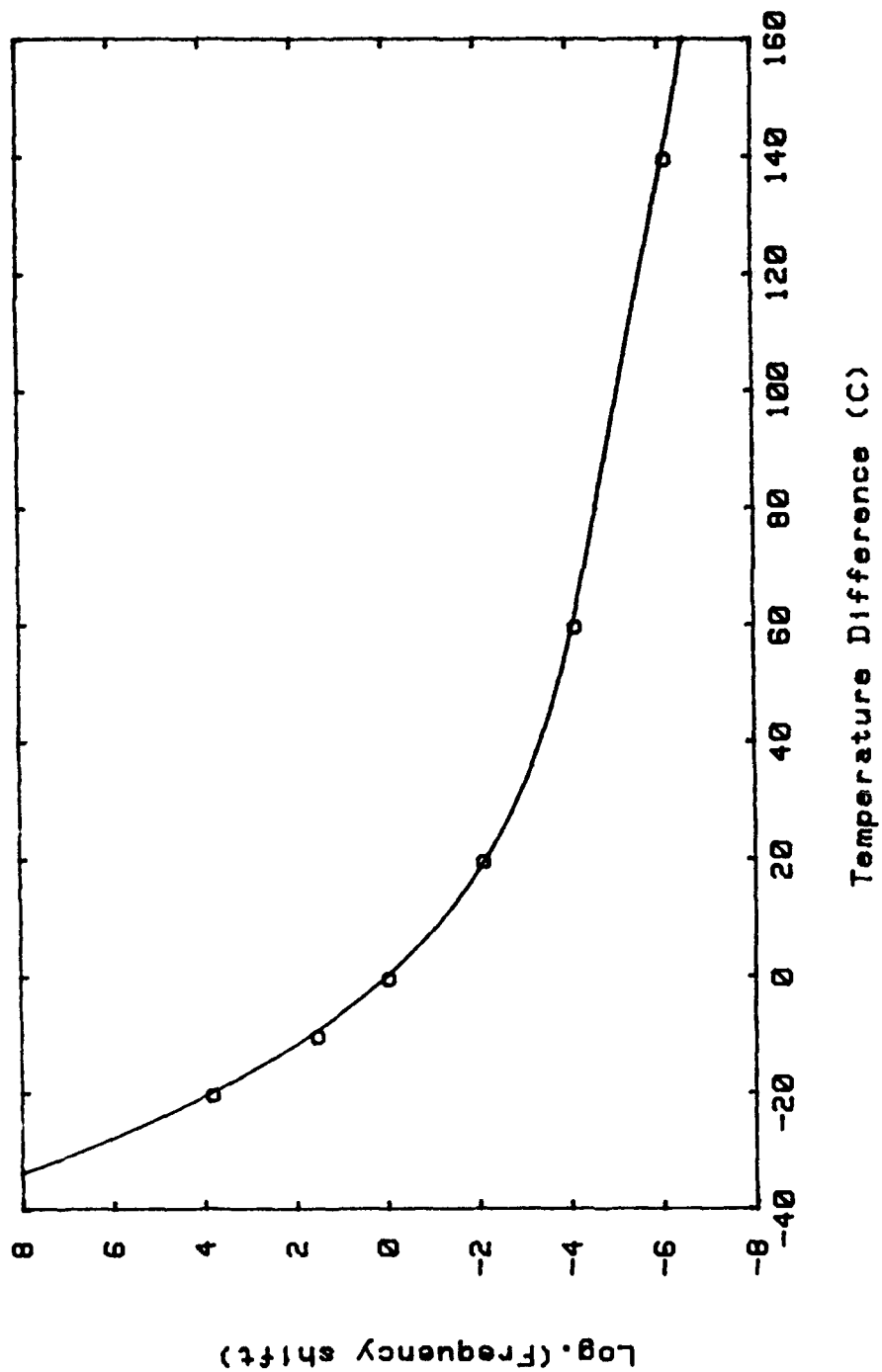


FIGURE 9 : SHIFT FACTOR CURVE FOR WIDE FREQUENCY BAND DATA

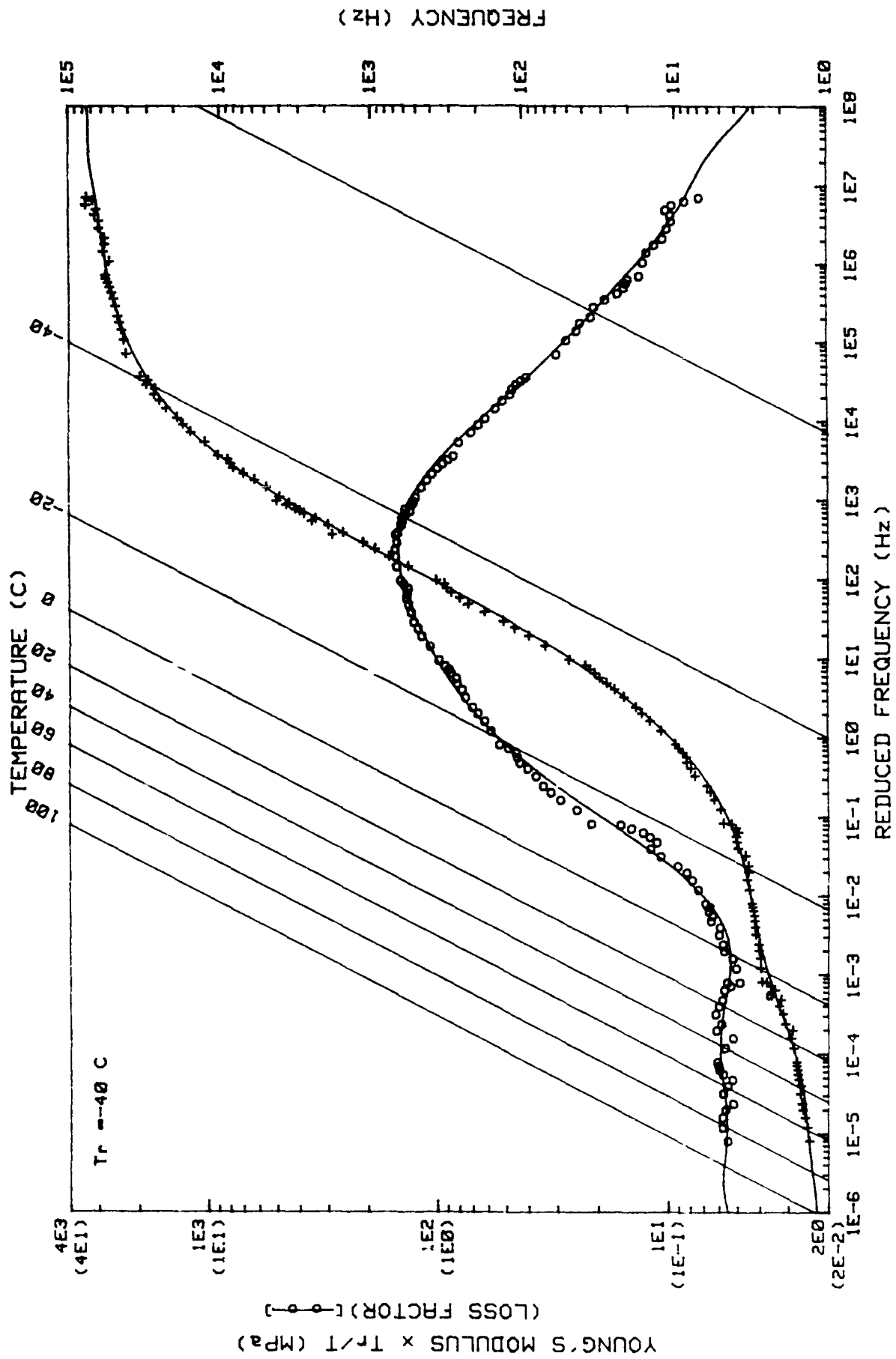


FIGURE 10 : INTERNATIONAL PLOT OF COMPLEX YOUNG'S MODULUS FOR POLYISOPRENE RUBBER
(WIDE FREQUENCY BAND DATA)

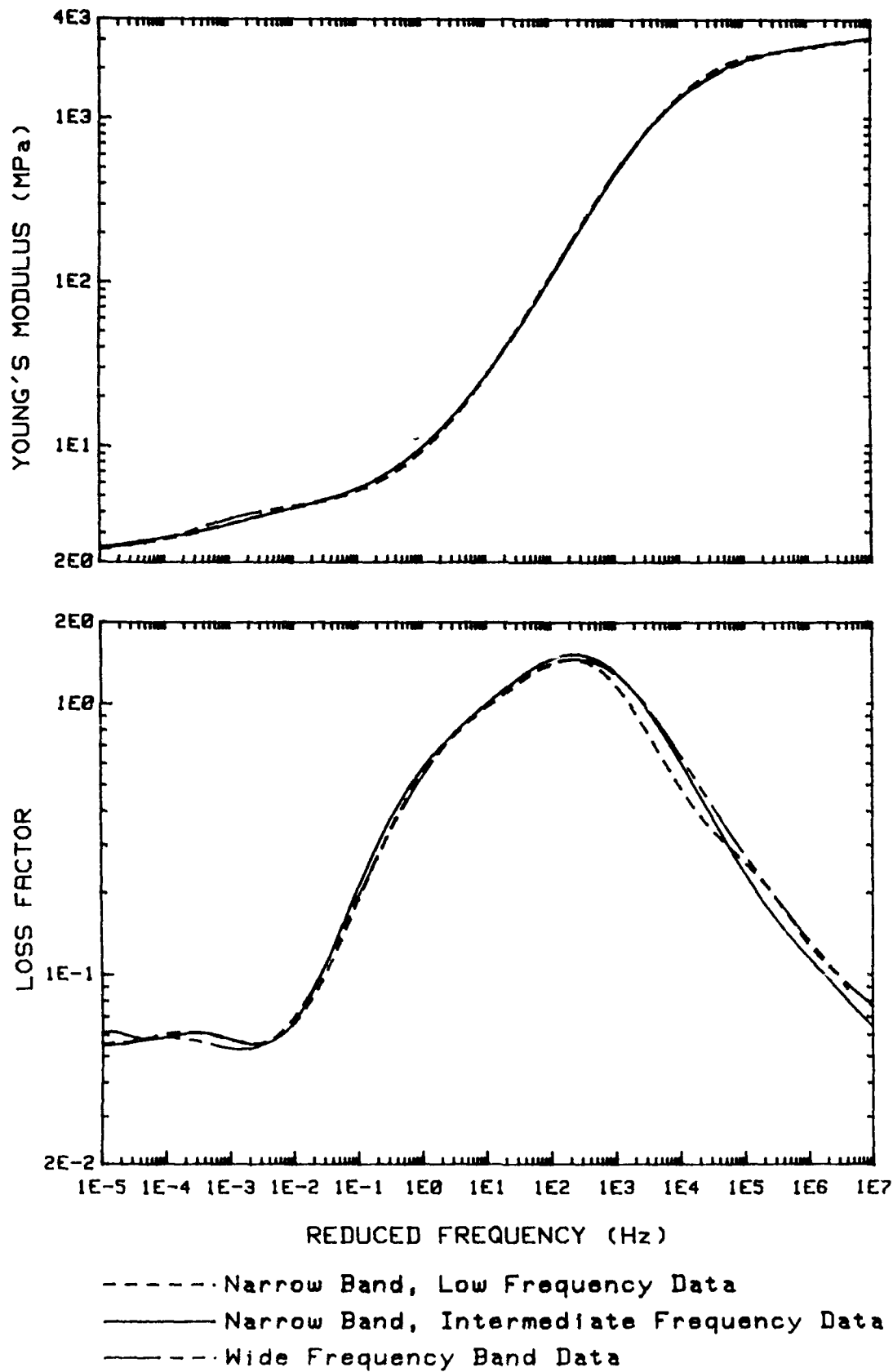


FIGURE 11 : MASTER CURVES OF COMPLEX YOUNG'S MODULUS
 FOR POLYISOPRENE RUBBER

INTEGRATED OPTIMIZATION OF COMPOSITE STRUCTURES FOR ADVANCED DAMPED DYNAMIC CHARACTERISTICS

D. A. Saravanos¹
Case Western Reserve University
and
C. C. Chamis
NASA-Lewis Research Center

ABSTRACT

Polymer matrix composites exhibit significantly higher material damping compared to most common metals. The current paper summarizes recent research on the development of design methodologies for optimizing the damping and the damped dynamic performance of composite structures. The optimal tailoring involves multiple material/structural levels, that is, the micromechanics level (fiber/matrix properties, fiber volume ratio), laminate level (ply angles/thicknesses, stacking sequence), and structural level (structural geometry and shape). The dynamic response and the modal damping of the composite structure are simulated with finite element analysis based on a special composite element. A multi-objective constrained optimization scheme is proposed for the best handling of the many competing design criteria involved. Applications on basic structural components (beams and plates) demonstrate that properly tailored composite structures can exhibit significantly improved damped dynamic performance.

Keywords: damping; composite materials; composite structures; optimization; design; dynamic performance.

¹ Structures Division, Lewis Research Center, MS 49-8,
21000 Brookpark Rd., Cleveland, OH 44135; (216) 433-8466.

INTRODUCTION

Fiber composite materials are widely used in structural applications requiring high stiffness-to-weight and strength-to-weight ratios, as they readily provide high specific moduli, high specific strengths, and tailorable anisotropic elastic properties. Polymer matrix composites may also exhibit significantly higher damping compared to most common metals. The previously stated requirements for advanced light-weight structures virtually restrict the use of many traditional sources of passive damping, therefore, the option to utilize the damping capacity of polymer-matrix composites appears very attractive. Reported research on the damping of unidirectional composites and laminates [1-6] has shown that the damping of composites is highly-tailorable and is primarily controlled by constituent parameters (fiber/matrix properties, fiber volume ratio), and laminate parameters (ply angles/thicknesses, stacking sequence). Additional research work [7] demonstrated that the modal damping of composite structures depends also on the structural geometry and deformation (mode shapes). This work also suggested that properly designed composite structures can provide significant passive damping, and they may further improve the dynamic performance and fatigue endurance by attenuating undesirable elasto-dynamic phenomena such as structural resonances, overshooting, and long settling times. The previous studies have also demonstrated that any increase in damping typically results in decreased stiffness and strength, therefore, any tailoring of the composite material for optimal damped response will be based on trade-offs between damping, stiffness, and strength.

Although the optimization of composite structures for multiple design criteria including damping appears to be worthwhile and its significance has been acknowledged [8], reported research on the subject has been mostly limited to the laminate level [9,10]. Recent research performed by the authors has been focused on the optimal tailoring of composite structures for optimal transient or forced dynamic response [11-13]. This work is summarized herein and involves methodologies for the optimal design of polymer matrix composite structures. The methods are equally applicable to structures subject in steady or transient response, and they further entail: (1) multiple objectives to effectively represent the array of competing design requirements; (2) capability for tailoring of the basic composite materials and/or laminate; (3) capability for concurrent shape optimization; and (4) design criteria based on the global static and dynamic response of the composite structure.

The proposed design objectives are minimization of resonance amplitudes (or maximization of structural damping), minimization of structural weight, and minimization of material cost. Additional performance constraints are imposed on static deflections, dynamic resonance amplitudes, natural frequencies, static ply stresses, and dynamic ply stresses. The analysis involves unified composite mechanics, which entail micromechanics, laminate and structural mechanics theories for the passive damping and other mechanical

properties of the composite. The structural damping and the damped dynamic response are simulated with finite element analysis. Applications of the methodology on the optimization of a cantilever composite beams and a cantilever composite plate are presented. The results quantify the importance of structural damping in improving the dynamic performance of composite structures, and illustrate the effectiveness of the proposed design methodology.

DAMPED STRUCTURAL DYNAMIC RESPONSE

To enable the design of general composite structures, a finite element discretization is utilized. In such case, the dynamic response of a structure which is excited by a force $P(t)$ is expressed by the following system of dynamic equations:

$$[M]\{\ddot{u}\} + [C]\{\dot{u}\} + [K]\{u\} = \{P(t)\} \quad (1)$$

where $\{u\}$ is the discretized displacement vector. In the case of laminated composite structures, the stiffness, damping, and mass matrices, $[K]$, $[C]$, and $[M]$ respectively, are synthesized utilizing micromechanics, laminate, and structural mechanics theories representing the various material and structural scales in the composite structure.

The related theories for this multi-level simulation of structural composite damping are described in refs. 1,2, and 7. Analogous theories are utilized for the synthesis of other mechanical properties [14]. At the micromechanics level, the on-axis damping capacities of the basic composite material systems are calculated based on constituent properties, material microstructure, fiber volume ratio (FVR), temperature, and moisture. The off-axis damping capacities of the composite plies are calculated at the laminate level, and the local laminate damping matrices are predicted based on on-axis damping values, ply thicknesses, and laminate configuration. The damping contributions of the interlaminar matrix layers due to in-plane interlaminar shear are also incorporated [2].

The structural modal damping is synthesized by integrating the local laminate damping contributions over the structural volume. The modal specific damping capacity (SDC) of the n -th vibration mode ψ_n is:

$$\psi_n = \frac{\int_A \Delta W_{Ln} dA}{\int_A W_{Ln} dA} \quad (2)$$

where: A is the structural area; ΔW_{Ln} and W_{Ln} are the dissipated and maximum stored laminate strain energy distributions, respectively, of the n -th mode per unit area per cycle. Utilizing the finite element discretization scheme proposed in ref. 7, the modal

SDC is related to the element damping and stiffness matrices, $[C_e]$ and $[K_e]$ respectively:

$$\psi_n = \frac{\frac{1}{2} \sum_{i=1}^{nel} \{u_{ein}\}^T [C_{ei}] \{u_{ein}\}}{\frac{1}{2} \sum_{i=1}^{nel} \{u_{ein}\}^T [K_{ei}] \{u_{ein}\}} \quad (3)$$

where, nel is the total number of elements and $\{u_{ein}\}$ the nodal displacements of the i -th element corresponding to the n -th vibration mode.

The dynamic response of the structure is simulated based on modal superposition. The dynamic system in eq. (1) is transferred to the $p \times p$ modal space via the linear modal transformation $\{u\} = [\phi]\{q\}$. Assuming proportional damping, then the damping matrix is synthesized from the modal damping values. The frequency response (FRF) of the structure, or the transient dynamic response is subsequently calculated. Typically the resonance amplitudes, or the undamped amplitudes in transient response of most critical vibration modes are used as performance measures.

OPTIMAL DESIGN

Originally, the optimal design of composite structures was conceived as a single-objective constrained optimization problem [11,12]. Although this research demonstrated the advantages of damping tailoring, it indicated that the design of composite structures for optimal dynamic performance is a multi-objective task, and may be best accomplished as the constrained minimization of multiple objective functions. Increases in composite damping may typically result in stiffness/strength reductions and/or mass addition, for this reason, the minimization of weight and material cost was also included in the objectives. The material cost is a crucial factor, restricting in many cases the use of composite materials. Moreover, the distinction between weight minimization and material cost minimization is also stressed, because fiber reinforced composites are nonhomogeneous materials and the minimization of the weight does not also imply the minimization of the material cost. Therefore, the multi-objective formulation is summarized herein, as the more general case.

A constrained multi-objective problem involving minimization of I objective functions is described in the following mathematical form:

$$\min \{F_1(z), F_2(z), \dots, F_I(z)\} \quad (4)$$

subject to lower and upper bounds on the design vector z and inequality constraints

$G(z)$:

$$z^L \leq z \leq z^U \quad (5)$$

$$G(z) \leq 0 \quad (6)$$

In the rest of the paper, upper and lower values are represented by superscripts L and U respectively. Individual minimizations of each objective function subject to constraint set (5,6) will result in a set of ideal solutions which define a target point $F^* = (F_1^*, F_2^*, \dots, F_l^*)$. A solution of the multi-objective problem is then obtained by finding a feasible point $\{F\} = (F_1, \dots, F_l)$ as closely as possible to the target point $\{F^*\}$. This is achieved by minimizing the following scaled objective function:

$$\min \sum_{i=1}^l v_i \frac{(F_i - F_i^*)^2}{F_i^{*2}} \quad (7)$$

subject to constraints (5,6). The weighting coefficients are represented with v_i . Other metrics or scaling procedures may be utilized in eq. (7), but in general, they are expected to result in different solutions.

The design objectives typically include minimization of: (1) the maximum resonance amplitude ($\min F_1$); (2) the total structural weight ($\min F_2$); and (3) the material cost represented by the average cost of fibers ($\min F_3$). Alternatively, F_1 may represent the maximization of select modal damping values. The explicit maximization of modal damping may be preferred in the case of transient or a-priori unknown dynamic excitations. The fiber cost is used as a measure of the total material cost due to the high cost of fibers compared to the cost of matrix. The design vector includes fiber volume ratios (FVRs), ply angles, and shape parameters.

Performance constraints are imposed on static deflections u_s ,

$$\{u^s\} \leq \{u^{sU}\} \quad (8)$$

dynamic amplitudes,

$$\{U^d\} \leq \{U^{dU}\} \quad (9)$$

natural frequencies $\{f_n\}$,

$$\{f^L\} \leq \{f_n\} \leq \{f^U\} \quad (10)$$

and the static and dynamic stresses of each ply σ_i in the form of the modified

distortion energy criterion [14],

$$f(\sigma_p, S) - 1 \leq 0 \quad (11)$$

The constrained optimizations mentioned above are solved with the modified feasible directions non-linear programming method [15,16]. The feasible directions algorithm performs a direct search in the design space involving a series of iterations. In each iteration, a search direction is calculated based on first order derivatives of the objective function and active constraints. A line search is subsequently performed along the search direction and a suboptimum along the search direction is calculated. The iterations are repeated until convergence to a local optimum is achieved.

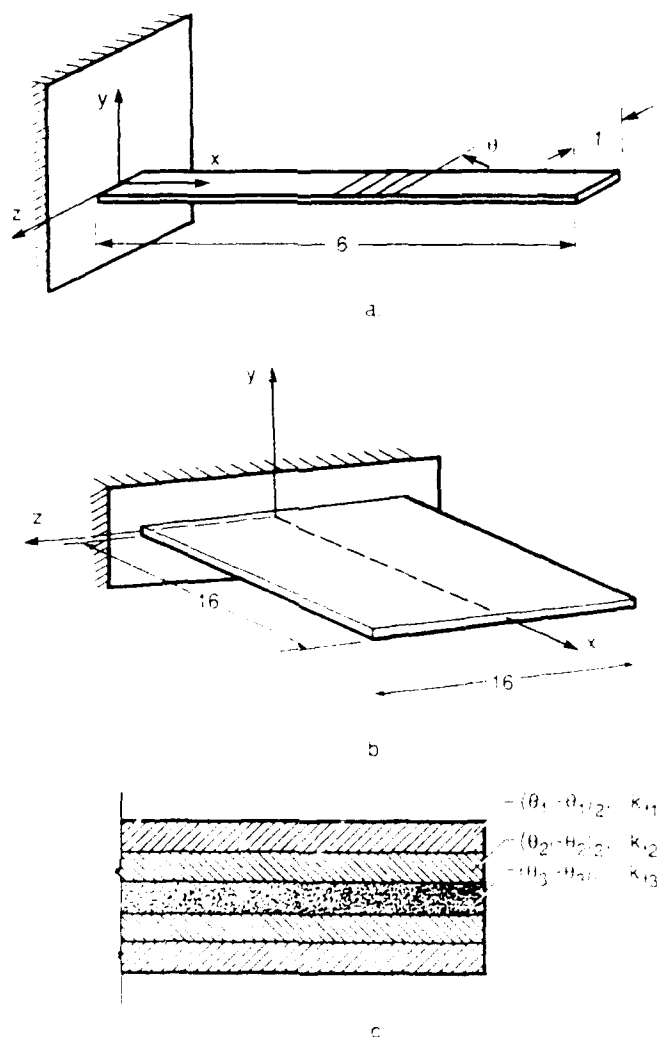


Fig. 1

Candidate composite structures. (a) Initial beam geometry; (b) Initial plate geometry; (c) Laminate configuration. Dimensions are in inches.

APPLICATIONS

Selected evaluations on the method on the optimal tailoring of a cantilever graphite/epoxy composite beam and a cantilever graphite/epoxy composite plate are presented (Fig. 1). The assumed laminate configuration in both structures is symmetric consisting of angle-ply sublaminae 1, 2, and 3 in each side. All sublaminae had plies of equal thickness (0.01 in). The ply angles θ_i and FVRs k_{fi} of each sublaminate, and the thicknesses h_i at 0%, 30%, 60%, and 100% (tip) of the span were optimized. The thickness at other sections was interpolated using a cubic spline fit. A unidirectional ply configuration was selected as the initial baseline composite design for both cases, because it provides high axial bending rigidity.

Composite Beam in Impulsive Excitation: Typical improvements in the predicted impulse response (y-axis) of an optimized composite beam design are shown in Fig. 2. In this particular case, a single objective function was implemented, such that, the modal damping corresponding to the mode with the higher undamped dynamic amplitude was maximized [11]. The optimization variables involved only composite parameters, that is, FVRs and fiber orientation angles. The baseline and resultant optimum design is shown in Table 1. Clearly, the free response of the optimized beam has been drastically improved, although the undamped dynamic amplitude was increased.

Table 1. Optimum design for Composite Beam in Impulsive Excitation

	Baseline Design	Optimum Design
Ply Angles, (degrees)		
θ_1	0.0	30.24
θ_2	0.0	30.49
θ_3	0.0	29.76
Fiber volume ratios		
k_{f1}	0.50	0.69
k_{f2}	0.50	0.53
k_{f3}	0.50	0.50

Multi-Objective Design of the Composite Beam in Forced Excitation: As a next application, a case of optimal design of the composite beam, involving the three objective functions mentioned above, is presented [13]. The assumed loading conditions involved a

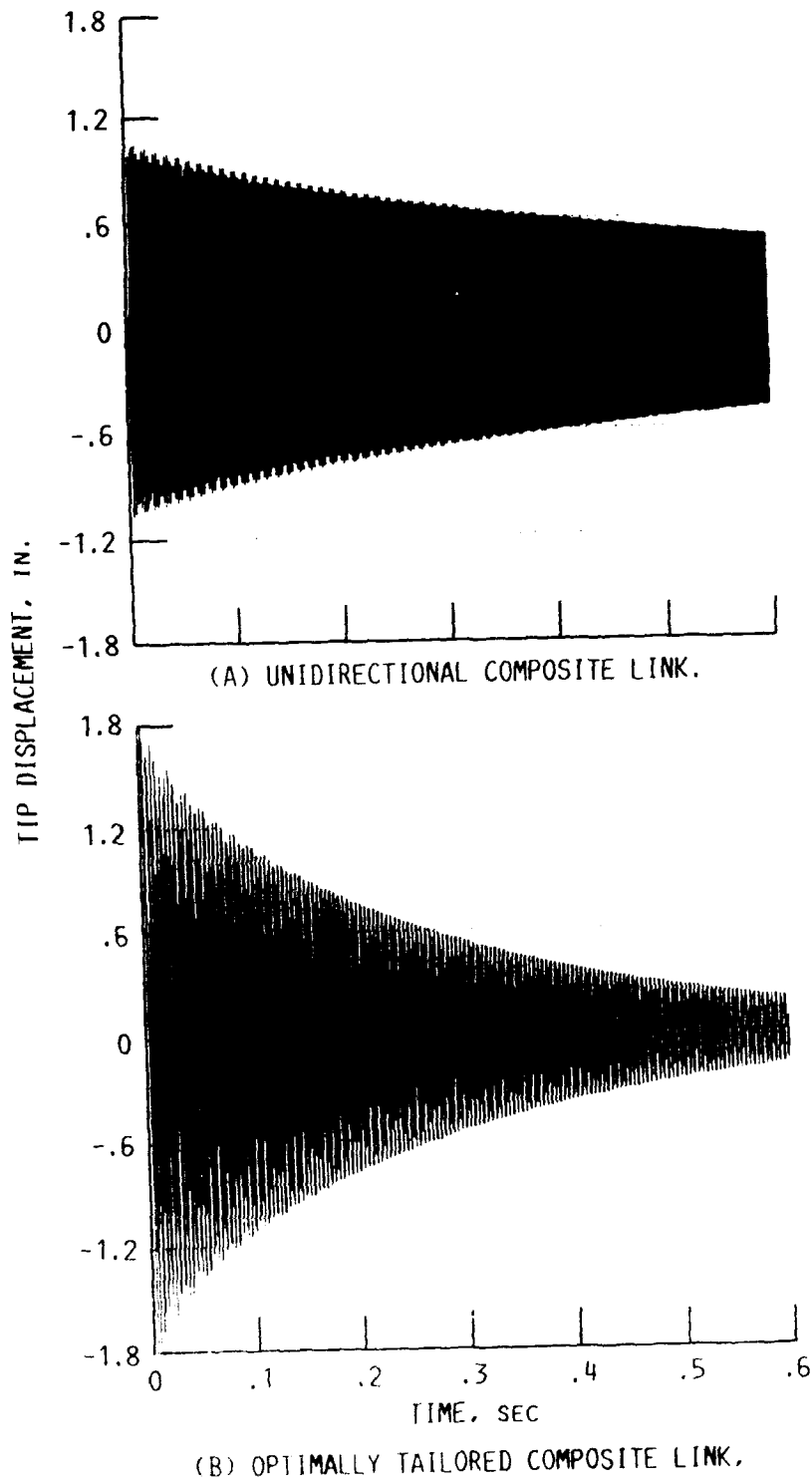


Fig. 2 Impulse response of the optimum and baseline (initial) composite beams.

combination of uniform static transverse out-of plane (y-axis) forces (50 lbs/in) and transverse out-of-plane harmonic forces (0.1 lbs/in amplitude) applied at the tip of the beam. The design variables included both composite parameters (FVRs and ply angles) and shape parameters (cross-sectional thicknesses). In addition to constraints (8) and (11), constraints included upper bounds on the transverse static deflections at the free end lower bounds on the first two natural frequencies, and upper bounds on the transverse resonance amplitudes at the tip, for each of the first four modes.

Table 2. Multi-objective optimum designs: Composite beam

	Baseline	Single-Objective Designs		Multi-Objective	
		min F1	min F2	min F3	
Ply Angles, (degrees)					
θ_1	0.0	24.68	13.55	4.306	24.46
θ_2	0.0	24.05	-41.19	41.150	53.53
θ_3	0.0	-50.33	-65.56	44.863	90.00
Fiber volume ratios					
k_{f1}	0.50	0.637	0.630	0.294	0.512
k_{f2}	0.50	0.700	0.021	0.010	0.010
k_{f3}	0.50	0.010	0.010	0.010	0.010

Table 2 also shows the baseline design, the three single-objective optimal designs (each objective function individually optimized), and the resultant multi-objective optimal design. All optimized designs have non-uniform thickness, being thicker at the proximal end and thinner at the distal end. The apparent differences among the optimal shapes demonstrate the significance of shape optimization. The relative improvements of each objective function with respect to the baseline design are plotted in Fig. 3. As seen in Fig. 3, the single-objective optimizations have failed to reduce all objective functions. Only the multi-objective optimal design produced simultaneous improvements in all design objectives.

The frequency response functions at the mid-point of the free-edge of the initial and optimized beams are shown in Fig. 4. The multi-objective optimum design has a better FRF than the minimum cost and minimum weight designs. This suggests that the incorporation of composite damping was crucial in obtaining these significant improvements in all objective functions illustrating, in this manner, the significance of composite damping in the design of high dynamic performance, light-weight, and low-cost composite

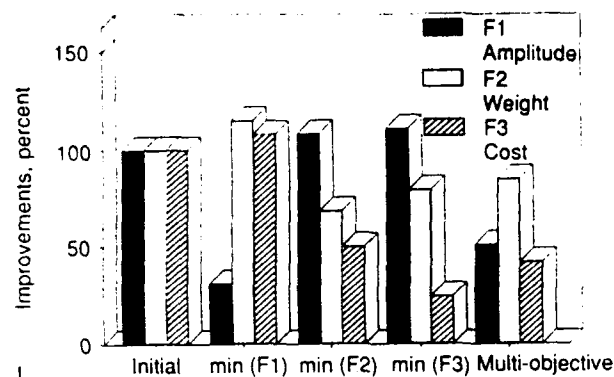


Fig. 3 Relative changes in the objective functions (composite beam).

structures.

Multi-Objective Design of the Composite Plate in Forced Excitation: The optimization of the composite plate involves additional structural complexity, therefore, the present application provides additional insight in the optimal design composite structures [13]. In this case, the loading conditions included combinations of a uniform static transverse out-of-plane (y-axis) force (3.12 lbs/in) at the free end, a uniform transverse out-of-plane harmonic force (0.0063 lbs/in amplitude) at the free end, and a harmonic moment (0.0313 lb-in/in amplitude) also applied along the free-edge of the plate. Under this type of dynamic loading, the maximum resonance amplitude at the tip typically occurs either at the first mode (first out-of-plane bending in the baseline design) or at the second mode (first torsion in the baseline design). Both composite parameters and shape variables were optimized. In addition to constraints (8), and (11), constraints included upper bounds on the transverse static deflections of the free-end, lower bounds on the first four natural frequencies, and upper bounds on the transverse resonance amplitudes of the free-end for the first four modes (Table 3).

Table 3 also presents the initial baseline design, the three single-objective optimal designs, and the resultant multi-objective optimal design. The relative changes in the objective function values with respect to the initial unidirectional plate are shown in Fig. 5. A strong tendency was observed in the optimum designs to result in "sandwich" type laminate configurations with a constrained thick matrix core (sublaminates 2, 3) and angle-ply composite skins (sublaminates 1) that provided stiffness and strength. The same tendency was also observed with the beam design but was less predominant. This inter-

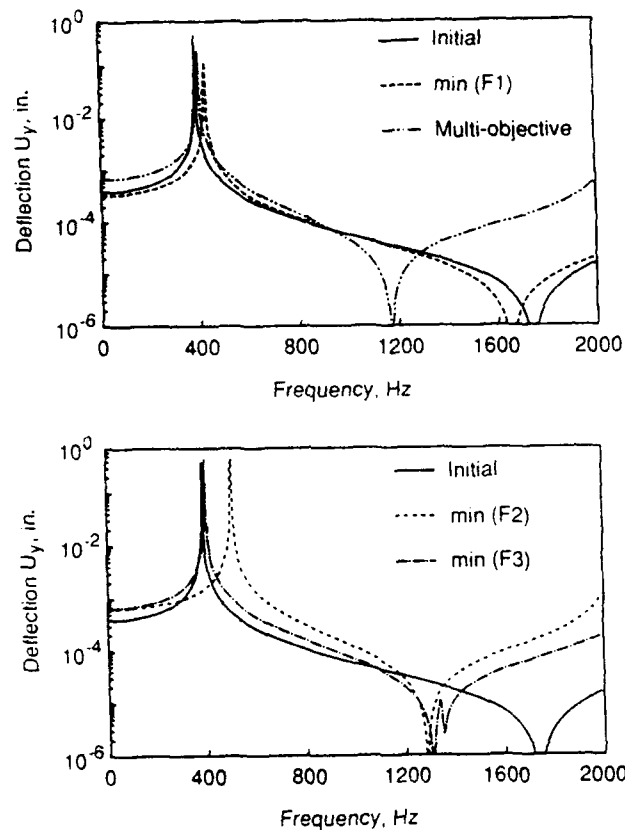


Fig. 4 Frequency response functions of the initial and optimal designs of the composite beam

esting result was the direct benefit of introducing unified micromechanics into the analysis, and consequently, the FVRs into the design parameters. The optimal designs varied drastically in optimal thickness shapes, ply angles, and FVRs, which demonstrated the inherent tendency of composite structures to get overdesigned.

The resultant frequency response functions of the transverse y-axis deflection at the foremost corner of the plate ($x=16$ in, $z=8$ in), where the maximum dynamic deflection was observed for almost all optimal designs, are plotted in Fig. 6. Interestingly, the minimum weight design has the higher resonance amplitudes, even than the baseline plate, illustrating the unsuitability of the minimum weight design for improving the dynamic performance. As both case studies illustrated, optimal design methodologies neglecting the damping capacity of composite materials and its controllable anisotropy may lead to structures with inferior dynamic performance near the resonance regimes, hence, they appear unsuitable for optimizing the dynamic performance of composite structures.

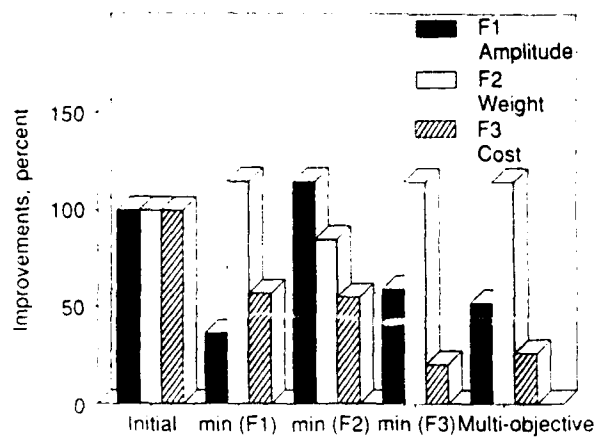


Fig. 5 Relative changes in the objective functions (composite plate).

Table 3. Multi-objective optimum designs: Composite Plate

	Baseline	Single-Objective Designs		Multi-Objective	
		min F1	min F2	min F3	
Ply Angles, (degrees)					
θ_1	0.0	11.74	24.91	33.97	24.23
θ_2	0.0	-83.10	50.38	68.88	49.92
θ_3	0.0	-4.06	56.22	-47.84	-52.70
Fiber volume ratios					
k_{f1}	0.50	0.700	0.698	0.225	0.301
k_{f2}	0.50	0.010	0.010	0.010	0.010
k_{f3}	0.50	0.010	0.010	0.010	0.010

SUMMARY

Research work at NASA-Lewis Research Center on the development of optimal design methodologies for optimizing the damping of composite structures and their dynamic performance was summarized. The design methodologies provide the option of multiple objective functions, and may tailor composite parameters at multiple scale levels of a

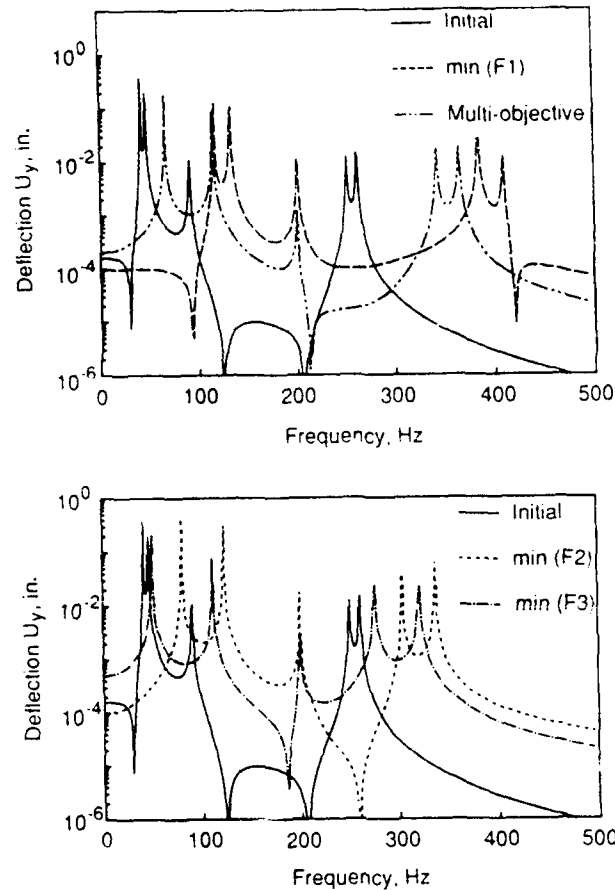


Fig. 6 Frequency response functions of the initial and optimal designs of the composite plate

composite structure. The structural dynamic analysis included the effects of composite passive damping on the dynamic response of composite structures via integrated micromechanics, laminate, and structural damping theories. Performance constraints were imposed on static displacements, static stresses, dynamic resonance amplitudes, natural frequencies, and dynamic stresses. The described method has been integrated into an in-house research code [16].

Basic application cases illustrating the optimal design of a cantilever composite beam and a cantilever plate were reviewed. All cases illustrated that optimal tailoring may significantly improve the damping capacity of composite structures and result in superior dynamic performance. It was also demonstrated that the damping capacity of composites is an important factor in designing light-weight, low-cost composite structures of improved dynamic performance. The multi-objective optimization was proved superior in minimizing the competing requirements involved. The optimizations with single-objective functions have shown a strong tendency to overdesign the structure and did not improve

all objectives. The resultant optimal designs illustrated that both material (fiber orientation angles, fiber volume ratios) and shape parameters contributed to the obtained improvements. Overall, the applications of the method appeared very encouraging. Additional studies on more complex structural configurations and dynamic excitations may well worth the effort, therefore, are recommended as future research topics.

REFERENCES

1. Saravanos, D. A. and Chamis, C. C., "Unified Micromechanics of Damping for Unidirectional and Off-Axis Fiber Composites," *Journal of Composites Technology and Research*, Vol. 12, No.1, Spring 1990, pp. 31-40.
2. Saravanos, D. A. and Chamis, C. C., "Mechanics of Damping for Fiber Composite Laminates Including Hygro-Thermal Effects," *AIAA Journal*, Vol. 28, No. 10, 1990, pp. 1813-1819.
3. Adams, R. D. and Bacon, D. G. C., "Effect of Fibre Orientation and Laminate Geometry on the Dynamic Properties of CFRP," *Journal of Composite Materials*, Vol. 7, Oct. 1973, pp. 402-428.
4. Ni, R. G. and Adams, R. D., "The Damping and Dynamic Moduli of Symmetric Laminated Composite Beams -- Theoretical and Experimental Results," *Journal of Composite Materials*, Vol. 18, March 1984, pp. 104-121.
5. Siu, C. C. and Bert, C. W., "Sinusoidal Response of Composite-Material Plates with Material Damping," *ASME Journal of Engineering for Industry*, May 1974, pp. 603-610.
6. Suarez, S. A., Gibson, R. F., Sun, C. T. and Chaturvedi, S. K., "The Influence of Fiber Length and Fiber Orientation on Damping and Stiffness of Polymer Composite Materials," *Experimental Mechanics*, Vol. 26, No. 2, 1986, pp. 175-184.
7. Saravanos, D. A. and Chamis, C. C., "Computational Simulation of Structural Composite Damping," *Journal of Reinforced Plastics and Composites*, in-press, 1991.
8. Bert, C. W., "Research on Dynamic Behavior of Composite and Sandwich Plates - IV," *The Shock and Vibration Digest*, Vol. 17, No.11, 1985, pp. 3-15.
9. Liao, D.X., Sung, C.K. and Thompson, B.S., "The Optimal Design of Laminated Beams Considering Damping," *Journal of Composite Materials*, Vol. 20, 1986, pp. 485-501.

10. Hajela, P. and Shih, C. J., "Optimum Synthesis of Polymer Matrix Composites for Improved Internal Material Damping Characteristics," *AIAA Journal*, Vol. 26, No. 4, 1988, pp. 504-506.
11. Saravanos, D. A. and Chamis, C. C., "Tailoring of Composite Links for Optimal Damped Elasto-Dynamic Performance," *Proceedings, ASME Design Automation Conference*, Vol. No. H0509C, Montreal, Canada, Sept. 17-20, 1989.
12. Saravanos, D. A. and Chamis, C. C., "A Methodology for Optimizing Structural Composite Damping," *Journal of Polymer Composites*, Vol. 11, No. 6, 1990, pp. 328-336.
13. Saravanos, D. A. and Chamis, C. C., "Multi-Objective Material and Shape Optimization of Composite Structures Including Damping," *AIAA Journal*, to appear, 1991. (Also, NASA TM-102579)
14. Murthy, P.L.N. and Chamis, C.C., "ICAN: Integrated Composite Analyzer," *AIAA Paper 84-0974*, May 1984.
15. Vanderplaats, G. N. "A Robust Feasible Directions Algorithm for Design Synthesis," *Proceedings, 24th AIAA/ASME/ASCE/AHS Structures, Structural Dynamics, and Materials Conference*, Lake Tahoe, NV, 1983.
16. Brown, K. W., "Structural Tailoring of Advanced Turboprops (STAT) - Interim Report," *NASA CR-180861*, Aug. 1988.

An Optimum Design Methodology for Passively Damped Truss Structures

R. A. Manning*
TRW Space and Technology Group
Redondo Beach, CA 90278
(213) 813-9125

ABSTRACT

Many of the complex space structures proposed for future space missions will utilize enhanced damping to meet stringent performance requirements. The enhanced damping is necessary to prevent excessive slew/settle times, unacceptable jitter levels, and harmful controls/structures interactions. There are currently no documented integrated design methodologies for designing damping into complex structures early in the design process.

In this paper, an optimum design methodology is presented for truss structures augmented with constrained layer viscoelastically damped members. The methodology is presented as a two stage procedure. In the first stage, efficient locations for the passive members are found heuristically, thus avoiding a computationally burdensome combinatoric optimization problem. In the second stage, a formal optimization procedure is used to simultaneously size both the truss members and the passive members. Values for the design variables at the optimum design are found by solving a sequence of approximate problems. Each approximate problem is constructed using design sensitivity information in conjunction with first order Taylor series expansions. The sizing-type design variables treated in the optimum design procedure are inert structural member cross sectional dimensions, passive member cross sectional dimensions, passive member viscoelastic layer and constraining layer thicknesses.

The complex space structure design problem is posed as a nonlinear mathematical programming problem in which an objective function critical to adequate mission performance (e.g., line-of-sight errors or settling time following slew) is to be minimized. Limitations considered during the design procedure include an upper bound weight cap, dynamic response constraints (which represent additional mission requirements), and side constraints on the design variables.

* Staff Engineer

INTRODUCTION

Stringent performance goals for future space missions will require minimum levels of "designed-in" damping. The necessary levels of damping can be added through either active or passive means. Active damping requires sensors and actuators, a source of power, and a compensator (control law) which gives good performance and remains stable in the wake of structural parameter uncertainty and change. Passive damping requires high loss viscoelastic or fluid materials and thermal control. For some space systems, the lack of adequate power margins and the potential for gross structural parameter perturbations suggest that passive damping methods are the method of choice.

Recent developments in analysis and fabrication techniques have led to the consideration of constrained layer viscoelastically damped members for vibration suppression. Bronowicki et al. [1] derived a special purpose finite element for use in analyzing such members. In addition, Reference 1 is notable for the fabrication and hardware verification of the passive members. Hedgepeth [2] derived simplified design equations for use with segmented constraining layer VEM damped members. His results yielded expressions for the real and complex stiffness of these members when loaded axially (i.e., when used as truss members). In order to utilize passive members on complex space structures, automated design procedures are needed which employ these analysis methods.

The approach used in the current work was to start at the element level and develop a *design-oriented procedure* for passively damped structures. Other approaches, Gibson and Johnson [3], for example, have developed system level optimization capability utilizing a prepackaged finite element code such as NASTRAN in conjunction with the ADS [4] optimizer. Because a prepackaged finite element code was used, the viscoelastic damping treatment had to be modeled using standard elements, such as the QUAD4, HEXA, and/or PENTA elements, and sensitivities had to be computed numerically. Starting at the element level allows the calculation of element design sensitivities in closed form for use with gradient-based optimization packages. The closed form element level sensitivities avoids the computational intensity of finite difference-based sensitivity information. Furthermore, the availability of inexpensive and accurate gradients gives credence to the construction of high quality approximations for use during the optimization procedure. These high quality approximations, in conjunction with a suitable nonlinear mathematical programming procedure, allows many optimum design problems to be solved in relatively few complete dynamic analyses.

In the current study, the design problem is posed as a combinatoric optimization problem in which passive member placement, inert member cross sectional dimensions, and passive member cross sectional dimensions are treated simultaneously as design variables. By designing the inert and passive members simultaneously, strain energy can be funneled into the passive members, thus yielding suitable levels of damping. The design optimization procedure is applied to a problem where purely mass and stiffness redistribution has little chance

for success due to the broadband nature of the disturbance.

OPTIMUM DESIGN PROBLEM STATEMENT

The optimum design problem used for this work is

$$\min \text{LOS}(d, t) \quad (1)$$

subject to

$$g(d, t) \leq 0 \quad (2)$$

along with the side constraints

$$d^l \leq d \leq d^u \quad (3)$$

where it is understood that d is the vector of design variables for the inert truss members and the passive members.

The design problem stated in equations (1) through (3) corresponds to a spacecraft design problem where maximum performance is obtained by minimizing a single specified performance index, such as a line-of-sight (LOS) pointing error. Other restrictions on the performance of the spacecraft, such as an upper bound mass cap, limits on the travel of key optical or sensor components, limits on the loads induced in fragile sensor/electrical assemblies, and dynamic stability margins for controlled structures, are specified as additional constraints, g .

Figure 1 contains schematics of the inert truss design elements and the passive member design elements. For the inert truss design elements, the inside diameter and wall thickness of the member are the design variables whereas the reciprocal of the cross sectional area is used as the optimization variables. For the passive members, the design variables are the inside diameter of the base tube and it's wall thickness, the thickness of the viscoelastic material, and the thickness of the constraining layer. Optimization variables for the passive members are the reciprocal of the area of the tube, the viscoelastic material, and the constraining layer. A 100% mass penalty was applied to each passive member to account for thermal control hardware.

The system optimization problem posed in equations (1) through (3) is an implicit combinatoric optimization problem. The task of placing the passive members on the structure for maximum effectiveness gives rise to the combinatoric nature of the problem. Furthermore, both the objective function and the constraints are complicated implicit functions of the design variables. A limited number of solution methods exist for this class of problems, all of which are computationally burdensome.

SOLUTION METHODOLOGY

An alternative solution methodology is to separate the combinatoric and implicit aspects of the problem and attack each subproblem individually. A flow diagram for such a procedure is shown in Figure 2. Placing the passive members at efficient locations on the structure involves solving a heuristic subproblem. One solution to the heuristic subproblem is to place the passive members in regions of high strain energy for the modes that are to be damped. Optimum values for the design variables are then found using a formal optimization procedure with the locations of the passive members fixed. The formal subproblem replaces the implicit problem posed in equations (1) through (3) with the explicit approximate problem [5]

$$\min \tilde{L}\tilde{O}S(d, t) \quad (4)$$

subject to

$$\tilde{g}(d, t) \leq 0 \quad (5)$$

along with the side constraints

$$d^l \leq d \leq d^u \quad (6)$$

where both the objective function and the constraints have been replaced by the explicit hybrid [6] first order Taylor series, $\tilde{L}\tilde{O}S$ and \tilde{g} , respectively.

Solution of the implicit optimum design problem posed in equations (1) through (3) proceeds by solving a sequence of heuristic and formal subproblems. Each formal subproblem involves solving a sequence of approximate problems (stated in equations (4) through (6)). A pictorial description of the complete solution sequence to the original optimum design problem is shown in Figure 2.

SYSTEM DESCRIPTION

The structural dynamic equations of motion for the class of problems dealt with here, namely truss structures augmented with passive members, can be written as

$$M\ddot{Z} + (K_r + K_p)Z = R \quad (7)$$

where R is the vector of externally applied loads, M is the mass matrix, K_r is the real portion of the structural stiffness matrix, and K_p is the complex portion of the stiffness matrix. The complex portion of the stiffness matrix arises due to the complex material properties of the viscoelastic material. Using the undamped normal modes of the structure, namely,

$$Z = \phi q \quad (8)$$

equation (7) can be cast in reduced size first order form as

$$\dot{X} = AX + BR \quad (9)$$

where the system plant matrix is given by

$$A = \begin{bmatrix} 0 & I \\ -\omega^2 & -\phi^T K_p \phi \end{bmatrix} \quad (10)$$

the state X is the vector of stacked modal displacements and velocities

$$X = \begin{Bmatrix} q \\ \dot{q} \end{Bmatrix} \quad (11)$$

and the input matrix is

$$B = \begin{bmatrix} 0 \\ \phi^T R \end{bmatrix} \quad (12)$$

The M and K_s matrices are computed for the truss elements in the usual finite element manner. The K_s and K_p matrices are computed for the segmented constrained layer passive members using the analysis methodology presented in Reference 2. The effective stiffness of the passive member can be written in terms of the stiffness of the tube wall, k_w , and the stiffness of the constraining layer, k_c , as

$$k_{eff} = \frac{k_w + k_c}{1 + \frac{k_c}{k_w} \frac{\tanh(Dl)}{D}} \quad (13)$$

The D parameter is related to the shear lag length τ by

$$D = \frac{l}{2\tau} \quad (14)$$

The shear lag length, which is used for determining the lengths of the segments of the constraining layer, is given by

$$\tau = \sqrt{\frac{E_c t_c t_{vem}}{G_{vem}}} \frac{1}{1 + \frac{E_c t_c}{E_w t_w}} \quad (15)$$

where G_{vem} is the complex shear stiffness of the VEM. Sensitivity information at the element level is found by taking the derivative of the effective stiffness of the passive member with respect to the design variables.

Solution of equation (9) for the system response due to external loads is accomplished by computing the complex modes of the system plant A and solving the resulting uncoupled equations in the frequency domain.

EXAMPLE PROBLEM

The structure shown in Figure 3 will be used to demonstrate the benefits of the previously-described optimization procedure. The structure is a scaled version of a proposed Space Based Interferometer [7]. Two 13 meter arms run out from the sides of the interferometer and hold light-collecting telescopes at the tips. The 11 meter tower contains a telescope running down its center while laser metrology equipment is mounted at the end of an additional 11 meter truss. In an undeformed, perfectly-aligned state, the two 13 meter arms give an optical path length (baseline) of 26 meters.

Dynamic disturbances from the attitude control system reaction wheels are fed into the structure at the central bay. The interferometer can acquire data when the relative alignment (tip and tilt) of the collecting telescopes is less than $8\mu\text{rad}$ and the optical path length does not substantially deviate from 26 meters. Therefore the design optimization problem is to minimize path length deviations from 26 meters while maintaining relative tip and tilt of the collecting telescopes within $8\mu\text{rad}$. An upper bound mass cap of 252 kg is also imposed on the system. This cap corresponds to the preliminary design mass of the completely inert system (without passive member augmentation).

The purely inert preliminary design of the SBI was used as the point of departure for the optimum design procedure. The performance of the interferometer at the preliminary design is shown in Figure 4. Unacceptable optical lengths and relative tip and tilt motion of the collecting telescopes exceeding $8\mu\text{rad}$ were obtained. The modes at 4.4, 16.4, 19.0, 27.7, and 36.9 Hz needed damping augmentation to achieve the performance goals. It should be noted that purely structural methods (i.e., mass and stiffness redistribution) are doomed to failure in this case because of the wide band disturbance and the stringent performance levels required. Locations for the passive members were determined by examining regions of high strain energy for the modes which needed damping augmentation. This, in effect, results in a solution to the heuristic placement subproblem. A total of 56 passive members were added to the system.

The performance of the interferometer following optimization is shown in Figure 4. Optical length deviations have been reduced from $3.16\mu\text{m}$ to $0.11\mu\text{m}$ while bringing the relative tip and tilt motion of the collecting telescopes down to acceptable levels. The peak tip and tilt motions at the optimum design are $7.5\mu\text{rad}$ and $7.8\mu\text{rad}$, respectively, having been reduced from $27.7\mu\text{rad}$ and $48.3\mu\text{rad}$ at the initial design. A comparison of damping levels at the initial design and the optimum design for each of the modes below 40 Hz are shown in Table 1. Though a large number of passive members were added, the design optimization procedure managed to meet the mass cap of 252 kgs and reduce the interferometer baseline by a factor of 28.7.

Table 1: Initial and Optimum Frequencies and Damping Ratios

Mode Number	Initial Design		Optimum Design	
	Frequency (Hz)	ζ (%)	Frequency (Hz)	ζ (%)
1-6	0.0	0.0	0.0	0.0
7	4.4	0.2	4.1	4.7
8	6.5	0.2	6.1	3.9
9	7.2	0.2	6.8	2.0
10	8.4	0.2	7.9	4.5
11	8.5	0.2	7.9	3.4
12	12.9	0.2	12.0	3.7
13	16.4	0.2	14.8	4.1
14	19.0	0.2	17.3	2.9
15	19.2	0.2	17.8	3.2
16	21.7	0.2	20.6	0.6
17	24.5	0.2	22.0	3.9
18	27.7	0.2	24.6	5.3
19	29.1	0.2	26.9	3.1
20	36.9	0.2	33.6	4.6

CONCLUDING REMARKS

An integrated inert truss/passive truss member design optimization methodology has been developed. The methodology treats both structural design variables and passive member design variables simultaneously in the optimization procedure. By employing a two stage heuristic/formal subproblem solution procedure, the computational burden associated with placing the passive members on the structure is avoided. A solution for the implicit formal subproblem is found in relatively few complete dynamic analyses by solving an explicit approximate problem. Design sensitivity information was efficiently computed by differentiating a closed form expression for the complex stiffness of the passive members. The design optimization procedure is a mission-enabling technology for future space missions with extremely stringent dynamic performance requirements where purely structural solutions fail.

REFERENCES

- [1] Bronowicki, A.J. and Diaz, H.P., "Analysis, Optimization, Fabrication and Test of Composite Shells with Embedded Viscoelastic Layers", *Proceedings of Damping '89*, West Palm Beach, Florida, February 8-10, 1989, pp. GCA-1-GCA-21.
- [2] Hedgepeth, J.M. and Mobren, M., "Investigation of Passive Damping of Large Space Truss Structures", *Proceedings of Damping '86*.

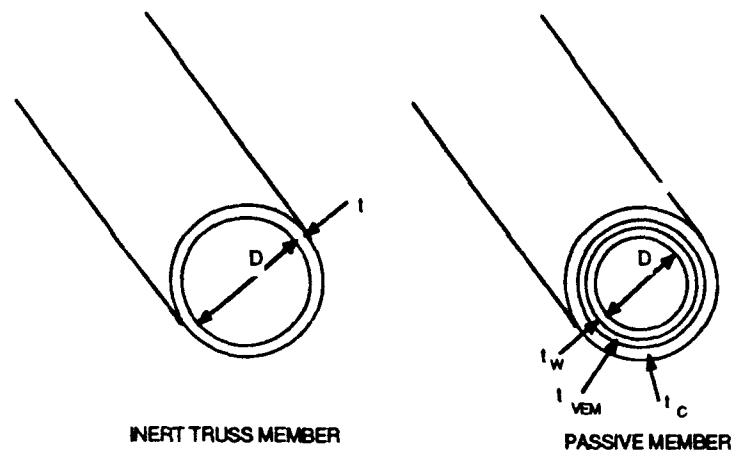


Figure 1: Inert Truss and Passive Member Design Elements

- [3] Gibson, W.C. and Johnson, C.D., "Optimized Designs of Viscoelastic Damping Treatment" *Proceedings of Damping '89*, West Palm Beach, Florida, February 8-10, 1989, pp. DBD-1-DBD-23.
- [4] Vanderplaats, G.N., "ADS - A Fortran Program for Automated Design Synthesis", Version 1.10, May 1985. Available from VMA Engineering, 5960 Mandarin Avenue, Suite F, Goleta, California, 93117.
- [5] Schmit, L.A. and Miura, H., "Approximation Concepts for Efficient Structural Synthesis", NASA CR 2552, March 1976.
- [6] Starnes, J.R. and Haftka, R.T., "Preliminary Design of Composite Wings for Buckling, Stress, and Displacement Constraints", *Journal of Aircraft*, Vol. 16, Aug. 1979, pp. 564-570.
- [7] Laskin, R.A., "A Spaceborne Optical Interferometer: The JPL CSI Mission Focus", *Proceedings of the NASA/DoD Controls-Structures Interaction Technology Conference*, NASA CP 3041, San Diego, California, January 29-February 2, 1989, PP. 1-16.

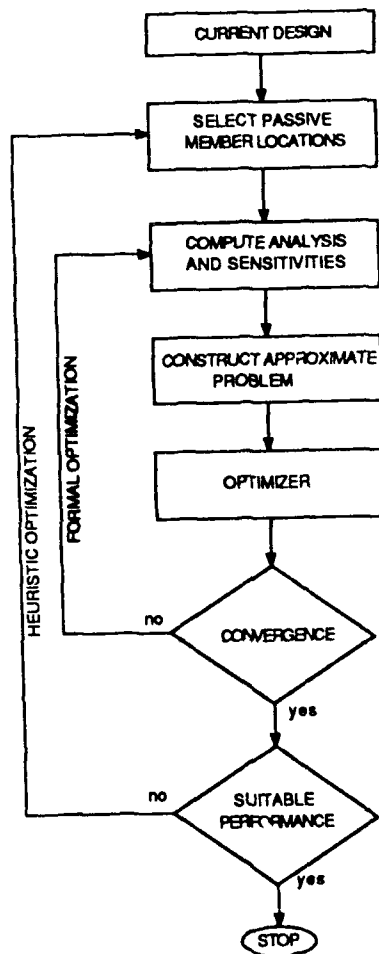


Figure 2: Optimum Design Solution Procedure

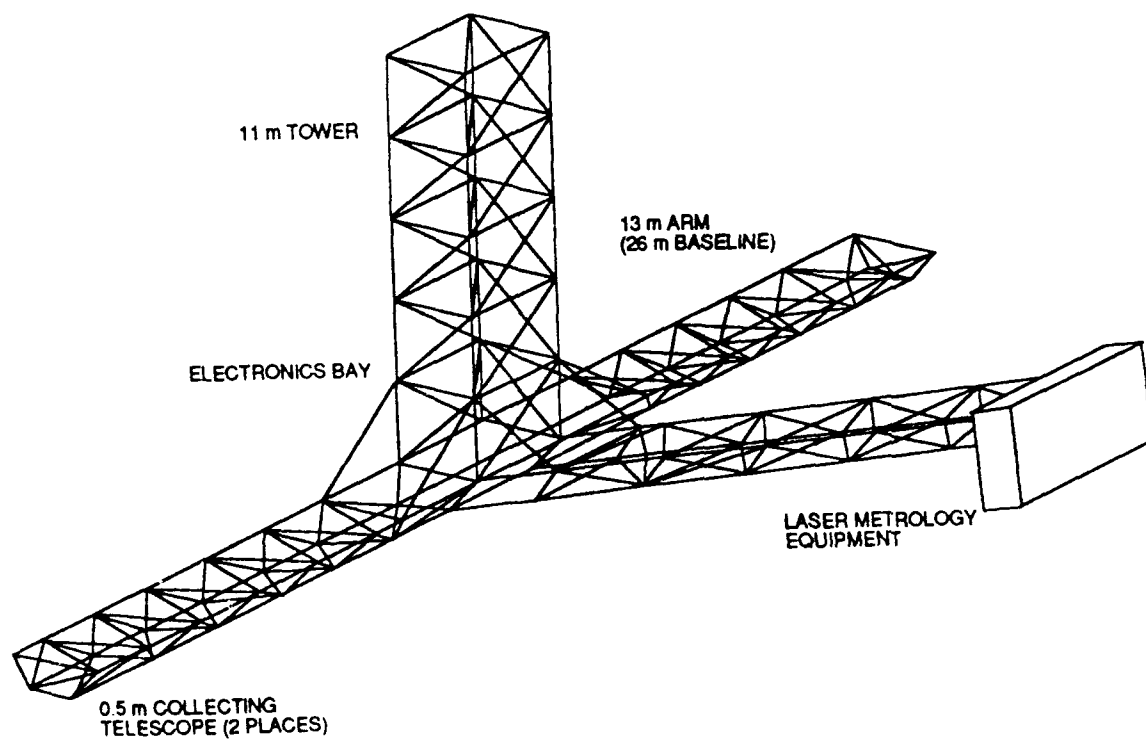


Figure 3: Space Based Interferometer

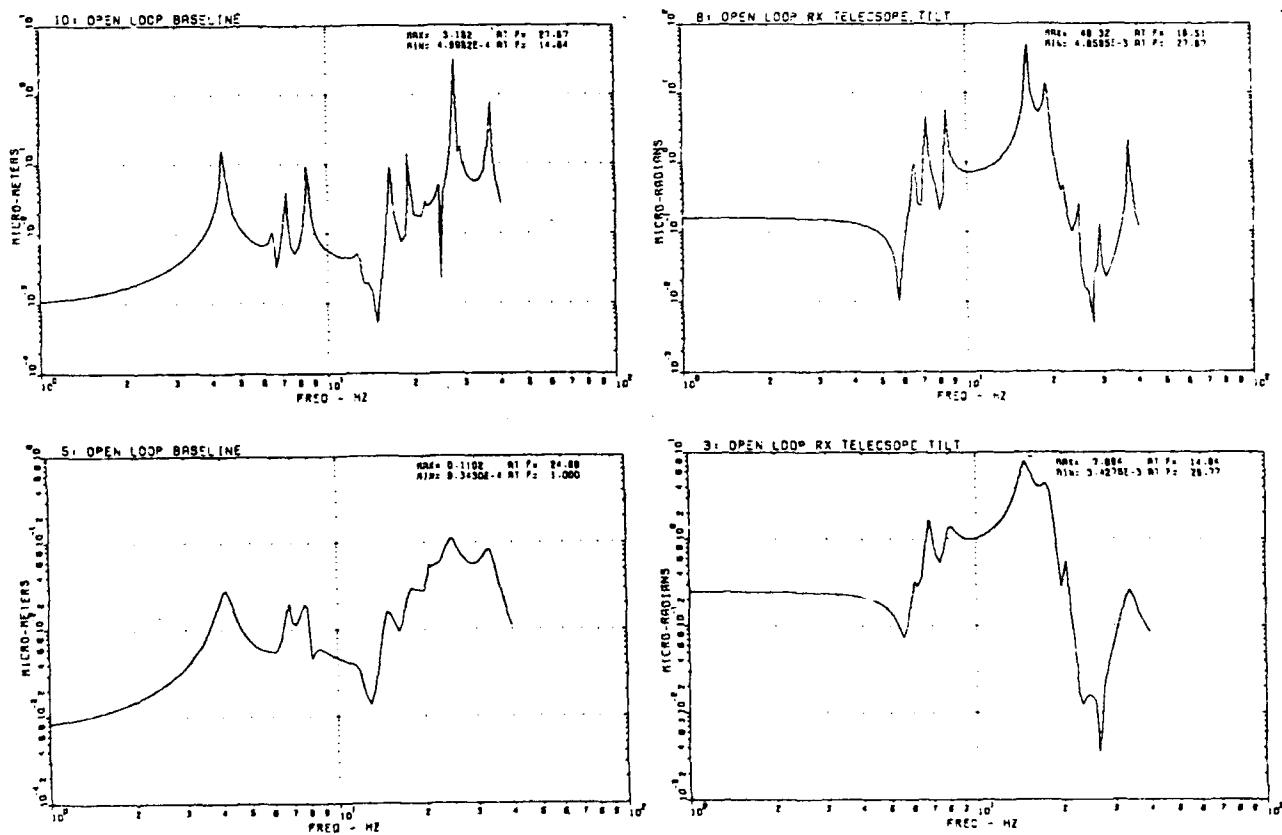


Figure 4: Initial and Optimum Design Dynamic Responses

ON AN APPLICATION OF COMPLEX DAMPING COEFFICIENTS

M. Tong, Z. Liang, and G. C. Lee

412 Bonner Hall
State University of New York at Buffalo
Amherst, NY 14260

ABSTRACT

Complex damping theory is a useful tool in analysis of energy transformations among modes of a vibration system. Based on this theory, there are many applications and improvements in the areas of system identification, vibration control and damper optimization design.

This paper presents an application of the theory in regard to finite element model corrections. First, a common shortfall of usual correction procedures is analyzed. In order to deal with this problem, a correct correspondence rule is then proposed. With the help of complex damping coefficients, improvements to certain correction procedures are discussed.

INTRODUCTION

The dynamic performance of a structure may be characterized by different mathematical models. Among them, the modal model and the physical model are most frequently seen. A modal model which consists of a set of modal parameters is often used in harmonic-related vibration control, in dynamic behavior analysis, and in physical model modification. Since a modal model is essentially a dynamic representation of the physical model in the modal domain. The transformation of physical coordinates into modal coordinates is always accompanied by a certain loss of information, a modal model is generally considered to be a weak model but relatively easy to obtain.

A physical model consists of three coefficient matrices: The mass, damping and stiffness matrices. If such a model is known, all the modal parameters can be calculated. Conversely, a physical model can not be determined in general from a modal model. In this regard, a physical model is considered superior than a modal model.

In engineering practice, a physical model is not always available because not all the coefficient matrices can be directly measured. The measurable quantities are often the various dynamic responses and modal parameters of the structural system. Based on these data, we can typically generate an approximate model - an analytical model, using the finite element method (FEM). In most cases, the analytical model is inaccurate and requires various adjustments or corrections. In the past decades, many attempts have been made to develop better algorithms to modify the FEM models. At present, the need to develop appropriate algorithms continues to exist.

From the analytical model to the physical model, an important step is to perform model corrections. In a general model correction procedure, the goal is to obtain a set of coefficient matrices, mass M , damping C and stiffness K . What we have at the beginning is the analytical model data $M^{(a)}$, $C^{(a)}$ and $K^{(a)}$, along with some dynamic parameters of the physical model, such as measured response $X^{(m)}$ and/or modal parameters: Undamped natural frequencies $\Omega^{(m)}$, damping ratios $\Xi^{(m)}$ and mode shapes $p^{(m)}$. In

each step of the corrections, we obtain certain corresponding matrices $M^{(1)}$, $C^{(1)}$ and $K^{(1)}$ as approximations to the real M , C and K . Then we typically compare the measured response $X^{(m)}$ and/or modal parameters $\Omega^{(m)}$, $\Xi^{(m)}$ and $P^{(m)}$, with the calculated response $X^{(1)}$, and/or modal parameters $\Omega^{(1)}$, $\Xi^{(1)}$ and $P^{(1)}$ from the revised analytical model. If the discrepancy between the two sets of data is less than a certain preset level, then the revised analytical model is accepted as the physical model. Otherwise, the correction procedure is continued.

In such a correction procedure described above, a number of factors can influence the final result. There are many existing algorithms that do not converge in general. For those that converge may have problems in targeting the correct M , C and K because the comparison criterion used is not sufficiently comprehensive.

In this paper, we propose an alternative judgment on the effectiveness of model corrections. Our discussions will be restricted to finite element models and their corrections under the assumption that the models are linear, time-invariant and have lumped-masses.

RESPONSE-FITTING

One of the simplest model correction methods is the time domain *response-fitting*. In order to carry out this method, a time history (or transfer function) of the testing structure must first be recorded. The time history can be a free decay response with an initial input such as sine-burst, white noise-burst, impulse, etc. Or it can be a forced response under an excitation such as sinusoidal, sine-sweep, sine-dwell, pseudo white-noise or simulated seismic ground motion. In a carefully conducted experiment, the measured response is considered "noise-free". Thus it is ready to be used as the correction reference. Once the reference is available, corresponding samples are collected from a calculated response of the analytical model with same initial phases and time intervals. Then by using certain mathematical techniques such as the least-square method or the maximum-likelihood method, a cost function is generated to measure the discrepancy between the two responses. Equation (1) gives a least-

square cost function (Natke, 1988).

$$J = \sum_{i=1}^p \sum_{j=1}^n \alpha_{ij} (x_{ij}^{(m)} - x_{ij}^{(a)})^2 \quad (1)$$

where, $x_{ij}^{(m)}$ and $x_{ij}^{(a)}$ are the i^{th} samples of measured and calculated responses from the j^{th} node respectively. The total number of samples from each source is p and the number of nodes is n . α_{ij} are weighted coefficients. In general, at certain nodes, samples are measured more accurately than at other places, the weighted coefficients of these samples will then be assigned with greater values. Conversely, the tail of a free decay response is thought to have poor signal-to-noise ratio, the weighted coefficients of samples from this portion will be assigned with smaller values.

The value of J indicates whether the analytical model is close to the physical model. When the response of the analytical model does not fit the response of the structural system, J will assume a large value. Corrections to the analytical model will then be made to reduce the value of J .

Due to several reasons, response-fitting is often considered unsatisfactory in terms of its model correction effect. First, when a given excitation with a nearly straight spectrum, the structural response should theoretically incorporate the influences of all modes of the structural system. However, lower modes are usually associated with large percentage of the total energy involved, these modes have dominate influence to the response. In fact, most engineering applications only require to consider the first mode. Therefore, information from the higher modes may be lost in the response.

Secondly, despite the measured response being assumed noise-free, noise can not be completely eliminated. The commonly used noise-reduction techniques in response-fitting are essentially pre-treatments such as averaging the noise in the frequency domain. Since the participating factors of higher modes are relatively small, these modes give poor signal-to-noise ratios. The existence of these modes can hardly be identified in a response function. Consequently, the order of the

reference can not be determined by the response-fitting method unless more sophisticated time domain modal analysis is used. It is conceivable that without prior knowledge of the reference order, response-fitting is more likely to accept a degenerate model with only the first few modes of the real structural system.

Thirdly, the higher modes decay faster than the lower modes in a free decay response. This may also induce the problem of losing information from the higher modes in a recorded response.

EXAMPLE 1: Figure 1 (a) shows a five story structure. This model steel frame is considered to have at least fifteen degrees-of-freedom. A free decay time history measured at a point on the third floor of the frame is shown in Figure 1 (b). Two other responses are also given here. They are calculated responses from two analytical models one with 2 DOF the other with 3 DOF. Although the 15 DOF structure should not be treated as a 2 or 3 DOF system, by using response-fitting, we could have accepted the 2 or 3 DOF analytical model as the real physical model.

FREQUENCY-FITTING

Frequency-fitting is another commonly applicable method for model corrections. The reference in this method is the measured natural frequencies which are either obtained directly from vibration test or extracted through modal analysis. The two ways give damped and undamped natural frequencies respectively. The number of the natural frequencies collected in the reference corresponds to the order of the structural system. So there has no problem in determining the number of modes in the system. The cost function is given by

$$J = \sum_{i=1}^n \alpha_i (\omega_i^{(m)} - \omega_i^{(a)})^2 \quad (2)$$

where $\omega_i^{(m)}$ and $\omega_i^{(a)}$ are the measured and calculated undamped natural frequencies of the i^{th} mode respectively. α_i are the corresponding weighted coefficients. Since this method utilizes information from all relevant natural frequencies, which have been accurately measured, it has

better overall performance over the response-fitting method. Especially, frequency-fitting is suitable for correcting models with many higher modes

Equation (2) can be further modified by including both the natural frequencies and the damping ratios in J .

$$J = \sum_{i=1}^n \alpha_i (\omega_i^{(m)} - \omega_i^{(a)})^2 + \beta_i (\xi_i^{(m)} - \xi_i^{(a)})^2 \quad (3)$$

where $\xi_i^{(\cdot)}$ denotes the i^{th} damping ratio of (m) or (a). This improved Equation (3) is suitable for correcting models demanding high accuracy for both natural frequencies and damping ratios.

A useful variation of the above method is the less accurate FRF curve-fitting technique. Similar to Equation (1), the cost function in this case is

$$J = \sum_{i=1}^p \alpha_i (f_i^{(m)} - f_i^{(a)})^2 \quad (4)$$

where $f_i^{(\cdot)}$ is the i^{th} sample taken from the reference FRF (m) or the analytical FRF (a). p is the total number of samples. Selection of weighted coefficients is empirical. If the FRF samples are collected from a forced response with a feedback controlled excitation whose input spectrum has been kept a straight line, then α_i are the same for all $i = 1, \dots, n$.

In using Equation (2), a correspondence between the referential and the analytical frequencies must be established first. One such correspondence is described below.

Consider the two sets of natural frequencies

$$\{ \omega_i^{(m)} \mid i = 1, \dots, n \} \quad \text{and} \quad \{ \omega_j^{(a)} \mid j = 1, \dots, n \}.$$

First, arrange them by a linear ordering

$$\begin{aligned} \omega_{i_1}^{(m)} &\leq \omega_{i_2}^{(m)} \leq \omega_{i_3}^{(m)} \leq \dots \leq \omega_{i_n}^{(m)} \\ \omega_{j_1}^{(a)} &\leq \omega_{j_2}^{(a)} \leq \omega_{j_3}^{(a)} \leq \dots \leq \omega_{j_n}^{(a)} \end{aligned} \quad (5)$$

where the subscripts are some permutations of $1, 2, \dots, n$. Then the frequencies are paired according to the ordering. With this one-one

correspondence, Equation (2) can be restated as

$$J = \alpha_1 (\omega_{i_1}^{(m)} - \omega_{j_1}^{(a)})^2 + \alpha_2 (\omega_{i_2}^{(m)} - \omega_{j_2}^{(a)})^2 + \dots + \alpha_n (\omega_{i_n}^{(m)} - \omega_{j_n}^{(a)})^2$$

Such a correspondence has the nice mathematical property that it gives the cost function J the smallest value when the weighted coefficients in Equation (2) are the same.

There are some problems with response-fitting method too. This can be seen from the following example.

EXAMPLE 2: A 4 DOF structure is shown in Figure 2 (a). Its physical model and an analytical model have the generalized damping and stiffness matrices as given in Table 1 (a), (b) respectively. Figure 2 (b) gives two FRF's, in which the dotted curve is from the physical model and the dashed curve is from the analytical model.

Table 1 (a) Generalized Damping Matrices $M^{-1}C$

Physical	Analytical
27.3598 -19.2436 -22.8993 24.2555	6.3384 -1.3278 -1.2976 0.6308
32.2713 1.7445 -23.1446	3.1574 -0.7730 -1.1894
43.2177 -32.4571	3.1408 -1.6335
49.1511	2.5634

Table 1 (b) Generalized Stiffness Matrices $M^{-1}K \quad 1,000 \times$

Physical	Analytical
8.3284 -2.7139 -2.6032 2.3111	8.3130 -2.7085 -2.5973 2.3056
1.8560 0.1289 -0.8413	1.8549 0.1266 -0.8398
2.3377 -1.5225	2.3361 -1.5209
1.4619	1.4607

It is clear that the generalized damping matrices of these two models are quite different. In fact, the physical model is non-proportionally damped whereas the analytical model is proportionally damped. (most finite element algorithms only generate proportionally damped models). Consequently, the mode shapes of these two models are different. The first

model has complex-valued mode shapes but the second has only real-valued ones. Such differences can not be detected in a single pair of frequency response functions. Therefore, curve-fitting FRF or frequency-fitting is inadequate for correcting errors in such category. This is seen in Figure 2 (b), where, in spite of the aforementioned differences between the two models, the two FRF still appear to be close.

COMPLETE MODAL-FITTING

A more sophisticated fitting method is developed by include the mode shape influences into the cost function, namely

$$J = \sum_{i=1}^n \alpha_i (\omega_i^{(m)} - \omega_i^{(a)})^2 + \beta_i (\xi_i^{(m)} - \xi_i^{(a)})^2 + (\mathbf{p}_i^{(m)} - \mathbf{p}_i^{(a)})^H \Gamma_i (\mathbf{p}_i^{(m)} - \mathbf{p}_i^{(a)}) \quad (6)$$

where $\mathbf{p}_i^{(\cdot)}$ is the i^{th} mode shape, and Γ_i is a diagonal matrix which consists of weighted coefficients. A simplified version of Equation (6) is

$$J = \sum_{i=1}^n \alpha_i (\omega_i^{(m)} - \omega_i^{(a)})^2 + (\mathbf{p}_i^{(m)} - \mathbf{p}_i^{(a)})^H \Gamma_i (\mathbf{p}_i^{(m)} - \mathbf{p}_i^{(a)}) \quad (7)$$

Since the complete set of modal parameters is employed in Equation (6), it is called the *complete modal-fitting*. However, complete modal-fitting does not always give a satisfactory correction to an analytical model. One problem is related to the mode shapes. For example, the error in a measured mode shape could reach as high as 500%. (Liang & Inman 1988). Under this circumstance, the weighted coefficients Γ_i must be assigned with very small values. Therefore, the modification effect from mode shapes is limited.

WEAKNESS OF AVAILABLE CORRECTION METHODS

In the preceding sections, we briefly reviewed some commonly used model correction procedures. None of these methods is sufficient in terms of the correction effectiveness. There are certain types of errors in the analytical model that may not be eliminated through the model corrections.

One of the shortfalls is that the cost function J is based on numerical judgments of some necessary but not sufficient properties of the model. Therefore, no matter how small the value of J could be reduced to, the correction effect still may not be greatly improved. In addition, there exist possible experimental errors as well. So it is necessary to establish more suitable criteria for evaluations of the correction effects.

The goal of model correction is to obtain the correct M , C , and K matrices. However, in many engineering applications, it is the properties of the structural system that are of our interests. As described at the introduction section, using the M - C - K model we can calculate these system's properties. On the other hand, when some of the properties the systems are known such as the order of the system, they may be used in model corrections. Following this line of thought, we can consider and treat model correction on the basis of its ability of preserving system properties in addition to its ability to satisfy the prescribed numerical criteria such as cost function J . Since there is no single property of the system that is strong enough to guarantee the correctness of the physical model (at least it is the case at present), the best analytical model is the one that preserves most properties of the system.

CORRECT CORRESPONDENCE AND ITS INTERPRETATION IN MODEL CORRECTIONS

Consider again the 5-story structure shown in Figure 1 (a). A diagrammatic finite element representation generated according to the real measurements is shown in Figure 3 (a). In Figure 3 (b) and (c), the modal deformations of the first and second modes of the structural system are illustrated. Figure 3 (b) shows a simple translational mode and Figure 3 (c) shows a simple torsional mode. In more complicated situations, modes of the structural system may not be as simple as the ones given in these figures. Nevertheless, they possess distinct modal deformations, which are the most basic dynamic performances of the structural system. Since the structural system for testing is also the object for finite element modeling, the modal deformations of the modes obtained from the two approaches should be essentially the same, despite of numerical disparities due to the errors of measurements and calculations. Based on

this observation, we investigate in the following some possible model correction methods that make the revised analytical model preserve similar modal deformations as the real structural system.

The invariance of modal deformations for the modes in both physical and analytical models can be characterized by the correct correspondence between the modes (system eigenvalues and system eigenvectors) of the two models. Conceptually, it is easy to understand that such a correspondence should relate the modes with similar deformations to each other. To establish such correspondence however, we have to define the correct correspondence in terms of model elements. In usual, the stiffness K and the mass M of the analytical model are obtained with more accuracy than damping matrix C , a correct correspondence can be obtained easily between the stiffness eigenvalues of the physical and analytical models. Since each individual mode is dominated by an unique stiffness eigenvalue, we can achieve the correct correspondence of modes of the physical and analytical models by first numbering the modes in each model with respect to the given subscripts of the stiffness eigenvalues in that model, and then relate the modes according to the correct correspondence between the stiffness eigenvalues of the two models.

Examine the governing equation

$$M\ddot{X} + C\dot{X} + KX = F \quad (8)$$

where M , C and K are mass, damping and stiffness matrices respectively. Vectors \ddot{X} , \dot{X} , X and F denote the acceleration, velocity, displacement and forcing function respectively. In free vibration, F is zero. Equation (8) becomes

$$M\ddot{X} + C\dot{X} + KX = 0 \quad (9)$$

Applying some matrix operations to Equation (9), we obtain the following D- Λ_k model

$$I\ddot{Y} + D\dot{Y} + \Lambda_k Y = 0 \quad (10)$$

where I is an identity matrix, and $Y = Q^T M^{1/2} X$

$$D = Q^T M^{-1/2} C M^{-1/2} Q \quad \text{and} \quad \Lambda_k^T = Q M^{-1/2} K M^{-1/2} Q = \begin{bmatrix} \omega_1^2 & & \\ & \omega_2^2 & \\ & & \ddots \\ & & & \omega_n^2 \end{bmatrix}$$

Q is an orthogonal matrix. This is called the canonical vibration model (Liang et al 1990). Its advantage over the general vibration model (9) lies in the simplification of M and K matrices. With Λ_k diagonal, the stiffness eigenvectors in this model are always e_i (the unit vectors) $i = 1, 2, \dots, n$. Now we discuss how to number the modes with respect to subscript i .

In the case of a proportionally damped system, it is known that Caughey's criterion (Caughey, 1976)

$$D \Lambda_k = \Lambda_k D \quad (11)$$

is satisfied. Using Equation (11), we can find an orthogonal matrix R . By applying R from the left and the Hermitian transpose of R from the right to Equation (10), we have a canonical model with both RDR^H and $R\Lambda_k R^H$ diagonal. Such a system is completely decoupled. There are n separate single DOF equations each of which corresponds to a mode of the system. The numbering is easily determined in the way that the eigenvalue of the i^{th} equation,

$$\ddot{y}_i + d_i \dot{y}_i + \omega_i^2 y_i = 0$$

is assigned with subscript i .

Let $\lambda_1, \lambda_2, \dots, \lambda_n$ denote the system eigenvalues and p_1, p_2, \dots, p_n denote the mode shapes of an canonical model. A recent result by Liang et al (1990) offers another convenient way to obtain the numbering. The result unfolds the following property of a proportionally damped system

$$\lambda_i \bar{\lambda}_i = \omega_i^2 \quad i = 1, 2, \dots, n \quad (12)$$

where ω_i^2 is the i^{th} eigenvalue of the stiffness matrix. The subscript i in (12) enumerates the system eigenvalues such that it gives an one-one correspondence between the system eigenvalues λ and eigenvalues ω^2 of the stiffness matrix. Since the inverse of this result is also valid, a system satisfying (12) is automatically proportionally damped and possesses the desired numbering.

Using complex-damping coefficients, the above numbering can be justified in terms of the system energy relations. By definition, a complex-damping coefficient is a generalized Rayleigh quotient

$$\alpha_i = a_i + b_i j = \frac{\mathbf{q}_i^T \mathbf{D} \mathbf{p}_{r_i}}{\mathbf{q}_i^T \mathbf{p}_{r_i}} \quad i = 1, 2, \dots, n$$

where \mathbf{q}_i is an eigenvector of stiffness matrix, \mathbf{p}_{r_i} is a system eigenvector. a_i and b_i are the real and imaginary parts of α_i . For a different numbering of the system's modes, we usually get a different set of corresponding complex-damping coefficients. Otherwise the generalized Rayleigh quotients are not defined at all. As reported by Liang and Lee (1990), there is one correct set of complex-damping coefficients which can be used to describe the energy transformations among the modes of a vibration system. In their report a complex damping ratio μ_i is defined as

$$\mu_i = \alpha_i / 2 \omega_i \approx \xi_i + j \zeta_i$$

where ω_i is the i^{th} undamped natural frequency and ξ_i is the i^{th} damping ratio. The ζ_i is a ratio of the energy transformed in a cycle over the total energy stored before the cycle in the i^{th} mode. If ζ_i is zero, μ_i has no imaginary part. Thus there is no energy transformed into or out of the i^{th} mode. Consequently, such a mode can be decoupled from the system. By this theory, the set of correct complex-damping coefficients for a proportionally damped canonical vibration model is a set of real-valued scalars, because in such model every mode can be decoupled. This condition is satisfied by the complex-damping coefficients calculated with the numbering described earlier. In fact, this numbering is the only one that satisfies the requirement $\mathbf{q}_i^T \mathbf{p}_{r_i} \neq 0$, for complex-damping coefficients.

For non-proportionally damped systems, the correct numbering is also associated with the correct set of complex-damping coefficients, which describe the energy transformations among the coupled modes. Although a natural generalization of the numbering discussed for proportionally damped systems, namely relating a stiffness eigenvalue ω^2 with a closest $\bar{\lambda}$, is not correct in general for non-proportionally damped systems, (see Tong et al), given the correct set of complex-damping coefficients, the correct numbering is shown to be unique (see Tong et al). Therefore, we can search the correct numbering from the complex-damping coefficients.

By using the correct correspondence of modes in model corrections, individual modes in the corrected model preserve their deformations. In most cases, we may produce a model having similar energy transformation pattern to the physical model. Due to the limit of space, we omit the examples.

COMPLEX DAMPING FITTING AND EIGEN-MATRIX FITTING

The first way to improve the correction procedures is to use the complex-damping coefficients to determine the correct correspondence. The imaginary part of a complex-damping ratio satisfies

$$\omega_i = \omega_{n_1} \exp(\zeta_i), \quad i = 1, 2, \dots, n \quad (13)$$

when the system is lightly damped, i.e.

$$|\mu_i| \leq 0.3, \quad i = 1, 2, \dots, n. \quad (14)$$

Equation (14) is satisfied with most engineering structures.

In Equation (14), ω_{r_1} is the square root of the r_1^{th} eigenvalue of the generalized stiffness matrix, where r_1 is a designated permutation of 1, 2, ..., n. Thus, by using equation (14) and μ_i , we can determine the correct correspondence quantitatively.

We propose a improved model correction criterion as follows.

$$J = \sum_{i=1}^n \alpha_i (\omega_i^{(m)} - \omega_i^{(a)})^2 + \beta_i (\xi_i^{(m)} - \xi_i^{(a)})^2 + \gamma_i (\zeta_i^{(m)} - \zeta_i^{(a)})^2 + (p_i^{(m)} - p_i^{(a)})^H \Gamma_i (p_i^{(m)} - p_i^{(a)}) \quad (15)$$

where γ_i are weighted coefficients for least square approximation of ratio $\zeta_i^{(\cdot)}$. The term $(\zeta_i^{(m)} - \zeta_i^{(a)})^2$ is a good monitor of non-proportionality.

With the complex-damping ratios available and the systems considered being lightly damped, The correct correspondence can be solved from Equation (13).

A second approach to deal with correct correspondence is to avoid using the modal parameters mode by mode. Instead we can use a more general convergence pattern so that the correct correspondence is assured through the convergence. In this regard we have a choice of either using the state matrix or using the eigen-matrix. Because the size of the state matrix is $2n \times 2n$, (supposing the order of the system is n), we consider the eigen-

matrix whose size is only $n \times n$.

An eigen-matrix \mathbf{A} is defined by

$$\mathbf{A} = \mathbf{P} \mathbf{\Lambda} \mathbf{P}^{-1} \quad (16)$$

where $\mathbf{\Lambda}$ is a diagonal matrix consists of all eigenvalues λ_i , $i = 1, \dots, n$, of the system, and

$$\lambda_i = -\xi_i \omega_i \pm j(1-\xi_i)^{1/2} \omega_i \quad (17)$$

A matrix \mathbf{A} has the eigen-decomposition (16), if and

only if \mathbf{A} satisfies the following quadratic matrix equation:

$$\mathbf{M} \mathbf{A}^2 + \mathbf{C} \mathbf{A} + \mathbf{K} = \mathbf{0} \quad (18)$$

where the coefficient matrices \mathbf{M} , \mathbf{C} and \mathbf{K} are defined as in Equation (8). From Equation (16), we can see intuitively, that convergence of an eigen-matrix \mathbf{A} involves global adjustments of all modal parameters. Therefore, the problem of correspondence will not occur here. The cost function can be established by

$$J = \|\mathbf{A}^{(m)} - \mathbf{A}^{(a)}\| \quad (19)$$

where $\|\cdot\|$ stands for a norm of matrix $\mathbf{A}^{(m)} - \mathbf{A}^{(a)}$. For example, it can be the Frobenius norm,

$$J = \|\mathbf{A}^{(m)} - \mathbf{A}^{(a)}\|_F = \left\{ \sum_{i=1}^n \sum_{j=1}^n |a_{ij}^{(m)} - a_{ij}^{(a)}|^2 \right\}^{1/2} \quad (20)$$

where $a_{ij}^{(\cdot)}$ is the ij^{th} entry of matrix $\mathbf{A}^{(\cdot)}$. Or it can be a p-norm, such as the 2-norm,

$$J = \|\mathbf{A}^{(m)} - \mathbf{A}^{(a)}\|_2 = \left\{ \lambda_{\max} [(\mathbf{A}^{(m)} - \mathbf{A}^{(a)})^H (\mathbf{A}^{(m)} - \mathbf{A}^{(a)})] \right\}^{1/2} \quad (21)$$

where $\lambda_{\max}[\cdot]$ is the maximum eigenvalue of matrix $[\cdot]$.

CONCLUDING REMARKS

In this paper, we first examined several model correction procedures and their common weaknesses. Most available methods emphasize the speed of numerical convergence. In this study we pay attention to the validity of the corrections. We suggested methods to improve some of correction procedures by using the correct correspondence between the modes of physical and analytical models. This study results in the improvement of finite element modeling. It is also shown that a strong connection exist between the theoretical studies such as the complex damping theory and the various practical applications.

ACKNOWLEDGEMENT

Funding for the research reported in this paper has been provided jointly by the State University of New York at Buffalo and the National Science Foundation through the National Center for Earthquake Engineering Research under master contract number ECF86-07591.

REFERENCES

- Caughey, T.K. and O'Kelly, M.M.J. "Classical Normal Mode in Damped Linear Dynamic Systems" J. of Appl. Mech. ASME Vol 32, pp.583-588, 1965.
- Clough, R. W. and Penzien, J. " Dynamics of Structures," McGraw-Hill, New York, 1975.
- Ewins, D.J "Modal Testing, Theory and Practice" Research Studies Press LTD. England (1986).
- Inman, D. "Vibration with Control, Measurement and Stability", Prentice-Hall, Englewood Cliffs, 1989.
- Kozin, F. and Natke, H.G. (1986). "System Identification Techniques", Structural Safety, vol.2, pp.269-316.
- Liang, Z and Inman, D.J, "Rank Decomposition Methods in Modal Analysis" Proc. of IMAC-6, 1988, pp.1176-1179.
- Liang, Z. and Lee, G.C. "On Complex Damping of MDOF Systems" Proc. of IMAC-8, 1990, pp.1048-1055.
- Liang, Z. and Lee, G.C. "On Damping of Structures", NCEER Technical report, to be published.
- Liang, Z. Lee, G. C. and Tong, M. "On a Theory of Complex Damping", Proc. of Damping '91, Feb. 13-15 1991, San Diego, CA., Sponsored by Wright Laboratory, Flight Dynamics Directorate, Wright-Patterson Air Force Base.
- Liang, Z. Lee, G. C. and Tong, M. "A Strong Criterion for Testing Proportionally Damped Systems", Proc. of Damping '91, Feb. 13-15 1991, San Diego, CA., Sponsored by Wright Laboratory, Flight Dynamics Directorate, Wright-Patterson Air Force Base.
- Liang, Z. Lee, G. C. and Tong, M. "On a Linear Property of Lightly Damped Systems", Proc. of Damping '91, Feb. 13-15 1991, San Diego, CA., Sponsored by Wright Laboratory, Flight Dynamics Directorate, Wright-Patterson Air Force Base.

Liang, Z., Tong, M. and Lee, G. C. "Complex Modes in Linear Dynamic Systems"
Submitted to Inter. J. of Analytical and Experimental Modal Analysis.

Tong, M., Liang, Z. and G. C. Lee "On Correction Criteria of Finite
Element Modeling in Structural Dynamics", (to be submitted) Journal of
Applied Mechanics.

Natke, H. G. "Updating Computational Models in the Frequency Domain Based
on Measured Data: A Survey", Probabilistic Engineering Mech. Vol. 3, No.1
1988.

Shinozuka, M., Yun, C-B. and Imai, H. (1982). " Identification of Linear
Structural Dynamic Systems", J. of Structural Engineering, ASCE, Vol. 108,
No. EM6, pp.1371-1390.

Tong, M., Liang, Z. and Lee, G. C. "Techniques in Design and Using VE
Dampers", Proc. of Damping '91, Feb. 13-15 1991, San Diego, CA., Sponsored
by Wright Laboratory, Flight Dynamics Directorate, Wright-Patterson Air
Force Base.

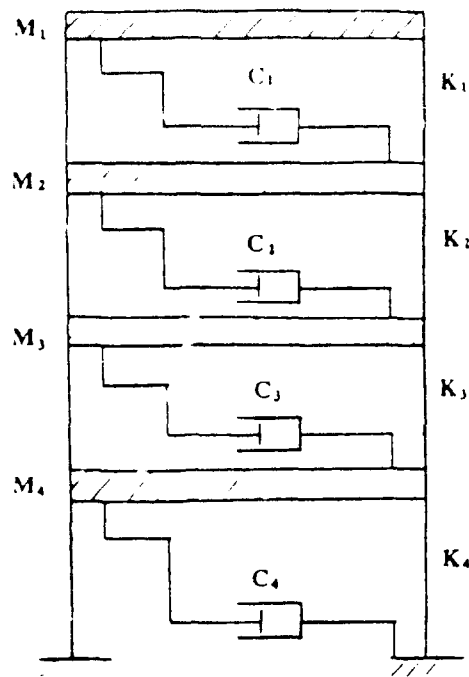


Figure 2 (a) 4 Degree-of-Freedom Structure

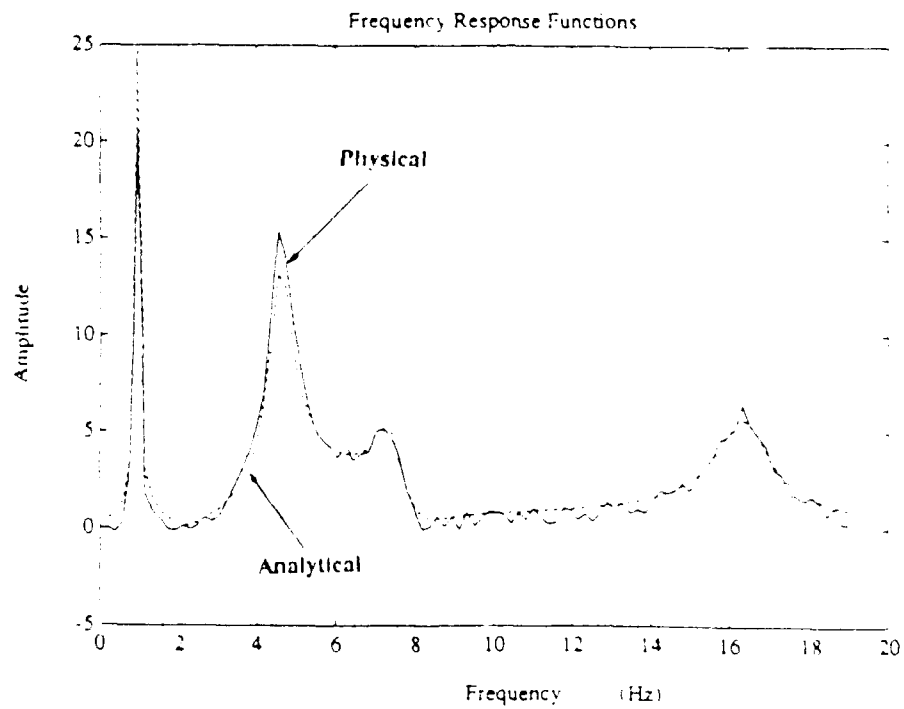


Figure 2 (b) FRF Curves

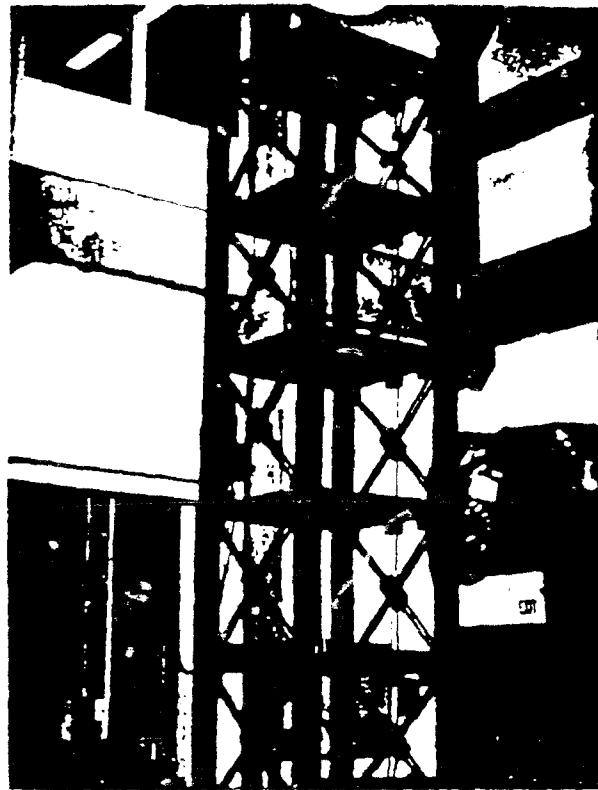


Figure 1(a) Five Floor Structure

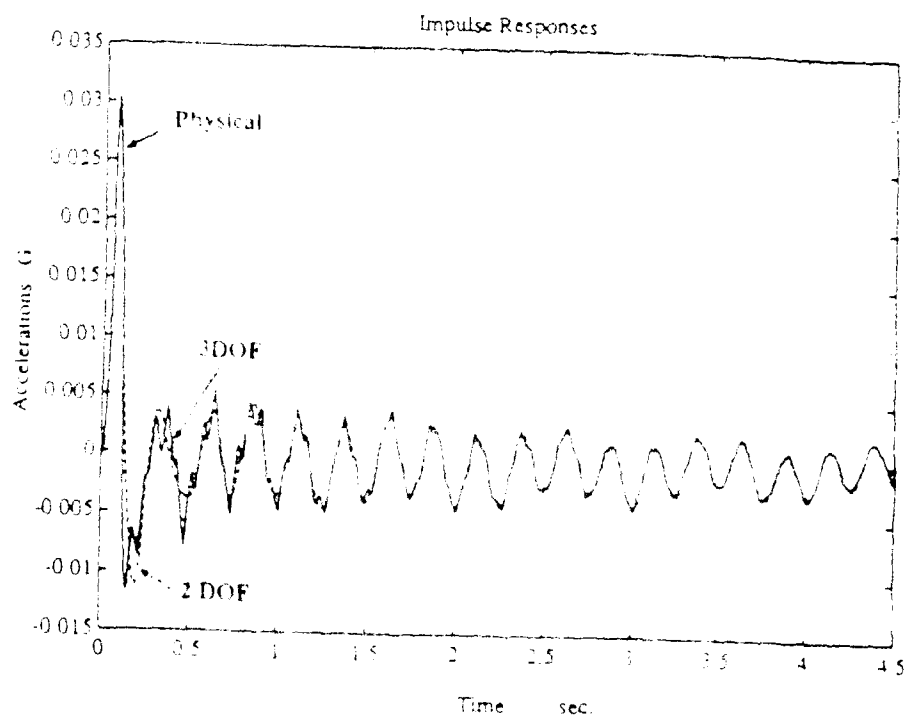
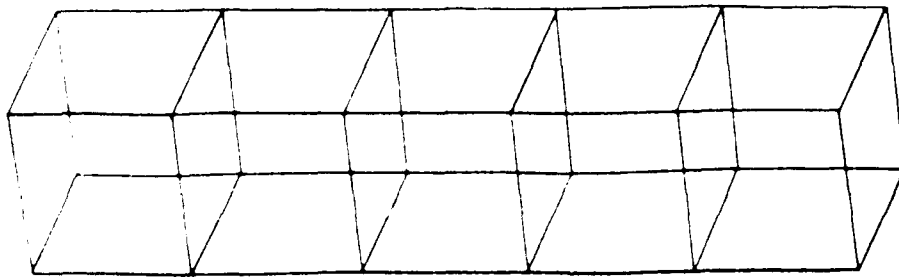
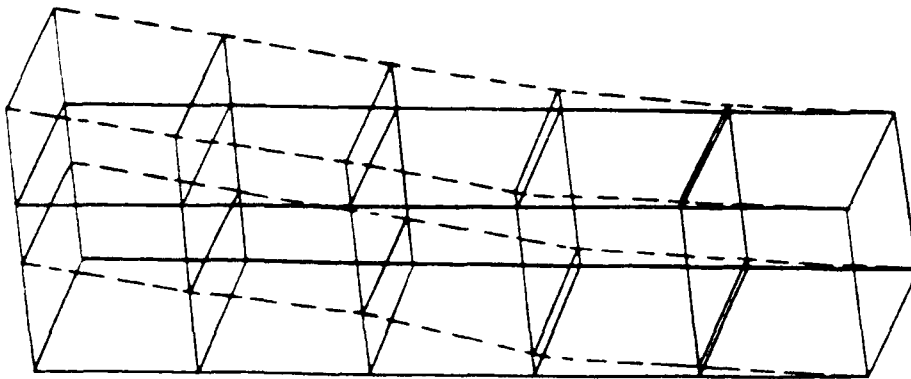


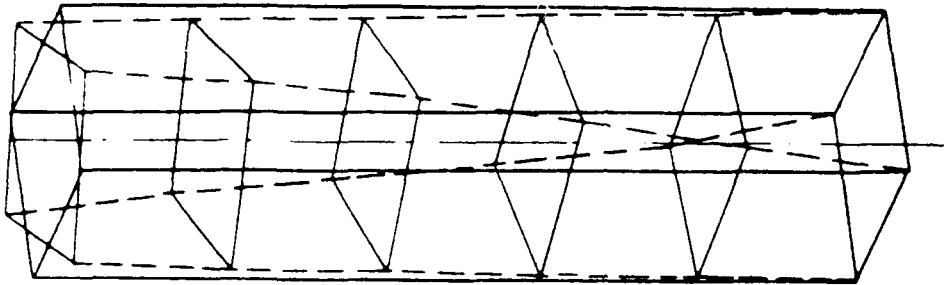
Figure 1 (b) Three Responses
DCC-18



Original Structure (a)



Translational Mode Shape (b)



Torsional Mode Shape (c)

Figure 3 Structure and Mode Shapes